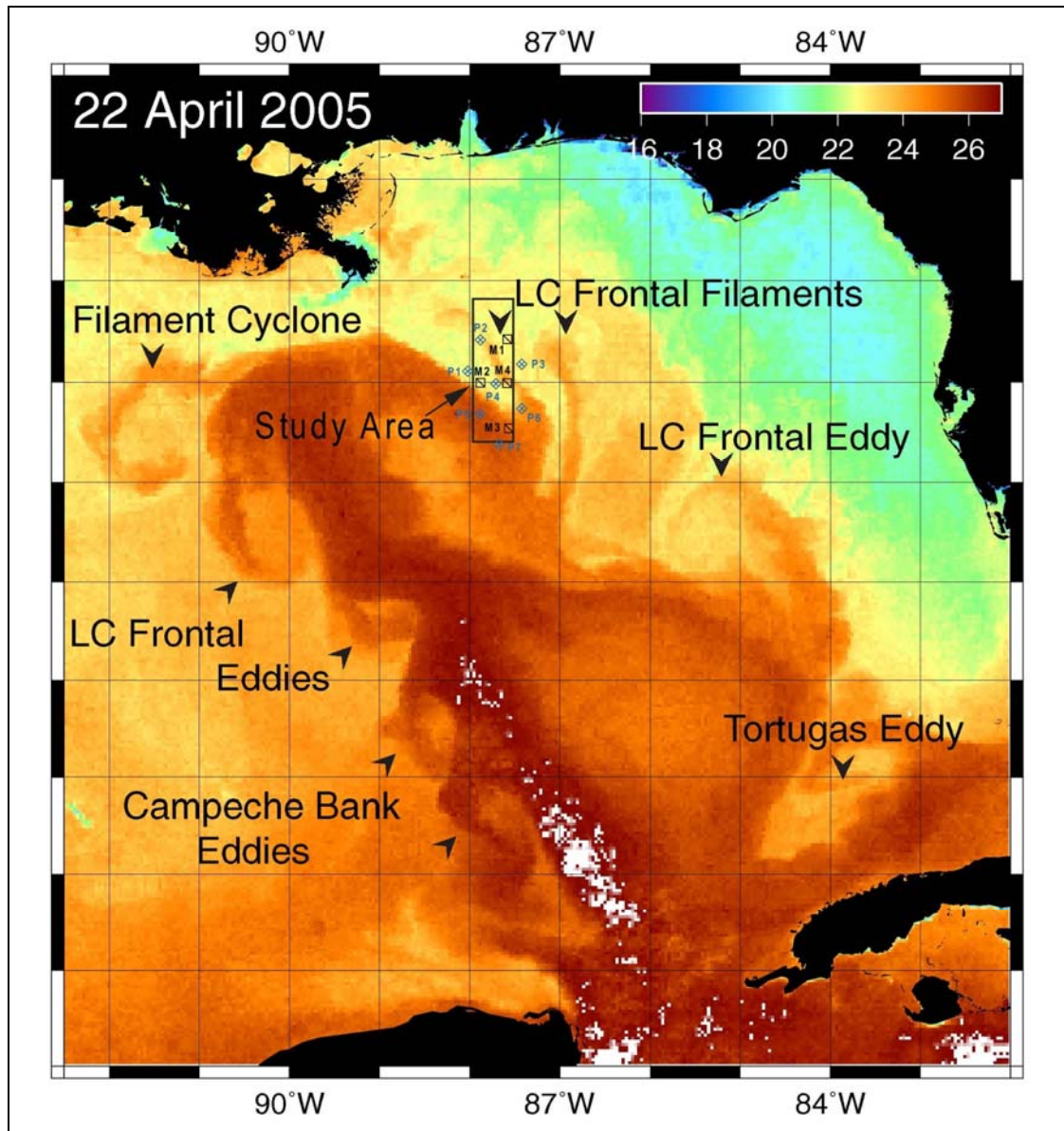




Study of Deepwater Currents in the Eastern Gulf of Mexico



Study of Deepwater Currents in the Eastern Gulf of Mexico

Authors

Jeff Cox
Carol Coomes
S. DiMarco
Kathleen Donohue
George Forristall
Peter Hamilton
Robert Leben
D.R. Watts

Prepared under BOEMRE Contract
M04PC00008 (1435-01-04-CT-34239)
by
Evans-Hamilton, Inc.
4608 Union Bay Place
Seattle, WA 98105

Published by

U.S. Department of the Interior
Bureau of Ocean Energy Management,
Regulation and Enforcement
Gulf of Mexico OCS Region

**New Orleans
December 2010**

DISCLAIMER

This report was prepared under contract between the Bureau of Ocean Energy Management, Regulation and Enforcement (BOEMRE) and Evans-Hamilton, Inc. (EHI). This report is undergoing review by the BOEMRE, and it has been approved for publication. Approval does not signify that the contents necessarily reflect the views and policies of the BOEMRE, nor does mention of trade names or commercial products constitute endorsement or recommendation for use. It is, however, exempt from review and compliance with the BOEMRE editorial standards.

REPORT AVAILABILITY

This report is available only in compact disc format from the Bureau of Ocean Energy Management, Regulation, and Enforcement, Gulf of Mexico OCS Region, at a charge of \$15.00, by referencing OCS Study BOEMRE 2010-041. The report may be downloaded from the BOEMRE website through the [Environmental Studies Program Information System \(ESPIS\)](#). You will be able to obtain this report also from the National Technical Information Service in the near future. Here are the addresses. You may also inspect copies at selected Federal Depository Libraries.

U.S. Department of the Interior
Bureau of Ocean Energy Management,
Regulation, and Enforcement
Gulf of Mexico OCS Region
Public Information Office (MS 5034)
1201 Elmwood Park Boulevard
New Orleans, Louisiana 70123-2394
Telephone requests may be placed at
(504) 736-2519, 1-800-200-GULF, or
Rush Orders: 1-800-553-6847
Fax: (504) 736-2620

U.S. Department of Commerce
National Technical Information Service
5285 Port Royal Road
Springfield, Virginia 22161
Phone: (703) 605-6040
Fax: (703) 605-6900
Email: bookstore@ntis.gov

CITATION

Cox, J., C. Coomes, S. DiMarco, K. Donohue, G.Z. Forristall, P. Hamilton, R.R. Leben, and D.R. Watts. 2010. Study of deepwater currents in the Eastern Gulf of Mexico. U.S. Dept. of the Interior, Bureau of Ocean Energy Management, Regulation, and Enforcement, Gulf of Mexico OCS Region, New Orleans, LA. OCS Study BOEMRE 2010-041. 473 pp.

ABOUT THE COVER

The cover shows the location of the study area (rectangle) within the eastern Gulf of Mexico, and the locations of the four current measurement moorings (M1-M4) plus the locations of the seven PIES measurement moorings (P1-P7) overlaid on a sea surface temperature image of 22 April 2005. On that date, warm (red) loop current waters extended well north into the Gulf of Mexico, and contained several frontal eddies, cyclones, and filaments around its periphery. Both a portion of the Loop Current, and filaments from it, can be seen impacting a portion of the study area.

ACKNOWLEDGEMENT

Many outstanding individuals contributed to the overall success of this program. While there are too many to identify all of them individually, the following deserve special recognition. Mr. Keith Kurrus and Mr. Kevin Redman of EHI planned and very successfully led the field operations. PIES field operations were ably performed by Mr. G. Chaplin from URI. Thanks also to the captains and crew of the R/V Pelican from which the field operations were conducted.

Data reduction, QA/QC, final edited data files, and initial graphical displays of mooring, hydrographic, and ancillary data were conducted by Mrs. Kari Walker and her team at EHI. Mr. Paul Blankinship at SAIC, and Dr. Matt Howard and Ms. Kelly Cole at Texas A&M University provided extensive analysis assistance to the PIs in their organizations.

Compilation, blending, and editing of all the PI inputs to the report, and adapting the inputs to the BOEMRE report format, was ably conducted by Mrs. Rachel Halfhill of EHI.

Lastly, the support, encouragement, and patience of Dr. Alexis Lugo-Fernandez, the BOMRE COTR, was critical to the project's success.

TABLE OF CONTENTS

	Page
LIST OF FIGURES	XI
LIST OF TABLES	XXXI
EXECUTIVE SUMMARY	XXXV
1.0 INTRODUCTION AND OBJECTIVES.....	1-1
1.1 Background.....	1-1
1.2 Study Area	1-3
1.3 Study Approach	1-5
1.4 Study Objectives.....	1-6
1.5 Study Team.....	1-7
1.6 Report Organization.....	1-8
2.0 EXPERIMENT DESIGN AND METHODOLOGY	2-1
2.1 Moorings.....	2-1
2.1.1 Instrumentation	2-1
2.1.2 Instrumentation and Moorings Preparation	2-1
2.1.3 Moorings Deployment, Servicing, and Recovery.....	2-5
2.1.4 Processing and QA/QC of Mooring Measurements	2-8
2.1.5 Mooring Data Coverage.....	2-12
2.1.6 Mooring Data Graphical Products and Analyses.....	2-12
2.2 Hydrography	2-20
2.2.1 Survey Pattern and Instrumentation.....	2-21
2.2.2 Hydrography Data Processing and QAQC	2-26
2.2.3 CTD vs XBT Data	2-30
2.2.4 Comparison to Historical Data.....	2-31
2.3 PIES	2-33
2.3.1 Gravest Empirical Mode Method.....	2-34
2.3.1.1 Determine τ Index.....	2-34
2.3.1.2 Assemble Regional Hydrographic Data Set	2-34
2.3.1.3 Sort Hydrographic Data by τ Index	2-39
2.3.1.4 Seasonal Correction	2-39
2.3.2 Conversion of Measured τ to $\tau(150-1000)$	2-39
2.3.3 Upper-Ocean Maps.....	2-50
2.3.4 Bottom Pressure.....	2-50
2.3.5 Reference-Level Maps.....	2-52
2.3.6 Total Maps	2-54
2.3.7 Mooring Comparisons	2-55
2.4 Remote Sensing	2-57
2.4.1 Altimetry.....	2-60

2.4.1.1	Alongtrack Altimeter Data.....	2-62
2.4.1.2	Mesoscale Analysis.....	2-63
2.4.1.3	Mean Reference Surface and Model Mean SSH	2-63
2.4.1.4	Objective Mapping.....	2-64
2.4.1.5	Objective Analysis Procedure.....	2-64
2.4.2	Ocean Color Imagery	2-66
2.4.3	SST Imagery	2-67
2.5	PIES/Altimeter Comparison	2-67
2.5.1	Altimetric Sampling and Aliasing	2-67
2.5.2	Signal-to-Noise	2-75
2.5.3	Sea Surface Height Time Scales.....	2-78
2.5.4	Comparison of CCAR Mesoscale and PIES SSH.....	2-80
2.6	Ancillary Data.....	2-83
2.6.1	River Discharge	2-84
2.6.2	Coastal and Offshore Winds	2-84
2.6.3	Coastal Water Levels	2-84
2.6.4	Hurricanes and Tropical Storms	2-84
2.6.5	Horizon Marine Eddy Watch and Drifting Buoys	2-90
3.0	LOOP CURRENT EVENTS AND HISTORICAL PERSPECTIVE	3-1
3.1	Loop Current and Loop Current Eddies.....	3-1
3.1.1	LC and LCEs During the Study Period.....	3-1
3.1.2	Loop Current Metrics and Statistics	3-9
3.1.3	Loop Current Eddy Metrics and Statistics.....	3-12
3.1.4	Loop Current Frontal Eddies and Other Cyclonic Eddies	3-20
3.2	Study Time Period in the Context of the Historical Record	3-22
3.2.1	Loop Current.....	3-22
3.2.2	Loop Current Eddies.....	3-23
4.0	LC AND LCE DYNAMICS	4-1
4.1	Kinematic Analysis.....	4-1
4.1.1	Drifting Buoy Data and Analysis Approach.....	4-1
4.1.2	Eddy Vortex	4-2
4.1.3	Cyclones.....	4-2
4.1.4	Combined Kinematic and Altimetric Analysis.....	4-3
4.2	Dynamic Analysis.....	4-8
4.2.1	Mapped Surface Circulation and Sea Surface Height from PIES.....	4-8
4.2.2	Relative Vorticity Calculated from the PIES.....	4-16
4.2.3	Anticyclonic and Cyclonic Events in PIES Relative Vorticity Time Series.....	4-19
5.0	MOORING AND HYDROGRAPHY RESULTS	5-1
5.1	Mooring Measurements	5-1
5.1.1	Velocity Time-Series	5-1

5.1.2	Current Roses, Joint Probability Distributions of Speed by Direction	5-6
5.1.3	Current Speed Persistence Tables	5-6
5.1.4	Velocity Spectra	5-7
5.1.4.1	Upper Ocean Spectra	5-7
5.1.4.2	Deep Ocean Spectra	5-11
5.1.5	Coherency Spectra	5-11
5.1.5.1	Current – Wind Coherence	5-11
5.1.5.2	Vertical Current – Current Coherence	5-12
5.1.5.3	Horizontal Current – Current Coherency Spectra	5-16
5.1.6	Mean, Minimum and Maximum Currents	5-17
5.1.7	Extreme Current Value Distributions	5-20
5.1.8	Responses to Hurricanes	5-26
5.1.8.1	Inertial Oscillations	5-26
5.1.8.2	Wavelet Analysis of the Inertial Oscillations	5-42
5.1.8.3	1-D Turbulence Closure Model	5-47
5.2	Hydrography Measurements	5-52
6.0	DEEP CIRCULATION	6-1
6.1	Overview of Observations of Topographic Rossby Waves in the Deep Gulf	6-1
6.1.1	Background	6-1
6.1.2	Data	6-4
6.1.2.1	Moorings	6-4
6.1.2.2	RAFOS Floats	6-4
6.1.3	Gulf-Wide Overview of Deep Currents	6-6
6.2	Basic Statistics from Moorings	6-18
6.2.1	Event Analysis	6-19
6.3	Topographic Rossby Waves North of the Loop Current	6-24
6.3.1	Wavelet Analysis	6-38
7.0	VERTICAL COUPLING	7-1
7.1	CEOFs	7-1
7.1.1	Potential Vorticity	7-4
7.2	Dynamic Modes	7-8
7.2.1	Vertical Structure of Low-Frequency Variability	7-8
7.2.1.1	Empirical Orthogonal Function (EOF) Analysis	7-8
7.2.1.2	Dynamical Mode Analysis	7-18
7.2.1.3	Model Utility Test for Dynamic Modes	7-32
7.2.1.3.1	Temporal Correlation of First Baroclinic Mode and Sea Surface Height Gradient	7-32
7.2.1.3.2	Spectra and Temporal Scales of Modes	7-45
7.3	Upper/Lower-Layer Coupling Analysis Using PIES Data	7-45
8.0	SUMMARY AND CONCLUSIONS	8-1
8.1	Summary of the Results	8-1

8.2	Conclusions.....	8-3
8.3	Recommendations.....	8-4
9.0	LITERATURE CITED	9-1
	APPENDIX A Hurricanes and Tropical Storm Events	A-1
	APPENDIX B Color Vector Plots of Current Magnitude and Direction.....	B-1
	APPENDIX C Basic Statistics for Current Measurements	C-1
	APPENDIX D Barotropic Tides.....	D-1
	APPENDIX E Elliptical Fit Parameters.....	E-1
	APPENDIX F Ocean Response to Hurricane Katrina in Presence of a Cyclone.	F-1

LIST OF FIGURES

	Page
Figure 1.1-1. Locations of the BOEMRE Gulf of Mexico regions and other major features of the Gulf of Mexico.....	1-2
Figure 1.2-1. Map of the study area (outlined in red) including locations of moorings M1, M2, M3 and M4 in black, and PIES in purple.	1-4
Figure 2.1-1. Design of the tall (M1, M2, and M3) and short (M4) moorings.....	2-2
Figure 2.1-2. Example current rose diagram: Mooring M1, deployment 1.....	2-18
Figure 2.1-3. Example persistence table: Mooring M1, deployment 1.	2-19
Figure 2.1-4. Kinetic energy spectra of unfiltered (blue) and detided (red) versions of ADCP data during deployment 1 at mooring 1.	2-19
Figure 2.2-1. Grid pattern proposed for hydrography cruises.	2-23
Figure 2.2-2. Grid pattern of Hydrography Cruise 1.....	2-24
Figure 2.2-3. Grid pattern of Hydrography Cruise 2.....	2-25
Figure 2.2-4. Pinwheel station grid for intensive Hydrography Cruise 3.....	2-27
Figure 2.2-5. Station pattern for Hydrography Cruise 3.....	2-28
Figure 2.2-6. CTD vs. XBT profile information for Hydrographic Cruise 3 January 2006.....	2-31
Figure 2.2-7. Profiles from all three hydrographic cruises plotted as potential temperature vs salinity superimposed on the historical data boundaries.....	2-32
Figure 2.3-1. Time series of τ (tau) anomaly in seconds plotted according to approximate geographic location.....	2-35
Figure 2.3-2. Time series of bottom pressure anomaly in dbar plotted according to approximate geographic location.....	2-36
Figure 2.3-3. Two views of the temperature structure in the region for August 5, 2005 provided by the PIES.	2-37
Figure 2.3-4. Several views of the current structure in the region for August 5, 2005 provided by the PIES and current meter measurements.	2-38
Figure 2.3-5. Spatial and temporal distribution of hydrocasts used to construct the Gravest Empirical Mode.....	2-41

Figure 2.3-6. Temperature profiles interpolated every 10 dbar and sorted by $\tau(150-1000)$.	2-42
Figure 2.3-7. Scatter plots of temperature versus $\tau(150-1000)$ for six representative pressure levels.	2-43
Figure 2.3-8. Contour plot of the cubic smoothing spline fits for the temperature GEM field.	2-44
Figure 2.3-9. The GEM-determined temperature and salinity profiles agree well with measured profiles.	2-45
Figure 2.3-10. Upper panels: Scatter plots of temperature versus $\tau(150-1000)$ for surface (left), 50 dbar (middle) and 100 dbar (right) with the cubic spline fit shown as a solid dark line.	2-46
Figure 2.3-11. Seasonal temperature correction/amplitude contoured as function of year/day and pressure.	2-47
Figure 2.3-12. $\tau(150-1000)$ for each time series.	2-48
Figure 2.3-13. Upper panel: Scatter plots of $\tau(0-150)$ versus $\tau(150-1000)$.	2-49
Figure 2.3-14. Correlation coefficient between pairs of τ records longer than one year.	2-51
Figure 2.3-15. Top Panel: Common mode subtracted from bottom pressure records before mapping deepwater dynamical properties.	2-53
Figure 2.3-16. Time series of bottom pressure anomaly with the common mode removed in dbar plotted according to approximate geographic location.	2-54
Figure 2.3-17. Correlation coefficient between pairs of pressure records.	2-55
Figure 2.3-18. Comparison between the moorings (red) and PIES-derived (blue) temperatures near 400 m depth.	2-58
Figure 2.3-19. Comparison between the M2 mooring (red) and PIES-derived (blue) zonal (top) and meridional (middle) velocities at 415 m depth.	2-59
Figure 2.4-1. Satellite altimeter groundtrack coverage in study region.	2-61
Figure 2.5-1. Maps of PIES barotropic unaliased variance for 10-day, 17-day, and 35-day sampling.	2-71
Figure 2.5-2. Maps of PIES baroclinic unaliased variance for 10-day, 17-day, and 35-day sampling.	2-72

Figure 2.5-3. Maps of PIES SSH unaliased variance for 10-day, 17-day, and 35-day sampling.....	2-73
Figure 2.5-4. Maps of PIES SSH signal-to-noise ratio (SNR) for 10-day, 17-day, and 35-day sampling.....	2-77
Figure 2.5-5. Spatial maps of the half-power period, T, computed from the PIES barotropic, baroclinic, and combined SSH anomaly time series.	2-79
Figure 2.5-6. Spatial map of the CCAR/PIES SSH temporal correlation.	2-81
Figure 2.5-7. Scatterplot and correlation values of PIES time series points located on altimeter groundtracks with the coincident points from the along-track detrended altimeter data.	2-82
Figure 2.6-1. River discharge in $m^3 s^{-1}$ during the first deployment (Rivers 1-7). Note Mississippi River is at larger scale.....	2-85
Figure 2.6-2. River discharge in $m^3 s^{-1}$ during the first deployment (Rivers 8-15).	2-85
Figure 2.6-3. River discharge in $m^3 s^{-1}$ during the second deployment (Rivers 1-7). Note Mississippi River is at larger scale.	2-86
Figure 2.6-4. River discharge in $m^3 s^{-1}$ during the second deployment (Rivers 8-15).	2-86
Figure 2.6-5. Vector plots of wind speed (mph) and direction (degrees from) for the first deployment (Winds 1-5).	2-87
Figure 2.6-6. Vector plots of wind speed (mph) and direction (degrees from) for the first deployment (Winds 6-10).	2-87
Figure 2.6-7. Vector plots of wind speed (mph) and direction (degrees from) for the second deployment (Winds 1-5).	2-88
Figure 2.6-8. Vector plots of wind speed (mph) and direction (degrees from) for the second deployment (Winds 6-10).	2-88
Figure 2.6-9. Predicted and measured tide height (m) from gauges located on the coast from Louisiana to Florida for deployment 1.....	2-89
Figure 2.6-10. Predicted and measured tide height (m) from gauges located on the coast from Louisiana to Florida for deployment 2.	2-89
Figure 2.6-11. Timing and paths of all six storm events that passed near the study area during the study period.	2-91
Figure 3.1-1. Eight-day composite image of chlorophyll concentration overlaid with the SSH contour map from 15 September 2005 showing the recent separation of LCE Vortex from the LC.....	3-3

Figure 3.1-2. Three-day composite SST images overlaid with SSH contour maps showing the detachment of LCE Vortex from the LC in late February 2005.....	3-4
Figure 3.1-3. Three-day composite SST images overlaid with SSH contour maps showing the reattachment of LCE Vortex to the LC in early April 2005.....	3-5
Figure 3.1-4. Three-day composite SST images overlaid with SSH contours showing LCE Vortex detachment (upper panels) and reattachment (lower panels) for events #1 and #2.....	3-7
Figure 3.1-5. Eight-day composite chlorophyll concentration images overlaid with SSH contours showing LCE Vortex detachment (upper panels) and reattachment (lower panels) for events #3 and #4.....	3-8
Figure 3.1-6. SST and chlorophyll concentration images overlaid with SSH showing the four LCE detachment events identified in the altimeter record.....	3-10
Figure 3.1-7. Loop Current maximum northern/western extension and length time series with percent occurrence histograms.....	3-13
Figure 3.1-8. Loop Current area, volume, and circulation time series with percent occurrence histograms.....	3-14
Figure 3.1-9. Loop Current maximum northern/western extensions and length time series with percent occurrence histograms during the EGOM study.....	3-15
Figure 3.1-10. Loop Current area, volume, and circulation time series with percent occurrence histograms during the EGOM study.....	3-16
Figure 3.1-11. Histograms of Loop Current metrics during the EGOM study (red bars) versus the historical time period (blue bars).....	3-17
Figure 3.1-12. LCE separation events identified in the altimeter record.....	3-19
Figure 3.1-13. Nighttime composite SST image from 22 April 2005 showing the LC and its associated cyclonic features.....	3-21
Figure 3.2-1. Histograms of yearlong running averages of Loop Current metrics from the historical altimetry record.....	3-24
Figure 3.2-2. Histogram of the LCE separation period using data from Table 3.2-2 are shown for selected time intervals.....	3-27
Figure 3.2-3a. Zoomed SSH maps of LCEs 1 through 8 at the time of separation from the LC.....	3-28

Figure 3.2-3b. Zoomed SSH maps of LCEs 9 through 16 at the time of separation from the LC.....	3-29
Figure 3.2-3c. Zoomed SSH maps of LCEs 17 through 20 at the time of separation from the LC.....	3-30
Figure 3.2-4. The 17-cm tracking contour at the time of separation for all 20 LCEs observed from 1 January 1993 through 30 June 2006.	3-31
Figure 3.2-5. Composite of LCE Vortex detachment and reattachment events.	3-32
Figure 4.1-1. Ocean color images overlaid with SSH at 3-day intervals from July 9-18, 2005.....	4-4
Figure 4.1-2. Ocean color images overlaid with SSH at 3-day intervals from July 21-30, 2005.....	4-5
Figure 4.1-3. Ocean color images overlaid with SSH at 3-day intervals from August 2-11, 2005.....	4-6
Figure 4.1-4. Ocean color images overlaid with SSH at 3-day intervals from August 14-23, 2005.....	4-7
Figure 4.2-1. Top Panel: Time-average mean sea surface height (contours) and currents (black vectors) at the surface.	4-10
Figure 4.2-2. Upper panel: Mean surface eddy kinetic energy averaged between 27 January to 19 January 2006 contoured every $200 \text{ cm}^2 \text{ s}^{-2}$	4-11
Figure 4.2-3. 16 February 2005 to 28 February 2005.....	4-12
Figure 4.2-4. 19 May 2005 to 31 May 2005.....	4-13
Figure 4.2-5. 15 June 2005 to 27 June 2005.....	4-14
Figure 4.2-6. 12 December 2005 to 24 December 2005.....	4-15
Figure 4.2-7. Diagrams #1 and #2 show schematics used to compute relative vorticity from the Eastern Gulf PIES stations.	4-18
Figure 4.2-8. Altimeter-derived SSH overlaid on 8-day composite chlorophyll-concentration image from 16 Feb 2005.	4-20
Figure 4.2-9. Altimeter-derived SSH overlaid on 8-day composite chlorophyll-concentration image for 15 June 2005.....	4-21
Figure 4.2-10. Altimeter-derived SSH overlaid on 8-day composite chlorophyll-concentration images for selected dates before Eddy Vortex separation.	4-22

Figure 4.2-11. Altimeter-derived SSH overlaid on 8-day composite chlorophyll-concentration images for selected dates after Eddy Vortex separation.	4-23
Figure 5.1-1. Color contour of speed (top) and direction (bottom) for M1 during deployment 1 showing the effects of mooring draw down due to high currents.....	5-2
Figure 5.1-2. Color contour of temperature for M3 during deployment 1.	5-3
Figure 5.1-3. Color contour of speed (top) and direction (bottom) for M3 during deployment 2 showing inertial oscillations on the mooring due to hurricanes.....	5-4
Figure 5.1-4a. Gap-filled, gridded current speed from five moored ADCP depths and moored current meters M1 for deployments 1 (left) and 2 (right).....	5-5
Figure 5.1-4b. Gap-filled, gridded current speed from five moored ADCP depths and moored current meters M2 for deployments 1 (left) and 2 (right).....	5-5
Figure 5.1-4c. Gap-filled, gridded current speed from five moored ADCP depths and moored current meters M3 for deployments 1 (left) and 2 (right).....	5-6
Figure 5.1-5. Panels A and B give power spectral density of detided, gap-filled u and v velocity components, respectively, at 6 depths at mooring M1 from deployment 1.....	5-8
Figure 5.1-6. Panels A and B give power spectral density of detided, gap-filled u and v velocity components, respectively, at 6 depths at mooring M2 from deployment 1.....	5-9
Figure 5.1-7. Panels A and B give power spectral density of detided, gap-filled u and v velocity components, respectively, at 6 depths at mooring M3 from deployment 1.....	5-10
Figure 5.1-8. Detided, gap-filled, gridded u velocity time-series at mooring 1 during deployment 1 at 100 m and 428 m.....	5-13
Figure 5.1-9. (Clockwise from top left) Coherence, admittance, power, and phase spectra between u velocity components at 100 m and 428 m at mooring 1 during deployment 1.	5-14
Figure 5.1-10. (Clockwise from top left) Coherence, admittance, power, and phase spectra of north-south (v) velocity components at 70 m and 494 m at mooring M2 during deployment 2.	5-15
Figure 5.1-11. (Clockwise from top left) Coherence, admittance, power, and phase spectra between v velocity components at 749 m at mooring M1 and mooring M2 during deployment 1.	5-17

Figure 5.1-12. Detided, gap-filled, gridded east-west velocity time-series at mooring M2 and mooring M3 during deployment 1 at 1995 m and 2699 m respectively.	5-18
Figure 5.1-13. (Clockwise from top left) Coherence, admittance, power, and phase spectra between u velocity components at mooring 2 and mooring 3 during deployment 1 at 1995 m and 2699 m respectively.	5-19
Figure 5.1-14. Vertical profiles of record-length mean, standard deviation, minimum, and maximum velocity components for mooring M1 (left: east-west component; right: north-south component).	5-21
Figure 5.1-15. Vertical profiles of record-length mean, standard deviation, minimum, and maximum velocity components for mooring M2 (left: east-west component; right: north-south component).	5-22
Figure 5.1-16. Vertical profiles of record-length mean, standard deviation, minimum, and maximum velocity components for mooring M3 (left: east-west component; right: north-south component).	5-23
Figure 5.1-17. Extreme value fits for current speeds at Mooring 1, Depths 749 – 1492 m.	5-27
Figure 5.1-18. Extreme value fits for current speeds at Mooring 1, depth 2499 m and Mooring 2, depths 749 – 1244 m.	5-28
Figure 5.1-19. Extreme value fits for current speeds at Mooring 2, depths 1492 – 1995 m and Mooring 3, Depths 750 – 997 m.	5-29
Figure 5.1-20. Extreme value fits for current speeds at Mooring 3, depths 1245 – 2499 m.	5-30
Figure 5.1-21. Extreme value fits for current speeds at Mooring 3, depth 2699 m, and Mooring 4, depths 2530 – 2630 m.	5-31
Figure 5.1-22. Total current speed and diurnal bandpass current speed for the first deployment at mooring 1.	5-32
Figure 5.1-23. Total current speed and diurnal bandpass current speed for the first deployment at mooring 2.	5-32
Figure 5.1-24. Total current speed and diurnal bandpass current speed for the first deployment at mooring 3.	5-33
Figure 5.1-25. Total current speed and diurnal bandpass current speed for the second deployment at mooring 1.	5-33
Figure 5.1-26. Total current speed and diurnal bandpass current speed for the second deployment at mooring 2.	5-34

Figure 5.1-27. Total current speed and diurnal bandpass current speed for the second deployment at mooring 3.	5-34
Figure 5.1-28. Total current speed and diurnal bandpass current speed during Hurricane Katrina at mooring 1.	5-35
Figure 5.1-29. Total current speed and diurnal bandpass current speed during Hurricane Katrina at mooring 2.	5-36
Figure 5.1-30. Total current speed and diurnal bandpass current speed during Hurricane Katrina at mooring 3.	5-36
Figure 5.1-31. Total current speed and diurnal bandpass current speed during Hurricane Rita at mooring 1.	5-37
Figure 5.1-32. Total current speed and diurnal bandpass current speed during Hurricane Rita at mooring 2.	5-38
Figure 5.1-33. Total current speed and diurnal bandpass current speed during Hurricane Rita at mooring 3.	5-38
Figure 5.1-34. Scatter plot of band passed current speed vs. total current speed at 100 m depth.	5-39
Figure 5.1-35. Scatter plot of band passed current speed vs. total current speed at 200 m depth.	5-39
Figure 5.1-36. Scatter plot of band passed current speed vs. total current speed at 300 m depth.	5-40
Figure 5.1-37. Scatter plot of band passed current speed vs. total current speed at 400 m depth.	5-40
Figure 5.1-38. Ratio of band passed speed to total current speed.	5-41
Figure 5.1-39. (Top left) Wavelet power spectrum of the hourly east-west current time-series at ~ 80 m depth at mooring 3 during deployment 2.	5-43
Figure 5.1-40. Contours of the frequency-averaged wavelet power in the inertial band (0.5 – 2 day period) during the weeks after Hurricanes Katrina and Rita in the upper 500 m of the water column at moorings M1 (top), M2 (middle), and M3 (bottom).	5-44
Figure 5.1-41. Principal component time-series for the leading modes from the combined three-mooring, full water column vertical EOF analysis of the frequency-averaged wavelet power in the inertial band (0.5 – 2 day period) during deployment 2.	5-45

Figure 5.1-42. Amplitudes of leading modes for moorings M1 (left), M2 (center), M3 (right), for combined three-mooring full water-column vertical EOF analysis of the frequency-averaged wavelet power in the inertial band (0.5 – 2 day period) during deployment 2.....	5-46
Figure 5.1-43. Eddy Vortex just before Hurricane Katrina.....	5-48
Figure 5.1-44. Measurements at Mooring 3 compared to a one dimensional turbulence model. 5-49	
Figure 5.1-45. Diurnal bandpass currents at Mooring 3.....	5-50
Figure 5.1-46. Diurnal bandpass currents at Mooring 1.....	5-51
Figure 5.1-47. Lowpass current speed at Mooring 3 compared to the diurnal bandpass speed.	5-52
Figure 5.2-1. Color contour of the depth of the 20° isotherm during Hydrographic Cruise 1 in January 2005.....	5-53
Figure 5.2-2. Color contour of the depth of the 20° isotherm during Hydrographic Cruise 2 in August 2005.	5-54
Figure 5.2-3. Color contour of the depth of the 20° isotherm during Hydrographic Cruise 3 in January 2006.....	5-55
Figure 5.2-4. Hydrocruise 3 Transect 1 temperature from XBT and CTD casts.....	5-56
Figure 5.2-5. Hydrocruise 3 Transect 2 temperature from XBT and CTD casts.....	5-57
Figure 5.2-6. Hydrocruise 3 Transect 3 temperature from XBT and CTD casts.....	5-58
Figure 6.1-1. Locations of the principal full-depth moorings used in the analyses.....	6-3
Figure 6.1-2. Spaghetti plot of all 36 RAFOS float smoothed trajectories at all depths (1000 to 2500 m) in the Exploratory Study.	6-6
Figure 6.1-3. Depth-integrated EKE for the CEOF mode 1 lower-layer currents at the locations identified in Table 6.1-2 (thick vertical bars).....	6-11
Figure 6.1-4. CEOF mode 1 normalized amplitudes for lower-layer currents.	6-12
Figure 6.1-5. Spectra, in variance preserving form, for the normalized CEOF mode 1 amplitudes of the lower-layer currents.	6-13
Figure 6.1-6. a) Depth-integrated EKE as a function of frequency band.	6-14
Figure 6.1-7. Lower-layer mean currents from RAFOS floats (red) and lower-layer current meters (purple).....	6-16

Figure 6.2-1.	Mean (LH panel) and standard deviation ellipses (RH panel) for currents 100 to 500 m above bottom (red) and ~ 1200 m depth (blue) except for 42375 where the upper level is at 1560 m.	6-19
Figure 6.2-2.	Stick plots of the 40-HLP currents for the indicated moorings and depths.	6-21
Figure 6.2-3.	Tracks of the center low pressures of tropical storms and hurricanes that passed over the Gulf of Mexico in 2005.	6-22
Figure 6.2-4.	Upper panel: Mean lower-layer (2500 m) eddy kinetic energy averaged between 27 January to 19 January 2006 contoured every 20 cm ² s ⁻²	6-25
Figure 6.2-5a.	The LH panel shows the 3-day composite SST overlaid with CCAR altimeter-derived SSH for April 25, 2005.	6-26
Figure 6.2-5b.	The LH panel shows the 3-day composite SST overlaid with CCAR altimeter-derived SSH for May 22, 2005.	6-27
Figure 6.2-5c.	The LH panel shows the 3-day composite chlorophyll concentration overlaid with CCAR altimeter-derived SSH for August 1, 2005.	6-28
Figure 6.2-5d.	The LH panel shows the 3-day composite SST overlaid with CCAR altimeter-derived SSH for December 6, 2005.	6-29
Figure 6.2-5e.	The LH panel shows the 3-day composite SST overlaid with CCAR altimeter-derived SSH for December 26, 2005.	6-30
Figure 6.2-5f.	The LH panel shows the 3-day composite SST overlaid with CCAR altimeter-derived SSH for January 16, 2006.	6-31
Figure 6.2-6.	Snapshot of upper and lower layer circulation on May 23 (bottom panel) with surface geopotential referenced to 2500 m denoted by colored lines and bottom streamfunction indicated by filled colored contours.	6-32
Figure 6.2-7.	Upper layer 40-HLP currents, temperatures (solid contours) and salinities from mooring M3.	6-33
Figure 6.3-1.	Variance preserving kinetic energy spectra for selected lower-layer velocity observations at.	6-35
Figure 6.3-2.	Variance preserving kinetic energy spectra for near-bottom velocity observations on the indicated moorings.	6-36
Figure 6.3-3.	West of 89°W, the near-bottom (100 to 500 MAB) EKE is contoured for the 335-33 day EOF mode 1 velocities from the Exploratory Program.	6-39
Figure 6.3-4.	West of 89°W, the near-bottom (100 to 500 MAB) EKE is contoured for the 33-17 day EOF mode 1 velocities from the Exploratory Program.	6-40

Figure 6.3-5.	RH panels show the local wavelet power spectrum of the velocity components from M3 at 2490 m for the indicated time interval using the Morlet wavelet normalized by the variances of the respective series.....	6-42
Figure 6.3-6.	RH panels show the local wavelet power spectrum of the velocity components from L3 at 2500 m for the indicated time interval using the Morlet wavelet normalized by the variances of the respective series.....	6-43
Figure 7.1-1.	Depth profiles of CEOF amplitudes (cm/s) from a) separate analyses of upper and lower layer currents at M3, and b) full water column analysis of normalized currents at M3.	7-2
Figure 7.1-2.	Mode 1 amplitude vector time series (top panel: upper-layer; bottom panel: lower-layer) from the M3 CEOF layer analysis.....	7-3
Figure 7.1-3.	Relative vorticity (as a fraction of f) contoured for the upper layer, and as time series for the lower layer (1500 and 2300 m) calculated for the M1, M2 and M3 moorings.....	7-7
Figure 7.1-4.	Coherence squared and phase differences between upper and lower layer averaged ζ (red lines), and ζ at 300 and 2300 m (blue lines).....	7-8
Figure 7.1-5.	Potential vorticity anomalies and their component relative vorticity and stretching terms for the upper and lower layers with interface defined by the 8 °C isotherm (lower panel).....	7-9
Figure 7.2-1.	Vertical EOFs of east-west and north-south current velocity at mooring M1 during deployment 1.....	7-12
Figure 7.2-2.	Vertical EOFs of east-west and north-south current velocity at mooring M1 during deployment 2.....	7-13
Figure 7.2-3.	Vertical EOFs of east-west and north-south current velocity at mooring M2 during deployment 1.....	7-14
Figure 7.2-4.	Vertical EOFs of east-west and north-south current velocity at mooring M2 during deployment 2.....	7-15
Figure 7.2-5.	Vertical EOFs of east-west and north-south current velocity at mooring M3 during deployment 1.....	7-16
Figure 7.2-6.	Vertical EOFs of east-west and north-south current velocity at mooring M3 during deployment 2.....	7-17
Figure 7.2-7.	Location of BOEMRE Eastern Gulf of Mexico Circulation Study (EGOM) moorings and MMS Deepwater Physical Oceanography Reanalysis and Synthesis of Historical Data stations in the eastern Gulf of Mexico (east of 89° W) that were used to estimate dynamic modes.	7-19

Figure 7.2-8. T-S plot of CTD, XBT, and Nansen/Niskin bottle data collected between 1915 and 2000 and analyzed in the MMS-funded Physical Oceanography Reanalysis and Synthesis of Historical Data Report (Nowlin et al. 2001) and CTD cast data from three EGOM cruises taken near each of the three EGOM mooring sites.	7-20
Figure 7.2-9. Vertical profiles of Brunt-Vaisala frequency at or nearest to each mooring site based on three EGOM hydrographic cruises in January 2005, August 2005, and January 2006.	7-21
Figure 7.2-10. Normalized barotropic and first two baroclinic modes calculated with averaged casts at mooring M1 from cruises in January and August of 2005.....	7-22
Figure 7.2-11. Normalized barotropic and first two baroclinic modes calculated with averaged casts at mooring M1 from cruises in August 2005 and January 2006.....	7-22
Figure 7.2-12. Normalized barotropic and first two baroclinic modes calculated with averaged casts at mooring M2 from cruises in January and August of 2005.....	7-23
Figure 7.2-13. Normalized barotropic and first two baroclinic modes calculated with averaged casts at mooring M2 from cruises in August 2005 and January 2006.....	7-23
Figure 7.2-14. Normalized barotropic and first two baroclinic modes calculated with averaged casts at M3 from cruises in January and August of 2005.....	7-24
Figure 7.2-15. Normalized barotropic and first two baroclinic modes calculated with averaged casts at M3 from cruises in August 2005 and January 2006.	7-24
Figure 7.2-16. (Top) Spatial correlation between observed u velocity at mooring M1 from deployment 1 and the modeled u velocity from CTD cast data on the EGOM hydrographic cruises.	7-26
Figure 7.2-17. (Top) Spatial correlation between observed v velocity at mooring M1 from deployment 1 and the modeled v velocity from CTD cast data on the EGOM hydrographic cruises.	7-26
Figure 7.2-18. (Top) Spatial correlation between observed u velocity at mooring M1 from deployment 2 and the modeled u velocity from CTD cast data on the EGOM hydrographic cruises.	7-27
Figure 7.2-19. (Top) Spatial correlation between observed v velocity at mooring M1 from deployment 2 and the modeled v velocity from CTD cast data on the EGOM hydrographic cruises.	7-27

Figure 7.2-20. (Top) Spatial correlation between observed u velocity at mooring M2 from deployment 1 and the modeled u velocity from CTD cast data on the EGOM hydrographic cruises.	7-28
Figure 7.2-21. (Top) Spatial correlation between observed v velocity at mooring M2 from deployment 1 and the modeled v velocity from CTD cast data on the EGOM hydrographic cruises.	7-28
Figure 7.2-22. (Top) Spatial correlation between observed u velocity at mooring M2 from deployment 2 and the modeled u velocity from CTD cast data on the EGOM hydrographic cruises.	7-29
Figure 7.2-23. (Top) Spatial correlation between observed v velocity at mooring M2 from deployment 2 and the modeled v velocity from CTD cast data on the EGOM hydrographic cruises.	7-29
Figure 7.2-24. (Top) Spatial correlation between observed u velocity at mooring M3 from deployment 1 and the modeled u velocity from CTD cast data on the EGOM hydrographic cruises.	7-30
Figure 7.2-25. (Top) Spatial correlation between observed v velocity at mooring M3 from deployment 1 and the modeled v velocity from CTD cast data on the EGOM hydrographic cruises.	7-30
Figure 7.2-26. (Top) Spatial correlation between observed u velocity at mooring M3 from deployment 2 and the modeled u velocity from CTD cast data on the EGOM hydrographic cruises.	7-31
Figure 7.2-27. (Top) Spatial correlation between observed v velocity at mooring M3 from deployment 2 and the modeled v velocity from CTD cast data on the EGOM hydrographic cruises.	7-31
Figure 7.2-28. Temporal amplitudes of first baroclinic (bc) mode of the east-west velocity at M1 during deployment 1 (blue) and the SSH gradient in the north-south direction (green).	7-33
Figure 7.2-29. Coherency (top) and phase (bottom) spectra of the temporal amplitudes of the first baroclinic mode for the east-west velocity at M1 during deployment 1 and the SSH gradient in the north-south direction.	7-33
Figure 7.2-30. Temporal amplitudes of first baroclinic mode of the north-south velocity at mooring M1 during deployment 1 (blue) and the SSH gradient in the east-west direction (green).	7-34
Figure 7.2-31. Coherency (top) and phase (bottom) spectra of the temporal amplitudes of the first baroclinic mode for the north-south velocity component at mooring M1 during deployment 1 and the SSH gradient in the east-west direction.	7-34

Figure 7.2-32. Temporal amplitudes of first baroclinic mode of the east-west velocity at mooring M1 during deployment 2 (blue) and the SSH gradient in the north-south direction (green).	7-35
Figure 7.2-33. Coherency (top) and phase (bottom) spectra of the temporal amplitudes of the first baroclinic mode for the east-west velocity component at mooring M1 during deployment 2 and the SSH gradient in the north-south direction.	7-35
Figure 7.2-34. Temporal amplitudes of first baroclinic mode of the north-south velocity at mooring M1 during deployment 2 (blue) and the SSH gradient in the east-west direction (green).	7-36
Figure 7.2-35. Coherency (top) and phase (bottom) spectra of the temporal amplitudes of the north-south velocity first baroclinic mode at M1 during deployment 2 and the SSH gradient in the east-west direction.	7-36
Figure 7.2-36. Temporal amplitudes of first baroclinic for the east-west velocity mode at mooring M2 during deployment 1 (blue) and the SSH gradient in the north-south direction (green).	7-37
Figure 7.2-37. Coherency (top) and phase (bottom) spectra of the temporal amplitudes of the first baroclinic mode of the east-west velocity component at mooring M2 during deployment 1 and the SSH gradient in the north-south direction.	7-37
Figure 7.2-38. Temporal amplitudes of first baroclinic mode of the north-south velocity at mooring M2 during deployment 1 (blue) and the SSH gradient in the east-west direction (green).	7-38
Figure 7.2-39. Coherency (top) and phase (bottom) spectra of the temporal amplitudes of the first baroclinic mode for the north-south velocity component at mooring M2 during deployment 1 and the SSH gradient in the east-west direction.	7-38
Figure 7.2-40. Temporal amplitudes of first baroclinic mode for the east-west velocity at mooring M2 during deployment 2 (blue) and the SSH gradient in the north-south direction (green).	7-39
Figure 7.2-41. Coherency (top) and phase (bottom) spectra of the temporal amplitudes of the first baroclinic mode for the east-west velocity component at mooring M2 during deployment 2 and the SSH gradient in the north-south direction.	7-39
Figure 7.2-42. Temporal amplitudes of first baroclinic mode for the north-south velocity at mooring M2 during deployment 2 (blue) and the SSH gradient in the east-west direction (green).	7-40

Figure 7.2-43. Coherency (top) and phase (bottom) spectra of the temporal amplitudes of the first baroclinic mode for the north-south velocity component at mooring M2 during deployment 2 and the SSH gradient in the east-west direction.	7-40
Figure 7.2-44. Temporal amplitudes of first baroclinic mode for the east-west velocity at mooring M3 during deployment 1 (blue) and the SSH gradient in the north-south direction (green).	7-41
Figure 7.2-45. Coherency (top) and phase (bottom) spectra of the temporal amplitudes of the first baroclinic mode for the east-west velocity component at mooring M3 during deployment 1 and the SSH gradient in the north-south direction.	7-41
Figure 7.2-46. Temporal amplitudes of first baroclinic mode for the north-south velocity at M3 during deployment 1 (blue) and the SSH gradient in the east-west direction (green).	7-42
Figure 7.2-47. Coherency (top) and phase (bottom) spectra of the temporal amplitudes of the first baroclinic mode for the north-south velocity at M3 during deployment 1 and the SSH gradient in the east-west direction.	7-42
Figure 7.2-48. Temporal amplitudes of first baroclinic mode for the east-west velocity at M3 during deployment 2 (blue) and the SSH gradient in the north-south direction (green).	7-43
Figure 7.2-49. Coherency (top) and phase (bottom) spectra of the temporal amplitudes of the first baroclinic mode for the east-west velocity at M3 during deployment 2 and the SSH gradient in the north-south direction.	7-43
Figure 7.2-50. Temporal amplitudes of first baroclinic (bc) mode for the north-south velocity at M3 during deployment 2 (blue) and the SSH gradient in the east-west direction (green).	7-44
Figure 7.2-51. Coherency (top) and phase (bottom) spectra of the temporal amplitudes of the first baroclinic (bc) mode for the north-south velocity at M3 during deployment 2 and time series of the SSH gradient in the east-west direction.	7-44
Figure 7.2-52. Power spectra of the time-series amplitudes of the first three theoretical modes (top: barotropic mode; middle: first baroclinic mode; bottom: second baroclinic mode) time-series for fits to the east-west (left) and north-south (right) velocity data at mooring M3 during deployment 1.	7-46
Figure 7.2-53. Normalized autocovariance function (NACF) of mode amplitudes from the fit to east-west and north-south velocity component data at mooring M3 during deployment 1.	7-47

Figure 7.3-1.	Measurement array mean eddy kinetic energy (EKE) at the surface (blue) and at 2500 m (red).	7-48
Figure 7.3-2.	Top (bottom) panel: Mean (standard deviation) lower-layer potential vorticity.	7-51
Figure 7.3-3.	Top (middle) panel: Mean (standard deviation) of lower-layer thickness.	7-52
Figure 7.3-4.	Top (middle) panel: Mean (standard deviation) of lower-layer relative vorticity divided by the local Coriolis parameter (f).	7-53
Figure 7.3-5.	Top panel: Snapshot of upper and deep circulation on August 3, 2005. PIES derived SSH (thick lines) and 2500 m streamfunction (solid color; blue shades cyclonic, pink shades anticyclonic).	7-54
Figure 7.3-6.	Top panel: Snapshot of upper and deep circulation on August 3, 2005. PIES derived SSH (thick lines) and 2500 m streamfunction (solid color; blue shades cyclonic, pink shades anticyclonic).	7-55
Figure 7.3-7.	Properties of event c cyclone.	7-56
Figure A-1.	Storm track and wind extent of tropical storm Arlene.	3
Figure A-2.	Storm track and wind extent of hurricane Cindy.	4
Figure A-3.	Storm track and wind extent of hurricane Dennis.	5
Figure A-4.	Storm track and wind extent of hurricane Katrina.	6
Figure A-5.	Storm track and wind extent of hurricane Rita.	7
Figure A-6.	Storm track and wind extent of hurricane Wilma.	8
Figure B-1.	Mooring 1 current vectors for Deployment 1.	3
Figure B-2.	Mooring 1 current vectors for Deployment 2.	4
Figure B-3.	Mooring 2 current vectors for Deployment 1.	5
Figure B-4.	Mooring 2 current vectors for Deployment 2.	6
Figure B-5.	Mooring 3 current vectors for Deployment 1.	7
Figure B-6.	Mooring 3 current vectors for Deployment 2.	8
Figure B-7.	Mooring 4 current vectors for Deployment 1.	9
Figure B-8.	Mooring 4 current vectors for Deployment 2.	10

Figure D-1.	Amplitude (left column) and phase (right column) of the O1, K1, Q1, and P1 constituents determined with the tidal response method (Munk and Cartwright, 1966) from the six bottom pressure records	3
Figure D-2.	Amplitude (left panels) and phase (right panels) of the M2, K2, N2, and S2 constituents determined with the tidal response method (Munk and Cartwright, 1966) from the six bottom pressure records.	4
Figure E-1.	Latitude of the center of Eddy Ulysses.	5
Figure E-2.	Longitude of the center of Eddy Ulysses.	5
Figure E-3.	Orbital period in Eddy Ulysses.	6
Figure E-4.	Eccentricity of Eddy Ulysses.	6
Figure E-5.	Orientation of the major axis of Eddy Ulysses.	7
Figure E-6.	Latitude of the center of Eddy Vortex early in 2005.	8
Figure E-7.	Longitude of the center of Eddy Vortex early in 2005.	8
Figure E-8.	Orbital period of Eddy Vortex early in 2005.	9
Figure E-9.	Eccentricity of Eddy Vortex early in 2005.	9
Figure E-10.	Orientation of the major axis of Eddy Vortex early in 2005.	10
Figure E-11.	Latitude of the center of Eddy Vortex late in 2005.	11
Figure E-12.	Longitude of the center of Eddy Vortex late in 2005.	11
Figure E-13.	Orbital period of Eddy Vortex late in 2005.	12
Figure E-14.	Eccentricity of Eddy Vortex late in 2005.	12
Figure E-15.	Orientation of the major axis of Eddy Vortex late in 2005.	13
Figure E-16.	Latitude of the center of Eddy Walker.	14
Figure E-17.	Longitude of the center of Eddy Walker.	14
Figure E-18.	Orbital period of Eddy Walker.	15
Figure E-19.	Eccentricity of Eddy Walker.	15
Figure E-20.	Orientation of the major axis of Eddy Walker.	16
Figure E-21.	Latitude of the center of Cold Eddy 1.	17

Figure E-22.	Longitude of the center of Cold Eddy 1.....	17
Figure E-23.	Orbital period of Cold Eddy 1.	18
Figure E-24.	Eccentricity of Cold Eddy 1.....	18
Figure E-25.	Orientation of the major axis of Cold Eddy 1.....	19
Figure E-26.	Latitude of the center of Cold Eddy 2.....	20
Figure E-27.	Longitude of the center of Cold Eddy 2.....	20
Figure E-28.	Orbital period of Cold Eddy 2.	21
Figure E-29.	Eccentricity of Cold Eddy 2.....	21
Figure E-30.	Orientation of the major axis of Cold Eddy 2.....	22
Figure E-31.	Latitude of the center of Cold Eddy 3.....	23
Figure E-32.	Longitude of the center of Cold Eddy 3.....	23
Figure E-33.	Orbital period of Cold Eddy 3.	24
Figure E-34.	Eccentricity of Cold Eddy 3.....	24
Figure E-35.	Orientation of the major axis of Cold Eddy 3.....	25
Figure E-36.	Latitude of the center of Cold Eddy 4.....	26
Figure E-37.	Longitude of the center of Cold Eddy 4.....	26
Figure E-38.	Orbital period of Cold Eddy 4.	27
Figure E-39.	Eccentricity of Cold Eddy 4.....	27
Figure E-40.	Orientation of the major axis of Cold Eddy 4.....	28
Figure E-41.	Latitude of the center of the Loop Current.	29
Figure E-42.	Longitude of the center of the Loop Current.	29
Figure E-43.	Orbital period in the Loop Current.	30
Figure E-44.	Eccentricity of the Loop Current.	30
Figure E-45.	Orientation of the major axis of the Loop Current.	31
Figure F-1.	Mooring map for the Eastern GOM observational program.....	10

Figure F-2.	Locations of tall moorings M1-M3 (shown with red stars) overlaid on the real-time analysis of surface fronts for August 29, 2005 (provided by Horizon Marine Inc.)	11
Figure F-3.	Near-inertial response to hurricane Katrina at Mooring 1 (Forristall, 2007).....	12
Figure F-4.	Near-inertial response to hurricane Katrina at Mooring 3 (Forristall, 2007).....	13
Figure F-5.	Surface frontal analysis provided by Horizon Marine Inc. for August 20, 2005.....	14
Figure F-6.	Surface frontal analysis provided by Horizon Marine Inc. for August 27, 2005.....	15
Figure F-7.	Surface currents simulated during the “spinup” initialization on August 24, 2005.....	16
Figure F-8.	Surface currents simulated during the “spinup” initialization on August 25, 2005.....	17
Figure F-9.	Surface currents simulated during the “spinup” initialization on August 26, 2005.....	18
Figure F-10.	Surface currents simulated during the “spinup” initialization on August 27, 2005.....	19
Figure F-11.	Observed (upper panel) and simulated (lower panel) current speed at the northern mooring.	20
Figure F-12.	Observed (upper panel) and simulated (lower panel) current speed at the middle mooring.	21
Figure F-13.	Observed (upper panel) and simulated (lower panel) current speed at the southern mooring.	22

LIST OF TABLES

	Page
Table 2.1-1. Deployment locations of the moorings for Deployment 1.....	2-3
Table 2.1-2. Deployment locations of the moorings for Deployment 2.....	2-4
Table 2.1-3. Deployment information of the tall (M1, M2, and M3) and short (M4) moorings for each instrument deployed.....	2-7
Table 2.1-4. Summary of data coverage by each instrument and their sensors for Mooring 1 during January 2005 to January 2006.....	2-13
Table 2.1-5. Summary of data coverage by each instrument and their sensors for Mooring 2 during January 2005 to January 2006.....	2-14
Table 2.1-6. Summary of data coverage by each instrument and their sensors for Mooring 3 during January 2005 to January 2006.....	2-15
Table 2.1-7. Summary of data coverage by each instrument and their sensors for Mooring 4 during January 2005 to January 2006.....	2-16
Table 2.1-8. Data return statistics for each mooring and each instrument type during both deployments.....	2-16
Table 2.3-1. Temperature Differences.....	2-56
Table 2.3-2. Velocity Differences.....	2-57
Table 2.4-1. Satellite Altimeter Missions during the Eastern Gulf Program.....	2-60
Table 2.5-1. Satellite Periods.....	2-70
Table 2.5-2. Variance Statistics.....	2-74
Table 2.5-3. PIES Statistics.....	2-75
Table 2.5-4. SNR Statistics.....	2-76
Table 2.5-5. Half-power Period of PIES Barotropic, Baroclinic, and Total SSH Signals.....	2-80
Table 2.5-6. Satellite Altimeter and PIES SSH Correlation.....	2-83
Table 2.6-1. Storm Events.....	2-90
Table 3.1-1. LCE Vortex Detachment and Reattachment Events.....	3-6
Table 3.1-2. Altimeter-derived Summary Statistics.....	3-12

Table 3.1-3.	Ring Separation Events from the Altimetric Record: 1 January 1993 through 30 June 2006.....	3-18
Table 3.2-1.	Intrusion Events.....	3-23
Table 3.2-2.	LCE Separation Periods.....	3-25
Table 5.1-1.	Extreme current speed distributions at Mooring 1.....	5-24
Table 5.1-2.	Extreme current speed distributions at Mooring 2.....	5-24
Table 5.1-3.	Extreme current speed distributions at Mooring 3.....	5-25
Table 5.1-4.	Extreme current speed distributions at Mooring 4.....	5-25
Table 6.1-1.	Moorings Deployed by Observational Studies in the Deep GOM.	6-5
Table 6.1-2.	Lower-Layer EOF Analysis of Currents by Mooring.....	6-9
Table 6.1-3.	Time Scales and Degrees of Freedom for Lagrangian and Eulerian Velocity Statistics	6-17
Table 6.3-1.	EOF and Wavenumber Analysis of Eastern GOM Deep Currents.....	6-34
Table 7.1-1.	Potential Vorticity Parameters	7-6
Table 7.2-1.	EOF Mode Variance	7-11
Table C-1.	Statistics from Mooring 1 Deployment 1 ADCP for the u and v components of the currents measured.....	C-3
Table C-2.	Statistics from Mooring 1 Deployment 1 single point current meters for the u and v components of the currents measured.....	C-5
Table C-3.	Statistics from Mooring 2 Deployment 1 ADCP for the u and v components of the currents measured.....	C-6
Table C-4.	Statistics from Mooring 2 Deployment 1 single point current meters for the u and v components of the currents measured.....	C-8
Table C-5.	Statistics from Mooring 3 Deployment 1 ADCP for the u and v components of the currents measured.....	C-9
Table C-6.	Statistics from Mooring 3 Deployment 1 single point current meters for the u and v components of the currents measured.....	C-11
Table C-7.	Statistics from Mooring 4 Deployment 1 single point current meters for the u and v components of the currents measured.....	C-11

Table C-8.	Statistics from Mooring 1 Deployment 2 ADCP for the u and v components of the currents measured.....	C-12
Table C-9.	Statistics from Mooring 1 Deployment 2 single point current meters for the u and v components of the currents measured.	C-14
Table C-10.	Statistics from Mooring 2 Deployment 2 ADCP for the u and v components of the currents measured.....	C-15
Table C-11.	Statistics from Mooring 2 Deployment 2 single point current meters for the u and v components of the currents measured.	C-17
Table C-12.	Statistics from Mooring 3 Deployment 2 ADCP for the u and v components of the currents measured.....	C-18
Table C-13.	Statistics from Mooring 3 Deployment 2 single point current meters for the u and v components of the currents measured.	C-20
Table C-14.	Statistics from Mooring 4 Deployment 2 single point current meters for the u and v components of the currents measured.	C-20
Table D-1.	Amplitude in cm and phase in degrees for the eight major tidal constituents (O1, K1, Q1, P1, M2, K2, N2, S2) constituents determined with the tidal response method (Munk and Cartwright, 1966).	D-5

EXECUTIVE SUMMARY

Project Background

The major source of energy forcing currents in the surface waters of the Gulf of Mexico (GOM) is the Loop Current (LC) which flows northward through the Yucatan Channel into the GOM, and then turns eastward and exits through the Straits of Florida to join the Gulf Stream. The LC varies in its penetration into the GOM, sometimes constraining itself to the southern Gulf, and sometimes penetrating far northward into the northern Gulf. During most periods when the LC has penetrated northward, cold core eddies and warm water filaments can be found migrating around its periphery. Often when extended far northward, the LC pinches off, forming a Loop Current Eddy (LCE) that migrates through the northern Gulf, eventually moving westward to die within its western regions. LCEs detach from the LC at periods ranging from 3 to 17 months, with a mean frequency of separation near 10 months (Sturges and Leben 2000). Very energetic LCEs interact with one another, the LC, and bathymetry, forming cyclonic eddies with which they also interact. There are times, however, that the LC retreats southward without shedding an eddy.

All this activity by the LC, LCE's, and associated features, imparts significant energy to the surface waters of the GOM. While the overall net circulation of the surface waters in the GOM based on drifter records is generally understood to be a clockwise circulation pattern around the basin (DiMarco et al. 2005), the magnitude of the velocity and variance of the surface currents are known to be greatest in the vicinity of the LC, where speeds often exceed 1.5 m s^{-1} .

In deeper waters of the GOM, previous studies (Hamilton 1990; Donohue et al. 2006) have identified energetic, deep, barotropic (below about 1000 m) motions with some indications of bottom intensification at various locations on the slope and rise of the North-central Gulf, particularly along the Sigsbee Escarpment. With time scales of 10 d or more and amplitudes up to 1 m s^{-1} , the phenomena responsible for these motions are generally attributed to topographic Rossby waves (TRWs). In general, little coupling of upper and lower layer circulation in the GOM appears to occur. However, some instances of coupling have been observed in other observation programs. Also, modeling studies output suggest that deep cyclonic (anti-clockwise) and anti-cyclonic (clockwise) eddies form in the Eastern and Central Gulf and propagate into the Western Gulf guided by topography. Some modeling results (Welsh and Inoue 2000) suggest that an anticyclone/cyclone pair form in the lower level in response to an anti-cyclonic LCE in the upper layer.

Recent agency studies have investigated the circulation features and their characteristics and vertical variations over the coastal shelf off Texas and Louisiana (Nowlin et al. 1998a, Nowlin et al. 1998b), and in the deeper waters of the central (Donohue et al. 2006) and western Gulf of Mexico (Donohue et al. 2008). A lack of current measurements and understanding of the circulation in the deep northeastern Gulf of Mexico prompted the BOEMRE to develop and fund a study titled: *Survey of Deepwater Currents in the Eastern Gulf of Mexico*. In July 2004 a contract was awarded to Evans-Hamilton, Inc. (EHI) and its science team to perform this study. This study is part of a larger research effort by the BOEMRE to gain a better understanding of the surface and deep dynamic processes in the GOM.

Study Area

The study area is located within the Eastern GOM. This area consists of the area of the Eastern Gulf Lease Sale 181. The study area is located south of Mobile Bay in water depths ranging from 2000 to 2800 m, and is bounded approximately by the following coordinates:

NW Corner: 28.848 °N, 87.918 °W	NE Corner: 28.850 °N, 87.523 °W
SW Corner: 27.453 °N, 87.907 °W	SE Corner: 27.455 °N, 87.516 °W

Bathymetrically, the area is bounded as follows.

To the north: by the ~2000 m isobath, & by a slope incised by hills & valleys
To the east: the northern half by the steep slope of the West Florida Escarpment
To the east: the southern half by a flat plain at 2500-2800 m depth
To the south: by a relatively flat featureless plain
To the west: by a slope with isobaths directed NNE to SSW

Key bathymetric features of the study area include that the:

1. Area lies to NE of the Sigsbee Escarpment, and SW of the DeSoto Canyon.
2. Area contains primarily NNE to SSW oriented isobaths, rather than E-W isobaths
3. Area contains the farthest northward extent of the 2000 m isobath in the Gulf of Mexico, plus NNE of the study area is located the farthest northward extent of the 200 m isobath. As a result, the area provides the best opportunity for the most northerly penetration of the LC or a LCE within the Gulf of Mexico.
4. Area surrounding the study area has the largest separation between the 2000 and 3000 m isobaths within the Gulf of Mexico. This area is a large, relatively flat area.
5. The West Florida Escarpment intersects the eastern boundary of the study area at ~ 28.4° N, or approximately one-third the distance from the NE to the SE corners of the study area.

Study Objectives

The goal of this study was to investigate and document the deepwater circulation in the Eastern GOM. This is an area of sparse previous deepwater current measurements. Specific study objectives were to:

- Conduct measurements of currents using moorings to increase the regional database of ocean currents in the Eastern GOM.
- Improve the scientific community's overall knowledge and understanding of circulation features in this deepwater area.
- Collect hydrographic, remote sensing, and other relevant measurements useful to understanding what controls the region's circulation.
- Assess the key processes energizing the circulation.
- Add to the database of LC and LCE characteristics, and how these features affect the study area.

- Establish an improved base of knowledge to help design future circulation studies in this part of the GOM.
- Provide measurements and knowledge which could assist with future calculations of horizontal and vertical trajectories of released oil and its dispersion.

The objectives of the study were met by conducting a one-year measurement program to collect an integrated set of current, hydrography, remote sensing, and ancillary measurements that could provide an excellent understanding of the circulation processes in the area. These measurements were collected from January 2005 to January 2006 and included current measurements and water properties collected from four moorings in water depths from ranging from 2500 to 2800 m. The mooring measurements were supplemented with measurements from bottom-moored PIES, three hydrography (profiling CTD and XBT) cruises, and satellite imagery and altimetry. Satellite-tracked drifting buoy data along with Eddy Watch maps were obtained from Horizon Marine, Inc. for the period of the study's measurements, and utilized under a limited license for additional analyses of the characteristics of the LC and LCE's. Publicly available river discharge data, coastal and offshore wind data, and coastal water level data during the measurement period were also obtained.

Study Team

The Science Team Principal Investigators (PIs) for the study all have conducted research and analysis of the circulation of the Gulf of Mexico for several years. Drs. Peter Hamilton, Robert Leben, Kathleen Donohue, and Randolph Watts have participated in recent MMS studies of the deep central and western GOM, and were selected to provide continuity of their past work to the planning and analyses performed for this study. Dr. Steven DiMarco led the compilation and analysis of all available current measurements in the GOM for MMS (Nowlin et al. 2001), and was selected for his overall understanding of the circulation features within the GOM. Dr. George Forristall was a Senior Oceanographer at Shell Oil Company who studied extreme and operational oceanographic conditions within the GOM, and was selected to provide his knowledge and an oil industry perspective to the science team.

All PIs contributed to the design of the study, analyses of the measurements and remote sensing data, and participated in the writing of this report. Extensive collaboration occurred between PIs, both during planning of the study and during analysis of the measurements resulting from this study. In addition to the Science Team PI's, the following personnel led the organization and conduct of the project:

Mr. Jeffrey Cox, EHI – Program Manager
 Mrs. Carol Coomes – Assistant Program Manager, Data Manager
 Mr. Keith Kurrus and Mr. Kevin Redman, EHI – Cruise Chief Scientists
 Mrs. Kari Walker, EHI – Data Processing & QA/QC Team Leader

Many additional personnel in all team member organizations contributed significantly to the performance of work conducted for this study.

Study Design

The current measurement moorings consisted of three tall moorings and one short mooring. The tall moorings reached from ~70 m depth to bottom in water depths between 2600 to 2800 m. The one short mooring reaching 250 m above the bottom to the bottom at 2750 m depth. The design of the moorings was to provide measurement of current velocity and temperature over the full water column, but at higher vertical resolution over the top 500 m where the LC and LCE's most strenuously influence the currents. Horizontally the moorings were spaced close enough to examine correlations between them and assess regional vorticity, but far enough apart to provide regional coverage of the study area.

The three tall moorings contained upward-looking 75 kHz ADCPs at 500 m depth, with single point current meters spaced at intervals from 750 m to near bottom. The short mooring contained two single point current meters in the lower 100 m of the water column. Overall, excellent data coverage was achieved from the moorings.

An array of seven inverted echo sounders with pressure gauges (PIES) was deployed in order to increase the spatial extent of the moored current meter array. Also, two PIES instruments were deployed at two of the seven PIES deployment sites for a portion of the study. Data return from the PIES was excellent. Full deployment records are available from all PIES with two exceptions: first, the initial instrument at PIES site 6 did not have valid τ records and therefore only the second deployment's data from this site were used; and second, the PIES at site 7 was not recovered, although the full daily average data set was received by acoustic transmission.

Three hydrography cruises were conducted during the 12-month measurement period. The hydrography cruises used a combination of CTD casts and XBT profiles designed to ensure sufficient data density, efficiency of operations during the cruise, and coverage of the study area. The first hydrography cruise was conducted January 17-23, 2005 and followed a grid pattern as no LC features were located near the study area at the time. The second hydrography cruise was conducted August 18-25, 2005 and again followed the grid pattern and the general station type. Additional XBT profiles were collected every 10 km as the ship crossed the loop eddy on the way back to shore. Hydrographic Cruise 2 finished one day ahead of Hurricane Katrina entering the GOM.

The third hydrography cruise was conducted January 20-28, 2006 and did not use the grid design. As the time was approaching for retrieval of all the moorings and PIES and the third hydrography cruise, satellite imagery showed the LC was moving northeastward toward the study area, and two cold core eddies appeared to be located in the southern half of the study area along with some other frontal features. A cruise plan was devised to intensively sample the edge of the LC and the cold core eddies.

All data from the moorings and hydrographic cruises were processed, QA/QC'd, and converted to standard format files. Graphical displays and tabular summaries of these data were then created. These were then distributed along with the processed data files to all PI's for their specific analyses of the measurements.

Remote sensing (satellite) data collected for the study included sea surface height (SSH) data, high-resolution sea surface temperature (SST), and ocean color imagery. These data were collected, processed, and the results distributed to team members by the Colorado Center for Astrodynamic Research (CCAR).

Five hurricanes and one tropical storm passed through the GOM during the measurement program in 2005. Information on the tracks of the storms was obtained from the National Hurricane Center (NHC) website <http://www.nhc.noaa.gov>.

Results

Loop Current Events

From the remote sensing data, statistics of LC intrusion as well as LCE detachment, reattachment, and final separation events that occurred during the program time period were developed based on an objective method (Leben 2005) for tracking the LC and detecting LCE separation events that gives separation periods comparable to those determined by subjective tracking methods. Continuous altimeter mapping of the sea surface height in the GOM since 1993 provided the ability to place the LC and LCE events during the study period into perspective with this historical period. Additional historical perspective back to July 1973 is also provided based on previous LCE identifications using SST imagery (Vukovich 1988). Herein LC and LCE statistics are presented both for the study period and for these historical periods.

During the study period, the LC penetrated and remained far north in the central and eastern portions of the GOM, often influencing the study area. Only a single large anticyclonic eddy, which was given the name “Vortex”, separated from the LC during the study period. However, Eddy Vortex detached and re-attached from the LC four times prior to its final separation from the LC on 13 September 2005. For historical perspective, although eddies may detach from and reattach to the LC, ultimate LCE separation occurs most frequently at intervals of about 6, 9 and 11.5 months based on the available historical measurements (Leben 2005).

The extended intrusion of the LC into the northern GOM associated with Eddy Vortex was one of the most northerly intrusions of the LC on record, only exceeded by the intrusion that generated Eddy Sargassum during the Exploratory Study. This far northerly intrusion of the LC and Eddy Vortex during late summer 2005 contributed to the intensification of Hurricanes Katrina and Rita (Walker et al. 2005). After the separation of Eddy Vortex, the LC did not retreat substantially to the south. As a result the LC remained intruded into the eastern-central GOM close to the study area during the remainder of the study’s measurement period.

The extended LC intrusion associated with the repeated detachment and reattachment of LCE Vortex before ultimate separation in September 2005 significantly impacted the study region upper ocean circulation during the first half of the EGOM program. Once Eddy Vortex separated, fewer LC or LC frontal feature impacts to the circulation in the study area occurred, and the character of the circulation returned to conditions more typical of this northern location in the eastern deepwater GOM basin.

The 13.5 year historical altimetry record (1993-June 2006) showed that LC or LCE intrusions into the study area averaged about 22 days per year, whereas during the study, the LC or Eddy Vortex intruded into the study area 52 days total in 2005, over twice the historical average. Only one other calendar year had a greater occurrence of intrusion, which was 91 days in 2003 associated with Eddy Sargassum.

Mooring Measurements

During the mooring measurements the study area experienced the influence of either the LC, Eddy Vortex, or frontal features multiple times. In addition, several hurricanes and a tropical storm passed through the GOM during 2005, some of them close enough to the study area to result in distinguishable impacts to the current measurements. The end result is that the moorings captured a robust set of measurements showing the impacts to the eastern GOM circulation by the LC, an LCE, frontal features, and hurricanes. The measurements were collected during two deployments, with the servicing of the moorings occurring just prior to the arrival of Hurricane Katrina.

During the first deployment all three tall moorings experienced significant periods of stronger currents primarily but not entirely generated by the LC, Eddy Vortex, or LC or LCE frontal features. At M3, nearly the entire first deployment contained stronger currents. Currents at M2 were quite similar to those at M3, whereas the strength and duration of stronger currents at M1 were reduced as compared to those at M2 and M3. During the second deployment, periods of stronger currents were normally shorter, and current strengths reduced as compared to the first deployment, although Mooring M3 continued to show influences on the currents due to both hurricanes and the LC/LCE/frontal features.

Currents during both deployments at all three tall moorings showed a high degree of coherency at water depths above 500 m, with weak coherence extending down to 750 m, and with only occasional coherence at deeper depths. However, during those occasional events, the observations indicated a strong barotropic component to the flow structure. For example, in mid-August 2005, at mooring M3, there was a barotropic event associated with the detachment and reattachment of an LCE. The feature was coherent throughout the water column and peaked in the upper ocean with only gradual diminishment with depth. In October through mid-December 2005, there was a second barotropic current event that was seen in the velocity data collected at M2 and M3. During this second event, the increase in current speed was associated with a LC meander into the study area.

Large-amplitude inertial oscillations in the study area were excited immediately after the passages of Hurricanes Katrina in late August 2005 and Rita on 21 September 2005. These oscillations persisted for at least two weeks after the passage of the storms. The inertial motions were strongest at M3 and penetrated down to 500 m. Hurricane Dennis, which entered the Gulf on July 9th and later passed very close to the study area, also generated less intense inertial oscillations at M1.

During the first deployment, the moorings each had similar inertial energy amplitudes. During the second deployment, moorings M2 and M3 had significantly more energy in the inertial band than mooring M1, owing to the closer proximity of these mooring to the centers of Hurricanes Katrina and Rita. Hurricane Katrina came closest to all three moorings late on August 28. All the moorings were to the right of the storm track and roughly the same distance from it. The resulting clockwise rotating wind stress vector had about the same potential for generating inertial oscillations at all the moorings. The inertial oscillations were much stronger at M3 than at the other moorings. This difference in strength cannot be explained by any large difference in the wind forcing at the moorings. The very strong inertial response at M3 is believed to have been caused by the coincidence of the hurricane and a cyclonic eddy.

The inertial motions generated by Hurricanes Katrina and Rita were also investigated using the wavelet transform. This method estimates the temporal variability of energy in specified frequency bands. Looking at the wavelet power spectrum, it was clear that inertial motions were excited immediately following hurricanes Katrina and Rita and persisted for around 2 weeks at this depth. Not only did the storms amplify inertial motions; energy was elevated throughout the sub-inertial frequency domain. The average variance in the inertial band time-series was constructed by integration of the wavelet power spectrum in the period band 0.5 – 2 days. The significant peaks in the variance in early September further illustrate the effects of the passage of the two hurricanes.

There were generally two subsurface maxima of energy present after the storms and two paths for inertial energy were revealed. There was a direct influence on the entire water column that occurred during or immediately after the storm due to the storm's intensity. There was also the downward propagation of inertial energy, evidenced by the diagonal streak of high energy following the storm.

Inertial waves after Katrina were present more than 2 weeks after the storm and penetrated quickly to the base of the upper layer. The amplitudes of the inertial oscillations after Hurricane Rita were not as large as the motions excited by Hurricane Katrina and didn't penetrate as deep, but appeared to persist at the surface longer. The rate of downward inertial energy propagation was roughly 30 m day^{-1} .

A full water column vertical empirical orthogonal function (EOF) of the average variance in the inertial band was performed. Modes 1, 2, and 3 explain ~71%, ~8%, and ~4% respectively of the variance in the inertial band energy.

Spectral energy from the currents was greatest in the shallow ocean (< 300 m depth). Surface records (~ 50 m) contained larger weather-band variance than deeper records as expected since the influence of winds on currents generally diminishes with depth. This was especially true at moorings M2 and M3, where the variance steadily increased between 0.9 cpd and 0.1 cpd.

Near-surface spectral energy associated with periods of 20-60 days was typically associated with mesoscale processes such as the LC and LCEs. Low-frequency spectral estimates in the upper ocean at all tall moorings were roughly equal. There was slightly more sub-inertial energy present during deployment 1, especially at the 20 – 60 day period. This is likely attributable to the penetrations of the LC and Eddy Vortex into the study area multiple times.

Relative to the surface, spectral energy in deeper currents were less energetic. The overall shapes of the trends of the spectra energy of the deeper records closely resembled those of the upper ocean. Subinertial variability, particularly in the lowest bands shown, decreased from south to north. This may be attributed to the motions associated with the LC and LCE events at each mooring. There were some cases where low frequency variance (20 – 60 day period band) in the deepest record (usually 2500 m) was greater than the energy in the record at ~ 1000 m, which could be evidence of topographic Rossby waves.

The vertical coherence of the currents at low frequencies between velocity time-series at 100 m and records to depths of ~500 m depth were mostly significant for every mooring deployment. Coherency was also observed at near-inertial frequencies. Coherency in the inertial band between near-surface velocity and records between 100 – 200 m diminished owing to the location of the pycnocline at these depths. Below this depth, inertial motions may be attributable to other forcing processes such as eddy features. Inertial oscillations at the surface and at depth therefore would not be expected to be coincident or phase locked. The exception to this is when a powerful hurricane is able to affect layers below the pycnocline.

Estimates of the coherency spectra for horizontal separations were calculated between moorings for all velocity combinations at the same depth. East-west velocity at moorings M1 and M2 were coherent at the lowest frequency band (~90 days) and with zero phase lag. Near the inertial frequency in the upper water column, coherency was found at 750 m, 1244 m, and 1492 m. The phase of the correlation at the near inertial peak was variable with depth. The east-west velocity component at mooring M1 and north-south velocity component at mooring M2 were also coherent at low frequencies but with a phase difference of about 1 radian (~90°) at the lowest frequency, which indicated that the M1 velocity lead the M2 velocity.

Coherency between mooring M1 v velocity and mooring M2 u velocity, as well as coherency between v velocity at both moorings indicated coherency at low frequency with a phase of ~-1.0 radian, which meant that M2 lead M1. The phase relationship of the two components likely indicated the influence of the eddy fields. Deeper current meter records at M1 and M2, except for the records at 1995 m, were only significantly correlated between north-south velocity components at both moorings in the inertial band and at low frequencies (~ 80 - 90 days). This may be an indication of topographic steering along the bathymetry.

Mooring M1 and mooring M3 east-west velocities were coherent at near-inertial frequencies at every depth in the upper layers. M1 u and M3 v were correlated at the fundamental frequency (~90 days) at a phase of ~2 radians (180°) throughout the water column and near inertial peaks were present down to 998 m. v velocity at M1 and M3 were correlated at low frequencies down to 998 m with zero phase difference. Only near-inertial correlation was present between M1 v and M3 u .

East-west velocity at moorings M2 and M3 illustrated very little significant coherency beyond some intermittent near-inertial correlations in the upper water column; however, the east-west velocity was coherent between moorings M2 and M3 in all current meter records in the deep ocean at periods of about 50 days. North-south velocity was correlated at low frequencies in the upper water column, and there was correlation at 20-day periods and above between the data from the deep current meters at 750, 998, and 1245 m. There were some near-inertial peaks in the upper water column between M2 east-west (north-south) velocity and M3 north-south (east-west) velocity.

The mean current velocity at mooring M3 was predominantly to the southeast during deployment 1 and eastward during deployment 2. We attribute this to the relative location of the mooring near the northern edge of the LC and Eddy Vortex during the first deployment, while during deployment 2 portions of a frontal cyclonic eddy passed over this region producing mostly eastward-directed currents. Mooring M3 was also closest to Hurricanes Katrina and Rita; therefore, the minimum/maximum current velocity envelopes were greatest here than for any other moorings. The mean current velocity during the first deployment was primarily southeastward at mooring M2, and to the east at mooring M1. However, during the second deployment, currents were dominated by various cold core frontal eddies moving in and out of the study area resulting in relatively small mean current velocities at both moorings.

For engineering applications, one often needs an estimate of the extreme value of the current speed over some return interval. Herein, we developed such estimates for the measurements made by the Aanderaa current meters on the moorings, but not for the ADCP measurements. The extremes were developed using weekly maximum current speed values for each Aanderaa current meter record. The weekly maxima were fit to the generalized extreme value (GEV) distribution. The GEV is the limit distribution of the maxima of a sequence of independent and identically distributed random variables. In general, the extreme values near 750 m depth and near the bottom were largest, with smaller values at intermediate depths. By far the largest were at 749 m depth on Mooring 1. The extrapolated near-bottom current speeds at Mooring 1 near the Florida Escarpment were no larger than those at Mooring 3 on the abyssal plane.

Hydrography Measurements

To gain additional perspective on the influence of the LC and LCE's on the study area, hydrographic measurements were acquired during the mooring deployment, servicing, and recovery cruises. The hydrographic conditions during the cruises were as follows. During Hydrography Cruise 1 (17-23 January 2005) the southwest section of the study area was being impacted by the edge of the LC, which can be seen as deep warm water mesoscale feature in the hydrographic data. The LC was close to, but had not yet reached, the mooring locations. During Hydrography Cruise 2 (18-25 August 2005) the LC and Eddy Vortex were not over the study area as evidenced by the 20° isotherm remaining fairly shallow throughout much of the study area during the cruise. A cold core eddy sitting atop Mooring 3 was quite clearly visible in the data.

Hydrographic Cruise 3 (20-28 January 2006) saw the most dramatic and intensive influence from the LC. During this period, the edge of the Loop current lay just to the southwest of the study area, and was advancing toward it. In addition, a cold core eddy lay over the southern portion of the study area in the vicinity of Mooring 3. Intensive hydrographic sampling resulted in excellent data across the edge of the LC and within the cold core eddy. However, due to both the rapid advancement of the LC towards the moorings, and the resultant rapid evolution and movement of the cold core eddy during the nine-day period of the cruise, it was difficult to capture a representative static snapshot of these conditions over the entire area. Changes to the edge of the LC as it migrated toward the study area were captured in selected transects that were repeated during the cruise.

Deep Circulation

Previously Hamilton (1990) showed that much of the current variability under the LC in the north central and northwest Gulf of Mexico had the characteristics of topographic Rossby waves (TRWs). Such characteristics included high coherence through the lower water column, bottom intensification, and period and wavevector agreements with the dispersion relation as given by Rhines (1970). Hamilton (1990) speculated that pulsations of the LC were the primary source of the lower-layer TRWs, and evoked the Malanotte-Rizzoli et al. (1987) model of broad-band radiation from a pulsating meander in a channel over a sloping bottom as an explanation of the observations. Hamilton (1990) suggested that the TRW-trains propagate generally westward at higher group speeds than LCE's, therefore motions in the lower layer are largely decoupled from the eddy currents in the upper layer.

To assess the motions in the deep circulation, mean current and standard deviation ellipses were calculated of the deep current measurements from the study area, and from a mooring maintained by Louisiana State University (LSU) to the south of the study area (L7). The deep mean flows were north-northwestward at L7, which is similar to the 2003-2004 results for the same location. Near-bottom mean flows at M3 and M4 are westward towards the escarpment south of the delta. At M3, and to a lesser extent at M2, the mean currents at 1200 m are essentially negligible, which is a contrast to the more depth independent mean flows at L7. Where the slope is steeper (M1) the mean flows tend to follow the isobaths.

The current fluctuations were more energetic at L7 than at moorings M1, M2, and M3 within the study area. Under the LC at L7, the fluctuations of the currents were predominantly northwards with few reversals, depth independent from 1200 to 3200 m, with relatively long periods (~ 30 days or more), and with the maximum speeds ($\sim 30 \text{ cm s}^{-1}$ in late December 2005) of all the deep measurements versus moorings M1, M2, and M3. The standard deviation ellipses at M2 and M3 clearly show evidence of bottom intensification, with principal axes directed westward and southwestward, respectively, across the isobaths into shallower water, which is characteristic of TRW motions. The lower water column still contained considerably more eddy kinetic energy (EKE) because of the approximate doubling of the thickness of the lower water column between M3 and L7.

For the M2, M3 and M4 moorings, the fluctuations were more variable in amplitude, had more frequent reversals, and had somewhat shorter periods than at L7. There was clearly a decrease in energy moving from south to north over the 45 km spacing from M3 to M4 and M2. Near the slope at M1 the fluctuations were much less energetic, with amplitudes mostly less than 5 cm s^{-1} , and characteristic periods much shorter, generally less than ~ 20 days.

As discussed earlier, during the study period the LC and Eddy Vortex impacted the study area multiple times, and several hurricanes passed close by. Evidence of some of these events was seen in the deep currents. For example, in the deep current records, there was evidence of low-frequency pulses at some of the moorings when storms were intense and passed fairly close to the moorings. The center of Hurricane Katrina passed close to L7 on August 28, 2005 at which time it was classified as a category 4 hurricane. A short-lived northward pulse of $\sim 20 \text{ cm s}^{-1}$ was observed in the lower water column at L7 at this time, which stood out from the background flows. A month later, a similarly intense Hurricane Rita passed by L7 at a greater distance, but there was no obvious pulse from the hurricane at L7.

In contrast, deep currents at moorings M2, M3 and M4 on the abyssal rise showed no discernable response to the passage of these major storms. However, the near-bottom currents at M1 did show consistent short period pulses at the times of the closest approaches of the major hurricanes Dennis, Katrina and Rita.

Deep circulation was also punctuated by a number of energetic low-frequency events. The six largest EKE peaks were analyzed. Maps of SST overlaid with altimeter-derived SSH were used to analyze these six high EKE events in context of the LC and Eddy Vortex movements. High resolution lower-layer streamlines and geostrophic bottom currents overlaid with PIES derived SSH were used to show the relationship of the bottom flows to the upper-layer.

One event occurred in late April 2005, where the deep circulation contained south or southwestward flows over the main part of the array and northwest flows at M1. During this period, the LC was extended well towards the delta and bordered moorings M2 and M3. The study region was dominated by a LC frontal eddy resulting upper layer southeastward flows at M2 and M3 along the LC front and reversed flows on the north side of the cyclone at M1. The lower layer streamlines were approximately normal to the upper-layer flows and the strong deep currents were caused by a deep cyclone in the southern part of the array; however the present view is that apparent deep cyclones and anticyclones are primarily the result of packets of dispersive TRWs.

The LC remained in this configuration for most of April, May and June, though the cyclonic LC frontal eddy propagated along the front towards the southeast and possibly merged with another cyclone during this interval. The upper-layer flows at M3 persisted through this interval as the LC front moved further over the mooring in May. In the lower-layer, the deep anticyclone in the northeast part of the study area strengthened and moved southeastward. The cyclone decayed in early May or possibly moved out of the study area towards the southeast, which was approximately in the direction of the surface LC front. The deep cyclone either moved into the study area from the east at the beginning of the event or intensified in place. The apparent growth and decay of deep vortexes without any direct connection to upper-layer forcing could be considered evidence for the planetary wave-like nature of lower-layer circulations.

The three following events in May, August and early December, respectively, at M3 had similar behavior to each other, which consisted of a northward pulse accompanied by a cyclonic rotation of the velocity vectors. In all three cases, cyclonically rotating velocity vectors were caused by an anticyclone-cyclone pair translating fairly rapidly southeastward through the array. This was again the general orientation of the surface LC front, and moorings M2 and M3 were on the northeast edge of this front. In all these three cases the cyclone – anticyclone pair appeared to propagate southeastward, intensify in the southeast corner of the mooring array and possibly decay in place. There was an intriguing consistency with the surface layer LC flows, because the deep cyclone tended to follow and remain locked to an upper-ocean high.

An event at the end of December had very similar characteristics, for both upper and lower layer flows, to the event in April. The LC and an incipient LC eddy extended to the northwest, and a fairly stationary cyclonic frontal eddy dominated the upper-layer flows in the study area. This cyclone was larger and more vigorous than the one in April-May. The lower layer flows at M3 and M4, and to a lesser extent at M2 were dominated by a cyclone, which, similar to the event in April, intensified in place and then decayed while moving out of the study area towards the southeast. At the same time, the deep anticyclone to the north began to strengthen. The deep strong northward flows at L7 that began in the middle of December appear to be unrelated to the deep circulations in the study area during this event.

The final event occurred in the middle of January 2006. At the time a LC eddy was still attached but had moved westward, and the study area moorings were primarily on the northern side of a cyclonic frontal eddy. In the lower-layer however, a cyclone and anticyclone were in the reversed positions with the cyclone to the northeast of the anticyclone, which produced large northeast flows at M2. The deep cyclone may have moved in from the west and intensified. The deep eddy pair began to move southwards just before the end of the data records.

The common characteristics of these events were the presence of deep high and low pressure centers with separation length scales of ~ 50 to 100 km that intensified and decayed while propagating south or southeastwards in the general direction of the overlying front along the east-side of the LC. Lower and upper layer streamlines invariably crossed at right angles during the more energetic lower-layer events. The significance of this is not clear at present.

Kinetic energy spectra was computed for the lower-layer currents. The M1 spectra show very low energy and have very little in common with the spectra from the moorings located further south. M2, M3, and M4 have a prominent spectral peak at 20 days, while M3 and L7 also have energy at longer periods with peaks at 30 to 35 days. M2, M3 and L7 show bottom intensification at the depth levels deeper than 1000 m, whereas at M4 the fluctuations are essentially depth independent through the 100 m separation of the measurements. Therefore, except for M1, the lower layer signals have spectra characteristic of TRWs. Low frequency near-bottom EKE increases towards the west and south from M4.

TRW wavelengths were estimated by calculating the frequency domain EOF modes for the records at 100 to 500 m above the bottom for moorings M2, M3 and M4. Based on the spectra, two frequency bands were analyzed. In the M2, M3 and M4 moorings, the highest 60-day energy was at M3 reflected by mode 1. The wavelength calculated from the phase differences was 162 km, which was within the range of previously derived estimates in the deep GOM (Hamilton 1990; 2007). The direction of the major axes of the 1st mode ellipses indicated that phase propagation was south or southeastwards and thus corresponded to the propagation direction of the deep eddies described earlier. The second mode was barely significant and the derived wavelength was larger than expected, suggesting that this weak signal was not a propagating wave.

TRW ray tracing from the full dispersion relation showed that a TRW could reach the upper escarpment in about 40 to 45 days, but the region of impact was an area of low energy as measured by the earlier study. However, if the ray is moved slightly southward so that it favors the larger fluctuations at M3, then it is apparent that the EGOM region could potentially supply some energy to the northern part of the high EKE region below the escarpment. Southward displacement of the ray could also be caused by the westward mean flow along the escarpment; this effect was not included in the ray tracing calculations conducted here.

The EOF analyses of wavelengths were also conducted for 20 to 25 day periods. For the EGOM moorings, the first two modes were significant and the directions of the major axes of the ellipses at M3 and M4 implied that energy was propagating up-slope (mode 1) and down-slope (mode 2). With the estimated wavelengths from the phase analysis, the ray tracing produced two similar ray paths towards the escarpment because the down-slope ray was reversed by the topography. The backward ray paths were also similar and pointed to the M1 location, which had very low energy in this frequency band. This implied again that the generation zone was fairly local to the deeper parts of the study area. The 25-day forward ray paths implied that the EGOM moorings could be an upstream source for the relatively weak fluctuations at the shallower eastern end of the escarpment. Transit times would be in the range of ~ 12 to 15 days.

The wavelet power spectra were calculated for the cross (*u*) and along (*v*) isobath components of the 2500 m currents at M3. The results indicated that there was significant variance at shorter periods in the *u*- than the *v*-component, and that the *v*-component dominated at longer periods. This was expected from the dispersion relation for TRWs, because the principal major axis of the fluctuations rotates from across to along isobaths as the wave period increases. This further confirms that the lower-layer motions in the study area are dominated by TRWs as such a pattern would not be expected from translating eddies.

The analyses also showed that the fluctuations were intermittent but that times of significant power occurred throughout the summer (May through August, 2005) when the LC was extended to the northwest and Eddy Vortex was undergoing a sequence of detachments and reattachments. After the final separation and the rapid translation of Eddy Vortex to the west at the beginning of September, the power decreased below the 95% significance levels, particularly at shorter periods, suggesting that the presence of the LC or a LCE over the study area had a direct influence on the amplitudes of the lower-layer TRWs.

Vertical Coupling

Establishing relationships between observations of upper and lower circulations in the deep GOM has proved to be difficult over the years. Generally, currents above 800 m and below 1200 m have not been correlated at significant time scales. There have been occasional intriguing events where flows appear to be similar through the whole water column; however, they were not long lasting and generally quite rare.

To further evaluate potential vertical coupling between the upper and lower layers, several analyses were undertaken. First, a complex empirical orthogonal function (CEOF) analysis was utilized similar to that employed on just the deeper currents. Time domain CEOFs were used rather than frequency domain EOFs because the 1-year time series of upper-layer currents does not resolve the ~ 6 to 18 month fluctuations of the LCE shedding cycle. Another approach using dynamical normal modes, which are a theoretical decomposition of current profiles based on the vertical profiles of the Brunt-Vaisala (buoyancy) frequency, was also used. This analysis has many similarities to the purely statistical CEOFs. A limitation of dynamic modes is that the bottom is assumed to be level, and this precludes any bottom intensification of the currents.

Initially upper and lower layer CEOF were calculated for 6 levels of demeaned currents in each the upper and lower layer at M3, with the 987 m level being common to both. The first CEOF mode for each layer accounted for > 90% of the total variance of each set of 6 records. The upper-layer mode was strongly sheared, and approximately unidirectional with the principal axis directed approximately north – south. The 987 m level currents were only weakly coherent with the mode. The lower-layer currents were highly coherent with the lower-layer mode 1 from 1000 m to the bottom. The mode CEOFs were unidirectional, with the principal axes being more along the isobaths trending southwest to northeast, and showed an increase in amplitude towards the bottom.

The complex mode 1 amplitude time series (normalized to unit variance) of the upper and lower layers shows the observed 40-HLP currents at one upper and two lower layer measurement depths at M3. The upper and lower layer modes closely resembled the observed currents from the upper layer (179 m) and lower layer (987 and 1985 m), respectively. The two-layer CEOF analysis thus indicated that there was minimal connection between the modes that account for > 90% of the variance in each layer.

Currents at 983 m and below were highly coherent with mode 1. The correlations then decayed towards the surface. This mode did indicate that some of the signal above 1000 m was attributable to TRW motions.

Mode 2 was primarily surface intensified and was clearly similar to the upper-layer mode 1. However, it also had a weak almost depth-independent expression, in the opposite direction below 1000 m, that had small, barely significant correlation coefficients. The zero crossover point was at about 800 m, and this mode closely resembled the dynamical normal mode 1. The lower layer had a small contribution from upper-layer LC or eddy fluctuations through dynamical coupling, just as the upper layer had a small contribution from TRW flows decaying upwards through the water column. Therefore, the separate layer and full water column CEOF velocity modes were essentially equivalent and indicated only very weak interactions.

Analyses of the CEOF velocity modes for M1 and M2 generated similar results of the interactions of the upper and lower layers as occurred at M3.

Potential vorticity (*PV*) of the upper and lower layers was calculated from the current measurements at M1, M2, and M3. Layer thicknesses were estimated by averaging isotherm depths, calculated by linear interpolation between temperature sensors at M1, M2 and M3. Only two layers were considered: between the surface and the 8 °C isotherm, and between the 8 °C isotherm and the bottom. The depth of the 8 °C isotherm was used to delineate the lower parts of the LC eddies.

The relative vorticity was at a maximum near the surface and decreased with depth through the upper layer. It then showed a slight increase towards the bottom, similar to the vertical profile of velocity variances. There was some correspondence between the lower and upper layer peaks in relative vorticity, indicating a connection that was not apparent in the velocity fluctuations.

For the most part the 8 °C isotherm lies between 400 and 750 m where relative vorticity has smaller magnitudes and showed the expected relations with deep and shallow excursions corresponding to anticyclonic and cyclonic flows, respectively. The mean relative vorticity in both the upper and lower layers was positive. In the upper layer the relatively large mean value was a consequence of the array being on the east and cyclonic side of the LC front for most of the study interval, as well as from the frequent passage of cyclonic frontal eddies.

The upper and lower layer vertically averaged relative vorticities were significantly correlated though some of the correlation was caused by the upper layer relative vorticity leaking below the 8 °C isotherm depth. There was significant coherence at TRW frequencies in the 20 to 35 day period band, with the upper layer lagging the lower layer by $\sim 90^\circ$, that was suggestive of baroclinic instability mechanisms (McWilliams 2006).

Time series of potential vorticity anomaly (*PVA*; potential vorticity with stretching effect, sometimes defined as the Sverdrup *PVA*) and its constituent terms (relative vorticity and stretching) were calculated for both layers. For many events the stretching term dominated (e.g., the warm and cold eddy events in May-June and October-November, respectively), and because the stretching terms were inversely correlated in the two layers, this contributed to the overall coherence of the total *PVA* of the layers. However, there were other events when the stretching was weak and relative vorticity dominated the total *PVA* (e.g., the events in March-April, and at the beginning of August and the middle of December).

An analysis of potential upper and lower layer coupling was also performed using primarily the PIES data. The array-averaged EKE for the upper (surface) and deep (2500 m) layers did not indicate a direct one-to-one correspondence between the major surface and deep energetic current events. To help elucidate potential vertical coupling between the layers during any of the higher energy events, the lower-layer potential vorticity was analyzed.

The resolution of the PIES and moorings array allowed investigation of both the advective and tendency terms in the deep potential vorticity budget. The mean and standard deviation of the lower layer potential vorticity, layer thickness, and relative vorticity were therefore computed. Lower-layer potential vorticity exhibited maximums along the northwestern edge of the array, whereas the largest fluctuations of potential vorticity occurred along the southwestern edge of the array which is coincident with the location of the largest fluctuations in lower-layer thickness. Lower layer relative vorticity exhibited the largest variability in the southern portion of the array where the Rossby number reached maximum values near 0.28 during strong cyclonic events and varied from -0.12 to 0.28.

The contributions of lower layer stretching and relative vorticity were investigated. Both thickness and relative vorticity variability contributed to the local rate of change in the total potential vorticity. The potential vorticity associated with one of the energetic deep circulation events showed that cyclone's potential vorticity was nearly constant, while its relative vorticity and thickness increased over time. Thus the production of relative vorticity was balanced by lower-layer stretching as the cyclone propagated southeastward into deeper water. The thickness increase was due almost entirely to the change in ocean depth as the feature propagated to the southeast. The depth of the thermocline showed no discernable increase over time. The cyclone spun up over time as a consequence of its propagation into deeper ocean depths. This result was similar to two other events.

EOF analysis was also conducted on the current meter data in a manner consistent with previous studies (Nowlin et al. 2001). The results of the EOF analyses of the current measurements from this study affirm that the horizontal current structure in this region of the Gulf resembles a 2-layer system. The eddy field causes intensification of the surface currents, which exponentially decay in magnitude with depth to ~ 800 meters. This structure is observed in the Mode 1 amplitudes, which contains the largest percentage of variance (~ 80 - 95 %). This mode shows maximum amplitudes at the surface that decrease with depth to nearly zero below 1000 m. The dynamic effect of eddies are rarely seen below 800 m.

Mode 2 explains the second largest percentage of variance. In general, the amplitude crosses zero near 200 meter depth and is nearly constant or gradually increasing with increasing depth. During deployment 1, the amplitude of Mode 2 at mooring M1 shows a mid-water maximum 300 and 1000m. The structure of this mode, however, is more similar to the vertical structure found in Mode 3 at moorings M2 and M3. Further, the percentage of variance in the second and third modes increases from M1 to M3, indicating more variance in the higher order modes closer to the Loop Current. During the second deployment, Mode 2 at mooring M1 again resembles higher order modes at M2 and M3. However, the percentage of variance in modes 2 and greater is a maximum in the east-west velocity component of mooring M2 and generally greater during deployment 2 than deployment 1.

The vertical structure of Mode 3 is more complex with two zero crossings typically in the upper 1000 m and relatively constant in water depths below 1000 m. The amount of variance contained in this mode is a small fraction of the current variance (< 4 %).

Stability profiles were derived from temperature and salinity (CTD) data from hydrographic data collected adjacent to mooring sites M1, M2, and M3. The CTD data were used to calculate vertical buoyancy modes that represent the mean horizontal current structure at the three mooring locations. Vertical profiles of Brunt-Vaisala frequency for the three EGOM hydrographic cruises were computed in which a maximum occurred between 100 - 200 m during the winter and near the surface (< 20 m depth) during the summer.

Dynamic modes calculated from CTD casts at (or closest to) the mooring sites during the three cruises were used to create a normalized set of modes to fit to the velocity measurements. The barotropic mode was simply equal to one throughout the water column. First and second baroclinic modes had similar shapes at each mooring. The first mode crossed zero around 600 m; the second mode crossed zero twice, around 200 and 900 m. Below 1200 m all modes were barotropic, i.e., nearly constant with increasing depth. The general shape of these modes was the same for each deployment. The relative amplitudes were nearly identical; the principal difference between casts was the depth of zero-crossing of the modes.

The temporal variation of the barotropic and first two baroclinic modes were estimated using a least squares minimization that fits the calculated set of vertical modes to synoptic vertical profiles of the moored ADCP and single-point current meter data. Three modes were used in the least squares fit. Generally, the barotropic time series amplitudes were significantly smaller than the baroclinic amplitudes at all moorings for both velocity components during both deployments.

As found previously in the EOF analysis, most of the variance in the observed velocity data can be explained by a surface trapped mode that decays exponentially with depth. Therefore, we expect that the temporal amplitudes of the first baroclinic mode to be large and to indicate the presence of surface trapped, i.e., eddy related, motions. The amplitudes of the second dynamic mode were more variable, i.e., possessed higher frequency motions, than the first baroclinic mode and were small relative to the amplitudes of the first baroclinic mode.

During the first deployment, the east-west velocity amplitudes were mostly positive, i.e., eastward, because of the location of the mooring relative to the location of the northeastern edge of the LC. In general, mode amplitudes were greater during the first deployment, as more surface intensified, high-speed current eddy events were encountered in the spring and summer of 2005 than during the fall and winter of 2005–2006. The high correlation between mode 1 amplitudes and CTD pressure records, which fluctuated due to mooring draw down, were also validation of the first baroclinic mode amplitudes as indicators of eddy activity in the EGOM.

Spatial correlation at every sample time between observed and modeled velocity from the least squared fit of dynamic modes showed that when the first baroclinic mode amplitudes were close to zero, the correlation was poor. The low correlation could possibly indicate times of relative quiescence in the wake of eddies.

Two types of model utility tests were performed on the modal fit to the observed currents in the space domain. The first test utilized the F statistic to assess whether a useful relationship between the observed data and any of the modal predictors existed. The goodness of the fit test confirmed that the barotropic and at least one of the baroclinic modes are necessary to the regression approximately 80-90 % of the time. The second statistical test is an inference for a single mode coefficient, which determines if a certain mode needs to be included in the fit. This test indicated that the first baroclinic mode was the only mode necessary to explain the current structure at moorings M1, M2, and M3 during most of their deployment; however, the second baroclinic mode was necessary to the fit of velocity data during portions of the deployments, and particularly to the data collected at mooring M3 during periods within its second deployment.

Power spectra and autocorrelation functions were generated for the dynamic mode time series using FFT methods. The results from these analyses were consistent between data from each mooring deployment. Spectra for mode fits to u and v velocity exemplified a typical energy and enstrophy-conserving velocity spectrum, with an energy cascade in the red direction, i.e., from high to low frequencies. The barotropic amplitudes exhibited less energy than the first baroclinic modes at low frequencies. The second baroclinic mode spectra are nearly white (constant) at frequencies less than 1 cpd.

All of the above analyses and results provide an intriguing but limited view of the dynamics and coupling between the upper layer and deep circulation features. The results are highly suggestive of upper and deep layer coupling under certain conditions not yet well understood.

Conclusions

Prior to the study, the study team had a significant concern if the eastern GOM would experience any sizable current energetics. The primary conclusion from the study is that the eastern GOM is a very active region in terms of circulation, especially when the LC or an LCE is present. The circulation characteristics of the region are very similar to those in the north-central GOM when similar processes are at work, whether they be the presence of the LC, and LCE, frontal features, or major storms. Significant advancement in the understanding of the circulation in the eastern GOM was achieved including:

- Extended LC intrusion significantly impacted the study area upper ocean circulation during the first half of the EGOM program. Once Eddy Vortex finally separated, fewer LC or frontal features impacted the circulation and the character of the circulation returned to conditions more typical for this region.
- Cyclones are an important dynamical component of the general circulation of the GOM and significantly impacted the study region during the program.
- Comparisons were drawn between the mean surface circulation over the first six months of measurements versus the last six months. The mean for the first six months revealed southeast flow from the presence of Eddy Vortex while the last six months had comparatively weak circulation.
- The PIES array captured the mesoscale frontal meanders along the periphery of the LC and while well resolved provided a limited window.

- Cyclonic events occurred more frequently than anticyclonic events in the EGOM vorticity record.
- Currents during both deployments at all three tall moorings showed a high degree of coherency at water depths above 500 m, with weaker coherence extending down to 750 m, and with only occasional coherence at deeper depths.
- Large amplitude inertial oscillations are evident immediately after the passages of Hurricanes Katrina and Rita. These current oscillations persisted for at least two weeks after the passage of these storms.
- The passage of Hurricane Katrina near the study's moorings while a cyclonic (cold core) eddy was sitting over the southern portion of the study area, is believed to have generated stronger than normal currents.
- In general, spectral energy was greatest in the shallow ocean depth (<300 m). Surface records (~ 50 m) contained larger weather-band variance than deeper records.
- The extrapolated near-bottom current speeds at M1 near the Florida Escarpment were no larger than those at M3 on the abyssal plane. This was an interesting contrast to near-bottom currents near the Sigsbee Escarpment farther west, where bottom currents were much stronger in proximity to the Escarpment.
- The lower-layer motions in the study area are dominated by TRWs. The presence of the LC or LCE over the study area had a direct influence on the amplitudes of the lower-layer TRWs.
- Deep circulation experiences TRW packets, though generation of TRWs that translate into the north-central GOM do not appear to be generated in this region. TRW generated currents are also not affected significantly by steep bathymetry in this region.
- The lower layer had a small contribution from upper LC or eddy fluctuations through dynamical coupling, just as the upper layer had a small contribution from TRW flows decaying upwards through the water column.
- The horizontal current structure in this region of the Gulf resembles a 2-layer system. The eddy field causes intensification of the surface currents, which exponentially decay in magnitude with depth to ~ 800 m., while the lower layer was influenced primarily by TRWs propagating through the region.

Recommendations

The one year measurement program in the eastern GOM was judicious in timing in that it caught significant penetrations of the LC and an LCE into the region, as well as multiple large storms. The study region, however, was actually fairly small, and fairly limited in measurement locations, to extrapolate the study results to a much larger portion of the eastern GOM. The primary recommendations for future studies to further assess the larger eastern GOM circulation features, and to better explore the dynamics and interactions of the water column with the LC and its eddies, are as follows:

- Conduct a larger-scale circulation study of the eastern GOM spanning more of this area to better assess the geographic extent of the circulation and processes found during this study.
- Conduct in-situ measurements at both small (25km) and large (50-100km) scales so as to observe currents over a wider area, yet maintain the ability to calculate vorticity, coherence between measurement sites, and to assess the small scale interactions at the edges of the LC and LCEs which are imparting significant energy into the water column.
- Add gliders so as to better map hydrography changes in critical areas, such as the LC and LCE edges, and so as to provide hydrography measurements over much longer time scales than can be achieved by hydrography cruises using CTDs and XBTs.
- Concentrate a set of moorings in the path of, and at the boundaries of, the LC and LCEs, as best as they can be positioned, to improve understanding of the frontal features and how they affect and control LC movements and eddy shedding.
- Continue to employ remote sensing (satellite measurements) in future studies, as these provide such a great basis of understanding of the features that affect specific in-situ measurement sites.
- Conduct coordinated programs geographically to obtain measurements in the southern portion of the LC as well as the northern portion so as to better understand what drives and controls its northward intrusions and southward retractions.
- Conduct coordinated programs with other institutions, in particular those institutions conducting oceanographic measurements of major storms, so as to make use of their fast response measurement capabilities in front of the storms.
- Finally, keep funding quality research in the GOM.

1.0 INTRODUCTION AND OBJECTIVES

1.1 *Background*

The major source of energy forcing currents in the surface waters of the Gulf of Mexico is the Loop Current (LC) which flows northward through the Yucatan Channel into the Gulf of Mexico, and then turns eastward and exits through the Straits of Florida to join the Gulf Stream. The LC varies in its penetration into the Gulf of Mexico, sometimes constraining itself to the southern Gulf, and sometimes penetrating far northward into the northern Gulf. During most periods when the LC has penetrated northward, cold core eddies and warm water filaments can be found migrating around its periphery. Often when extended far northward, the LC pinches off, forming a Loop Current Eddy (LCE) that migrates through the northern Gulf, eventually moving westward to die within its western regions. LCEs detach from the LC at periods ranging from 3 to 17 months, with a mean frequency of separation near 10 months (Sturges and Leben 2000). Very energetic LCEs interact with one another, the LC, and bathymetry, forming cyclonic eddies with which they also interact. There are times, however, that the LC retreats southward without shedding an eddy.

All this activity by the LC, LCE's, and associated features, imparts significant energy to the surface waters of the Gulf of Mexico. While the overall net circulation of the surface waters in the Gulf of Mexico based on drifter records is generally understood to be a clockwise circulation pattern around the basin (DiMarco et al. 2005), the magnitude of the velocity and variance of the surface currents are known to be greatest in the vicinity of the Loop Current, where speeds often exceed 1.5 m s^{-1} .

The other main source of energy to surface waters are winds generated by strong storms and hurricanes. Tropical storms and hurricanes provide the greatest storm-related energy, and primarily occur during summer and fall months.

In deeper waters of the Gulf of Mexico, previous studies (Hamilton 1990; Donohue et al. 2006) have identified energetic, deep, barotropic (below about 1000 m) motions with some indications of bottom intensification at various locations on the slope and rise of the North-central Gulf, particularly along the Sigsbee Escarpment. With pseudo-periods of 10 d or more and amplitudes up to $1 \text{ m}\cdot\text{s}^{-1}$, the phenomena responsible for these motions are generally attributed to topographic Rossby waves (TRWs).

In general, little coupling of upper and lower layer circulation in the Gulf of Mexico appears to occur. However, some instances have been observed in other observation programs. Also, the modeling studies of Sturges et al. (1993), Inoue and Welsh (1997), and Welsh and Inoue (2000), and the CUPOM (University of Colorado Princeton Ocean Model) output suggest that deep cyclonic (anti-clockwise) and anti-cyclonic (clockwise) eddies form in the Eastern and Central Gulf and propagate into the Western Gulf guided by topography. Some modeling results (Welsh and Inoue 2000) suggest that an anticyclone/cyclone pair form in the lower level in response to an anti-cyclonic LCE in the upper layer.

Recent Minerals Management Service (MMS) studies have investigated the circulation features and their characteristics and vertical variations over the coastal shelf off Texas and Louisiana (Nowlin et al. 1998a, Nowlin et al. 1998b), and in the deeper waters of the central (Donohue et al. 2006) and western Gulf of Mexico (Donohue et al. 2008). These regions are shown in Figure 1.1-1. A lack of current measurements and understanding of the circulation in the deep northeastern Gulf of Mexico prompted the BOEMRE to develop and fund a study titled: *Survey of Deepwater Currents in the Eastern Gulf of Mexico*. In July 2004 a contract was awarded to Evans-Hamilton, Inc. (EHI) and its science team to perform this study. This study is part of a larger research effort by the Minerals Management Service to gain a better understanding of the surface and deep dynamic processes in the Gulf of Mexico (GOM).

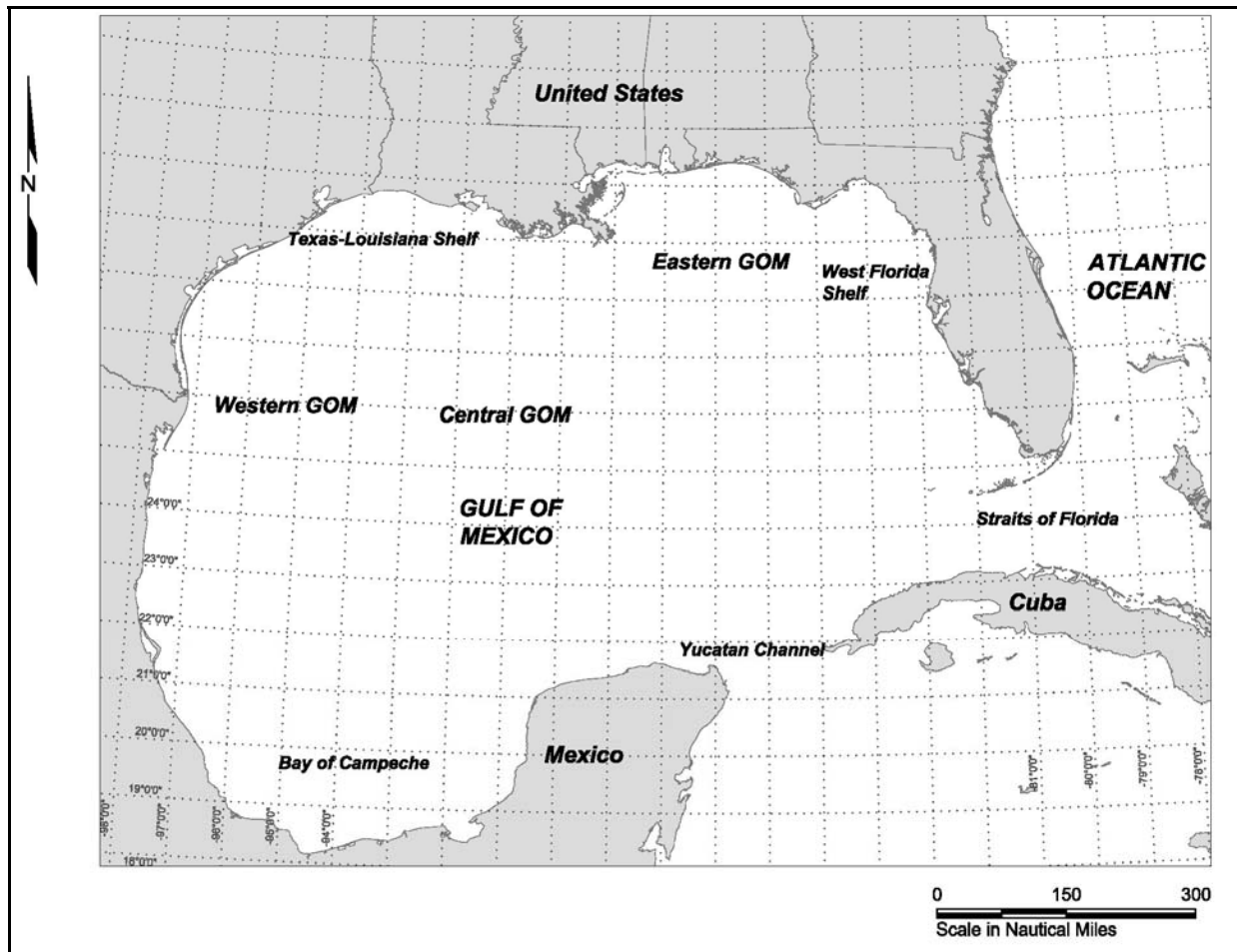


Figure 1.1-1. Locations of the BOEMRE Gulf of Mexico regions and other major features of the Gulf of Mexico.

1.2 Study Area

The study area is located within the Eastern GOM (Figure 1.2-1). This area consists of the area of the Eastern Gulf Lease Sale 181. The study area is located south of Mobile Bay in water depths ranging from 2000 to 2800 m, and is bounded approximately by the following coordinates:

NW Corner:	28.848 °N, 87.918 °W	NE Corner:	28.850 °N, 87.523 °W
SW Corner:	27.453 °N, 87.907 °W	SE Corner:	27.455 °N, 87.516 °W

Bathymetrically, the area is bounded as follows.

To the north: by the ~2000 m isobath, & by a slope incised by hills & valleys
To the east: the northern half by the steep slope of the West Florida Escarpment
To the east: the southern half by a flat plain at 2500-2800 m depth
To the south: by a relatively flat featureless plain
To the west: by a slope with isobaths directed NNE to SSW

Key bathymetric features of the study area include that the:

- Area lies to NE of Sigsbee Escarpment, and SW of the DeSoto Canyon.
- Area contains primarily NNE to SSW oriented isobaths, rather than E-W isobaths
- Area contains the farthest northward extent of the 2000 m isobath in the Gulf of Mexico, plus NNE of the study area is located the farthest northward extent of the 200 m isobath. As a result, the area provides the best opportunity for the most northerly penetration of the LC or a LCE within the Gulf of Mexico.
- Area surrounding the study area has the largest separation between the 2000 and 3000 m isobaths within the Gulf of Mexico. This area is a large, relatively flat area.
- The West Florida Escarpment intersects the eastern boundary of the study area at ~ 28.4° N, or approximately one-third the distance from the NE to the SE corners of the study area.

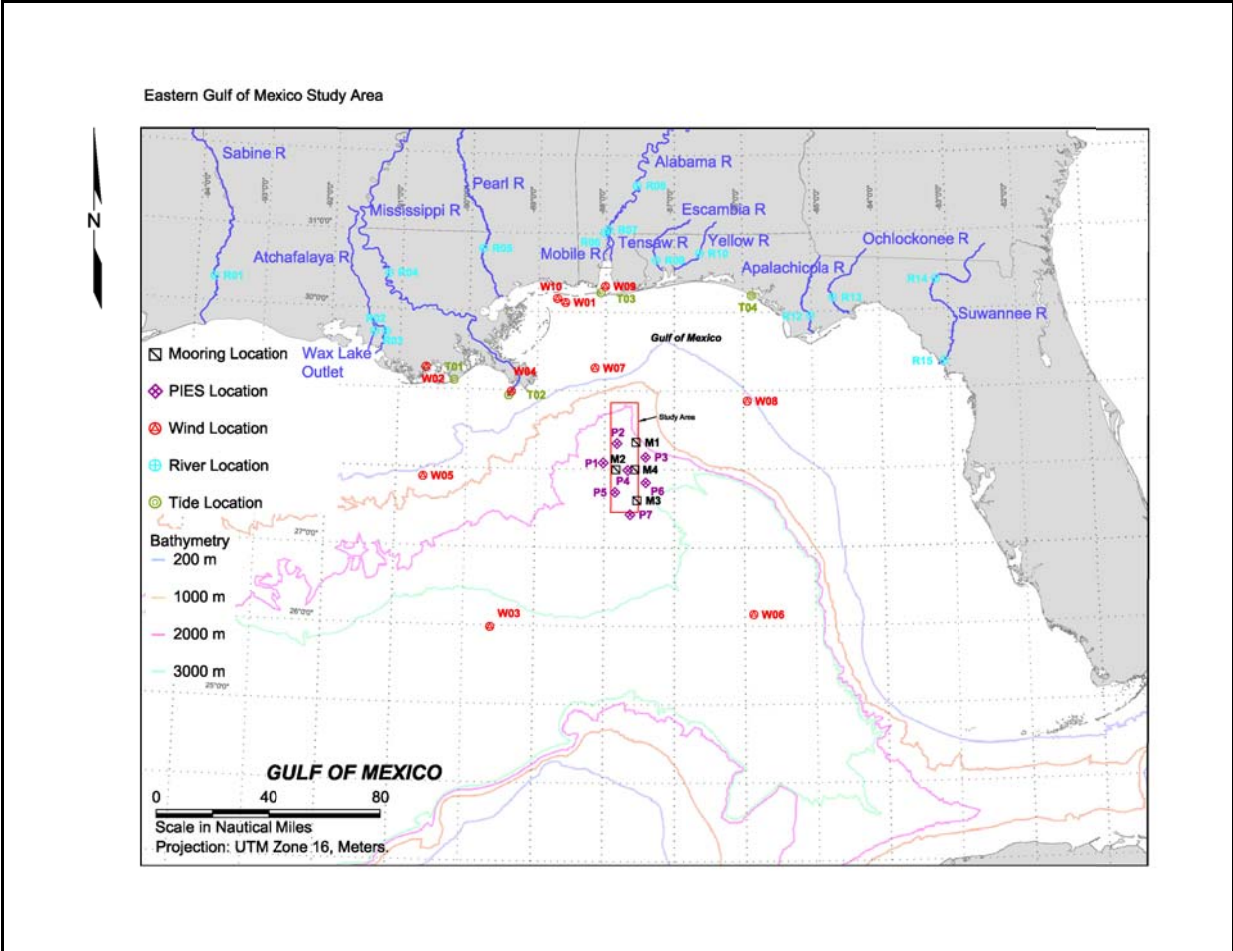


Figure 1.2-1. Map of the study area (outlined in red) including locations of moorings M1, M2, M3 and M4 in black, and PIES in purple. Ancillary data set locations are marked for wind gauges (red), river discharge and flow gauges (blue) and tide gauges (green). Major rivers that drain into the Northern Gulf are also marked.

1.3 Study Approach

The study called for a one-year measurement program to collect an integrated set of current, hydrography, remote sensing, and ancillary measurements that could provide an excellent understanding of the circulation processes in the area. The one-year measurement period allowed for observations across all seasons, as well as potentially capturing the effects of some tropical storms or hurricanes. As a result, from January 2005 to January 2006 one year of current measurements were collected from four moorings in water depths from ranging from 2500 to 2800 m. The moorings also contained measurements of water temperature and conductivity in the upper 500 m. The mooring measurements were supplemented with measurements from bottom-moored PIES, three hydrography (profiling CTD and XBT) cruises, and satellite imagery and altimetry. Eddy Watch, a proprietary operational oceanographic product that tracks, maps, and forecasts the LC and its eddies, along with drifting buoy data used in the Eddy Watch analysis, were obtained from Horizon Marine, Inc. for the period of the study's measurements, and utilized under a limited license for additional analyses of the characteristics of the LC and LCE's. Publicly available river discharge data, coastal and offshore wind data, and coastal water level data during the measurement period were also obtained as ancillary data.

The current measurement moorings consisted of three tall (M1, M2, & M3) and one short (M4) moorings (Figure 1.2-1). The tall moorings were full water column moorings designed to reach within 70 m of the surface. The short mooring was 250 m tall, and was designed to provide additional near-bottom current measurements. The current meter moorings were deployed from January 2005 to January 2006, with servicing of the moorings occurring in August 2005 just a few days prior to the arrival of hurricane Katrina. The tall moorings contained upward-looking 75 kHz ADCPs at 500 m depth, with single point current meters spaced at intervals from 750 m to near bottom.

PIES measurements were obtained from seven locations (Figure 1.2-1). The PIES were deployed in December 2004, interrogated in August 2005 plus additional PIES added to the array, and recovered in January 2006.

In positioning the moorings and PIES, the approach was taken to place at least one tall mooring as far south as possible within the study area so as to maximize the potential for the LC, its frontal features, or an LCE to impact the mooring. Positions of the other two tall moorings were selected to maximize coverage of the study area while maintaining scales and a triangular configuration to conduct along and across isobath coherence and vorticity analyses. The northern tall mooring was also positioned to assess the potential intensification of the current along the Florida Escarpment. PIES were positioned surrounding and within the moorings to as to provide a more regional perspective on the conditions affecting the moorings. Positioning of the moorings and PIES, as well as the hydrography stations, was intended to provide an ability to conduct both regional (50-200 km) as well as smaller scale (10-25 km) analyses.

Hydrographic measurements consisting of CTD casts and XBT profiles were collected in January and August 2005, and January 2006 during mooring deployment, servicing, and recovery cruises. The hydrographic measurements were targeted to capture interesting loop current, eddy, or other related features affecting the study area. The final hydrographic survey was targeted to capture small scale interactions between the edge of a Loop Current Eddy (LCE) and a Cold Core Eddy (CCE) that lay over a portion of the study area.

To help place the study's measurement data in perspective, ancillary coastal wind and runoff data were obtained from the National Climatic Data Center (NCDC), National Data Buoy Center (NDBC), and from the US Geological Survey for the sites shown in Figure 1.2-1.

1.4 Study Objectives

The goal of this study was to investigate and document the deepwater circulation in the Eastern GOM. This is an area of sparse previous deepwater current measurements. Specific study objectives were to:

- Conduct measurements of currents using moorings to increase the regional database of ocean currents in the Eastern GOM.
- Improve the scientific community's overall knowledge and understanding of circulation features in this deepwater area.
- Collect hydrographic, remote sensing, and other relevant measurements useful to understanding what controls the region's circulation.
- Assess the key processes energizing the circulation.
- Add to the database of LC and LCE characteristics, and how these features affect the study area.
- Establish an improved base of knowledge to help design future circulation studies in this part of the GOM.
- Provide measurements and knowledge which could assist with future calculations of horizontal and vertical trajectories of released oil and its dispersion.

Anticipated key circulation processes in this area included:

- Loop Current (LC) intrusions Loop Current Eddy (LCE) dynamics LCE frontal features including cyclonic and anti-cyclonic eddies
- Eddy-topography interactions
- Potential TRW genesis and propagation
- Potential deep cyclone and anti-cyclone pairs
- Interactions between upper and lower layers
- Response to hurricanes and storms

The data acquired by this study was used to look for and better understand the key processes listed above as they occurred within or affected the circulation within the study area.

1.5 Study Team

The Science Team Principal Investigators (PIs) for the study, listed below along with their primary areas of responsibility for this project, all have conducted research and analysis of the circulation of the Gulf of Mexico for several years. Drs. Peter Hamilton, Robert Leben, Kathleen Donohue, and Randolph Watts have participated in recent MMS studies of the deep central and western GOM, and were selected to provide continuity of their past work to the planning and analyses performed for this study. Dr. Steven DiMarco led the compilation and analysis of all available current measurements in the GOM for MMS (Nowlin et al. 2001), and was selected for his overall understanding of the circulation features within the GOM. Dr. George Forristall was a Senior Oceanographer at Shell Oil Company who studied extreme and operational oceanographic conditions within the GOM, and was selected to provide his knowledge and an oil industry perspective to the science team.

All PIs contributed to the design of the study, analyses of the measurements and remote sensing data, and participated in the writing of this report. Extensive collaboration occurred between PIs, both during planning of the study and during analysis of the measurements resulting from this study. The primary data sets they utilized and the focus of their analyses were as follows:

Remote Sensing:

Dr. Robert Leben, University of Colorado, Colorado Center for Astrodynamic Research (CCAR) – Dr. Leben acquired and provided the remote sensing products to the study team for this project. His focus was on the analysis of the movement and characteristics of the Loop Current, LCEs, and LC frontal features, and in placing the characteristics of these features during the study period into historical perspective.

In-Situ Current and Hydrographic Measurements:

Dr. Steven DiMarco, Texas A&M University – Dr. DiMarco’s focus was on the analysis of the upper Gulf of Mexico circulation features, and coupling of the upper and lower layers.

Dr. Peter Hamilton, SAIC – Dr. Hamilton’s focus was on the analysis of deep Gulf of Mexico circulation features.

Dr. George Forristall, Forristall Ocean Engineering – Dr. Forristall’s focus was on the kinematics of LCEs, the analysis of current extremes, and the analysis of storm-induced inertial oscillations.

PIES:

Dr. Kathleen Donohue and Dr. Randolph Watts, University of Rhode Island – Dr. Donohue and Dr. Watts’ team conducted the PIES measurements. The focus of their analysis was on the PIES data and geostrophic flow patterns.

Program Management Team:

In addition to the Science Team PI’s, the following personnel led the organization and conduct of the project:

Mr. Jeffrey Cox, EHI – Program Manager
Mrs. Carol Coomes – Assistant Program Manager, Data Manager
Mr. Keith Kurrus and Mr. Kevin Redman, EHI – Cruise Chief Scientists
Mrs. Kari Walker, EHI – Data Processing & QA/QC Team Leader

Many additional personnel in all team member organizations contributed significantly to the performance of work conducted for this study. EHI was responsible for the preparation, deployment, servicing, and recovery of the current meter moorings for the study, along with the initial data processing, QA/QC, and preparation of final data sets for distribution to the Science Team PIs. EHI was also responsible for conducting the hydrographic cruises that were performed in conjunction with the mooring deployment, servicing, and recovery cruises. URI was responsible for the preparation, deployment, servicing, and recovery of the PIES, and all processing of the PIES data.

1.6 Report Organization

The report is organized to provide a background to the purpose and objectives of the study, the methods used and data acquired, and a description of the circulation processes identified in the upper and lower layers of Eastern Gulf of Mexico during the study period. Chapters contained within the report include:

- Executive Summary.
- Chapter 1: Introduction and objectives.
- Chapter 2: Experiment design and methodology.
- Chapter 3: Measurement results from the moorings.
- Chapter 4: Loop current events.
- Chapter 5: Upper layer circulation.
- Chapter 6: Deep circulation.
- Chapter 7: Vertical coupling.
- Chapter 8: Summary and conclusions.
- Chapter 9: Literature cited.
- Chapter 10: Appendices

2.0 EXPERIMENT DESIGN AND METHODOLOGY

2.1 Moorings

Direct measurement of current velocity of the full water column was designed to provide estimates of subinertial (low-frequency), inertial (temporal periods of about 24 hours), and superinertial (periods less than one day) band motions and oscillations. Because anticyclones separate from the Loop Current in this area and cyclonic Loop Current frontal eddies frequently may develop or pass through this region, the moorings were designed to obtain high vertical resolutions (~8 m) in the upper 500 m of the water column.

The current measurement moorings program consisted of the follow key components:

- 3 tall moorings reaching from 70 m depth to bottom at between 2600 to 2800 m depths
- 1 short mooring reaching from bottom at 2750 m depth to 2500 m depth

2.1.1 Instrumentation

Three tall (designated M1, M2, and M3) and one short (M4) moorings were deployed from January 2005 to January 2006, with servicing of the moorings occurring in August 2005 just a few days prior to the arrival of Hurricane Katrina (August 26, 2005). The tall moorings contained upward-looking 75 kHz ADCPs at 500 m depth, with single point current meters spaced at intervals from 750 m to near bottom Figure 2.1-1. The tall moorings also contained combinations of temperature, or temperature-conductivity-pressure sensors at various depths. The short mooring contained two single point current meters in the lower 100 m of the water column. The instrumentation contained on the moorings, the parameters measured, and the planned and actual depth of the instrumentation at the start of each deployment is provided in Tables 2.1-1 and 2.1-2.

2.1.2 Instrumentation and Moorings Preparation

Upon determining the final planned mooring locations and instrumentation, designs of the subsurface taut-wire moorings were initiated. The moorings were designed using a standard mooring design software package along with the same current profile representative of a LC event that was utilized by SAIC for design of the deepwater current moorings for the Exploratory Study in the North-central GOM (Donohue et al. 2006). The program permits using a variety of flotation, current meters, anchor configurations, mooring wire, and mooring hardware components to assess mooring performance under different current profile conditions. Moorings for this study were designed to:

- Minimize bending
- Minimize vertical displacement of instruments
- Ensure the moorings have sufficient anchor weight to remain in place
- Ensure if the mooring parted at any location, flotation is sufficient to bring all components to the surface once released from the anchor

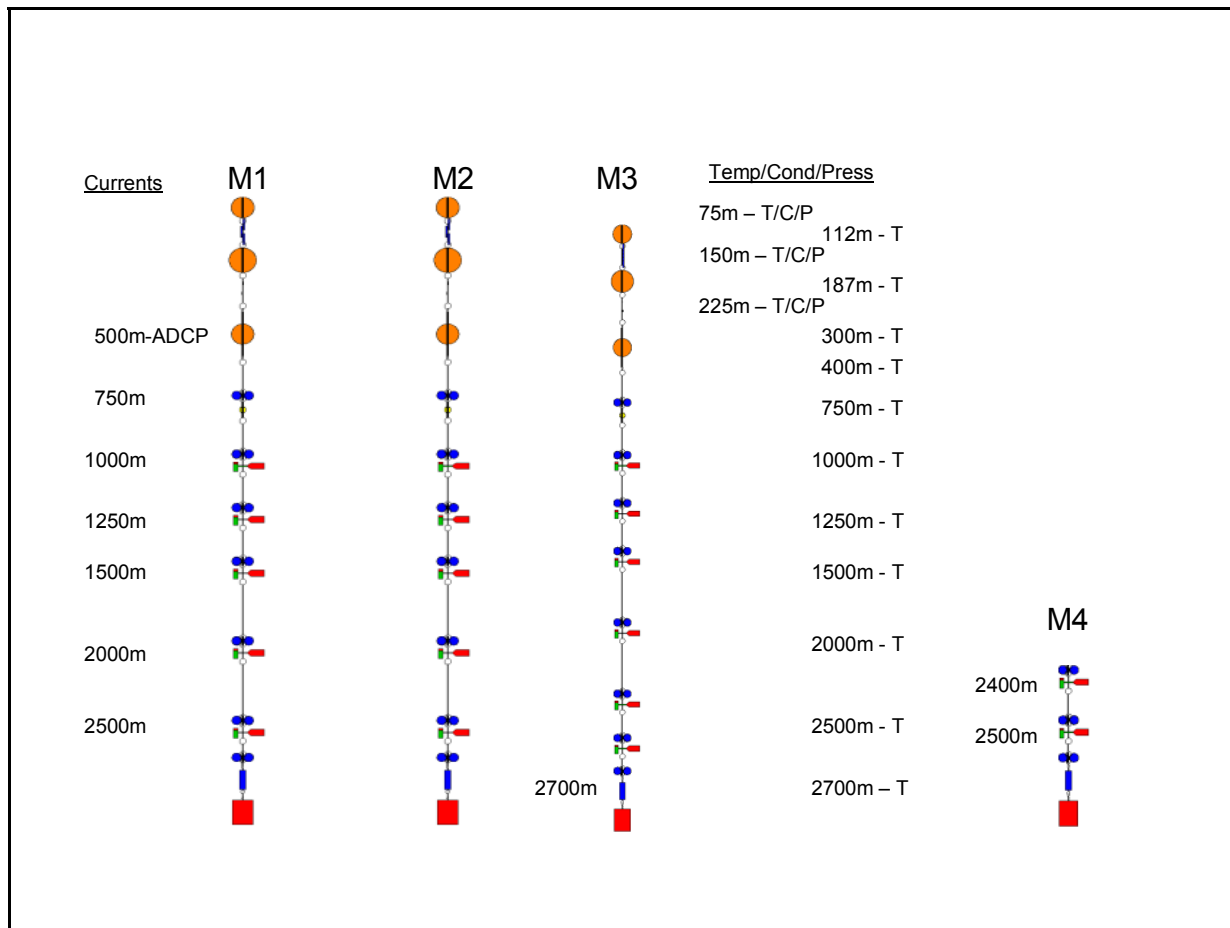


Figure 2.1-1. Design of the tall (M1, M2, and M3) and short (M4) moorings. The column labeled Currents indicates the depths of the meters for M1 – M3. The column Temp/Cond/Press indicates the depths of sensors measuring temperature, conductivity, and pressure on the tall moorings (T/C/P had all three sensors, T is only temperature).

To maximize recovery of the moorings, each mooring also included dual acoustic releases that, upon triggering either release, would release the mooring from the anchor allowing the mooring to surface. The dual releases thus provided redundancy. The top flotation buoy containing the ADCP also contained an ARGOS satellite transmitting device that upon surfacing, began transmitting its position to aid mooring recovery, especially if the mooring surfaced prematurely. A flashing light that also activates upon surfacing and aids recovery of the mooring at night was also mounted on the ADCP flotation buoy.

Table 2.1-1

Deployment locations of the moorings for Deployment 1.

Shaded instrument types had a pressure sensor. Abbreviations for measured parameters: c – conductivity, t – temperature, p – pressure, u,v – north and east current component.

	Type and Model	Serial Number	Other Sensors	Planned Depth (m)	Deployed Depth (m)
D1M1	SeaBird SBE37	59	c,t,p	75	11
	StarOddi Hugrun	c919	t	112	47
	SeaBird SBE37	2697	c,t,p	150	85
	StarOddi Hugrun	c926	t	187	122
	SeaBird SBE37	2698	c,t,p	225	159
	StarOddi Hugrun	c932	t	300	233
	StarOddi Hugrun	c933	t	400	331
	TRDI ADCP LR	4487	t,p,u,v	499	446
	InterOcean S4	7801745	c,t,u,v	749	679
	Aanderaa RCM7/8	7223	c,t,u,v	997	926
	Aanderaa RCM7/8	7692	t,p,u,v	1244	1173
	Aanderaa RCM7/8	9722	t,u,v	1492	1426
	Aanderaa RCM7/8	10053	t,p,u,v	1995	1939
	Aanderaa RCM7/8	12085	t,p,u,v	2499	2423
D1M2	SeaBird SBE37	57	c,t,p	75	6
	StarOddi Hugrun	c937	t	112	42
	SeaBird SBE37	2699	c,t,p	150	79
	StarOddi Hugrun	c939	t	187	116
	SeaBird SBE37	2700	c,t,p	225	153
	StarOddi Hugrun	c940	t	300	226
	StarOddi Hugrun	c944	t	400	322
	TRDI ADCP LR	5165	t,p,u,v	499	435
	InterOcean S4	8161753	c,t,u,v	749	676
	Aanderaa RCM7/8	7507	c,t,u,v	997	933
	Aanderaa RCM7/8	7771	t,p,u,v	1244	1189
	Aanderaa RCM7/8	12803	t,u,v	1492	1464
	Aanderaa RCM7/8	9807	t,p,u,v	1995	2022
	Aanderaa RCM7/8	12807	t,u,v	2499	2526
D1M3	SeaBird SBE37	2701	c,t,p	76	49
	StarOddi Hugrun	c946	t	113	85
	SeaBird SBE37	2702	c,t,p	151	122
	StarOddi Hugrun	c950	t	188	159
	SeaBird SBE37	2703	c,t,p	226	196
	StarOddi Hugrun	c959	t	301	269
	StarOddi Hugrun	c960	t	401	366
	TRDI ADCP LR	5699	t,p,u,v	500	479
	InterOcean S4	2129	c,t,u,v	750	713
	Aanderaa RCM7/8	12084	c,t,u,v	998	961
	Aanderaa RCM7/8	10643	t,p,u,v	1245	1208
	Aanderaa RCM7/8	9480	c,u,v	1292	1254
	Aanderaa RCM7/8	9809	t,p,u,v	1996	1945
	Aanderaa RCM7/8	12808	t,u,v	2499	2448
Aanderaa RCM7/8	12809	t,u,v	2699	2648	
D1M4	Aanderaa RCM7/8	10112	t,p,u,v	2530	2513
	Aanderaa RCM7/8	12810	t,u,v	2630	2613

Table 2.1-2

Deployment locations of the moorings for Deployment 2.

Shaded instrument type indicates it had a pressure sensor. Abbreviations for measured parameters: c – conductivity, t – temperature, p – pressure, u,v – north and east current component (current speed and direction).

	Type and Model	Serial Number	Other Sensors	Planned Depth (m)	Deployed Depth (m)
D2M1	SeaBird SBE37	59	c,t,p	75	74
	StarOddi Hugrun	c919	t	112	110
	SeaBird SBE37	2697	c,t,p	150	148
	StarOddi Hugrun	c926	t	187	185
	SeaBird SBE37	2698	c,t,p	225	222
	StarOddi Hugrun	c932	t	300	296
	StarOddi Hugrun	c933	t	400	395
	TRDI ADCP LR	4487	t,p,u,v	499	509
	InterOcean S4	7801745	c,t,u,v	749	742
	Aanderaa RCM7/8	12805	t,u,v	997	990
	Aanderaa RCM7/8	7692	t,p,u,v	1244	1238
	Aanderaa RCM7/8	9722	t,u,v	1492	1493
	Aanderaa RCM7/8	10053	t,p,u,v	1995	2011
	Aanderaa RCM7/8	12085	t,p,u,v	2499	2428
D2M2	SeaBird SBE37	2693	c,t,p	75.2	80
	StarOddi Hugrun	c937	t	112.2	117
	SeaBird SBE37	2699	c,t,p	150.2	155
	StarOddi Hugrun	c939	t	187.2	191
	SeaBird SBE37	2700	c,t,p	225.2	229
	StarOddi Hugrun	c940	t	300.2	297
	StarOddi Hugrun	c944	t	400.2	389
	TRDI ADCP LR	5165	t,p,u,v	527.3	520
	InterOcean S4	8161753	c,t,u,v	749	741
	Aanderaa RCM7/8	7507	c,t,u,v	997	1007
	Aanderaa RCM7/8	7771	t,p,u,v	1244	1271
	Aanderaa RCM7/8	12803	t,u,v	1492	1544
	Aanderaa RCM7/8	9807	t,p,u,v	1995	2097
	Aanderaa RCM7/8	12807	t,u,v	2499	2601
D2M3	SeaBird SBE37	2701	c,t,p	75.7	56
	StarOddi Hugrun	c946	t	112.7	93
	SeaBird SBE37	2702	c,t,p	150.7	130
	StarOddi Hugrun	c950	t	187.7	166
	SeaBird SBE37	2703	c,t,p	225.7	204
	StarOddi Hugrun	c959	t	300.7	277
	StarOddi Hugrun	c960	t	400.7	374
	TRDI ADCP LR	5699	t,p,u,v	499.85	487
	InterOcean S4	8111780	c,t,u,v	750	720
	Aanderaa RCM7/8	12084	c,t,u,v	997	967
	Aanderaa RCM7/8	10643	t,p,u,v	1245	1214
	Aanderaa RCM7/8	9480	c,u,v	1492	1452
	Aanderaa RCM7/8	9809	t,p,u,v	1996	1939
	Aanderaa RCM7/8	12808	t,u,v	2499	2442
Aanderaa RCM7/8	12809	t,u,v	2699	2642	
D2M4	Aanderaa RCM7/8	10112	t,p,u,v	2530	2513
	Aanderaa RCM7/8	12810	t,u,v	2630	2613

All instrumentation used on the moorings were inspected early in the program, and determinations made for whether instrumentation needed to be sent back to the manufacturers for checkout, refurbishment, and recalibration. Aanderaa single point current meters were sent to Aanderaa Instruments in Norway for factory checkout and recalibration. InterOcean S4 current meters were sent to InterOcean Systems for checkout and refurbishment. Seabird SBE37 CTDs that did not have recent factory calibrations were sent to Seabird Instruments for checkout and recalibration. All Hugren temperature only sensors were returned to Star-Oddi for factory checkout and new batteries. Four acoustic releases also were sent to Benthos for checkout and refurbishment prior to use.

After return of the instruments, and prior to shipping to the vessel mobilization site, all instrumentation was inspected, prepared, and run through standard pre-deployment checkout procedures, including tests in water in EHI's test tank. All instrumentation and mooring components were then packed up and transported to the Louisiana Universities Marine Consortium (LUMCON) facility at Cocodrie, Louisiana where they were loaded onto the R/V Pelican.

Aboard the vessel and prior to deployment, all instrumentation was again run through pre-deployment checkouts.

2.1.3 Moorings Deployment, Servicing, and Recovery

After arrival at each mooring deployment location, a small bathymetric survey of the planned mooring location was performed to confirm the water depth, as the accuracy of water depth information for deployment sites often varies, and variations in water depth can affect the depths of instrument measurements and sometimes also affect instrument performance. Extra mooring wire and chain was carried aboard the R/V Pelican and used to adjust the mooring length as necessary so as to keep the sensors at their planned depths.

Next, a ship drift test was performed to help assess the proper distance and direction from the deployment site to begin spooling out the mooring into the water as the ship steams towards the deployment site. Locations to begin deploying the mooring, and to release the anchor, were chosen based on the drift test, the length of the mooring, and the anticipated fall-back of the mooring due both to currents and drag on the mooring flotation as it descends through the water column.

Upon confirmation of the water depth, conclusion of final mooring adjustments, and selection of the ship's approach to the deployment site and the anchor drop location, the mooring deployment was initiated. The mooring was deployed using the top first, anchor last deployment method. Using this method, the top of the moorings was first put over the stern of the vessel, and then the mooring paid out as the vessel slowly steamed ahead. Payout of the mooring was halted and instruments attached at pre-designated and tagged points in the mooring which correspond to specific end pieces of mooring cables. Once the entire mooring was trailing astern of the vessel, the anchor was attached to the bottom of the mooring, and the anchor positioned at the very stern of the vessel and secured using a Quick-Release hook attached to the vessel with cables and safety taglines. Upon arriving at the planned anchor drop location, the Quick-Release was triggered and the mooring dropped anchor first.

After the mooring's anchor had reached the bottom, the mooring's exact deployed location was checked by both ranging from three locations on the acoustic releases that are contained on the mooring just above the anchor so as to triangulate a fix, and by passing over the mooring and identifying the buoy on the ship's fathometer. This also permitted confirming the depth of the top flotation buoy on the mooring against its planned depth.

After each deployment, the final mooring locations were determined utilizing a series of acoustic ranges which were interrogated from the acoustic releases attached at the bottom of the mooring. Triangulation of these ranges, from cardinal locations around the mooring location, determined the final mooring positions. The final mooring positions for each deployment, along with the measurement dates and instrument setup details, are provided in Table 2.1-3.

To release and recover the moorings for either servicing or their final recovery, several steps were undertaken. First, upon arriving at a mooring's location and prior to its recovery, the position of the mooring was checked by ranging on the acoustic releases to obtain a new fix so as to insure the mooring had not moved. The vessel was then positioned a short distance away from the confirmed mooring location, and an acoustic signal was transmitted to trigger the acoustic releases on the mooring.

Upon surfacing of the mooring, the ship was maneuvered to acquire the bottom end of the mooring first. This end was grabbed by means of a boat hook or rope and hook device, after which a snaphook, which is attached to the end of the main lifting cable of the deck winch, was attached to appropriate hardware on the mooring to lift the acoustic releases and other mooring hardware aboard. Once the bottom end of the mooring and the acoustic releases were onboard, the mooring was pulled aboard the ship by pulling the mooring wire with the deck winch. This wound the bottom end of the mooring on the deck winch first, resulting in the mooring cable being in the best position for re-deployment after servicing. As each instrument or flotation component reached the back end of the ship, the mooring line was secured with a safety line, the instrument or flotation components removed from the mooring, the mooring hardware reattached, and recovery of the mooring continued until all components were onboard.

Once removed from the moorings, each instrument was carefully cleaned and visually checked for damage, and properly turned off to end data recording. Next, the instruments were serviced to download their data, install new batteries as needed, replace parts and anodes as needed, and restart the instruments. In addition, downloaded data from each instrument underwent an initial QA/QC inspection aboard the vessel to confirm proper functioning of the instrument. After servicing, all instruments were run through the standard pre-deployment checkout procedures prior to release for redeployment.

All data recovered during the service trip in August 2005 and the final recovery trip in January 2006 were downloaded initially to computer hard drives. Backup copies of the raw data files were also made to CDs.

Table 2.1-3

Deployment information of the tall (M1, M2, and M3) and short (M4) moorings for each instrument deployed.

	= Instruments with Pressure Sensors			Deployment 1										Deployment 2									
	Instrument Type	Serial Number	Measured Parameters	Start Date	Start Time	End Date	End Time	Latitude	Longitude	Sampling Interval	Samples Averaged	Bin Size	Magnetic Declination	Start Date	Start Time	End Date	End Time	Latitude	Longitude	Sampling Interval	Samples Averaged	Bin Size	Magnetic Declination
Mooring 1	SeaBird SBE37	59	c,t,p	1/21/05	22:00	8/20/05	13:00	28 20.89770	87 32.86178	0:30:00	8	n/a	n/a	8/22/05	2:00	1/24/06	13:00	28 20.82604	87 32.83353	0:30:00	8	n/a	n/a
	StarOddi Hugrun	c919	t	1/21/05	22:00	8/20/05	13:00	28 20.89770	87 32.86178	0:30:00	1	n/a	n/a	8/22/05	2:00	1/24/06	13:00	28 20.82604	87 32.83353	0:30:00	1	n/a	n/a
	SeaBird SBE37	2697	c,t,p	1/21/05	22:00	8/20/05	13:00	28 20.89770	87 32.86178	0:30:00	8	n/a	n/a	8/22/05	2:00	1/24/06	13:00	28 20.82604	87 32.83353	0:30:00	8	n/a	n/a
	StarOddi Hugrun	c926	t	1/21/05	22:00	8/20/05	13:00	28 20.89770	87 32.86178	0:30:00	1	n/a	n/a	8/22/05	2:00	1/24/06	13:00	28 20.82604	87 32.83353	0:30:00	1	n/a	n/a
	SeaBird SBE37	2698	c,t,p	1/21/05	22:00	8/20/05	13:00	28 20.89770	87 32.86178	0:30:00	8	n/a	n/a	8/22/05	2:00	1/24/06	13:00	28 20.82604	87 32.83353	0:30:00	8	n/a	n/a
	StarOddi Hugrun	c932	t	1/21/05	22:00	8/20/05	13:00	28 20.89770	87 32.86178	0:30:00	1	n/a	n/a	8/22/05	2:00	1/24/06	13:00	28 20.82604	87 32.83353	0:30:00	1	n/a	n/a
	StarOddi Hugrun	c933	t	1/21/05	22:00	8/20/05	13:00	28 20.89770	87 32.86178	0:30:00	1	n/a	n/a	8/22/05	2:00	1/24/06	13:00	28 20.82604	87 32.83353	0:30:00	1	n/a	n/a
	TRDI ADCP LR	4487	t,p,u,v	1/21/05	21:00	8/20/05	13:00	28 20.89770	87 32.86178	1:00:00	60	8m	-0.87	8/22/05	1:00	1/24/06	12:00	28 20.82604	87 32.83353	1:00:00	60	8m	-0.87
	InterOcean S4	7801745	c,t,u,v	1/21/05	22:00	8/20/05	13:00	28 20.89770	87 32.86178	1:00:00	360	n/a	-0.87	8/22/05	2:00	1/24/06	13:00	28 20.82604	87 32.83353	1:00:00	360	n/a	-0.87
	Aanderaa RCM7/8	7223/12805	c,t,u,v,t,u,v	1/21/05	21:59	8/20/05	12:57	28 20.89770	87 32.86178	1:00:00	50	n/a	-0.87	8/22/05	1:59	1/24/06	13:00	28 20.82604	87 32.83353	1:00:00	50	n/a	-0.87
	Aanderaa RCM7/8	7692	t,p,u,v	1/21/05	21:59	8/20/05	12:59	28 20.89770	87 32.86178	1:00:00	50	n/a	-0.87	8/22/05	1:59	1/24/06	12:59	28 20.82604	87 32.83353	1:00:00	50	n/a	-0.87
	Aanderaa RCM7/8	9722	t,u,v	1/21/05	21:59	8/20/05	12:59	28 20.89770	87 32.86178	1:00:00	50	n/a	-0.87	8/22/05	1:59	1/24/06	12:59	28 20.82604	87 32.83353	1:00:00	50	n/a	-0.87
	Aanderaa RCM7/8	10053	t,p,u,v	1/21/05	21:59	8/20/05	12:55	28 20.89770	87 32.86178	1:00:00	50	n/a	-0.87	8/22/05	1:59	1/24/06	12:56	28 20.82604	87 32.83353	1:00:00	50	n/a	-0.87
	Aanderaa RCM7/8	12085	t,p,u,v	1/21/05	21:59	8/20/05	12:54	28 20.89770	87 32.86178	1:00:00	50	n/a	-0.87	8/22/05	1:40	1/24/06	12:35	28 20.82604	87 32.83353	1:00:00	50	n/a	-0.87
Mooring 2	SeaBird SBE37	57/2693	c,t,p	1/20/05	22:00	5/1/05	8:30	27 59.89942	87 50.33546	0:30:00	8	n/a	n/a	8/25/05	17:00	1/23/06	18:00	27 59.89942	87 50.33546	0:30:00	8	n/a	n/a
	StarOddi Hugrun	c937	t	1/20/05	22:00	5/1/05	8:30	27 59.89942	87 50.33546	0:30:00	1	n/a	n/a	8/25/05	17:00	1/23/06	18:00	27 59.89942	87 50.33546	0:30:00	1	n/a	n/a
	SeaBird SBE37	2699	c,t,p	1/20/05	22:00	8/24/05	11:00	27 59.89942	87 50.33546	0:30:00	8	n/a	n/a	8/25/05	17:00	1/23/06	18:00	27 59.89942	87 50.33546	0:30:00	8	n/a	n/a
	StarOddi Hugrun	c939	t	1/20/05	22:00	5/1/05	8:30	27 59.89942	87 50.33546	0:30:00	1	n/a	n/a	8/25/05	17:00	1/23/06	18:00	27 59.89942	87 50.33546	0:30:00	1	n/a	n/a
	SeaBird SBE37	2700	c,t,p	1/20/05	22:00	8/24/05	11:00	27 59.89942	87 50.33546	0:30:00	8	n/a	n/a	8/25/05	17:00	1/23/06	18:00	27 59.89942	87 50.33546	0:30:00	8	n/a	n/a
	StarOddi Hugrun	c940	t	1/20/05	22:00	5/1/05	8:30	27 59.89942	87 50.33546	0:30:00	1	n/a	n/a	8/25/05	17:00	1/23/06	18:00	27 59.89942	87 50.33546	0:30:00	1	n/a	n/a
	StarOddi Hugrun	c944	t	1/20/05	22:00	5/1/05	8:30	27 59.89942	87 50.33546	0:30:00	1	n/a	n/a	8/25/05	17:00	1/23/06	18:00	27 59.89942	87 50.33546	0:30:00	1	n/a	n/a
	TRDI ADCP LR	5165	t,p,u,v	1/20/05	21:00	8/24/05	10:00	27 59.89942	87 50.33546	1:00:00	60	8m	-0.617	8/25/05	17:00	1/23/06	18:00	27 59.89942	87 50.33546	1:00:00	60	8m	-0.617
	InterOcean S4	8161753	c,t,u,v	1/20/05	22:00	8/24/05	11:00	27 59.89942	87 50.33546	1:00:00	360	n/a	-0.617	8/25/05	17:00	1/23/06	18:00	27 59.89942	87 50.33546	1:00:00	360	n/a	-0.617
	Aanderaa RCM7/8	7507	c,t,u,v	1/20/05	21:59	8/24/05	10:59	27 59.89942	87 50.33546	1:00:00	50	n/a	-0.617	8/25/05	16:59	1/23/06	17:59	27 59.89942	87 50.33546	1:00:00	50	n/a	-0.617
	Aanderaa RCM7/8	7771	t,p,u,v	1/20/05	22:00	8/24/05	10:59	27 59.89942	87 50.33546	1:00:00	50	n/a	-0.617	8/25/05	16:59	1/23/06	17:59	27 59.89942	87 50.33546	1:00:00	50	n/a	-0.617
	Aanderaa RCM7/8	12803	t,u,v	1/20/05	22:00	8/24/05	11:02	27 59.89942	87 50.33546	1:00:00	50	n/a	-0.617	8/25/05	16:59	1/23/06	18:01	27 59.89942	87 50.33546	1:00:00	50	n/a	-0.617
	Aanderaa RCM7/8	9807	t,p,u,v	1/20/05	21:59	8/24/05	10:57	27 59.89942	87 50.33546	1:00:00	50	n/a	-0.617	8/25/05	16:59	1/23/06	17:58	27 59.89942	87 50.33546	1:00:00	50	n/a	-0.617
	Aanderaa RCM7/8	12807	t,u,v	1/20/05	21:59	8/24/05	10:57	27 59.89942	87 50.33546	1:00:00	50	n/a	-0.617	8/25/05	16:59	1/23/06	17:58	27 59.89942	87 50.33546	1:00:00	50	n/a	-0.617
Mooring 3	SeaBird SBE37	2701	c,t,p	1/20/05	0:00	8/22/05	11:00	27 36.55084	87 31.95179	0:30:00	8	n/a	n/a	8/23/05	19:00	1/24/06	19:00	27 36.38936	87 32.45470	0:30:00	8	n/a	n/a
	StarOddi Hugrun	c946	t	1/20/05	0:00	8/22/05	11:00	27 36.55084	87 31.95179	0:30:00	1	n/a	n/a	8/23/05	19:00	1/24/06	19:00	27 36.38936	87 32.45470	0:30:00	1	n/a	n/a
	SeaBird SBE37	2702	c,t,p	1/20/05	0:00	8/22/05	11:00	27 36.55084	87 31.95179	0:30:00	8	n/a	n/a	8/23/05	19:00	1/24/06	19:00	27 36.38936	87 32.45470	0:30:00	8	n/a	n/a
	StarOddi Hugrun	c950	t	1/20/05	0:00	8/22/05	11:00	27 36.55084	87 31.95179	0:30:00	1	n/a	n/a	8/23/05	19:00	1/24/06	19:00	27 36.38936	87 32.45470	0:30:00	1	n/a	n/a
	SeaBird SBE37	2703	c,t,p	1/20/05	0:00	8/22/05	11:00	27 36.55084	87 31.95179	0:30:00	8	n/a	n/a	8/23/05	19:00	1/24/06	19:00	27 36.38936	87 32.45470	0:30:00	8	n/a	n/a
	StarOddi Hugrun	c959	t	1/20/05	0:00	8/22/05	11:00	27 36.55084	87 31.95179	0:30:00	1	n/a	n/a	8/23/05	19:00	1/24/06	19:00	27 36.38936	87 32.45470	0:30:00	1	n/a	n/a
	StarOddi Hugrun	c960	t	1/20/05	0:00	8/22/05	11:00	27 36.55084	87 31.95179	0:30:00	1	n/a	n/a	8/23/05	19:00	1/24/06	19:00	27 36.38936	87 32.45470	0:30:00	1	n/a	n/a
	TRDI ADCP LR	5699	t,p,u,v	1/19/05	23:00	8/22/05	11:00	27 36.55084	87 31.95179	1:00:00	60	8m	-0.77	8/23/05	18:00	1/24/06	19:00	27 36.38936	87 32.45470	1:00:00	60	8m	-0.77
	InterOcean S4	2129/8111780	c,t,u,v	1/20/05	0:00	8/22/05	11:00	27 36.55084	87 31.95179	1:00:00	360	n/a	-0.77	8/23/05	19:00	1/24/06	19:00	27 36.38936	87 32.45470	1:00:00	360	n/a	-0.77
	Aanderaa RCM7/8	12084	c,t,u,v	1/19/05	23:59	8/22/05	10:58	27 36.55084	87 31.95179	1:00:00	50	n/a	-0.77	8/23/05	18:59	1/24/06	18:58	27 36.38936	87 32.45470	1:00:00	50	n/a	-0.77
	Aanderaa RCM7/8	10643	t,p,u,v	1/19/05	23:59	8/22/05	10:57	27 36.55084	87 31.95179	1:00:00	50	n/a	-0.77	8/23/05	18:59	1/24/06	18:57	27 36.38936	87 32.45470	1:00:00	50	n/a	-0.77
	Aanderaa RCM7/8	9480	c,u,v	1/19/05	23:59	8/22/05	10:57	27 36.55084	87 31.95179	1:00:00	50	n/a	-0.77	8/23/05	18:59	1/24/06	18:58	27 36.38936	87 32.45470	1:00:00	50	n/a	-0.77
	Aanderaa RCM7/8	9809	t,p,u,v	1/19/05	23:59	8/22/05	10:59	27 36.55084	87 31.95179	1:00:00	50	n/a	-0.77	8/23/05	18:59	1/24/06	19:00	27 36.38936	87 32.45470	1:00:00	50	n/a	-0.77
	Aanderaa RCM7/8	12808	t,u,v	1/20/05	0:00	8/22/05	11:01	27 36.55084	87 31.95179	1:00:00	50	n/a	-0.77	8/23/05	19:00	1/24/06	19:01	27 36.38936	87 32.45470	1:00:00	50	n/a	-0.77
Aanderaa RCM7/8	12809	t,u,v	1/20/05	0:00	8/22/05	11:02	27 36.55084	87 31.95179	1:00:00	50	n/a	-0.77	8/23/05	19:00	1/24/06	19:01	27 36.38936	87 32.45470	1:00:00	50	n/a	-0.77	
Mooring 4	Aanderaa RCM7/8	10112	t,p,u,v	1/19/05	2:59	8/19/05	12:56	27 59.98225	87 33.59521	1:00:00	50	n/a	-0.82	8/19/05									

2.1.4 Processing and QA/QC of Mooring Measurements

Initial processing and quality assurance/quality control (QA/QC) of the measurements from the four moorings were performed by EHI. This resulted in final edited data sets for the mooring measurements being prepared and released to all Science Team PIs for their analyses. EHI also formatted the final data sets to NODC standards and provided the data to NODC.

Initial data processing and QA/QC of the mooring measurements utilized a combination of instrument manufacturer software and EHI software. Data processing steps involved conducting QA/QC of overall instrument performance (tilt, battery life, etc.), cutting data recorded by the instruments out-of-water prior to and after deployment, cutting data from the ADCPs for measurement bins near surface, and identifying and removing or providing caveats of bad or questionable data. Listed below are the steps involved in the processing and QA/QC of the different types of mooring data collected.

ADCP Data

To help assess overall performance of the ADCP instruments, a series of data plots were viewed in the RDI software. These plots included information on the orientation of the meter, water temperature, backscatter intensity, vertical velocity, pitch, roll, heading, pressure, battery voltage, and other parameters related to the quality of data.

The parameters used to cut the ADCP data for periods prior to and after deployment, and for measurement bins near the surface experiencing acoustic side lobe interference, were percent good as well as per-beam values of correlation and echo amplitude. For each data file, the percent good cut off value was set so that all data falling below a designated percent good value was cut from the data set. The correlation and echo amplitude gate values were set so that all data with a per-bin correlation or echo amplitude difference greater than the designated respective values were cut from the data set. Because of the presence of both the LC and hurricanes during the deployment periods, “maximum magnitude not to exceed” current velocities were not used as a cutting parameter. Remaining bad data points not cut by the before mentioned procedures were hand-cut from the data set using the above parameters. All remaining questionable data were flagged using “999.99”.

Following are the detailed steps used in the processing and QA/QC of the ADCP data:

Step 1 Utilizing Teledyne RD Instruments Software:

- Determined first and last good ensembles due to out-of-water times
- Verified that in- and out-of-water times matched start and end of good data, respectively
- Verified instrument settings
- Performed initial visual QA/QC of the data
- Exported all data variables as *.MAT files (The MathWorks, Inc MATLAB compatible)

Step 2 Utilizing EHI Data Cleaning Software:

- Cut bad data using percent good threshold
- Cut bad data using correlation gate
- Cut bad data using echo amplitude gate
- Converted current magnitude from mm s^{-1} to cm s^{-1}
- Applied mooring location-specific magnetic declination
- Checked for and flag data file anomalies such as time jumps

Step 3 Utilizing EHI Data QA/QC and Graphing Software:

- Hand cut bad data near surface that was not caught by the above defined parameters values using surface bin differences in per-bin values of percent good, correlation, and echo amplitude.
- Plotted contours of current magnitude and direction
- Plotted vectors of current magnitude and direction
- Plotted contours of vertical velocities, average correlation, and average echo amplitude
- Plotted line plots of temperature, pressure, pitch, roll, and heading

Aanderaa Current Data

Following are the steps used in the processing and QA/QC of the Aanderaa RCM7/8 data:

Step 1 Utilizing Aanderaa Software:

- Applied calibration information for each sensor per instrument
- Converted data from raw voltages to engineering units
- Determined first and last good ensembles due to out-of-water times
- Verified that in- and out-of-water times match start and end of good data, respectively
- Verified instrument settings
- Removed instrument time stamps
- Performed initial visual QA/QC of the data
- Exported all data into an ASCII format

Step 2 Utilizing EHI Data Cleaning Software:

- Applied mooring location-specific magnetic declination
- Checked for and flagged data file anomalies such as time jumps

Step 3 Utilizing EHI Data QA/QC and Graphing Software:

- Cut bad current speed data due to rotor loss or malfunction
- Cut bad current direction data due to vane malfunction
- Checked for and hand cut bad data spikes
- Plotted vectors of current magnitude and direction

- Plotted line plots of temperature, and pressure and/or conductivity when present

Interocean S4 Current Data

Following are the steps used in the processing and QA/QC of the Interocean S4 data:

Step 1 Utilizing InterOcean Systems, Inc. Software:

- Determined first and last good ensembles due to out-of-water times
- Verified that in- and out-of-water times match start and end of good data, respectively
- Verified instrument settings
- Performed initial visual QA/QC of the data
- Exported all data into an ASCII format

Step 2 Utilizing EHI Data Cleaning Software:

- Applied mooring location-specific magnetic declination
- Checked for and flagged data file anomalies such as time jumps

Step 3 Utilizing EHI Data QA/QC and Graphing Software:

- Checked for and hand cut bad data spikes
- Plotted vectors of current magnitude and direction
- Plotted line plots of temperature, conductivity, pitch, roll, and heading

Seabird SBE-37 Single Point CTD Data

Following are the steps used in the processing and QA/QC of the Seabird Instruments SBE-37 CTD data:

Step 1 Utilizing SeaTerm Processing Software:

- Exported data to ASCII file

Step 2 Utilizing EHI Data QA/QC and Graphing Software:

- Determined first and last good data values due to out-of-water times
- Verified that in- and out-of-water times match start and end of good data, respectively
- Calculated salinity and density from the temperature, conductivity and pressure records using the seawater toolbox routines (Phil Morgan ,CSIRO)
- Plotted line plots of temperature, conductivity, calculated salinity, and pressure
- Performed initial visual QA/QC of the data
- QA/QC the data for spikes in temperature records, removed and interpolated across excursions greater than 1.5° C

Step 3 Additional QA/QC

- Data were further hand checked for spikes in temperature

Of special note is that during Deployment 1, Mooring 2 lost the top flotation buoy part way through the deployment in March, after which the top portion of the mooring down to about 400 m depth, fell over and hung suspended below that point. For all CTD instruments that did not contain a pressure sensor to accurately position their depth after the loss of the buoy, the data record for those instruments was cut at the time of the buoy loss because the depth of the instruments could not be positively identified for the remainder of the deployment. If an instrument did contain a pressure sensor and it did not become over-pressured, two data files were written for the instrument, one prior to and one for after the buoy loss.

Star-Oddi Hugrun Single Point CTD Data

Step 1 Utilizing Seamon Processing Software:

- Exported data to ASCII file

Step 2 Utilizing EHI Data QA/QC and Graphing Software:

- Determined first and last good data values due to out-of-water times
- Verified that in- and out-of-water times match start and end of good data, respectively
- Plotted line plots of temperature
- Performed initial visual QA/QC of the data
- QA/QC'd the data for spikes in temperature records, removed and interpolated across excursions greater than 1.5° C
- These instruments did not have pressure; therefore, pressure was calculated from instruments on the same mooring based on known cable lengths and pressure records of those instruments above and below the Hugrun. Given an instrument H with no pressure sensor and instruments S1 above and S2 below with pressures PS1 and PS2, and given each instrument's mooring cable position: MS1, MH, MS2;

$$P_H = P_{S1} + \frac{(P_{S2} - P_{S1}) * (M_H - M_{S1})}{M_{S2} - M_{S1}}, \quad (2.1.1)$$

Step 3 Additional QA/QC

- Data were further hand checked for spikes in temperature

2.1.5 Mooring Data Coverage

Overall, excellent data coverage was achieved from the moorings. Tables 2.1-4 through 2.1-7 depict the periods of good data coverage for each instrument over the two deployments. Some problems were encountered with particular instruments, and with identifying the measurement depth of some instruments after the loss of the top flotation buoy on Mooring 2 during Deployment 1. Statistical computations for each deployment of the percent data return by instrument type, and per mooring including all instruments on the mooring, are provided in Table 2.1-8.

2.1.6 Mooring Data Graphical Products and Analyses

Utilizing the processed and QA/QC'd mooring measurements data, a number of additional analyses were conducted, and graphical and tabular displays of the data prepared. While these data products are presented and discussed within Chapter 3, a listing of these products and the analyses performed is presented below.

The graphical and tabular displays of the mooring data include:

- Vector plots of current speed and direction vs. time for selected measurement depths
- Color contours of current speed and direction vs. time and depth
- Color contours of water temperature vs. time and depth
- Color contours of water salinity vs. time and depth
- Current roses
- Joint probability distributions of current speed vs. direction
- Current speed persistence tables
- Spectral analysis plots for current speeds
- Basic statistics of the u and v components of the current

Prior to conducting some of the above analyses, mooring drawdown due to the influence of the LC at the mooring sites was assessed. It was determined that when the LC was affecting a mooring location, mooring drawdown was significant enough (50 m) to warrant correction for those analyses presenting results at defined depths. It was determined that the mooring drawdown primarily affected the depth of current measurements and CTD data in the upper 500 m. ADCP data was therefore corrected by fitting u and v velocity component time series to a regular grid. From the gridded fields, a single time series for each 8 m depth range was constructed. Because the ADCP was originally configured to record in 8 m bins and the number of bins remained constant throughout the deployment, this method assures there is only one measurement in a given bin for each sample time

For those analyses requiring regularly spaced, gapless time series, time series above ~ 60 m were excluded from analysis due to gaps longer than 2 weeks resulting in a large portion of the record being affected by gaps. For some mooring deployments, the shallowest time series is around 100 m.

Table 2.1-4

Summary of data coverage by each instrument and their sensors for Mooring 1 during January 2005 to January 2006.

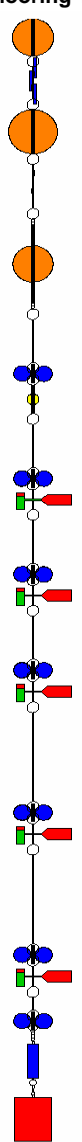
Mooring Schematic	Instrument Type	Measured Parameters	Deployment 1								Deployment 2																			
			Jan	Feb	Mar	Apr	May	Jun	Jul	Aug	Sep	Oct	Nov	Dec	Jan															
	SeaBird SBE37	c																												
		t																												
		p																												
	StarOddi Hugrun	t																												
	SeaBird SBE37	c																												
		t																												
		p																												
	StarOddi Hugrun	t																												
	SeaBird SBE37	c																												
		t																												
		p																												
	StarOddi Hugrun	t																												
	StarOddi Hugrun	t																												
	TRDI ADCP LR	t																												
		p																												
		dir																												
		mag																												
	InterOcean S4	c																												
		t																												
		dir																												
		mag																												
	Aanderaa RCM7/8	c																												
		t																												
		dir																												
		mag																												
	Aanderaa RCM7/8	t																												
		p																												
		dir																												
	mag																													
Aanderaa RCM7/8	t																													
	dir																													
	mag																													
Aanderaa RCM7/8	t																													
	p																													
	dir																													
	mag																													
Aanderaa RCM7/8	t																													
	p																													
	dir																													
	mag																													

Table 2.1-5

Summary of data coverage by each instrument and their sensors for Mooring 2 during January 2005 to January 2006.

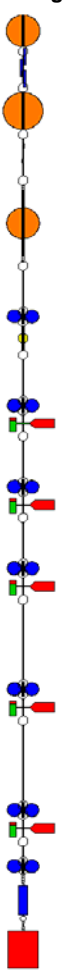
Mooring Schematic	Instrument Type	Measured Parameters	Deployment 1								Deployment 2																
			Jan	Feb	Mar	Apr	May	Jun	Jul	Aug	Sep	Oct	Nov	Dec	Jan												
	SeaBird SBE37	c																									
		t																									
		p																									
	StarOddi Hugrun	t																									
	SeaBird SBE37	c																									
		t																									
		p																									
	StarOddi Hugrun	t																									
	SeaBird SBE37	c																									
		t																									
		p																									
	StarOddi Hugrun	t																									
	StarOddi Hugrun	t																									
	TRDI ADCP LR	t																									
		p																									
		dir																									
		mag																									
	InterOcean S4	c																									
		t																									
		dir																									
		mag																									
	Aanderaa RCM7/8	c																									
		t																									
		dir																									
		mag																									
	Aanderaa RCM7/8	t																									
	p																										
	dir																										
	mag																										
Aanderaa RCM7/8	t																										
	dir																										
	mag																										
Aanderaa RCM7/8	t																										
	p																										
	dir																										
	mag																										
Aanderaa RCM7/8	t																										
	dir																										
	mag																										

Table 2.1-6

Summary of data coverage by each instrument and their sensors for Mooring 3 during January 2005 to January 2006.

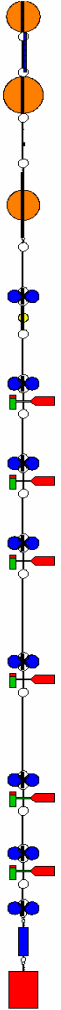
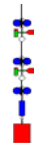
Mooring Schematic	Instrument Type	Measured Parameters	Deployment 1								Deployment 2																
			Jan	Feb	Mar	Apr	May	Jun	Jul	Aug	Sep	Oct	Nov	Dec	Jan												
	SeaBird SBE37	c																									
		t																									
		p																									
	StarOddi Hugrun	t																									
	SeaBird SBE37	c																									
		t																									
		p																									
	StarOddi Hugrun	t																									
	SeaBird SBE37	c																									
		t																									
		p																									
	StarOddi Hugrun	t																									
	StarOddi Hugrun	t																									
	TRDI ADCP LR	t																									
		p																									
		dir																									
		mag																									
	InterOcean S4	c																									
		t																									
		dir																									
		mag																									
	Aanderaa RCM7/8	c																									
		t																									
		dir																									
	mag																										
Aanderaa RCM7/8	t																										
	p																										
	dir																										
	mag																										
Aanderaa RCM7/8	c																										
	dir																										
	mag																										
Aanderaa RCM7/8	t																										
	p																										
	dir																										
	mag																										
Aanderaa RCM7/8	t																										
	dir																										
	mag																										
Aanderaa RCM7/8	t																										
	dir																										
	mag																										
Aanderaa RCM7/8	t																										
	dir																										
	mag																										

Table 2.1-7

Summary of data coverage by each instrument and their sensors for Mooring 4 during January 2005 to January 2006.

Mooring Schematic	Instrument Type	Measured Parameters	Deployment 1						Deployment 2						
			Jan	Feb	Mar	Apr	May	Jun	Jul	Aug	Sep	Oct	Nov	Dec	Jan
	Aanderaa RCM7/8	t													
		p													
		dir													
		mag													
	Aanderaa RCM7/8	t													
		dir													
	mag														

-  = Good Data
-  = Bad or Missing Data
-  = Current Data: Speed Only
-  = Current Data: Direction Only
-  = CTD Data: Depth Change - Good Data
-  = CTD Data: Data not provided due to unknown depth of instrument
-  = Instruments with Pressure Sensors

Table 2.1-8

Data return statistics for each mooring and each instrument type during both deployments.

Totals:	Deployment 1			Deployment 2		
	# Data Points Exp	# Data points Ret	% Return	# Data Points Exp	# Data points Ret	% Return
Doppler Data:	61508	61508	100%	44212	44116	100%
Aanderaa Data:	332932	321450	97%	236796	232029	98%
S4 Data:	61500	61500	100%	44208	44208	100%
Hugrun CTD Data:	123000	100901	82%	88416	88408	100%
SeaBird CTD Data:	276750	260169	94%	198936	198918	100%
Mooring 1	267919	259372	97%	194457	191893	99%
Mooring 2	268996	227381	85%	188500	186175	99%
Mooring 3	283089	283089	100%	203284	203284	100%
Mooring 4	35686	35686	100%	26327	26327	100%

As a consequence of this method and the constant bin number, gaps in the surface-most bins occur in the velocity data when the mooring was depressed in depth. Temporal gaps in the time series that lasted less than 2 weeks and more than 1 day were filled using the spectral method of Maximum Likelihood, a method which uses data before and after the gap to weight and predict values in the gap that are spectrally consistent with observations surrounding the gap (Nowlin et al. 1982). Gaps of less than one day were filled using linear interpolation. The same gap filling procedure was performed on the single point current meter data when needed

Several types of statistical data products were prepared for each current meter file or depth bin from the ADCP observations for each deployment period. First, the record length mean, standard deviation, and minimum and maximum values were calculated to produce an overall climatology of the dataset to help identify the physical processes that occurred during the field study. The measurements were then investigated to characterize their record-length structures. As part of this effort, joint distributions of direction and speed were tabulated for each deployment period using unfiltered hourly versions of the quality-controlled data. The joint speed versus direction information indicates the percentage of time the current observations fall within the indicated speed range and 45°-intervals of direction centered on the 8-principal compass directions. Speeds less than 1 cm s⁻¹ are categorized as calm and not assigned compass direction because those directions would likely not be meaningful. Also shown is the percentage of time when the currents are within each speed range and each direction bin. The average speed for each direction bin is included. From these tabulations, current roses were constructed for each single point current meter file and ADCP depth bin. The current roses are a graphical depiction of the joint distributions tabulations. On the current roses, the white and stippled segments indicate, from the rose center outward, the percentage of the currents that were in speed bins of 5 cm s⁻¹ increments up to speeds greater than 75 cm s⁻¹. The length of each segment corresponds to the percentage of time the current was in that speed bin; if the percentage is less than 1% for a particular speed bin, the corresponding segment is omitted. Calms are indicated in the center of the rose. An example is shown in Figure 2.1-2.

Persistence tables (also known as recurrence and duration statistics) were constructed for each current meter file. Persistence statistics were calculated using the unfiltered hourly versions of the quality controlled data sets. An example persistence table is shown below in Figure 2.1-3. Each persistence interval is defined by speed classes in the table. Speed classes are subdivided into several increments ranging from 1 to 10 cm s⁻¹. The duration (termed “run length”) in hours was computed for the time while consecutive values of the time series fell within a speed interval. Duration intervals are 0-6, 6-12, 12-18, 18-24, 24-32 hours. An occurrence is defined as a given speed class persisting for a given duration. The number of occurrences for each speed class and run length are shown in the tables. The mean, standard deviation, and maximum duration of the run length (in hours) for each interval are then calculated.

Kinetic energy spectra plots were constructed for each current meter file or ADCP depth bin. As for the persistence tables and rose diagrams, the spectral energy plots were generated for each deployment period using unfiltered hourly versions of the quality-controlled data. The spectra were estimated using Welch’s method using a segment length of 512 points with 50% overlap. A Kaiser-Bessel window was applied to the segment (Emery and Thomson 2001) to increase the statistical degrees of freedom and insure the greatest statistical reliability of the spectral estimates. The velocity vectors were divided into north-south and east-west current components prior to analysis. Shown also is the kinetic energy spectrum of a detided version of the data. An example of a kinetic energy spectra plot is shown in Figure 2.1-4.

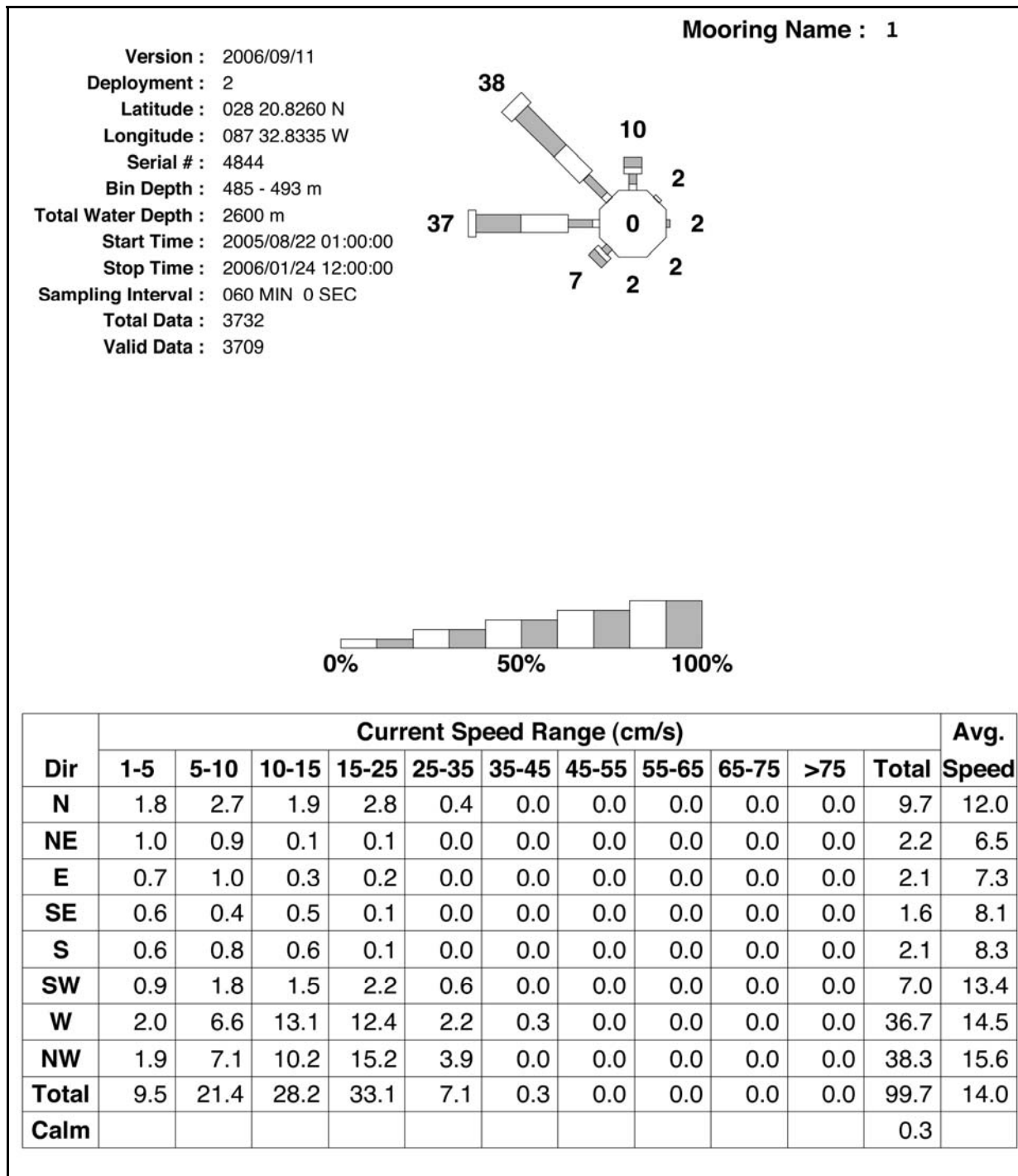


Figure 2.1-2. Example current rose diagram: Mooring M1, deployment 1.

Deployment : 1	Instrument Type : RDI Broadband 75 kHz Long-Ranger ADCP			
Mooring : 1	Serial # : 1307			
Latitude : 028 20.8977 N	Bin Depth : 424 - 432 m			
Longitude : 087 32.8618 W	Start Time : 2005/01/21 21:00:00			
Total Water Depth : 2600 m	End Time : 2005/08/20 13:00:00			

Speed (cm/s)	Duration limits (hours)					Duration statistics (hours)				
	0	6	12	18	24	32	total	max	mean	std.dev
0 <=S< 1	36	0	0	0	0	0	36	2.0	1.1	0.3
1 <=S< 2	63	0	0	0	0	0	63	2.0	1.1	0.3
2 <=S< 3	114	0	0	0	0	0	114	3.0	1.2	0.4
3 <=S< 4	150	0	0	0	0	0	150	3.0	1.2	0.4
4 <=S< 5	165	0	0	0	0	0	165	4.0	1.2	0.5
5 <=S< 10	569	60	3	0	0	0	632	15.0	2.5	2.1
10 <=S< 20	382	101	23	8	3	0	517	32.0	4.1	4.5
20 <=S< 30	115	28	10	1	0	0	154	20.0	3.9	3.8
30 <=S< 40	34	5	1	0	0	0	40	12.0	3.2	2.7
40 <=S< 44	6	0	0	0	0	0	6	3.0	1.8	0.7
Data gaps	0	0	0	0	0	0	0	0.0	0.0	0.0

Figure 2.1-3. Example persistence table: Mooring M1, deployment 1.

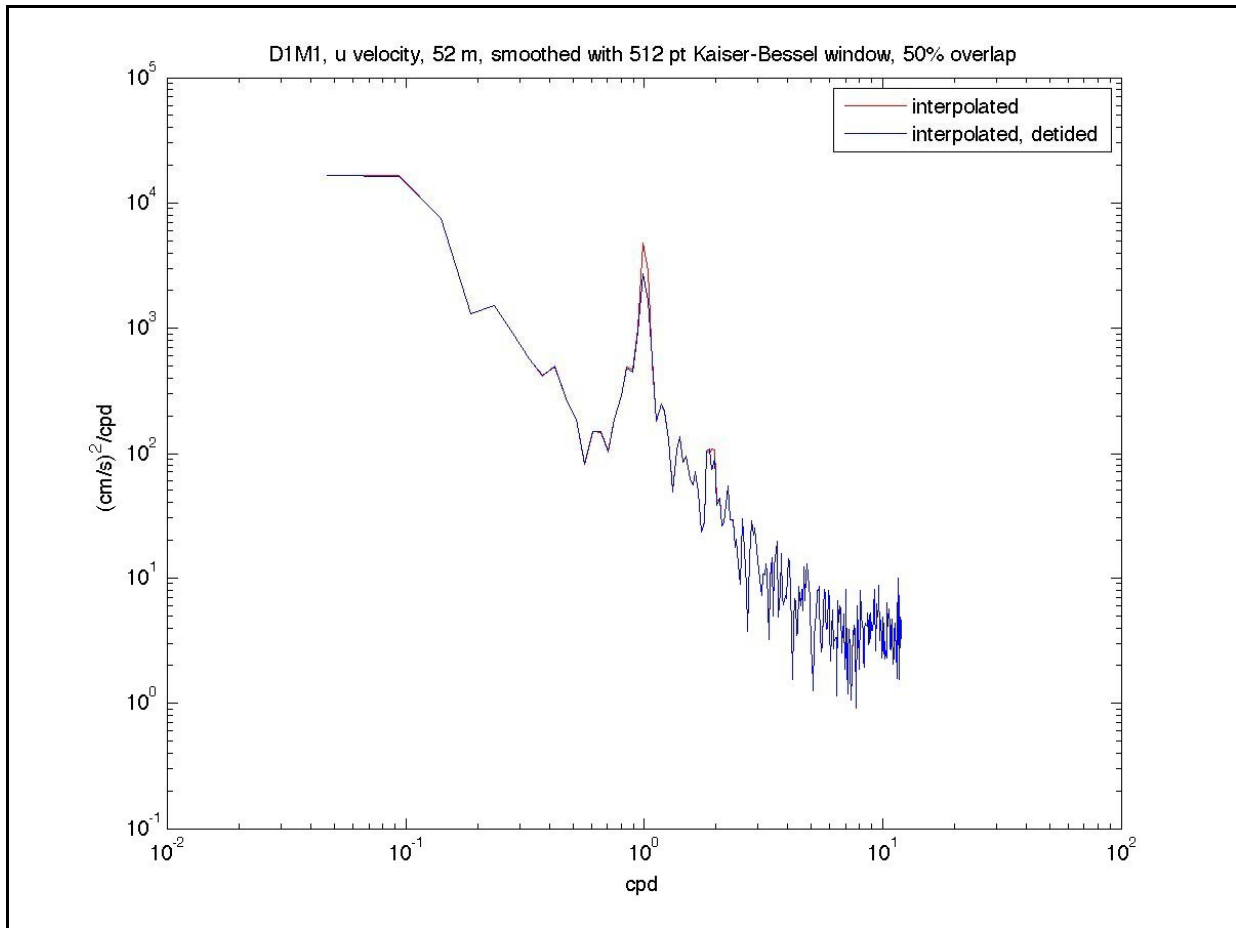


Figure 2.1-4. Kinetic energy spectra of unfiltered (blue) and detided (red) versions of ADCP data during deployment 1 at mooring 1. Bin depth is 52 m.

When analysis of the tidal components of the currents was needed either to understand the tidal currents, or to eliminate the tidal current signal so as to look at low frequency circulation, a couple of methods were utilized. Tidal analysis was performed on all current meter data using the iterative least squares method of cyclic descent (Bloomfield 1976). The eight tidal constituents with the largest gravitational potential were analyzed. Tidal ellipses (major/minor axes, ellipse directional orientation) and phase were calculated for each velocity component record.

For the study of low frequency circulation, all time series were filtered using a 96+1+96 point 40-hr low pass Lanczos-Cosine kernel (Harris 1978), which eliminates tidal and inertial signals from the data. For correlation between SSH anomaly and current, and wind and current, current data was 40 hour low pass filtered and resampled at 24-hour intervals and 3-hour intervals respectively.

Dynamic modes of the current were also calculated following the method of Klink (1999) using both historical hydrographic observations (Nowlin et al. 2001) and new observations collected specifically for this project. The dynamic modes give an estimation of the vertical structure of currents at a point for a given stability profile. Once identified, the dynamic modes were compared to full water column synoptic vertical profiles of current constructed from low-passed filtered versions of the upper ocean ADCP data (in the upper 500 m) and single point Aanderaa RCM11 current meters (typically below 500 m to near the bottom). The first three dynamic modes (barotropic plus first two baroclinic) were then fitted using linear regression at each time point. From this a time series of the dynamic modes was constructed and analyzed. The statistical significance of each modal time series was tested using a model utility test. The modal time series were then correlated and interpreted with respect to independent forcing such as sea surface height, sea surface height gradient, and wind speed. Coherency, phase, and gain spectra between various forcing and modal time series were computed to identify frequency bands in which correlation between parameters exist.

Additional spectral analysis was performed using wavelets to produce the time evolution of the spectral components. Wavelets were used principally to investigate inertial band energy, specifically those related to tropical storms. Wavelets associated with subinertial variability of about 10 days were also investigated. Long-period variability was addressed using the estimation of dynamic mode and empirical orthogonal function (EOF) decomposition of individual velocity components.

2.2 Hydrography

Three hydrography cruises were planned for the 12-month measurement period of the NE Gulf of Mexico Program: at initial deployment of the current meter moorings, at the six month servicing of the moorings, and during final retrieval. The hydrography cruises used a combination of CTD casts and XBT profiles designed to ensure sufficient data density, efficiency of operations during the cruise, and coverage of the study area.

2.2.1 Survey Pattern and Instrumentation

A grid pattern of stations (Figure 2.2-1) was devised consisting of deep CTD casts (~2000 m), shallow CTD casts (~1000 m), deep XBT profiles (T5 ~1830 m), and shallow XBT profiles (T7 ~760 m). This grid was to be utilized if no LC, LCE, or related features were within or approaching the study area at the time of the cruises. Grid spacing between stations was 10 nmi in the east to west direction and 5 nmi in the north to south direction. In addition, a grid pattern was devised with alternating lines of CTD and XBT stations where each west to east transect line would be the same type of probe (e.g., all shallow CTD, all deep XBT, etc). Deep CTD casts were to be taken at each mooring and PIES location.

Prior to each mooring and hydrography cruise, the position of the LC, and any LCEs or frontal features was checked using a combination of satellite imagery and altimetry, and other available information. If it was found that the LC, and LCE, or frontal features were affecting the study area at the time of an upcoming cruise, it was planned to adapt the hydrography cruise grid to better align the grid with the location and scale of the feature. Such was the case during the third hydrography cruise.

The CTD used to conduct the casts was CTD system on the R/V Pelican. This unit is a Seabird SBE-19. All XBTs used were purchased from Lockheed Martin Sippican.

The hydrography cruises were conducted as follows:

Hydrography Cruise 1

The first hydrography cruise was conducted January 17-23, 2005 and followed the initial grid design and general station type. The hydrography stations were timed around the daylight deployment of the moorings. Due to a lack of time, the far west N-S transect was not sampled. Figure 2.2-2 shows the final station grid.

Hydrography Cruise 2

The second hydrography cruise was conducted August 18-25, 2005 and again followed the initial grid design and the general station type. The hydrography stations were timed around the daylight mooring retrieval and redeployments and the download of the PIES. The eight day cruise allowed sampling of the far west N-S transect not collected during the first cruise. Additional XBT profiles were collected every 10 km as the ship crossed the loop eddy on the way back to shore (Figure 2.2-3).

Hydrographic Cruise 2 finished one day ahead of Hurricane Katrina entering the GOM. Hurricane Rita followed less than a month later and finally Hurricane Wilma came through the southern GOM one month after Rita. Of the three hurricanes, Katrina had the most potential for impact to the study area. The storm tracks provided in Appendix A show that hurricane force winds covered most of the study area and tropical storm winds covered the remainder during Hurricane Katrina. During Hurricane Rita, tropical storm force winds covered the southern half of the study area. Hurricane Wilma had the least direct impact to the study area having passed well to the south. Because of these major storm events, additional funds were earmarked for a post hurricane hydrographic cruise; however, no suitable vessels with appropriate CTD instrumentation were available well past the time of all three hurricanes.

Hydrographic Cruise 3

The third hydrography cruise was conducted January 20-28, 2006 and did not use the initial grid design. A decision had to be made on how best to use the additional funds to benefit the program. Discussions amongst the study team determined that conducting a fine scale (intensive) survey of the edge of the LC and any frontal features within or near the study area would provide heretofore unavailable detail on the hydrography of these processes. To conduct such an intensive hydrography survey, an eye was kept to the presence of the LC and its frontal features within the study area, as well as to the availability of vessels to conduct the cruise.

Finally, as the time was approaching for retrieval of all the moorings and PIES and the third hydrography cruise, satellite imagery showed some interesting features. The edge of the LC was moving northeastward toward the study area, and two cold core eddies appeared to be located in the southern half of the study area along with some other frontal features. It was also speculated that current jets were possibly being produced by water squeezed by bathymetry at the north side of study area.

LUMCON was able to extend our final cruise period by a few days and so final planning for a fine scale hydrography survey was commenced. Team members were assembled via teleconference to discuss strategies for the cruise plan. The end result was a pin wheel grid of stations (Figure 2.2-4) designed to capture in detail the hydrography of the edge of the LC, the cold core eddies, and any other frontal features within or near the study area.

The cruise plan called for starting at the NW corner and following a transect toward the center of the grid to find the cold core eddy. Next the vessel would transit directly south until crossing the edge of the LC. The vessel would continue transiting the pattern in a clockwise rotation thereby sampling “new” water as opposed to the possibility of sampling the same water if a counterclockwise rotation was scheduled. Sampling would be a combination of CTD casts and XBT profiles. Deep CTD casts were scheduled to be taken at each mooring and PIES location in addition to the outer corners of the pinwheel to maximize the area available for deep contours. The moorings and PIES would be retrieved as the vessel transited the grid pattern.

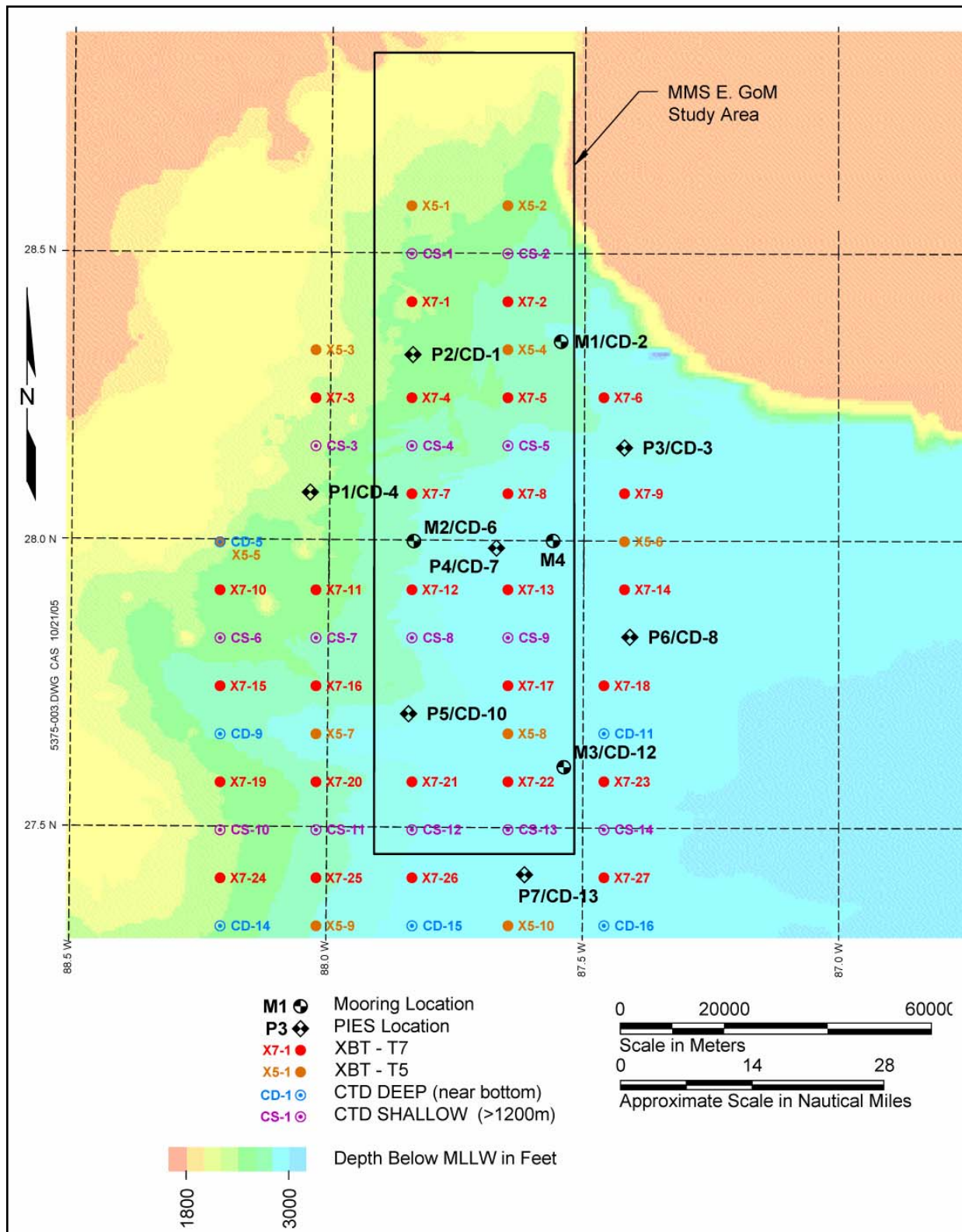


Figure 2.2-1. Grid pattern proposed for hydrography cruises. Legend denotes station type and naming scheme.

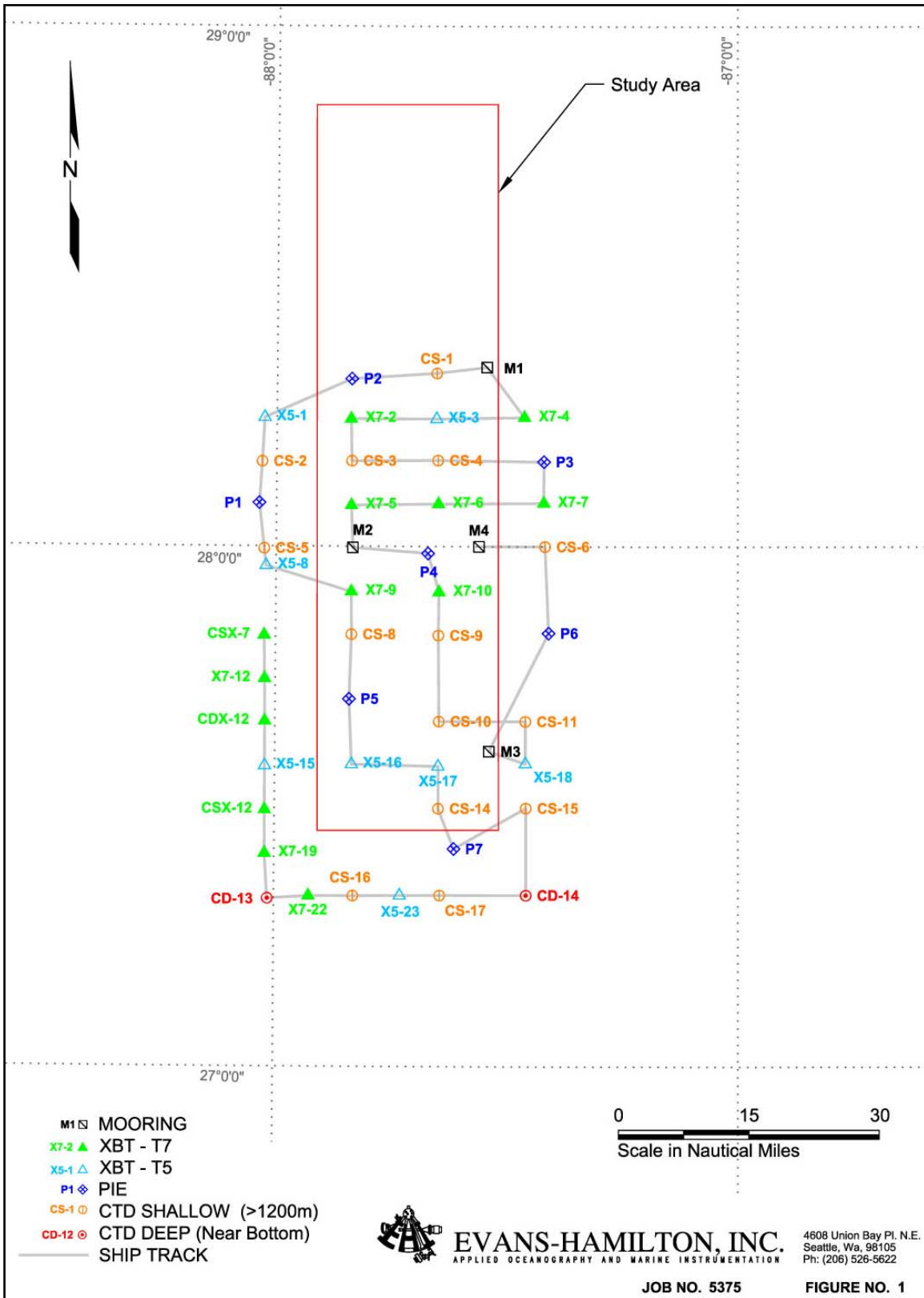


Figure 2.2-2. Grid pattern of Hydrography Cruise 1. Line indicates ship track.

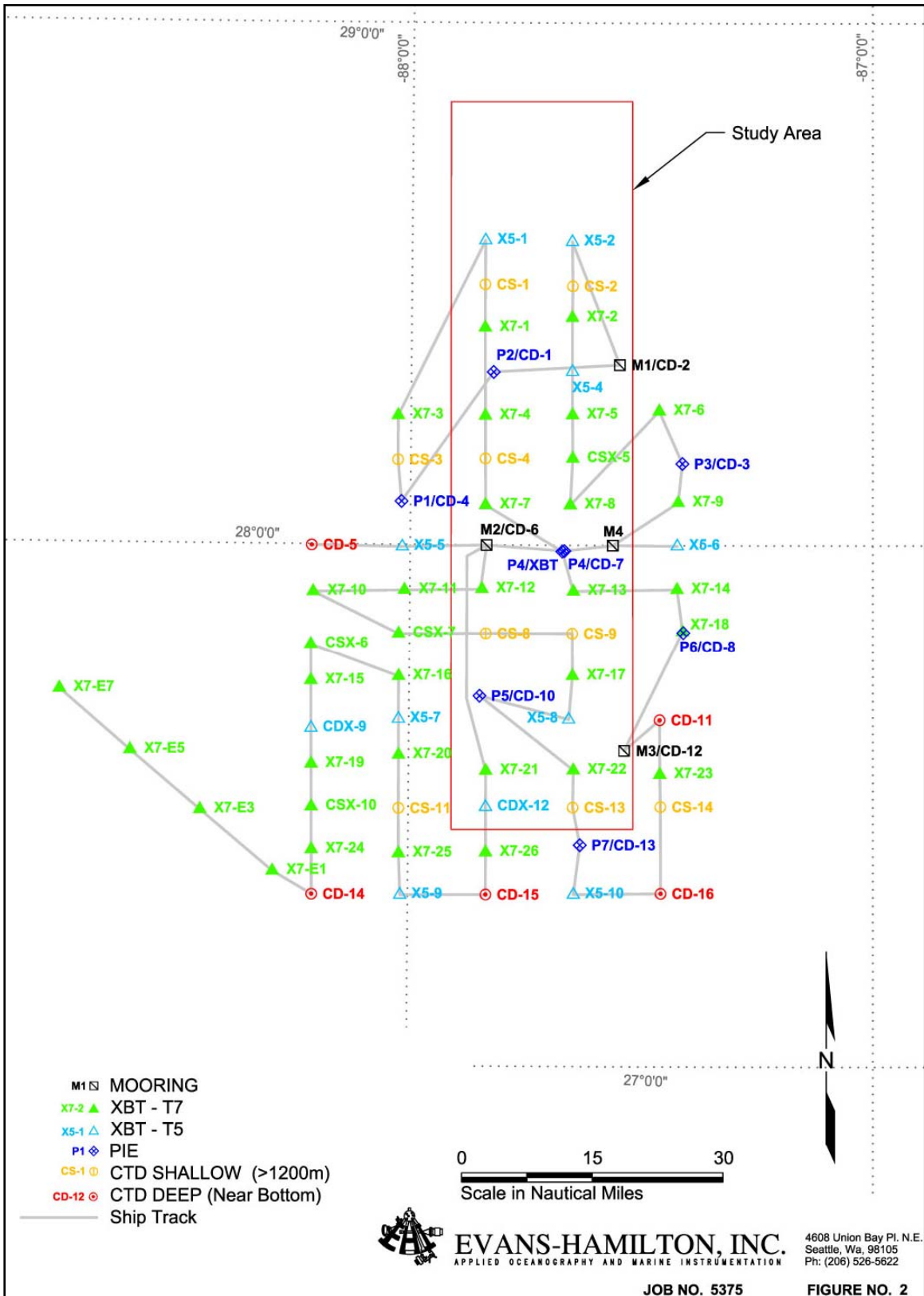


Figure 2.2-3. Grid pattern of Hydrography Cruise 2. Line through stations indicates ship track.

The actual cruise track pattern was modified once the vessel reached the study area (Figure 2.2-5). The edge of the Loop Current had slid northward so the legs along the south side of the grid pattern were shortened. The weather contributed to the modification of the cruise track as well. Immediately following completion of the most southern wedge of the pinwheel grid, the vessel headed north to take advantage of a good weather window to retrieve all moorings and PIES. The station plan was also modified once on site. Deep blue (DB) XBT probes (~870 m range) were available for this intensive cruise. At two of the PIES stations (P2 and P5) multiple XBT profiles (one each of T7, T5 and DB) were taken in conjunction with a deep CTD cast. Because of the modification to the cruise track, some stations were sampled more than once. One example is station 16 that was sampled with a T7 on 01/22/06 and again five days later as a shallow CTD site. A second example is the same transect line was sampled as the vessel transited into and out of the study area (NW quadrant).

2.2.2 Hydrography Data Processing and QAQC

The hydrography data were processed using a combination of SeaBird Electronics, Inc. (SBE), Sippican, and EHI processing software. The specific processing and QA/QC steps for each type of data are provided below.

Seabird Instruments SBE CTD Cast Data

Initial data processing began with the SBEDataProcessing-Win32 Software. Additional QAQC processing was completed using EHI CTD Processing Software.

Step 1 Data Conversion

- Data were converted from raw data to engineering units and saved as .cnv ASCII files.
- Scans to skip over: 200 (remove a portion of the soak time)
- Convert data from: Downcast and Upcast
- Output Variables:
 - a) Pressure, Digiquartz (decibars)
 - b) Depth (salt water, degrees C)
 - c) Primary Temperature (ITS-90, deg C)
 - d) Temperature 2 (ITS-90, deg C): (secondary Temp.)
 - e) Conductivity (Primary-s/m)
 - f) Conductivity 2 (Secondary-s/m)
 - g) Oxygen Saturation (mg/L)
 - h) Altimeter (m)

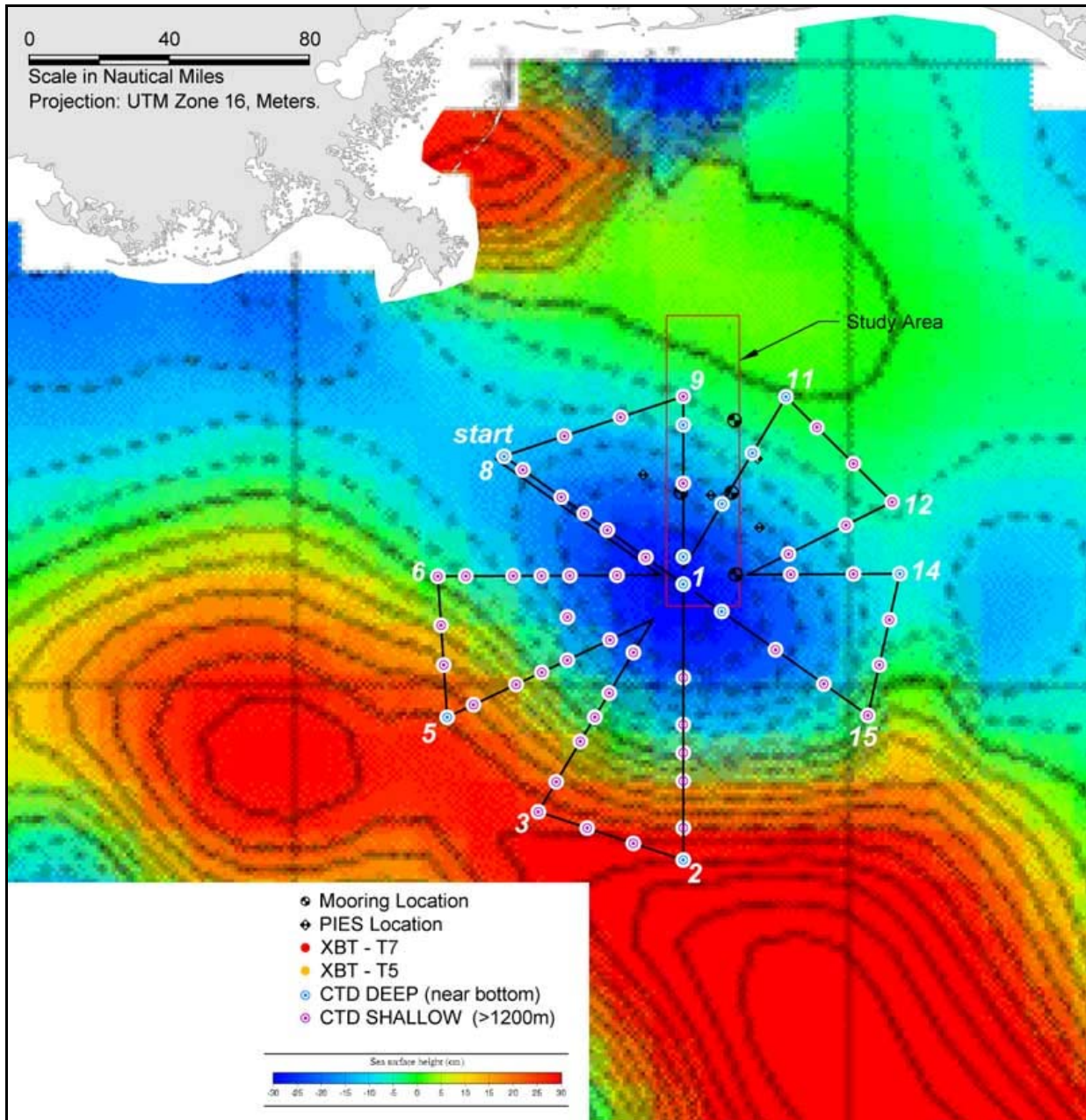


Figure 2.2-4. Pinwheel station grid for intensive Hydrography Cruise 3.

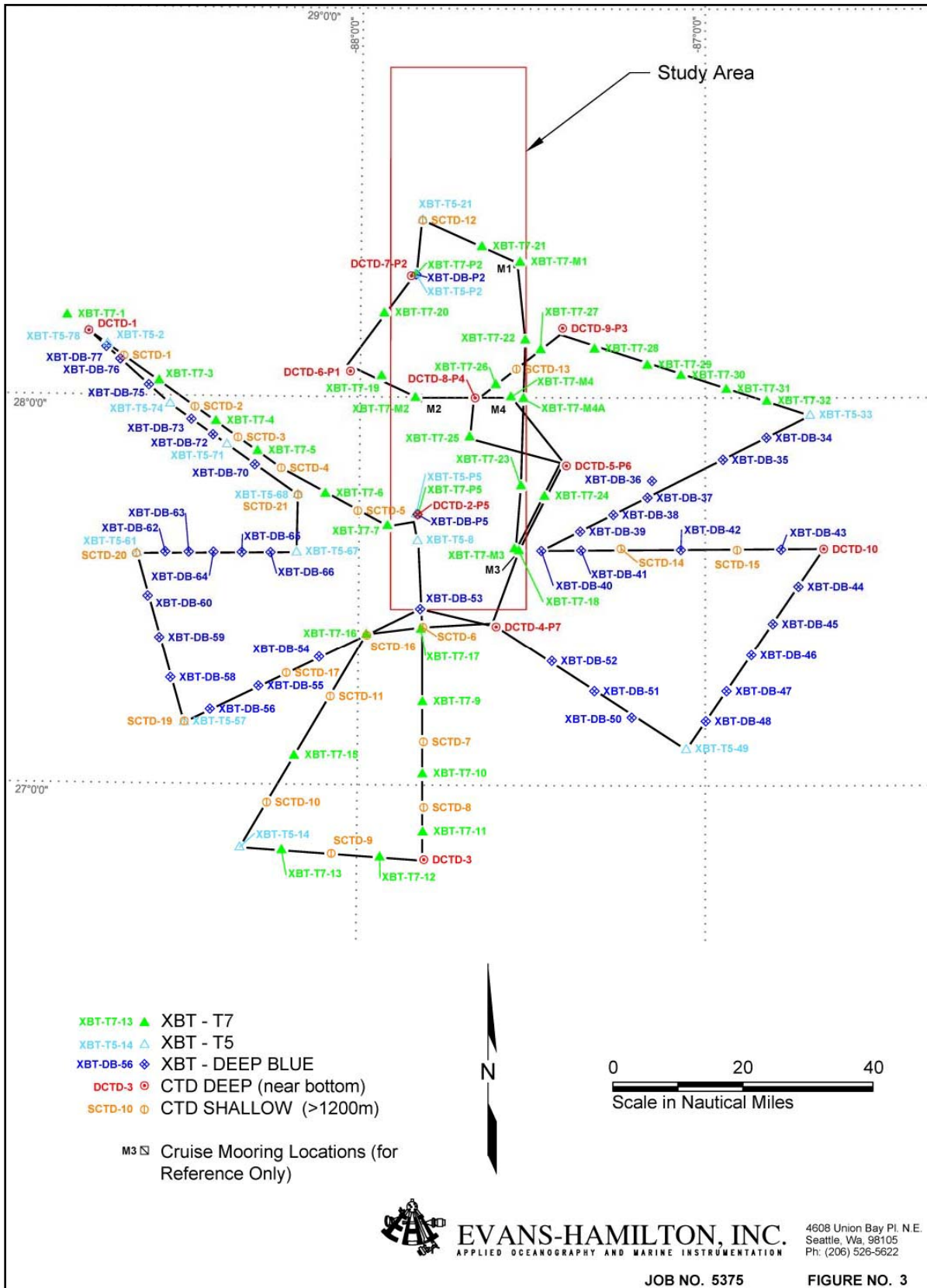


Figure 2.2-5. Station pattern for Hydrography Cruise 3.

Step 2 Filter

- Filtering smoothes high frequency data. Pressure data is typically filtered with a time constant equal to four times the CTD scan rate¹.
- CTD scan rate: 24 Hz = 0.0416667 s
- Pressure: $(4)(0.0416667) = 0.167\text{s}$
- Temperature: 0
- Conductivity: 0

Step 3 Align

- Align CTD aligns temperature, conductivity, and oxygen data relative to pressure to ensure calculated parameters such as salinity and dissolved oxygen concentration are from the same parcel of water.
- Shipboard Offsets: Temperature = 0
Conductivity = 0
Oxygen = 3

Step 4 Cell Thermal Mass

- Cell Thermal Mass uses a filter to remove cell thermal mass effects from the measured conductivity. In areas with steep temperature gradients, this correction is on the order of 0.005 PSU¹.
- Thermal anomaly amp (alpha): 0.03
- Thermal anomaly time constant (1/beta): 7.0

Step 5 Loop Edit

- Loop Edit flags scans as bad that have pressure slowdowns or reversals, thereby reducing the effects of ship heave.
- Minimum velocity type: Fixed
- Minimum CTD velocity (m s⁻¹): 0.25

Step 6 Derive

- Using pressure, temperature, and conductivity, Derive calculates parameters such as salinity and density.

Step 7 Sea Plot

- Sea Plot was used to make preliminary plots for QA/QC.

Step 8 EHI Software

- The EHI CTD processing software QA/QCs the data for spikes in pressure, temperature, salinity, density, conductivity, and oxygen. The maximum depth was found to cut the upcast from the file.

Step 9 QA/QC

- The data were hand checked to remove soak times and ensure high quality data.

Step 10. Bin Averaging

- Finalized data were averaged into 0.5 meter bins.

SIPPICAN XBT Cast Data

XBT data were first exported to ASCII format using the Sippican Winmk12 software. The data were then run through a series of checks and smoothing routines.

Step 1 EHI software

- The EHI CTD processing software QA/QCs the data for spikes in temperature.

Step 2 QA/QC

- The data were hand checked for surface spikes and/or spikes due to the wire coming in contact with the hull of the ship, and to ensure high quality data.

Step 3 Bin Averaging

- Finalized data were averaged into 0.5 meter bins.

2.2.3 CTD vs XBT Data

Hydrographic Cruise 3 was the most comprehensive of the three surveys and used several types of XBT probes. In addition, several stations were sampled with both the profiling CTD system and XBT probes and in some instances two or three types of XBT probe so as to provide an inter-comparison of the measurements from the different instruments. Figure 2.2-6 shows the comparisons of CTD and XBT multi-probe stations. Although the chief error is depth not temperature between the CTD and XBT, temperatures can be compared (Emery and Thomson 2001). Stations 2, 5, 6, and 12 show very close fits between all profiles. The mean XBT-CTD difference for each probe type in the 1-100 m depth range were 0.11° C for a T7 probe, 0.12° C for a T5 probe, and 0.18° C for a deep blue probe. These mean temperature differences were equal to (T7) or slightly less than the mean difference for the entire profile. The profiles for Station 16 differ because although they were taken at the same station, they were collected five days apart. The T7XBT was measured on 22 January 2006 and the shallow CTD was measured on 27 January 2006. This profile comparison indicates how much the area was changing, especially in the surface layers, due to circulation features passing through the area in the short time span of the hydrographic cruise.

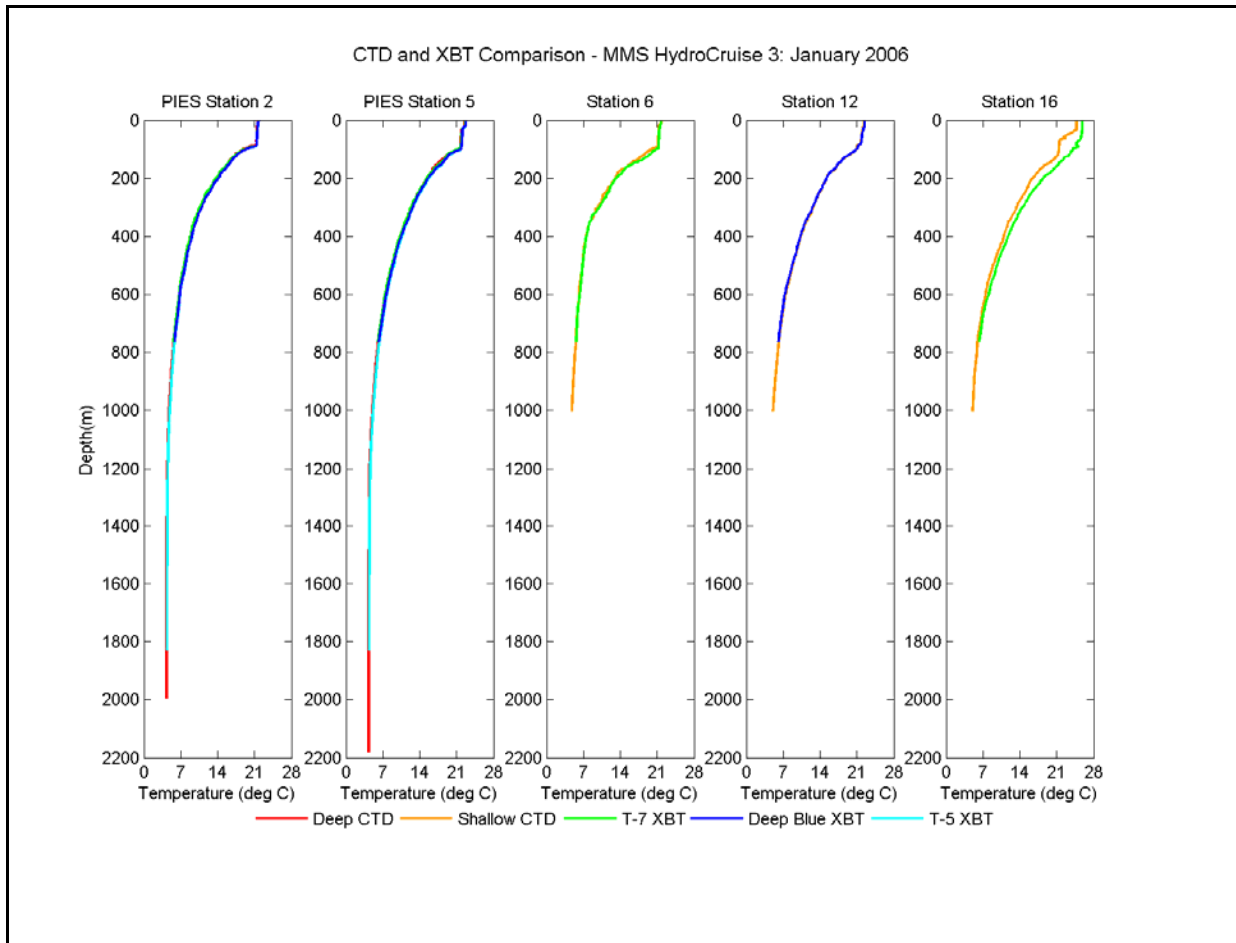


Figure 2.2-6. CTD vs. XBT profile information for Hydrographic Cruise 3 January 2006.

2.2.4 Comparison to Historical Data

Texas A&M University (TAMU) has gathered the electronic files of CTD profiles for most hydrography surveys conducted by researchers in the GOM. After reprocessing the historical data files and plotting the results, TAMU determined that all the historical profiles normally fell within a specified range when plotted as potential temperature versus salinity. Comparison of the CTD data from the present study with the boundaries of the historical data is shown in Figure 2.2-7. Data for the present study shows good agreement with the historical data in that the present data follows the shape of the historical set very closely. Many anomalies during the present study (e.g. number and force of storms, northward migration of LC, etc.) may have contributed to the slight variations.

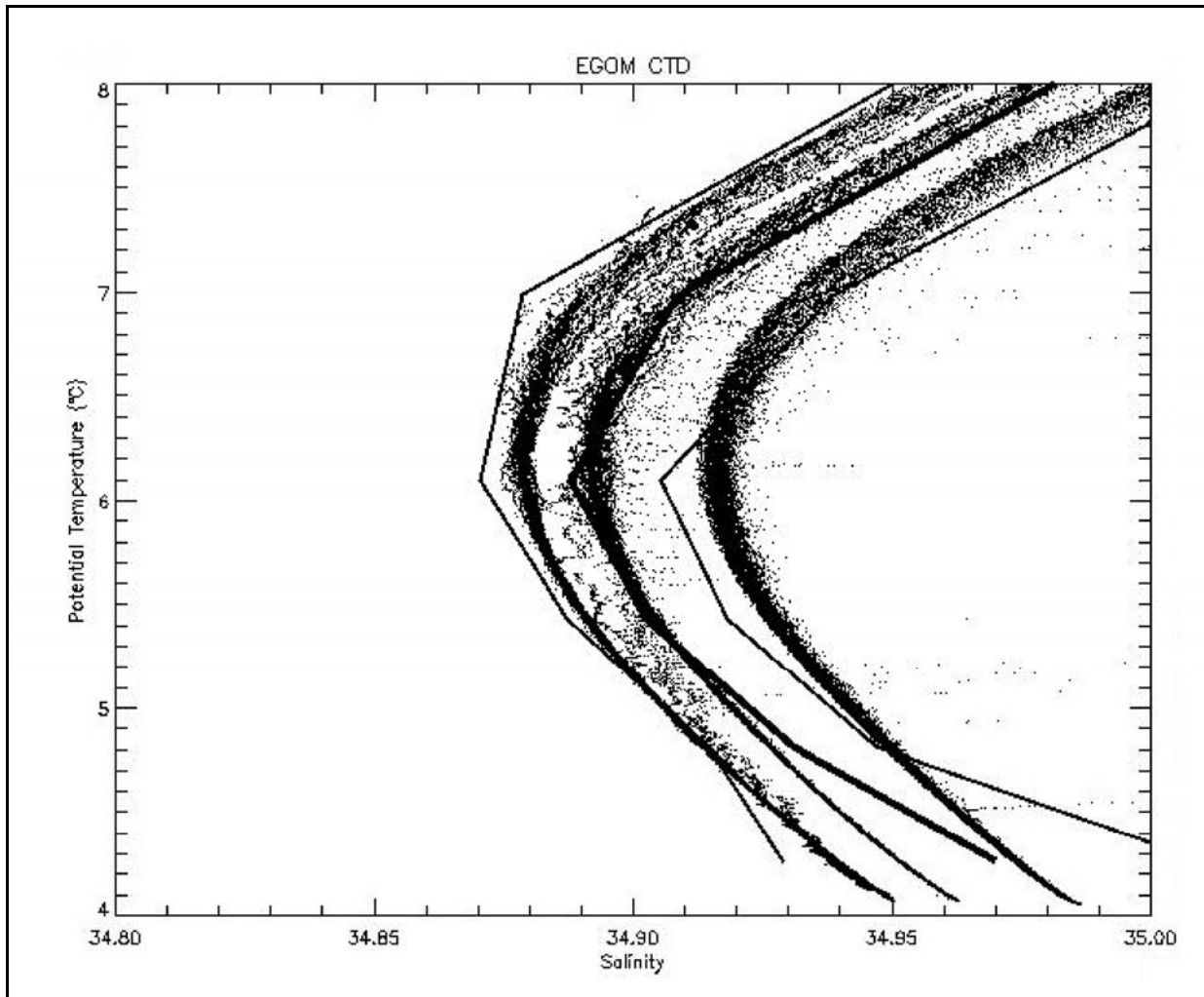


Figure 2.2-7. Profiles from all three hydrographic cruises plotted as potential temperature vs salinity superimposed on the historical data boundaries.

2.3 PIES

An array of seven inverted echo sounders with pressure gauges (PIES) was deployed late December 2004 and recovered in late January 2006 in order to increase the spatial extent to which the measurements of the moored current meter array could be applied (Figure 1.2-1). The PIES is a bottom-mounted instrument that emits 12 kHz sound pulses and measures the round trip travel times or τ (tau) of these acoustic pulses from sea floor to sea surface and back. The PIES, equipped with a pressure gauge, also measures bottom pressure. A detailed description of instrument and initial processing may be found in Hamilton et al. (2003) and Donohue et al. (2006); key steps are discussed in this section.

Prior to deployment, the PIES were serviced, tested, and mobilized by the University of Rhode Island. Deployment of the PIES occurred in late December 2004 on a separate cruise from the initial current moorings deployment which occurred in January 2005.

In late August 2005 during the servicing and redeployment of the current meter moorings, the PIES were acoustically interrogated from the ship and daily-averaged pressure and τ data for each PIES successfully telemetered to the ship. During this trip, two additional PIES were also deployed at sites 4 and 6, denoted as site 4_2 and 6_2.

During the mooring recovery cruise in January 2006, each of the PIES was again acoustically interrogated to download their daily-averaged pressure and τ data, and then acoustically released and recovered, with the exception that the PIES at site 7 did not release and was not recovered.

Data return from the PIES was excellent (Figures 2.3-1 and 2.3-2); full deployment records are available from all PIES with two exceptions. First, the initial instrument at PIES site 6 did not have valid τ records. The τ record from PIES 6_2 is therefore used for site 6. Second, even though the PIES at site 7 was not recovered, a full data set of its daily data was received by acoustic telemetry.

The array of PIES combined with measurements from the current meter moorings enabled a quantitative mapping of the regional circulation. The τ measurements from the PIES allowed for estimates of vertical profiles of temperature, salinity, and density by utilizing empirical relationships (Gravest Empirical Mode) established with historical hydrography. Pressure was leveled via geostrophy using the current measurements. Deep pressure records combined with estimated horizontal density gradients yielded referenced geostrophic velocities. With this array we produced 4-D maps of temperature, salinity, density, and velocity. We mapped the circulation for the year, January 21, 2005 to January 20, 2006 that encompasses the current meter records. Figures 2.3-3 and 2.3-4 illustrate the various views of temperature and current structure provided by the PIES and deep current meter mooring array for August 5, 2005. More details on this process are provided in the following sections.

2.3.1 Gravest Empirical Mode Method

The initial processing of the PIES data included filtering the time series data with a 72-hour 4th order Butterworth filter and subsampling the results at 6-hour intervals. Next, the PIES τ measurements were converted into profiles of temperature, salinity, and specific volume anomaly through the use of a look-up table.

A relationship has been previously established between a τ index and vertical profiles of temperature, salinity, and specific volume anomaly using historical hydrography. This is the so-called Gravest Empirical Mode (GEM) representation (e.g., Meinen and Watts 2000). The procedure consists of two branches. First an empirical relationship was created. Second we converted the PIES measured τ to the τ index of the look-up table.

2.3.1.1 Determine τ Index

Round trip travel time between the 150 and 1000 dbar surface, $\tau(150-1000)$ was used as the τ index. The 150 dbar upper limit of the τ integration avoided the influence of the seasonal cycle. Further refinements discussed below detail a seasonal correction. The 1000 dbar lower limit of the τ integration balanced two needs: to extend the integration below the thermocline and to retain as many of the acquired historical hydrocasts as possible.

2.3.1.2 Assemble Regional Hydrographic Data Set

The hydrography data set was derived from historical hydrography supplemented by CTD hydrocasts taken during the hydrography cruises of this study, and also by hydrocasts from profiling floats used in previous studies (Figure 2.3-5). Due to the integral nature of τ we used only high vertical resolution CTD hydrocasts. The historical database contains 597 hydrography stations from the GOM HYDRO Database compiled by TAMU as part of the BOEMRE-funded Deepwater Reanalysis Project as well as additional stations provided by SAIC and EHI. The GOM is well sampled; 876 hydrocasts represent about 20 years of sampling; hydrocasts sample most of the annual cycle except in May and December; the bulk of casts extend between 1000 to 2000 dbar with relatively few casts below 2000 dbar. Also included were 242 hydrocasts taken by profiling floats used on the MMS sponsored Exploratory Study of Deepwater Currents in the Gulf of Mexico (Donohue et al. 2006). They substantially increased the spatial and temporal sampling. These casts reached maximum pressures of 1000 m.

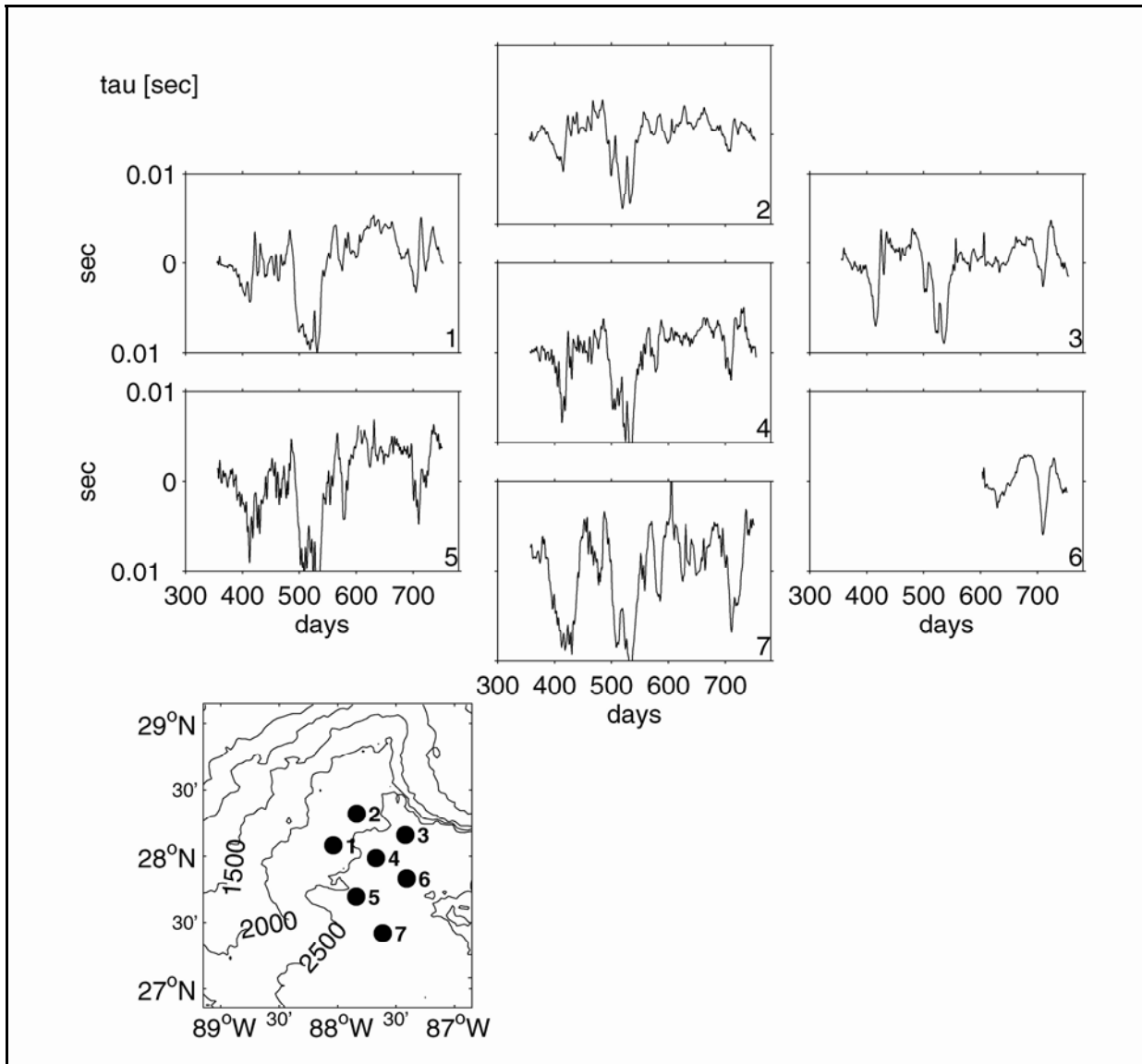


Figure 2.3-1. Time series of τ (tau) anomaly in seconds plotted according to approximate geographic location. Instrument number noted in the lower left corner of each subplot. Bathymetry contoured every 500 m depth. PIES are denoted as filled circles.

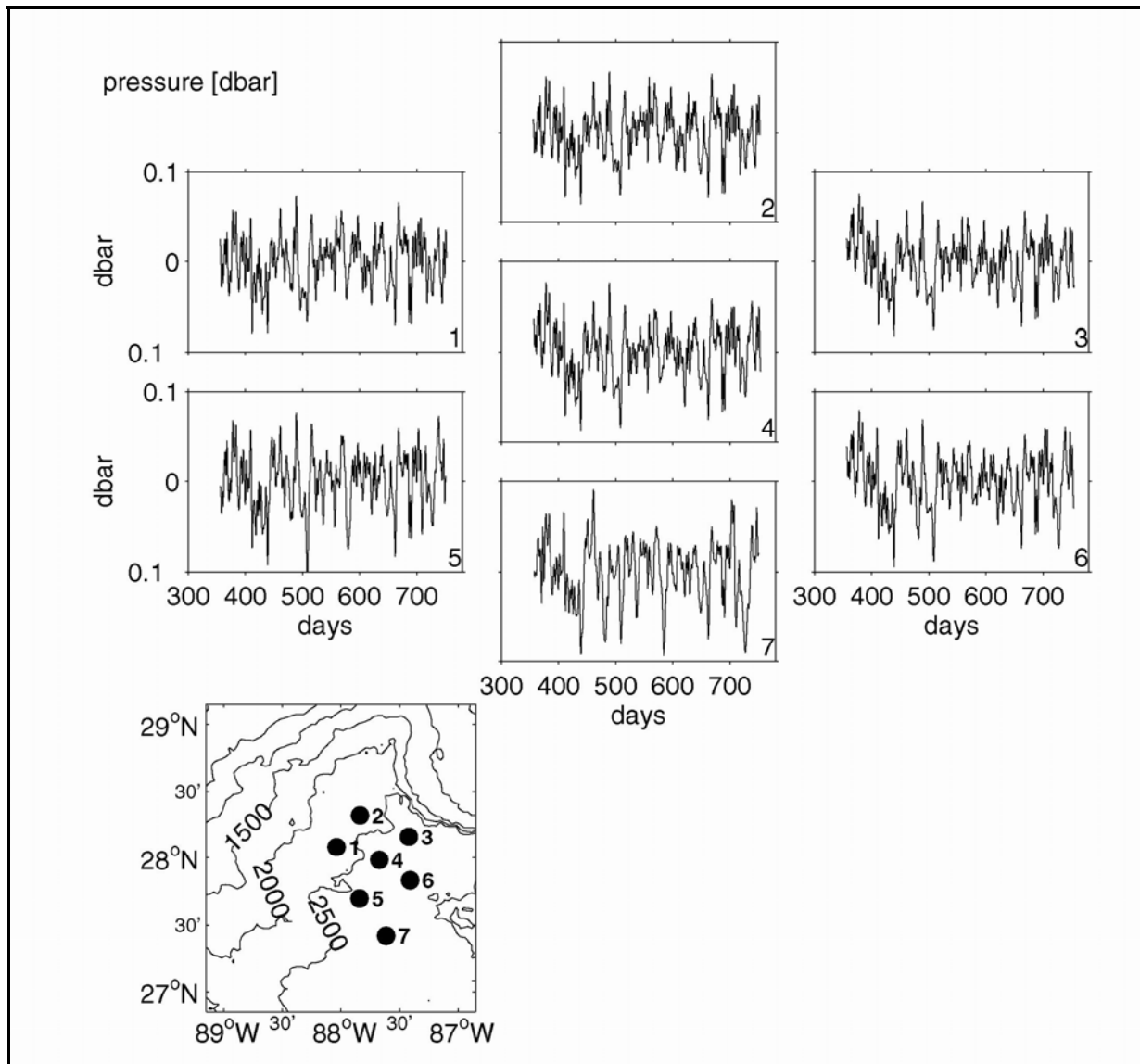


Figure 2.3-2. Time series of bottom pressure anomaly in dbar plotted according to approximate geographic location. Instrument number noted in the lower left corner of each subplot. Bathymetry contoured every 500 m depth.

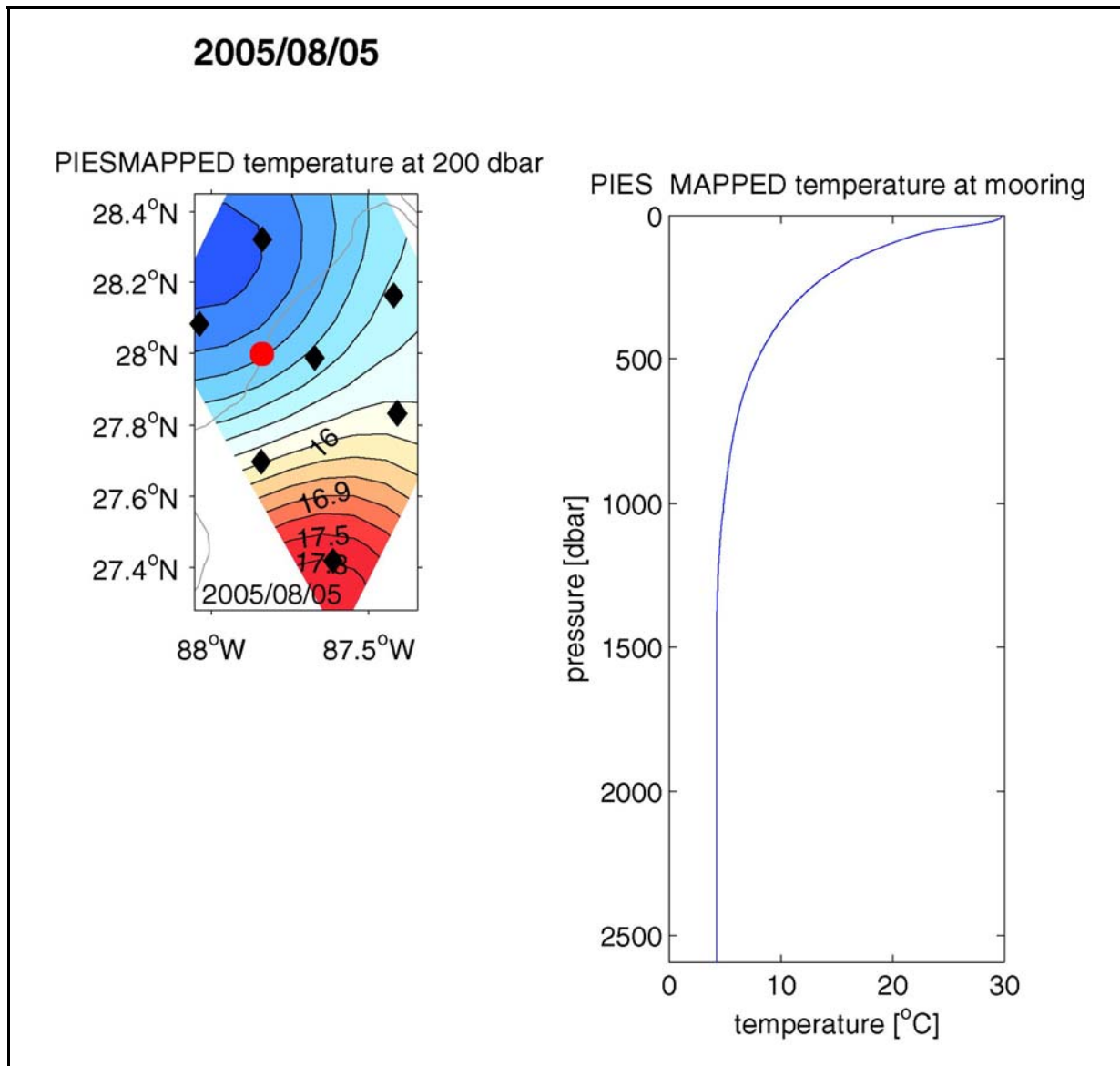


Figure 2.3-3. Two views of the temperature structure in the region for August 5, 2005 provided by the PIES. Left panel: Temperature at 200 dbar in plan view. PIES sites denoted by the diamonds; current meter moorings indicated by the circles. Right panel: Temperature determined from the PIES array at the red dot in the left.

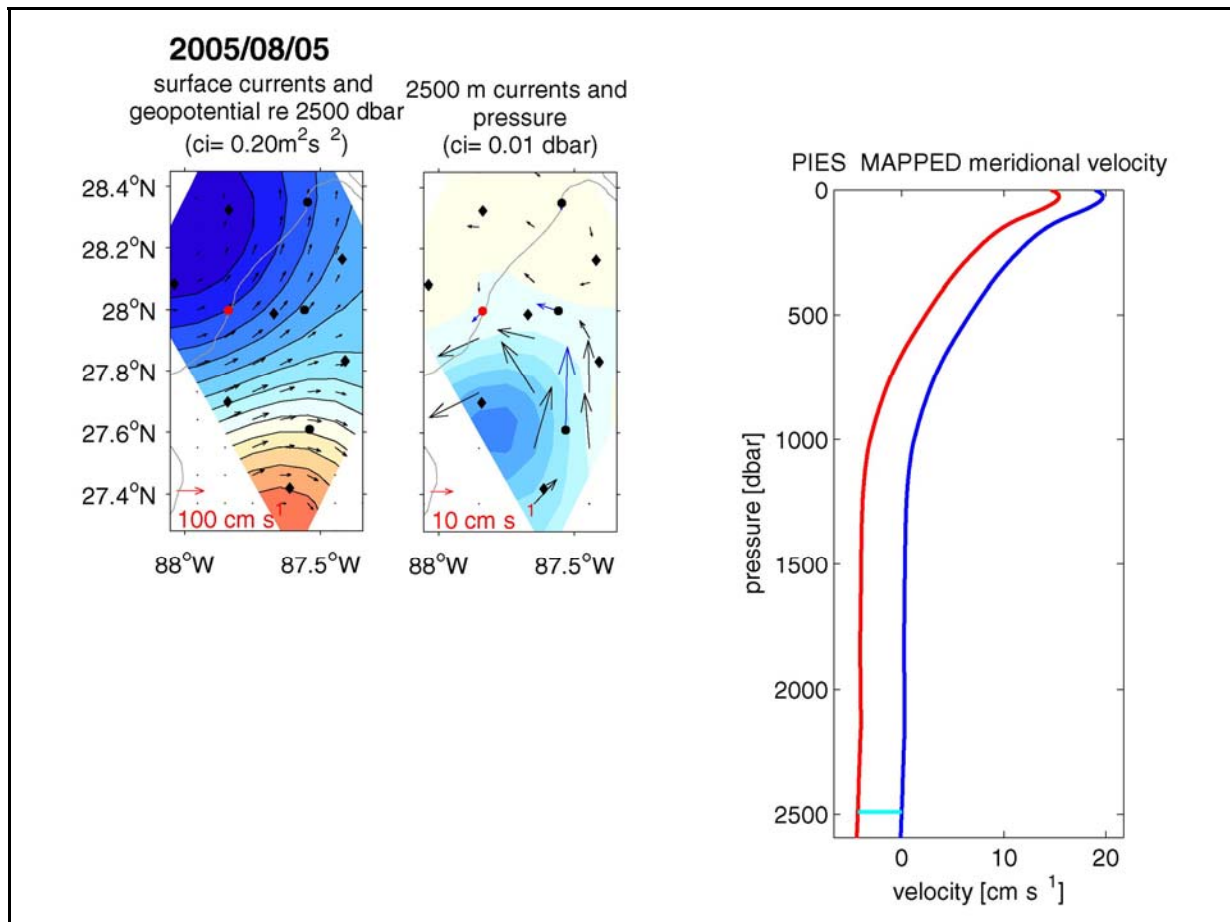


Figure 2.3-4. Several views of the current structure in the region for August 5, 2005 provided by the PIES and current meter measurements. Left two panels: Surface geopotential referenced to 2500 m and surface currents (left) and pressure at 2500 m (right) in plan view. Contour intervals given in the title of each panel. Anticyclonic circulations are shown by reddish hues; cyclonic circulations by bluish hues. PIES sites denoted by the diamonds; current meter moorings indicated by the circles. Right panel: Mapped meridional velocity determined by the PIES array at the red dot in the left and middle panels. The blue line indicates the baroclinic (geostrophic) shear referenced to zero at 2500 m depth derived from the PIES-GEM technique. This shear is referenced by 2500 m mapped velocities (light blue) to yield the absolute geostrophic velocity (red line).

2.3.1.3 Sort Hydrographic Data by τ Index

Hydrocasts were linearly interpolated to a uniform 10-dbar grid and sorted by $\tau(150-1000)$. In Figure 2.3-6 we show results for temperature. The methodology was also applied to salinity and specific volume. Every 10 dbar, a cubic smoothing spline was fit to temperature as a function of $\tau(150-1000)$ (Figure 2.3-7). Root-mean-square residual, rms, for each curve provides an indication of the departure any individual profile might have from the GEM curve. The rms values for temperature were small, 0.25°C, within the thermocline and decrease with increasing pressure. The curves showed that a functional relationship exists between the integrated variable, $\tau(150-1000)$ and vertical profiles of temperature. The two-dimensional GEM fields are shown in Figure 2.3-8. Note that there is little structure in the fields below 1000 dbar, and this reflects the uniform deep-water properties in the GOM.

An example of how the GEM look-up table works is illustrated in Figure 2.3-9. $\tau(150-1000)$ calculated from a hydrocast taken during the MMS-sponsored Survey of Deepwater Currents in the Northwestern Gulf of Mexico project (Donohue et al. 2008) is plotted as the vertical line in the GEM field. The temperature and salinity profiles (blue lines) are 'looked up' given the calculated $\tau(150-1000)$. GEM-determined profiles agreed well with the measured profiles. Note that for this illustration the GEM fields did not include this hydrocast.

2.3.1.4 Seasonal Correction

Finally, a seasonal correction to the upper 150 dbar of the temperature GEM field was made (Figures 2.3-10 and 2.3-11). This procedure utilized all available data and was performed as follows. First a cubic spline under tension was fit every 10 dbar from the surface to 150 dbar. Next the residual from the cubic spline curve was determined. Lastly, the residual was sorted by time of year and created a smoothed empirical relationship for the residual as a function of time of year. This became the 'correction' to the profile determined by the GEM field. The amplitude of the temperature seasonal correction was about 3°C at the surface and decayed to less than 0.5°C by 90 dbar. No seasonal correction was applied to salinity because while there was variability in the surface layer that did not appear to be seasonal.

2.3.2 Conversion of Measured τ to $\tau(150-1000)$

In order to use the GEM fields with the PIES τ measurements, the measured τ was converted to $\tau(150-1000)$. This was accomplished based on the fact that τ at any deep pressure is linearly related to τ at any other deep pressure:

$$\tau(150-1000) = A \times \tau_{p1} + B .$$

Historical hydrography established the slope of this relationship and hydrocasts taken during the PIES deployment and PIES and mooring recovery cruises determined B for each time series. Each PIES typically had two calibration casts except for PIES 6 which had a single cast available for calibration. Calibrations at each PIES with two hydrocasts agreed with each other within 1.5 milliseconds. The mean pressure of each instrument was determined from the record average pressure adjusted for the vertical offset between the pressure sensor and the transducer (0.6 dbar) and mean atmospheric pressure (10.16 dbar). The final $\tau(150-1000)$ records are shown in Figure 2.3-12.

Before measured τ records were converted to $\tau(150-1000)$, a seasonal τ signal was subtracted from the τ records. This seasonal signal was determined from the historical hydrography in a manner similar to the seasonal temperature adjustment. Here we considered the influence of the seasonal cycle in τ between the surface and 150 dbar because the hydrography showed that there is little seasonal signal below 150 dbar. The scatter plot of $\tau(0-150)$ versus $\tau(150-1000)$ was largely due to the seasonal cycle and we determined the amplitude of the residual to be 0.3320 milliseconds (Figure 2.3-13). The correction was small, about 2% of the total range in $\tau(150-1000)$.

We estimated the error in $\tau(150-1000)$ to be near 0.0006 sec. This error derives from the measured hourly τ error, 0.0004 sec, a calibration error, 0.0001 sec, the uncertainty in the seasonal τ correction, 0.0003 sec, and the uncertainty in the slope of the τ to $\tau(150-1000)$ look-up, 0.0003 sec. These errors add independently of each other. The hourly error was estimated as follows: individual τ records have an error of 0.002 sec which, when divided by the square root of twenty four (the number of samples) yielded 0.0004 sec. Note that we calibrated the CTD τ to the hourly measured τ . A potential spatial offset between PIES and the calibration CTD was the largest contribution to the calibration error (see Meinen and Watts, 1998) and was estimated as 0.0001 sec.

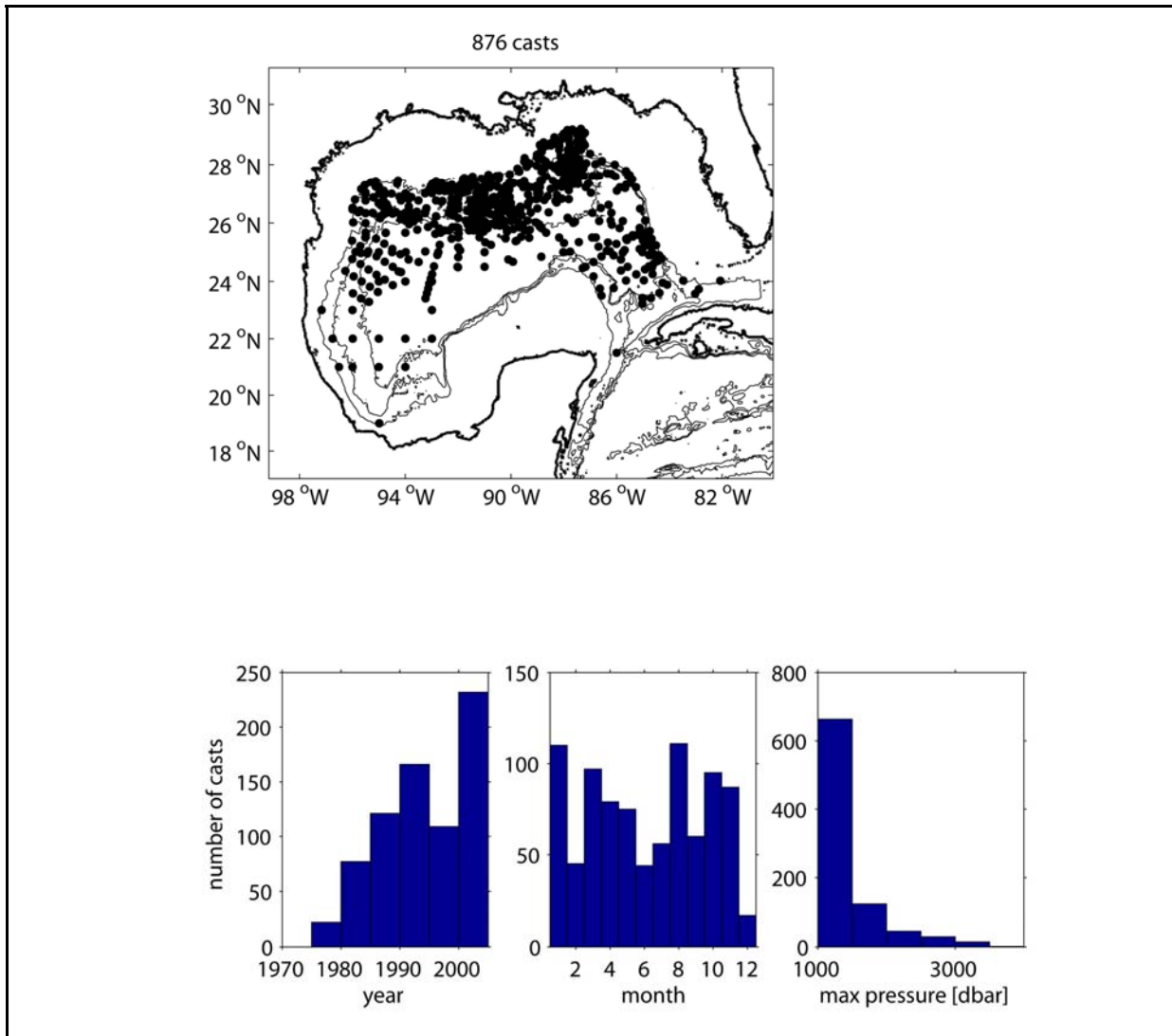


Figure 2.3-5. Spatial and temporal distribution of hydrocasts used to construct the Gravest Empirical Mode. Data provided by the GOM HYDRO Database compiled by TAMU as part of the MMS-funded Deepwater Reanalysis Project and additional stations provided by SAIC, profiling float hydrocasts, and hydrocasts taken during this experiment. Top panel: Spatial distribution of the hydrocasts with bathymetry contoured every 100 m. Bottom panels: Histograms of the maximum hydrocast pressure (bottom left), year of hydrocast (middle), and month of hydrocast (right).

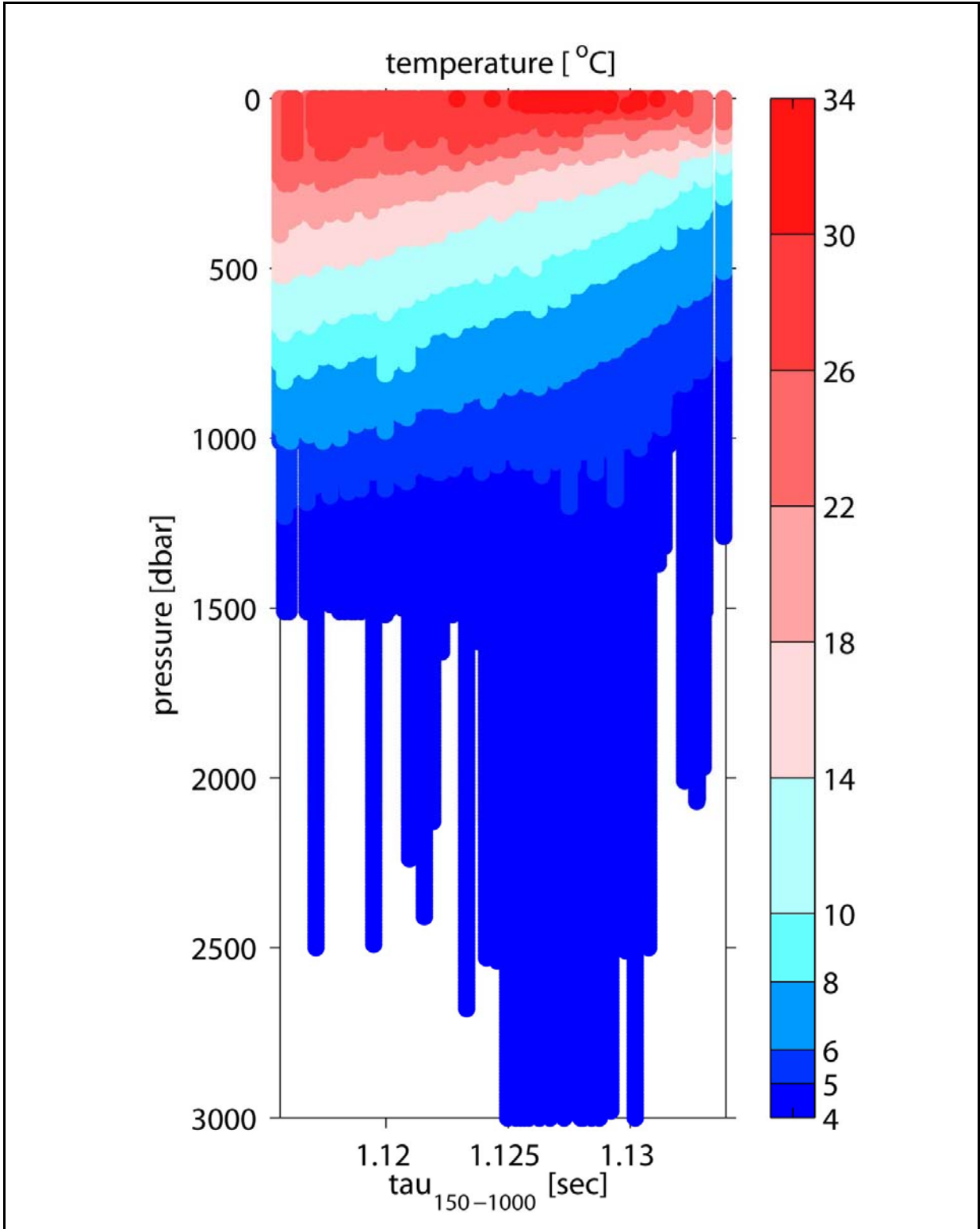


Figure 2.3-6. Temperature profiles interpolated every 10 dbar and sorted by $\tau(150-1000)$.

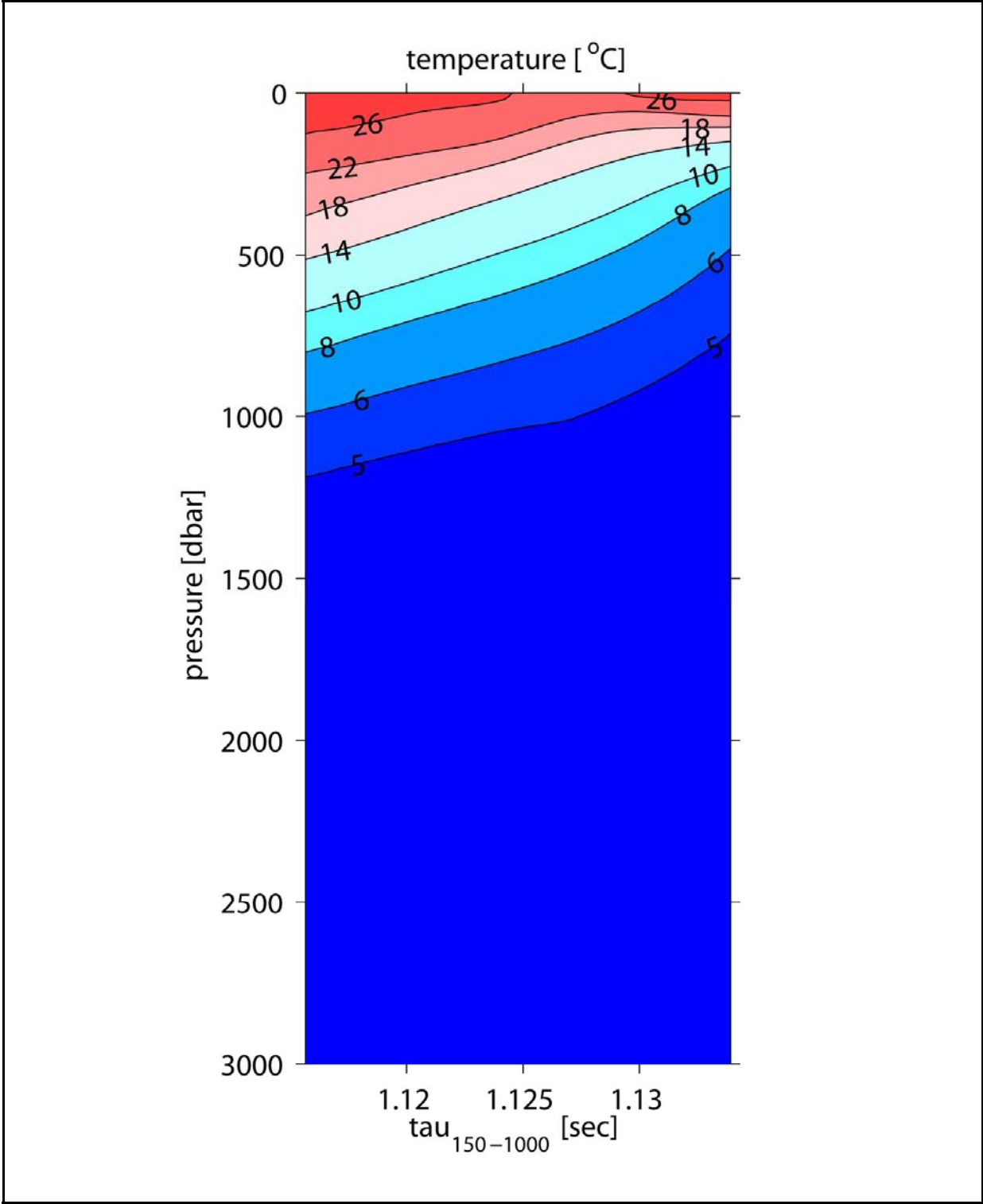


Figure 2.3-7. Scatter plots of temperature versus $\tau(150-1000)$ for six representative pressure levels. At each pressure, the temperature versus $\tau(150-1000)$ data were fit by a cubic smoothing spline (solid curve).

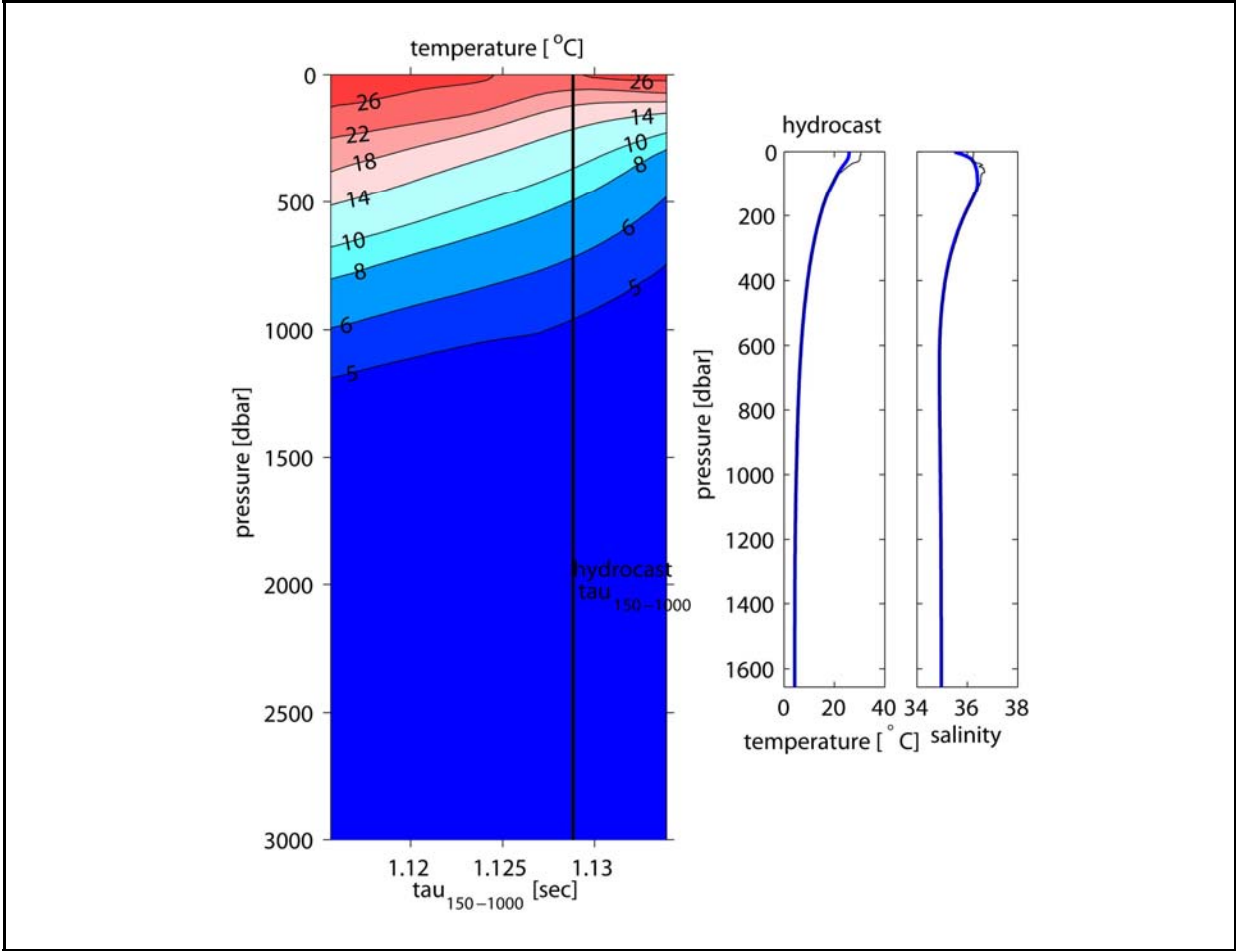


Figure 2.3-8. Contour plot of the cubic smoothing spline fits for the temperature GEM field.

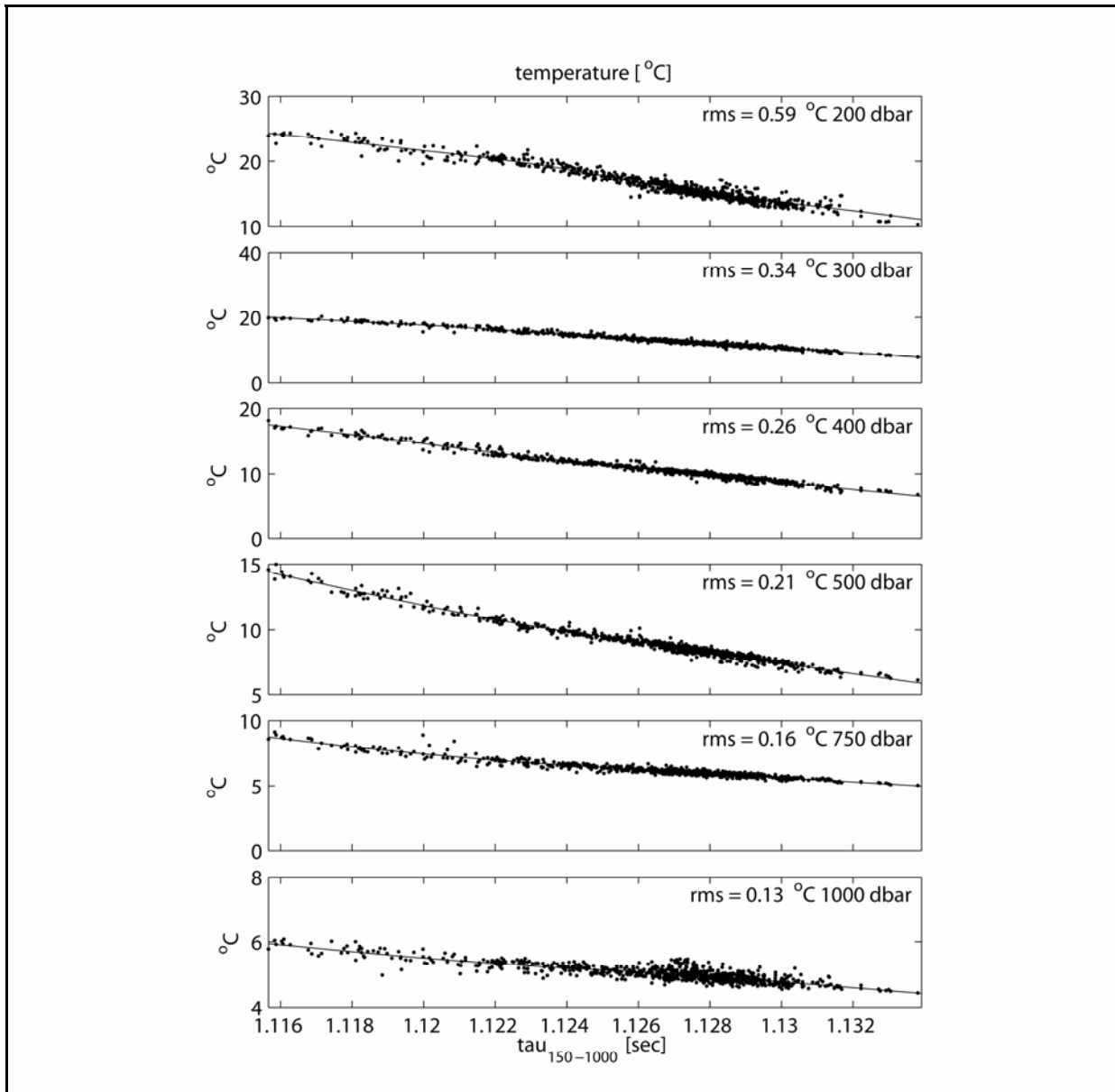


Figure 2.3-9. The GEM-determined temperature and salinity profiles agree well with measured profiles. $\tau(150-1000)$ from a hydrocast is plotted as a vertical line in the temperature GEM field (left panel). Middle and right panels show the temperature and salinity profiles from the hydrocast (black). The temperature and salinity profiles were ‘looked up’ given the calculated $\tau(150-1000)$ and produced estimates shown with the blue line.

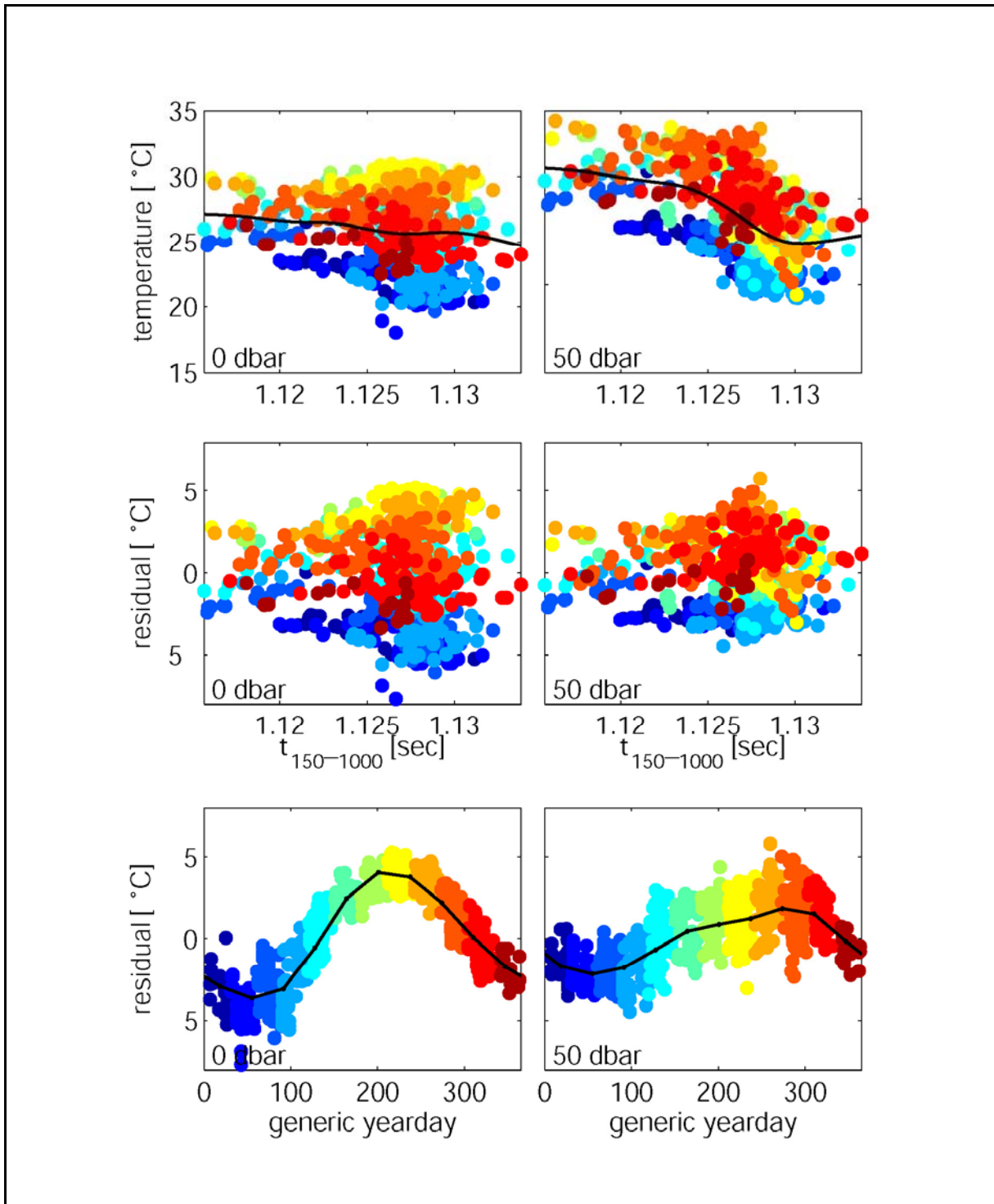


Figure 2.3-10. Upper panels: Scatter plots of temperature versus $\tau(150-1000)$ for surface (left), 50 dbar (middle) and 100 dbar (right) with the cubic spline fit shown as a solid dark line. All samples in all panels are color coded by generic yearday transitioning from blue in January to red in December. Middle panels show the residual from the cubic spline fit. Lower panels: A clear seasonal signal in temperature emerges when the residual is sorted by time of year.

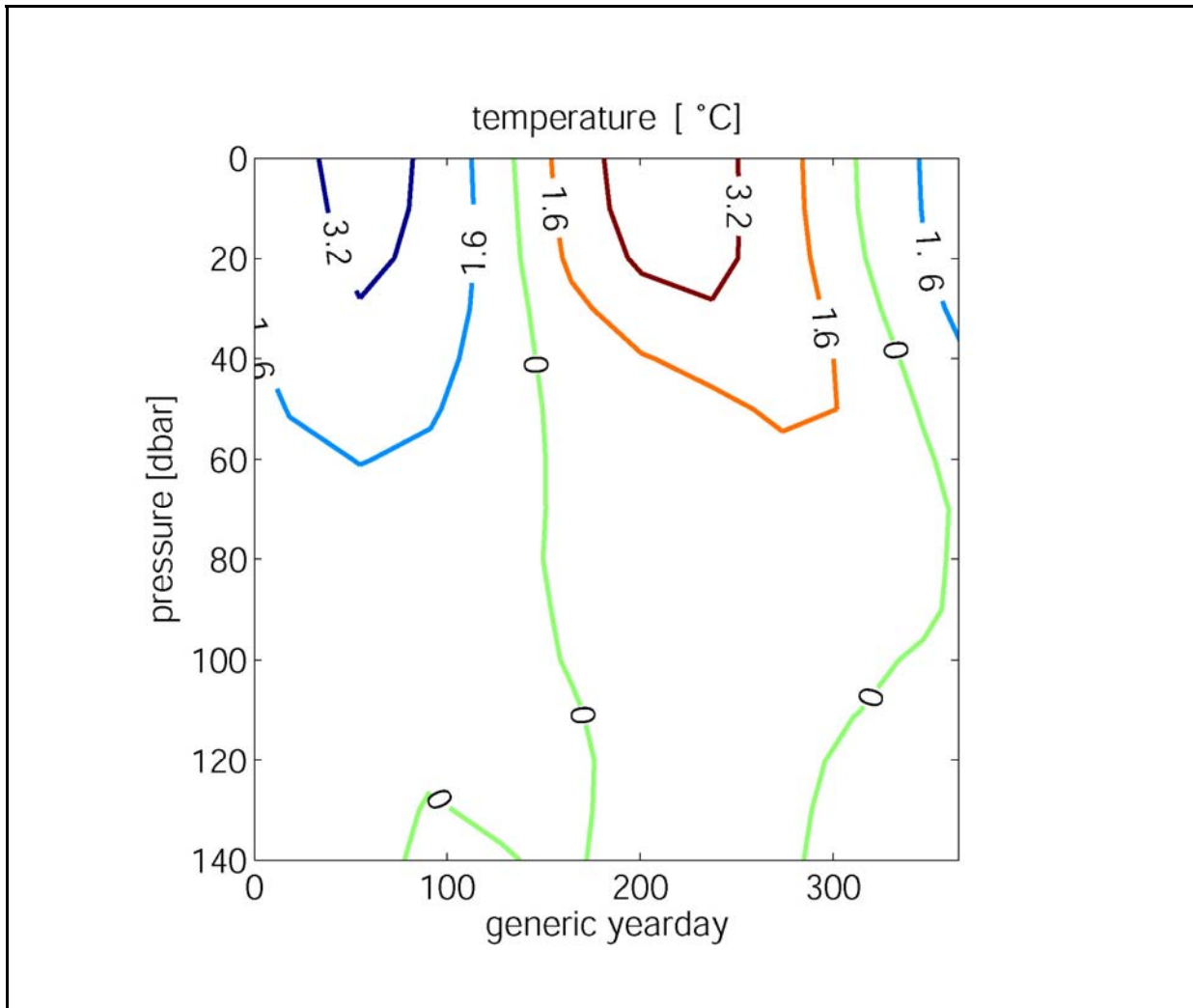


Figure 2.3-11. Seasonal temperature correction/amplitude contoured as function of yearday and pressure. The amplitude of the temperature seasonal correction is about 3°C at the surface and decays to less than 0.5°C by 90 dbar.

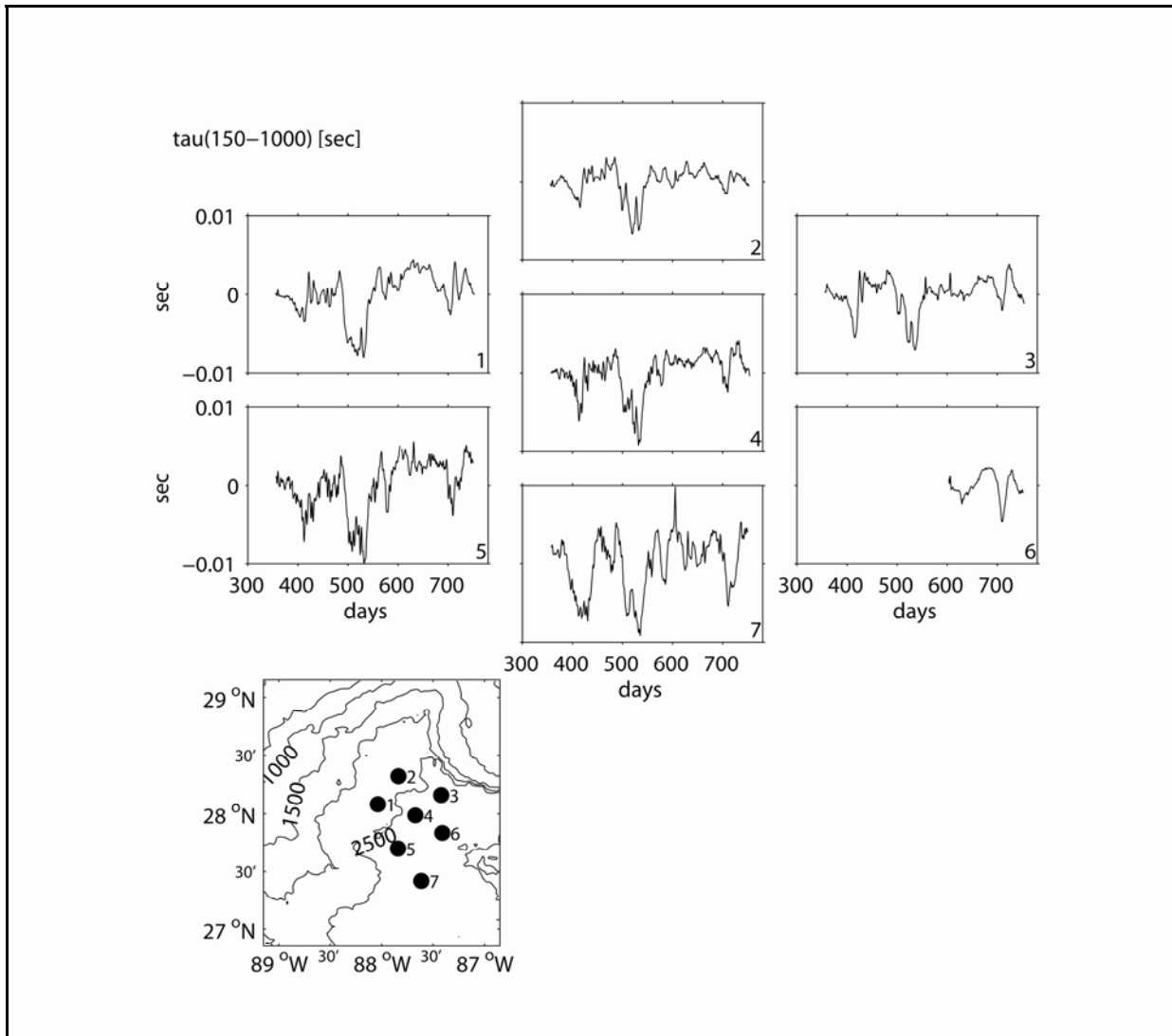


Figure 2.3-12. $\tau(150-1000)$ for each time series. The time series are shown in approximate geographic location. Instrument number is in the lower left corner of each subplot. Bathymetry contoured every 500 m depth.

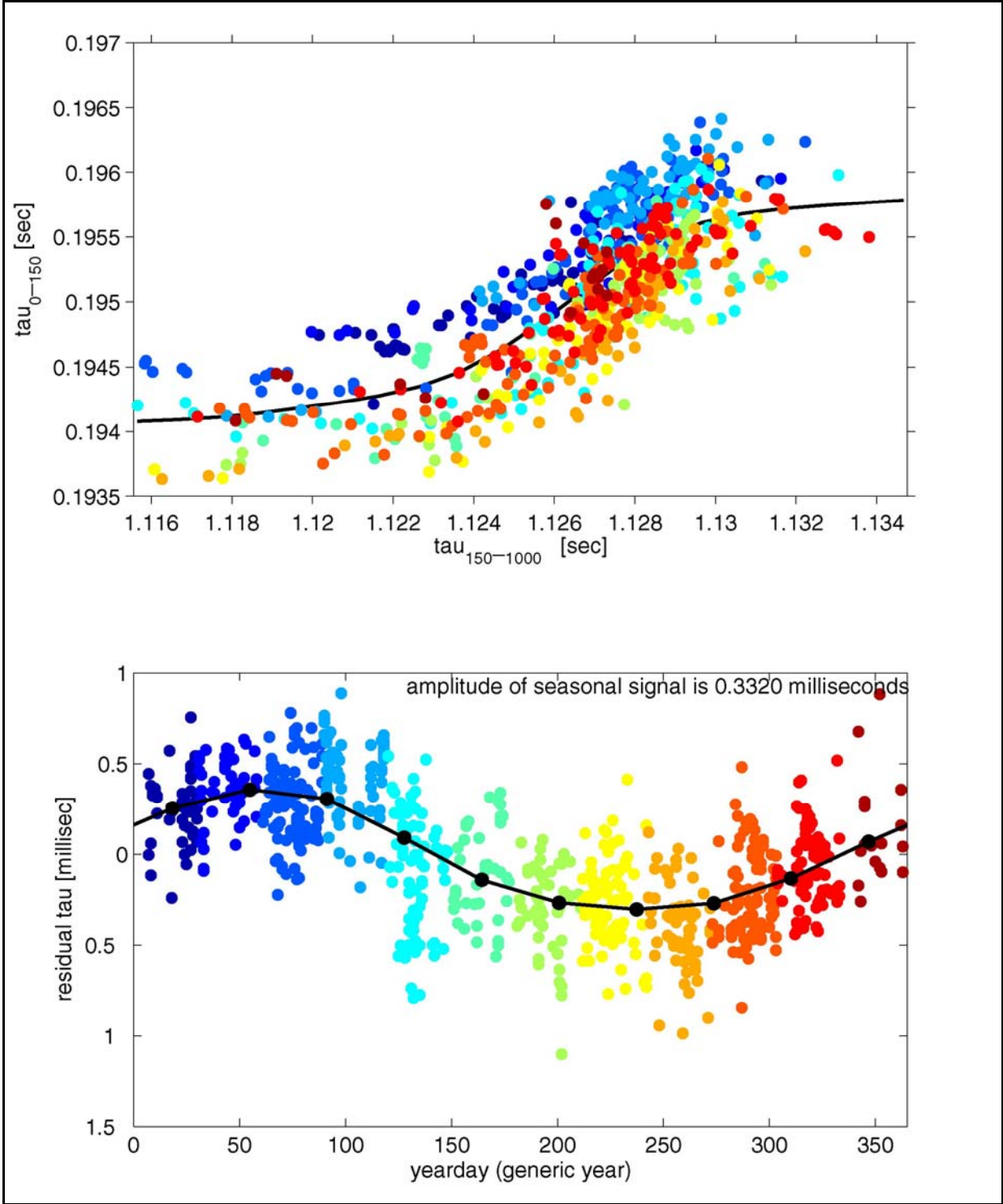


Figure 2.3-13. Upper panel: Scatter plots of $\tau(0-150)$ versus $\tau(150-1000)$. Each point is color coded by generic yearday transitioning from blue in January to red in December. The scatter about the spline fit (solid dark line) is largely due to the seasonal cycle. Lower panel: The residual from the cubic spline fit shown in the upper panel sorted by generic yearday showed a clear annual signal.

2.3.3 Upper-Ocean Maps

Maps were produced with optimal interpolation techniques adapted from Bretherton et al. (1976) and outlined in Watts et al. (1989, 2001). Optimal interpolation requires that the input fields have zero mean and uniform variance. In order to meet this requirement, a mean field must be subtracted from the fields before mapping and then added back to produce maps of the total field. The mean was removed in such a way that the mapped fields behaved well outside the measurement sites. Additionally, the cross-correlations among the measurements determined the correlation function and length scales utilized in the optimal interpolation to map anomalies. A Gaussian correlation function was employed to construct the maps. A multivariate optimal interpolation mapped the geopotential and velocity, which was constrained to be geostrophic.

The maps of upper-ocean fields such as temperature and geostrophic shear were calculated by subtracting a 40-day low-passed field mapped with a correlation length scale of 100 km. We then mapped an anomaly field with a shorter correlation length scale of 45 km. Correlation functions of the measurement anomalies determined the correlation length scales (Figure 2.3-14). The measurement correlation functions were nearly isotropic indicating that the use of an isotropic Gaussian correlation function for the objective analysis was appropriate.

2.3.4 Bottom Pressure

Several bottom-pressure processing details for the PIES are noteworthy. First, our experience indicates that preconditioning of the pressure sensors in the PIES greatly reduces pressure drift. Therefore the PIES pressure sensors were subjected to pressures near 3000 dbar for 1-2 months in the lab prior to their first deployment. Second, the pressure data were detided. Tidal response analysis (Munk and Cartwright 1966) determined the eight major tidal constituents for each instrument. Tidal amplitudes are generally small. The largest tidal amplitudes are near 14 cm for O1 and K1, near 5 cm for P1, and less than 5 cm for Q1 and for the remaining semidiurnal constituents. Estimated tides and phases vary smoothly across the array. Finally, pressure drift was removed using techniques found in Watts and Kontoyiannis (1990); an exponential-plus-linear drift curve determined by a least-squares fit was removed from the measurements. The instruments experienced small drifts with the maximum drift at 0.06 dbar.

To achieve mapping the near-bottom circulation, the bottom-pressure measurements must be leveled to produce spatially consistent maps since each dedrifted pressure record has an undetermined additive constant offset relative to the other records. ‘Leveled bottom pressures’ refers to bottom pressures that have been adjusted to the same geopotential surface. Mean near-bottom currents and bottom pressures were dynamically constrained to be in geostrophic balance. Watts et al. (2001) provides a detailed description of the leveling procedure; here we highlight methods specific to this study.

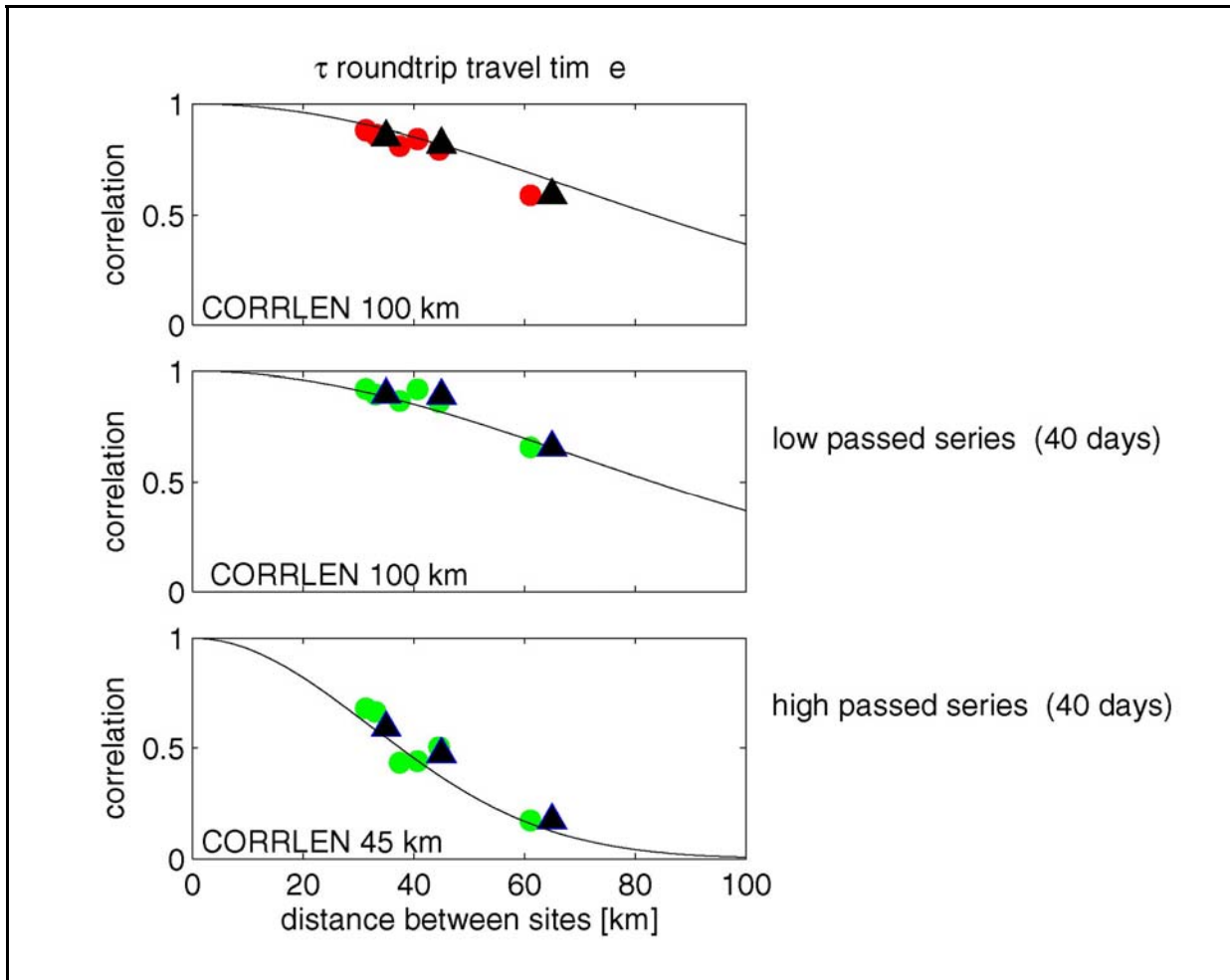


Figure 2.3-14. Correlation coefficient between pairs of τ records longer than one year. Correlations coefficient plotted as a function of separation distance and binned every 10 km (black triangles). Top panel: Time series have been 3-day low-pass filtered. A 100 km Gaussian function is plotted with black line. Middle panel: Time series have been 40-day low-pass filtered. A 100 km Gaussian function is plotted with black line. Lower panel: Time series have been 40-day high-pass filtered. A 45 km Gaussian function is plotted with black line.

First, we chose a deep reference level of 2500 dbar for the pressure records. Any depth could serve as the reference level, but a deep reference level reduces error because the level is close to the velocity and pressure measurements. Furthermore a deep reference level results in two modes that can be identified with physical modes, a baroclinic mode which contains the shear/steric signal and a barotropic mode which is depth independent. Thus the methodology yields absolute current profiles composed of two vertical modes, a geostrophic shear referenced to zero at the reference level and a depth-independent component that is equivalent to the velocity at the reference level. Figure 2.3-4 illustrates this approach. The deep reference-level currents were derived from the measured 2500 m currents at M1, M3, M4 and the 2000 m currents at M2. The M2 2500 m current record was not continuous through January 2005 to January 2006. Comparison between common time segments of the 2000 and 2500 m M2 records indicated that there was little vertical shear between these depths.

2.3.5 Reference-Level Maps

Lower-ocean mapping paralleled the upper-ocean procedure. Before mapping, a common mode (array-average pressure) was subtracted from the 2500-dbar pressures (Figure 2.3-15). The common mode in the deep pressures simply adds a time-dependent array-wide constant which has no dynamical significance for the mesoscale circulation so it is better to subtract it from all records prior to mapping. Spectra of the common mode revealed dominant peaks near 32, 14 and 6 days. The 6-day signal is likely the barotropic oceanic response to the atmospheric Rossby-Haurwitz wave (Park and Watts 2006). The 14-day peak had a slightly lower period compared to the nearly 16-day period found in the Exploratory Study bottom pressure data set (Donohue et al. 2006). This signal remains unexplained; however, this signal was coherent and in phase with the 14-day signal found in deep pressures in the Survey of Deepwater Currents in the Northwestern Gulf of Mexico (Donohue et al. 2008) suggesting that it is a basin-wide signal. Figure 2.3-16 shows the bottom pressure records with the common mode removed. The mean field was derived from fitting a plane to the mean 2500-dbar pressures. A 30-km correlation length scale determined from the near-bottom-pressure correlations was used to map anomaly fields (Figure 2.3-17). Similar to the τ time series, the near-bottom-pressure autocorrelations were nearly isotropic. Streamfunction maps were created by inputs from both pressure and current meter data. The inclusion of the current meter data sharpens the gradients.

Finally, we compared a 30-day low-pass streamfunction computed with deep current meters alone to a 30-day low-pass streamfunction computed only with the pressure gauges. The difference between these curves indicated possible errors in our initial dedrift technique. Recall that the initial procedure dedrifted bottom pressure by the subtraction of a linear plus exponential fit, however this method did not differentiate between short-term pressure drift and real ocean signals. Final drift curves changed slightly and the maximum drift remained small, 0.06 dbar.

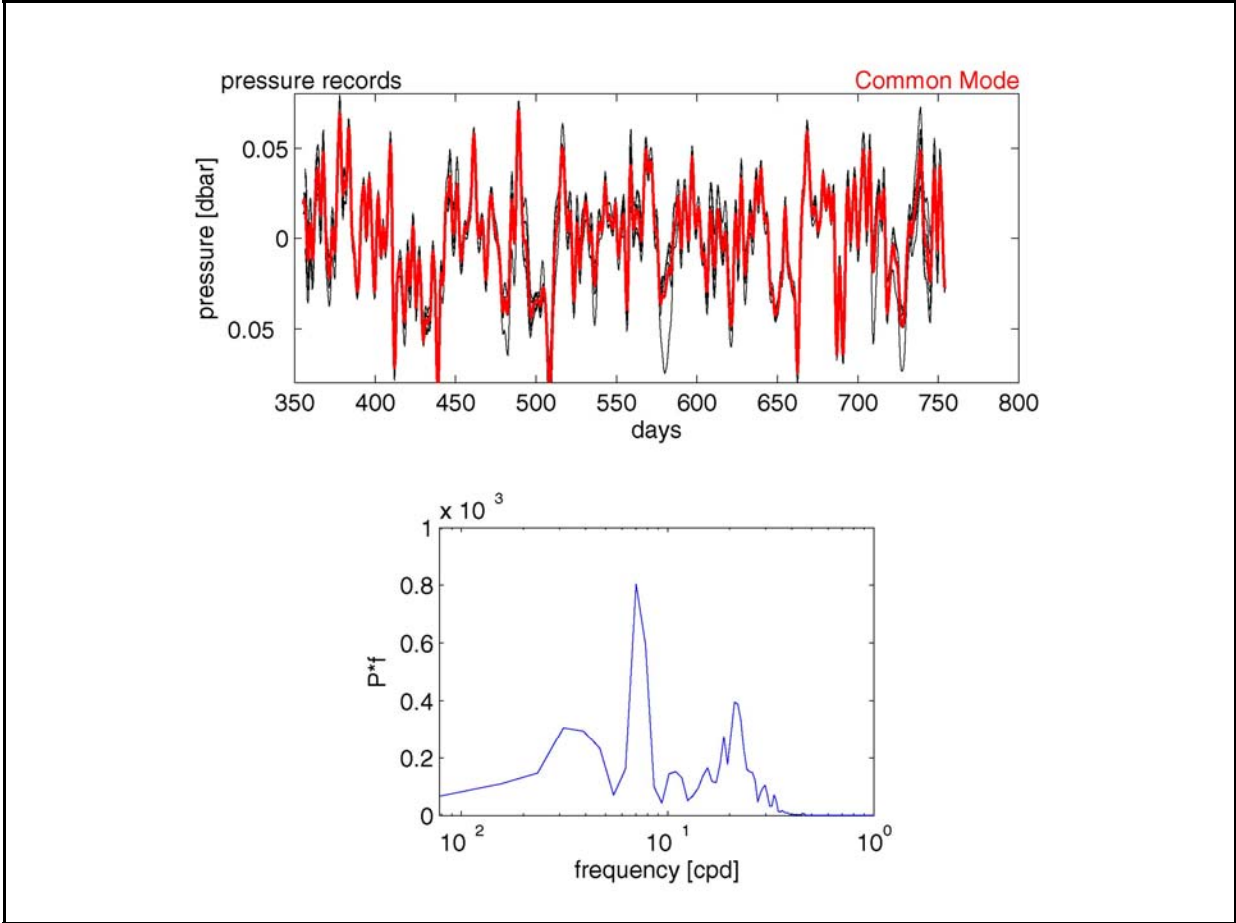


Figure 2.3-15. Top Panel: Common mode subtracted from bottom pressure records before mapping deepwater dynamical properties. Bottom Panel: Spectra of common mode reveal dominant peaks near 32, 14 and 5 days.

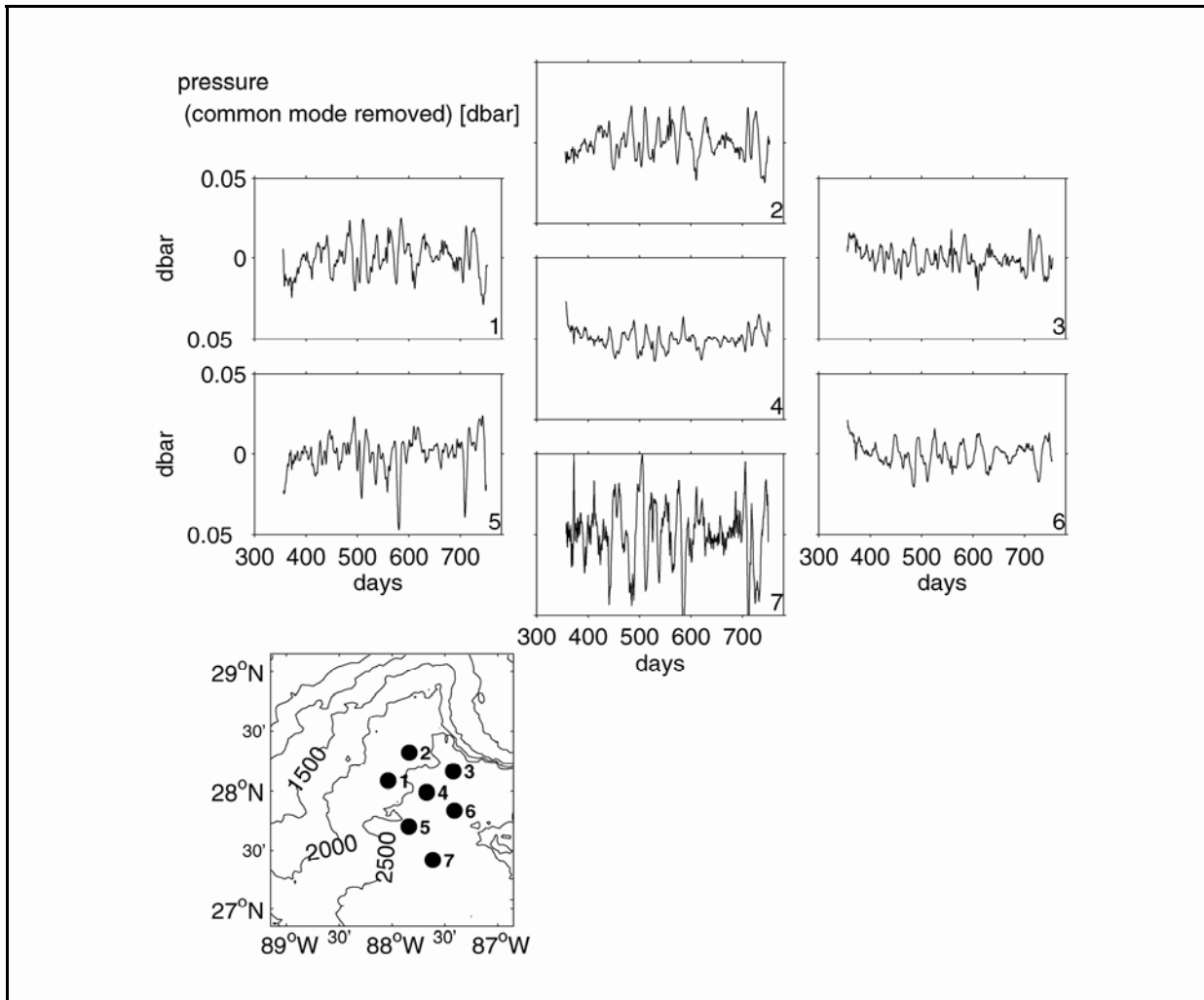


Figure 2.3-16. Time series of bottom pressure anomaly with the common mode removed in dbar plotted according to approximate geographic location. Instrument number noted in the lower left corner of each subplot. Bathymetry contoured every 500 m depth.

2.3.6 Total Maps

The combination of upper and lower circulation maps estimated absolute velocities throughout the water column. Upper-ocean relative velocities were created by mapping velocities referenced to zero at 2500 dbar. The 2500 dbar-level velocities, created with the bottom pressure and current meter records, then referenced these to generate absolute upper-ocean relative velocities. Absolute sea surface heights were also determined. First, 2500-dbar pressures were converted to their height equivalent (pressure divided by gravity and density). Second, surface geopotentials referenced to 2500 dbar were converted to their height equivalent (geopotential divided by gravity). The 2500-dbar referenced and 2500-dbar fields were combined to yield absolute sea surface height.

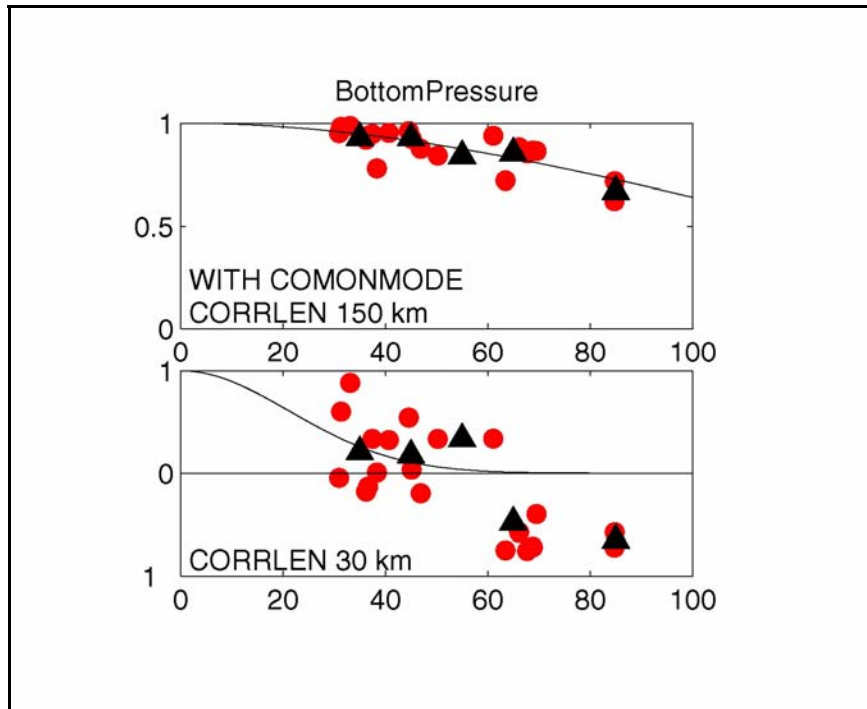


Figure 2.3-17. Correlation coefficient between pairs of pressure records. Upper panel: Correlations coefficient plotted as a function of separation distance (open red circles) and binned every 10 km (black triangles). The common mode produces long correlations. A 150 km Gaussian function is plotted with black line. Lower panel: Correlation coefficients contoured as a function of separation distance (open red circles) and binned every 10 km (black triangles) after the common mode has been removed. A 30 km Gaussian function is plotted in black.

2.3.7 Mooring Comparisons

Measurements of temperature and current from the current meters were compared to PIES-derived estimates. This comparison is not strictly a validation of the PIES methodology because the design of the array does not lend itself to strict verification as point measurements differ intrinsically from mapped estimates. In addition, the mooring measurements have errors as well. After accounting for possible differences, the comparisons below show that the measurements and PIES-derived estimates track each other and generally agree within anticipated bounds.

Three tall moorings (M1, M2, and M3) embedded in the middle of the array provided measurements to evaluate our PIES-derived fields of temperature. The tall moorings experienced some vertical motion when stronger ocean currents caused the sensors on the upper portion of the moorings to deviate in depth. The proper comparison was thus between measured and estimated $T(t,p(t))$. The comparison was made at a nominal 450 m depth because the temperature sensors at that depth were the most stable in depth of those temperature sensors in the upper thermocline level. The temperatures compare well (Figure 2.3-18). Differences derive from instrument errors (both from the moorings and the PIES), the GEM parameterization and from mapping uncertainty. Table 2.3-1 documents the anticipated differences between the moorings and the PIES. The first column indicates the error due to IES instrument noise (0.0006 sec), the GEM parameterization, and mapping error. The difference between point measurements and mapped estimates was determined by the optimal interpolation mapping error based upon a correlation length scale of 45 km (Bretherton 1976). The second column includes the impact of a 10 dbar uncertainty in the pressure sensor. The final column of Table 2.3-1 shows the rms differences between the mooring data and mapped temperature. The observed differences are lower for the M1 and M3 mooring time series. In the case of the M2 comparison, the observed rms is 0.05°C larger than anticipated.

Table 2.3-1

Temperature Differences.

Predicted differences between measured and PIES-estimated temperature for each mooring at a nominal depth of 450 m. The second column presents the predicted difference between mapped and measured temperature considering errors in the GEM table look-up due to τ uncertainty, scatter in the GEM table and the mapping uncertainty. The third column includes the impact of the uncertainty in absolute mooring sensor pressure (column 4).

Mooring	Predicted Difference (PIES and mapping errors) [°C]	Predicted Difference (PIES, mapping and mooring errors) [°C]	Observed Difference [°C]
M1	0.54	0.62	0.51
M2	0.56	0.63	0.68
M3	0.72	0.77	0.64

The PIES-mapped currents were also compared to the moored currents measurements. Figure 2.3-19 shows a comparison for the M2 mooring, again at a nominal depth of 450 m. Both series track each other well. The rms differences for all mooring current comparisons are listed in Table 2.3-2 which also includes an estimate of anticipated errors due to instrument error, the GEM parameterization, and mapping differences. Ageostrophic motion such as high vertical wavenumber inertial currents were not reproduced in the maps of geostrophic velocity. Additionally, in regions of strong curvature the gradient wind balance rather than geostrophic balance may be more appropriate. Table 2.3-2 does not account for the contribution of ageostrophic motion which is hard to anticipate a priori nor does the table include an error in mooring velocity due to uncertainty in the sensor pressure record because the velocity shears are relatively weak here.

The observed rms differences are very close to the anticipated differences. Although not explicitly tabulated, current meter measurements are not without error. As an example during the first deployment of mooring M2 the ADCP record contained gaps owing to cable interference during portions of the time when the mooring's surface buoy was lost.

Table 2.3-2

Velocity Differences.

Predicted differences between measured and PIES-estimated velocity for each mooring at a nominal depth of 450 m. The second column presents the predicted difference between mapped and measured velocities considering errors in the GEM table look-up due to τ uncertainty, scatter in the GEM table and the mapping uncertainty. The third column shows the observed differences.

Mooring	Predicted difference [cm s ⁻¹]	Observed Difference [cm s ⁻¹]
M1 zonal	8.0	8.5
meridional	5.9	5.8
M2 zonal	6.4	8.4
meridional	7.8	7.2
M3 zonal	7.2	7.9
meridional	6.3	7.9

2.4 Remote Sensing

The remote sensing component of the study acquired remotely sensed (satellite) data to aid in the interpretation of mesoscale oceanographic features during the period of time of the physical oceanographic measurements in the study area. A combination of satellite observing systems was used.

To carry out this task, the Colorado Center for Astrodynamic Research (CCAR) collected and processed a complementary suite of satellite observations from satellite altimeter and radiometer remote sensing data systems. This suite incorporated sea surface height (SSH) data with high-resolution sea surface temperature (SST) and ocean color imagery. Satellite altimetry provided the all-weather multi-satellite monitoring capability required to map mesoscale circulation variability in the GOM. During cloud-free conditions, multi-channel radiometry was used to supplement the altimetric sampling by providing high-resolution synoptic SST and ocean color imagery for monitoring the rapidly evolving LC and its associated eddies including small-scale frontal features in and around the study region.

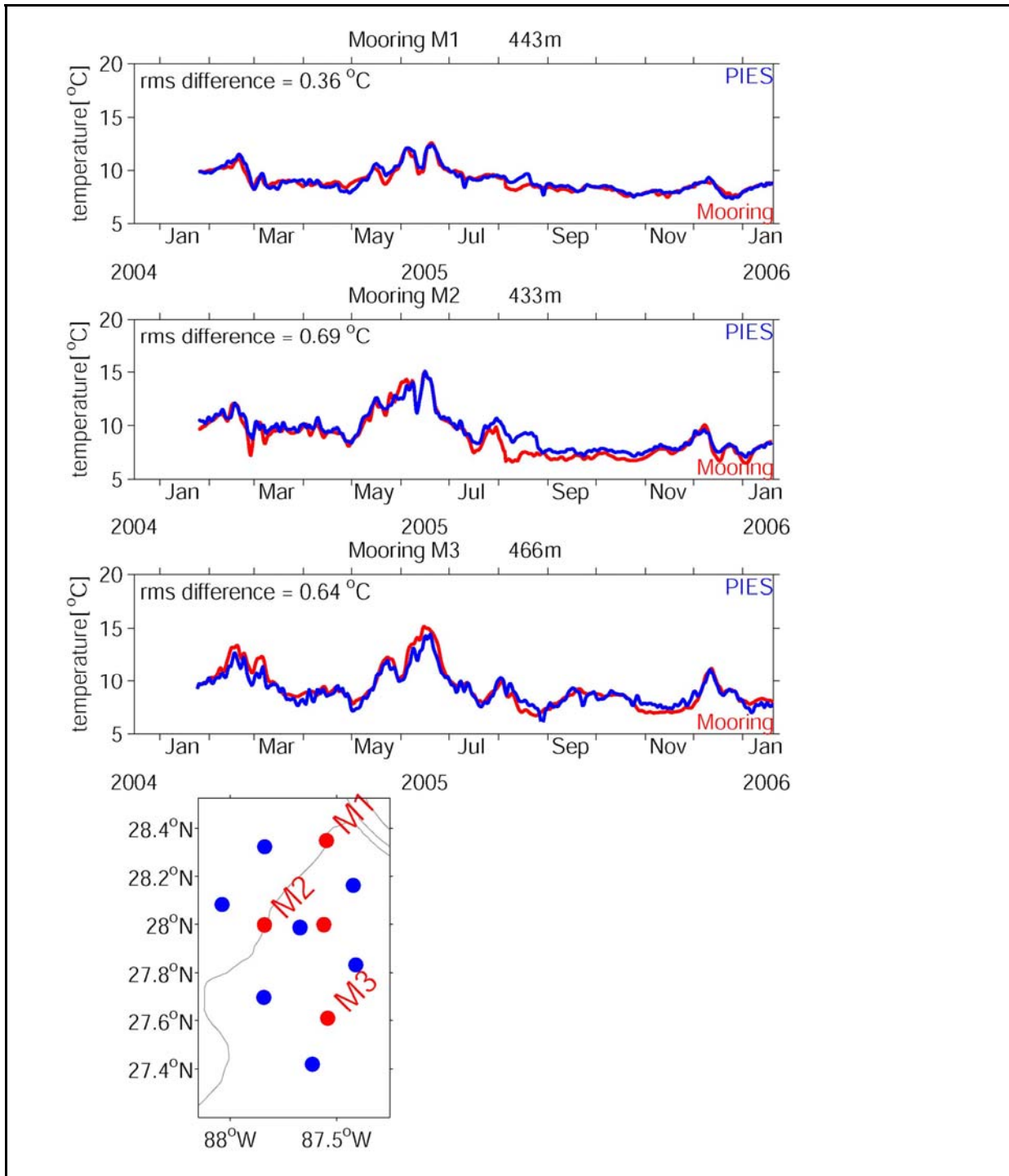


Figure 2.3-18. Comparison between the moorings (red) and PIES-derived (blue) temperatures near 400 m depth. The nominal depth and rms difference between PIES and the moorings are noted in the title and top right of each panel, respectively. The bottom panel shows the location of the PIES (blue) the moorings (red). Bathymetry contoured every 1000 m depth.

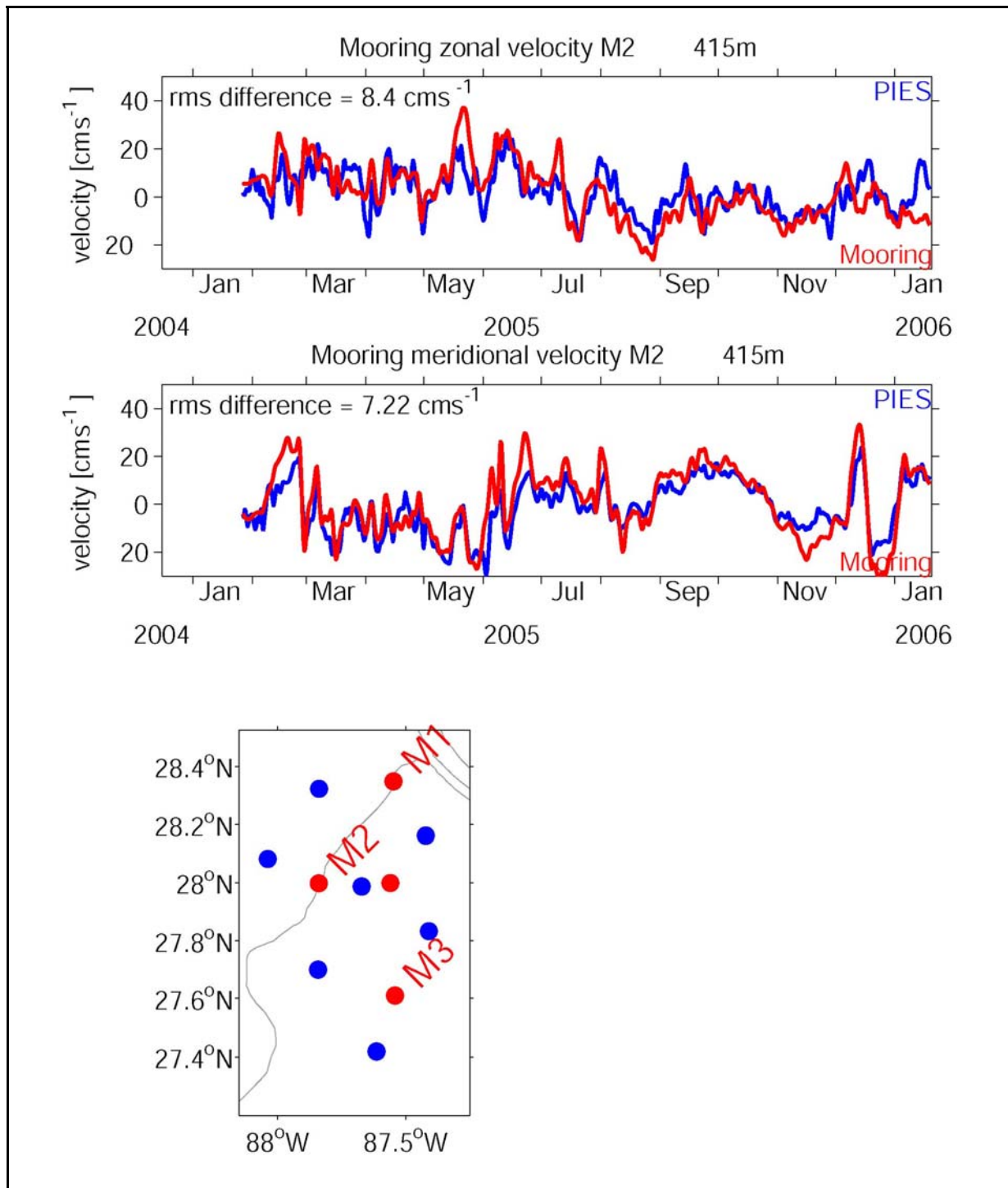


Figure 2.3-19. Comparison between the M2 mooring (red) and PIES-derived (blue) zonal (top) and meridional (middle) velocities at 415 m depth. The rms difference between PIES and the M2 mooring are noted in the upper left of each panel. The bottom panel shows the location of the PIES (blue) and the moorings (red). Bathymetry contoured every 1000 m depth.

2.4.1 Altimetry

Altimeter data collected and used during the study were the near real-time and archival data streams available from TOPEX/Poseidon (TOP/POS), ERS-2, Geosat Follow-on (GFO), Jason-1, and Envisat satellite missions. Processing of the SSH data was based on near real-time mesoscale analysis techniques designed to exploit the multi-satellite altimetric sampling (Leben et al. 2002). This method has been used to operationally monitor the GOM since November 1995. Altimeter data from a total of five satellites were available during the program time period. Basic information on each of the missions is given in Table 2.4-1. The groundtrack coverage provided by these satellites in the study region is shown in Figure 2.4-1.

Table 2.4-1

Satellite Altimeter Missions during the Eastern Gulf Program.

Satellite	Launch Date	Agency	Repeat Period (days)	Crosstrack Spacing	
				Degrees of Longitude	km*
TOPEX/Poseidon	10 Sep 1992	NASA/CNES	10	2.83	278
ERS-2	21 Apr 1995	ESA	35	0.72	71
Geosat Follow-On	10 Feb 1998	U. S. Navy	17	1.47	144
Jason-1	18 Dec 1999	NASA/CNES	10	2.83	278
Envisat	1 Mar 2002	ESA	35	0.72	71
Tandem/Interleaved Mission: 20 Sep 2000 to 6 Jan 2006.					
TOPEX/Poseidon/Jason-1 Interleaved			10	1.42	140

*at 28°N

Note that during the study, the TOP/POS and Jason-1 satellites were in tandem orbits with interleaved groundtracks. NASA/CNES scientists selected this configuration to improve the sampling of mesoscale ocean circulation by precision altimeters (Fu et al. 2003). The space/time sampling provided from the 10-day repeat orbit of the TOP/POS satellite, which was selected to map the ocean topography associated with large-scale variations in SSH, is not sufficient for monitoring mesoscale variability because of the large distance between neighboring ascending or descending tracks. In the GOM, this spacing is 2.83° of longitude or about 278 km at 28°N, which is also the distance between crossover points between ascending and descending tracks. Moving TOP/POS onto a parallel groundtrack that is midway between two adjacent groundtracks of the original TOP/POS orbit, which Jason-1 now occupies, reduced this distance by half to a crosstrack spacing of 140 km at 28°N. At latitudes midway between intra- and inter-satellite crossover points, the ascending/descending groundtrack sampling improves by another factor of two to a crosstrack spacing of just 71 km. Thus, the average crosstrack sampling from the tandem mission data alone is 70 to 140 km within the study region. The addition of GFO and ERS/Envisat data augments this spatial sampling but at irregular sampling times.

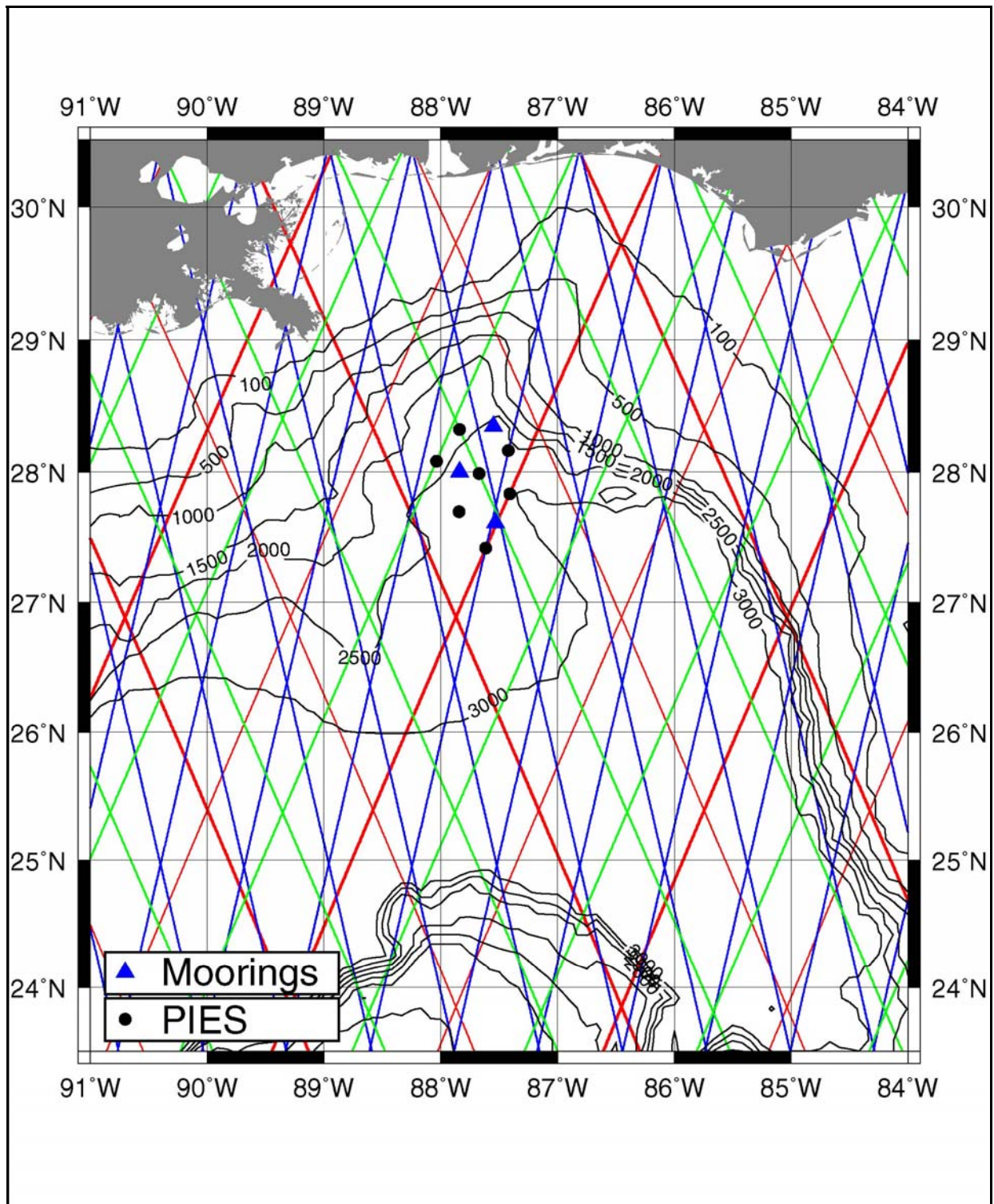


Figure 2.4-1. Satellite altimeter groundtrack coverage in study region. TOP/POS (thin red), Jason-1 (thick red), GFO (green), and ERS-2/Envisat (blue) are shown with a schematic of the instrument array.

Intuitively, sampling should improve by combining data from multiple altimeters. SSH fields produced by combining multi-mission altimetry; however, may not be better than those constructed from TOP/POS or Jason data alone if uniform errors and wavelength/frequency resolution satisfying the Nyquist criteria are required of the space/time gridded product as has been proposed by Greenslade et al. (1997). While these metrics may be reasonable for theoretical sampling studies or mission design, the constraints are too limiting for mesoscale mapping. Operational multiple satellite objective mapping of the mesoscale circulation must therefore rely on suboptimal smoothing to resolve eddy-scale wavelength albeit with the commensurate errors caused by non-uniform sampling and aliasing. This is true of both formal “optimal” interpolation and suboptimal objective analysis schemes. Nevertheless, the efficacy of the suboptimal interpolated fields can be evaluated by comparing the interpolated altimetry with coincident in situ data to quantitatively assess the processing and gridding strategies. PIES data are an ideal in-situ measurement type for these comparisons. PIES deployment locations for the study were therefore selected in part to provide in-situ measurements along altimeter groundtracks where possible so as to allow accurate assessment of not only the space/time gridded products but the alongtrack data as well.

2.4.1.1 Alongtrack Altimeter Data

Alongtrack data were collected from the agencies providing archival altimeter geophysical data records (GDRs). The TOP/POS and Jason-1 data are from the Physical Oceanography Distributed Active Archive Center (PO.DAAC) at the Jet Propulsion Laboratory. ERS-2 and Envisat data are from the "Centre ERS d'Archivage et de Traitement" (CERSAT), the French Processing and Archiving Facility for ERS-1, ERS-2, and Envisat data. GFO data are from the NOAA/NESDIS Laboratory for Satellite Altimetry.

All of the altimeter datasets were processed in as consistent a fashion as possible to produce accurate analysis maps based on the blended altimetric observations. Standard corrections were applied to the alongtrack data including inverted barometer, electromagnetic bias, ionosphere, and wet/dry troposphere corrections. Ocean tides were removed using the tide model supplied on the GDRs for TOP/POS, Jason, and Envisat. GFO and ERS-2 ocean tides were removed using the tide solution derived from the CCAR tide model (Tierney et al. 1998). The alongtrack coverage provided by the altimeter satellites during the time period was very good.

Each cycle of corrected 10-day repeat TOP/POS and Jason, 17-day repeat of GFO, and 35-day repeat of ERS-2 and Envisat data was linearly interpolated to reference groundtracks based on precision orbit determination ephemerides for each satellite at once-per-second alongtrack spacing. The TOP/POS and Jason reference track used the computed groundtrack for TOP/POS cycle 18. The TOP/POS interleaved mission reference groundtrack was the same groundtrack with an offset in longitude corresponding to the nominal interleaved orbit. The ERS-2 and Envisat 35-day reference groundtracks were based on repeat cycle 6 of the ERS-1 Multidisciplinary 1 Mission. The GFO reference groundtrack was based on cycle 2 from the GEOSAT Exact Repeat Mission.

2.4.1.2 Mesoscale Analysis

The processing of the altimeter data was designed to retain mesoscale signals while filtering out longer wavelength altimetric errors. This filtering also removed long wavelength oceanographic signals. A detailed description of this processing and its implementation and validation in the GOM can be found in Leben et al. (2002). The procedure incorporates data from all of the available satellites, treating each data set in a consistent fashion as follows:

1. All sub-satellite data were referenced to an independent gridded mean sea surface by subtracting the mean sea surface value at the sub-satellite point from each observation.
2. Alongtrack loess filtering was used to remove residual orbit and environmental correction errors. The loess filter removes a running least squares fit of a tilt plus bias within a sliding window from the alongtrack data. The window width is approximately 15° of latitude (200 once-per-second alongtrack data points).
3. A multigrid preconditioned Cressman analysis with temporal weighing was used to objectively interpolate the alongtrack data to a $1/4^\circ$ grid.
4. A model mean SSH field was added to the mapped SSH anomaly field to provide an estimate of the total SSH in the GOM.

2.4.1.3 Mean Reference Surface and Model Mean SSH

All alongtrack data were referenced to an existing altimetric mean sea surface. The data were treated as non-repeating groundtracks and were referenced directly to the mean sea surface by interpolating the mean sea surface value to the sub-satellite point and subtracting it from the sea surface height. This applies an implicit crosstrack geoid gradient correction to the alongtrack data before interpolation to the reference groundtracks.

The GSFC00.1_MSS, which was computed by Y. M. Wang of Raytheon ITSS (Wang 2001), was used as the reference surface. This mean sea surface is based on 6-years of TOP/POS data (Cycles 11 to 232), multiple years of ERS-1&2 35-day exact repeat data (ERS-1 Phase C: Cycles 1 to 18; Phase G: Cycles 1 to 13; ERS-2: Cycles 1 to 29), Geosat 17-day exact repeat data (Cycles 1 to 41), Geosat Geodetic Mission data, and both cycles of the ERS-1 168-day repeat data. All the altimeter data used to calculate the mean sea surface came from the GSFC's Altimeter Pathfinder products (Koblinsky et al. 1999).

To calculate the synthetic SSH estimates, we used the model mean sea surface height computed for the time period 1993-1999 from a data assimilation hindcast experiment performed by Drs. Lakshmi Kantha and Jei Choi for the MMS Deepwater Physical Oceanography Reanalysis and Synthesis Program (Nowlin et al. 2001). The data assimilation experiment used the University of Colorado-Princeton Ocean Model (CUPOM) and assimilated alongtrack TOPEX and ERS-1&2 sea surface height anomalies into CUPOM on a track-by-track basis as subsurface temperature anomalies (Kantha et al. 2005). Before adding the model mean to the gridded SSH anomaly fields, we averaged the 1993-1999 SSH anomaly fields and removed the residual anomalous altimetric mean over the time period. This referenced the SSH anomaly fields to a mean spanning the same time period as determined from the CUPOM hindcast data assimilation experiment. The anomalous altimetric mean reflected the difference between the mean circulation contained in the GSFC mean sea surface and the 1993-1999 data assimilation mean. More discussion of these differences is found in Leben et al. (2002).

2.4.1.4 Objective Mapping

Daily analysis maps of height anomaly relative to the mean sea surface were estimated using an objective analysis procedure (Cressman 1959) to interpolate the alongtrack data to a $1/4^\circ$ spatial grid. The method used an iterative difference-correction scheme to update an initial guess field and converge to a final gridded map. A multigrid procedure provided the initial guess. Five iterations were used with radii of influences of 200, 175, 150, 125, and 100 km while employing a 100-km spatial decorrelation length scale in the isotropic Cressman weighting function. The data were weighted in time using a 12-day decorrelation time scale relative to the analysis date using a ± 10 day window for the TOP/POS and Jason data and a ± 17 day window for the ERS-2, Envisat, and GFO data. The details of the space and time-weighted version of the multigrid preconditioned Cressman analysis is described next. The weighted version was based on the space-weighting only technique described in Hendricks et al. (1996).

2.4.1.5 Objective Analysis Procedure

An objective analysis (OA) procedure is used to interpolate the alongtrack sea surface height anomalies onto a regularly spaced $1/4^\circ$ global grid. The OA algorithm is based on the iterative difference-correction scheme of Cressman (1959). The initial guess field for the Cressman algorithm was supplied by an efficient multigrid procedure.

A rough estimate of the $1/4^\circ$ field was created by collecting the alongtrack SSH anomaly data into $1/4^\circ$ grid cells. In grid cells where at least one SSH measurement was available, the average of all measurements within the cell was computed. Some of the grid cells may not contain data depending on the spacing of groundtracks. The OA procedure is designed to fill in these data gaps by creating an SSH anomaly field that is consistent with the alongtrack measurements.

The 1/4°-binned data can be used as an initial guess in the Cressman algorithm; however, having initial values in the empty grid cells can enhance the efficiency of the iteration procedure. A simple multigrid procedure was used to estimate values in cells where no altimeter measurements are available. Multigrid methods (Briggs 1987) rapidly solve a set of equations by working at several grid resolutions. In this case, if the alongtrack data are binned into 1° or 2° grid cells, there would be fewer or even no empty ocean grid cells. Using a multigrid interpolation strategy to efficiently compute the means, a set of progressively coarser grids (1/2°, 1°, 2°, ...) are created from the global 1/4° grid, and the average SSH is computed at all coarser grid resolutions in each cell containing data. The mean values are transferred back to the original 1/4° grid from the finest-scale grid containing a mean value coincident with that location. Finally, a fast red-black smoothing operator (e.g., see Press et al. 1992) is used on the 1/4° initial guess field to smooth high-frequency noise introduced by the multigrid interpolation.

Cressman objective analysis uses an iterative-difference corrections scheme in which a new estimate of the SSH value for a given grid cell is equal to the sum of the previously estimated SSH at that location and a correction term. The correction term is forced by the difference between the estimated heights and the original data values over all grid cells within a specified radius of influence. A weight based on the number of original measurements within a grid cell is included in the correction term, as is a weight based on the distance of a grid cell from the point being updated.

The n th iteration for the SSH at grid cell i is computed using:

$$h_i^n = h_i^{n-1} + \frac{\sum w_m n_m^* (h_m^* - h_m^{n-1})}{\sum w_m n_m^*}, \quad (2.4.1)$$

where the sums are taken over all m grid cells within the specified radius of influence R from the grid cell i being updated. The variables in (Eq. 2.4.1) are defined as:

h_i^n the n th iteration of SSH at grid cell i ;

h_m^{n-1} the $(n-1)$ th iteration of SSH at grid cell i ;

h_m^* the average height at grid cell m based on the original data;

h_m^{n-1} the $(n-1)$ th iteration of SSH at grid cell m ;

n_m^* the number of original measurements within grid cell m .

The weights in the correction term are defined by:

$$w_m = \exp(-ar_m^2/R^2) \quad \text{for } r \leq R;$$

$$w_m = 0 \quad \text{for } r > R;$$

where r_m is the distance between grid cell m and the grid cell being updated and R is the maximum radius of influence. The parameter a is an adjustable weighting factor that scales the exponential spatial weighting of the data.

To incorporate weighting of the data in time, the data and the number of original measurements within a grid cell are each scaled by the weighting function:

$$w_i = \exp(-b\Delta t_m^2 / T^2) \quad \text{for } \Delta t \leq T;$$

$$w_i = 0 \quad \text{for } \Delta t > T;$$

where Δt_m is the difference between the measurement time and the time corresponding to the analyzed field. The parameter b is the time weighting factor, and T is the maximum time window of influence.

The empirical weighting parameters, a and b , are selected to map the mesoscale structure within the limitation of the scales resolvable by the crosstrack altimeter sampling. The mesoscale analysis used $a = 4$ and $b = 2$, which correspond to decorrelation space and time scales of 100 km and 12 days, respectively, for $R = 200$ km and $T = 17$ days. The maximum radius of influence, R , was decreased between the Cressman iterations to allow smaller scales to converge more quickly and to increase resolution when alongtrack sampling was available. For this study, R was decreased from 200 to 100 km over five iterations giving a decorrelation length scale of 50 km on the final Cressman iteration.

2.4.2 Ocean Color Imagery

Daily ocean color imagery was downloaded from the OceanColor group web and ftp sites (<http://oceancolor.gsfc.nasa.gov/>) at the NASA Goddard Space Flight Center (GSFC). These images are a 9-km resolution blended product incorporating data from the Sea-viewing Wide Field-of-view Sensor (SeaWiFS) satellite and the Moderate Resolution Imaging Spectroradiometer (MODIS) instrument onboard the Aqua satellite. The empirical chlorophyll algorithms OC4v4 and OC3M (O'Reilly et al. 1998) are used with measured radiances from SeaWiFS and MODIS, respectively, to calculate the individual chlorophyll fields from each satellite image. Both SeaWiFS and MODIS data were Level-3 processed before being merged. This processing involved the spatial and temporal binning of Level-2 data into 4 and 9-km equi-rectangular projections and is described in detail by Hooker et al. (1995). Combining the data from the two missions increased the coverage over a single mission product, on average, by over 50% for the daily product and by over 20% for the 8-day composite product. A variety of multi-day composites were made to help with the detection and tracking of oceanographic features in and around the study region. GSFC MODIS Level-2 ocean color imagery at 2-km resolution was also downloaded and used for some of the higher resolution analyses in this report.

2.4.3 SST Imagery

SST products were acquired for remote sensing and data synthesis activities. We used Advanced Very High Resolution Radiometer (AVHRR) imagery from the Johns Hopkins University/Applied Physics Laboratory (JHU/APL) Ocean Remote Sensing Group. Three-day warmest pixel composite images in Portable Network Graphics (PNG) format were downloaded from the JHU/APL Ocean Remote Sensing Group website. These images have 1-km resolution with image values (0-255) corresponding to the rounded integer SST values. The full precision values before rounding were calculated by the multi-channel algorithm used in the TerraScan software that converts raw antenna brightness temperatures to SST values in the APL ground station. Although the rounding limits the accuracy to only 0.5°C, which is less than required for most scientific work, the capability to detect spatial features was not compromised, and the data was sufficiently accurate for data synthesis activities. The images collected for the study were once-per-day 3-day composite images from January 1, 2005 through June 30, 2006.

2.5 *PIES/Altimeter Comparison*

PIES and satellite altimetry are complementary data types. Although the two measurement systems measure completely different physical quantities, they both yield an estimate of the height of the ocean surface relative to some datum, which is commonly referred to as sea surface height (SSH).

For this study,, we evaluated the altimeter SSH measurement system using PIES data as a benchmark for theoretical analyses and for comparison of PIES SSH directly to the coincident altimeter-derived SSH collected during the study. This is the third opportunity for these types of analyses and comparisons in the GOM, supplementing the results in the central and western Gulf reported in the Exploratory and the Northwestern GOM Study technical reports (Donohue et al. 2006; Donohue et al. 2008). Some of the statistics prepared for those reports will be presented again here and discussed in light of the results obtained in eastern GOM. These types of analyses and comparisons have the potential to identify problems in current datasets and to develop and test improvements in the altimeter data processing techniques used to produce future data products. This will facilitate the synthesis of altimetry data and PIES data from current and future arrays deployed in the deepwater GOM, which will improve observing and understanding of deepwater circulation patterns and dynamics throughout the water column.

2.5.1 Altimetric Sampling and Aliasing

Satellite altimeters provide discrete SSH measurements at sub-satellite points spaced approximately 5–7 km along groundtracks that repeat every 10, 17, or 35 days for the satellites used during the study program (Table 2.5-1). Orbital dynamics determine the space/time sampling pattern achieved on orbit, and there is a trade-off between spatial and temporal resolution when selecting an orbit during the mission design phase of a satellite program. As an example, see the discussion of the TOP/POS mission in Parke et al. (1987). For single satellite sampling, high spatial resolution using a nadir pointing altimeter is achieved only at the expense of less frequent sampling of the sea surface in time, and vice versa.

Unlike ground-based instruments where the sampling rate can be selected to satisfy a specific Nyquist criterion, satellite-based measurement systems in non-geosynchronous orbits have a temporal sampling rate imposed by the period at which a point on the Earth's surface is sampled from orbit. Increasing the temporal sampling rate for a nadir-pointing altimeter requires either the addition of more satellites in the same orbit or a shorter repeat period resulting in a loss of spatial sampling density. Neither option can usually be justified from an economic, scientific, or operational perspective. Anecdotally, when additional sampling became available from TOP/POS after the commissioning phase of the TOP/POS and Jason-1 tandem mission, the decision made was to increase the spatial sampling density (Fu et al. 2003) and, by default, accept the existing level of temporal aliasing of the 10-day repeat sampling. A number of studies have addressed spatial/temporal aliasing issues (Schlax and Chelton 1994; Parke et al. 1998) including assessment of the aliasing of well known periodic signals such as tides; however, few studies have assessed the SSH variance associated with the aliased signal from under-sampled SSH ocean measurements.

The temporal aliasing of ocean signals by satellite altimeter sampling can be addressed using the high-rate in-situ SSH data provided by PIES measurements. Hendry et al. (2002) performed the first study along these lines using PIES data collected within the North Atlantic Current in the Newfoundland Basin. They found that the time scales of motion observed in the region are such that 86-95% of the subinertial period SSH variability was not aliased by the approximately 10-day TOP/POS repeat period sampling. Gille and Hughes (2001) performed an earlier study of sampling using only bottom pressure records; however, that type of study would not be appropriate in the GOM where the time scales associated with the bottom pressure variability are not representative of the time scales of the SSH variability.

Following the methodology of Hendry et al. (2002), we made an assessment of the SSH signal in the Exploratory and Northwest GOM Study regions (Donohue et al. 2006; Donohue et al. 2008), and now report similar analyses for the Eastern GOM for the approximately 10-day, 17-day, and 35-day repeat period sampling available from the ongoing satellite altimeter missions. We computed power spectra for each of the SSH time series (barotropic, baroclinic, and combined) and calculated the percentage of cumulative power in the spectra up to each of the Nyquist frequencies associated with the 10-day, 17-day, and 35-day repeat sampling periods. The periods corresponding to the Nyquist frequency for each of the altimeter satellites are tabulated in Table 2.5-1. Figures 2.5-1, 2.5-2, and 2.5-3 show maps of the unaliased variance associated with 10-day, 17-day, and 35-day repeat sampling periods in the study region for the current altimeter missions from the barotropic, baroclinic, and combined SSH signals, respectively. Eastern GOM summary statistics are tabulated in Table 2.5-2 along with the statistics from the Exploratory Program and Northwest GOM PIES arrays. Tabulated values for each of the Eastern GOM PIES stations are listed in Table 2.5-3.

The aliasing of the barotropic SSH signal is the most severe because of the shorter time scales associated with that signal in the GOM. The mean value over the Eastern GOM array of 10-day sampling period unaliased variance was 63%, comparable to the 59% and 62% estimated from the Exploratory Program and Northwest GOM PIES arrays. The Eastern GOM individual station results ranged from a minimum of 59% at PIES 1 to a maximum of 70% at PIES 7, which is comparable to the 56% to 72% range found for the Northwest GOM program. The range, however, is smaller than the 44% to 77% range found in the Exploratory program array, which covered a larger aerial extent and included instruments above the Sigsbee Escarpment. The spatial pattern of aliasing was similar for 17-day sampling, with the least amount of aliasing at the southern-most station. However with 35-day sampling, the station with the greatest percentage of unaliased signal was station 3, which moves the region with the least amount of aliasing to the northeastern part of the array. The overall mean value was 35%, and the individual values ranged from a minimum of 31% at PIES 5 to a maximum of 39% at PIES 3. The Eastern GOM mean value of 35% is comparable to the Exploratory program and Northwest GOM program mean values of 37% and 42%, respectively. The generally low mean values for all of the altimetric sampling frequencies in both the NW and central Gulf are attributable to the aliasing of the frequencies associated with the 6-day barotropic oceanic response to an atmospheric Rossby-Haurwitz wave (Park and Watts 2006) and the 14-day to 16-day Gulf-wide common mode.

The unaliased variance of the baroclinic and total SSH signal was much higher than the barotropic-only case because of the longer period baroclinic signals and the dominance of the more energetic baroclinic component on the total SSH. Still, there were large differences between the 10-day and 35-day patterns, while the 10-day and 17-day patterns were more similar. For a 10-day sampling period of the baroclinic signal in the Eastern GOM, the unaliased variance mean value over the array was 93% and ranged from a minimum of 84% at PIES 6 to a maximum of 97% at PIES 7. The 35-day sampling mean value was only 76% and ranged from a minimum of 68% at PIES 6 to a maximum of 85% at PIES 1. The total combined baroclinic and barotropic SSH signal showed similar patterns. The SSH 10-day period unaliased variance mean value over the array was 92% and ranged from a minimum of 84% at PIES 6 to a maximum of 97% at PIES 7. The 35-day sampling mean value decreased to 75% and ranged from a minimum of 67% at PIES 6 to a maximum of 83% at PIES 1. These overall averages and ranges were comparable to those found in our analyses of the Exploratory program and Northwest GOM program PIES, further confirming the similarity of the baroclinic signals in the GOM deepwater even over separate and distinct observational time periods.

Table 2.5-1

Satellite Periods.

Satellite altimeter mission exact-repeat periods and periods associated with the Nyquist sampling frequency.

Satellite	Approximate Repeat	Repeat Period (days)	Nyquist Sampling Period (days)
TOPEX/Poseidon	10-day	9.9156	19.8313
ERS-2	35-day	35	70
Geosat Follow-On	17-day	17.0505	34.1010
Jason-1	10-day	9.9156	19.8313
Envisat	35-day	35	70

In summary, 84% to 97%, 84% to 98%, and 87% to 99% of the subinertial period SSH variability in the Eastern GOM, Northwest GOM, and Exploratory Study regions, respectively, are unaliased by the TOP/POS 10-day repeat period sampling. This is comparable to the 86% to 95% estimated from the Newfoundland Basin array by Hendry et al. (2002). However, the results for the 17-day and 35-day repeat sampling show that there can be significant aliasing of the GOM SSH signals in satellite altimetry even with the dominance of the longer period baroclinic signals associated with the LC and LCEs in the Gulf deepwater. The degree to which this affects the space/time interpolated maps of altimetric SSH needs to be investigated in more detail. It is also unclear whether the weak surface signature of topographic Rossby waves can be mapped effectively using satellite altimetry given the presence of the strong baroclinic SSH and the difficulties associated with aliasing of the barotropic signal. Also, the presence of the ubiquitous common mode needs to be considered when processing sea surface height. In most cases, this signal will be removed by standard altimetric processing techniques, and the aliasing will be mitigated. However, the signal may be retained as more sophisticated processing and higher frequency corrections are applied to the data.

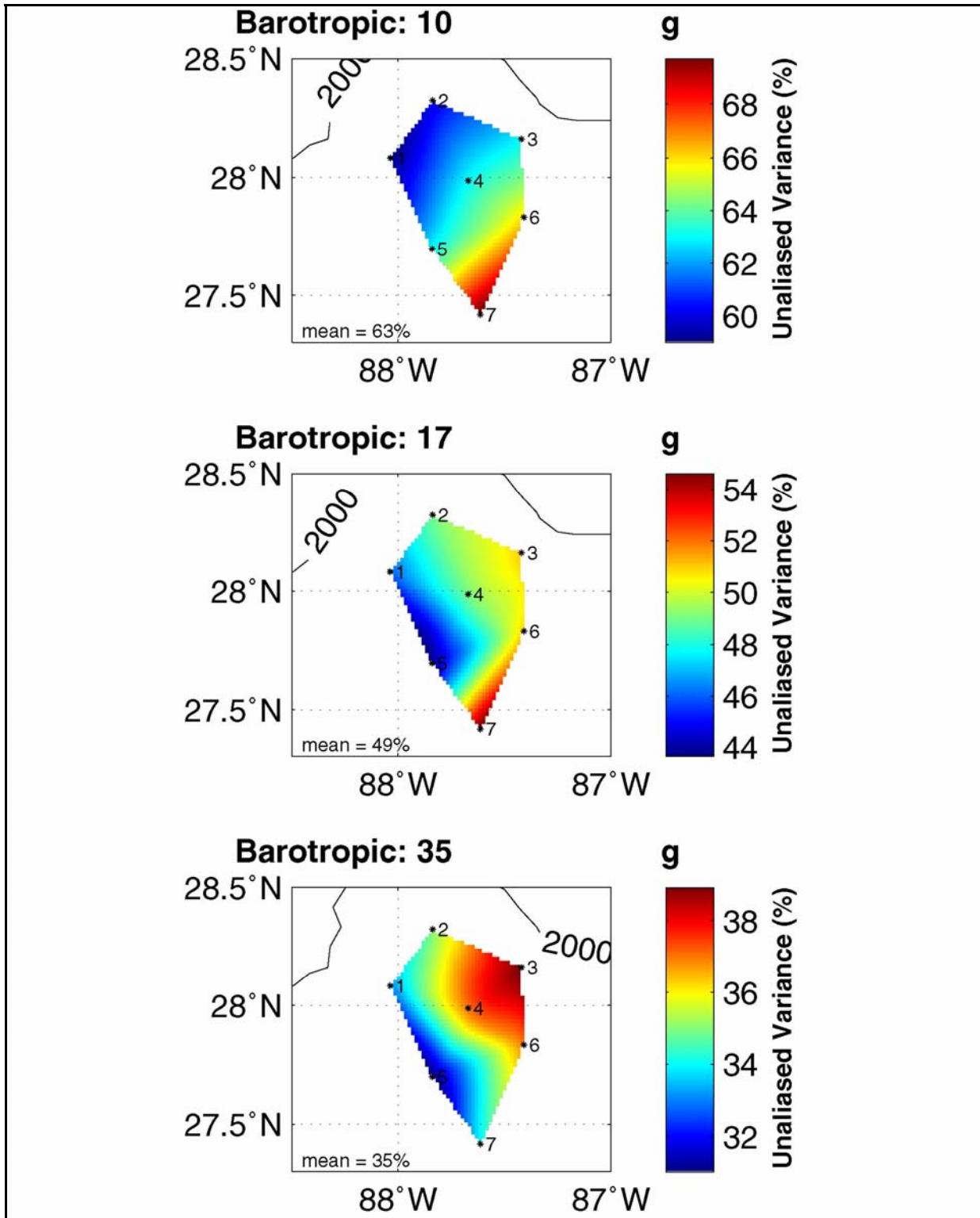


Figure 2.5-1. Maps of PIES barotropic unaliased variance for 10-day, 17-day, and 35-day sampling.

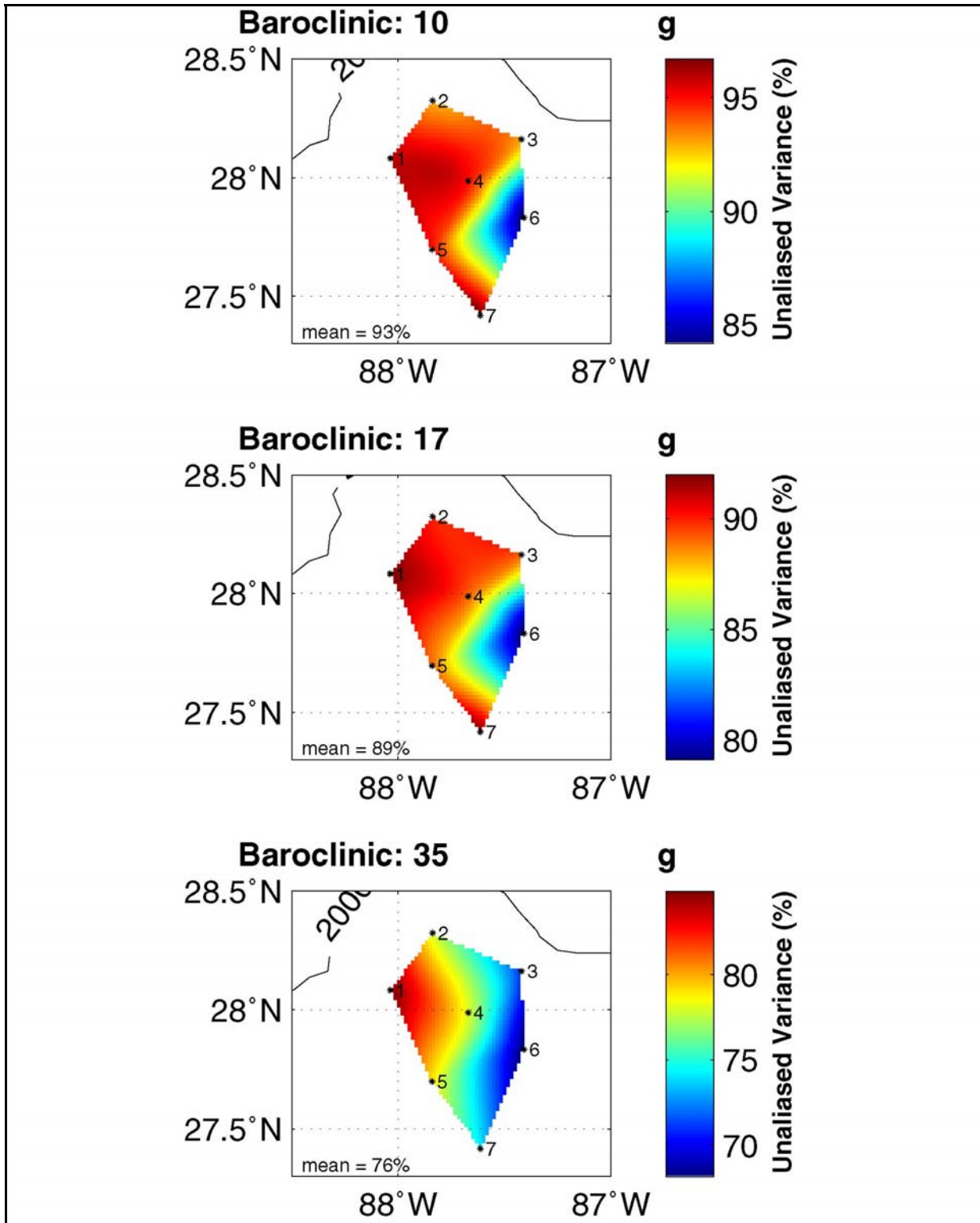


Figure 2.5-2. Maps of PIES baroclinic unaliased variance for 10-day, 17-day, and 35-day sampling.

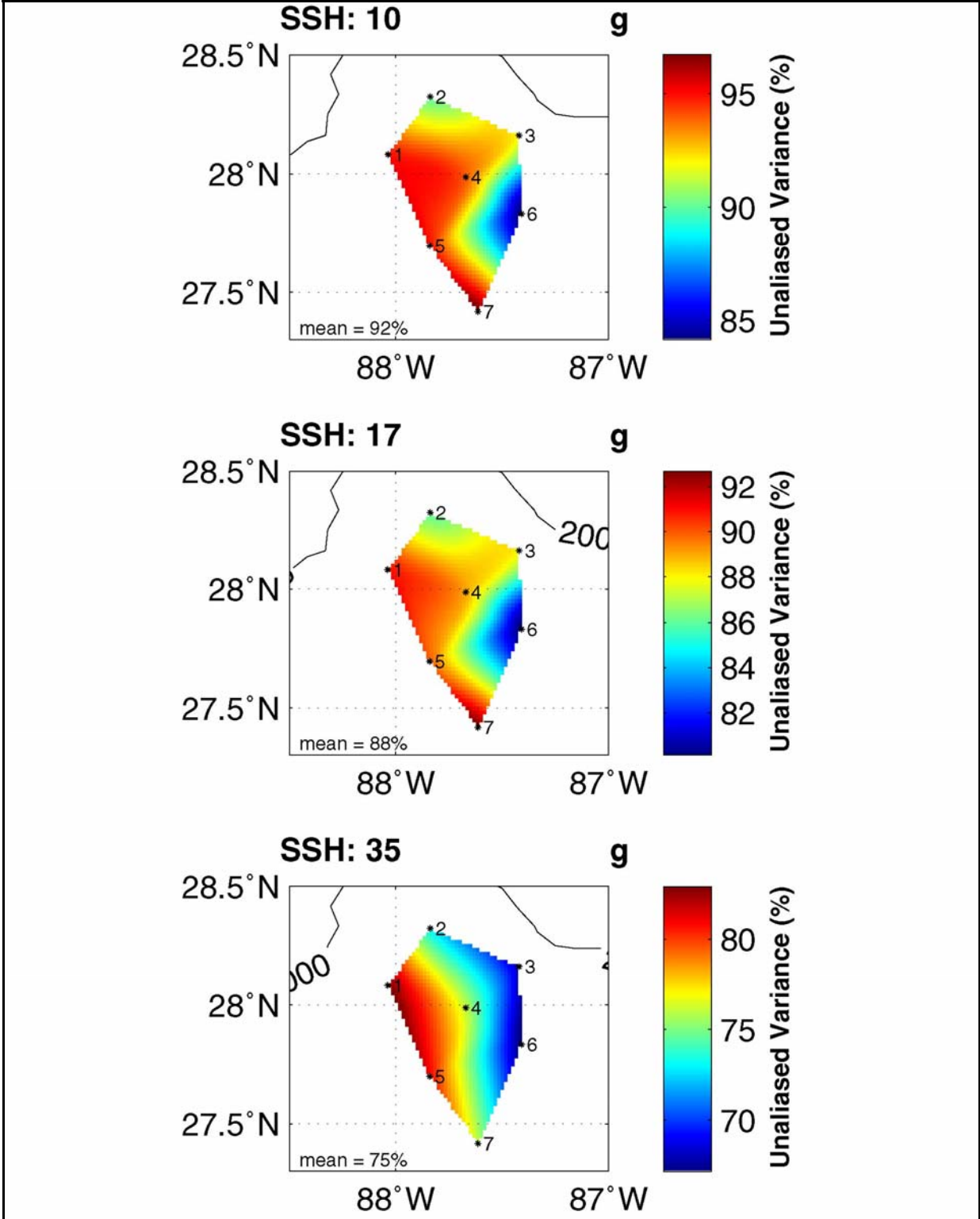


Figure 2.5-3. Maps of PIES SSH unaliased variance for 10-day, 17-day, and 35-day sampling.

Table 2.5-2

Variance Statistics.

Unaliased variance statistics for 10-day, 17-day, and 35-day exact repeat sampling of the PIES barotropic, baroclinic, and combined SSH signals.

Stations	Barotropic Signal Mean (%)			Baroclinic Signal Mean (%)			Total SSH Signal Mean (%)		
	10-day	17-day	35-day	10-day	17-day	35-day	10-day	17-day	35-day
Repeat:	10-day	17-day	35-day	10-day	17-day	35-day	10-day	17-day	35-day
Eastern Gulf Program									
all stations	63	49	35	93	89	76	92	88	75
NW Gulf Program									
all stations	62	53	42	97	92	76	94	89	75
Exploratory Program									
all stations	59	47	37	97	93	78	95	92	78
above escarpment	56	45	39	96	93	75	94	91	75
below escarpment	61	49	36	97	93	80	96	93	79
Stations	Barotropic Signal Maximum (%)			Baroclinic Signal Maximum (%)			Total SSH Signal Maximum (%)		
	10-day	17-day	35-day	10-day	17-day	35-day	10-day	17-day	35-day
Repeat:	10-day	17-day	35-day	10-day	17-day	35-day	10-day	17-day	35-day
Eastern Gulf Program									
all stations	70	55	39	97	92	85	97	93	83
NW Gulf Program									
all stations	72	64	47	99	97	90	98	95	87
Exploratory Program									
all stations	77	60	45	99	98	93	99	98	93
above escarpment	60	50	42	99	98	90	97	96	90
below escarpment	77	60	45	99	98	93	99	98	93
Stations	Barotropic Signal Minimum (%)			Baroclinic Signal Minimum (%)			Total SSH Signal Minimum (%)		
	10-day	17-day	35-day	10-day	17-day	35-day	10-day	17-day	35-day
Repeat:	10-day	17-day	35-day	10-day	17-day	35-day	10-day	17-day	35-day
Eastern Gulf Program									
all stations	59	44	31	84	79	68	84	80	67
NW Gulf Program									
all stations	56	47	36	93	86	52	84	79	53
Exploratory Program									
all stations	44	38	29	92	86	54	87	82	54
above escarpment	51	42	36	92	86	54	87	82	54
below escarpment	44	38	29	93	87	56	92	85	56

Table 2.5-3

PIES Statistics.

PIES SSH, baroclinic, and barotropic statistics and percent of unaliased variance measured by satellites in 10-day, 17-day, and 35-day exact repeat orbits. The time series' length, standard deviation (std), and half power period ($T_{0.5}$) are also shown.

PIES	Signal	Length (days)	Std (cm)	$T_{0.5}$ (days)	Unaliased Variance (%)		
					10-day	17-day	35-day
1	SSH	397	15.8	158	95	91	83
	Baroclinic	397	15.9	158	96	92	85
	Barotropic	397	2.7	16	59	46	33
2	SSH	397.5	11.0	102	90	86	73
	Baroclinic	397.5	10.7	108	93	90	78
	Barotropic	397.5	2.6	16	60	49	35
3	SSH	398.5	12.5	102	92	88	68
	Baroclinic	399	12.2	108	93	89	71
	Barotropic	398.5	2.7	21	63	51	39
4	SSH	397	13.4	128	94	89	76
	Baroclinic	397	13.6	128	95	89	78
	Barotropic	397	2.8	21	63	49	37
5	SSH	394	18.1	146	95	90	81
	Baroclinic	390.5	18.9	137	95	89	79
	Barotropic	390.5	3.1	21	63	44	31
6	SSH	397.5	16.5	102	84	80	67
	Baroclinic	288.5	16.8	102	84	79	68
	Barotropic	288.5	2.9	23	66	51	37
7	SSH	393	20.6	108	97	93	76
	Baroclinic	391	21.4	108	97	92	74
	Barotropic	391	3.3	25	70	55	34

2.5.2 Signal-to-Noise

A useful metric for assessing the accuracy of altimeter-derived estimates of SSH is the ratio of the unaliased variance to the aliased variance of the SSH signal, which is an estimate of the signal-to-noise ratio (SNR) of a perfect on-orbit measurement system. The amount of aliasing is also a function of the repeat sampling period of the satellite altimeter as can be seen in Figure 2.5-4. Note that we do not consider the barotropic and baroclinic components separately because they cannot be distinguished from on-orbit measurements alone. Also, the “noise” in the unaliased to aliased SNR is colored noise associated with undersampled geophysical signals that are very difficult to remove without excessive smoothing or filtering of the alongtrack data before interpolation. This is the primary reason that the requirement of uniform errors and wavelength/frequency resolution satisfying the Nyquist criteria as proposed by Greenslade et al. (1997) for gridded altimeter products is unrealistic in practice.

Table 2.5-4 shows a summary of the SNR statistics estimated from the Eastern GOM, Northwest GOM, and Exploratory Study PIES data. In nearly all cases, the Eastern GOM SNR is lower than both the Northwest GOM and Exploratory Study statistics for all three sampling scenarios. Nevertheless, the SNR in all of the study regions was very good for 10-day and 17-day altimetric sampling. The 35-day sampling was more problematic. The 35-day sampling spatial map (Figure 2.5-4 lower panel) shows SNR ratios in the low single digits over much of the Eastern GOM array, which would make it difficult to distinguish between signal and aliased signal at that sampling frequency from a single-point measurement. Similar low SNR regions were found in the western and central GOM. Quantifying the SNR for combined sampling by multiple altimeters will be reported in future work.

Table 2.5-4

SNR Statistics.

Signal-to-noise ratio (SNR) statistics for 10-day, 17-day, and 35-day exact repeat sampling of the PIES barotropic, baroclinic and combined SSH signals.

Stations	Mean SNR			Minimum SNR			Maximum SNR		
	10-day	17-day	35-day	10-day	17-day	35-day	10-day	17-day	35-day
Eastern Gulf Program									
all stations	16	8	3	5	4	2	32	13	5
NW Gulf Program									
all stations	22	11	4	5	4	1	49	19	7
Exploratory Program									
all stations	28	16	5	7	5	1	99	49	13
above escarpment	20	13	4	7	5	1	32	24	9
below escarpment	33	19	5	12	6	1	99	49	13

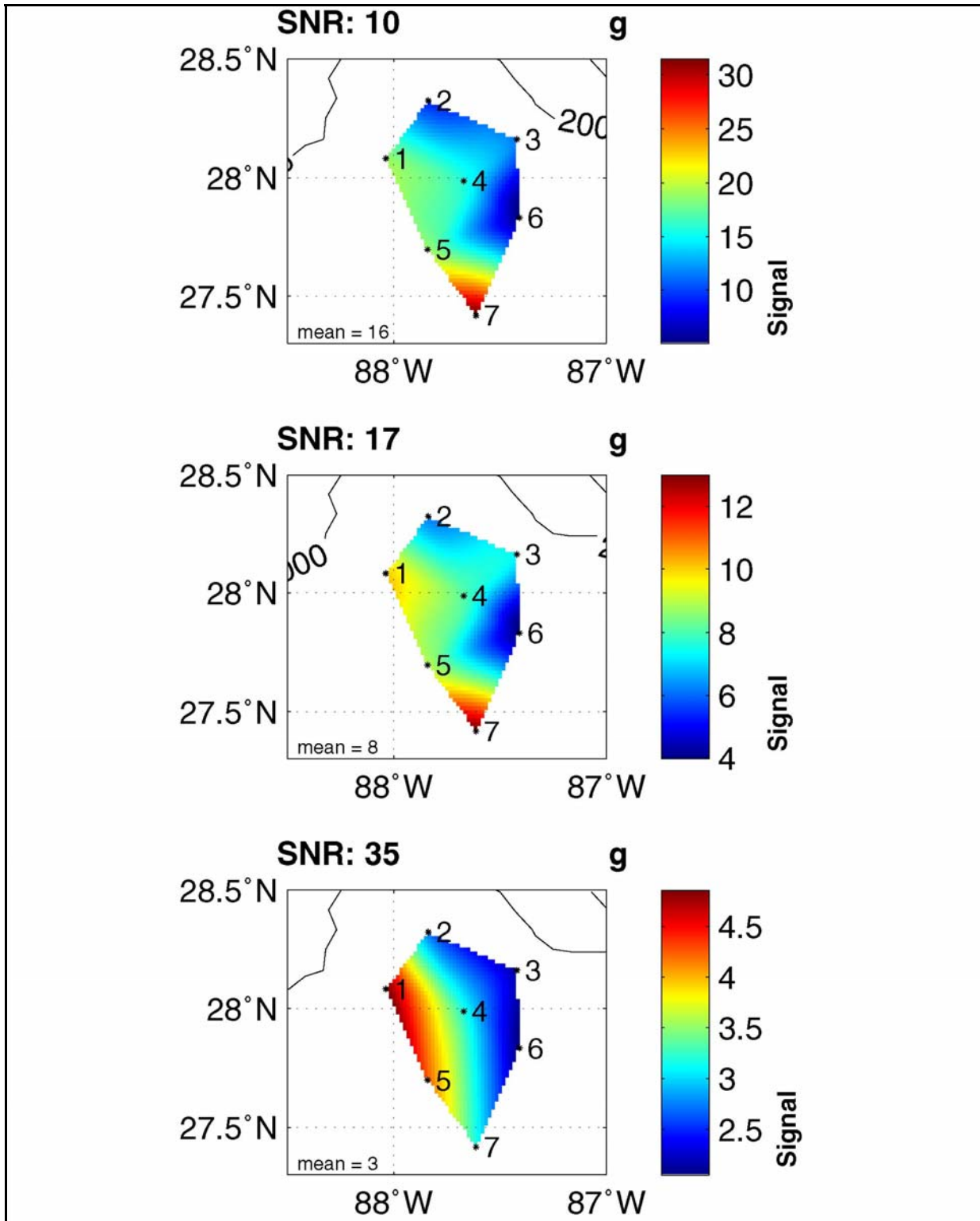


Figure 2.5-4. Maps of PIES SSH signal-to-noise ratio (SNR) for 10-day, 17-day, and 35-day sampling. SNR is estimated from the ratio of unaliased to aliased variance.

2.5.3 Sea Surface Height Time Scales

Following the methodology of Hendry et al. (2002), the period corresponding to the frequency at which the cumulative power spectrum reaches 50% of the total variance, the half-power period ($T_{0.5}$), was determined from the spectral analysis of each of the PIES SSH anomaly time series. $T_{0.5}$ is a more robust measure of time scale than the temporal autocorrelation zero crossing, T_0 , and is the preferred scale to be used to define the effective degrees of freedom of a time series (Fofonoff and Hendry 1985). This robustness is due in large part to the global and integral nature of the $T_{0.5}$ metric which is less sensitive to competing time scales within the time series. In contrast, the calculation of T_0 is a less robust measure because the first zero crossing of the temporal autocorrelation function is quite sensitive to the presence of multiple time scales and/or secular trends in the time series.

The half-power periods were computed from the 13-month Eastern GOM, 9-month Northwest GOM, and 12-month Exploratory Study PIES barotropic, baroclinic, and SSH anomaly time series. Spatial maps of $T_{0.5}$ in the Eastern Gulf for each of the three signals are shown in Figure 2.5-5. We did not detrend the time series before calculating the spectra because of the relatively short duration of the records. This allowed estimation of the longer time scales of variability associated with the LC and LCEs that occurred in most of the records. Mean $T_{0.5}$ values are listed in Table 2.5-5 for each program showing the average time scales for each of the signals at all PIES stations. The Exploratory Study averages for stations above and below the Sigsbee Escarpment are also shown.

The mean half-power periods of the barotropic signals were quite similar between the three regions and were dominated by the Gulf-wide common mode. The spatial distributions were notably different. In the Eastern GOM, the longer period signals were located along the southeast margin of the array located in the deepest water. This was similar to the central GOM where the longer period signals were in the south-central part of the Exploratory array in the deepwater below the Sigsbee Escarpment. In contrast, the longer period barotropic signals in the Northwest GOM were on the upper slope.

The time scales of the baroclinic and combined barotropic and baroclinic SSH anomaly signals were very similar because of the small contribution by the barotropic mode to the total signal. The long half-power periods associated with these signals show the dominance of the low-frequency LC and LCE variability observed in the three regions during the observational records. In the Eastern GOM, the 150-day and longer periods were located on the western margin of the array where LC and LCE variability reached into the array during the LC intrusion that ultimately formed LCE Vortex. The shortest half-power periods, less than 150 days, were found over much of the Eastern GOM array. The higher frequency signals associated with these shorter periods likely arise from the SSH variability generated by frontal or filament eddies on the periphery of LC and detached LC eddies.

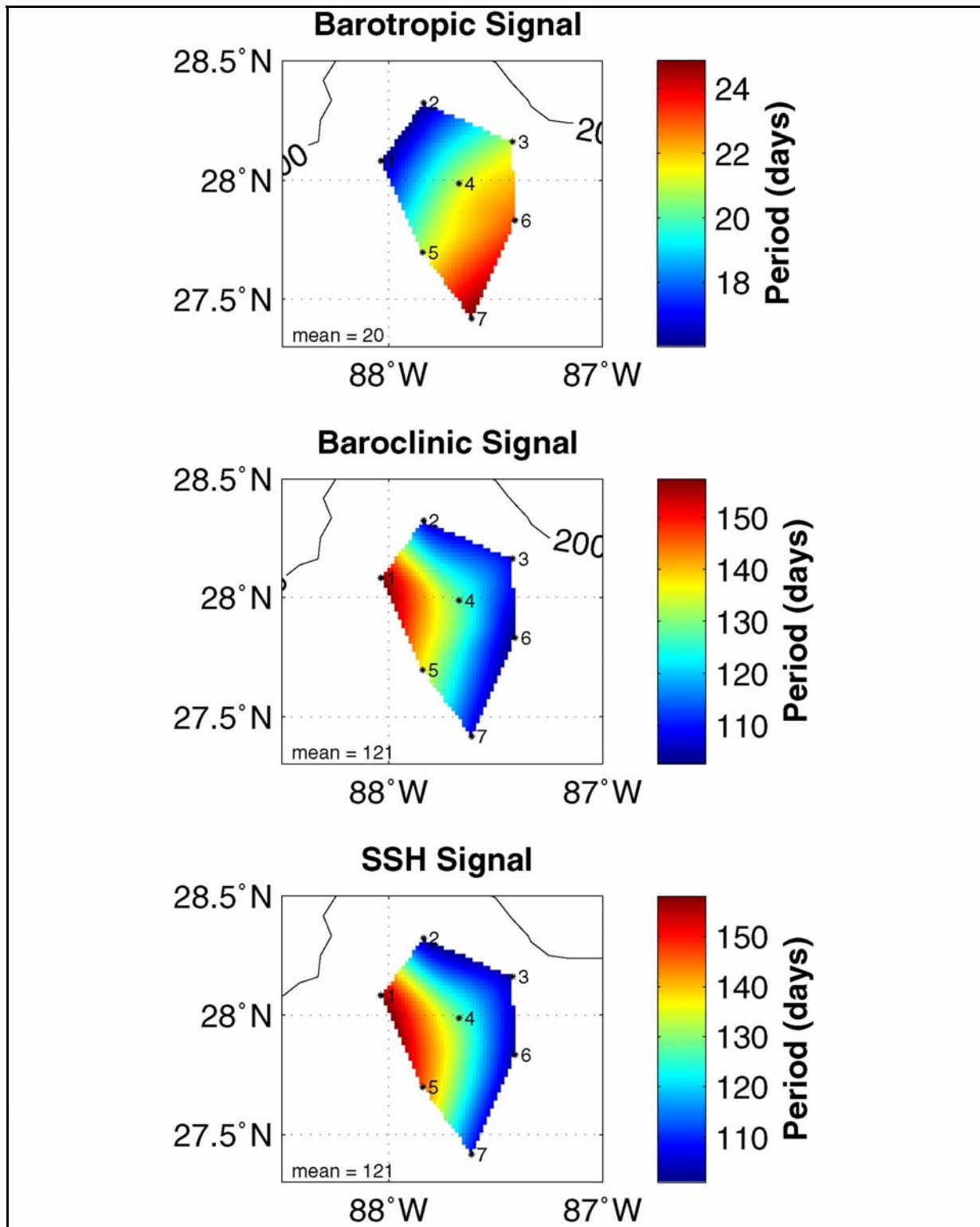


Figure 2.5-5. Spatial maps of the half-power period, T , computed from the PIES barotropic, baroclinic, and combined SSH anomaly time series. Mean values over all stations are also shown.

Table 2.5-5

Half-power Period of PIES Barotropic, Baroclinic, and Total SSH Signals.

Stations	Barotropic Signal Half-Power Period (days)			Baroclinic Signal Half-Power Period (days)			Total SSH Signal Half-Power Period (days)		
	mean	max	min	mean	max	min	mean	max	min
Eastern Gulf Program									
all stations	20	25	16	121	158	102	121	158	102
NW Gulf Program									
all stations	21	47	14	155	293	66	148	293	66
Exploratory Program									
all stations	19	34	12	230	34	12	232	512	60
above escarpment	16	18	14	188	18	14	195	341	64
below escarpment	21	34	12	262	34	12	260	512	60

2.5.4 Comparison of CCAR Mesoscale and PIES SSH

The CCAR mesoscale SSH gridded altimeter data product that was distributed and used for data synthesis activities in this report was evaluated by comparison with the coincident PIES SSH time series at each of the PIES stations in the Eastern Gulf array. A spatial map of the CCAR/PIES correlation is shown in Figure 2.5-6. The nearest $1/4^\circ$ grid point from the CCAR product was used to calculate the temporal correlation coefficient. The overall mean correlation for the Eastern GOM program datasets was 87%, which was better than both the Northwest GOM program and Exploratory program mean values of 76% and 82%, respectively. The lowest correlations were in the northeastern corner of the study array. The correlations were highest along the eastern and southern margins of the array where LC and LCE influences were more pronounced during the measurement time period.

Taking advantage of the placement of PIES on satellite groundtracks (Figure 2.4-1), we compared the alongtrack detrended SSH anomaly data from each altimeter to the coincident PIES SSH data gathered on collocated groundtrack points. Scatterplots and correlation coefficients for the collocated altimeter and PIES measurements are shown in Figure 2.5-7 for each of the four satellites that flew directly over a PIES station location during the study program. Note that no PIES were placed on a TOP/POS groundtrack during the Eastern GOM program. In all cases, the correlations during the Eastern GOM program were as good as or better than the Northwest Gulf and Exploratory Programs (Table 2.5-6). This is attributed to the longer time scales and higher amplitude signals associated with the primarily deepwater measurements made during the Eastern GOM program.

CCAR Mesoscale/PIES SSH Correlation

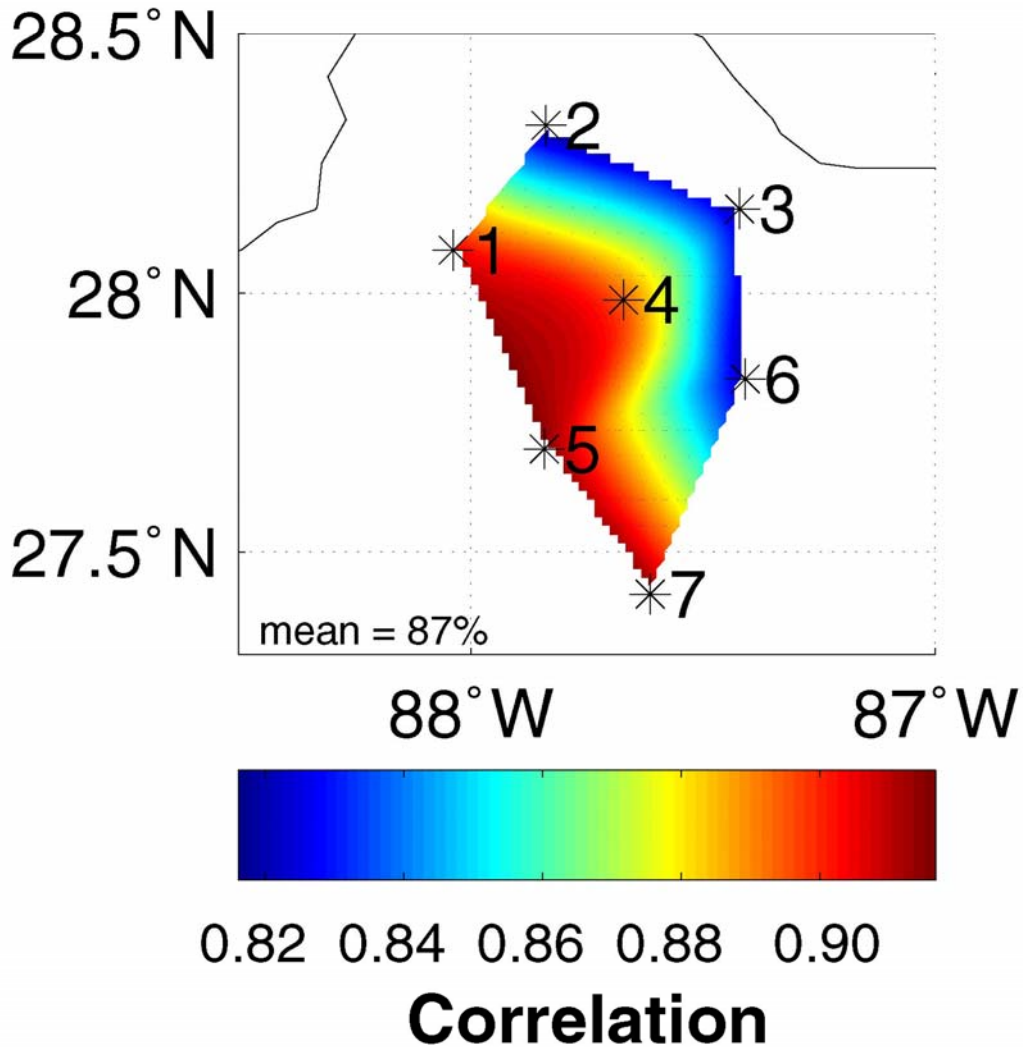


Figure 2.5-6. Spatial map of the CCAR/PIES SSH temporal correlation. Average over all stations of the correlation of the CCAR gridded mesoscale SSH data product to the collocated PIES time series is 87%. The 2000-m isobath is shown.

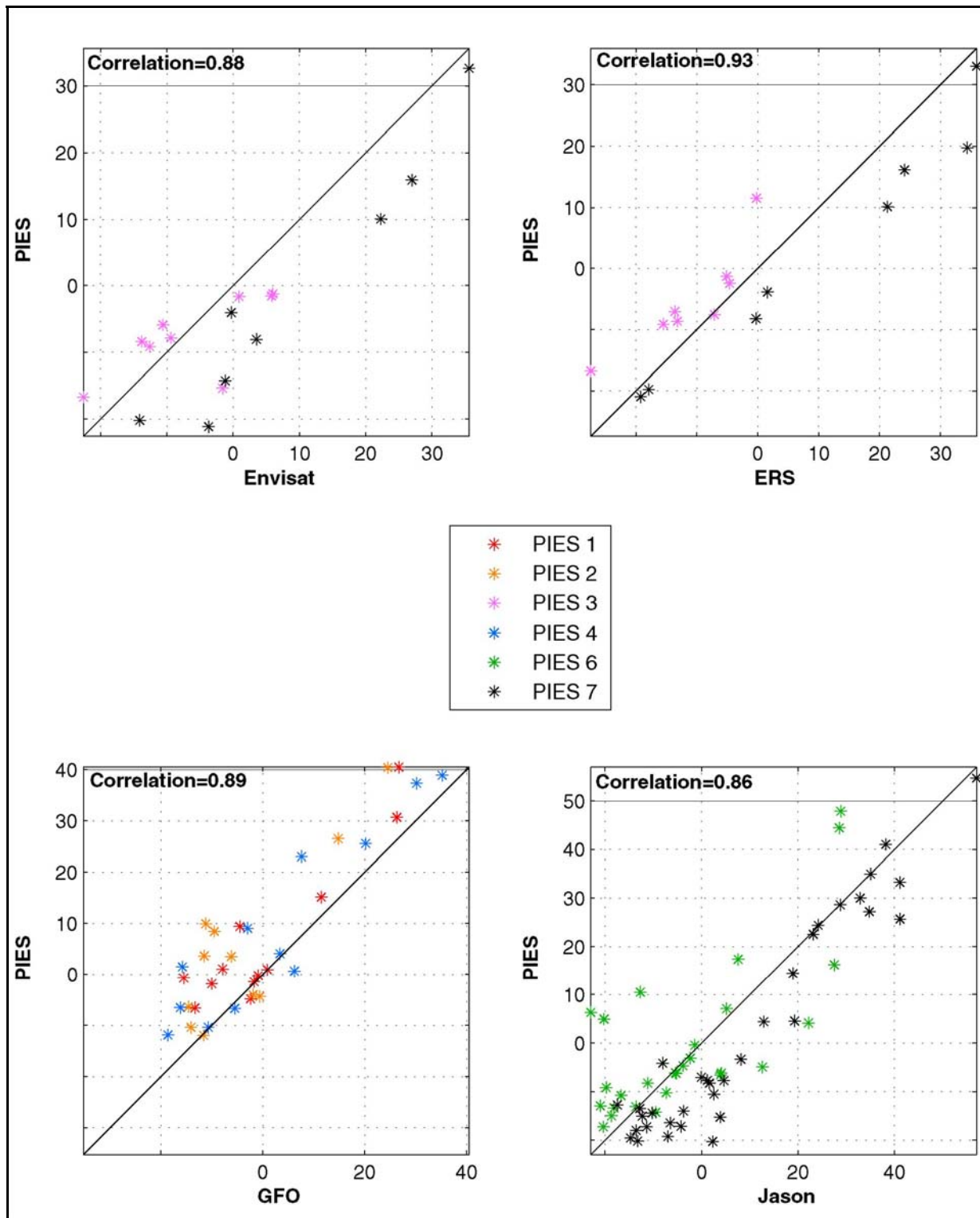


Figure 2.5-7. Scatterplot and correlation values of PIES time series points located on altimeter groundtracks with the coincident points from the along-track detrended altimeter data. Results derived from all four satellites that overflow a PIES station: Envisat, ERS-2, GFO, and Jason.

Table 2.5-6

Satellite Altimeter and PIES SSH Correlation.

Satellite altimeter and PIES SSH correlation at groundtrack points coincident with PIES stations during the Eastern Gulf, NW Gulf, and Exploratory Programs.

Satellite	Eastern Gulf Program	NW Gulf Program	Exploratory Program
Envisat	88%	81%	79%
ERS-2	93%	73%	72%
GFO	89%	78%	81%
Jason-1	86%	86%	77%
TOP/POS	NA	63%	56%

As we noted in the Northwest GOM and Exploratory Study reports, the correlation values are very sensitive to the alongtrack smoothing/gridding employed to interpolate the raw sub-satellite measurement points to a reference groundtrack. The CCAR alongtrack gridding technique does not smooth the raw alongtrack data and uses linear interpolation between sub-satellite points. This method was consistently applied to produce all of the alongtrack data for each satellite. The Cressman objective analysis that was used to interpolate the alongtrack data to a regular space/time grid does apply some filtering/smoothing to the data, which is why the gridded product correlations with the PIES SSH time series can, in some cases, be higher than the alongtrack correlations. The low correlation found between the TOP/POS alongtrack and PIES SSH data may be residual geoid error caused by referencing the alongtrack data to the GSFC mean sea surface. This mean sea surface predates the Tandem Mission therefore no SSH data along the TOP/POS interleaved groundtrack was used in the estimation of the mean. Updated mean sea surfaces that include TOP/POS Tandem Mission data in the estimation procedure are now becoming available. When one of these updated mean sea surfaces is incorporated into the CCAR data processing system, an improvement in the TOP/POS correlation with the PIES should be observed. Thus, PIES data can help to improve satellite altimeter data processing and to evaluate the performance of the satellite-based observing systems.

Ongoing work at the University of Colorado is directed toward improving the CCAR SSH product by using optimal interpolation techniques and space/time correlation functions tuned to the SSH variability in the Gulf. The ultimate goal is to combine altimeter and PIES SSH in a single data product exploiting the full sampling capabilities of both systems.

2.6 Ancillary Data

Ancillary data for river discharge, coastal and offshore winds, and coastal water levels were obtained as available from public sources. These data were used to assist in assessing if coastal influences significantly influenced the circulation structure in the study area.

2.6.1 River Discharge

River discharge data was obtained from the US Geological Survey (USGS) website <http://waterdata.usgs.gov/nwis/rt> for major rivers discharging into the central and eastern GOM north of the study area (Figure 1.2-1). Time series of these discharge data are shown in Figures 2.6-1 through 2.6-4. Timing of tropical storms and hurricanes is depicted on the plots. These discharge data provide an excellent perspective on the dominance of the Mississippi River discharge over the other sources, requiring some changes in the discharge scale so as to plot the data. The greatest river discharge occurred in April for most rivers. For the Wax Lake Outlet and the Lower Atchafalaya River, the greatest discharge occurred from January through April. The Mississippi River consistently had a higher discharge than all other rivers in the area followed by the Wax Lake Outlet, Lower Atchafalaya River and the Alabama River.

2.6.2 Coastal and Offshore Winds

Coastal wind data was obtained from the National Data Buoy Center (NDBC) website <http://www.ndbc.noaa.gov> for several coastal and offshore locations (Figure 1.2-1). Time series vector plots of these data are provided in Figures 2.6-5 through 2.6-8. Timing of tropical storms and hurricanes is depicted on the plots. Wind sensors 3 and 5-8 were located offshore on buoys surrounding the study area while the other sensors were located on or near-shore from Louisiana to Alabama. Some datasets were sparse after hurricane events. Sensors 4-8 had the highest wind speeds. The highest wind speeds approached 70 mph during Hurricane Katrina at sensors 6 and 7. For each sensor, the highest wind speeds occurred during hurricane events.

2.6.3 Coastal Water Levels

Coastal water level data was obtained from the National Oceanic and Atmospheric Administration (NOAA) website <http://tidesandcurrents.noaa.gov> for several coastal locations (Figure 1.2-1). Time series plots of these data are provided in Figures 2.6-9 and 2.6-10. Timing of tropical storms and hurricanes is depicted on the plots. Tidal variation was similar for each location. The largest differences between predicted and measured tide height occur during or shortly after hurricane events; however, the measured tide height varied from the predicted height at other times as well.

2.6.4 Hurricanes and Tropical Storms

Five hurricanes and one tropical storm passed through the GOM during the measurement program in 2005. A listing of the storms and dates is provided in Table 2.6-1. Information on the tracks of the storms was obtained from the National Hurricane Center (NHC) website <http://www.nhc.noaa.gov>. The paths and timing of all six storm events are shown in Figure 2.6-1. The aerial extent of the tropical storm and hurricane winds for each storm, as provided by the NHC, and their position versus our study area and moorings, is displayed in Appendix A. Timing of these tropical storms and hurricanes has also been depicted on various data plots in Appendices B and C.

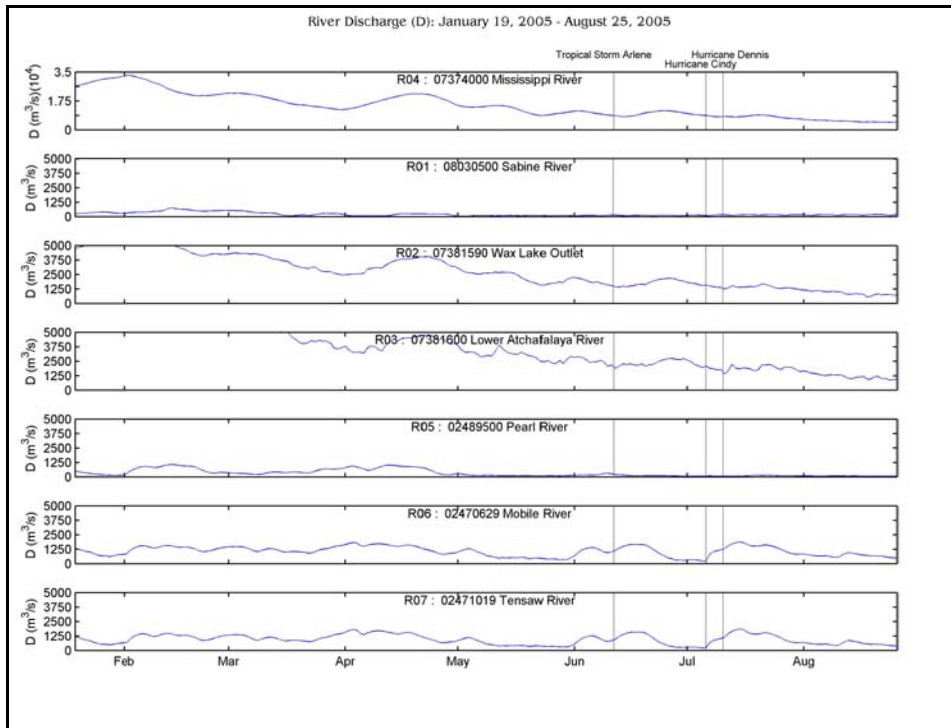


Figure 2.6-1. River discharge in $m^3 s^{-1}$ during the first deployment (Rivers 1-7). Note Mississippi River is at larger scale.

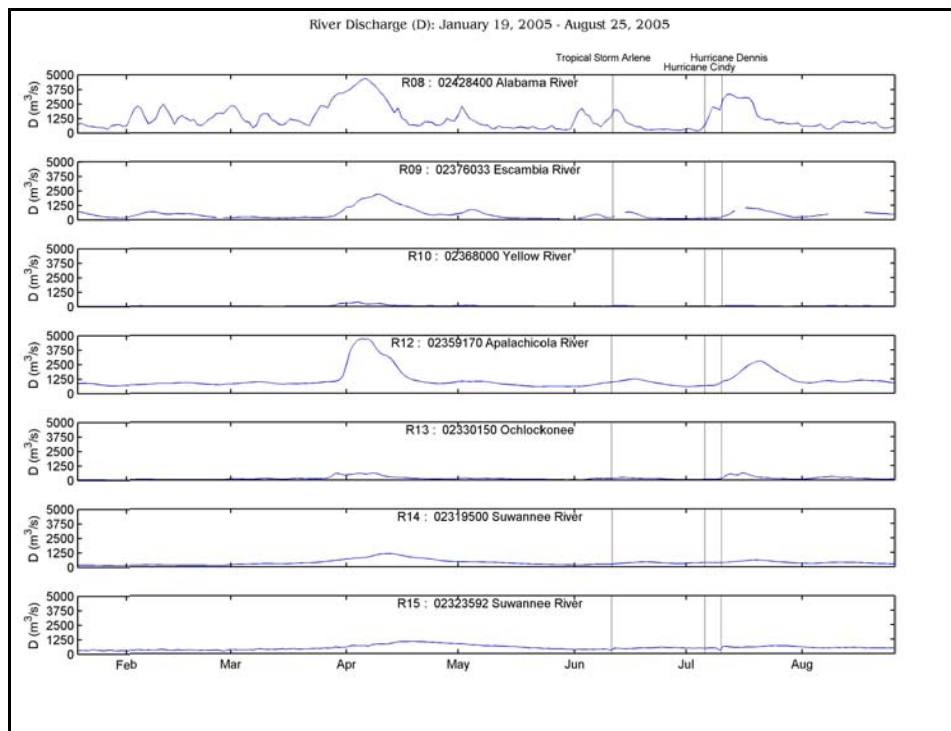


Figure 2.6-2. River discharge in $m^3 s^{-1}$ during the first deployment (Rivers 8-15).

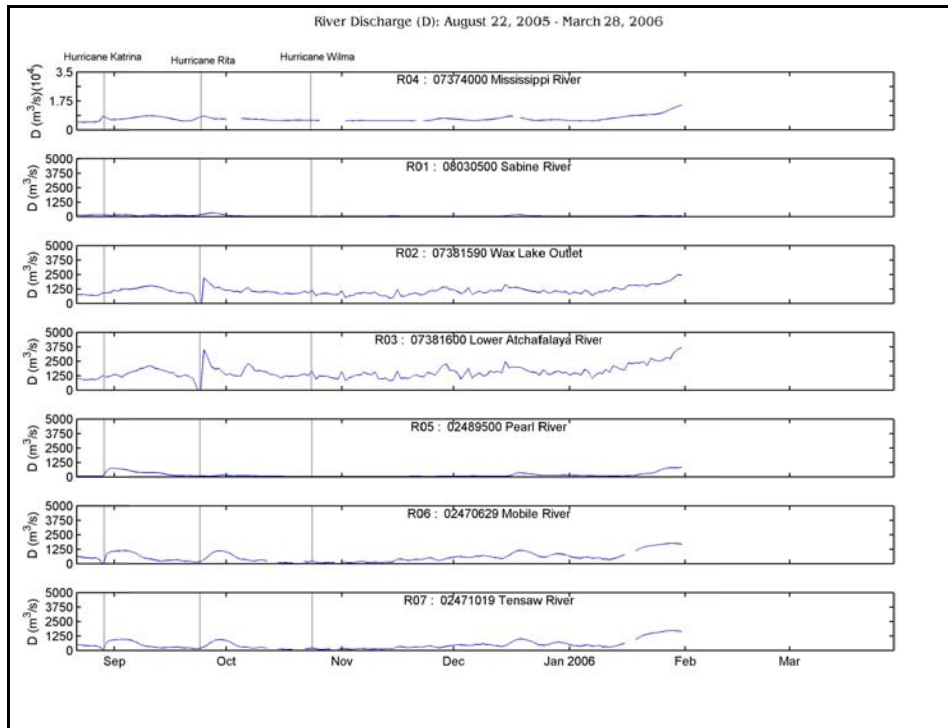


Figure 2.6-3. River discharge in $m^3 s^{-1}$ during the second deployment (Rivers 1-7). Note Mississippi River is at larger scale.

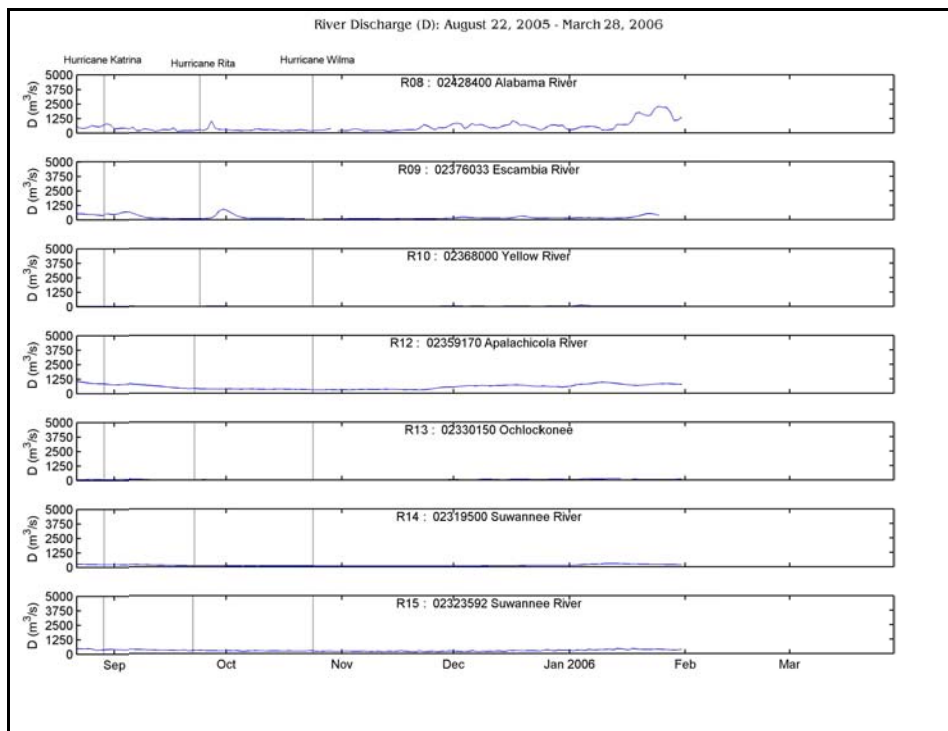


Figure 2.6-4. River discharge in $m^3 s^{-1}$ during the second deployment (Rivers 8-15).

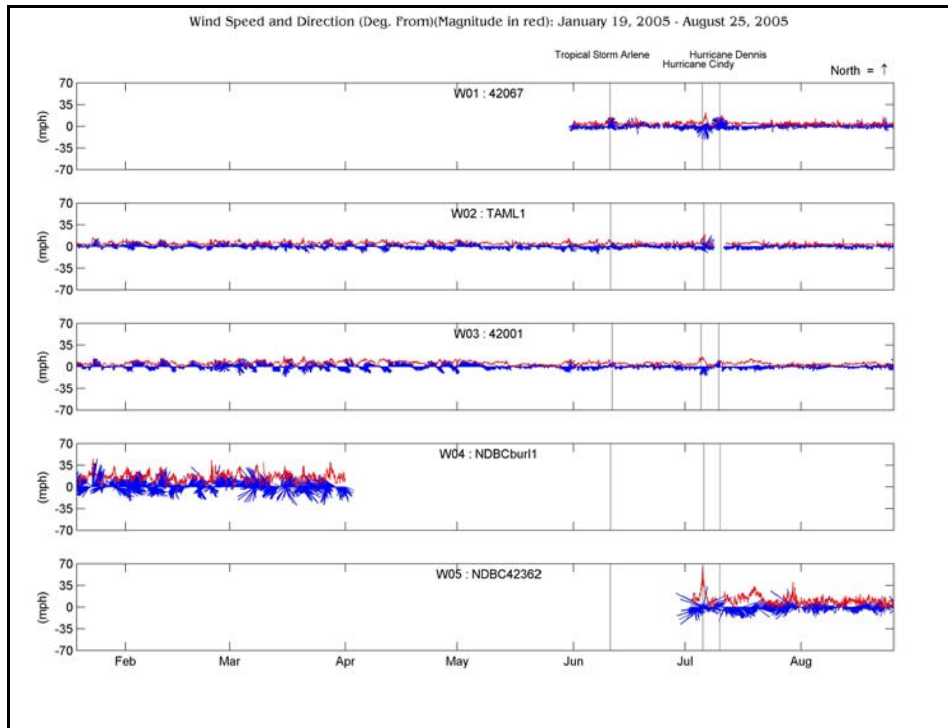


Figure 2.6-5. Vector plots of wind speed (mph) and direction (degrees from) for the first deployment (Winds 1-5).

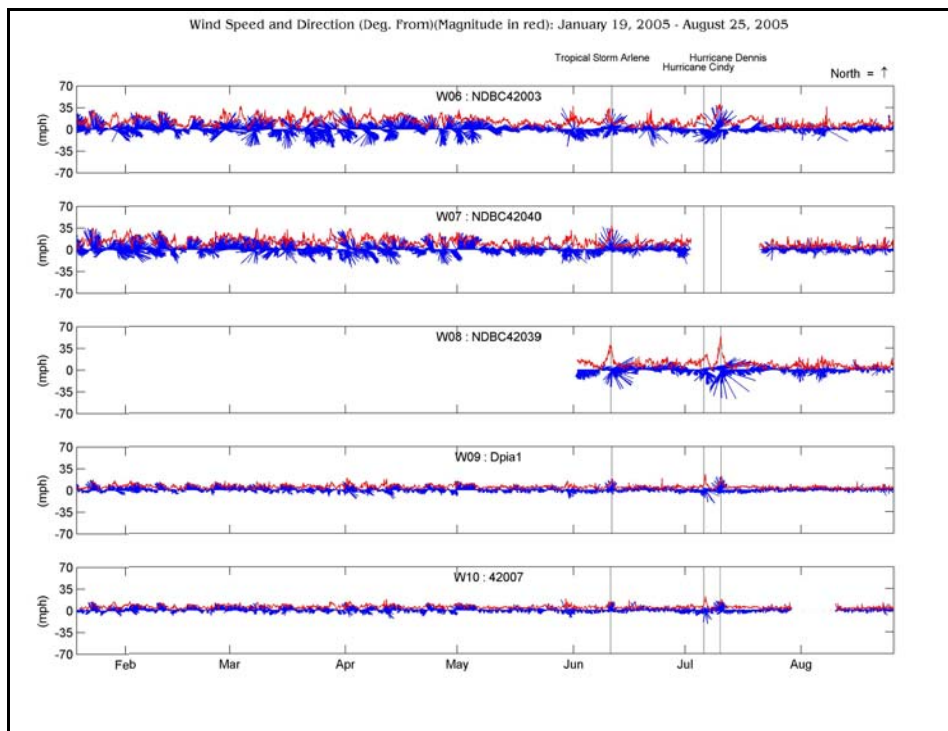


Figure 2.6-6. Vector plots of wind speed (mph) and direction (degrees from) for the first deployment (Winds 6-10).

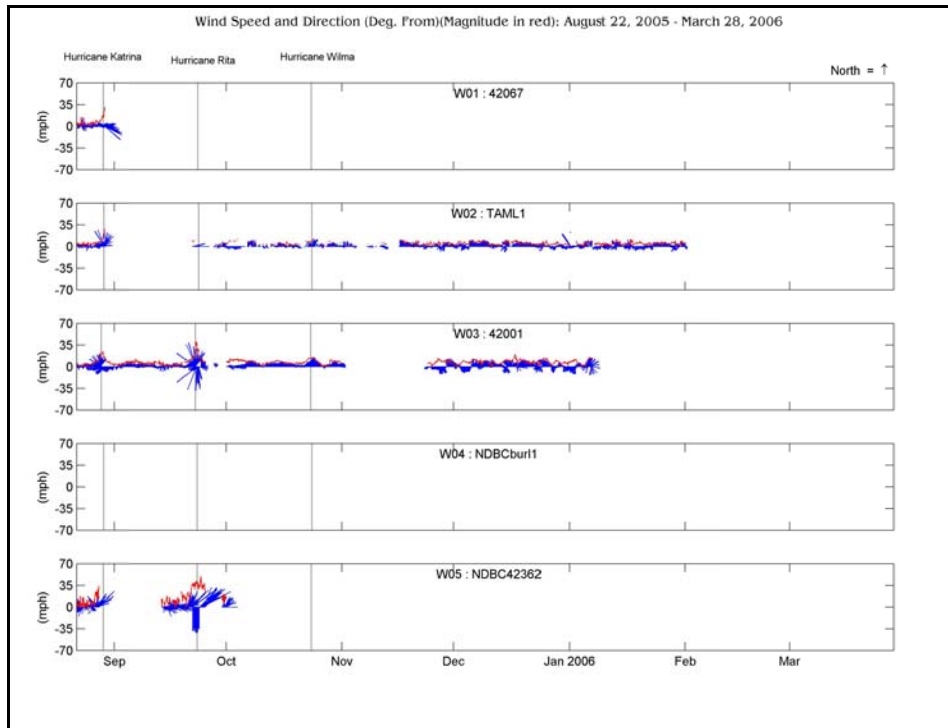


Figure 2.6-7. Vector plots of wind speed (mph) and direction (degrees from) for the second deployment (Winds 1-5).

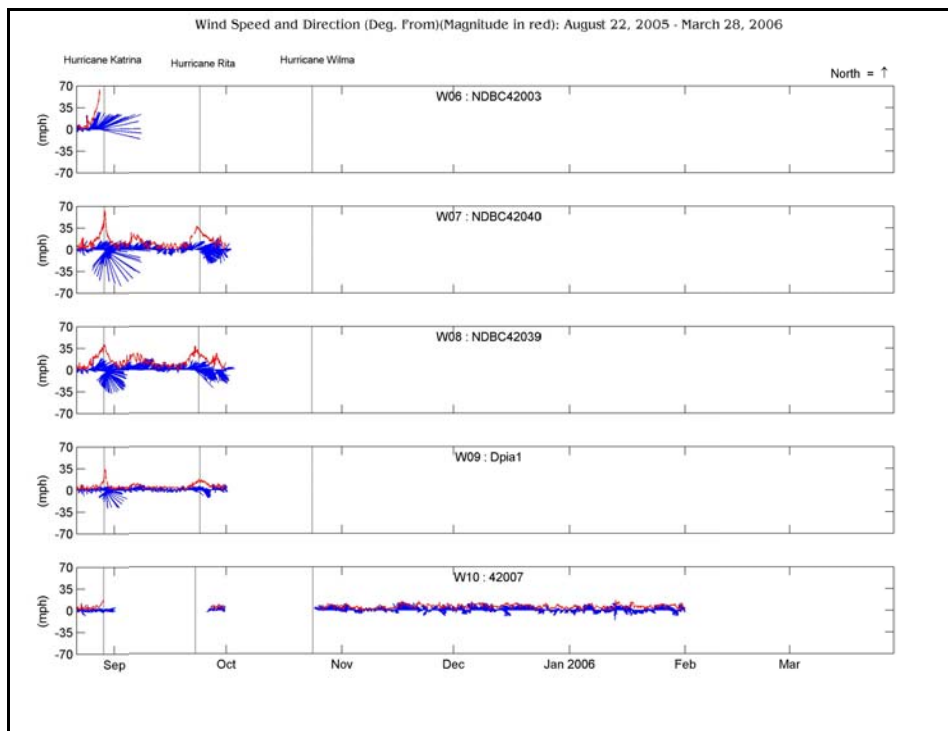


Figure 2.6-8. Vector plots of wind speed (mph) and direction (degrees from) for the second deployment (Winds 6-10).

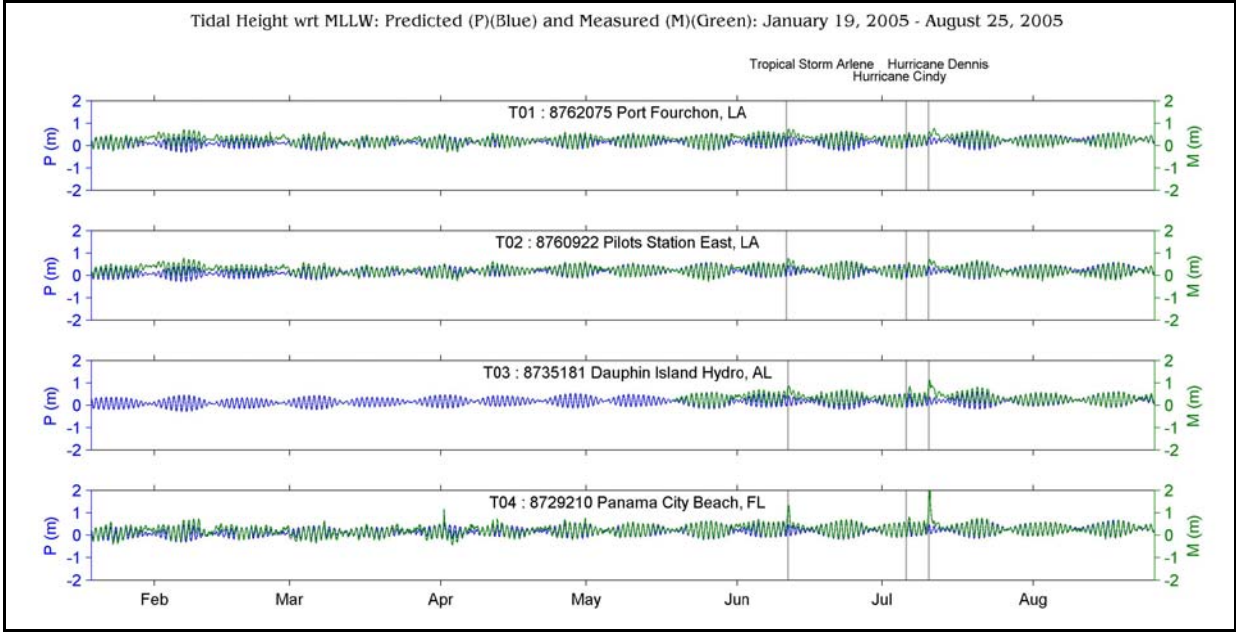


Figure 2.6-9. Predicted and measured tide height (m) from gauges located on the coast from Louisiana to Florida for deployment 1.

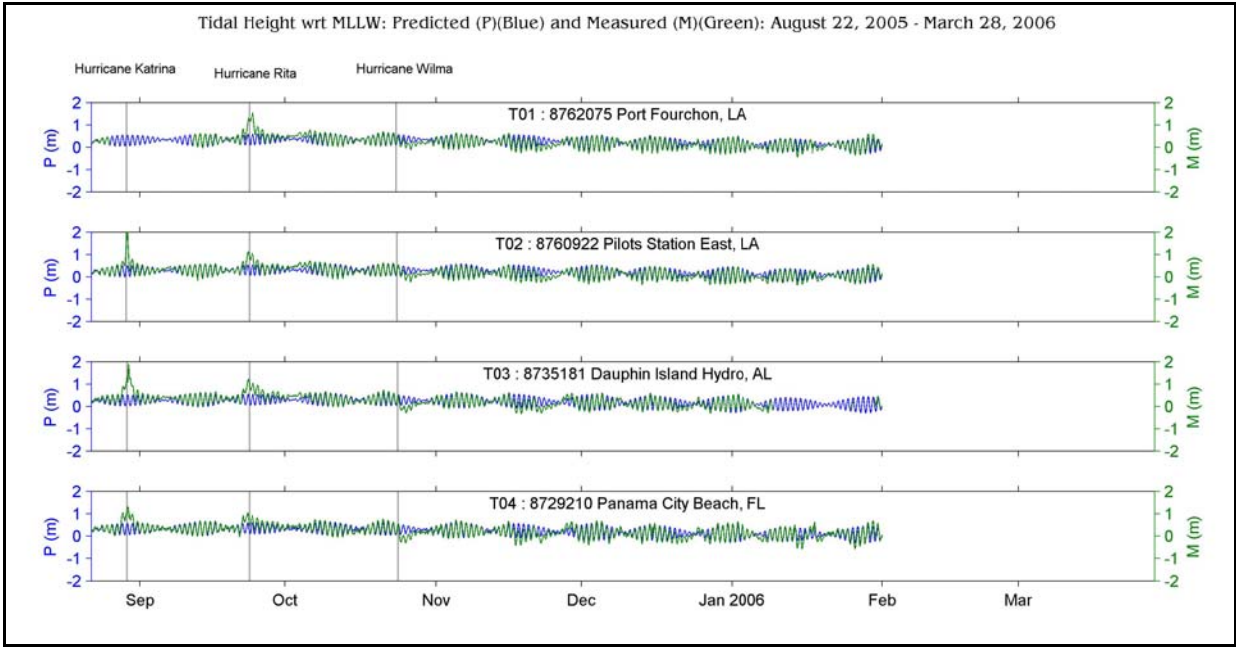


Figure 2.6-10. Predicted and measured tide height (m) from gauges located on the coast from Louisiana to Florida for deployment 2.

2.6.5 Horizon Marine Eddy Watch and Drifting Buoys

Horizon Marine, Inc. produces a proprietary operational oceanographic product called Eddy Watch that tracks, maps, and forecasts the LC and its eddies and frontal features. Horizon Marine uses a variety of information to create this oceanographic product, including satellite imagery and altimetry information, circulation modeling output, as well as trajectories from satellite-tracked drifting buoys that they deploy into the LC. The Eddy Watch product and the drifting buoys trajectory information are proprietary products with non-disclosure rules for a period of one year. The study team secured a limited use license to obtain and utilize both the Eddy Watch reports and the drifting buoy trajectory data for the period of 2005 for the purpose of performing some additional analyses on LC and LCE metrics and kinematics.

Table 2.6-1

Storm Events.

A list of the storm events that passed near the study area during the study period.

Storm Name	Category at Site	Date in Gulf	Date Closest to Site	Landfall Date
Tropical Storm Arlene	Tropical Storm	6/10/2005	6/11/2005	6/11/2005
Hurricane Cindy	Tropical Storm	7/4/2005	7/5/2005	7/5/2005
Hurricane Dennis	Category 4	7/8/2005	7/10/2005	7/10/2005
Hurricane Katrina	Category 5	8/26/2005	8/28/2005	8/29/2005
Hurricane Rita	Category 5	9/20/2005	9/22/2005	9/24/2005
Hurricane Wilma	Category 3	10/21/2005	10/23/2005	10/24/2005

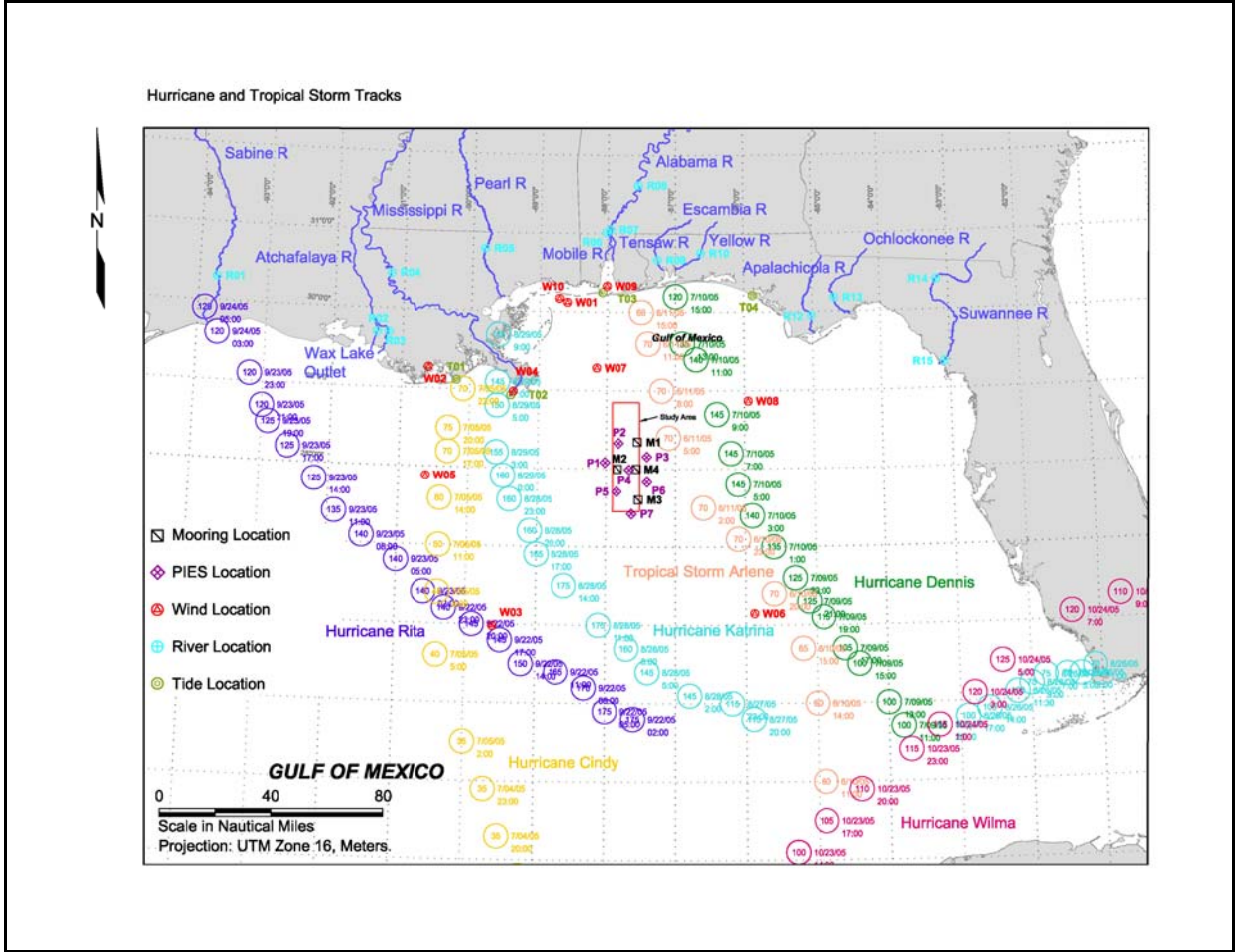


Figure 2.6-11. Timing and paths of all six storm events that passed near the study area during the study period.

3.0 LOOP CURRENT EVENTS AND HISTORICAL PERSPECTIVE

3.1 *Loop Current and Loop Current Eddies*

The Loop Current dominates the upper ocean circulation in the eastern deepwater basin of the GOM; therefore, no description of observations in the Eastern GOM study region is complete without accounting for the position and movement of the LC and its associated eddies. In this section, we describe the LC and LCE events impacting the study array during the program time period to put into perspective the results obtained from the measurement array. Remote sensing data were used to monitor oceanographic conditions in and around the array to achieve this perspective. The remote sensing data also allowed the measurement year to be placed into the context of "typical" conditions in the Eastern GOM. This could be achieved because continuous altimeter mapping of the sea surface height in the Gulf has been conducted since 1993 which provides this historical perspective. We used the available satellite altimeter time series to monitor the position of the LC and track individual LCEs over the 13.5-year altimeter record covering 1 January 1993 through 30 June 2006 and then compared those results with similar analyses made during the study time period from 1 January 2005 through 15 January 2006.

3.1.1 LC and LCEs During the Study Period

Sea surface temperature (SST) and ocean color images overlaid with sea surface height (SSH) contours provided synoptic views of the ocean surface thermal and color patterns associated with the altimeter-inferred circulation during the study program. These satellite images overlaid with altimetric SSH provided a basic overview of LC intrusion and LCE detachment and separation events during the study time period.

LCE separation events were identified by the breaking of the 17-cm SSH contour that closely tracks the edge of the high-velocity core of the LC. This is an objective method for tracking the LC and detecting LCE separation events that gives separation periods comparable to those determined by subjective tracking methods (Leben 2005). The day that the tracking contour breaking occurs is identified as the "time" of eddy separation. Occasionally a detached eddy will reattach to the LC. In those cases, the time associated with the final detachment of the LCE from the LC is referred to as the eddy separation time. We selected an exact day of separation determined by the breaking of the tracking contour; however, estimated uncertainties in the separation period may be as great as one month. Although eddies may detach from and reattach to the LC during intrusion, the ultimate detachment or separation occurs most frequently at intervals of about 6, 9 and 11.5 months based on the available historical measurements (Leben 2005).

During the Eastern GOM program only a single large anticyclonic eddy, which was given the name “Vortex”, separated from the LC. LCE Vortex nominally separated from the LC on 13 September 2005. Figure 3.1-1 shows an 8-day composite color image overlaid with SSH on 15 September 2005 just days after eddy separation. Negative SSH contour levels are shown by dashed lines, positive by solid. The contour increment is 5 cm and the 17-cm LC tracking contour is shown by the thick, solid contour line. The extended intrusion of the LC into the northern GOM associated with LCE Vortex was one of the most northerly on record; it was only exceeded by the intrusion that generated LCE Sargassum during the Exploratory Study. This far northerly intrusion of the LC and LCE Vortex during late summer 2005 contributed to the intensification of Hurricanes Katrina and Rita (Walker et al. 2005). After the separation of LCE Vortex, the LC did not retreat substantially to the south. As a result the LC remained intruded into the eastern-central GOM during the rest of the program time period. Although the LC later reentered into the north-central Gulf, it did not directly intrude into the study region again after the separation of LCE Vortex. The next two LCEs, Walker and Xtreme, separated on 6 Feb 2006 and 7 Mar 2006, respectively, after the program instruments were retrieved in January 2006.

Before ultimately separating from the LC in September 2005, LCE Vortex detached from and reattached to the LC a total of four times based on the 17-cm LC tracking contour depicted in the SSH maps. This was the largest number of detachment/reattachment events observed during a single LC intrusion cycle within the historical altimeter record. The first detachment was on 21 February 2005 and occurred shortly after the reentrusion of the LC into the northern GOM six months after the separation of the preceding LCE, Ulysses, from the LC in August 2004. Since the detachment/reattachment event occurred during late winter and early spring, SST imagery provides good contrast for identifying the surface signature of the upper ocean circulation during the event, as is seen in the series of 3-day composite SST images overlaid with SSH shown in Figures 3.1-2 and 3.1-3. This sequence of images at 10-day intervals clearly shows the detachment and reattachment of the eddy from the LC in the surface thermal signature of the eddy and current over the time period. During this detachment/reattachment event, the anticyclonic eddy remained detached from the LC for 52 days based on the altimeter tracking. The reconnection of the detached anticyclonic eddy to the LC in early April is confirmed by the wrapping of warm LC waters around the periphery of the eddy in the sequence of images shown in Figure 3.1-3. Only one other LCE detachment and reattachment event observed in the 13.5-year altimeter record exhibited a longer time period of detachment. That detachment event spanned 65 days and was associated with the LC intrusion that ultimately produced LCE Titanic in 2004, which was very well observed during the Exploratory Program (Donohue et al. 2006).

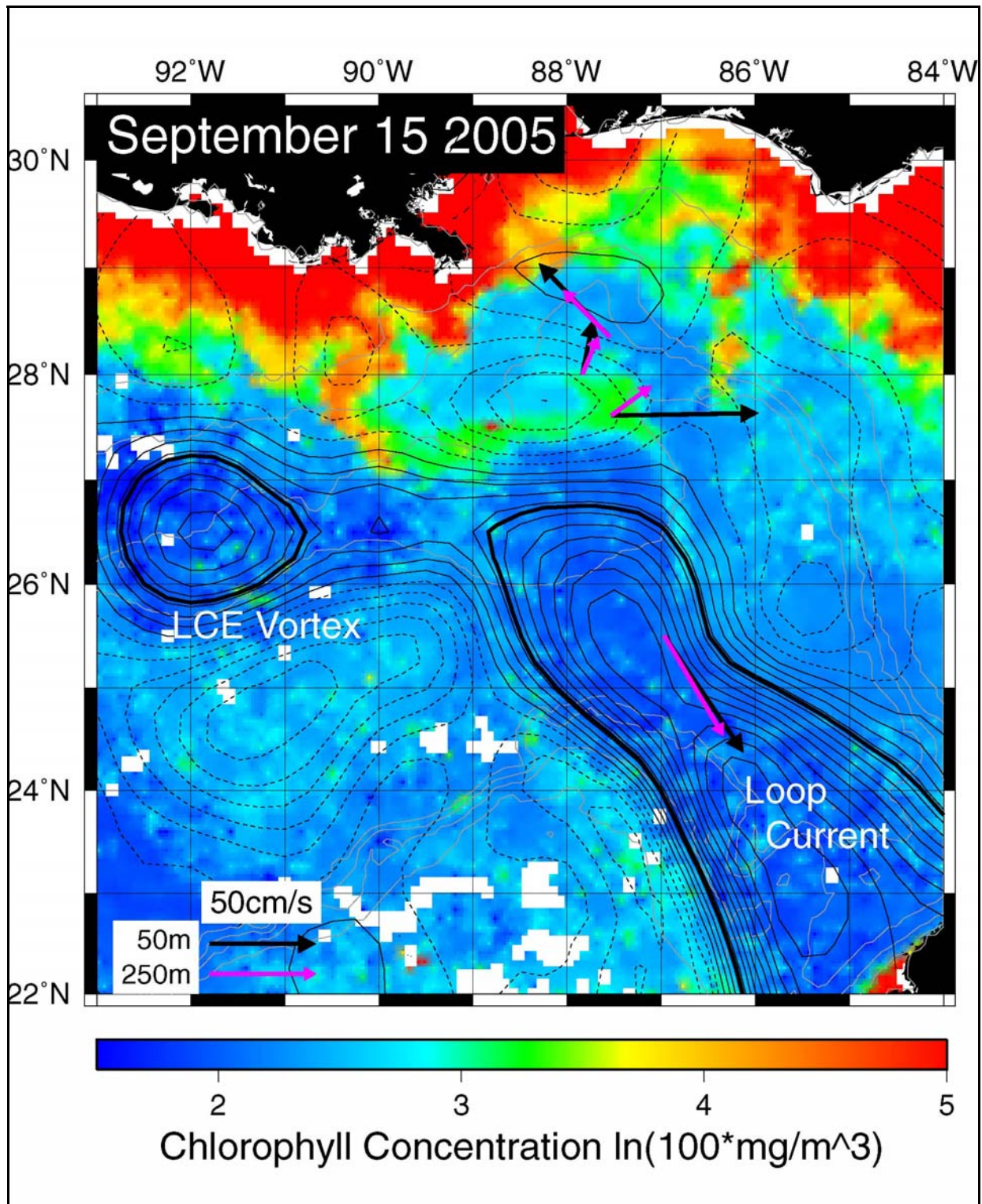


Figure 3.1-1. Eight-day composite image of chlorophyll concentration overlaid with the SSH contour map from 15 September 2005 showing the recent separation of LCE Vortex from the LC. The 17-cm LC tracking contour is the thick contour line. Current vectors from the study moorings at 50 and 250 m depth are also shown.

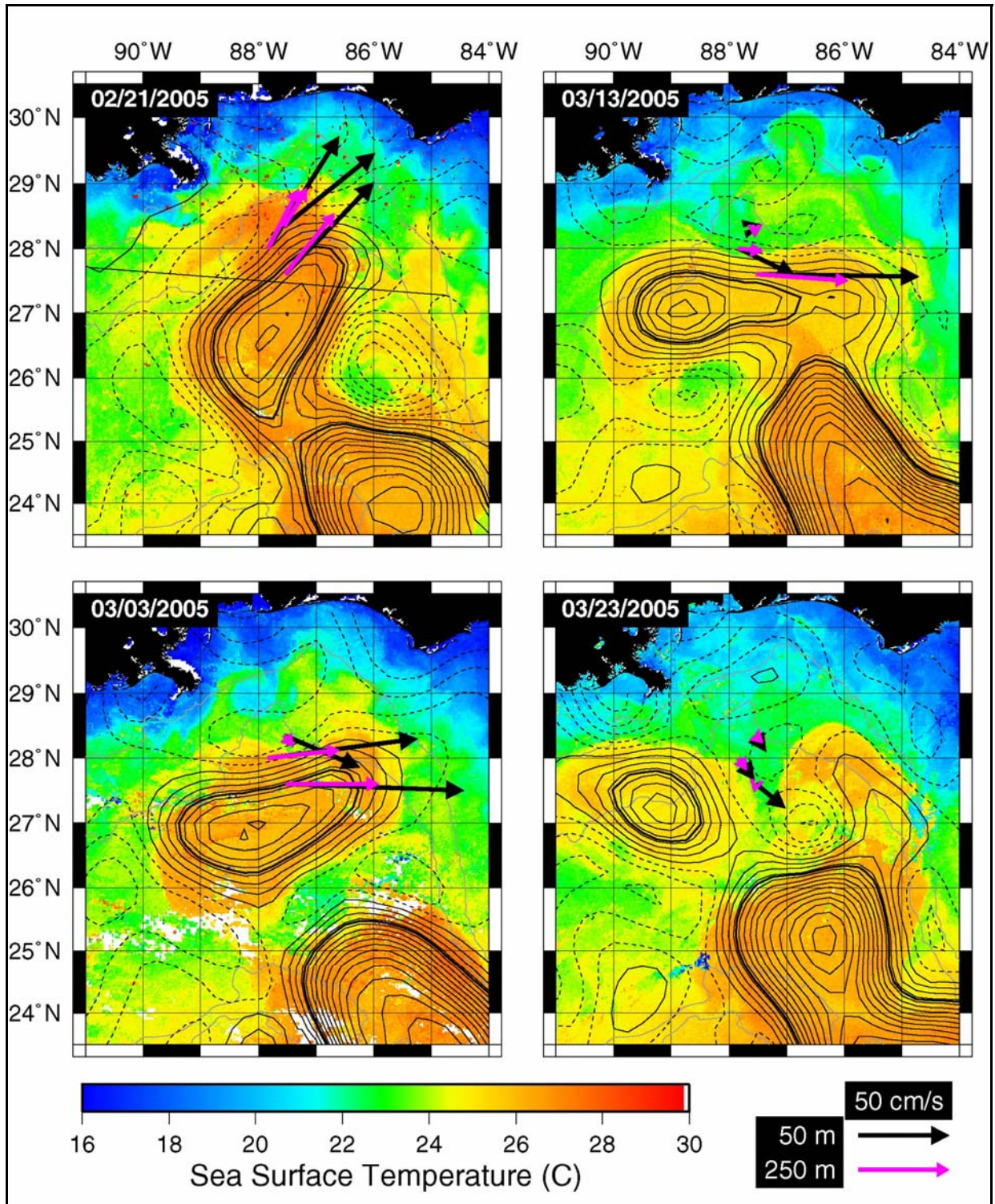


Figure 3.1-2. Three-day composite SST images overlaid with SSH contour maps showing the detachment of LCE Vortex from the LC in late February 2005. The interval between images is 10 days. The 17-cm LC tracking contour is shown by the thick line. Current vectors from the study moorings at 50 and 250 m depth are also shown.

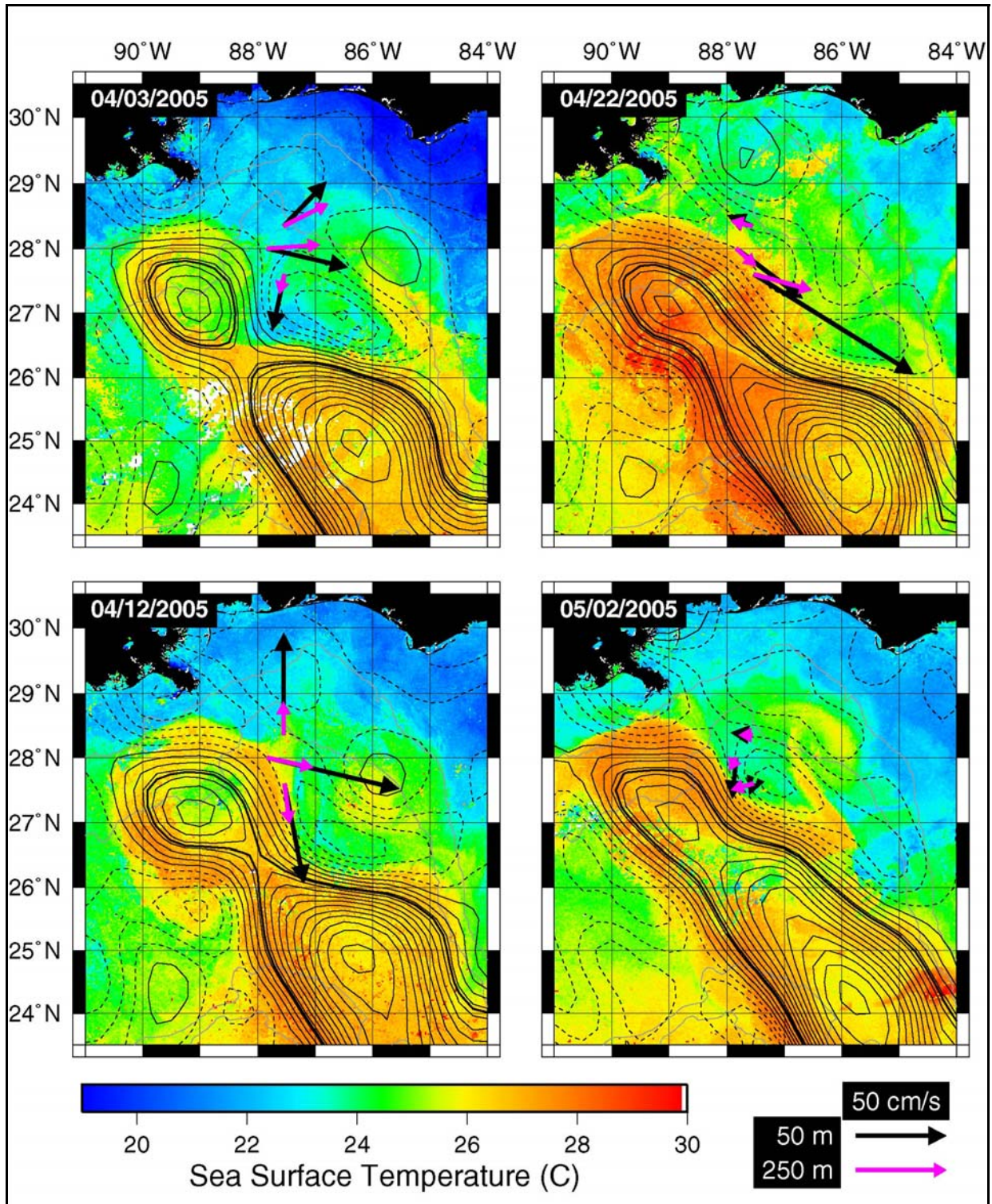


Figure 3.1-3. Three-day composite SST images overlaid with SSH contour maps showing the reattachment of LCE Vortex to the LC in early April 2005. The interval between images is about 10 days. The 17-cm LC tracking contour is shown by the thick line. Current vectors from the study moorings at 50 and 250 m depth are also shown.

After this initial detachment and reattachment, LCE Vortex detached and reattached three more times before ultimately separating from the LC in September. These detachment events were of shorter duration, lasting only one to three weeks. Satellite images with overlaid SSH corresponding to the detachment and reattachment times for each of the four events are shown in Figures 3.1-4 and 3.1-5. In all four detachment/reattachment events the LC was well intruded into the northern deepwater basin as eddy detachment occurred. As a result, in three of the four cases (#1, #2 and #3) the LC intruded directly into the study area. In the one case where intrusion did not occur (#4), the LC was positioned too far to the west of the study region to directly impact the observation array. Thus, the direct intrusions of the LC into the study region were confined to the time period before August 2005. Energetic events observed in the remainder of the observational record were associated with circulation peripheral to the LC, which in most cases was cyclonic.

The dates of all four Vortex detachment/reattachment events and their durations are listed in Table 3.1-1. Note that these dates were determined using the 17-cm LC tracking contour and the algorithm described in section 3.1.2 of this report. Because of the actual SSH contouring and masking algorithm applied in the MATLAB code used for automatic tracking, there are small differences in the configuration of the LC when SSH contours are plotted using the Generic Mapping Toolbox (GMT) contouring routine that was used to plot the figures shown. Dates nearest the MATLAB-determined dates were selected so that the plotted contours show a detached or attached eddy consistent with the automatic tracking results. In most cases, the GMT contouring causes differences of one day for the dates of detachment and reattachment when compared with the automated tracking results; the largest difference was only two days.

Table 3.1-1

LCE Vortex Detachment and Reattachment Events.

LCE Vortex detachment and reattachment events that occurred during the EGOM Study Program.

Event	Detachment Date	Reattachment Date	Duration (days)	Confirmation
#1	20 Feb 2005	12 Apr 2005	51	SST
#2	13 May 2005	20 May 2005	7	Not Confirmed
#3	15 Jun 2005	29 Jun 2005	14	Color/LSU Mooring
#4	01 Aug 2005	20 Aug 2005	19	Color

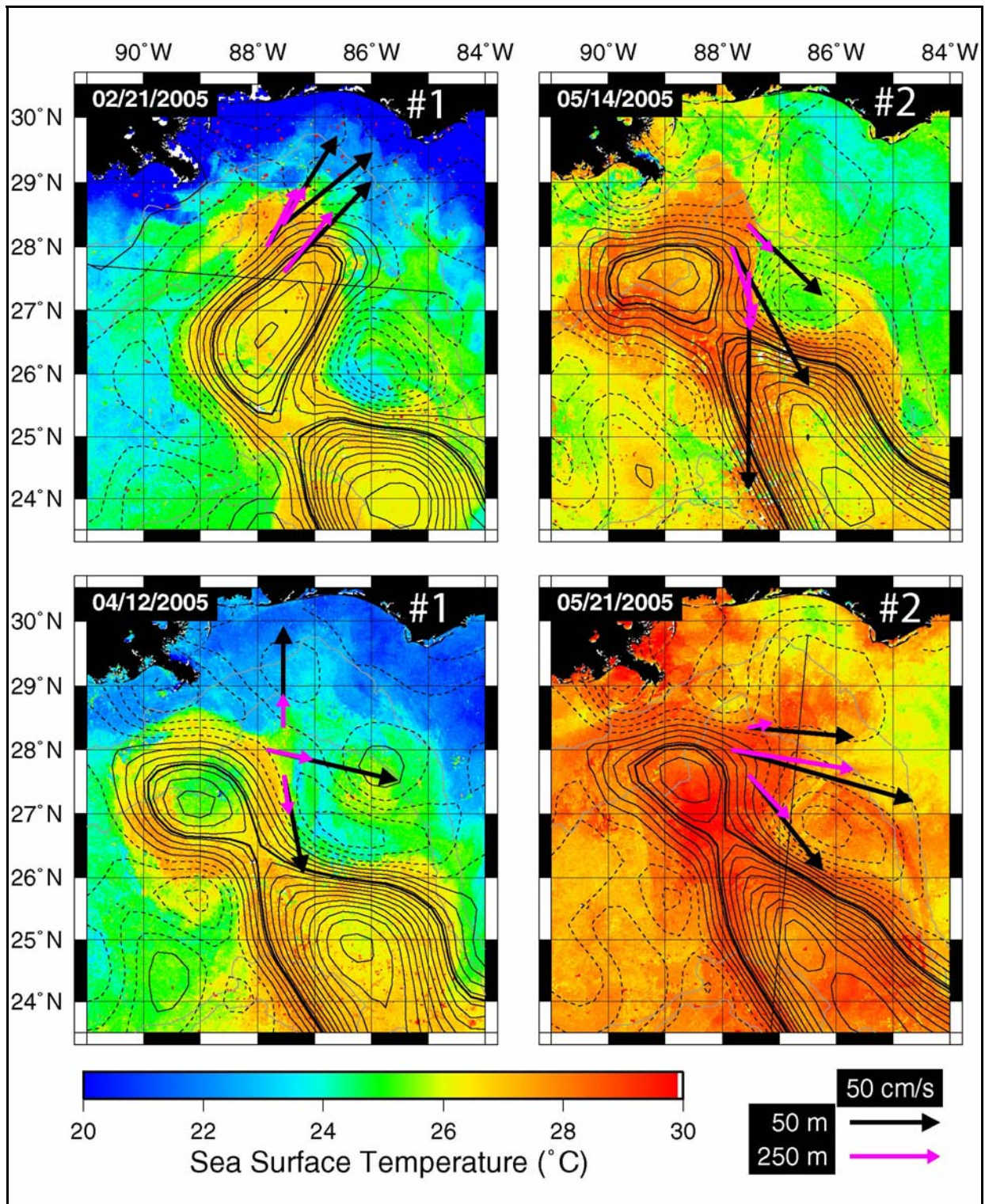


Figure 3.1-4. Three-day composite SST images overlaid with SSH contours showing LCE Vortex detachment (upper panels) and reattachment (lower panels) for events #1 and #2. The 17-cm LC tracking contour is shown by the thick contour line. Current vectors from the study moorings at 50 and 250 m depth are also shown.

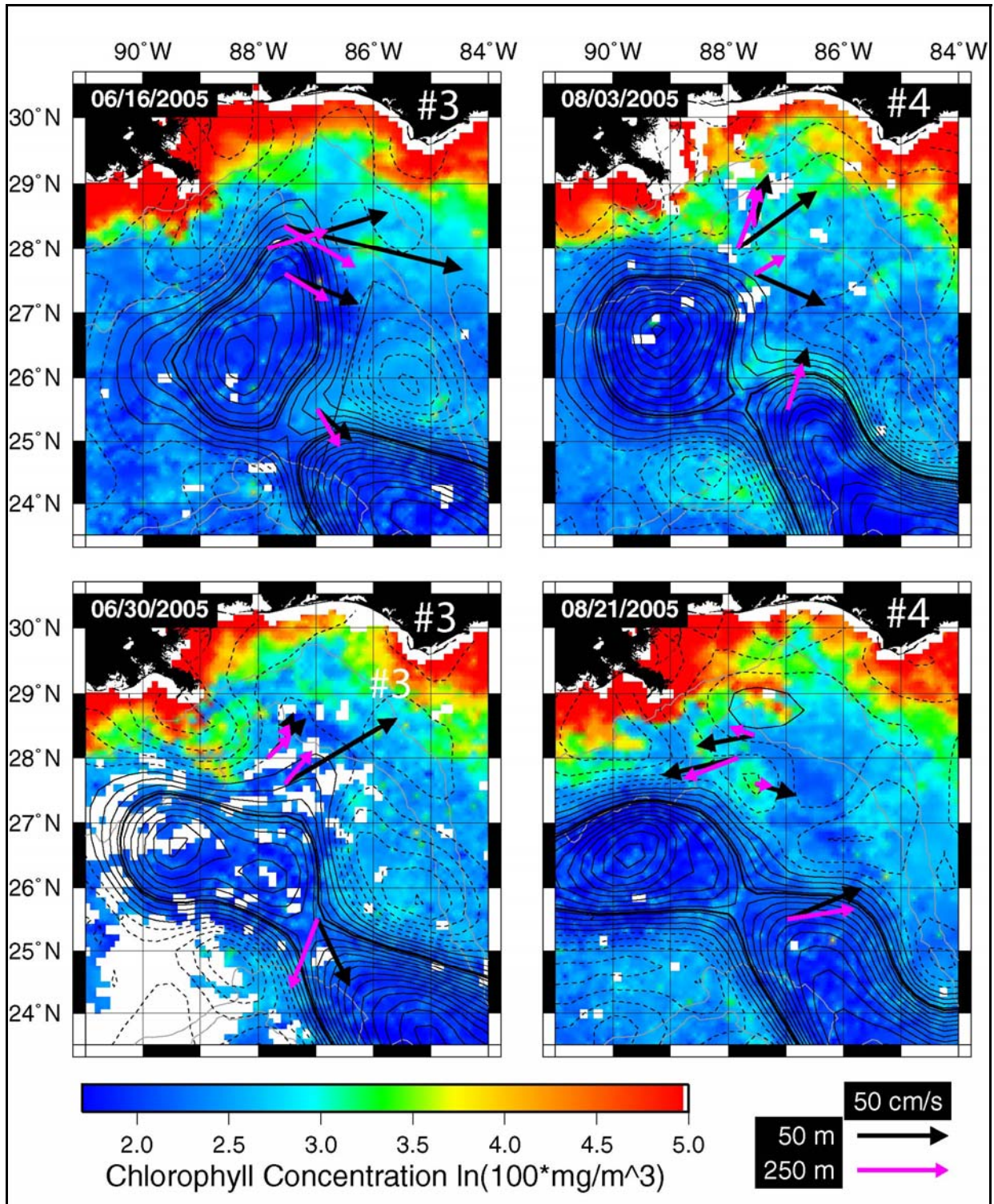


Figure 3.1-5. Eight-day composite chlorophyll concentration images overlaid with SSH contours showing LCE Vortex detachment (upper panels) and reattachment (lower panels) for events #3 and #4. The 17-cm LC tracking contour is shown by the thick contour line. Current vectors from the study moorings at 50 and 250 m depth are also shown.

Confirmation of the detachment of the eddy from the LC in the surface circulation was possible for three of the four eddy detachment events. SST and color images overlaid with SSH (Figure 3.1-6) show disconnection of the surface eddy signature from the LC in detachment events #1, #3, and #4. Further confirmation was found for detachment event #3 from the LSU mooring, which measured strong counter-current flow between the eddy and the LC at both 50 and 250-meter depths as shown in Figure 3.1-6. Only event #2 showed no clear evidence of the detachment of the eddy in the surface thermal or color patterns resolved in the SST or color images. Ancillary data including drifters were checked, but no clear evidence of detachment was found. Some displacement of closed eddy SSH contours relative to the LC was observed, which might be evidence of increasing disconnection between the eddy and the LC at depth, nevertheless, the displacement was apparently insufficient to completely detach the eddy.

The extended LC intrusion associated with the repeated detachment and reattachment of LCE Vortex before ultimate separation in September 2005 significantly impacted the study region upper ocean circulation during the first half of the eastern GOM program. Once LCE Vortex separated, the character of the circulation returned to conditions more typical of this northern location in the eastern deepwater GOM basin. This historical perspective is discussed in more detail in section 3.1.3 where the entire 13.5-year altimetry record of LC and LCE activity is presented.

3.1.2 Loop Current Metrics and Statistics

In addition to the objective identification of LCE separation, the objective tracking of the LC using the 17-cm SSH contour also allows detailed monitoring of LC metrics such as extent, boundary length, enclosed area, volume, and circulation. Previous studies (Hamilton et al. 2000; Leben et al. 2002; Leben 2005), developed and validated this objective tracking technique through qualitative and quantitative comparisons with satellite imagery and by direct comparisons with published subjective tracking results.

The altimeter dataset and objective tracking technique used to estimate the altimeter-derived LC metrics is described in detail in Leben (2005). The dataset used in this study is similar to that used for the revised estimates of the frequency of LCE shedding events published in Sturges and Leben (2000) with two notable improvements. First, we reprocessed the historical altimeter data using a new mean surface as described in Leben et al. (2002). Second, we incorporated altimeter data from the Envisat, Geosat Follow-On, Jason-1, and TOPEX/POSEIDON (TOP/POS) tandem missions to improve sampling during the time periods when those data are available.

The procedure for computing the metrics from the SSH fields has been automated by a MATLAB[®] program that accesses the GOM altimeter data archive and computes the values. Daily values for each metric were computed using the following algorithm:

1. Load the 0.25° gridded SSH field and generate the coordinates of the 17-cm contours within the Gulf.
2. Identify the Loop Current core, which is defined as the continuous 17-cm contour that enters the Gulf through the Yucatan Channel and exits through the Florida Straits.

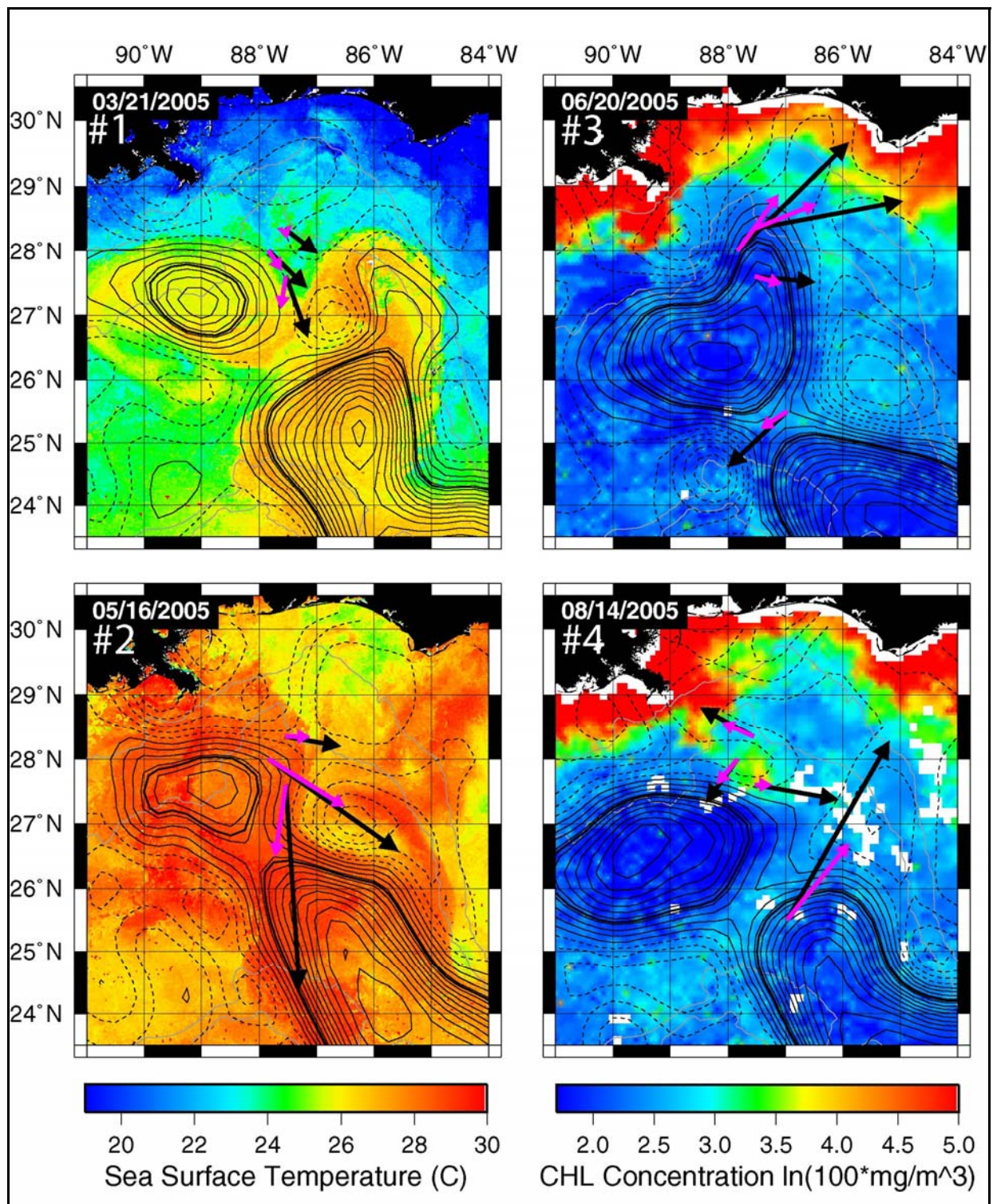


Figure 3.1-6. SST and chlorophyll concentration images overlaid with SSH showing the four LCE detachment events identified in the altimeter record. Three of the four detachments were confirmed by the coincident imager, only the second event (#2) was not. Current vectors from the study moorings at 50 and 250 m depth are also shown.

3. Find the maximum west longitude and north latitude coordinates to determine the extent of westward and northward penetration of the Loop Current.
4. Compute the length of the Loop Current by summing the distances between the coordinates on the 17-cm contour.
5. Identify all 0.25° grid cells bounded by the 17-cm contour and compute the total Loop Current area by summing the areas of the individual cells.
6. Estimate the Loop Current volume, assuming a one and a half-layer ocean and a reduced gravity approximation, by evaluating the following area integral over the region bounded by the 17-cm contour:

$$\iint \frac{g}{g'} h dx dy, \quad (3.1.1)$$

where h is the sea surface height; g is the acceleration of gravity; and g' the reduced gravity. (A value of 0.03 m s^{-2} was used for g' .)

7. Estimate the Loop Current circulation by the line integral of the geostrophic velocity along the 17-cm contour:

$$\oint \vec{V} \cdot ds = \int u dx + \int v dy, \quad (3.1.2)$$

where u and v are the geostrophic velocity components and dx and dy are the coordinate spacing in the east/west and north/south directions, respectively. The geostrophic velocity components at the midpoint locations are found by bilinear interpolation from the gridded geostrophic velocity components computed from the height field. (The sign convention employed here is such that the anticyclonic vorticity associated with the Loop Current is positive and therefore in positive correlation to the other metrics.)

The 13.5-year time series of LC maximum latitude/longitude extension and length are shown in Figure 3.1-7 and area, volume, and circulation in Figure 3.1-8 with the time period spanning the Exploratory Study program highlighted in black. Separate time series plots of the respective metrics during the program time period (1 January 2005 through 15 January 2006) are shown in Figures 3.1-9 and 3.1-10. Histograms of each metric are shown in the lower panels of each of the figures.

Histograms from the program record were overlaid on the histograms from the historical record (Figure 3.1-11) to allow direct comparison of the distribution of the LC metrics during the program and historical time periods. In general, the distributions were quite different, which was expected given the relatively short time period of the observational program and the energetic LC events that occurred therein. The mean LC values were also significantly different for the two time periods (Table 3.1-2). This was a result of the extended time period of LC intrusion associated with the repeated detachments and separation of LCE Vortex as well as the modest retreat and subsequent reintrusion of the LC after LCE Vortex separation.

3.1.3 Loop Current Eddy Metrics and Statistics

The primary goal of the objective LC tracking technique is to monitor the time-dependent behavior of the LC and its associated anticyclonic LCEs. As discussed previously, we identified the timing of LCE separation events using the LC length time series. The breaking of the 17-cm contour between the Loop and a detaching LCE into separate contours causes a discrete change in the LC length that is equal to the circumference of the separating eddy. The time associated with the final detachment of the eddy is referred to as the eddy separation time. The exact timing of a separation event is therefore dependent on the criteria selected to define separation and is complicated by the ambiguity of associating an exact time with what is clearly a continuous and complicated process. The tracking contour also impacts LC and LCE statistics, such as aerial extent, that are estimated using the tracking contour. Nevertheless, an objective definition of separation provides a useful benchmark for comparing LCE separation events that occurred during the study with those observed in the prior ten-year altimeter record.

Table 3.1-2

Altimeter-derived Summary Statistics.

Summary statistics for altimeter-derived LC metrics computed from the historical and eastern GOM program records.

	Maximum West Longitude	Maximum North Latitude	Length (km)	Area (km ²)	Volume (m ³)	Circulation (m ² sec ⁻¹)
Historical Record: 1 January 1993 through 30 June 2006						
Mean	88.01°W	26.28°N	1400	149,331	2.27x10 ¹³	1,408,600
Std. Dev.	1.25°	0.94°	369	28,989	0.36x10 ¹³	329,500
Maximum	93.07°W	28.10°N	2494	213,540	3.08x10 ¹³	2,311,200
Minimum	85.80°W	24.10°N	614	55,840	0.85x10 ¹³	611,420
EGOM Program Record: 1 January 2005 through 15 January 2006						
Mean	89.20°W	26.92°N	1678	170,077	2.44x10 ¹³	1,555,410
Std. Dev.	1.47°W	0.73°	346	21,398	0.23x10 ¹³	243,460
Maximum	92.80°W	28.07°N	2418	207,391	2.91x10 ¹³	2,134,550
Minimum	87.08°W	25.07°N	1017	124,488	1.86x10 ¹³	1,031,120

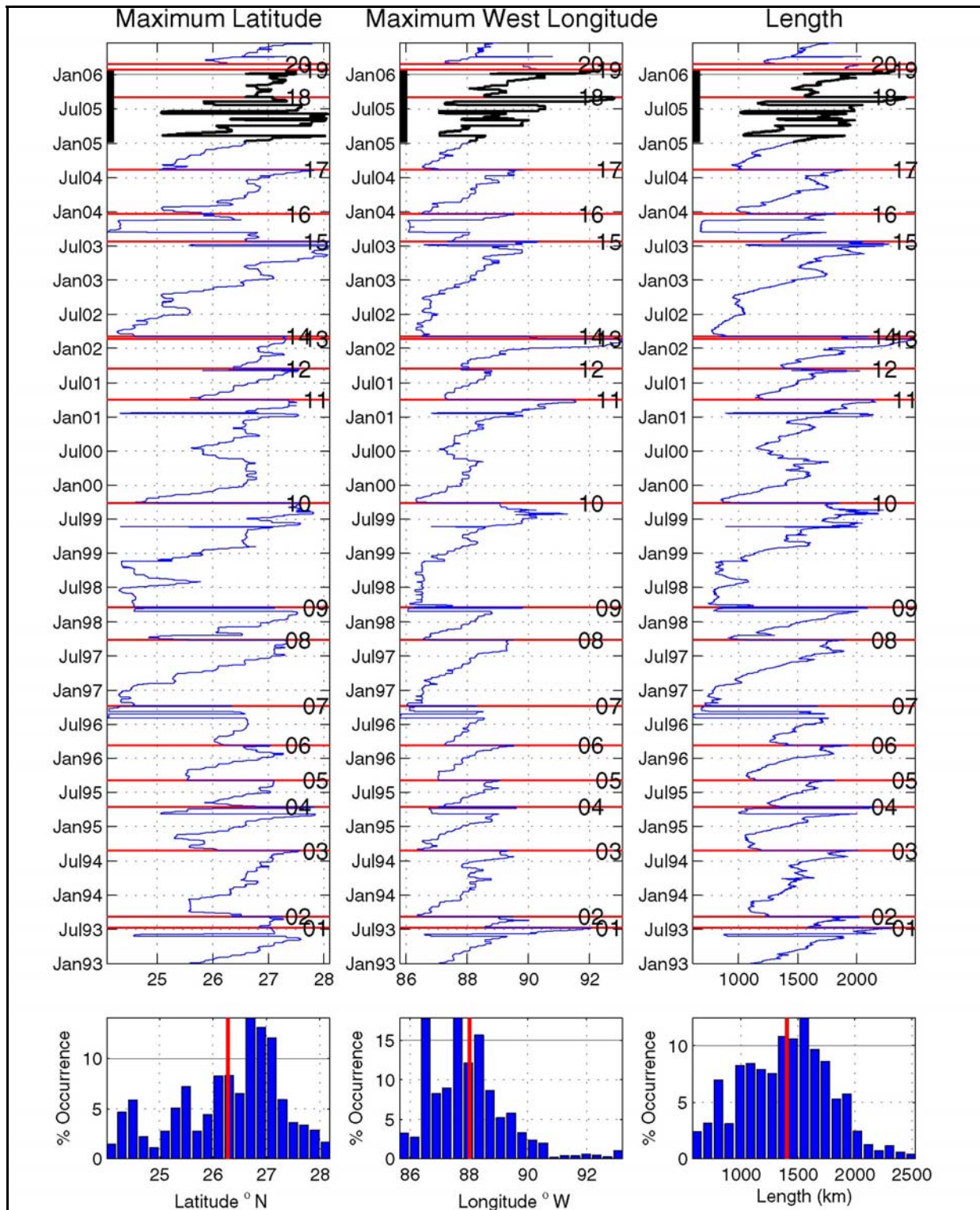


Figure 3.1-7. Loop Current maximum northern/western extension and length time series with percent occurrence histograms. The horizontal red lines identify the 20 LC eddy separation events and vertical red lines are the mean of the time series. The study time period is highlighted.

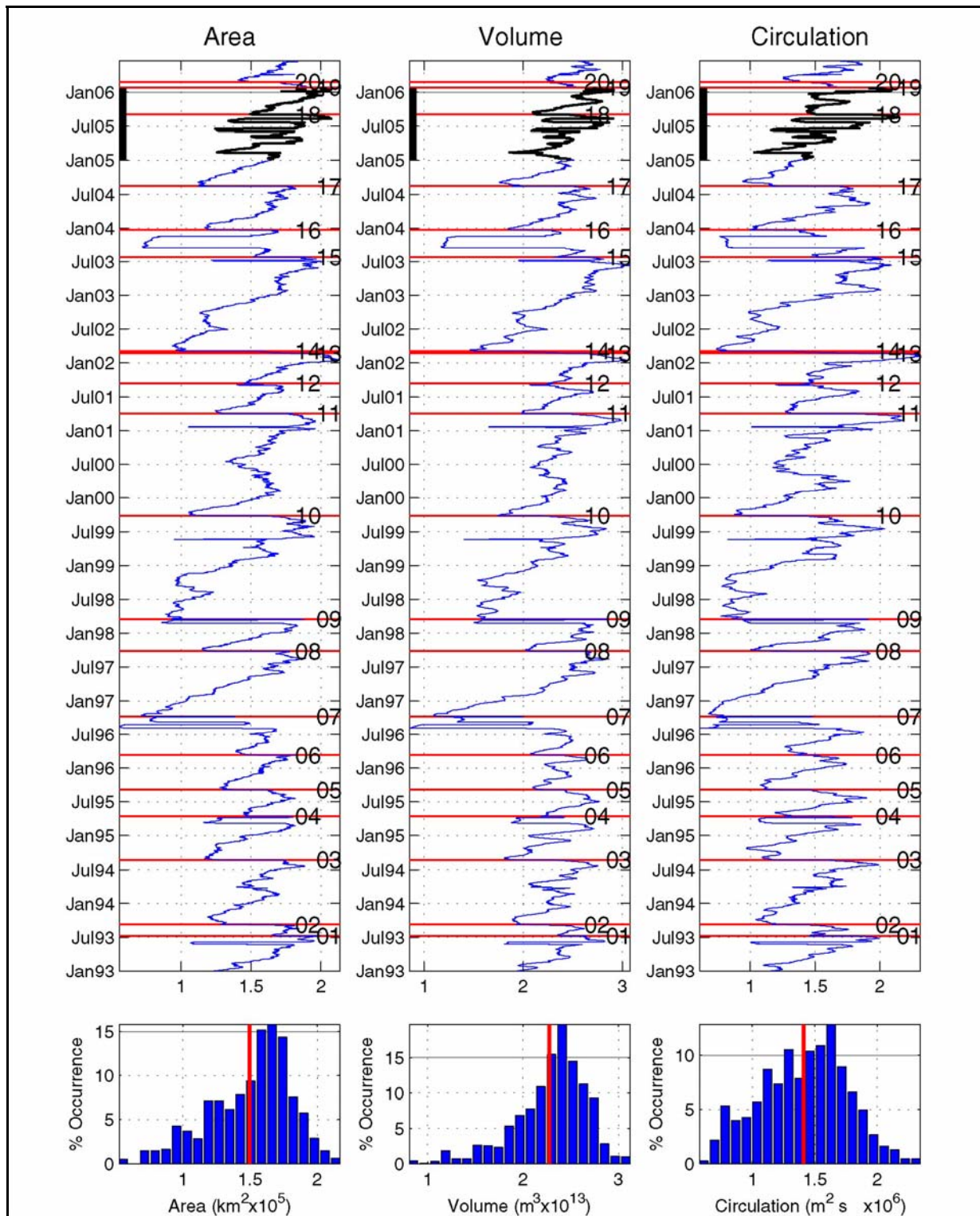


Figure 3.1-8. Loop Current area, volume, and circulation time series with percent occurrence histograms. The horizontal red lines identify the 20 LC eddy separation events and vertical red lines are the mean of the time series. The study time period is highlighted.

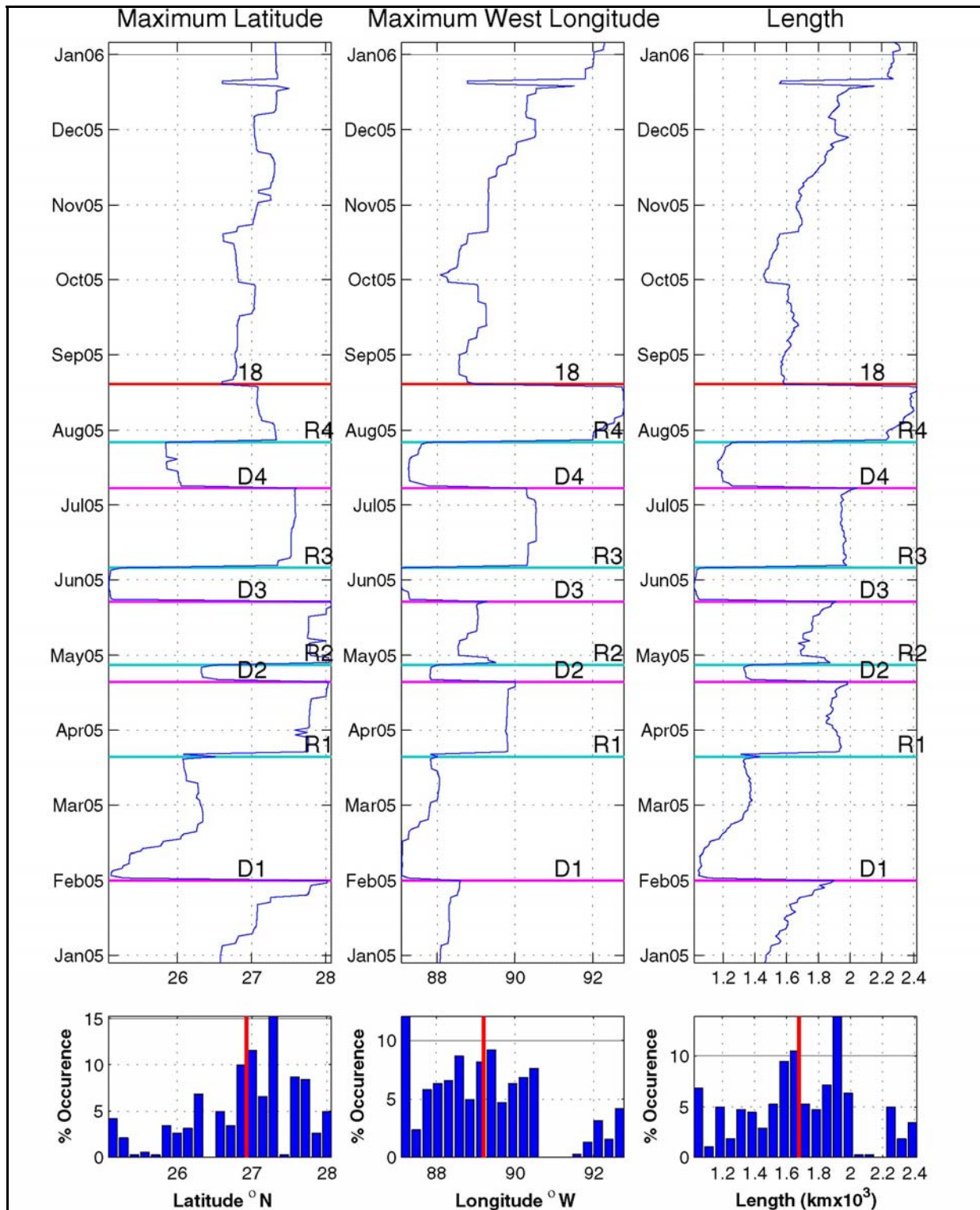


Figure 3.1-9. Loop Current maximum northern/western extensions and length time series with percent occurrence histograms during the EGOM study. Horizontal magenta, cyan, and red lines identify LCE Vortex detachment, reattachment and separation events, respectively. The vertical red lines are the means of the time series.

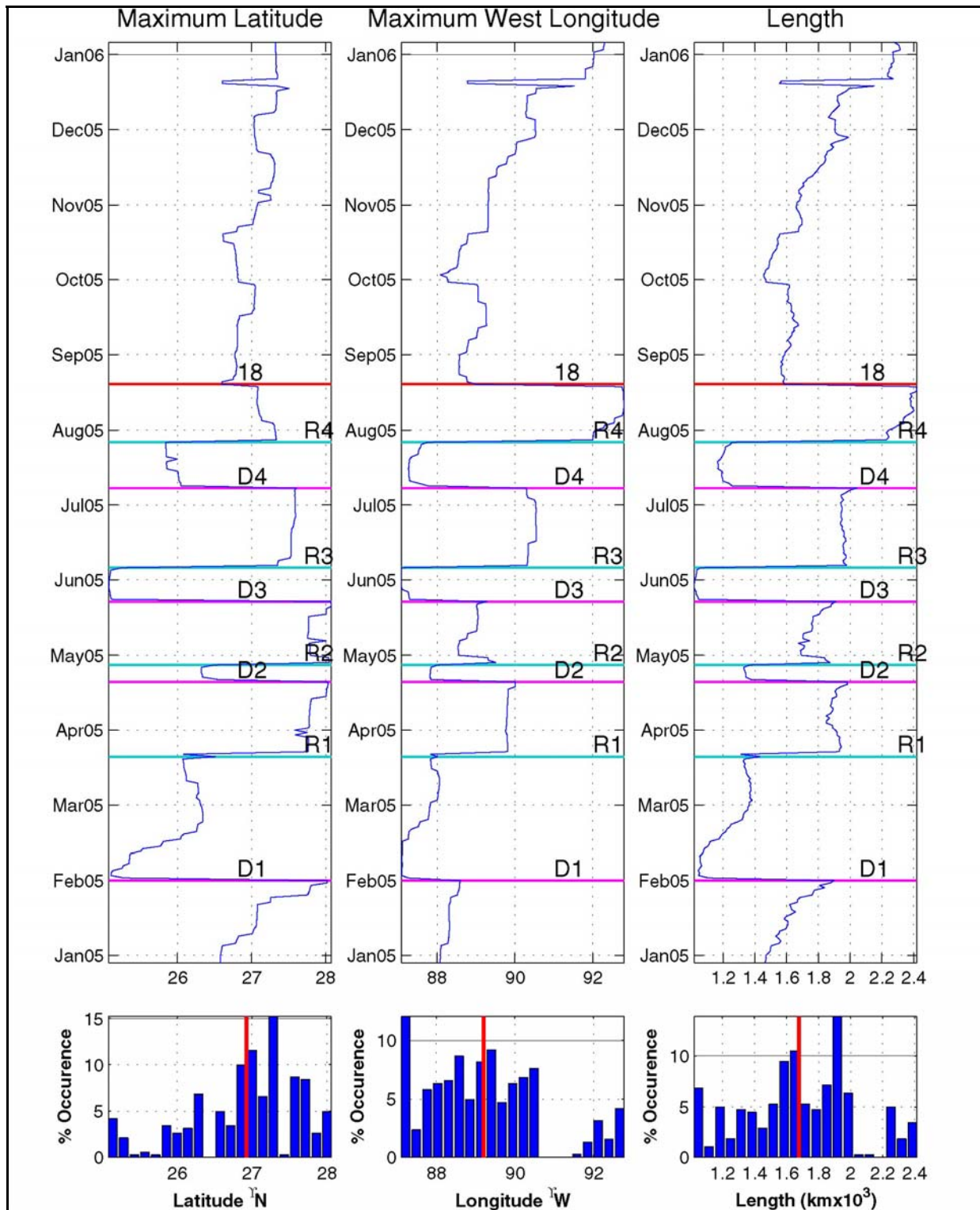


Figure 3.1-10. Loop Current area, volume, and circulation time series with percent occurrence histograms during the EGOM study. The horizontal magenta, cyan, and red lines identify LCE Vortex detachment, reattachment, and separation events, respectively. The vertical red lines are the means of the time series.

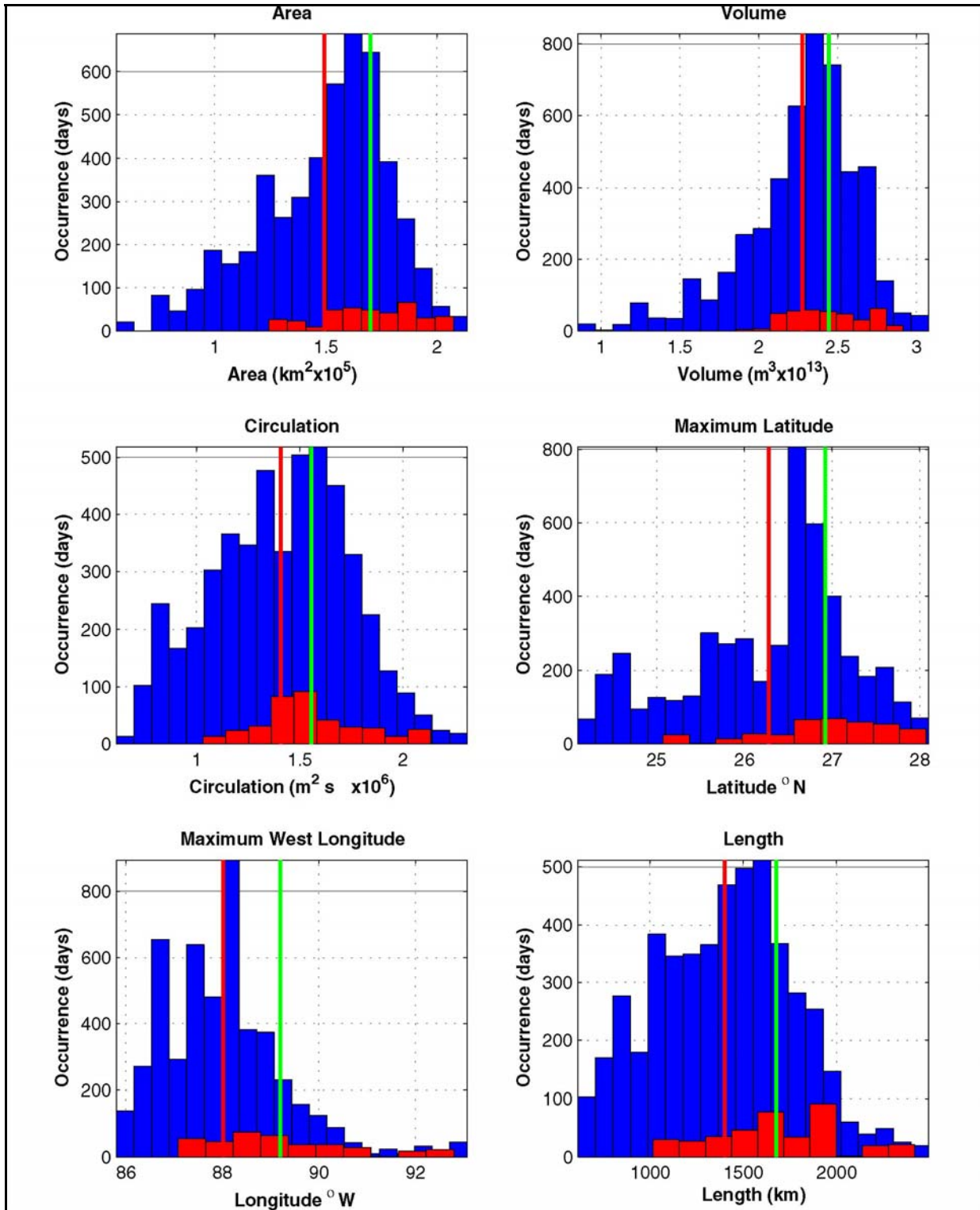


Figure 3.1-11. Histograms of Loop Current metrics during the EGOM study (red bars) versus the historical time period (blue bars). The vertical green and red lines are the mean values from the program and historical time periods, respectively. See Table 3.1-1 for tabulated values.

Twenty LCE separation events were identified in the 13.5-year altimeter record, which includes the study time period. The LC length time series and SSH maps of each of these events at the time of separation are shown in Figure 3.1-12. The separation date, separation period, eddy name, and eddy area at the time of separation are tabulated for each of the 20 observed events in Table 3.1-3. Horizon Marine, Inc. (HMI) names the eddies in alphabetical order as anticyclones shed from the LC. A complete list is published on the web at <http://horizonmarine.com/namedlces.html>. The names appear in the weekly EddyWatch™ reports provided to the GOM offshore oil and gas industry by subscription from HMI. All separation events identified using the SSH 17-cm tracking contour were monitored by the EddyWatch™ program, although a number of smaller anticyclonic eddies (7 total) were also named, causing breaks in the alphabetical sequence. Only one marginal eddy separation event was identified by the objective tracking procedure (Eddy Odessa/Nansen, Eddy 12), which dissipated so quickly that an estimate of the eddy area could not be made. These smaller eddies are of LC origin, but formed on the outer edge of the LC through the interaction of frontal cyclones with the current. This type of small anticyclonic eddy was observed in the northeast GOM during the DeSoto Canyon Eddy Intrusion Study (Hamilton et al. 2000). Other small anticyclonic eddies may originate as primary LCEs split and/or form smaller anticyclonic eddies after separation. An example of this type of event is the unnamed anticyclonic eddy that split off from the southwest quadrant of Eddy Sargassum during the final detachment of Sargassum from the LC during the Exploratory Program (Donohue et al. 2006).

Table 3.1-3

Ring Separation Events from the Altimetric Record: 1 January 1993 through 30 June 2006.

Eddy Number	Separation Date	Separation Period (months)	Industry Eddy Name	Area (km ²)	Eddy Maximum SSH (cm)
1	11 Jul 1993	11.5	Whopper	24,183	33
2	10 Sep 1993	2.0	Xtra	38,481	39
3	27 Aug 1994	11.5	Yucatan	43,022	39
4	18 Apr 1995	7.5	Zapp	21,337	36
5	8 Sep 1995	4.5	Aggie	24,899	36
6	14 Mar 1996	6	Biloxi	24,912	32
7	13 Oct 1996	7	Creole	49,644	69
8	30 Sep 1997	11.5	El Dorado	49,229	56
9	22 Mar 1998	5.5	Fourchon	89,143	72
10	2 Oct 1999	18.5	Juggernaut	40,325	39
11	10 Apr 2001	18.5	Millennium	45,705	44
12	22 Sep 2001	5.5	Odessa/Nansen	?	12
13	28 Feb 2002	5.5	Pelagic	22,119	41
14	13 Mar 2002	0.5	Quick	49,936	41
15	5 Aug 2003	17	Sargassum	25,302	49
16	31 Dec 2003	5	Titanic	33,278	43
17	23 Aug 2004	8	Ulysses	68,633	42
18	13 Sep 2005	12.5	Vortex	29,541	38
19	6 Feb 2006	5	Walker	11,366	29
20	7 Mar 2006	1	Xtreme	22,111	37

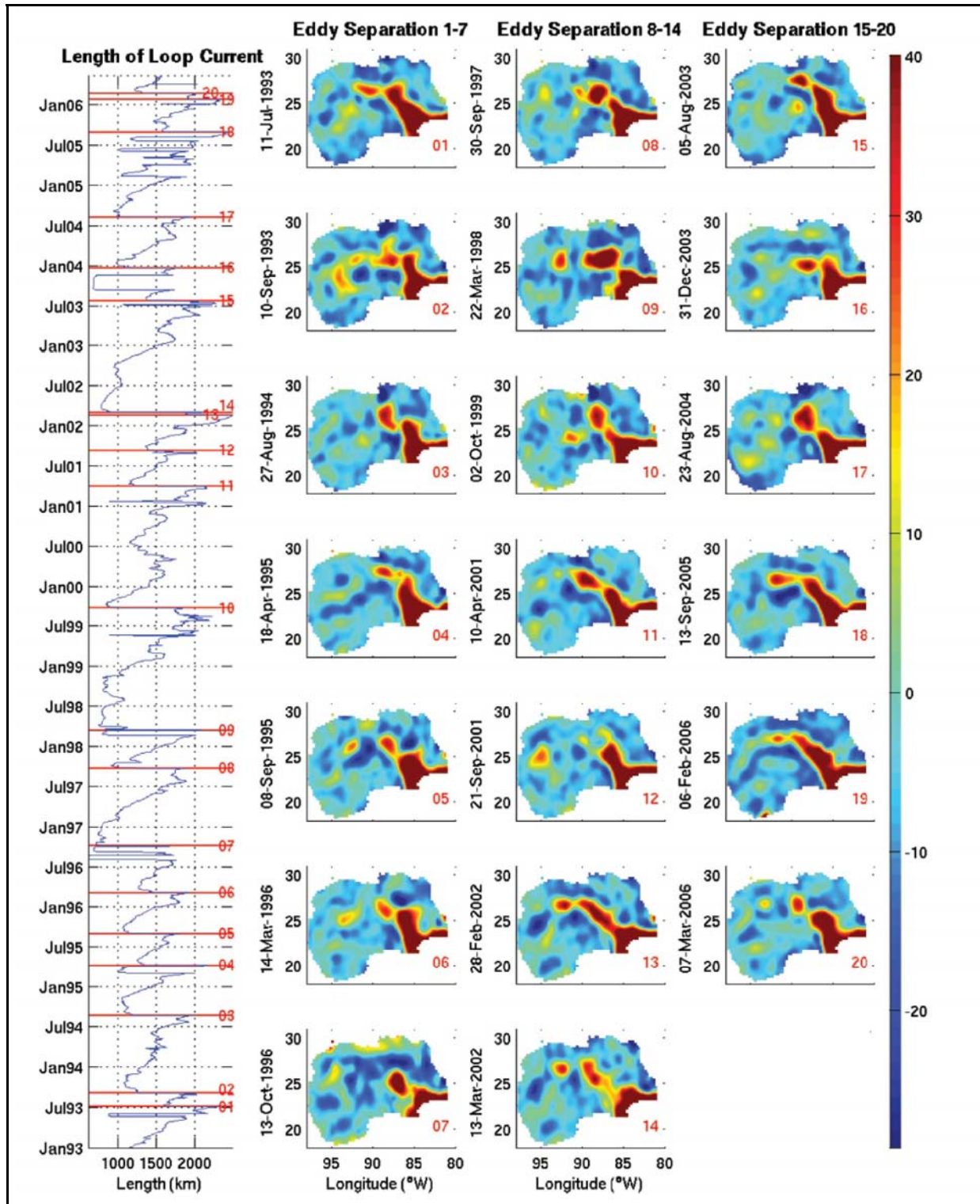


Figure 3.1-12. LCE separation events identified in the altimeter record. SSH maps on the separation dates are shown in the panels to the right (values above 40 cm and below -30 cm have been clipped). The LC length time series is overlaid with red lines corresponding to the separation dates.

3.1.4 Loop Current Frontal Eddies and Other Cyclonic Eddies

Cyclonic perturbations and eddies are common along the outer edge of the LC. Several observational studies have noted that these peripheral features, including LC frontal eddies (Vukovich and Maul 1985), Tortugas eddies (Lee et al. 1995; Fratantoni et al. 1998) and Campeche Bank eddies (Zavala-Hidalgo et al. 2003), are often associated with eddy separation events and are therefore thought to play a role in the detachment and/or separation of LCEs.

The combination of SSH maps and SST imagery has proven to be useful for detecting and tracking cyclonic features. This was demonstrated during the Desoto Canyon Eddy Intrusion Study when 12 LC frontal eddies were detected and tracked, 11 of which influenced the study region (Hamilton et al. 2000). In general, SST images are more useful for tracking LC frontal eddies because synoptic sampling is often required to map the rapid evolution of the features as they propagate around the LC at translation velocities of up to 25 km day⁻¹. Ocean color imagery is also useful for detecting and tracking cyclones because of the higher chlorophyll concentrations typically associated with upwelling within the eddy.

Continuous monitoring using SST or color radiometry imagery is not possible because of the frequent clouds over the GOM and the seasonal degradation of the surface thermal and biological signals. Even under good observing conditions, the surface temperature or color signature of an eddy in imagery can be difficult to interpret because the surface cyclonic circulation associated with a cyclonic eddy may advect filaments of warm chlorophyll-poor waters that mask the cold nutrient-rich conditions typical of cyclones. The cyclonic spiral of a warm filament within the eddy frequently identifies the presence of a cyclone. On the other hand, satellite altimetry can unambiguously detect cyclones by their lower SSH; however, the relatively small size of the eddies and their often rapid evolution can make detecting and tracking of these features difficult because of the non-synoptic sampling of the ocean surface by satellite-borne radar altimeters. Therefore, no systematic census of cyclones in the GOM, such as those performed for LCEs, has been attempted given the imaging and sampling limitations of the current operational satellite systems, although some topographically isolated features such as the Campeche Bank (Zavala-Hidalgo et al. 2003) and Tortugas Eddies (Fratantoni et al. 1998) have been studied in detail. Systematic comparisons of the cyclones observed during the program with those in the historical record will not be attempted. Nevertheless, cyclones are an important dynamical component of the general circulation of the GOM and significantly impacted the study region during the eastern GOM program. They are also quite common along the boundary of the LC during intrusions into the north-central GOM as was the case during nearly the entire eastern GOM program time period. As an example, in Figure 3.1-13 we identify a number of cyclones in the 22 April 2005 night time composite SST image from GOES-12 courtesy of Nan Walker of Louisiana State University.

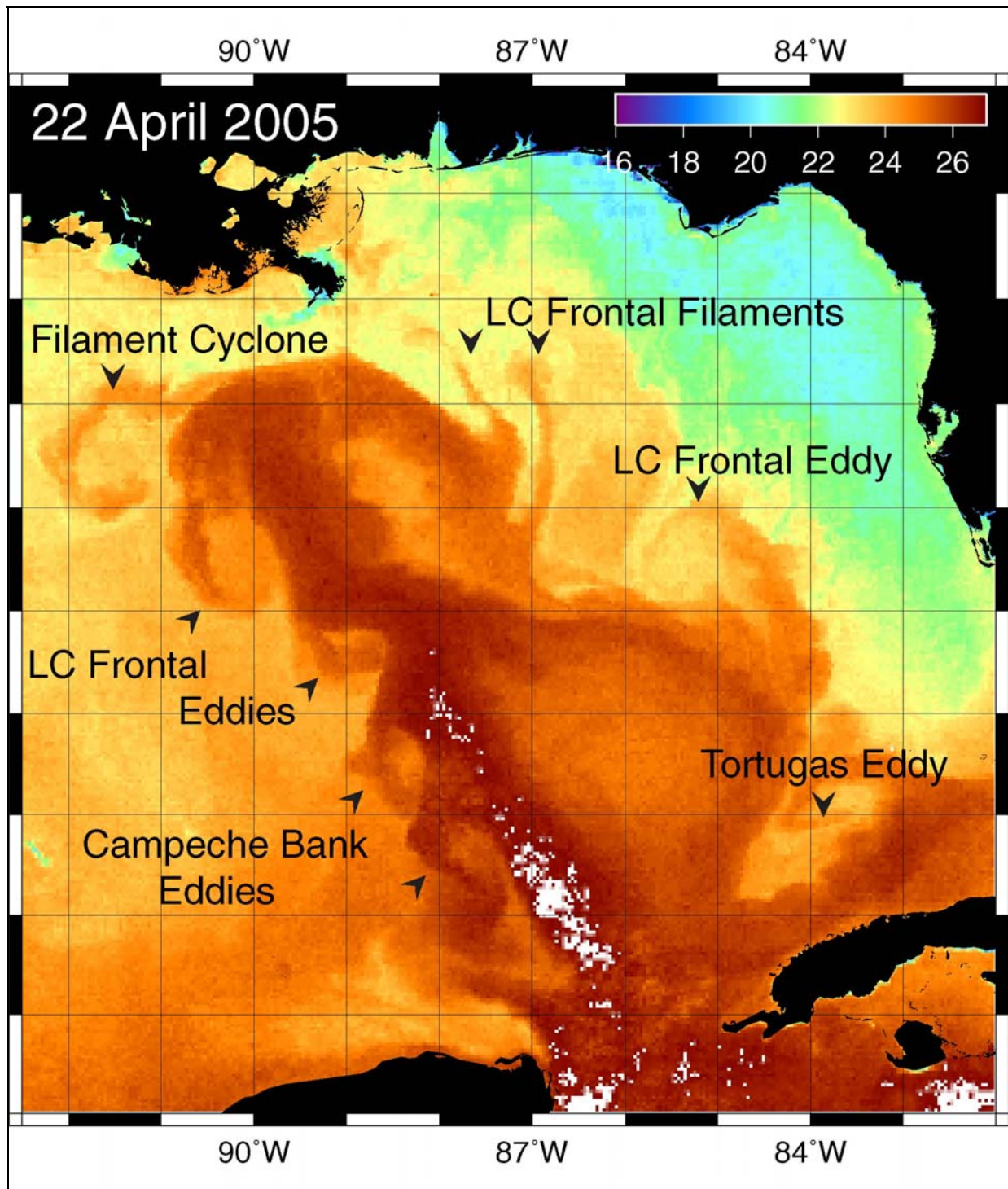


Figure 3.1-13. Nighttime composite SST image from 22 April 2005 showing the LC and its associated cyclonic features. The image is from the GOES-12 satellite and is courtesy of Nan Walker of Louisiana State University.

3.2 Study Time Period in the Context of the Historical Record

In this section, we give an overview of the eastern GOM program time period in the context of the 13.5-year altimeter record to gain a historical perspective on the LC and LCE activity in and around the study region.

3.2.1 Loop Current

The extended LC intrusion into the north-central GOM during the eastern GOM program, although not record-setting in terms of the maximum values of the LC metrics over the historical record (Table 3.1-2), was one of the most significant in terms of the overall extent of LC intrusion during the yearlong observational record.

The extent of LC penetration into the north-central Gulf during the program record is clearly demonstrated using yearlong running averages of the daily LC metric time series. Histograms of the running-averaged metrics are shown in Figure 3.2-1, overlaid with the yearlong mean values for 2005 representing the mean during the eastern GOM observational record. The total time where the yearlong running average values were greater than the mean over the observational record was quoted as a percent of the total occurrence for each of the metrics. The percentage occurrence exceeding the program record time period values range from 15.3% for LC circulation to only 4.2% for LC area, highlighting the remarkable extent of the LC intrusion over the yearlong eastern GOM program. In fact, the eastern GOM program yearlong averages of LC area and latitude of northern extent were not exceeded throughout the entire prior altimeter record. Average length and longitude were only exceeded briefly during a yearlong time period associated with the LC intrusion that formed LCE Millennium, the most westward intrusion on record. The remaining LC statistics, circulation and volume, were only exceeded during yearlong time periods immediately preceding the separation of LCEs Juggernaut, Millennium, and Sargassum.

Another way to characterize the extent of the LC intrusion during the eastern GOM program is by using the 13.5-year altimeter record in concert with automated LC tracking. Dates were identified in the historical record when altimeter-derived SSH values were greater than 17 cm at any of the eastern GOM PIES station locations. These events were categorized as a LC intrusion, a separated LCE, a detached LCE, or an anticyclonic eddy based on the configuration of the 17-cm LC and LCE tracking contour. A summary of these events is listed in Table 3.2-1. Remarkably, only one event of the 12 observed in the study region over the altimeter record was not directly related to the LC or a LCE. That singular event was a compact energetic anticyclonic eddy that formed in the northeastern corner of the Gulf and propagated through the study region in late July 1998. The remaining 11 intrusion events included 3 LC intrusions, 3 separated LCEs, and 5 mixed LC intrusions and LCE detachment/separation events. In summary, a total of 302 days occurred with SSH greater than 17 cm at the eastern GOM PIES station locations. LC or LCE intrusions were associated with a total of 296 days, which was approximately 6% of the 4929-day historical record, or an average of about 22 days per year where a LC or LCE was present in the array. This is less than half of the 52 days total in 2005 where the LC or a LCE intruded into the PIES array during the eastern GOM study program. Only one other calendar year had a greater occurrence of intrusion, which was 91 days in 2003 associated with LCE Sargassum during the Exploratory Study program.

Table 3.2-1

Intrusion Events.

Dates that the 17-cm SSH tracking contour intruded into eastern GOM study region based on the 1 January 1993 through 30 June 2006 altimetry record. Events are categorized as a LC intrusion, a separated LCE, a detached LCE, or an anticyclonic eddy based on the configuration of the 17-cm LC and LCE tracking contour.

Start Date	End Date	Duration	Event Type	Name
10 May 1993	19 May 1993	10 days	LC Intrusion	Whopper
14 Sep 1993	26 Sep 1993	13 days	Separated LC Eddy	Xtra
29 Aug 1994	4 Sep 1994	6 days	Separated LC Eddy	Yucatan
24 Feb 1995	14 Apr 1995	50 days	LC Intrusion/ Detached LC Eddy/ LC Intrusion	Zapp
27 Jul 1998	1 Aug 1998	6 days	Anticyclonic Eddy	
18 Aug 1999	9 Sep 1999	23 days	LC Intrusion	Juggernaut
16 Oct 1999	4 Nov 1999	20 days	Separated LC Eddy	Juggernaut
6 May 2003	4 Aug 2003	91 days	LC Intrusion/ Detached LC Eddy/ LC Intrusion	Sargassum
22 Aug 2004	13 Sep 2004	23 days	LC Intrusion/ Separated LC Eddy	Ulysses
14 Feb 2005	14 Mar 2005	29 days	LC Intrusion/ Detached LC Eddy	Vortex
3 Jun 2005	25 Jun 2005	23 days	LC Intrusion/ Detached LC Eddy	Vortex
23 Jun 2006	30 Jun 2006	8 days	LC Intrusion	Yankee

3.2.2 Loop Current Eddies

The altimeter-derived statistics provided a useful 13.5-year benchmark to compare the LCEs that occurred during the eastern GOM program to those of the historical record. An even longer time period can be addressed with LCE separation periods estimated using SST imagery available since 1973 (Vukovich 1988). The combined 33-year compilation of LCE separation periods from July 1973 through June 2006 is listed in Table 3.2-2. A total of 43 continuous events have been observed. A histogram of the distribution is shown in the upper panel of Figure 3.2-2. The 20 LCE separation events observed during the altimeter record are shown in red to highlight the contribution of the more recent events to the distribution of the entire observational record. The histograms of events before and after 1993 are shown in the middle and lower panels, respectively. The mean for the entire compilation of separation periods was 9.5 months and the mode was 6 months. Using only the pre-1993 record, the mean was 9.96, and the mode was 6 and 9 months over a range from a minimum of 6 to a maximum of 15 months. For the distribution of separation periods since 1993, which were based on altimeter-derived separation periods, the mean was 8.2, and mode was 5.5 and 11.5 months over a range from a minimum of 0.5 to a maximum of 18.5 months. The differences between the two measurement time periods were probably not significant; nevertheless, the change in the actual distribution was striking. This attests to the remarkable variability of the LCE separation period.

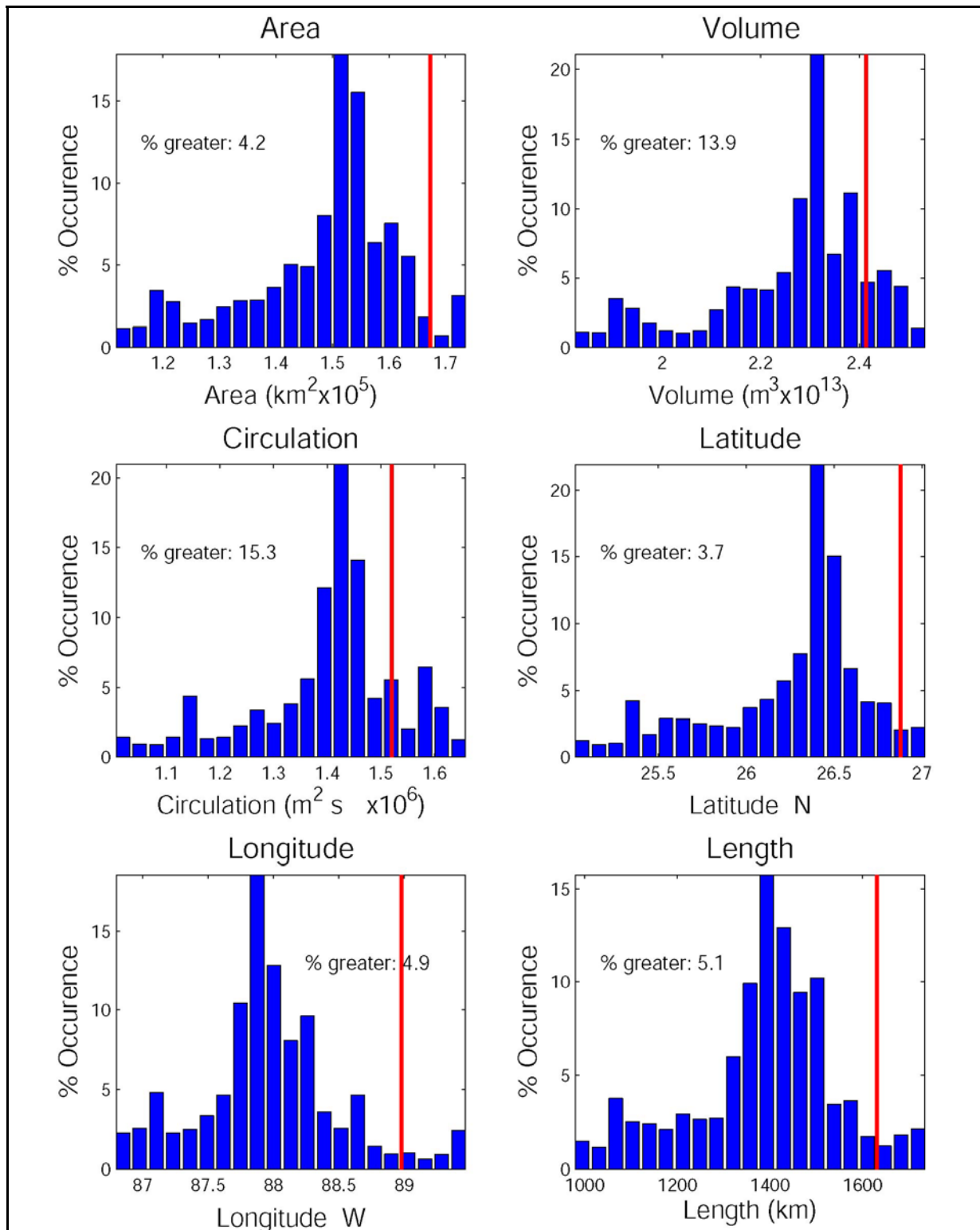


Figure 3.2-1. Histograms of yearlong running averages of Loop Current metrics from the historical altimetry record. Mean values during the Eastern Gulf program (annual mean from 2005) are shown along with the percent of historical values exceeding the program mean.

Zoomed maps of the SSH fields at the time of separation, including the maximum SSH values within the eddy and the 17-cm tracking contour (Figures 3.2-3 a, b, & c) are shown for all of the 20 LCEs observed in the altimeter record from 1 January 1993 through 30 June 2006. A composite of the tracking contours at the time of separation are shown in the upper panel of Figure 3.2-4. The three LCEs, Vortex, Xtreme, and Walker, that separated from the LC during or just after the eastern GOM program are highlighted in the bottom panel. These eddy separation locations show that the Vortex and Walker separation events were associated with some of the most western LC intrusions observed in the altimeter record, with only LCE Millennium separating farther to the west. Xtreme was also one of the more northern and western separation events relative to the historical distribution. In terms of eddy area and maximum SSH at the time of separation, these LCEs were some of the smaller area and weaker amplitude eddies observed in the altimeter record: LCE Vortex (#18) ranked 11th in eddy area and 13th in eddy maximum SSH, LCE Xtreme (#19) ranked 17th in eddy area and 14th in eddy maximum SSH, and LCE Walker (#20) ranked 19th in both eddy area and eddy maximum SSH.

Table 3.2-2

LCE Separation Periods.

A compilation of the 33-year record of separation periods for LCEs from July 1973 through June 2006 is tabulated below. A total of 43 consecutive events are listed. Entries through October 1986 are from Vukovich (1988); other entries prior to July 1992 are from Table 1 of Sturges (1994) using corrections based on Berger (1993). The separation event in July 1992 is from Sturges and Leben (2000). Data beginning in 1993 are based on objective tracking of the Loop Current using satellite altimeter data (Leben 2005).

Date	Separation Period (months)	Date	Separation Period (months)	Date	Separation Period (months)
July 1973		July 1985	11	13 Oct 1996	7
April 1974	9	January 1986	6	30 Sep 1997	11.5
January 1975	9	October 1986	9	22 Mar 1998	5.5
July 1975	6	September 1987	11	2 Oct 1999	18.5
August 1976	13	May 1988	8	10 Apr 2001	18.5
March 1977	7	May-June 1989	12.5	22 Sep 2001	5.5
June 1978	15	August 1990	14.5	28 Feb 2002	5
April 1979	10	Aug- Sep 1991	12.5	13 Mar 2002	0.5
January 1980	9	19 July 1992	11.5	5 Aug 2003	17
March 1981	14	11 Jul 1993	11.5	31 Dec 2003	5
November 1981	8	10 Sep 1993	2	23 Aug 2004	8
May 1982	6	27 Aug 1994	11.5	13 Sep 2005	12.5
March 1983	10	18 Apr 1995	7.5	6 Feb 2006	5
February 1984	11	8 Sep 1995	4.5	7 Mar 2006	1
August 1984	6	14 Mar 1996	6		

More important to the general circulation observed by the Eastern Gulf study array was the repeated detachment and reattachment of LCE Vortex during the observational record. Composites of the LCE tracking contour at detachment times and the LC tracking contour at reattachment times are shown in the upper and lower panels of Figure 3.2-5, respectively, along with mooring locations where subsurface currents were measured during the Eastern Gulf program including the LSU mooring. At the time of detachment, two of the four detached LCEs were located over the Eastern Gulf mooring locations based on the 17-cm tracking contour (upper panel of Figure 3.2-5). Given that the 17-cm tracking contour was offset from the surface thermal front by approximately 50 km (Leben 2005), each of these detachment events occurred with the LC/LCE surface circulation very near or over the moorings. Upon detachment from the LC, the eddies drifted westward due to the beta-effect and were found westward of the Eastern Gulf moorings when reattachment to the LC occurred (lower panel of Figure 3.2-5). In the historical record, time periods when a LCE detaches and reattaches to the LC are common even with the stringent definition of detachment based on the breaking of the 17-cm tracking contour. Eight of the 20 LCEs observed in the 13.5-year altimeter record detached and reattached before final separation (LCEs #1, 4, 7, 9, 11, 15, 16, and 18) including LCE Vortex (#18). No LCE, however, was observed to detach and reattach to the LC as frequently as LCE Vortex.

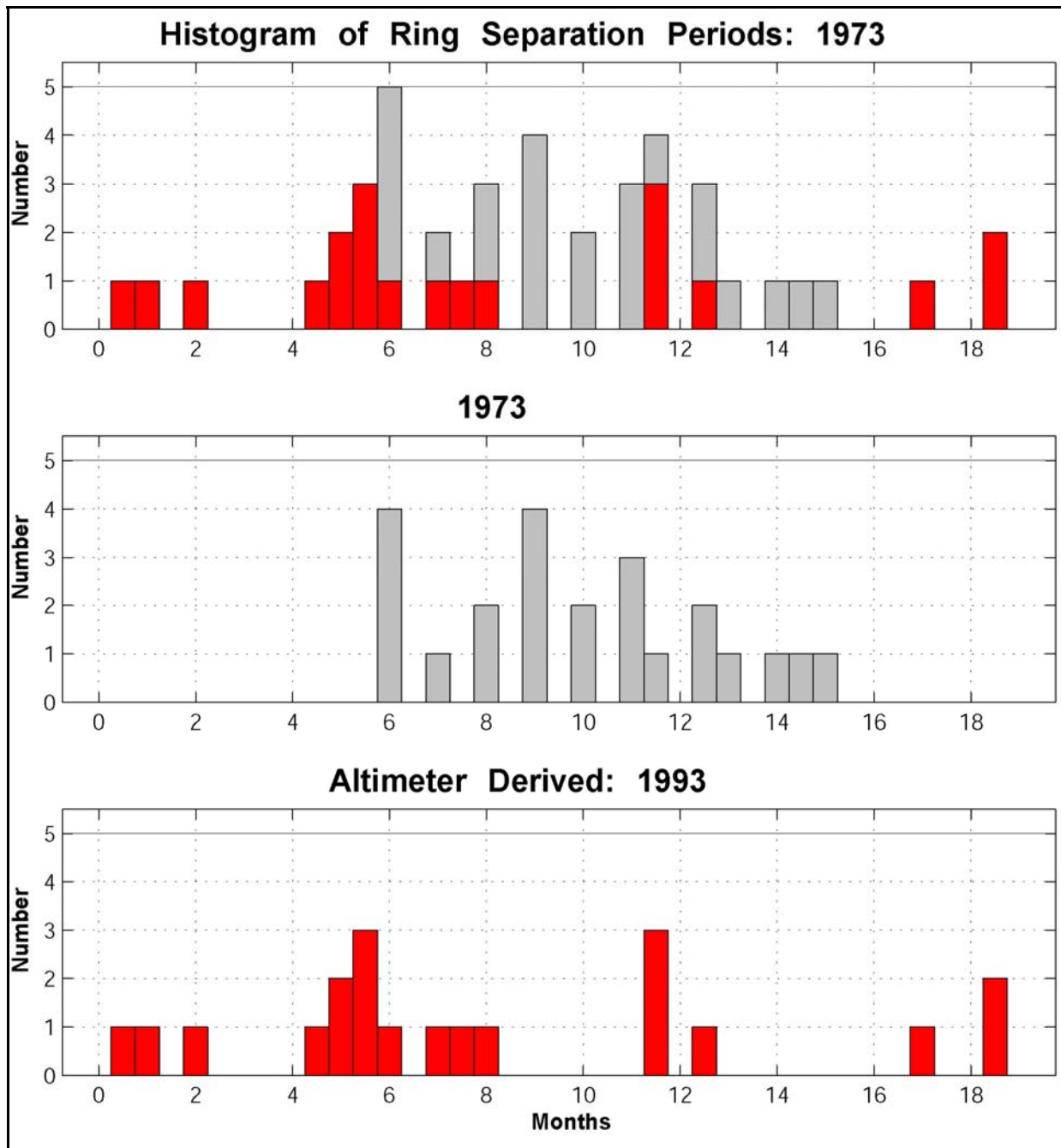


Figure 3.2-2. Histogram of the LCE separation period using data from Table 3.2-2 are shown for selected time intervals. The 20 LCE separation events observed during the altimeter record are shown in red, the prior in gray.

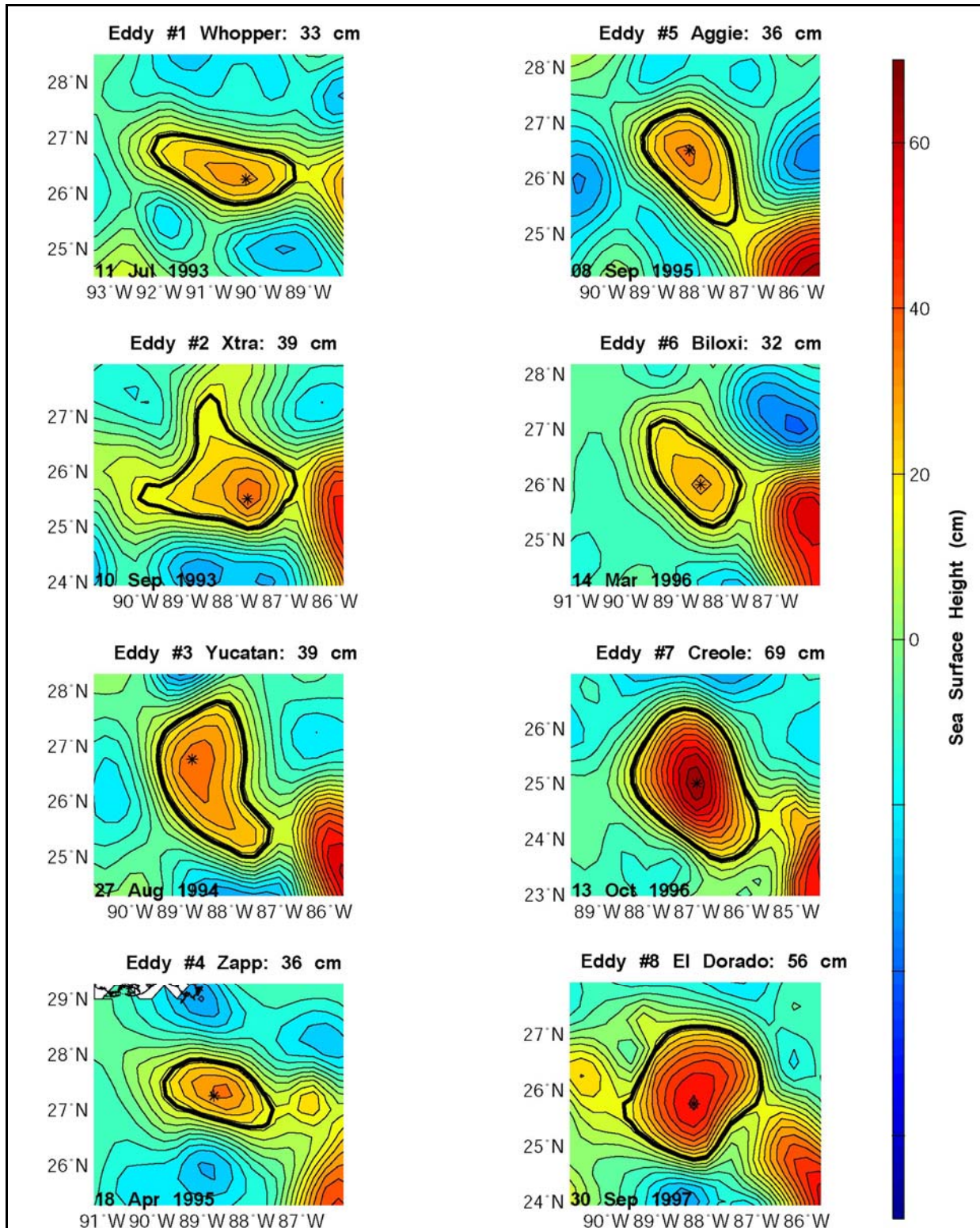


Figure 3.2-3a. Zoomed SSH maps of LCEs 1 through 8 at the time of separation from the LC. The 17-cm tracking contour and maximum SSH are shown for each eddy. Plots are equal area.

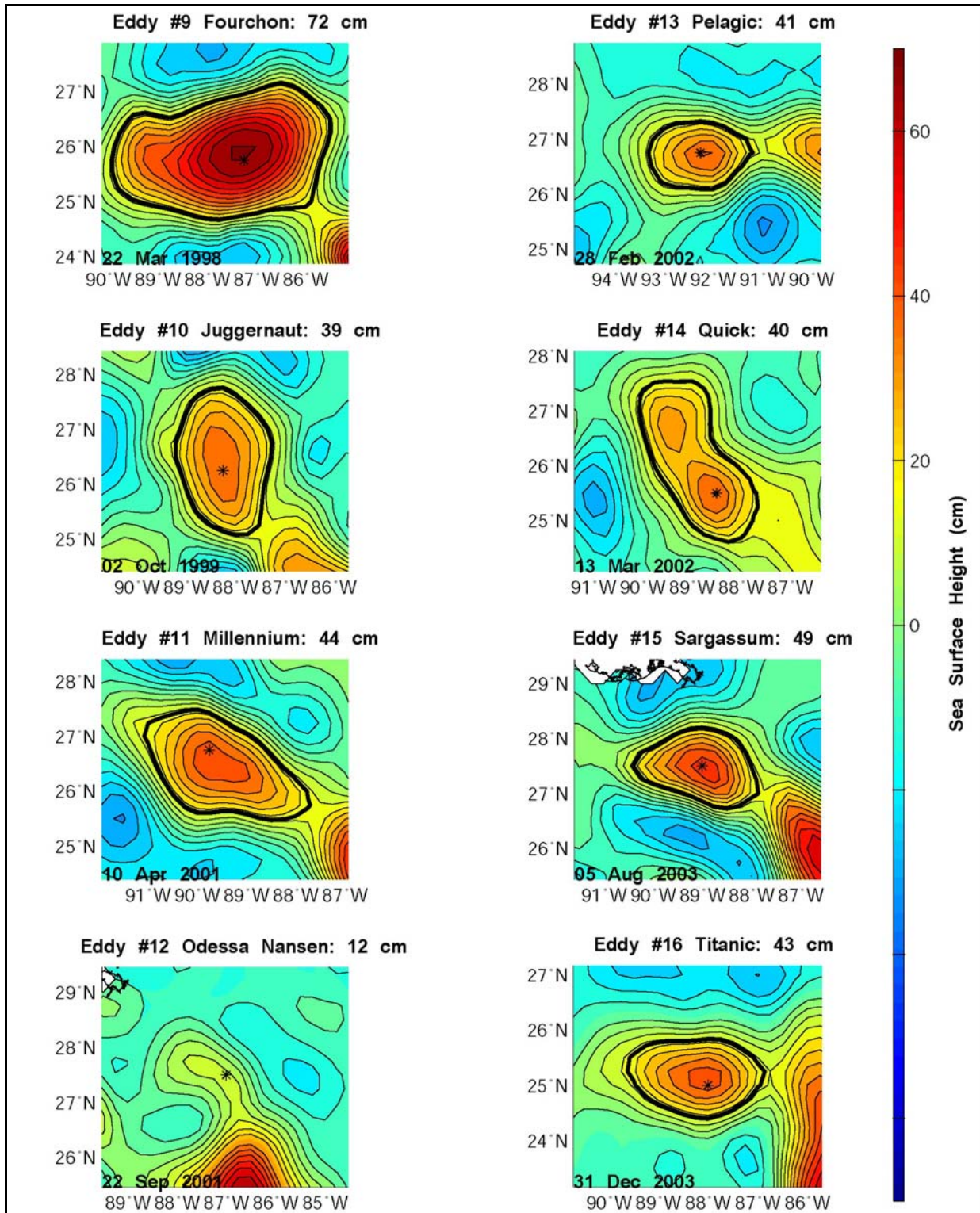


Figure 3.2-3b. Zoomed SSH maps of LCEs 9 through 16 at the time of separation from the LC. The 17-cm tracking contour and maximum SSH are shown for each eddy. Plots are equal area. Eddy #12 (Odessa/Nansen) dissipated rapidly and contained no tracking contour at the time of separation.

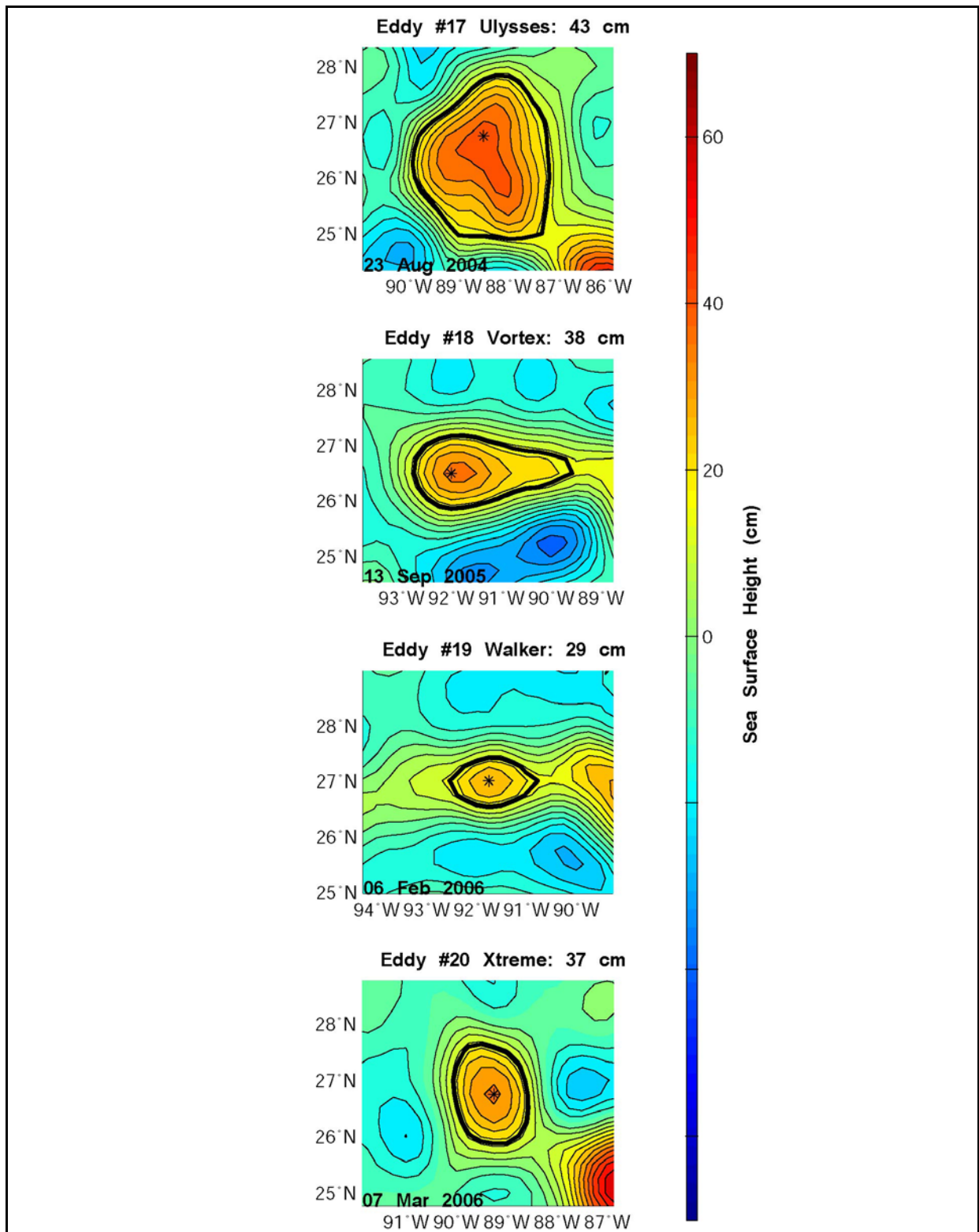


Figure 3.2-3c. Zoomed SSH maps of LCEs 17 through 20 at the time of separation from the LC. The 17-cm tracking contour and maximum SSH are shown for each eddy. Plots are equal area.

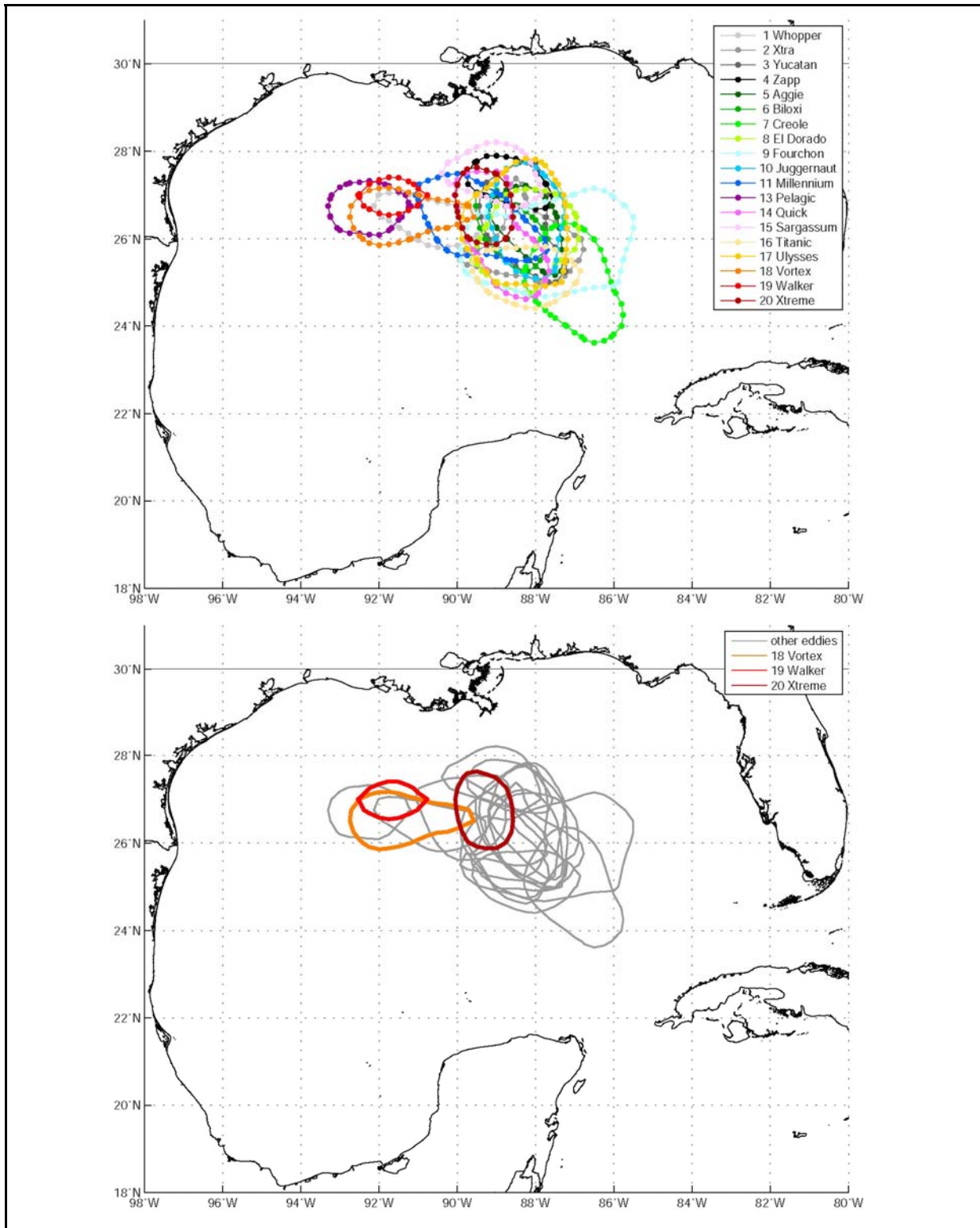


Figure 3.2-4. The 17-cm tracking contour at the time of separation for all 20 LCEs observed from 1 January 1993 through 30 June 2006. The LCEs that separated during or just after the Eastern Gulf study are highlighted in the bottom panel.

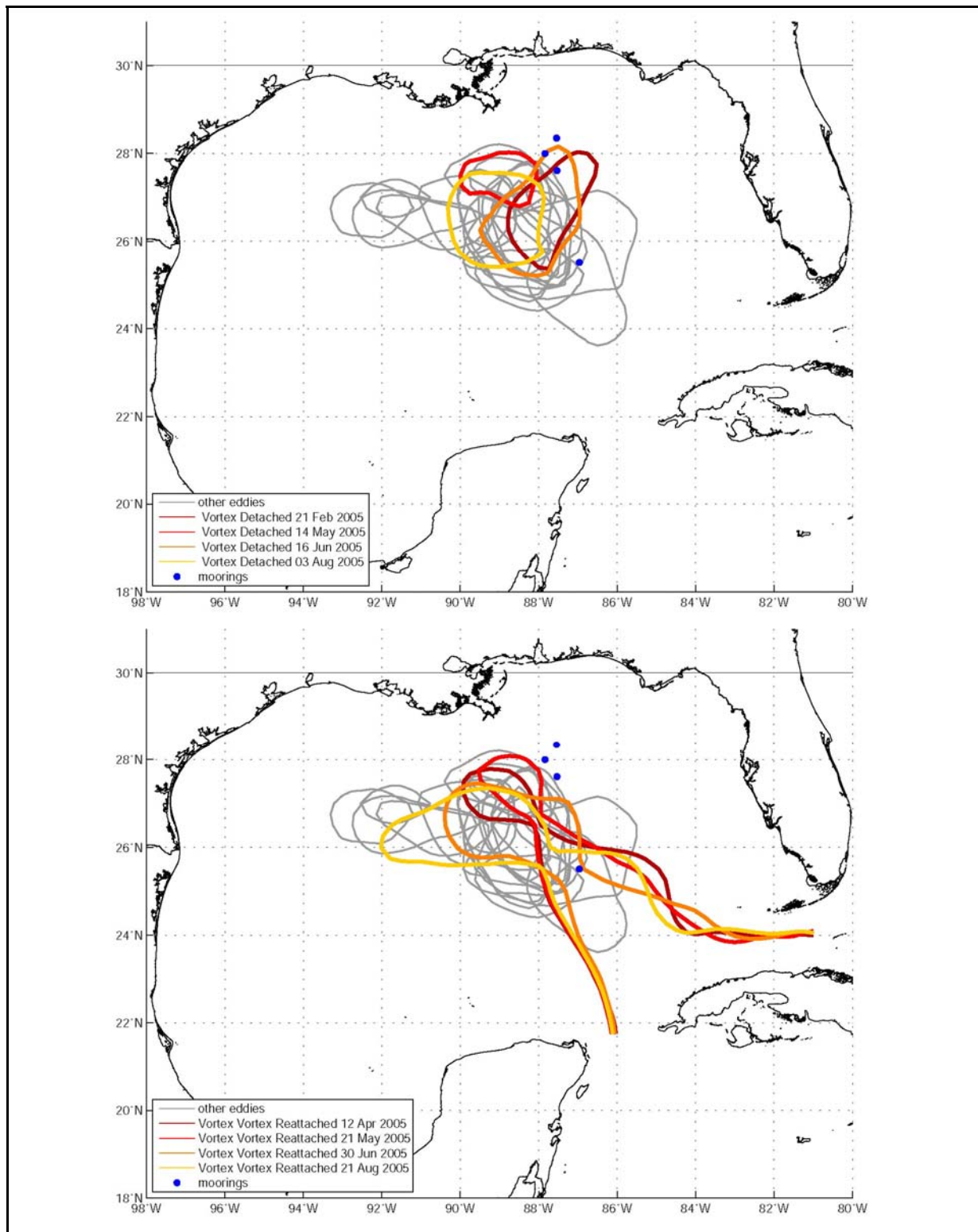


Figure 3.2-5. Composite of LCE Vortex detachment and reattachment events. The 17-cm LCE tracking contour at detachment and the 17-cm LC tracking contour at reattachment times are shown in the upper and lower panels, respectively.

4.0 LC AND LCE DYNAMICS

Two complementary approaches, one kinematic and one dynamic, were used to analyze LC and LCE dynamics and their affect upon the upper ocean circulation in the eastern GOM study array during the study time period. The kinematic analysis was performed using satellite-tracked drifter trajectories in combination with satellite altimetry to derive the kinematic properties of the dominant anticyclonic and cyclonic circulation events in the study region. The drifting buoy data used to perform this analysis were obtained from Horizon Marine, Inc. The dynamical analysis was performed based on vorticity calculated from the PIES array.

4.1 Kinematic Analysis

4.1.1 Drifting Buoy Data and Analysis Approach

Horizon Marine deployed over 200 drifting buoys during 2005 that tracked near surface currents in the GOM. The buoys had drogues at 50 m depth. Most of the buoys had relatively short lives or did not enter interesting features; however, the buoys that did orbit within cyclonic or anticyclonic eddies can be used to model and track individual eddies using the kinematics of the observed drifting buoy trajectories and a simplified feature model.

The feature model describes eddies as a translating and rotating ellipse. The model equations for the components of the position of the buoy x and y are

$$x(t) = x_0 + ut + a \cos \theta \cos(-\omega t + \phi) - b \sin \theta \sin(-\omega t + \phi), \quad (4.1.1)$$

$$y(t) = y_0 + vt + a \sin \theta \cos(-\omega t + \phi) + b \cos \theta \sin(-\omega t + \phi), \quad (4.1.2)$$

where u and v are the components of the center propagation velocity, x_0 and y_0 are the position of the center at time $t = 0$, a and b are semi-axis lengths of the ellipse, ω is the angular frequency of rotation of the buoy around the ellipse, θ is the angle between the x -axis and the a -axis of the ellipse, and ϕ is a phase angle. Note that the x -axis is toward the east and θ is measured counter-clockwise from east. Thus, $\theta = 90^\circ$ means that the long axis is oriented north to south. The parameters of this model were found using least squares fits to the observed positions as described by Glenn et al. (1990). Data from slightly more than one orbit of the center were used to give stable solutions to the least squares fit. The fits were made at one-day intervals and the resulting parameters were plotted at the center time of the data used in each fit.

Elliptical fits were found for Eddy Ulysses (Figures E-1 – E-5), Eddy Vortex, Eddy Walker, four small cyclonic eddies, and a brief period of closed circulation in the Loop Current. Graphs of the fit parameters for all of the features are included in Appendix E. The following sections present kinematic information for Eddy Vortex and two small cyclonic eddies, Cold Eddy 3 and 4, that impacted the study area. Graphs referred to in the summaries are included in Appendix E.

4.1.2 Eddy Vortex

The graphs for Eddy Vortex, shown in Appendix E, are broken into two sections. Figures E-6–E-10 describe the eddy from the end of February through the middle of April. Figures E-11–E-15 show its evolution from June through November. From April through June, the eddy reattached to the LC and there were no closed buoy orbits. During March, Eddy Vortex moved to the northwest. In the process, it got unusually close to the Mississippi Delta. At the end of April, the center of circulation moved back to the southeast as the eddy re-attached to the LC. The orbital period when the eddy was detached from the LC in March was rather low, only about 7 days. During that period, it was fairly elongated with an eccentricity of about 0.6. The long axis of the ellipse rotated clockwise at about 4° per day. The sense and speed of the rotation are as predicted for an isolated eddy by Cushman-Roisin et al. (1985).

After Eddy Vortex's separation in June, there are some gaps in the record because the eddy reattached to the LC several times, but the center of circulation moved steadily to the southwest. The various buoys gave very similar center positions. From June through August (Yeardays 160–240, 9 Jun through 28 Aug 2005) the orbital period was long for a fresh eddy, but during this time the eddy was rather large. The orientation of the ellipse changed rapidly during June and the early part of July (Yeardays 160 – 200, 9 Jun through 19 Jul 2005) but after that the regular clockwise rotation set in. Finally, buoy 1669 made a closed orbit in the middle of the Loop Current during the last half of September 2005 after Eddy Vortex separated. At first the center of circulation moved to the northwest, but then it moved to the northeast as the Loop Current leaned to the east. The change of the orientation of the ellipse from north-northwest to north was consistent with this lean. The period of rotation lowers as the orbit becomes more circular.

4.1.3 Cyclones

Several of the drifting buoys became trapped in small cyclonic (cold) eddies in and around the study array. The first cold eddy identified in the drifter data near the study region, Cold Eddy 3, was a persistent feature in drifter trajectories from the first of August through the middle of September. The eddy was located on the northeast edge of Eddy Vortex during the last detachment event and as Vortex was separating from the LC. The cyclone moved with Vortex as Vortex separated from the LC and moved to the west. There was a gap in the solution from Yeardays 238 – 248 (26 Aug through 5 Sep 2005), but the cyclonic circulation during the two time periods was apparently the same feature. The feature was small and its orbital period low until late in the record when the buoy moved out to a larger orbit.

Cold Eddy 4 was the final cold eddy that had closed buoy orbits. It was directly north of Eddy Walker as it began to separate from the LC in December 2005. This feature moved north as the LC extended and east as its meander propagated clockwise around the northern edge of what would become Eddy Walker. It was a small feature with an orbital period of only 4 days.

4.1.4 Combined Kinematic and Altimetric Analysis

A significant shortcoming of a kinematic feature model using only drifting buoy trajectories is that the area of eddy circulation is not uniquely determined by the trajectories of the drifters within the eddy. Differing estimates of eddy aerial extent or radius are obtained depending on the distance that a drifting buoy orbits relative to the eddy center. In view of this deficiency, a combined kinematic and altimetric analysis technique was developed to estimate eddy aerial extent to better determine the movement and extent of large closed anticyclonic circulation in and around the study region. The combined analysis used the eddy aerial extent estimated from daily altimeter-derived SSH maps to resize the elliptical eddy model parameters to equal area. After rescaling, the parameters estimated from each of the fit trajectories within the eddy were averaged to obtain a composite estimate of the size, shape, and orientation of the eddy for each day.

The altimeter-derived area was determined using an eddy-tracking program that automatically tracks SSH contours within an eddy. Once the eddy of interest was identified, the maximum height within that eddy was found along with all positive contours encircling the maximum. The area enclosed by each contour was calculated and a corresponding circular region was generated of equal area. The percentage of each contour that fits inside the corresponding circular area gave a measure of the circularity of the closed circulation. This percentage typically increased rapidly when the contour value increased to the level where secondary extrema, which were not part of the eddy, were no longer captured within the contour. This rapid change in percent of circularity was used to objectively identify the tracking contour to compute eddy area. When the maximum height in the eddy was at or above 30 cm, the automatic tracking contour level tended towards 17 cm, the level used for LC tracking (Leben 2005). When the maximum height dropped below 30 cm, the tracking contour tended toward values about half of the maximum height. This adaptive tracking was preferable to using a fixed tracking contour for calculating the area, especially as closed eddy circulation developed and decayed.

Figures 4.1-1 – 4.1-4 show 8-day composite ocean color images overlaid with SSH at 3-day intervals from 9 July 2005 through 23 Aug 2005. On each of the images, the rescaled ellipses and eddy centers determined from eddy tracking are plotted as red, green, and white dashed ellipses and crosses, respectively, to show the locations 3 days before (red), 3 days after (green), and on the analysis date (white). The 200 and 2000 meter isobaths are also shown. During this time period, Eddy Vortex was located in the north-central GOM to the west-southwest of the study area and was still attached to the LC. Tracking of the eddy centers showed that there was little movement of Eddy Vortex during July; however, the eddy underwent significant deformation, becoming elongated along a southeast to northwest oriented major axis. This elongation brought the northwest flank of the eddy onto the continental slope, which induced a cross-slope flow that showed up well in the ocean color imagery as a stream of high chlorophyll concentration water flowing along the northeast flank of the eddy. In early August, the eddy became more circular and moved to the west-southwest, detaching from the LC. The detached eddy elongated along a southwest to northeast oriented major axis, once again interacting with the continental slope. This produced a cyclonic eddy along the northeast flank of Vortex that was well sampled by the Horizon Marine drifters and identified above as Cold Eddy 3. The detached and elongated Eddy Vortex rotated clockwise and subsequently reattached to the LC after which kinematic tracking was no longer possible.

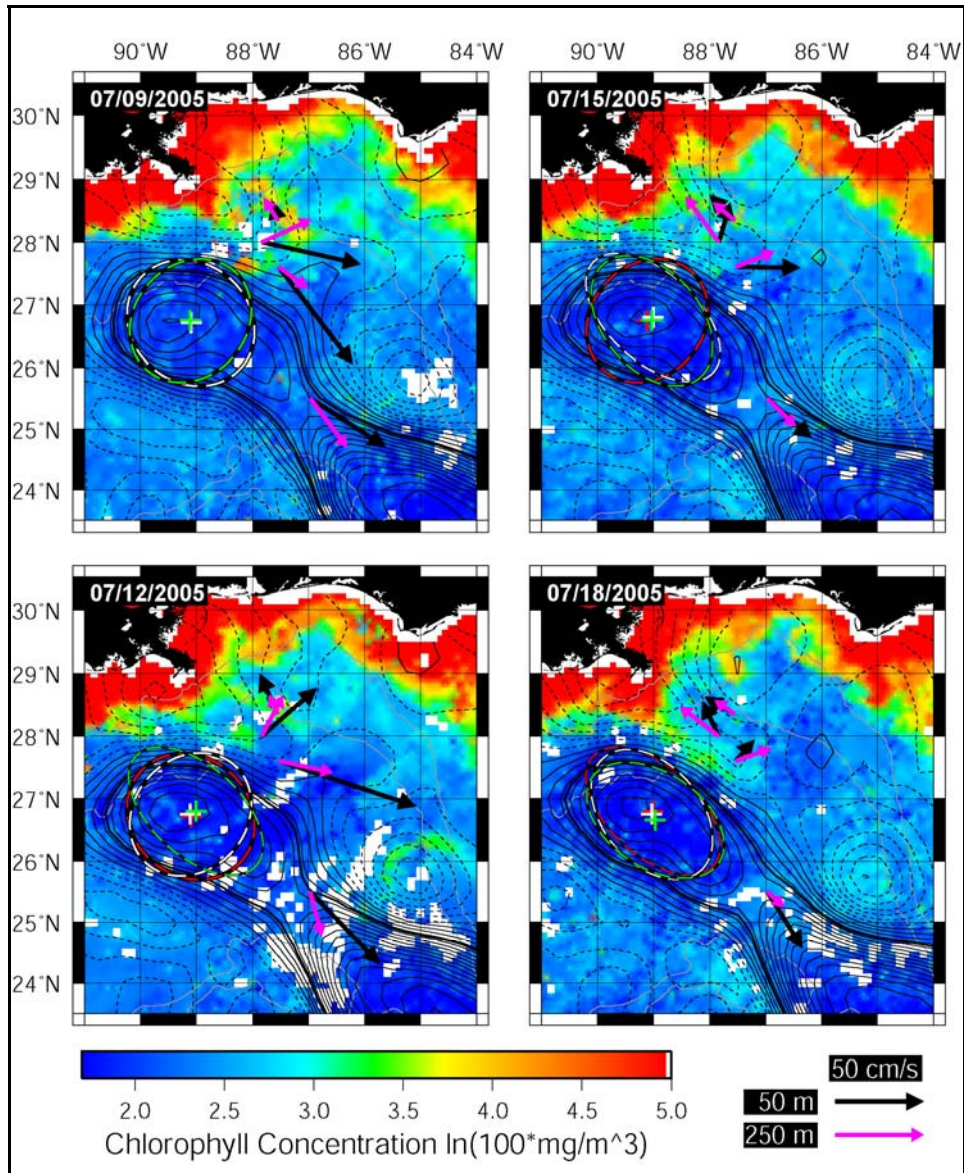


Figure 4.1-1. Ocean color images overlaid with SSH at 3-day intervals from July 9-18, 2005. Rescaled ellipses and eddy centers are plotted as red, green, and white dashed ellipses and crosses, respectively to show the eddy locations 3 days before (red), 3 days after (green), and on the analysis date (white).

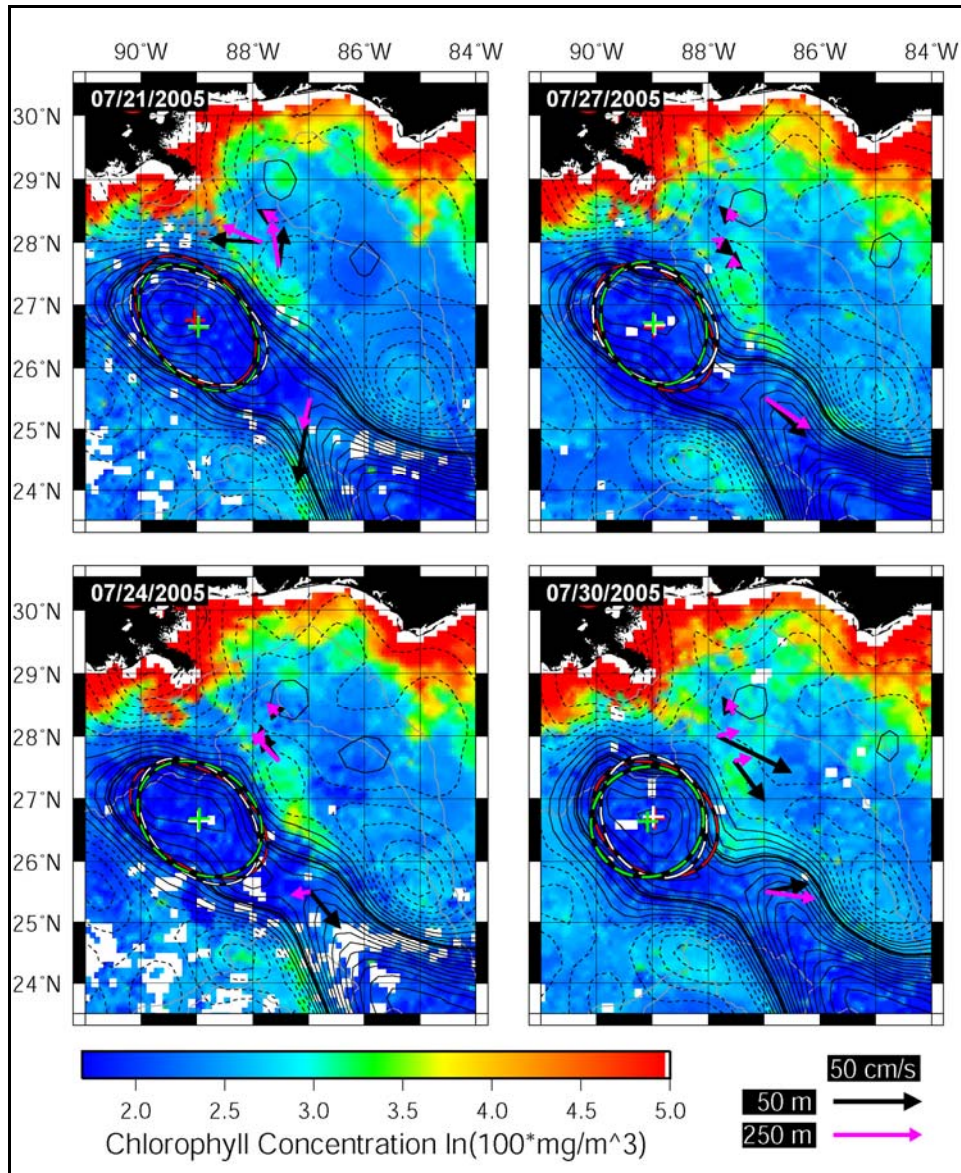


Figure 4.1-2. Ocean color images overlaid with SSH at 3-day intervals from July 21-30, 2005. Rescaled ellipses and eddy centers are plotted as red, green, and white dashed ellipses and crosses, respectively, to show the eddy locations 3 days before (red), 3 days after (green), and on the analysis date (white).

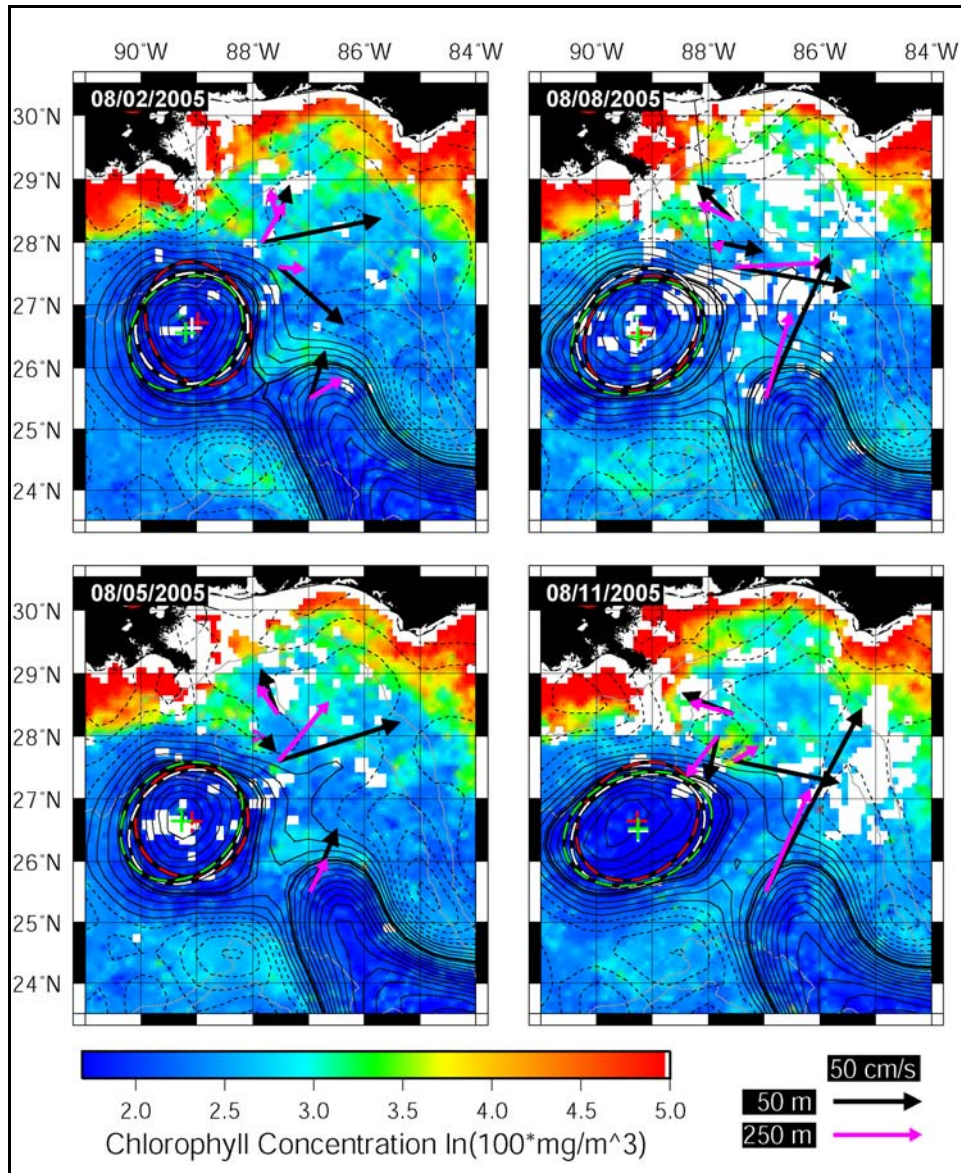


Figure 4.1-3. Ocean color images overlaid with SSH at 3-day intervals from August 2-11, 2005. Rescaled ellipses and eddy centers are plotted as red, green, and white dashed ellipses and crosses, respectively, to show the eddy locations 3 days before (red), 3 days after (green), and on the analysis date (white).

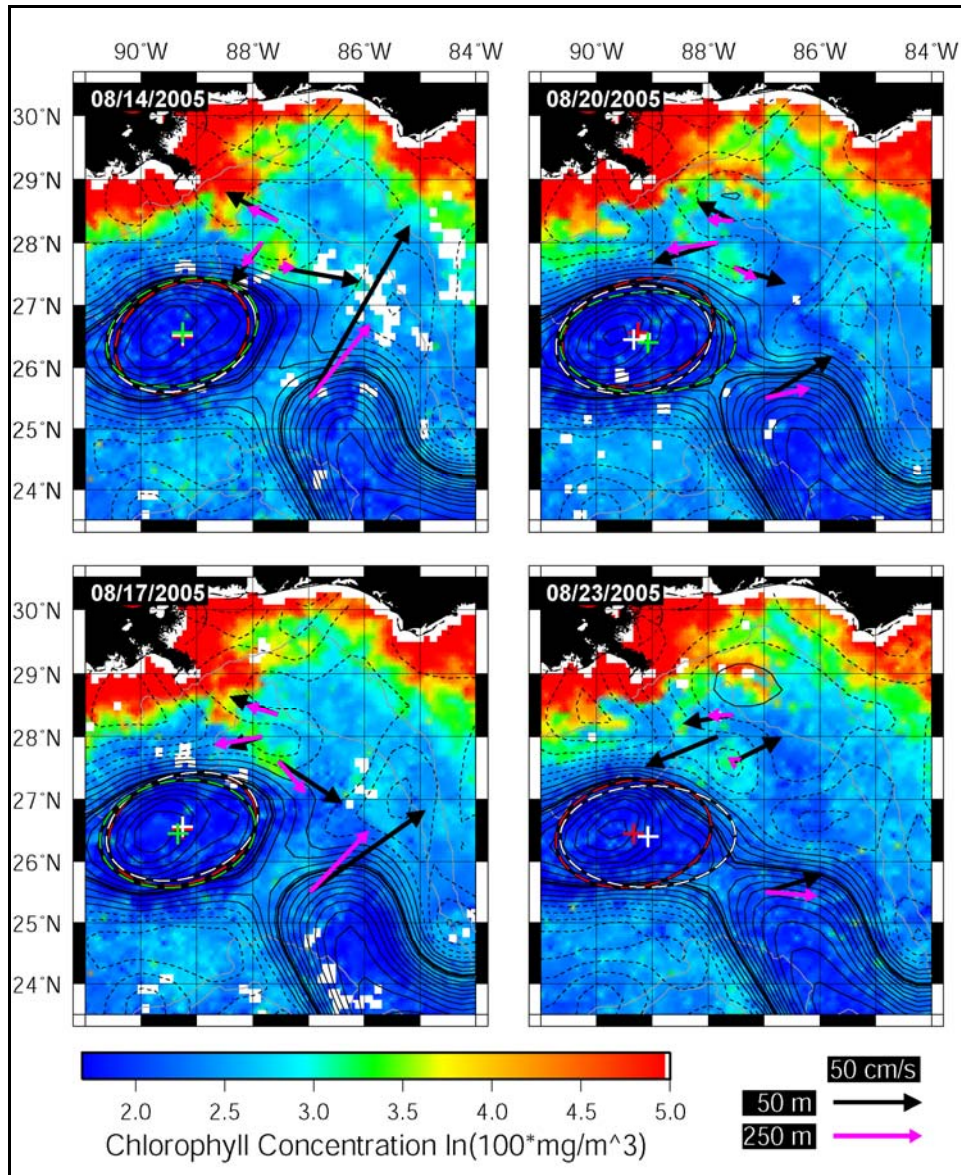


Figure 4.1-4. Ocean color images overlaid with SSH at 3-day intervals from August 14-23, 2005. Rescaled ellipses and eddy centers are plotted as red, green, and white dashed ellipses and crosses, respectively, to show the eddy locations 3 days before (red), 3 days after (green), and on the analysis date (white).

4.2 Dynamic Analysis

The dynamic analysis is based on relative vorticity calculated from the sea surface height estimates made using measurements from the PIES array. This analysis was used to objectively identify the dominant anticyclonic and cyclonic events sampled by the PIES array during the observational record.

4.2.1 Mapped Surface Circulation and Sea Surface Height from PIES

Time-averaged mapped surface currents and sea surface height determined from the PIES are shown in Figure 4.2-1. During the year-long observational period, the mean surface current was mainly to the east in the southern half of the array with mean speeds typically less than 25 cm s^{-1} . Currents in and above the thermocline tended to exhibit an "equivalent barotropic" structure, in which the currents decrease their speed with increasing depth but remain aligned in the same direction. The currents were observed to turn markedly with depth when subthermocline currents were strong, these events are discussed further in Chapters 6 and 7. Time-average currents were dominated by a few strong events; mean maps should not be interpreted as representative of the long-term mean. This point is emphasized by the comparison between the mean-surface circulation calculated over different time periods with nearly the same length. The mean from the first six months (January 27, 2005 to July 4, 2005; left panel of Figure 4.2-1) reveals southeast flow that results from the presence of Eddy Vortex within the southwestern portion of the array; the mean from the last six months (July 4, 2005 to January 19, 2006; right panel of Figure 4.2-1) has comparatively weaker currents and the mean cyclonic flow pattern results from several frontal cyclones.

The structure of the array-mean current can be clarified by looking at the major events. First, we determined current variability as expressed by mean eddy kinetic energy,

$$\text{EKE} = (1/2)\langle (u')^2 + (v')^2 \rangle, \quad (4.2.1)$$

where $\langle \rangle$ was the one-year mean. Figure 4.2-2 shows surface EKE superimposed on the mean surface current. The highest EKE values occurred in the middle of the array, slightly offset to the west. Current variance ellipses are also shown. The time history of the spatially-averaged EKE revealed four episodes of high EKE lasting 15-30 days, indicative of an event-dominated time series. The first three events occurred during an Eddy Vortex detachment and reattachment and more specifically when Eddy Vortex intruded into the array. After mid-July 2005, Eddy Vortex and the LC remained south of the array, the fourth event described here was a strong frontal cyclone. In order to capture these events, we mapped surface circulation at 4-day intervals over a 12-day period for each event (Figures 4.2-3 to 4.2-6, upper panels). In addition, we calculated surface relative vorticity ($\zeta = \partial v / \partial x - \partial u / \partial y$) divided by the Coriolis parameter (Figures 4.2-3 to 4.2-6, lower panels). Note that we mapped relative vorticity with optimal interpolation with a 50 km Gaussian correlation function.

These four events share the following characteristics: surface speeds in excess of 100 cm s^{-1} and absolute relative vorticity values that often exceed 0.4. A gradient-wind, rather than a geostrophic balance, may be a more appropriate balance in this region. Geostrophic wind overestimates (underestimates) velocity in strong cyclonic (anticyclonic) regimes by a factor on the order of the Rossby number (ζ/f). Here our calculation of relative vorticity did not distinguish between curvature and relative vorticity due to the limited spatial extent of the array. Figures 4.2-3 through 4.2-5 show the surface circulation during the major intrusions of the LC or LCE into the array. In these cases the PIES array was only influenced by the periphery of the LC/LCE. The following cases were noted:

16 through 28 February 2005, Eddy Vortex detachment #1: The LC extended northward and turned clockwise as Eddy Vortex formed and detached on February 21. We note the rapid change in ζ/f in the array center which changed from -0.4 to 0.7 in 4 days from February 24 to February 28. In addition, ζ/f spanned a range of 0.8, with values near 0.4 at PIES05 and values near -0.4 at PIES03. Mapped circulation for this day suggests that curvature dominated shear vorticity.

22 through 31 May 2005, Eddy Vortex reattachment #2: On May 21, Eddy Vortex reattached to the LC for a second time. Mapped currents reached peak values near 150 cm s^{-1} , and ζ/f values along the cyclonic side of the LC were near -0.8.

15 through 27 June 2005, Eddy Vortex detachment #3: A lobe of Eddy Vortex extended into the array and then retreated southward. Although Eddy Vortex extended furthest into the array during this time, vorticity values were weak compared to the other 'big' events.

12 through 24 December, Cyclone #2: Strong cyclonic vorticity associated with the frontal cyclone reached ζ/f values near 0.5, not quite as high as those associated with LC or LCE shears.

The PIES array captured the mesoscale frontal meanders along the periphery of the Loop Current. The array, while well resolved, provided a limited window.

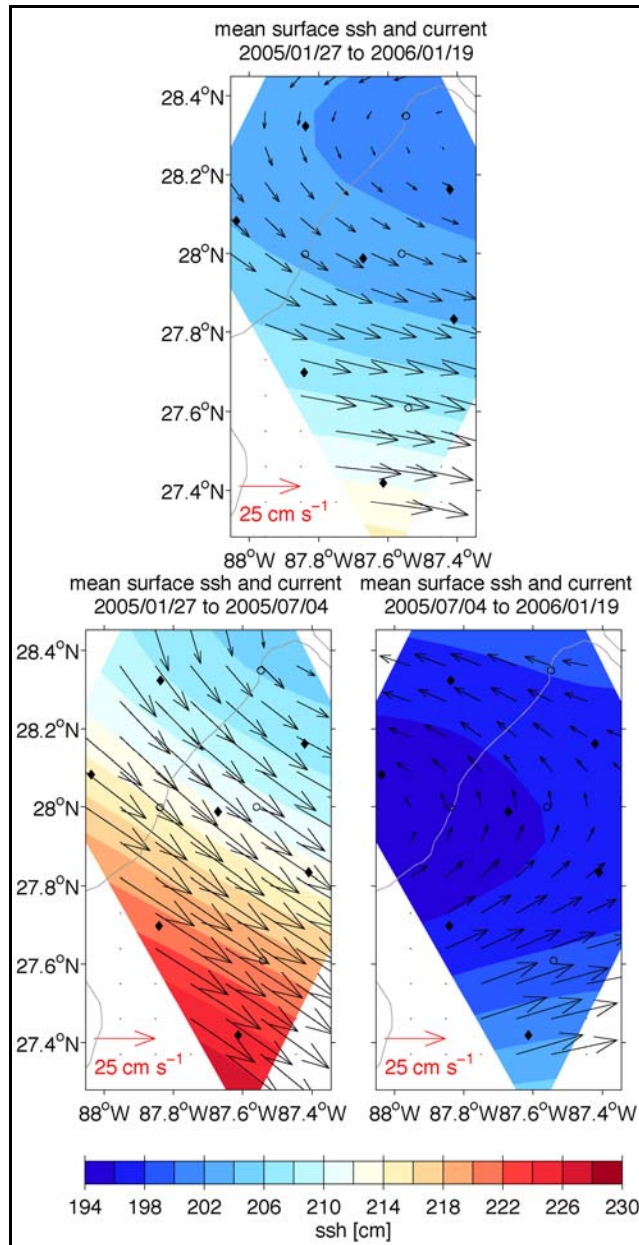


Figure 4.2-1. Top Panel: Time-average mean sea surface height (contours) and currents (black vectors) at the surface. Averaging period is from 27 January 2005 to 19 January 2006. Sea surface height is contoured every 2 cm with low (high) values shown with blue (red) hues. Current vectors plotted at 10-km spacing. PIES sites indicated by diamonds, current meters denoted by circles. Vector key is shown in lower left corner. Bathymetry contoured every 500 m depth with gray lines. Bottom Panels: Same as top panel except for the averaging period. Right Bottom Panel: 27 January 2005 to 4 July 2005. Right bottom panel: 4 July 2005 to 19 January 2005.

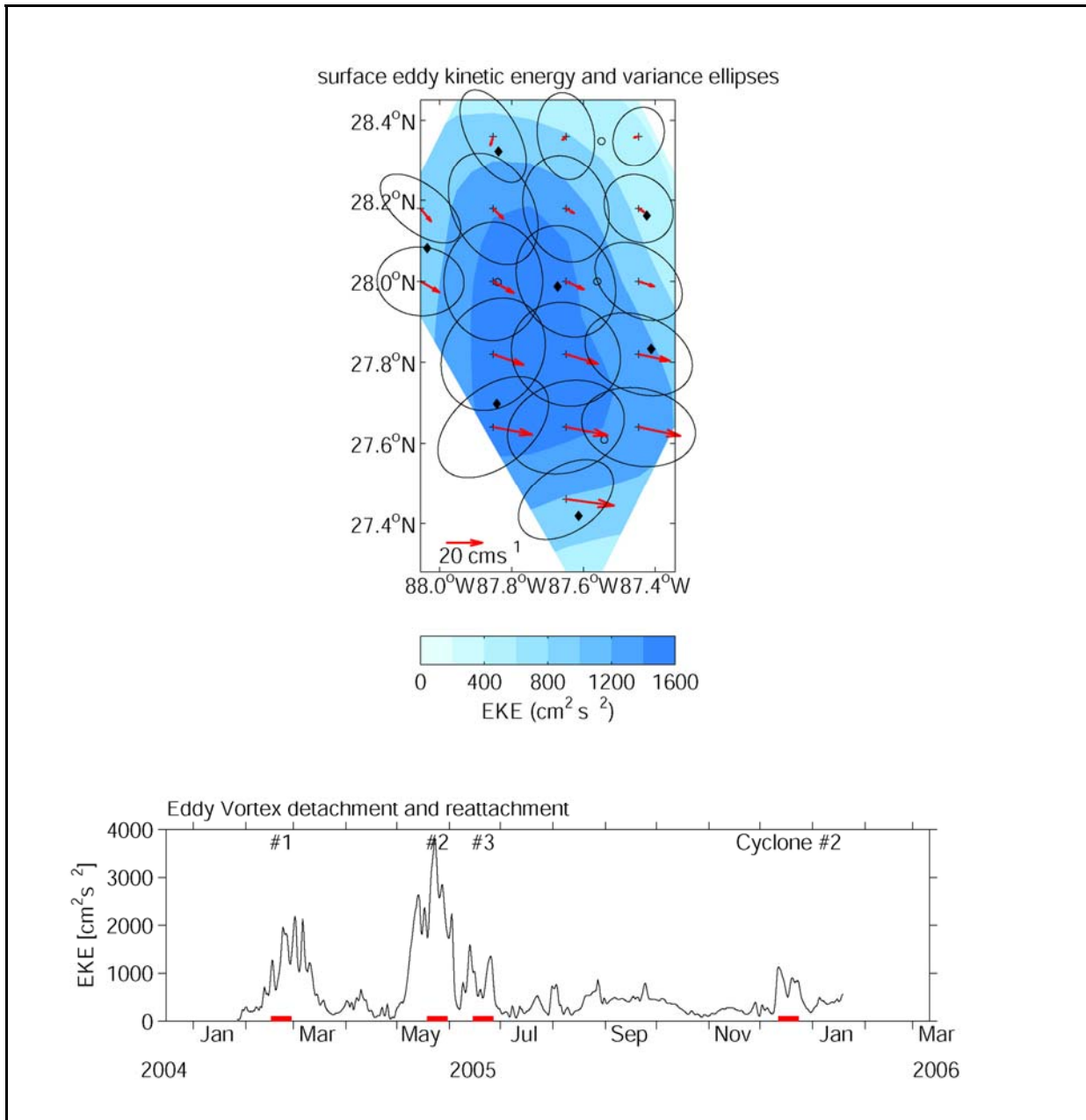


Figure 4.2-2. Upper panel: Mean surface eddy kinetic energy averaged between 27 January to 19 January 2006 contoured every 200 cm^2s^{-2} . Bathymetry contoured every 500 m depth with gray lines. PIES sites indicated by diamonds, current meters denoted by circles. Bottom panel: Array-average mean surface eddy kinetic energy. The four strongest events are highlighted by the red line along the x-axis and labeled consistently with the EGOM Upper Ocean Events Timeline.

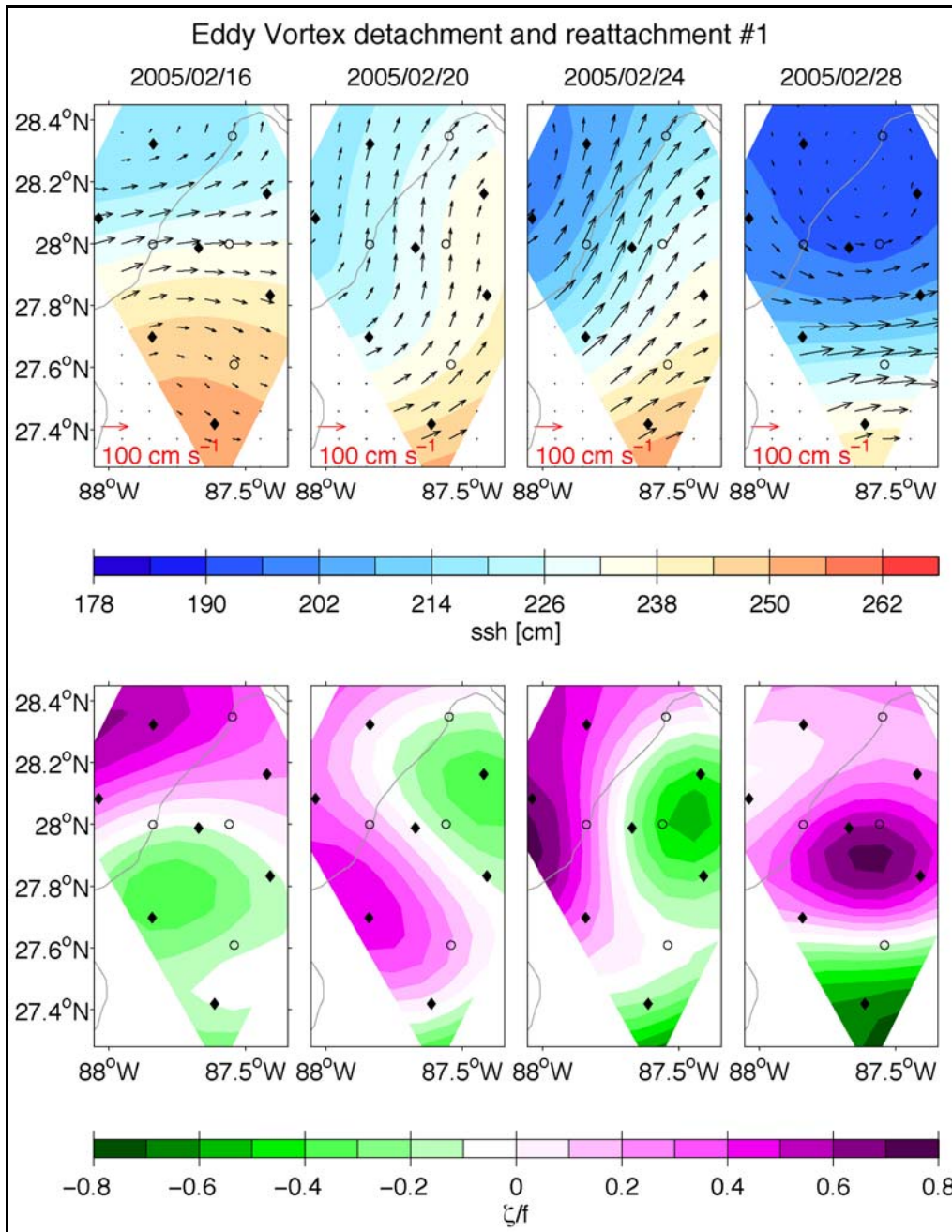


Figure 4.2-3. 16 February 2005 to 28 February 2005. Upper panels: Sea surface height (contours) and currents (black vectors) at the surface. Map date is stated in each panels' title. Sea surface height is contoured every 2.0 cm with low (high) values shown with blue (red) hues. Current vectors plotted at 10-km spacing. Vector key is shown in lower left corner Bottom panels: relative vorticity scaled by local Coriolis parameter. Low (high) values shown with magenta (green) hues. In all panels PIES sites indicated by diamonds, current meters denoted by circles and bathymetry contoured every 500 m depth with gray lines.

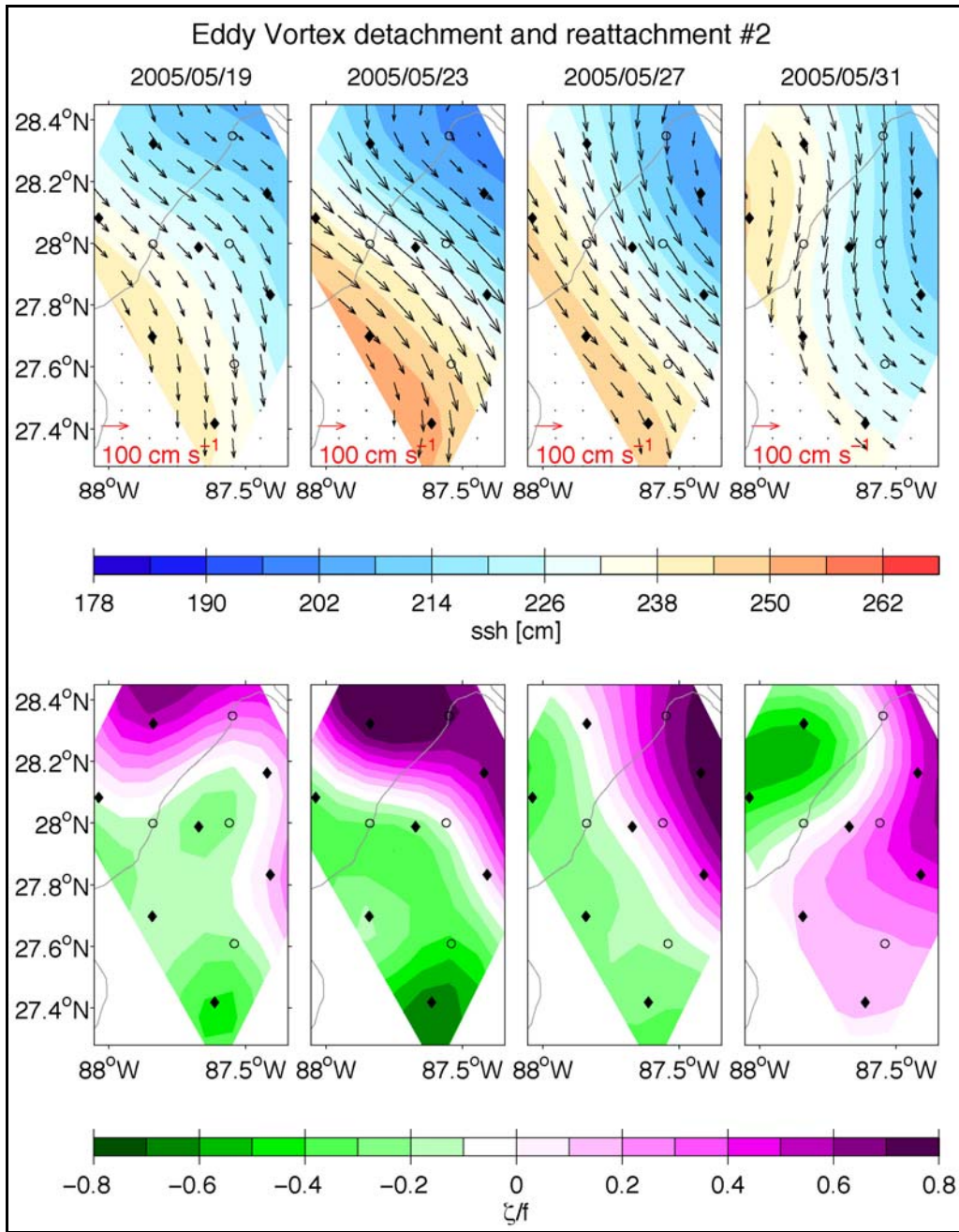


Figure 4.2-4. 19 May 2005 to 31 May 2005. Upper panels: Sea surface height (contours) and currents (black vectors) at the surface. Map date is stated in each panels' title. Sea surface height is contoured every 2.0 cm with low (high) values shown with blue (red) hues. Current vectors plotted at 10-km spacing. Vector key is shown in lower left corner Bottom panels: relative vorticity scaled by local Coriolis parameter. Low (high) values shown with magenta (green) hues. In all panels PIES sites indicated by diamonds, current meters denoted by circles and bathymetry contoured every 500 m depth with gray lines.

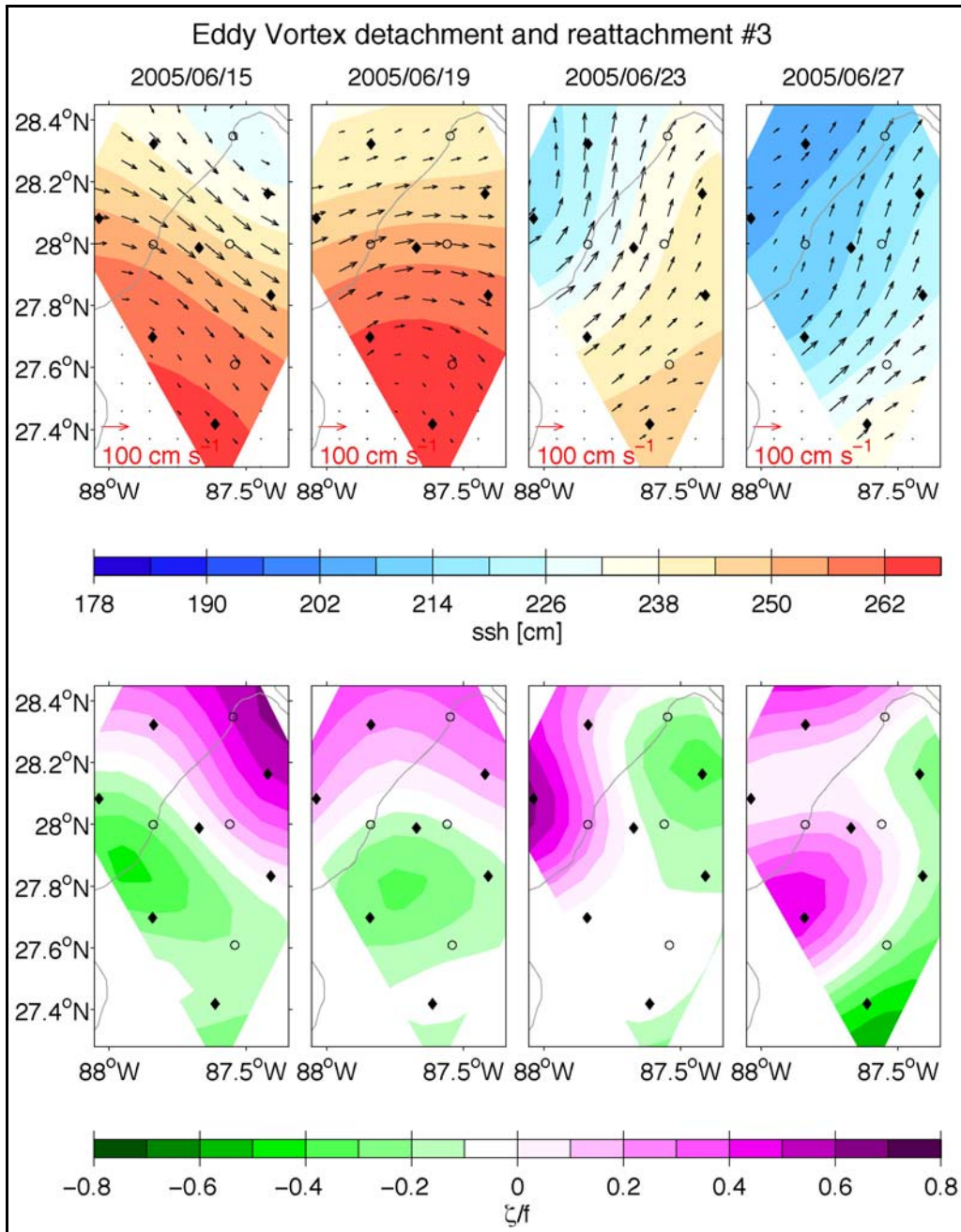


Figure 4.2-5. 15 June 2005 to 27 June 2005. Upper panels: Sea surface height (contours) and currents (black vectors) at the surface. Map date is stated in each panels' title. Sea surface height is contoured every 2.0 cm with low (high) values shown with blue (red) hues. Current vectors plotted at 10-km spacing. Vector key is shown in lower left corner Bottom panels: relative vorticity scaled by local Coriolis parameter. Low (high) values shown with magenta (green) hues. In all panels PIES sites indicated by diamonds, current meters denoted by circles and bathymetry contoured every 500 m depth with gray lines.

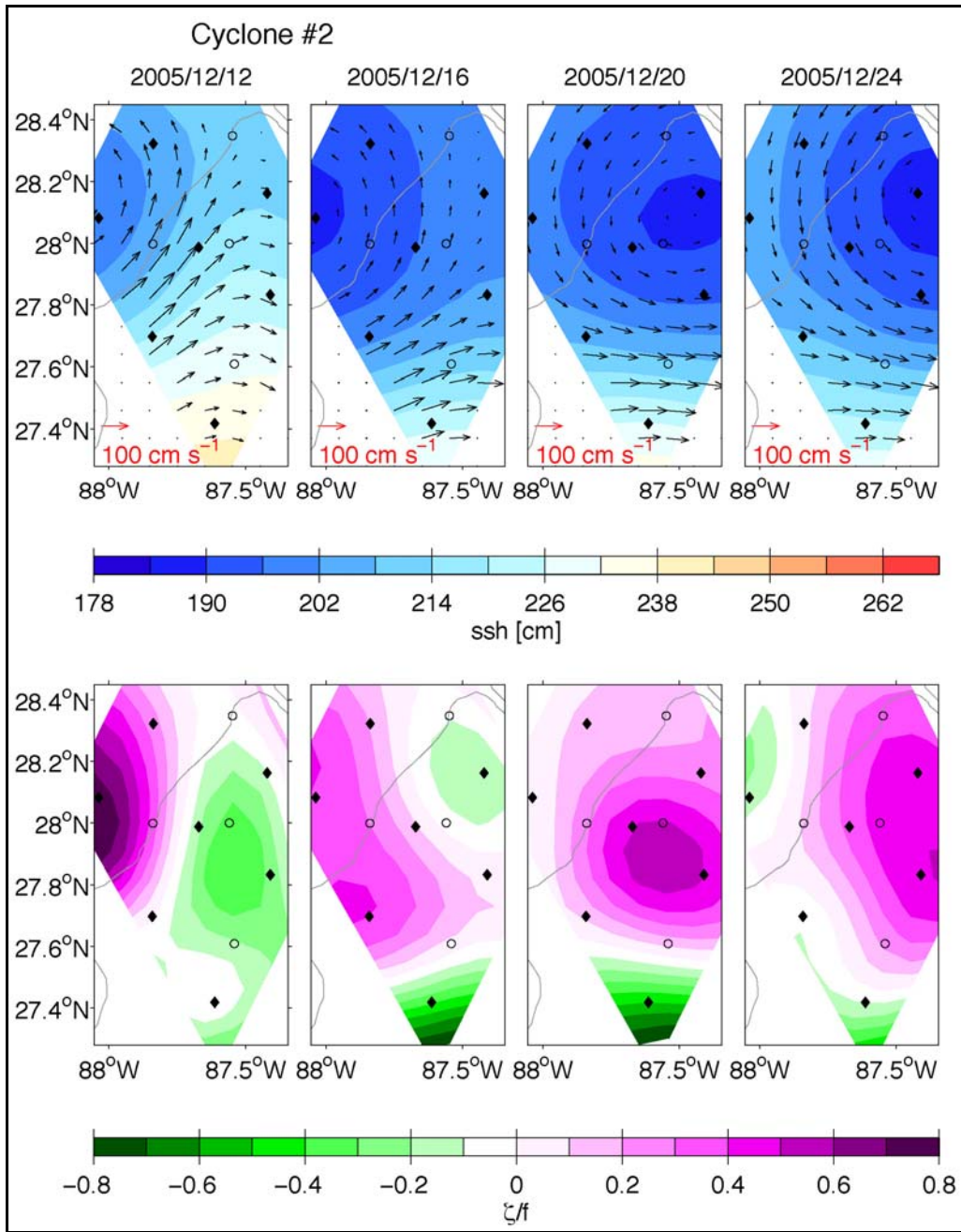


Figure 4.2-6. 12 December 2005 to 24 December 2005. Upper panels: Sea surface height (contours) and currents (black vectors) at the surface. Map date is stated in each panels' title. Sea surface height is contoured every 2.0 cm with low (high) values shown with blue (red) hues. Current vectors plotted at 10-km spacing. Vector key is shown in lower left corner Bottom panels: relative vorticity scaled by local Coriolis parameter. Low (high) values shown with magenta (green) hues. In all panels PIES sites indicated by diamonds, current meters denoted by circles and bathymetry contoured every 500 m depth with gray lines.

4.2.2 Relative Vorticity Calculated from the PIES

The relative vorticity was calculated from the PIES sea surface height time series by assuming geostrophy and using Stokes' theorem. The velocity and the vorticity are related through Stokes' theorem:

$$\oint_C \vec{v} \cdot d\vec{x} = \int_A \nabla \times \vec{v} \cdot \vec{n} \cdot d\vec{a} = \int_A \vec{\omega} \cdot \vec{n} \cdot d\vec{a}. \quad (4.2.2)$$

Assuming that the vorticity and area were constant over the region of interest, the above equations simplify to:

$$\omega = \frac{\sum(\vec{v} \cdot d\vec{s})}{A}, \quad (4.2.3)$$

for the vertical component of relative vorticity, ω . The horizontal components of the velocity field, u and v , are calculated from the sea surface height from the geostrophic approximation:

$$u = -\frac{g}{f} \frac{\partial h}{\partial y}, \quad v = \frac{g}{f} \frac{\partial h}{\partial x}. \quad (4.2.4)$$

By combining equations 4.2.3 and 4.2.4, the relative vorticity can be calculated directly from the PIES sea surface height. Diagram 1 in the upper panel of Figure 4.2-7 shows the configuration of the PIES used for the calculation. The method made use of triangles constructed between neighboring PIES stations and the center PIES station #4. PIES #6 was not used in these calculations because the sea surface height data from that instrument were only available during the second half of the year-long observational record. Based on the configuration of the individual PIES stations and the method used (see again Diagram #1), PIES #4 was selected as the location at which to find the vorticity since a circuit around a station is needed to evaluate the line integral of velocity defined by Stokes' theorem. The velocities in the direction along each face of the circuit were also needed to evaluate the integral. Diagram 2 (in Figure 4.2-7) shows the geometric configuration used to calculate the velocity between PIES stations #1 and #2. The velocity along each edge of the PIES array was calculated from the sea surface slope perpendicular to the line between each pair of PIES stations on the perimeter of the circuit. The steps below outline the process for completing the calculation of the velocities and the vorticity:

1. Found the locations of PIES #1 ($x_1, M1, h_1$) and PIES #2 ($x_2, M2, h_2$) relative to PIES #4 ($0, 0, h_4$) after moving the origin of the x, y coordinate system to the PIES #4 location.
2. Found the midpoint of the line connecting PIES #1 and PIES #2:

$$[(x_1+x_2)/2, (M1+M2)/2, (h_1+h_2)/2].$$

3. Set the point of intersection of the perpendicular (in red in Diagram #2) and the line connecting PIES #2 and PIES #4 to be (a, b, c) .

4. The line connecting PIES #2 to PIES #4 is given by the equation:

$$\vec{y} = (0,0,h_4) + t(x_2,y_2,h_2)$$

The point (a,b,c) will be a point on this line for some t , providing the three following equations:

$$a = x_2t$$

$$b = y_2t$$

$$c = h_4 + h_2t$$

5. A fourth equation was obtained using the Pythagorean theorem with the midpoint of the line connecting PIES #1 and PIES #2, the point at PIES #2, and the point (a,b,c) . This equation along with the 3 in step 4 is solved to obtain values for a,b,c and t .
6. Calculated the slope of the line connecting the midpoint between PIES #1 and PIES #2 and the point (a,b,c) , and multiplied by (g/f) which gives the velocity along the segment between PIES #1 and PIES #2.
7. Repeated steps 1 through 6 to find the velocities along all five line segments along the perimeter defining the path of integration around the PIES array.
8. Multiplied the velocity along each segment by the distance between the two respective PIES stations defining the individual segments and sum to calculate the total circulation around the full circuit of the array.
9. Divided the result from step 8 by the total area within the perimeter of the array to estimate the area-averaged vorticity.
10. Repeated the procedure for all times to calculate the time series of relative vorticity for the array.

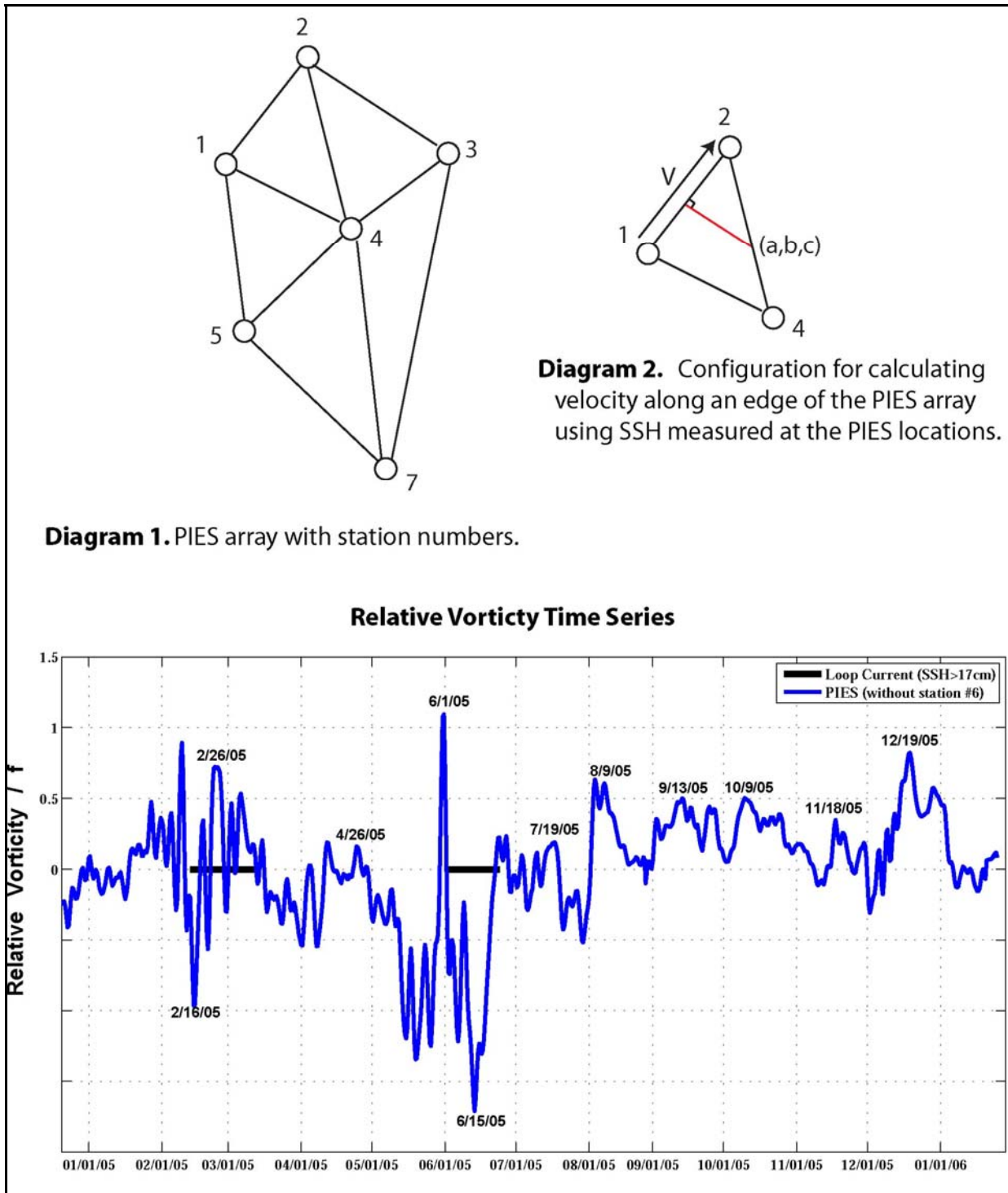


Figure 4.2-7. Diagrams #1 and #2 show schematics used to compute relative vorticity from the Eastern Gulf PIES stations. The lower panel shows the relative vorticity time series and the dates of selected events. Thick black lines span the time periods when the altimeter-derived SSH was above 17 cm within the PIES array.

4.2.3 Anticyclonic and Cyclonic Events in PIES Relative Vorticity Time Series

The time series of relative vorticity normalized by the planetary vorticity, f , is shown in the lower panel of Figure 4.2-7. The dates of selected anticyclonic and cyclonic events are identified by labels on the time series. Thick black lines show the time periods when the altimeter-derived SSH was above 17 cm within the PIES array, which corresponds to the strongest anticyclonic events observed in the record. The first time period of the 17-cm contour intrusion into the PIES array, from 14 Feb 2005 through 14 Mar 2005, was associated with the first detachment of Eddy Vortex (see Tables 3.1-1 and 3.2-2). The second time period of intrusion, from 3 June 2005 through 25 June 2005, was associated with the third detachment of Eddy Vortex. In these two cases, the peak anticyclonic vorticity events occurred just before a large anticyclonic eddy detached from the LC. Figures 4.2-8 and 4.2-9 show the altimeter-derived SSH overlaid on coincident chlorophyll concentration images on the dates of peak anticyclonic vorticity in the array: 16 February 2005 and 15 June 2005. Peak values during these events were of the same order of magnitude as the planetary vorticity. The two other LC intrusion and Eddy Vortex detachment events, which were in late May and early August, also influenced the anticyclonic vorticity observed in the array. In the last half of the record, the anticyclonic events were much less frequent and significantly weaker because of the more westward intrusion and ultimate retreat of the LC associated with the separation of Eddy Vortex on 13 September 2005.

Cyclonic events occurred more frequently than anticyclonic events in the eastern GOM vorticity record. In the first half of the time series, these events were associated with cyclonic frontal instabilities or eddies propagating in a clockwise direction along the frontal boundary of the intruded LC or detached Eddy Vortex. Figure 4.2-10 shows altimeter-derived SSH overlaid on coincident chlorophyll concentration images for four of the events with cloud-free imagery during this time period. A key feature in each of the images is the strong chlorophyll signature associated with the cyclonic frontal events. These plumes of enhanced chlorophyll originated upstream of the array through the interaction of the LC/LCE with the continental shelf/slope. In the latter half of the time series, the configuration of the LC in the eastern GOM changed as the LC retreated to just south of the study array following the separation of Eddy Vortex. The cyclonic events during this time period were associated with relatively stationary cyclones located along the northern frontal boundary of the retreated LC. Strong circulation events within the array, in these cases, were caused by the movement of large frontal eddies over and back into the array as they were jostled around by the LC that remained well-intruded, but south of the study region. Figure 4.2-11 shows altimeter-derived SSH overlaid on coincident chlorophyll concentration images for the four strongest events observed during this time period.

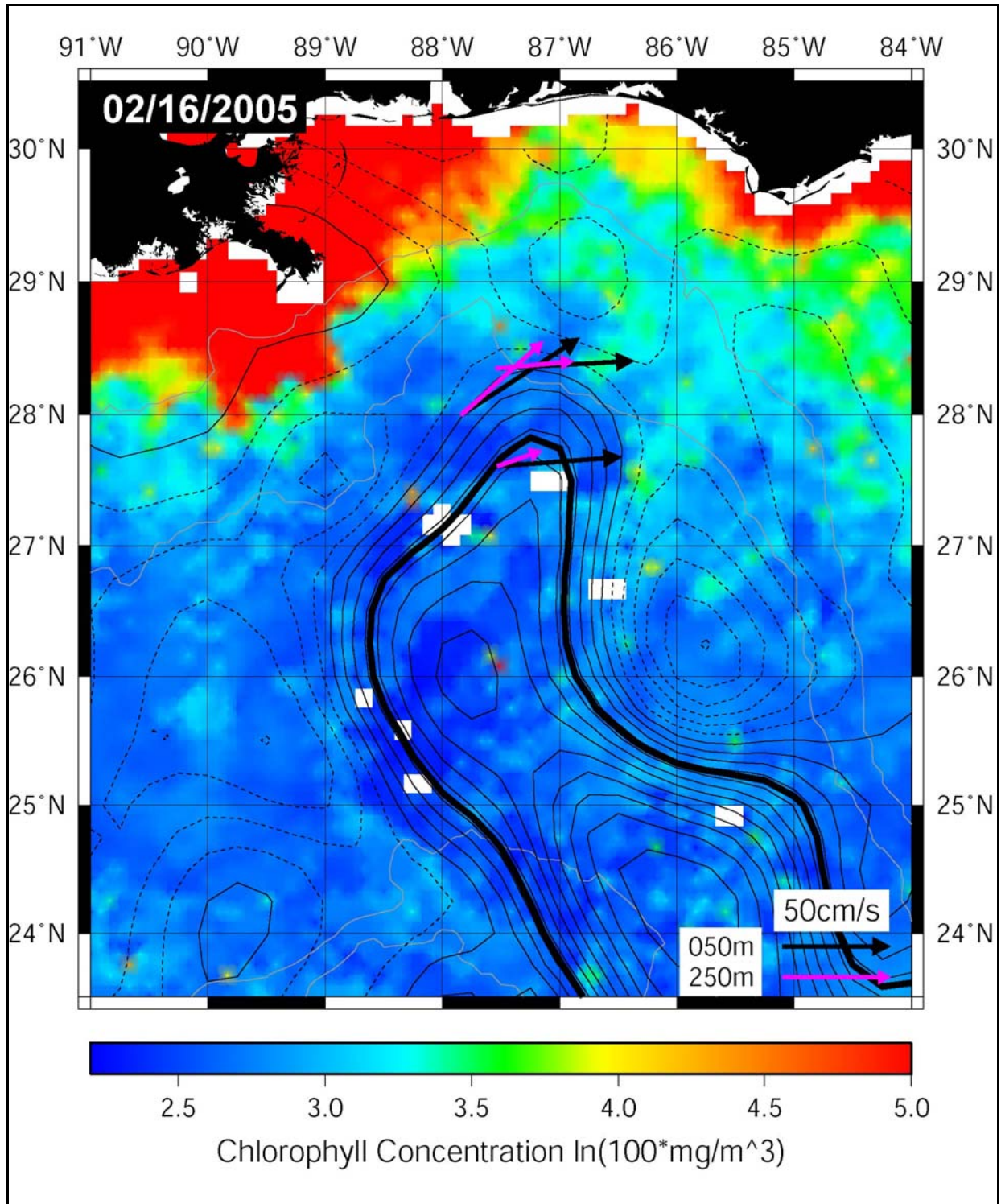


Figure 4.2-8. Altimeter-derived SSH overlaid on 8-day composite chlorophyll-concentration image from 16 Feb 2005. This day corresponds to the peak anticyclonic relative vorticity during the LC intrusion associated with the first detachment of Eddy Vortex.

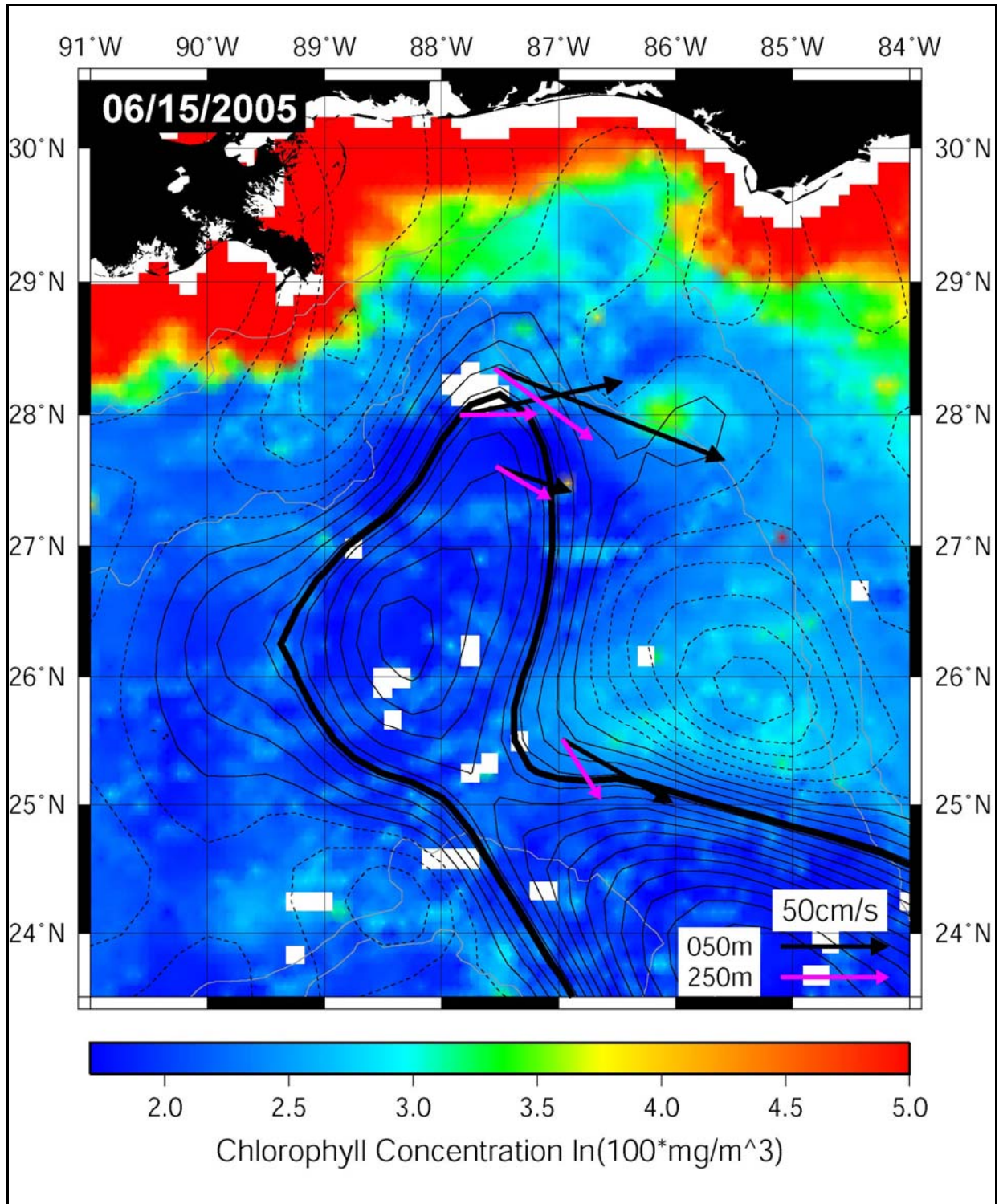


Figure 4.2-9. Altimeter-derived SSH overlaid on 8-day composite chlorophyll-concentration image for 15 June 2005. This day corresponds to the peak anticyclonic relative vorticity during the LC intrusion associated with the third detachment of Eddy Vortex.

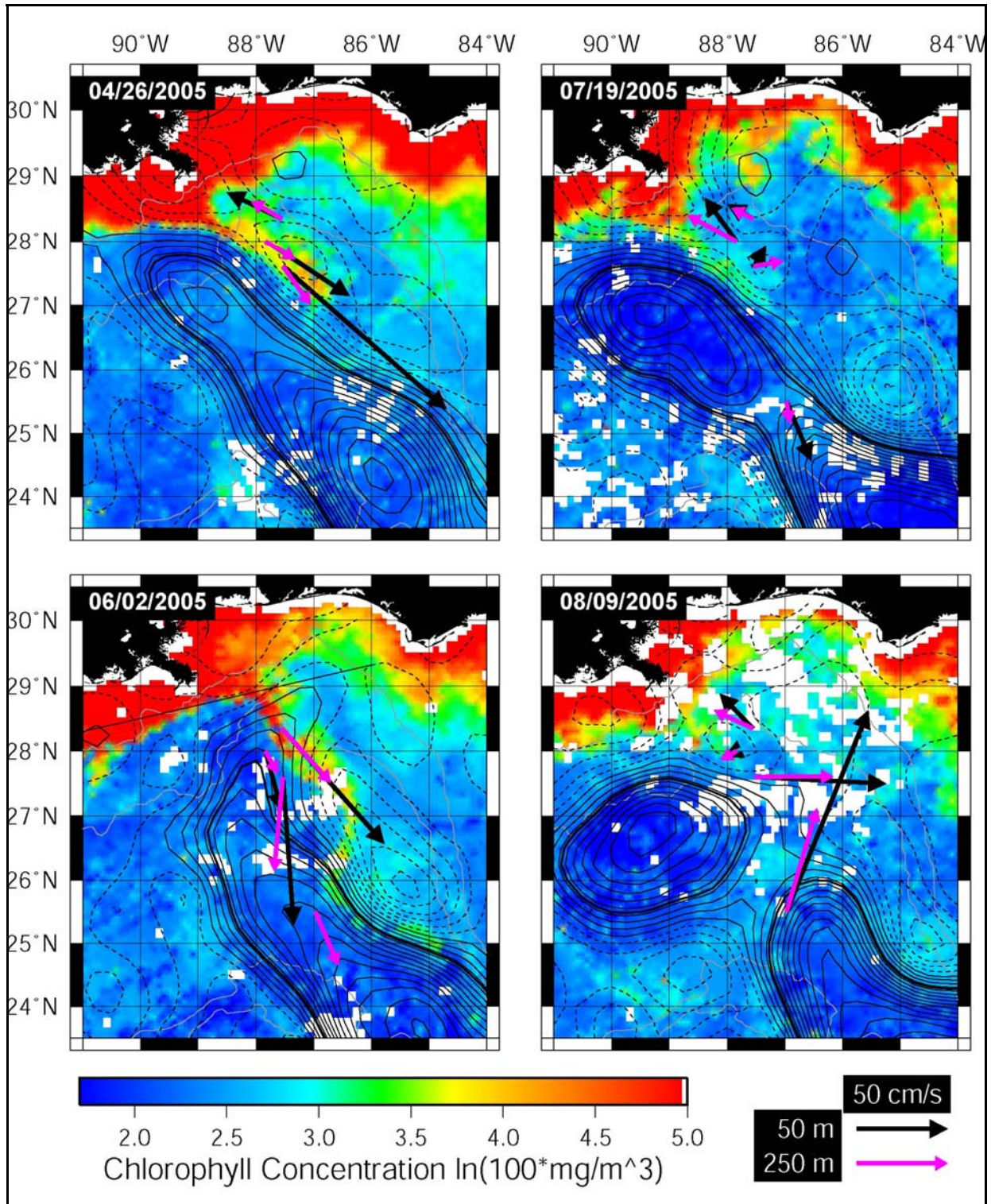


Figure 4.2-10. Altimeter-derived SSH overlaid on 8-day composite chlorophyll-concentration images for selected dates before Eddy Vortex separation. The dates correspond to the peak cyclonic vorticity events identified in the vorticity time series shown in the lower panel of Figure 4.2-7.

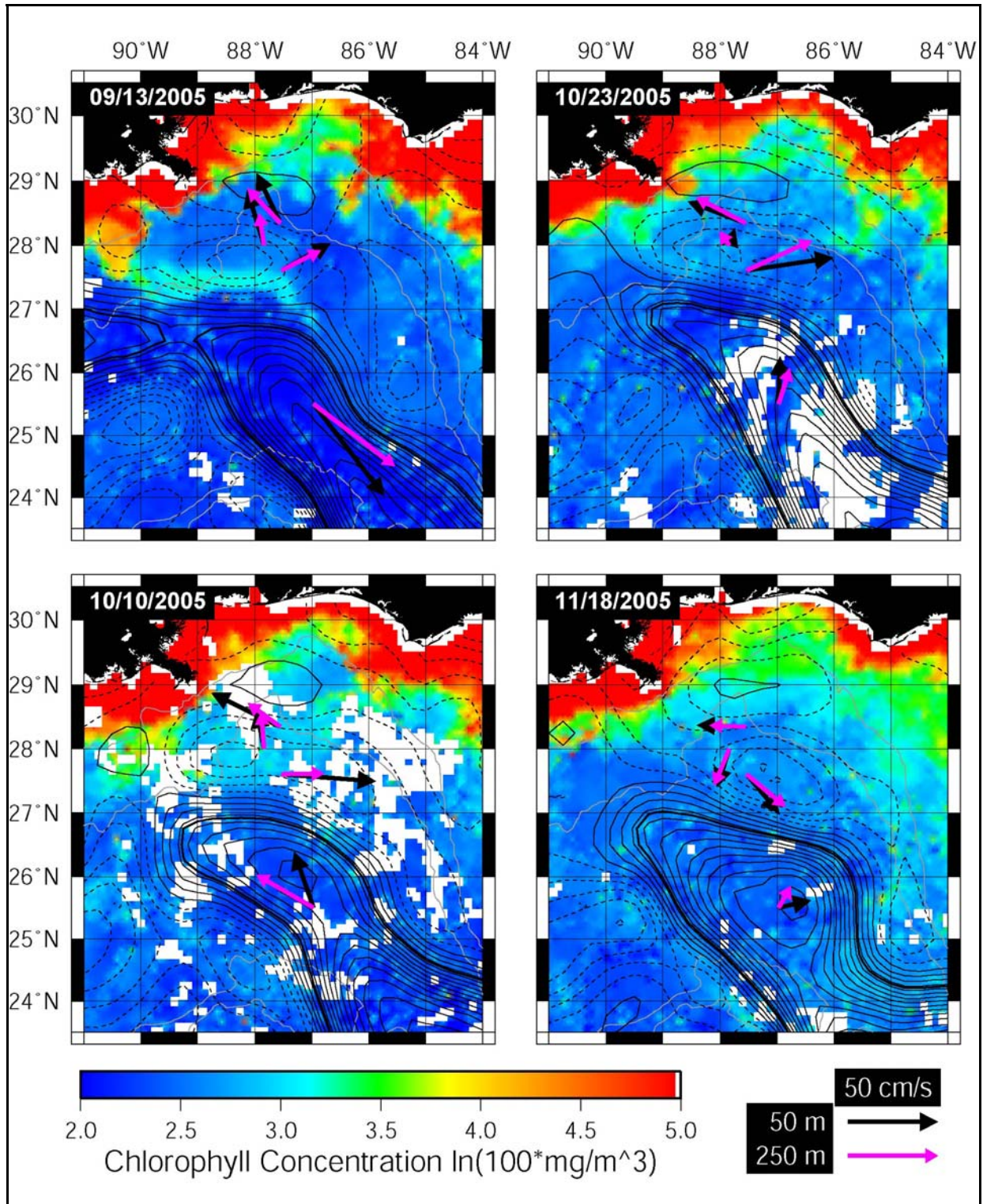


Figure 4.2-11. Altimeter-derived SSH overlaid on 8-day composite chlorophyll-concentration images for selected dates after Eddy Vortex separation. The dates correspond to the peak cyclonic vorticity events identified in the vorticity time series shown in the lower panel of Figure 4.2-7.

5.0 MOORING AND HYDROGRAPHY RESULTS

5.1 *Mooring Measurements*

As described previously herein, the mooring measurements were collected over two deployments spanning one year from January 2005 to January 2006. Servicing of the moorings occurred in August immediately prior to the arrival of Hurricane Katrina in the GOM. As shown in Chapters 3 and 4, portions of the study area experienced the influence of either the LC, Eddy Vortex, or frontal features associated with them multiple times. In addition, several hurricanes and a tropical storm passed through the GOM during 2005, some of them close enough to the study area (Appendix A) to result in distinguishable impacts to the currents measurements by the eastern GOM moorings. The end result is that the moorings captured a robust set of measurements showing the impacts to the eastern GOM circulation by both the LC, an LCE, frontal features, and hurricanes.

5.1.1 **Velocity Time-Series**

Velocity time series of the current measurements at multiple depths on the tall moorings M1, M2, and M3 for both the first and second deployments are shown in Appendix B. The time series are presented as vector plots, with the length of the vectors equal to the speed scale, and the direction of the vector pointed in the direction of current flow, with north toward the top of the page. A solid line superimposed on the vector plots also denotes the current speed. Data are presented for selected depths from the ADCPs, as well as from all single point current meters, so as to provide an initial full water column perspective on the timing and depths associated with stronger current events during each deployment. The depth axis is not to scale. Vertical lines represent the general timing of LC, LCE, frontal feature, or storm effects upon the currents.

As can be seen in these plots, a significant portion of the first deployment at all three tall mooring locations experienced stronger currents primarily but not entirely generated by LC, Eddy Vortex, or LC or LCE frontal features. At M3, nearly the entire first deployment contained stronger currents. Currents at M2 were quite similar to those at M3, whereas the strength and duration of stronger currents at M1 was reduced as compared to those at M2 and M3 during the first deployment. During the second deployment, periods of stronger currents were normally shorter, and current strengths reduced as compared to the first deployment, although Mooring M3 continued to show influences on the currents due to both hurricanes and the LC/LCE/frontal features for most of its record.

The effect on the currents by LC/LCE/frontal features and hurricanes is most prominent in the top 500 m of water depth. Color contours of the current speed, current direction and water temperature versus depth and time were created and analyzed to assess the periods of most impact by the different features. In these contours, thin horizontal lines depict the depth of various instruments that contained pressure sensors from which the mooring drawdown due to the currents was calculated. The depth of the current measurements was then adjusted as displayed in these contours. It is interesting to note that while hurricanes at times generated some higher current speeds, they caused minimal mooring drawdown as compared to the influence of the LC or and LCE. LC or LCE intrusions generated the strongest upper layer currents and caused more significant mooring blow-over, as is illustrated in some of the following figures.

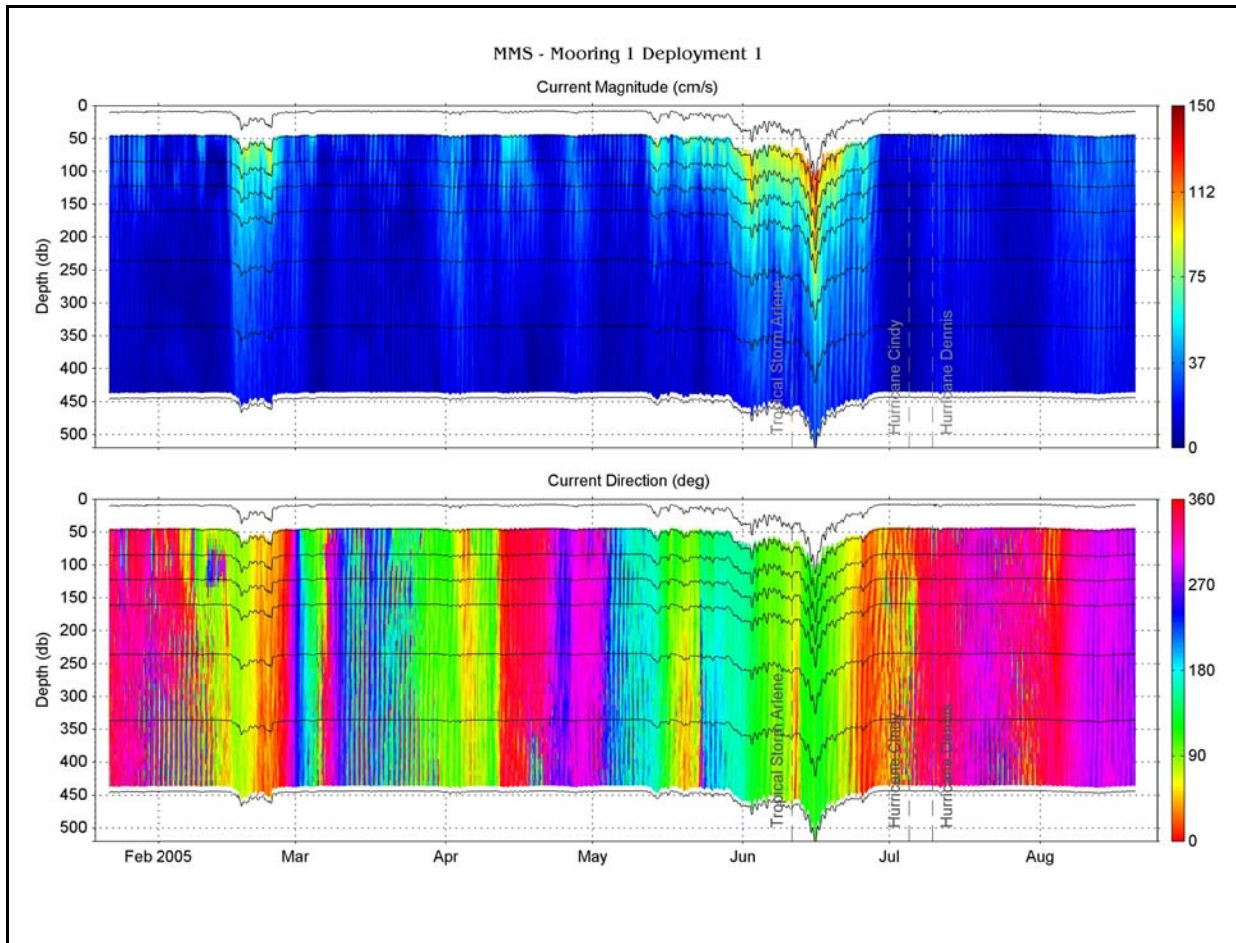


Figure 5.1-1. Color contour of speed (top) and direction (bottom) for M1 during deployment 1 showing the effects of mooring draw down due to high currents. Dark horizontal lines through the contours indicate the depth of each sensor on the mooring line including the ADCP.

For instance, Figure 5.1-1 shows a period when these currents pulled the mooring over compared with times that storms and hurricanes passed through the GOM. Note the large draw down in mid June between Tropical Storm Arlene and Hurricane Cindy. This is when Eddy Vortex is calculated to have detached for the third time from the LC. Also of note is the drawdown in the later part of February when Eddy Vortex detached for the first time from the LC. In one instance the blow over caused by the LC could be seen in the depth measurement for a current meter at nearly 200 m depth (Figure 5.1-2).

For perspective, an initial view of the influence of Hurricane Katrina which occurred in late August 2005 can be seen in Figure 5.1-3. Inertial oscillations of currents generated by Katrina are quite evident, yet are not as strong nor have the same drawdown effect on the moorings as the LC events. The effects of hurricanes on the circulation will be described in more detail in later sections of this Chapter.

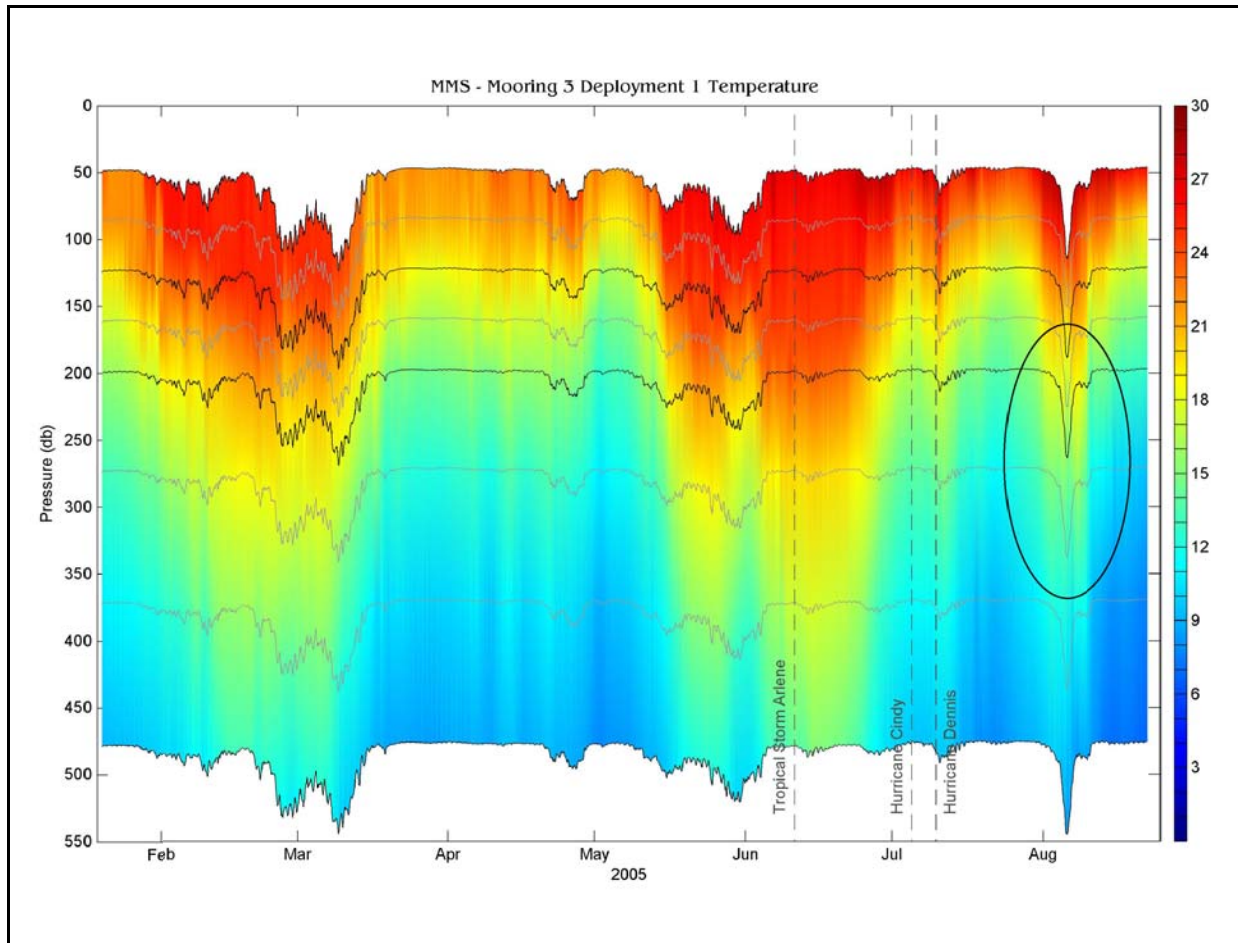


Figure 5.1-2. Color contour of temperature for M3 during deployment 1. Of note is the draw down effect on the meters by the Loop Current such as in early August (circled).

In all of these appendices, the variation in the depth of the measurements is displayed. The temperature data show best the influence of LC and LCE events. The pressure readings on the instruments, as depicted by the thin horizontal lines, provide good perspective on the periods within the mooring records showing the influence of the various tropical storms and hurricanes.

An initial understanding of the nature of the physical processes which occurred during the measurement period can be obtained by simple visual inspection of the moored time series data plotted in composite form at several depths that span the entire water column. Gridded, interpolated current speed at five ADCP depths and all single point current meters for each mooring deployment are illustrated in Figure 5.1-4a-c. Tick marks along the y axis are spaced at 50 cm s^{-1} intervals, tick labels indicate record depth. Clearly, currents during both deployments in this region showed a high degree of coherency at water depths above 500 m. High-speed current events (near surface speeds exceeding 100 cm s^{-1}) were strongest and more frequent at M3 than at M1 in particular due to the LC impacting M3 more frequently due to its position farther south in the study area.

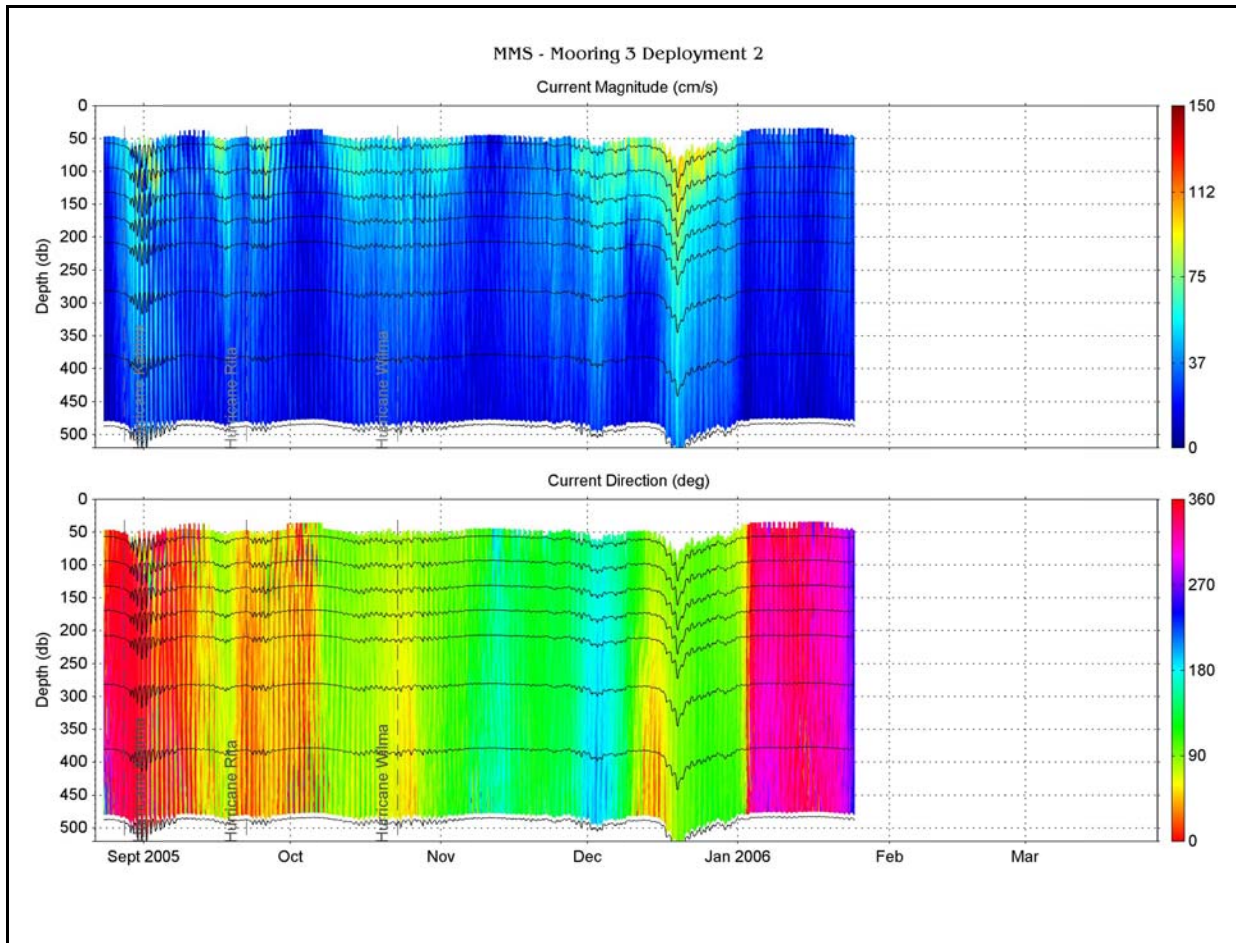


Figure 5.1-3. Color contour of speed (top) and direction (bottom) for M3 during deployment 2 showing inertial oscillations on the mooring due to hurricanes. Dark horizontal lines through the contours indicate the depth of each sensor on the mooring line including the ADCP.

Occasionally, the observations indicated a strong barotropic component to the flow structure. For example, in mid-August 2005, at mooring M3, there was a barotropic event associated with the detachment and reattachment of an LCE. The feature was coherent throughout the water column and peaked in the upper ocean with only gradual diminishment with depth. In October through mid-December 2005, there was a second barotropic current event that was seen in the velocity data collected at M2 and M3. During this second event, the increase in current speed was associated with a LC meander into the study area.

Large-amplitude inertial oscillations excited immediately after the passages of Hurricanes Katrina in late August 2005 and Rita on 21 September 2005, are easily identified in the time series. The current oscillations persisted for at least two weeks after the passage of the storms. Inertial motions were strongest at M3 and penetrated down to 500 m. Hurricane Dennis, which entered the Gulf on July 9th, and later passed very close to the study area, was evidenced in the less intense inertial oscillations at M1 around this time. A more detailed discussion of the effects on the circulation of the passage of these hurricanes is presented later in this Chapter.

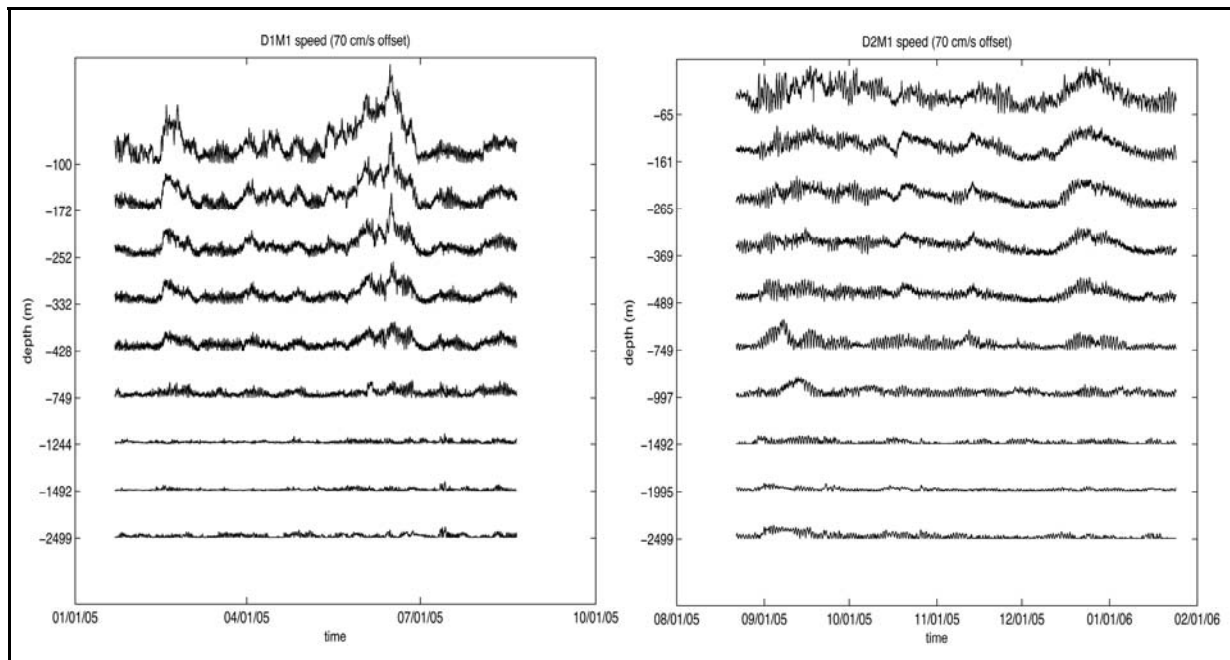


Figure 5.1-4a. Gap-filled, gridded current speed from five moored ADCP depths and moored current meters M1 for deployments 1 (left) and 2 (right). Instrument depth is indicated on the y-axis.

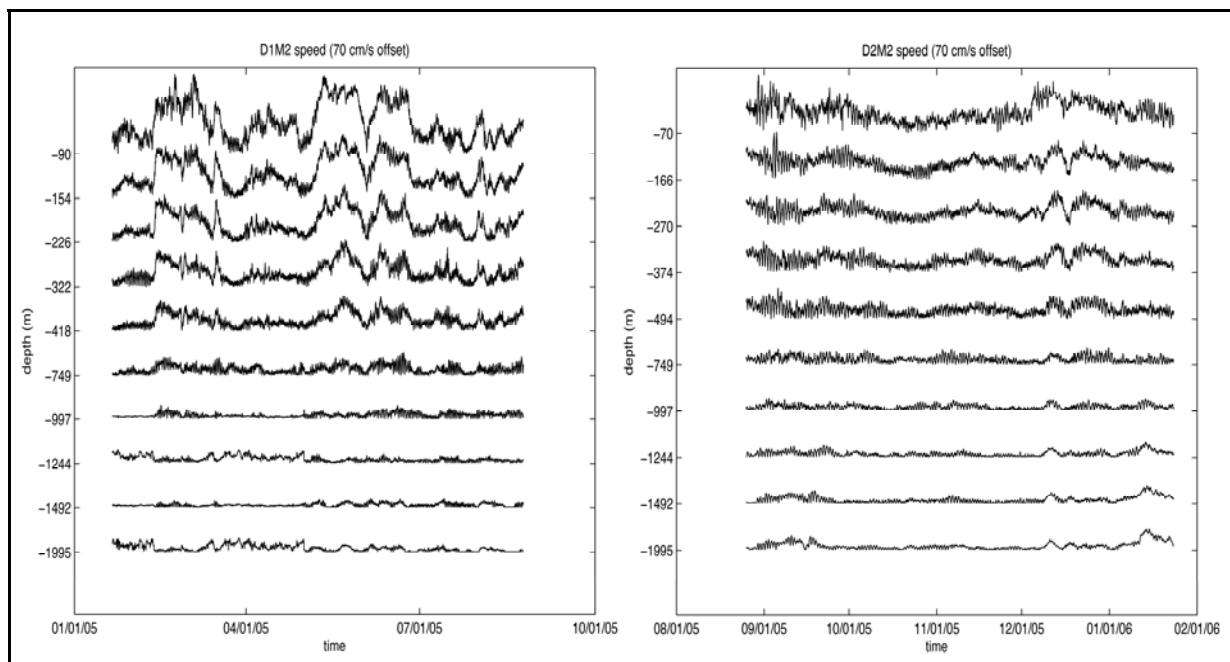


Figure 5.1-4b. Gap-filled, gridded current speed from five moored ADCP depths and moored current meters M2 for deployments 1 (left) and 2 (right). Instrument depth is indicated on the y-axis.

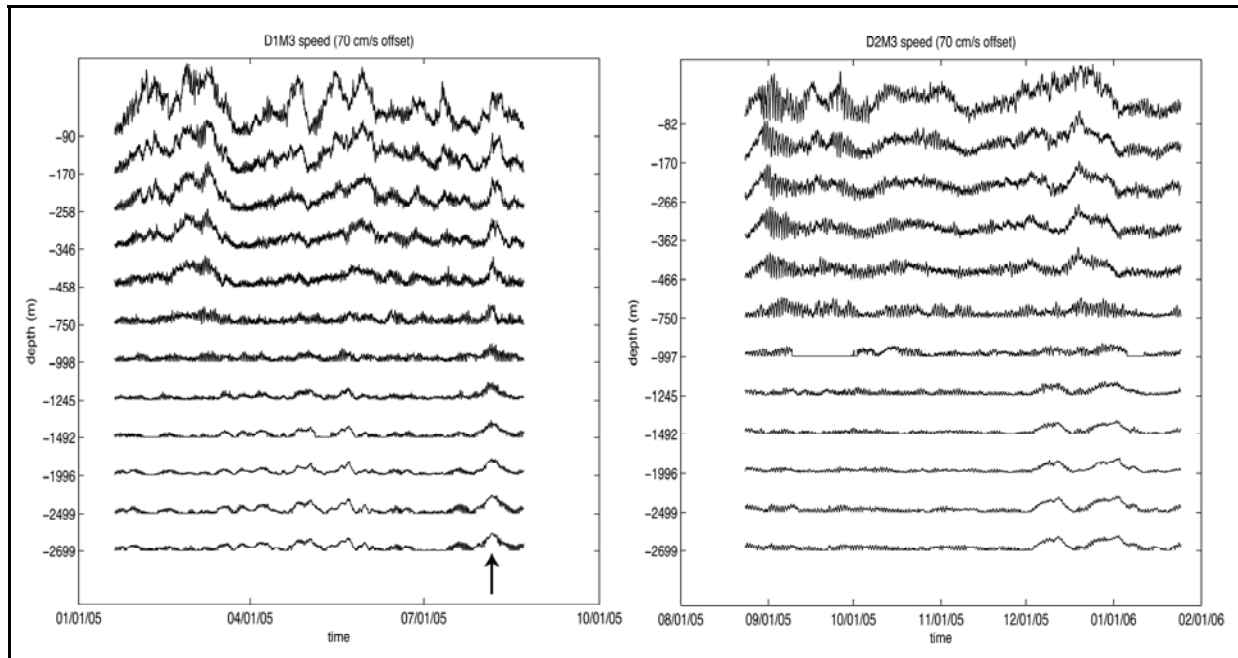


Figure 5.1-4c. Gap-filled, gridded current speed from five moored ADCP depths and moored current meters M3 for deployments 1 (left) and 2 (right). Instrument depth is indicated on the y-axis. Black arrow indicates barotropic event during August 2005. The flat periods in the current meter record at 997 m are periods of no data.

5.1.2 Current Roses, Joint Probability Distributions of Speed by Direction

Calculations of current speed within 5 cm s^{-1} speed ranges by eight directional quadrants were performed for all measurement depths for all moorings. These calculations were performed for each deployment period separately. From these, current roses were developed to aid interpretation of the current meter data.

5.1.3 Current Speed Persistence Tables

The persistence of various current speed ranges over five duration periods spanning up to 42 hours duration was also computed for all measurement depths for all moorings. Again, these calculations were performed for each deployment period separately.

5.1.4 Velocity Spectra

Power spectral density profiles for velocity components at all depth levels, for both mooring deployments, were generated using Fast Fourier Transform (FFT) methods. Following Welch's Method, the velocity time series were subsampled into overlapping segments of 512 points. Segments were preconditioned using a 512-point Kaiser-Bessel window; segments overlapped by 50%. The periodogram for each segment was computed using the FFT and then all periodograms for a given record were averaged to produce the spectra discussed in this section. A convenient property of the Kaiser-Bessel window is that it allows each 512-segment to be treated as statistically independent. This technique significantly increases the degrees of freedom and, therefore, the statistical confidence of each spectra estimate. If the size of the longest, gapless segment of the time series was less than 512 points, which was the case for some records at the surface, the data were sub-sampled, and a Kaiser-Bessel window the size of the sub-sample was used for preconditioning. As previously stated, records were corrected for mooring drawdown, interpolated, and eight tidal constituents were removed using the method of cyclic descent before analysis.

Spectra (non-variance preserving) estimates for moorings M1, M2, and M3 for u and v velocity components are presented at selected depths throughout the water column in loglog form for each deployment in Figures 5.1-5, 5.1-6, and 5.1-7, respectively. The purpose of these figures is to investigate how the spectral character of current velocity at each mooring location changes with depth.

The typical velocity spectrum derived from the velocity time series of historical GOM measurements display a red energy distribution (weighted to low frequencies), with a peak centered near the inertial frequency (i.e., close to 1 cpd). There is an energy minimum commonly seen in the 5 cpd range as well. Near-surface motions having periods ranging from 2-15 days are usually attributable to atmospheric weather conditions. Velocity spectra from the Eastern GOM moorings followed this energy partitioning.

5.1.4.1 Upper Ocean Spectra

In general, spectral energy throughout the frequency domain shown in Figures 5.1-5, 5.1-6 and 5.1-7 were greatest in the shallow ocean (< 300 m depth). As expected, surface records (~ 50 m) contained larger weather-band variance than deeper records since the influence of winds on currents generally diminishes with depth. This was especially true at moorings M2 and M3, where the variance steadily increased between 0.9 cpd and 0.1 cpd. Spectral peaks at periods of seven to eight days were evidenced in some near-surface records, in particular mooring M1 during deployment 2. Inertial band energy was present throughout the water column; however, the amplitude of the inertial peak tended to narrow and decrease with depth. During the first deployment, the moorings each had similar inertial energy amplitudes. Spectral estimates based on data from the second deployment show moorings M2 and M3 had significantly more energy in the inertial band than mooring M1, again owing to the closer proximity of these mooring to the centers of Hurricanes Katrina and Rita.

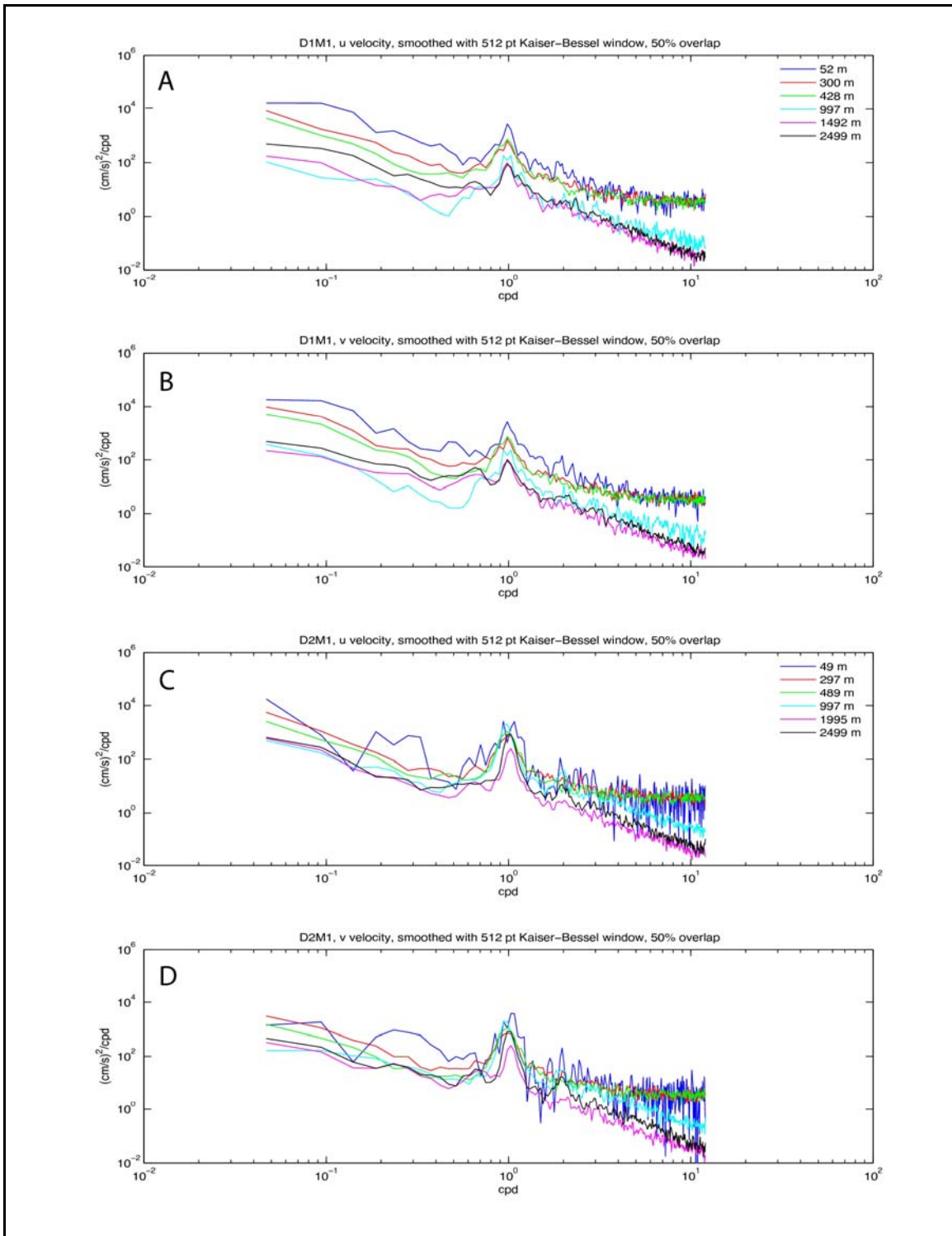


Figure 5.1-5. Panels A and B give power spectral density of detided, gap-filled u and v velocity components, respectively, at 6 depths at mooring M1 from deployment 1. Deployment 2: Panels C and D.

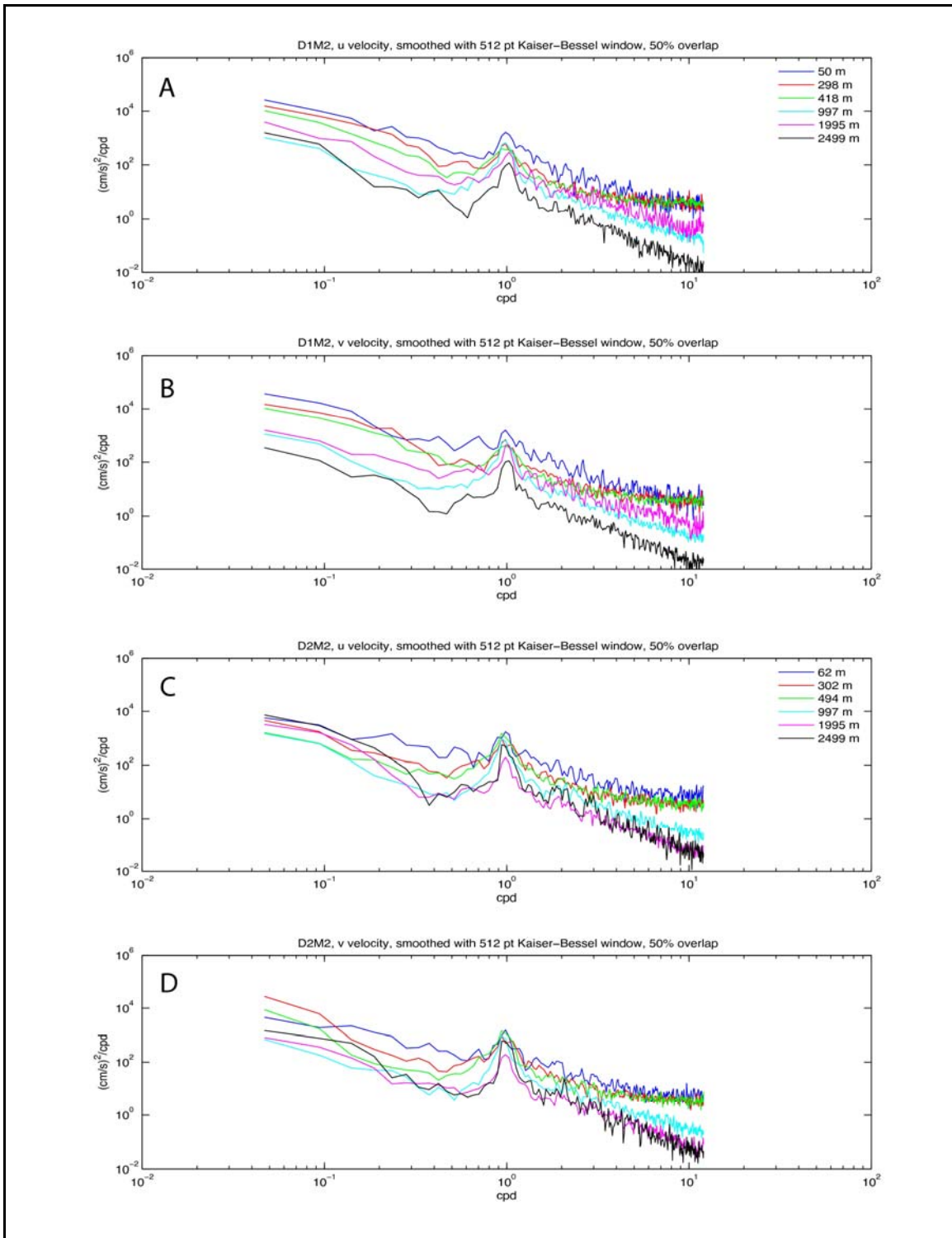


Figure 5.1-6. Panels A and B give power spectral density of detided, gap-filled u and v velocity components, respectively, at 6 depths at mooring M2 from deployment 1. Deployment 2: Panels C and D.

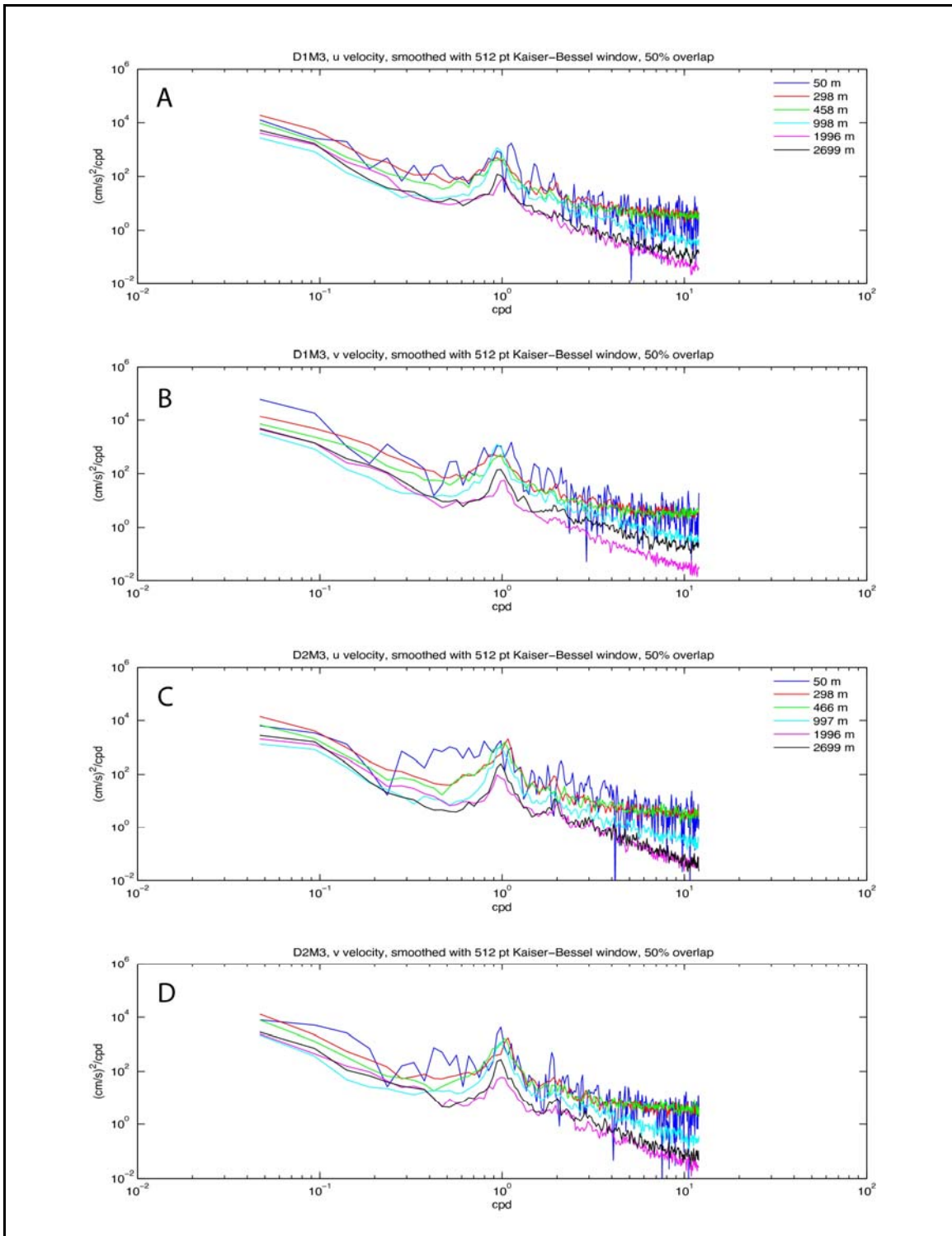


Figure 5.1-7. Panels A and B give power spectral density of detided, gap-filled u and v velocity components, respectively, at 6 depths at mooring M3 from deployment 1. Deployment 2: Panels C and D.

Near-surface spectral variance associated with periods of 20-60 days were typically associated with mesoscale processes such as the LC or its associated eddies. Low-frequency spectral estimates in the upper ocean at moorings M1, M2, and M3 were roughly equal. There was slightly more sub-inertial energy present during deployment 1, especially at the 20 – 60 day period. This is likely attributable to the penetrations of the LC and Eddy Vortex into the study area multiple times during deployment 1.

The super-inertial domain, i.e., frequencies greater than 1 cpd, generally decreased with increasing frequencies. There was some evidence of semi-diurnal variance, likely associated with semi-diurnal tides; however, the variance associated with the semi-diurnal tides rarely raised above background levels.

5.1.4.2 Deep Ocean Spectra

Relative to the surface, spectral estimates found in deeper records of the Eastern GOM moorings were less energetic. The overall shapes of the trends of the spectra estimates of the deeper records closely resembled those estimated from records of the upper ocean. Generally, estimates at super-inertial frequencies tended to decrease faster with increasing frequency in the deeper records. Subinertial variability, particularly in the lowest bands shown, decreased from south to north, i.e., from mooring M3 to M1. This may be attributed to the motions associated with the LC and LCE events at each mooring. There were some cases where low frequency variance (20 – 60 day period band) in the deepest record (usually 2500 m) was greater than the energy in the record at ~ 1000 m, which could be evidence of topographic Rossby waves. This is further considered in Chapter 6.

5.1.5 Coherency Spectra

5.1.5.1 Current – Wind Coherence

Coherency, coherence of spectral estimates of independent records, was estimated for all combinations of u and v wind velocity and u and v current velocity at all ADCP depths for all gapless time-series. In general, no statistical coherency of currents with wind was observed, except for incidental coherency near the inertial frequency. The coherency at this frequency was associated with random phase and were not seen deeper than the shallowest two or three velocity time-series for each mooring. The coherency near the inertial frequency was present at all moorings from data collected during deployment 2. This was likely related to the occurrences of Hurricanes Katrina and Rita, which caused high amplitude inertial currents in the study region for weeks after their passage.

At mooring M1, during deployment 1, there was a weak low frequency correlation between current and wind. The coherency between north-south current velocity and north-south wind velocity showed significant peaks at ~ 50 day period with constant phase. The coherency penetrated downward into the water column.

5.1.5.2 Vertical Current – Current Coherence

The coherency spectrum was estimated for current velocity components at different depths, i.e., vertically relative to the uppermost time-series at each mooring and horizontally between velocity components at similar depths at different moorings. To increase statistical reliability, the coherency spectra were smoothed in the frequency domain over 9 points.

The vertical coherence at low frequencies between velocity time-series at 100 m and records to depths of ~500 m depth were mostly significant for every mooring deployment. Coherency was also observed at near-inertial frequencies. Coherency in the inertial band between near-surface velocity and records between 100 – 200 m diminished owing to the location of the pycnocline at these depths. Below this depth, inertial motions may be attributable to other forcing processes such as eddy features. Inertial oscillations at the surface and at depth therefore would not be expected to be coincident or phase locked. The exception to this is when a powerful hurricane is able to affect layers below the pycnocline.

At mooring M1, deployment 1, there was significant low frequency coherency between current velocity at 100 and 428 m depth at periods above 7 to 8 days as evidenced by a comparison of the individual time series (Figure 5.1-8). The coherency spectrum (Figure 5.1-9: upper left) clearly shows significant coherency at the low frequencies (<0.2 cpd). The coherency phase spectrum (Figure 5.1-9: lower left) shows that the phase between the low frequency components being close to zero indicating in-phase oscillations. The admittance spectrum (Figure 5.1-9: upper right) shows the gain between the spectral components of the two series and indicates that the variance in the 428 m record was about 10% of that of the record at 100 m. The admittance at super-inertial frequencies was close to one, indicating nearly equal variances. Deployment 2 data indicated weaker low frequency coherency; however, the coherency was significant only at the lowest frequency, around 80 days, with zero phase difference.

At mooring M2, deployment 1, significant coherency was distributed similar to that seen at mooring M1. In the upper layer, low frequency coherency was seen at periods longer than about eight days and at near inertial peaks. This coherency extended deeper than at mooring M1. For example, north-south velocity was coherent with the surface at depths reaching 1244 m and east-west velocity was coherent with surface east-west velocity down to 750 m. For the second deployment, north-south velocity at mooring M2 was coherent throughout the upper water column (to about 500 m depth) at low frequencies with zero phase lag, which implied a significant correlation at zero lag between surface data and data throughout the upper 500 m, as seen in Figure 5.1-10. This was not the case for the east-west velocity component, as it was only correlated at the lowest frequency estimate (~80 days). The near-inertial correlation in both velocity components, between the surface and at depth, diminished around 120 m at mooring M2 during deployment 2.

Vertical coherency at mooring M3 during deployment 1 presented a similar picture to moorings M1 and M2, with significant zero lag low frequency correlation throughout the upper water column (to ~500 m) for east-west velocity component, but only to 350 m for the north-south velocity component. Data at mooring M3 from deployment 2 were only significantly correlated down to 300 m for the east-west velocity component and 100 m for the north-south velocity component.

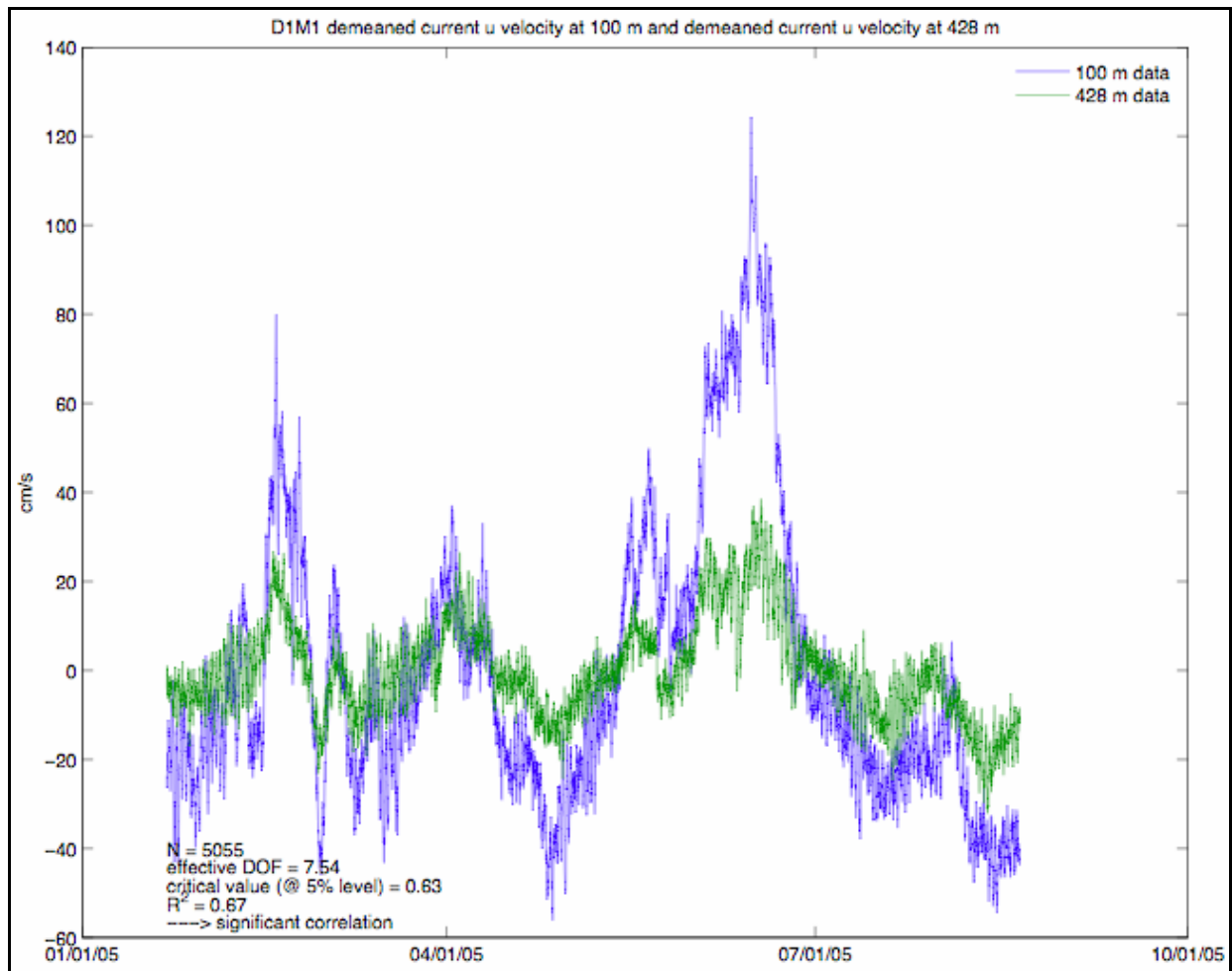


Figure 5.1-8. Detided, gap-filled, gridded u velocity time-series at mooring 1 during deployment 1 at 100 m and 428 m. Strong low frequency in phase coherency indicates significant correlations between currents at these two depths.

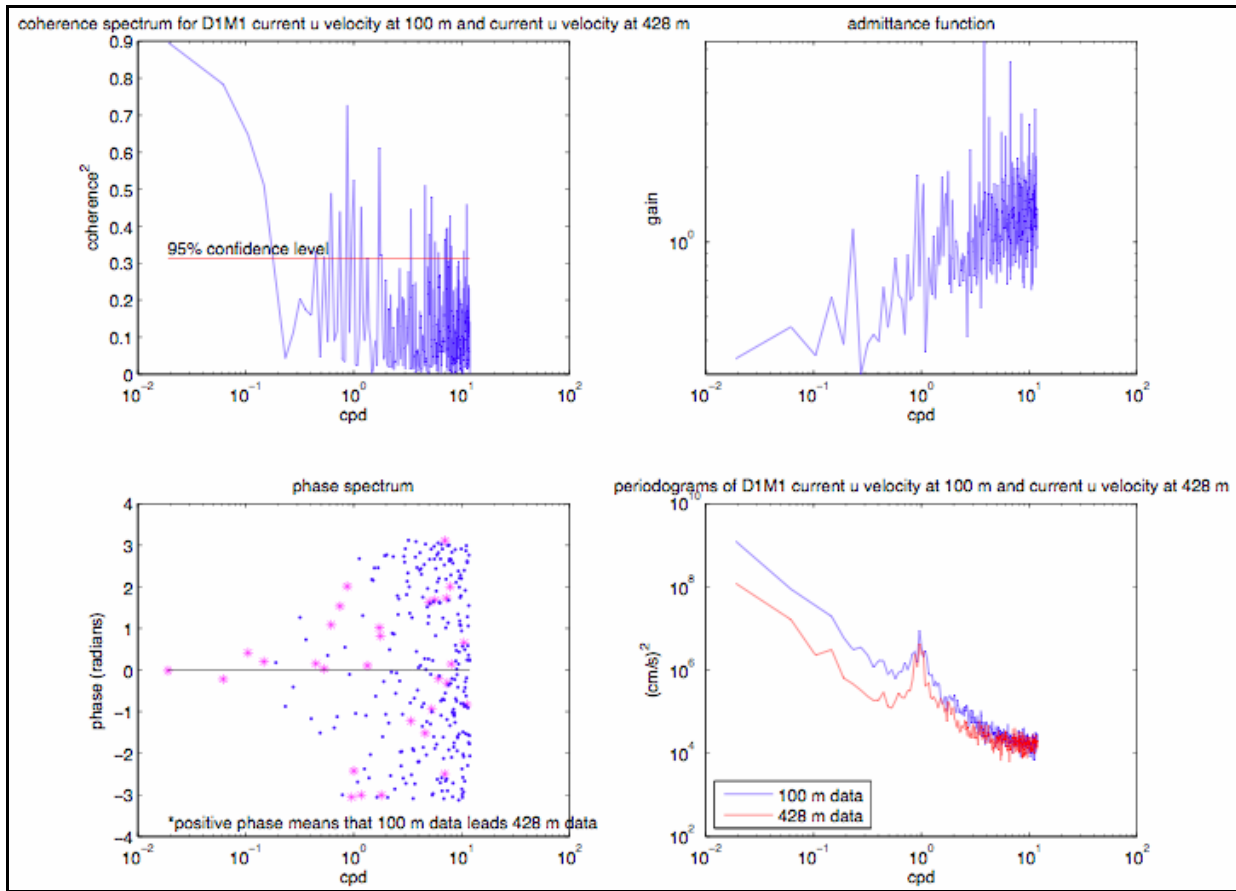


Figure 5.1-9. (Clockwise from top left) Coherence, admittance, power, and phase spectra between u velocity components at 100 m and 428 m at mooring 1 during deployment 1. Magenta asterisks in the phase spectrum indicate significant coherency at the corresponding frequency.

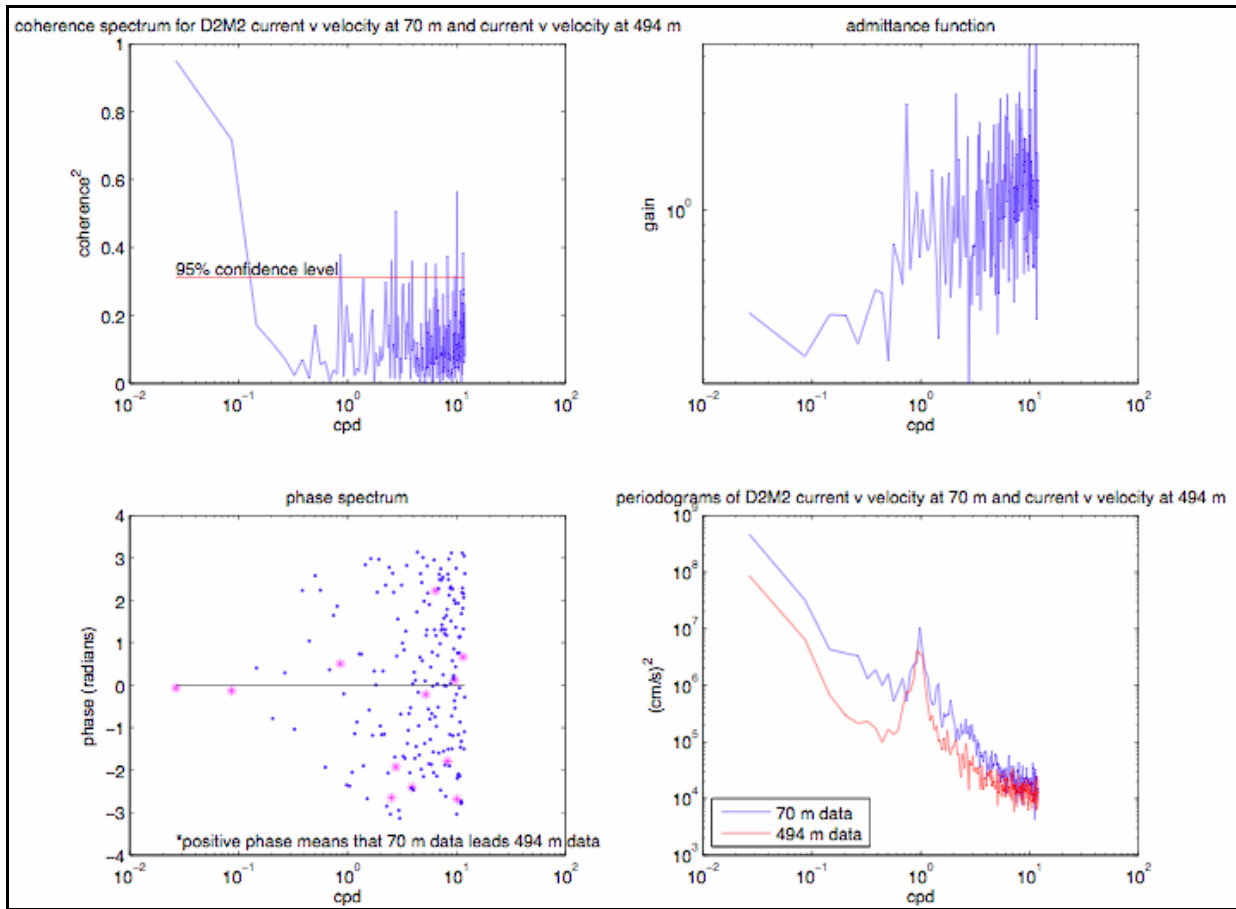


Figure 5.1-10. (Clockwise from top left) Coherence, admittance, power, and phase spectra of north-south (v) velocity components at 70 m and 494 m at mooring M2 during deployment 2. Magenta asterisks in the phase spectrum indicate significant coherence and phase at the corresponding frequency.

5.1.5.3 Horizontal Current – Current Coherency Spectra

Estimates of the coherency spectra for horizontal separations were calculated between moorings for all velocity combinations at the same depth. East-west velocity at moorings M1 and M2 were coherent at the lowest frequency band (~ 90 days) and with zero phase lag. Near the inertial frequency in the upper water column, coherency was found at 750 m, 1244 m, and 1492 m. The phase of the correlation at the near inertial peak was variable with depth. The east-west velocity component at mooring M1 and north-south velocity component at mooring M2 were also coherent at low frequencies but with a phase difference of about 1 radian ($\sim 90^\circ$) at the lowest frequency, which indicated that the M1 velocity lead the M2 velocity. Coherency between mooring M1 v velocity and mooring M2 u velocity, as well as coherency between v velocity at both moorings indicated coherency at low frequency with a phase of ~ -1.0 radian, which meant that M2 lead M1. The phase relationship of the two components likely indicated the influence of the eddy fields. Deeper current meter records, except for the records at 1995 m, were only significantly correlated between north-south velocity components at both moorings in the inertial band and at low frequencies ($\sim 80 - 90$ days), as seen in Figure 5.1-11. This may be an indication of topographic steering along the bathymetry.

Mooring M1 and mooring M3 east-west velocities were coherent at near-inertial frequencies at every depth in the upper layers. M1 u and M3 v were correlated at the fundamental frequency (~ 90 days) at a phase of ~ 2 radians (180°) throughout the water column and near inertial peaks were present down to 998 m. v velocity at M1 and M3 were correlated at low frequencies down to 998 m with zero phase difference. Only near-inertial correlation was present between M1 v and M3 u .

East-west velocity at moorings M2 and M3 illustrated very little significant coherency beyond some intermittent near-inertial correlations in the upper water column; however, the east-west velocity was coherent between moorings M2 and M3 in all current meter records in the deep ocean at periods of about 50 days (Figures 5.1-12 and 5.1-13). North-south velocity was correlated at low frequencies in the upper water column, and there was correlation at 20-day periods and above between the data from the deep current meters at 750, 998, and 1245 m. There were some near-inertial peaks in the upper water column between M2 east-west (north-south) velocity and M3 north-south (east-west) velocity.

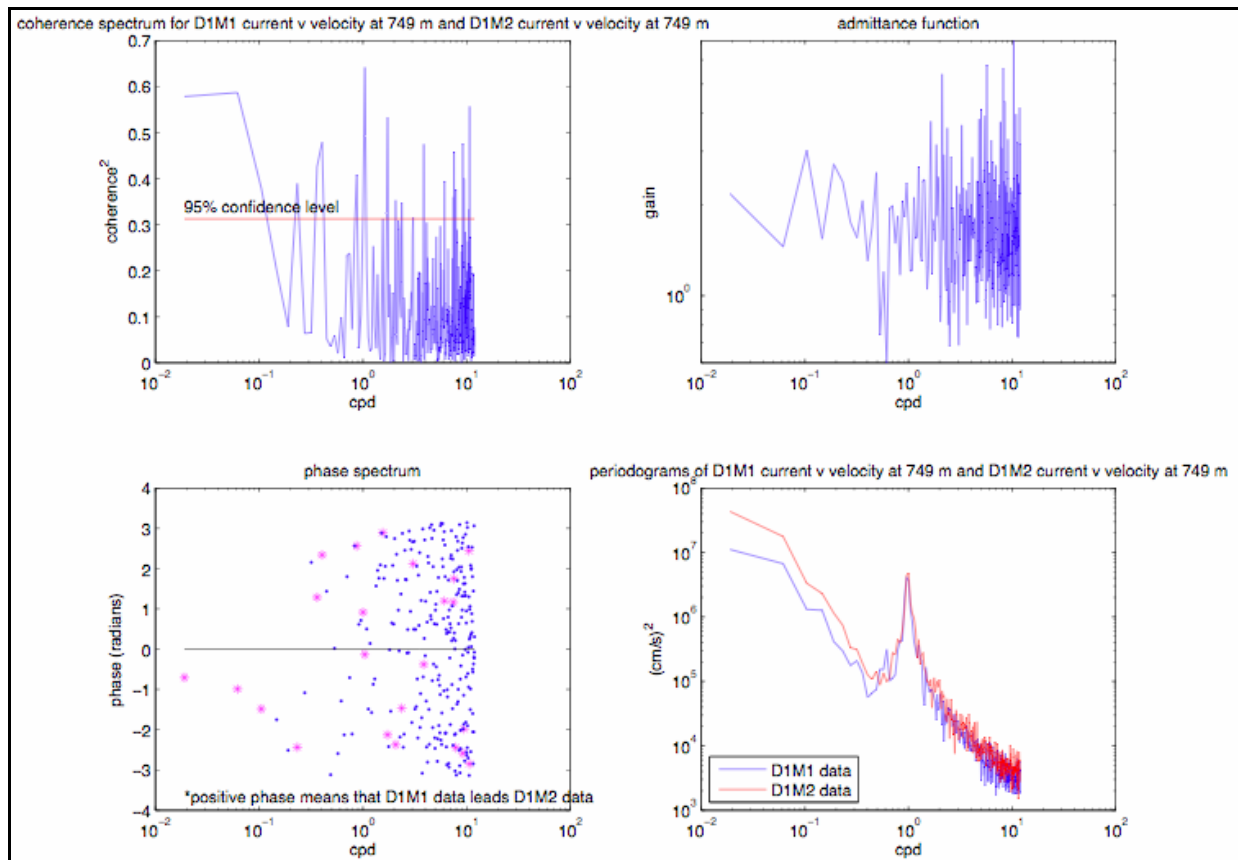


Figure 5.1-11. (Clockwise from top left) Coherence, admittance, power, and phase spectra between v velocity components at 749 m at mooring M1 and mooring M2 during deployment 1. Magenta asterisks in the phase spectrum indicate significant coherency at the corresponding frequency.

5.1.6 Mean, Minimum and Maximum Currents

Standard statistics were calculated for the current meter records, including the record-length mean current, its standard deviation, and the minimum and maximum currents that occurred in each record. Vertical profiles of the record-length mean, mean plus and minus one standard deviation, and minimum and maximum values for the u (east-west) and v (north-south) velocity components for all instruments and ADCP depth bins on moorings M1, M2, and M3 are plotted in Figures 5.1-14, 5.1-15 and 5.1-16, respectively. Appendix C contains the basic statistics in tabular form. The basic pattern revealed in this series of figures is that current velocity was generally greatest near-surface and decreased with depth. The statistics below depths of 1000 m were typically constant to the bottom. Some of the profiles showed that for the uppermost surface velocity bins the record-length mean, standard deviation, and minimum/maximum envelopes tended to have a slightly different character than measurements at deeper bins, i.e., around 100 m. This may have been because fewer observations were associated with the surface bins due to instrument drawdown and the effects of gridding the data to non-overlapping depth bins. This effect was particularly relevant since most data dropout at these levels occurred during strong current events.

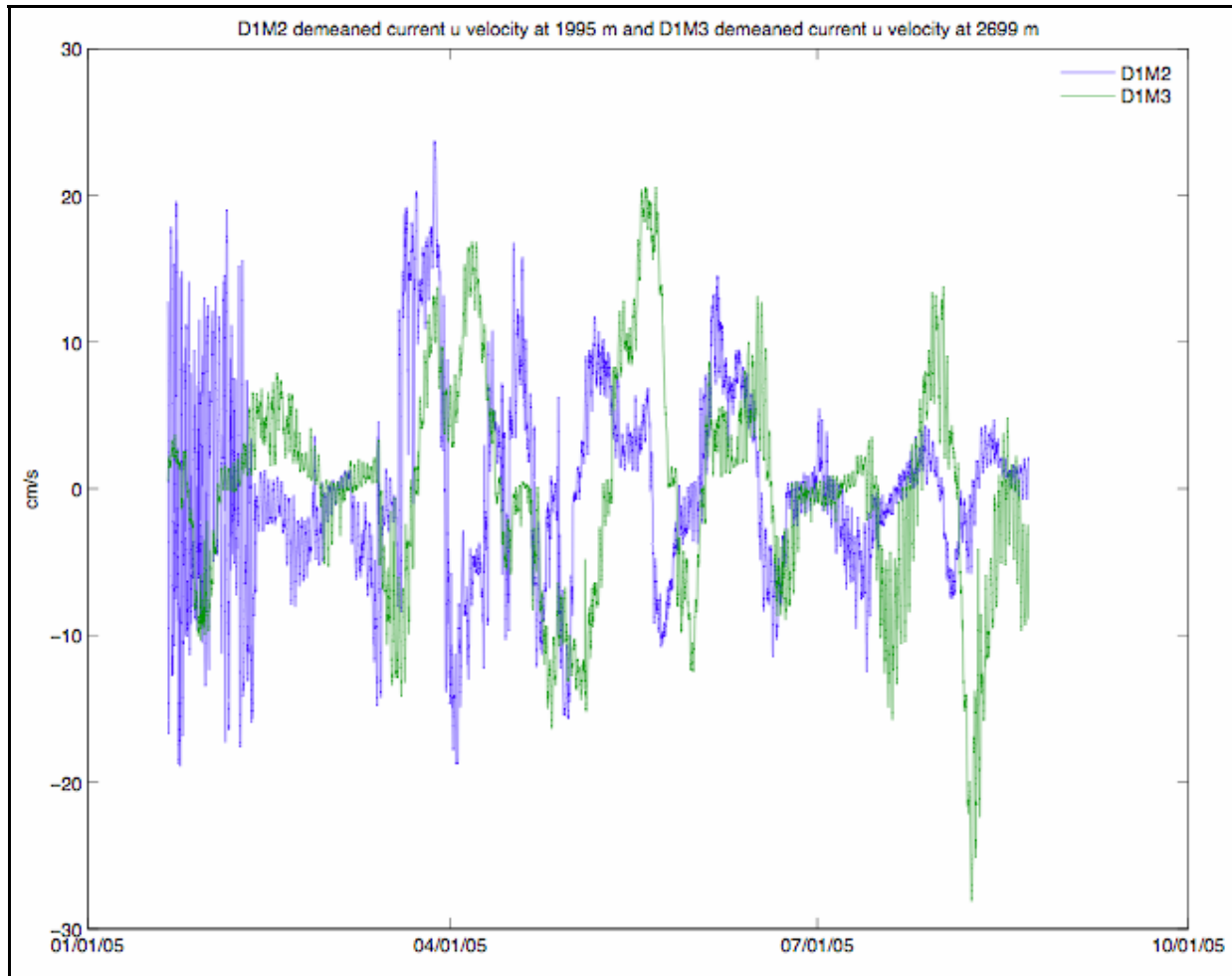


Figure 5.1-12. Detided, gap-filled, gridded east-west velocity time-series at mooring M2 and mooring M3 during deployment 1 at 1995 m and 2699 m respectively.

The mean current velocity at mooring M3 (Figure 5.1-16) was predominantly to the southeast during deployment 1 and eastward during deployment 2. We attribute this to the relative location of the mooring to the northern edge of the LC and the developing anticyclonic eddies during the early months of 2005. The southern limb of a frontal cyclonic eddy passed over this region during a large period of deployment 2 producing mostly eastward-directed currents. The southward velocity at M3 was attributed to the position of the LC relative to the mooring in early April 2005. In May, the northeastern limb of the LC moved into the study area, producing large southward current velocities. During the second deployment, the mean north-south velocity component at M3 was close to zero. Mooring M3 was also closest to Hurricanes Katrina and Rita; therefore, the minimum/maximum current velocity envelopes were greatest here than for any other mooring deployment.

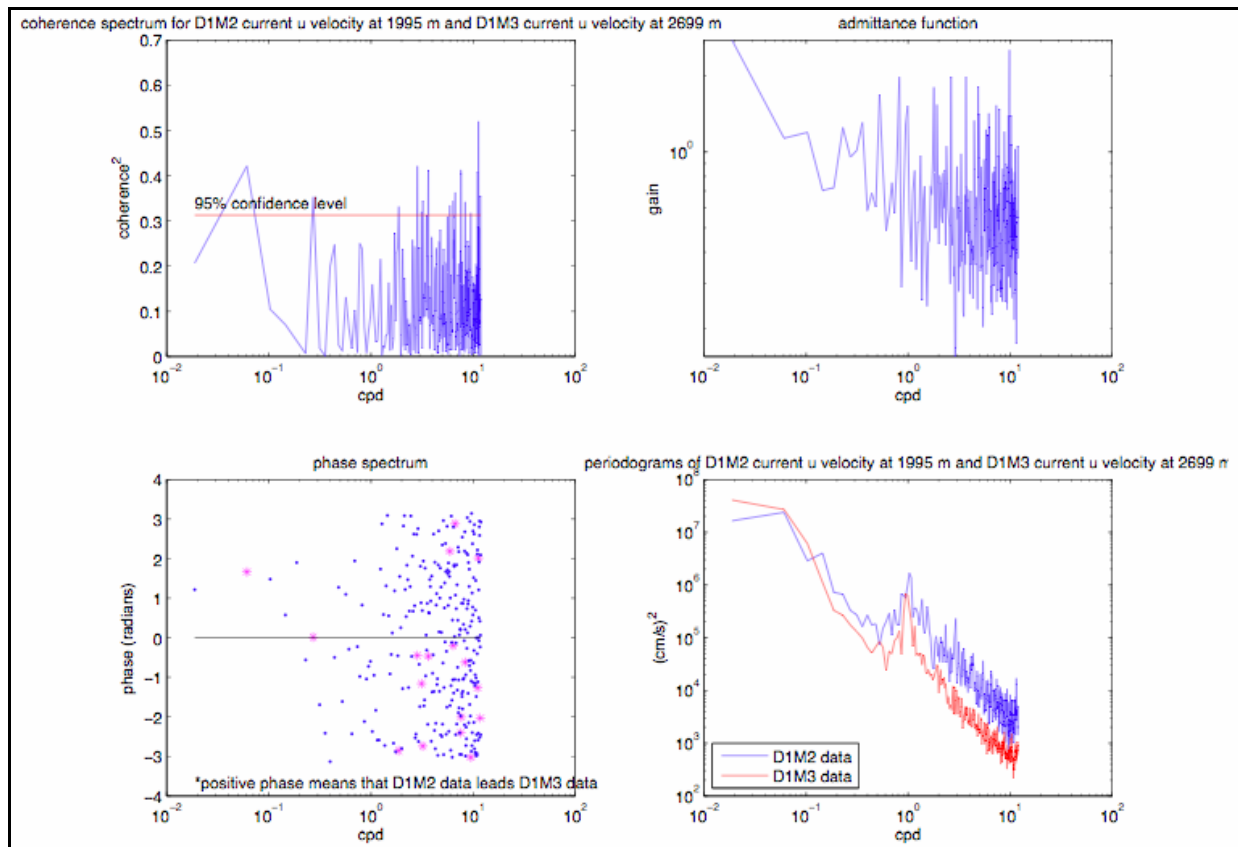


Figure 5.1-13. (Clockwise from top left) Coherence, admittance, power, and phase spectra between u velocity components at mooring 2 and mooring 3 during deployment 1 at 1995 m and 2699 m respectively. Magenta asterisks in the phase spectrum indicate significant coherency at the corresponding frequency.

Indications of energetic current events near the ocean surface were present at moorings M1 (Figure 5.1-14) and M2 (Figure 5.1-15) however to a lesser degree than that seen at M3. During deployment 1, current velocity was primarily southeastward at mooring M2, and to the east at mooring M1. However, during the second deployment, currents were dominated by various cold core frontal eddies moving in and out of the study area, and the result were relatively small mean current velocities.

At mid-water depths, i.e., around 750 m, the magnitude of the minimum and maximum currents for deployment 2 at mooring M1 was a maximum. An examination of the time series showed that the large currents associated with this peak occurred in early September 2005 as a long period oscillation with inertial motions superimposed. Comparison with records above and below showed little phase-locked or lagged correlation to any one particular event. The timing of these inertial oscillations at this depth were consistent with the interpretation that they were initiated at the surface by Hurricane Katrina on August 26 and propagated downward in the water column; however, the forcing of the longer period oscillation was not certain. Inertial band energy was seen at these depths at Moorings M2 and M3; however, there are no low frequency motions and therefore no mid-water peak in basic statistics.

Near-bottom (~2500 m) statistics from deployment 2 at mooring M1 showed slightly larger extreme values than values 500 m above bottom. This is the only deployment showing evidence of bottom intensification. We note that at M1 there was no indication of low-frequency oscillations that extended throughout the water column and that bottom motions were not coherent with surface motions.

Basic statistics for M4 were not plotted; a table containing these values was included in Appendix C. Record-length mean and standard deviation at M4 were near zero for both deployments and were consistent with values at similar depths at other moorings.

5.1.7 Extreme Current Value Distributions

In practical engineering applications, one often needs an estimate of the extreme value of the current speed over some return interval. In this section, we give examples of how that might be done for the measurements made by the Aanderaa current meters on the moorings.

Extreme value theory assumes that the sample distribution is made up from independent and identically distributed random variables. The hourly values of measured current speed are serially correlated so they cannot be used directly. Two methods are commonly used to produce independent variables from a serially correlated time series. The peaks over threshold (POT) method finds the peak values in intervals that exceed some specified threshold. The POT method is not very well suited to the Aanderaa current meter data because there are many closely spaced peaks that are likely not independent. The block maximum method finds the maxima in intervals of a specified duration. In cases where long time series are available, yearly maxima are often specified, such as for flood data. We only had one year of data, but the signal was highly variable on short time scales. It appeared that something like weekly maxima were statistically independent. Tests showed that taking maxima for a range of intervals around seven days did not change the results very much.

We fit the weekly maxima to the generalized extreme value distribution (GEV). The GEV is the limit distribution of the maxima of a sequence of independent and identically distributed random variables. The cumulative distribution function of the GEV is given by:

$$F(x) = \exp \left\{ - \left[1 + \xi \left(\frac{x - \mu}{\sigma} \right) \right]^{-1/\xi} \right\}, \quad (5.1.1)$$

where μ is the location parameter, σ is the scale parameter, and ξ is the shape parameter.

If ξ is negative the maximum value of x is bounded by $\mu - \sigma/\xi$. If ξ is positive the distribution is unbounded. The fits of the weekly maxima to equation 5.1.1 were made by the maximum likelihood method.

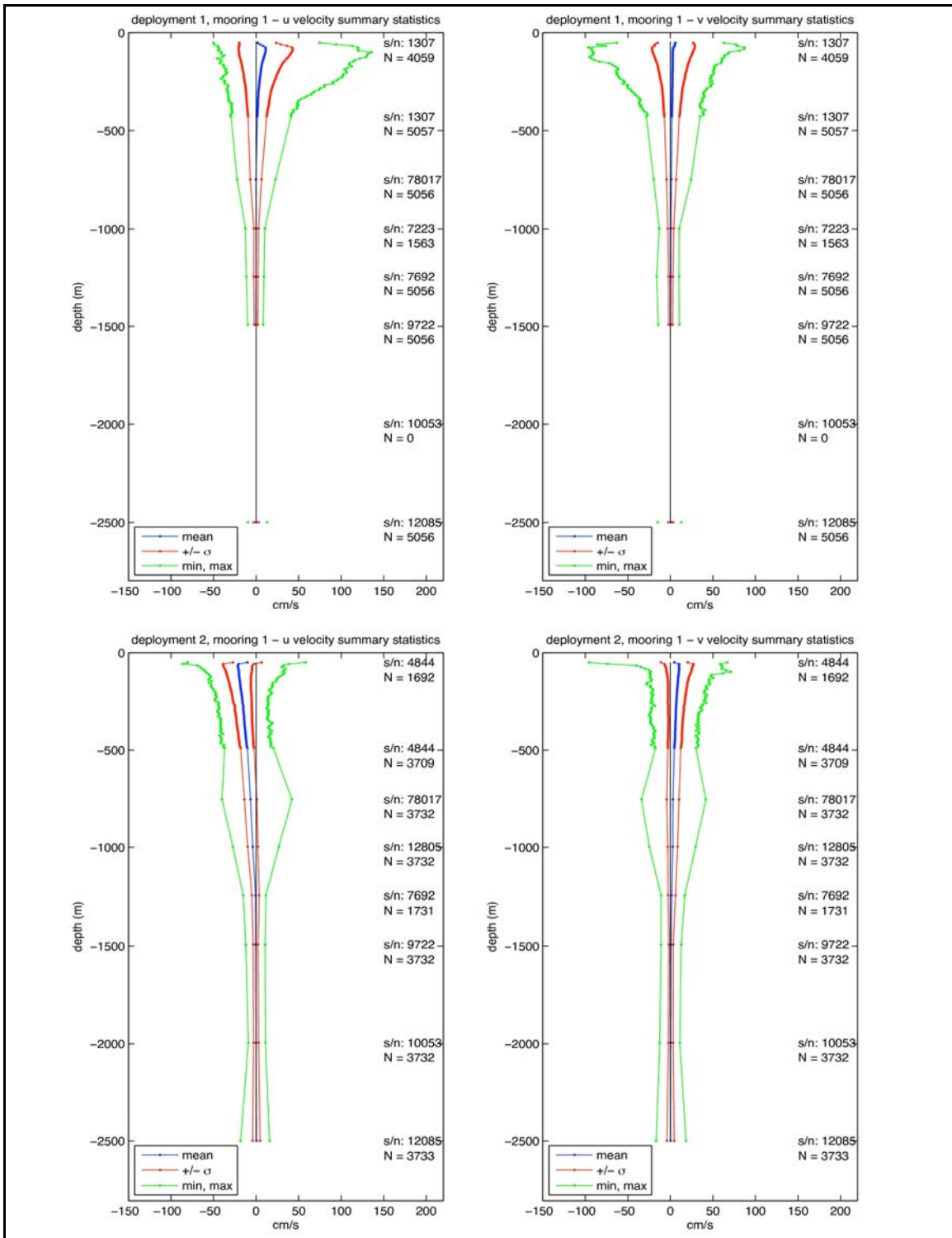


Figure 5.1-14. Vertical profiles of record-length mean, standard deviation, minimum, and maximum velocity components for mooring M1 (left: east-west component; right: north-south component). Top row: Deployment 1. Bottom row: Deployment 2.

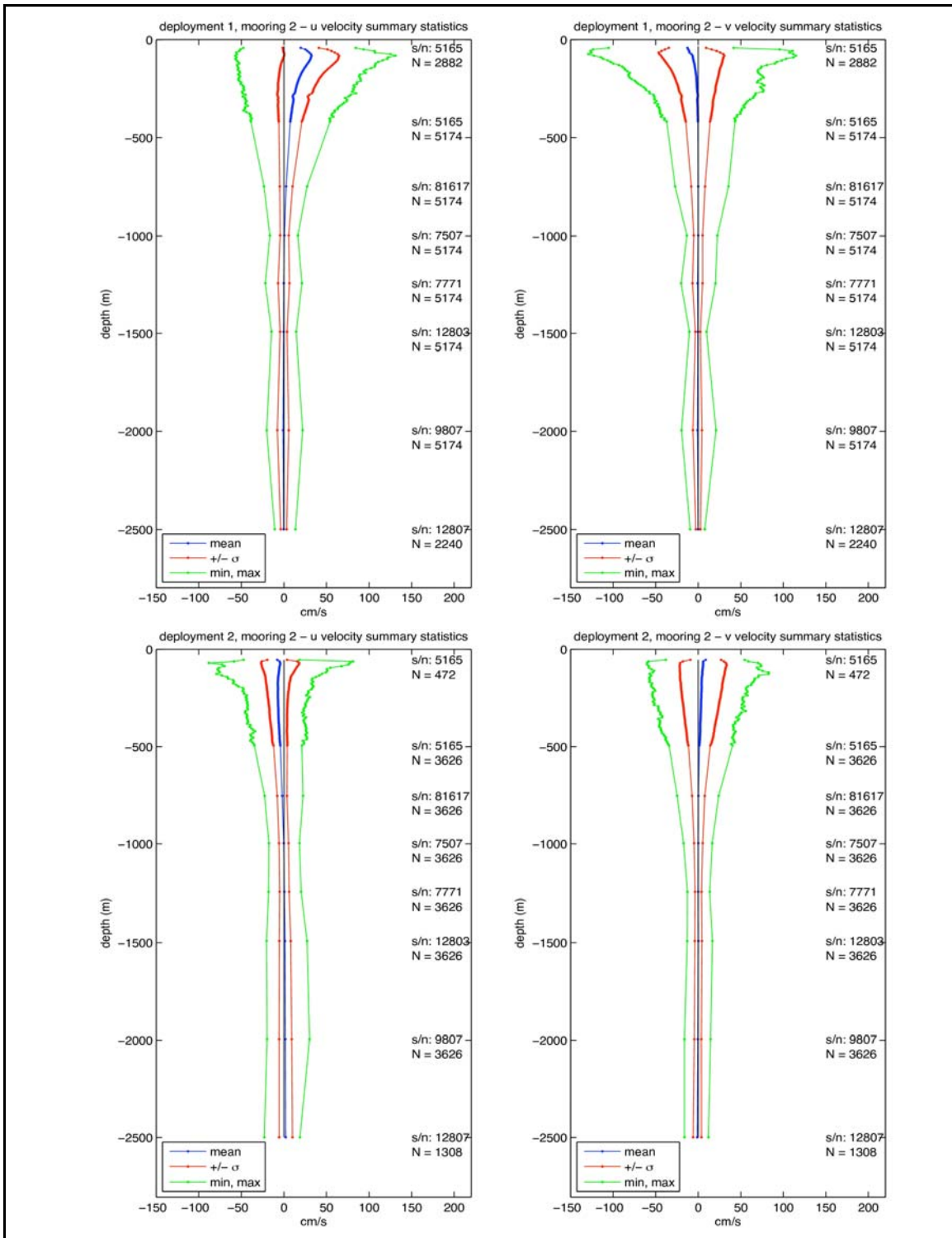


Figure 5.1-15. Vertical profiles of record-length mean, standard deviation, minimum, and maximum velocity components for mooring M2 (left: east-west component; right: north-south component). Top row: Deployment 1. Bottom row: Deployment 2.

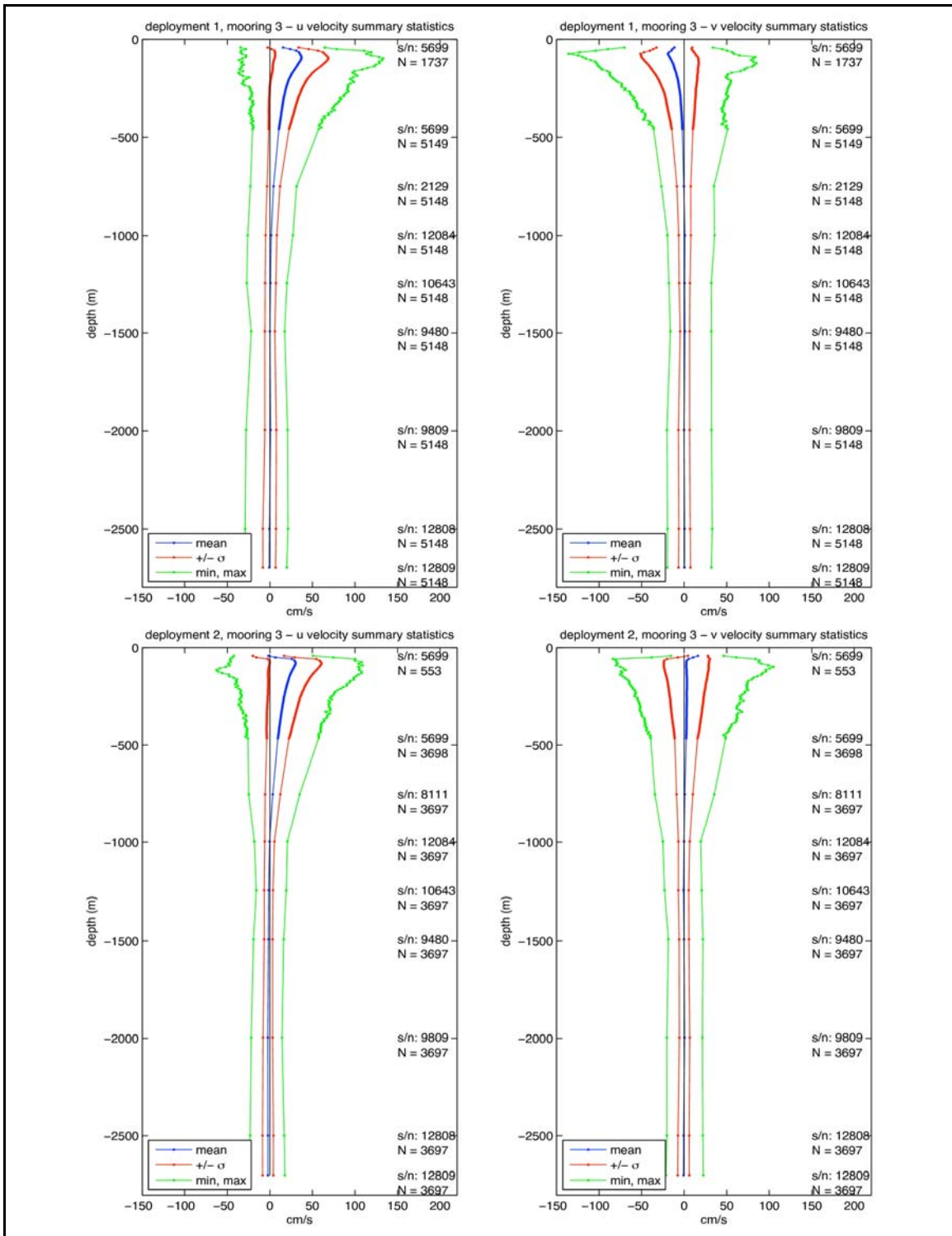


Figure 5.1-16. Vertical profiles of record-length mean, standard deviation, minimum, and maximum velocity components for mooring M3 (left: east-west component; right: north-south component). Top row: Deployment 1. Bottom row: Deployment 2.

The results of the fits are shown in Tables 5.1-1 – 5.1-4. The first three lines of the tables give the fitted parameters in equation 5.1.1 for each depth. N was the number of weekly maxima, generally 52. In some cases, the number was considerably lower. In those cases, the sample distribution was truncated below some speed because the higher maxima appeared to come from a different distribution than the lower maxima. Due to instrument failure, there was too little data at the 1995 m depth on mooring 1 and the 2499 m depth on mooring 2 for reliable fits. The row labeled Max is the maximum speed observed during the year of measurements. The last five lines of the tables give the extrapolated return period extreme values.

Table 5.1-1

Extreme current speed distributions at Mooring 1.

Depth	749	997	1244	1492	1995	2499
μ	15.74	7.87	7.63	6.31	--	9.34
σ	5.03	5.65	2.47	2.43	--	3.22
ξ	0.0799	-0.1249	0.0606	-0.1720	--	0.0300
N	52	52	52	52	--	51
Max	45.7	30.7	19.4	14.3	--	30.7
1 Yr	38.9	25.4	18.6	13.3	--	22.8
5 Yr	50.7	30.5	24.0	15.0	--	31.4
10 Yr	56.2	32.4	26.4	15.6	--	31.4
50 Yr	70.3	36.2	32.6	16.8	--	37.8
100 Yr	76.9	37.5	35.4	17.2	--	40.7

Table 5.1-2

Extreme current speed distributions at Mooring 2.

Depth	749	997	1244	1492	1995	2499
μ	18.38	12.17	11.62	7.89	16.78	--
σ	5.60	4.28	4.10	2.87	3.90	--
ξ	-0.2393	-0.3269	-0.1515	0.0239	-0.0260	--
N	52	52	52	49	24	--
Max	36.3	22.6	23.3	28.2	31.2	--
1 Yr	32.7	21.7	23.8	19.6	28.6	--
5 Yr	35.6	23.1	27.0	24.8	34.3	--
10 Yr	36.6	23.6	28.2	27.1	36.7	--
50 Yr	38.2	24.3	30.4	32.5	42.0	--
100 Yr	38.8	24.5	31.3	35.0	44.2	--

Table 5.1-3

Extreme current speed distributions at Mooring 3.

Depth	750	997	1245	1492	1996	2499	2699
μ	21.16	14.80	11.40	19.38	20.02	20.55	20.04
σ	5.87	5.87	3.41	3.66	4.51	4.51	4.01
ξ	-0.1979	-0.2161	-0.0122	-0.0714	-0.1707	-0.1481	-0.0279
N	52	52	50	12	14	15	16
Max	37.1	35.8	32.0	32.0	32.2	33.1	33.1
1 Yr	37.2	30.4	24.4	27.6	29.5	30.5	30.6
5 Yr	41.0	33.8	29.6	32.3	33.6	34.9	36.6
10 Yr	42.2	34.9	31.8	34.2	35.1	36.5	39.0
50 Yr	44.6	37.0	36.9	38.2	37.8	39.6	44.5
100 Yr	45.4	37.7	39.0	40.0	38.8	40.7	46.8

Table 5.1-4

Extreme current speed distributions at Mooring 4.

Depth	2530	2630
μ	9.05	8.92
σ	2.95	3.24
ξ	-0.0788	-0.1534
N	52	52
Max	18.0	17.8
1 Yr	19.0	18.5
5 Yr	22.3	21.0
10 Yr	23.6	21.9
50 Yr	26.3	23.7
100 Yr	27.4	24.3

Plots of the fits are shown in Figures 5.1-17 – 5.1-21. In general, the fitted distributions agreed reasonably well with the sample distributions. But there are some cases, for example the 2499 m depth at Mooring 1 where there were a couple of large maxima that did not agree with a smooth curve through the rest of the data. The maximum likelihood method did its best to honor all of the data, but recognized that the last few data points have a very large statistical uncertainty. The extrapolations to 100 years of 1 year of data also had a large uncertainty, but engineering calculations require answers.

Most of the fitted distributions had negative ξ values, showing that the distributions had an upper limit. On the other hand, the ξ values were generally rather close to zero, so that the limit was rather large compared to the extrapolated values.

In general, the extreme values near 750 m depth and near the bottom were largest, with smaller values at intermediate depths. By far the largest were at 749 m depth on Mooring 1. The extrapolated near-bottom current speeds at Mooring 1 near the Florida Escarpment were no larger than those at Mooring 3 on the abyssal plane. This was an interesting contrast to near-bottom currents near the Sigsbee Escarpment farther west, where bottom currents were much stronger in proximity to the Escarpment.

5.1.8 Responses to Hurricanes

During the Eastern GOM Study mooring deployments, five hurricanes and one tropical storm traversed the GOM; the most severe being Hurricanes Katrina and Rita, which caused devastating loss of life and property damage to the Gulf coast. Hurricane Katrina entered the GOM August 26, 2005 and was nearest to the study area on August 28, 2005; Hurricane Rita entered the GOM on September 20, 2005 and was nearest to the study region on September 22, 2005. As mentioned earlier, the paths of all the storms are presented in Appendix A.

5.1.8.1 Inertial Oscillations

A direct response of the ocean to this atmospheric forcing was a wake of near-inertial oscillations, characterized by the downward propagation of energy and upward propagation of leading phase. Near-inertial motions are an essential and ubiquitous element of ocean circulation. These motions were investigated herein using multiple methods.

The period in hours of inertial oscillations per hour as a function of latitude ϕ is given by

$$T_i = 12 / \sin(\phi), \quad (5.1.2)$$

At the latitude of moorings M1, M2, and M3, this period is close to 24 hours. A high-pass 9-pole Butterworth filter with a cutoff period of 48 hours followed by a low-pass 9-pole Butterworth filter with a cutoff period of 12 hours was used to isolate near-inertial oscillations in the data. The filter was run forward and backward to eliminate any phase lags. The filter was applied to the vector components of the measured currents in each ADCP bin. The currents were then interpolated to a uniform depth grid taking into account the measured set-down of the mooring.

Figures 5.1-22 – 5.1-27 show the total current speed and the band-passed current speed for the two deployments at each of the three ADCP moorings. The presentations show current speed instead of current components because the inertial oscillations usually rotate clockwise with slowly varying speed. During the first deployment (Figures 5.1-22 – 5.1-24) the strongest total current speeds were caused by incursions of the LC and Eddy Vortex. These features had the strongest effects on the southern-most mooring, M3, although strong currents from Eddy Vortex penetrated as far north as M1. The inertial band-passed speeds were generally small except for brief bursts at M3 at the end of the LC and Eddy Vortex events.

During the second deployment (Figures 5.1-25 – 5.1-27) the passages of Hurricanes Katrina and Rita occurred. The total current speeds were not as strong nor did they penetrate as deeply as the LC and Eddy events. On the other hand, these hurricanes produced by far the strongest inertial oscillations.

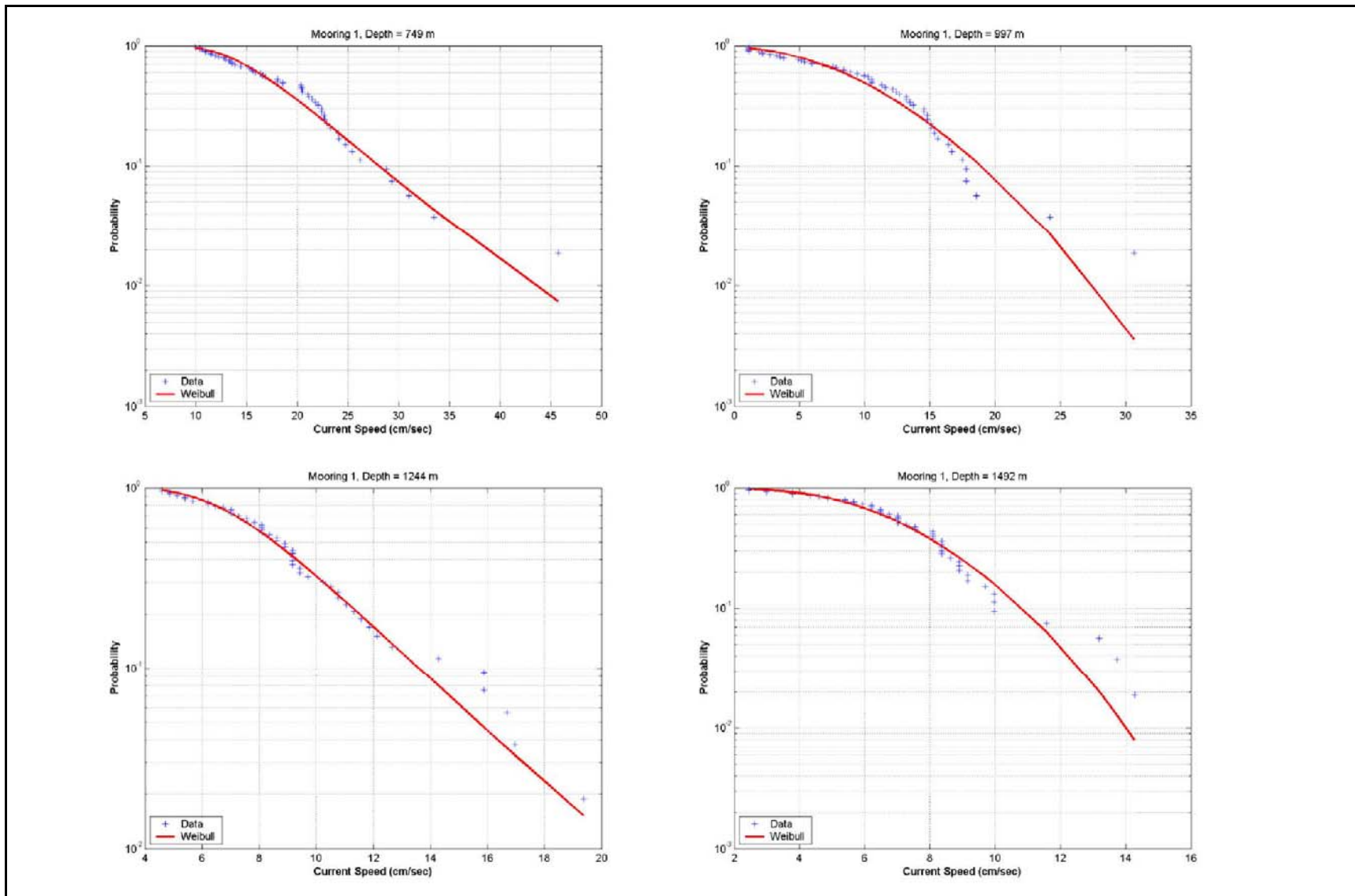


Figure 5.1-17. Extreme value fits for current speeds at Mooring 1, Depths 749 – 1492 m.

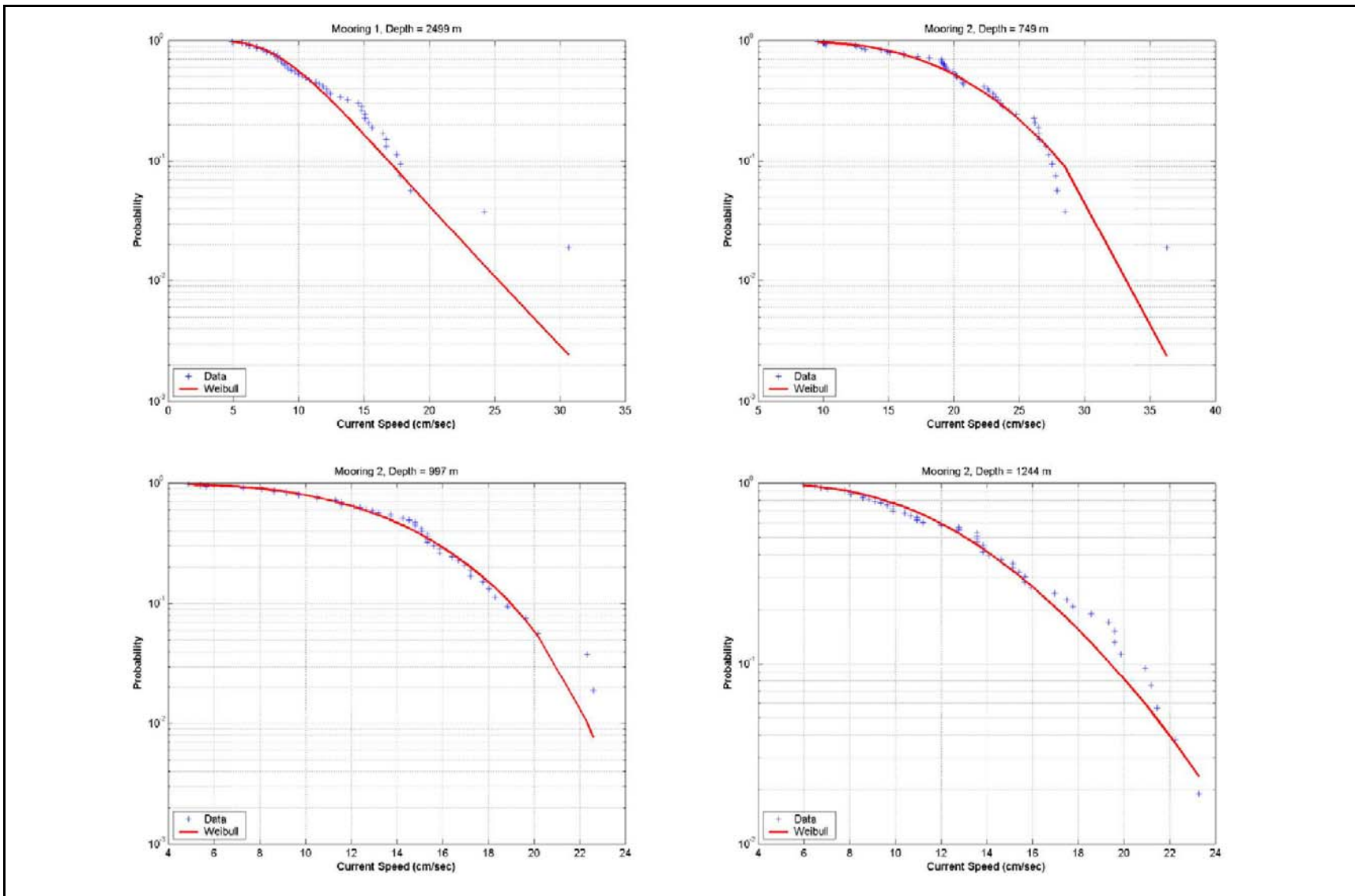


Figure 5.1-18. Extreme value fits for current speeds at Mooring 1, depth 2499 m and Mooring 2, depths 749 – 1244 m.

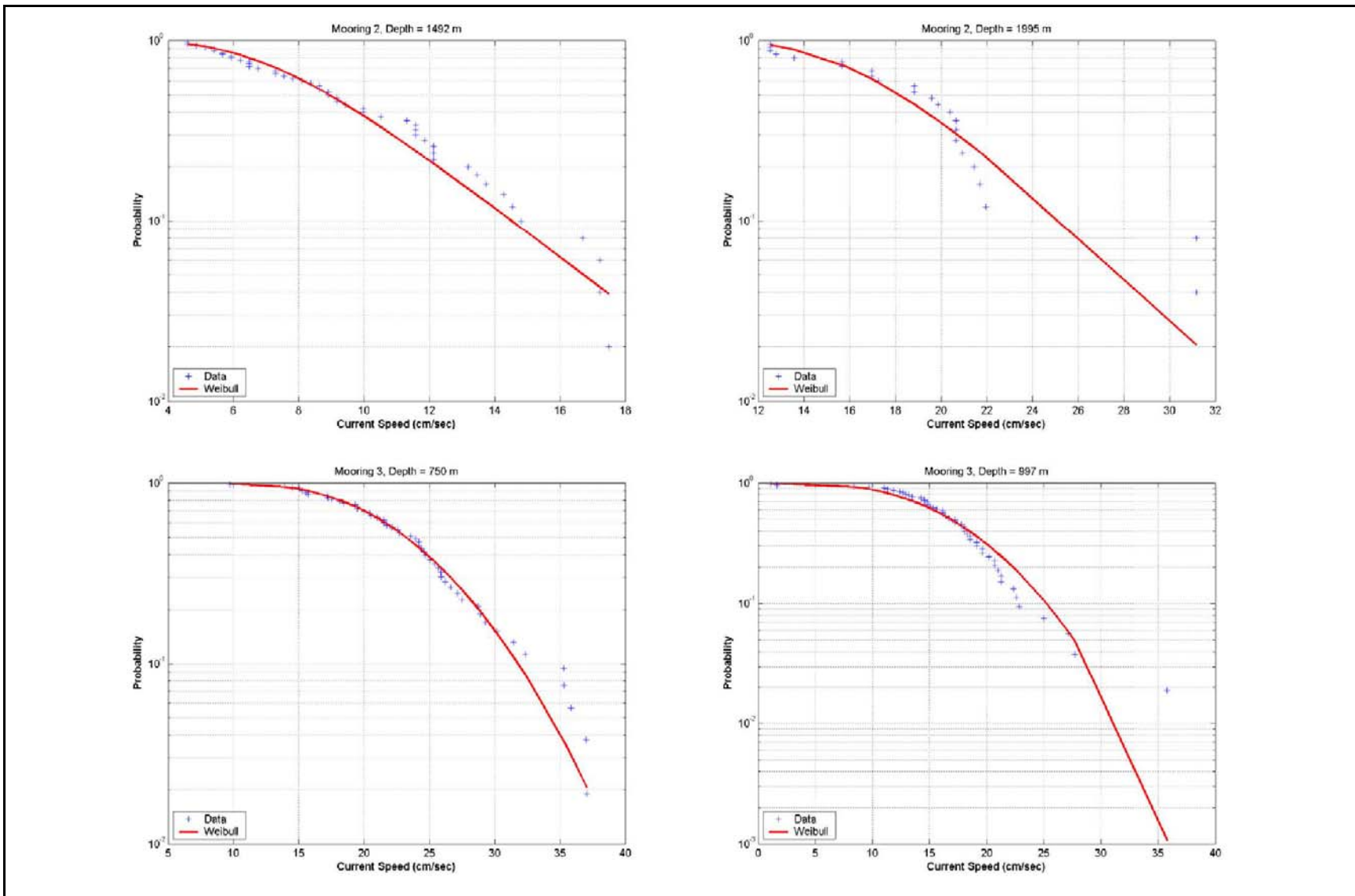


Figure 5.1-19. Extreme value fits for current speeds at Mooring 2, depths 1492 – 1995 m and Mooring 3, Depths 750 – 997 m.

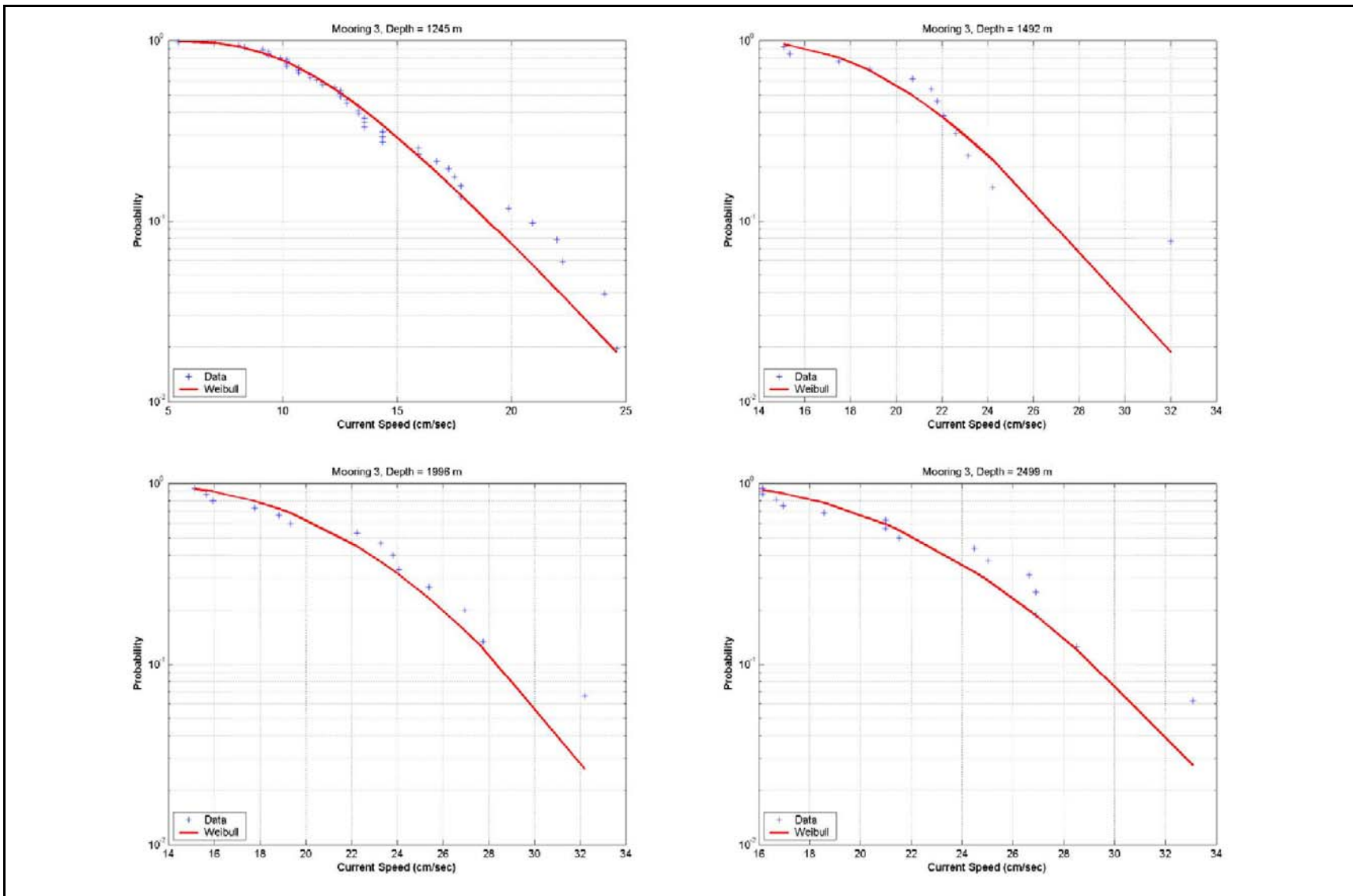


Figure 5.1-20. Extreme value fits for current speeds at Mooring 3, depths 1245 – 2499 m.

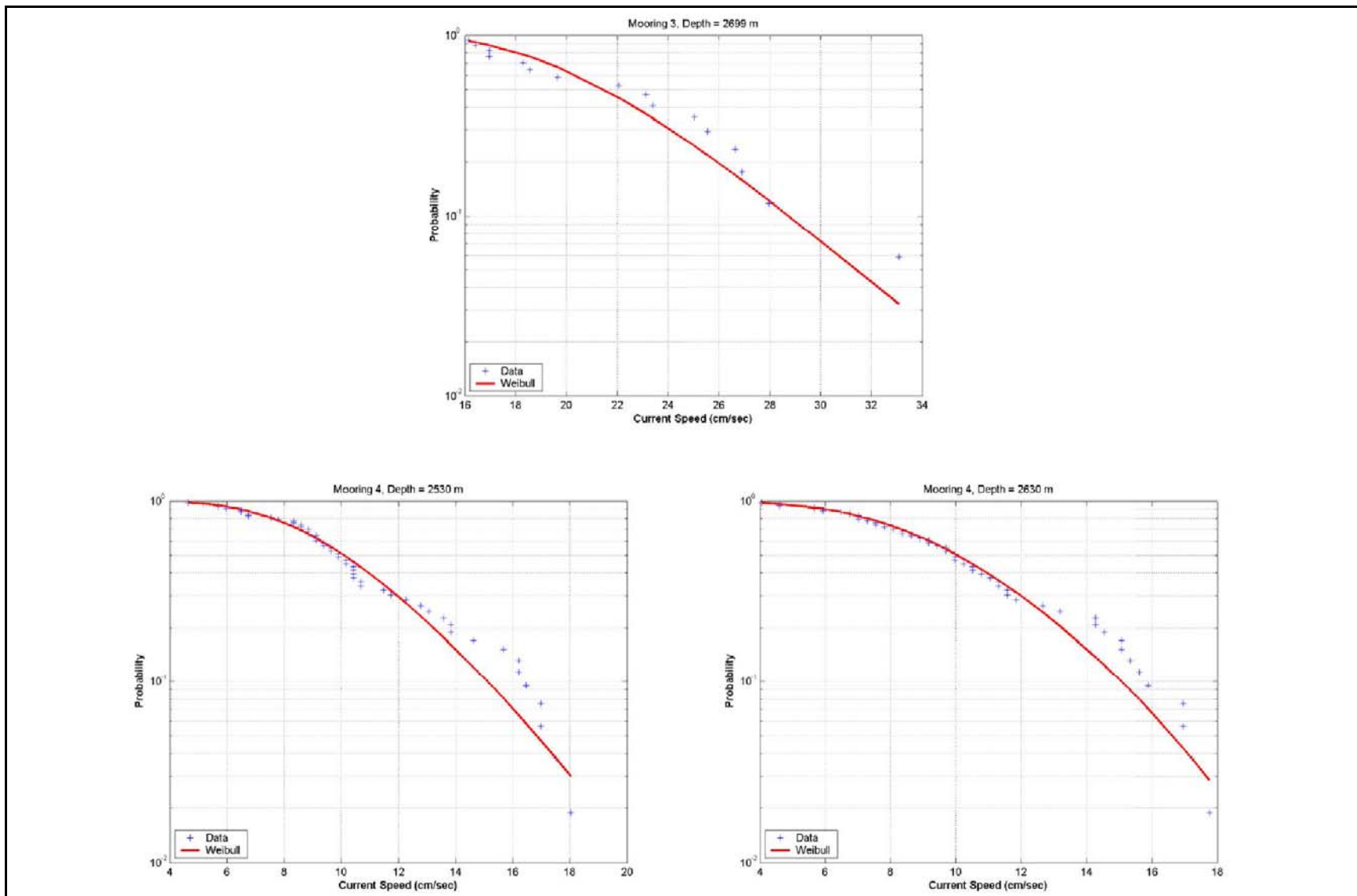


Figure 5.1-21. Extreme value fits for current speeds at Mooring 3, depth 2699 m, and Mooring 4, depths 2530 – 2630 m.

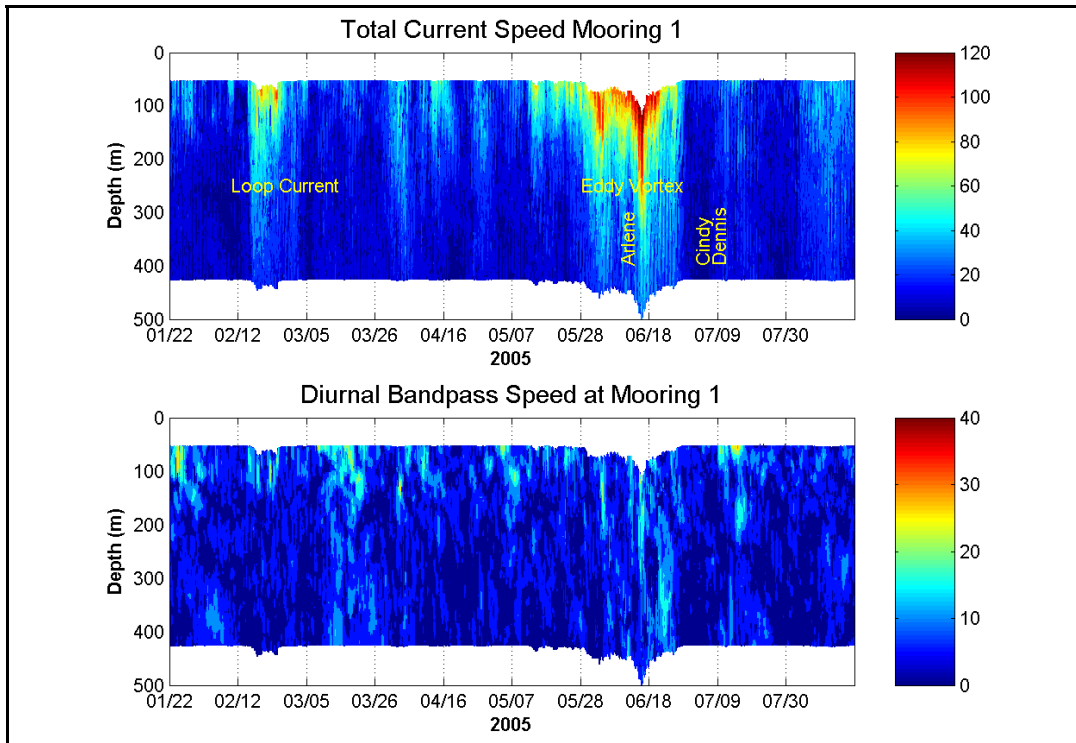


Figure 5.1-22. Total current speed and diurnal bandpass current speed for the first deployment at mooring 1.

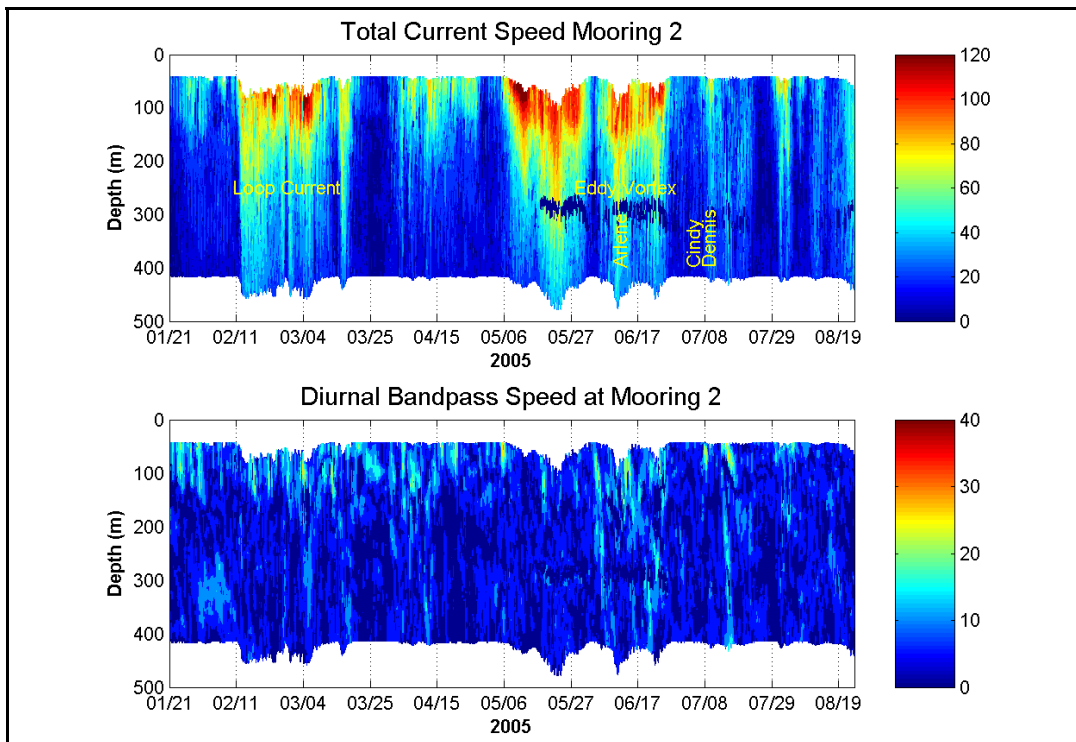


Figure 5.1-23. Total current speed and diurnal bandpass current speed for the first deployment at mooring 2.

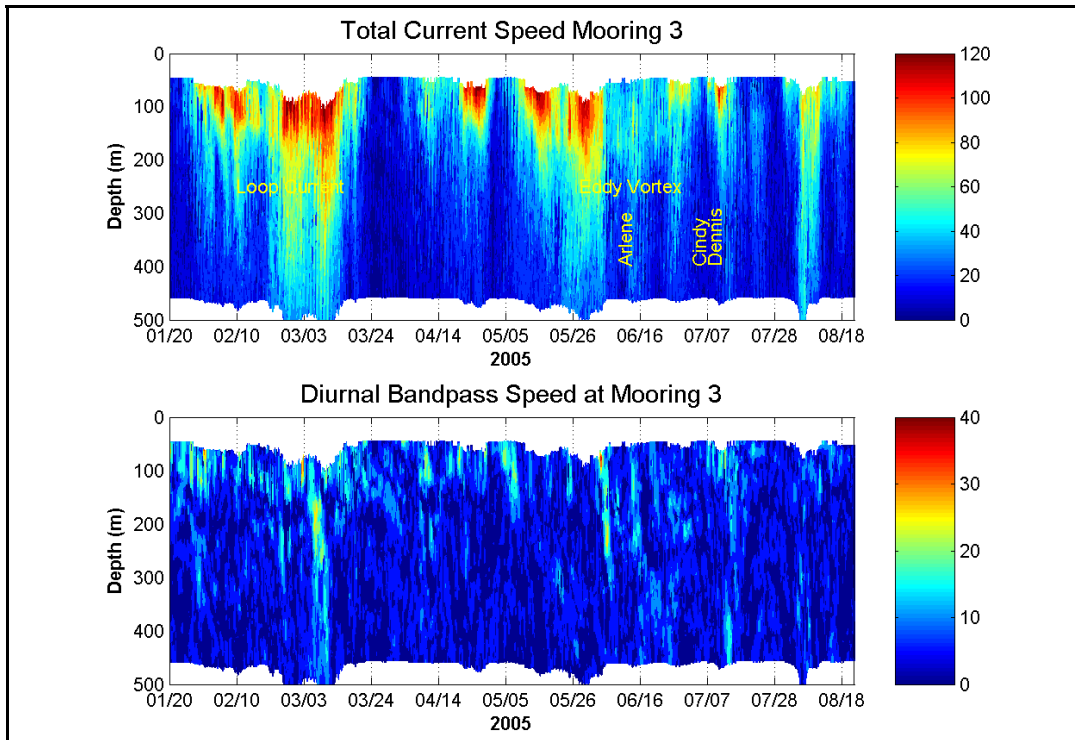


Figure 5.1-24. Total current speed and diurnal bandpass current speed for the first deployment at mooring 3.

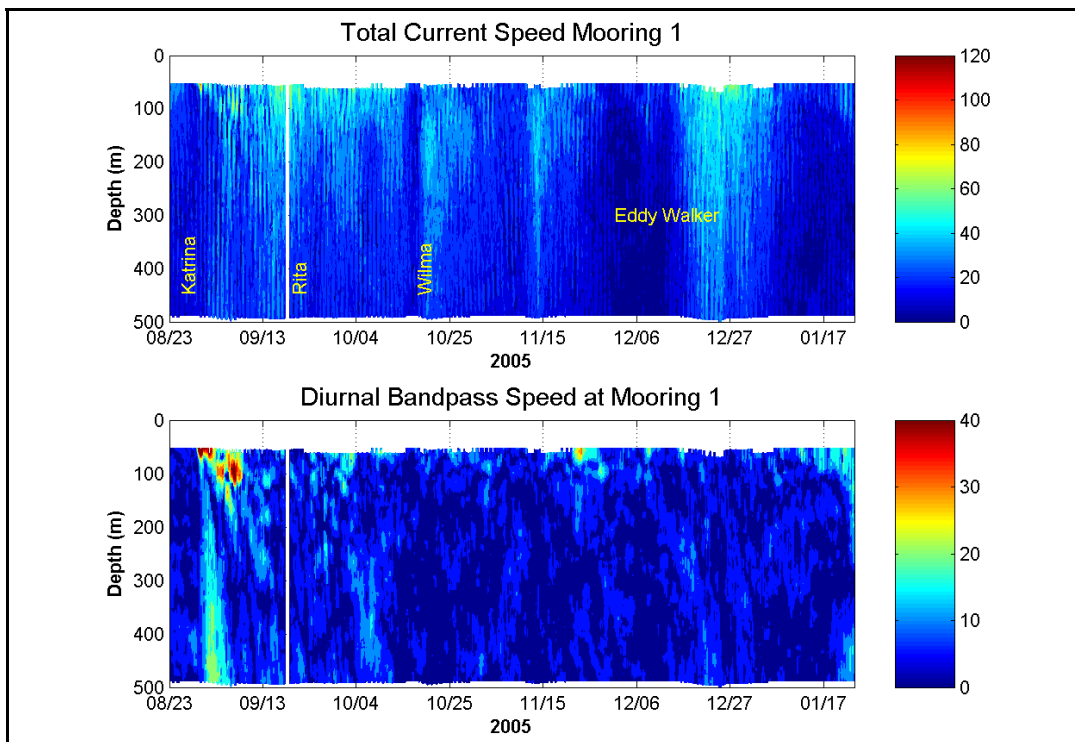


Figure 5.1-25. Total current speed and diurnal bandpass current speed for the second deployment at mooring 1.

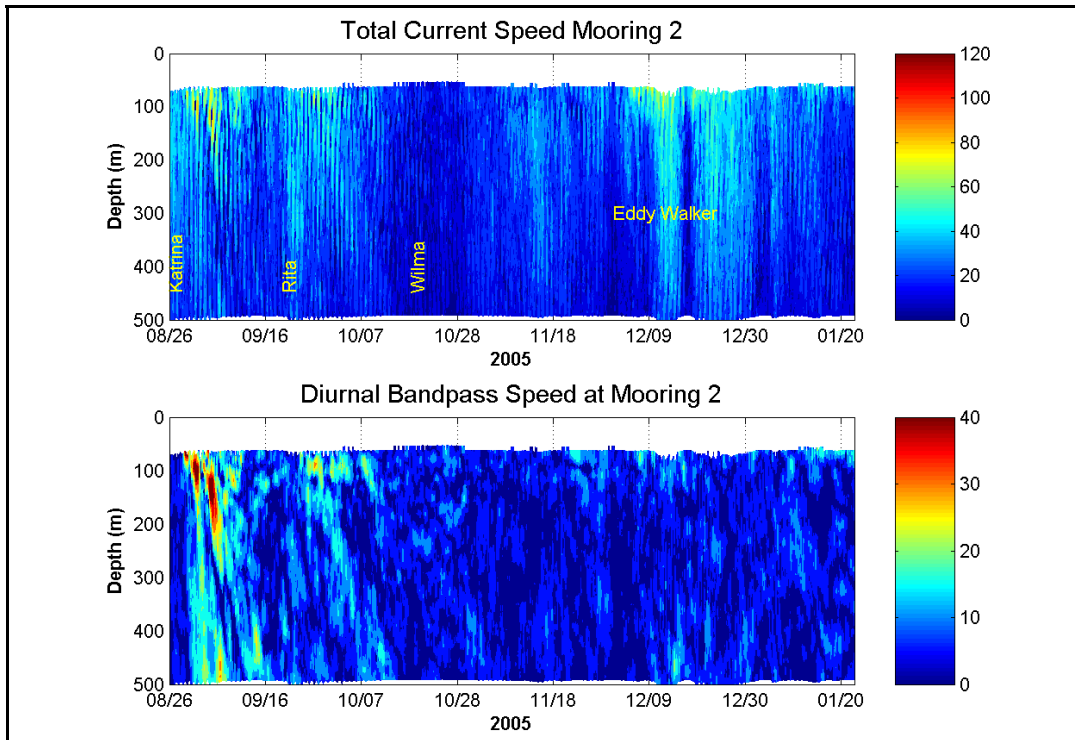


Figure 5.1-26. Total current speed and diurnal bandpass current speed for the second deployment at mooring 2.

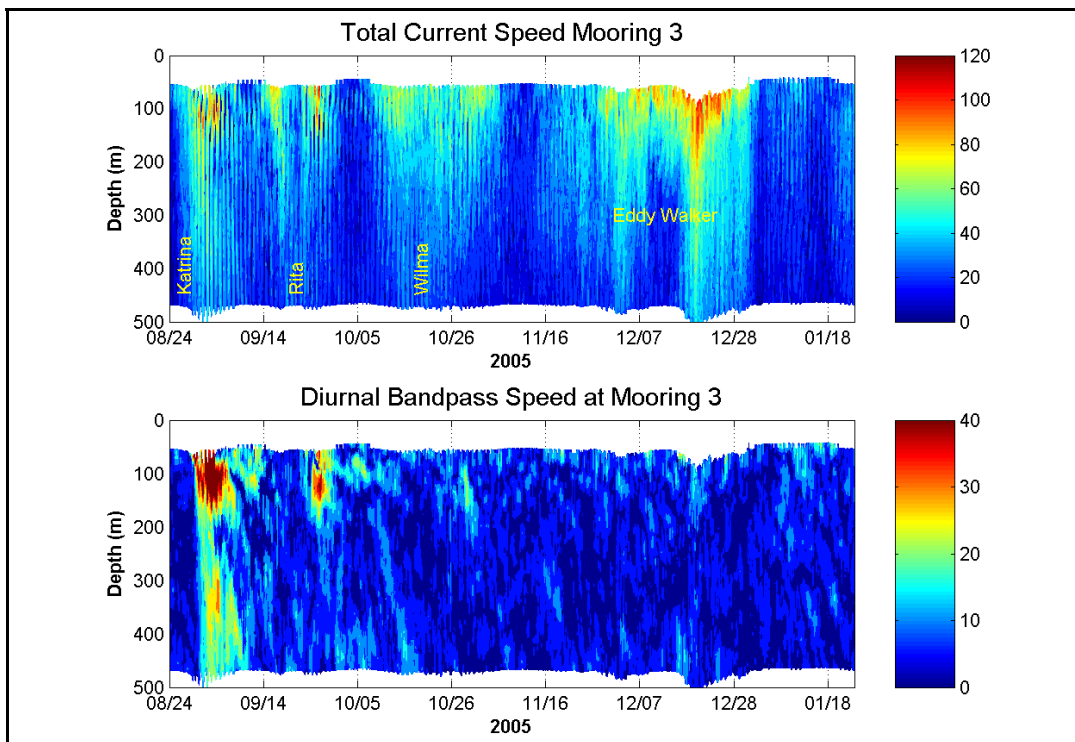


Figure 5.1-27. Total current speed and diurnal bandpass current speed for the second deployment at mooring 3.

Figures 5.1-28 – 5.1-30 show the response to Hurricane Katrina in more detail. The storm came closest to all three moorings late on August 28. All the moorings were to the right of the storm track and roughly the same distance from it. The resulting clockwise rotating wind stress vector had about the same potential for generating inertial oscillations at all the moorings. The initial response was confined above 50 m depth and thus not measured at the uppermost ADCP bins. After about a day, inertial pumping pushed the oscillations down to levels that were clearly registered by the ADCPs. These oscillations can be seen in the panels showing the total current (top) because the mean current is not zero, but they are more clearly seen on the panels that show only the band-passed current (bottom). The inertial oscillations were much stronger at M3 than at the other moorings. This difference in strength cannot be explained by any large difference in the wind forcing at the moorings. The very strong inertial response at M3 was caused by the coincidence of the hurricane and a cyclonic eddy. The combination of clockwise rotating winds and a pre-existing eddy was responsible for the strongest inertial response in these measurements.

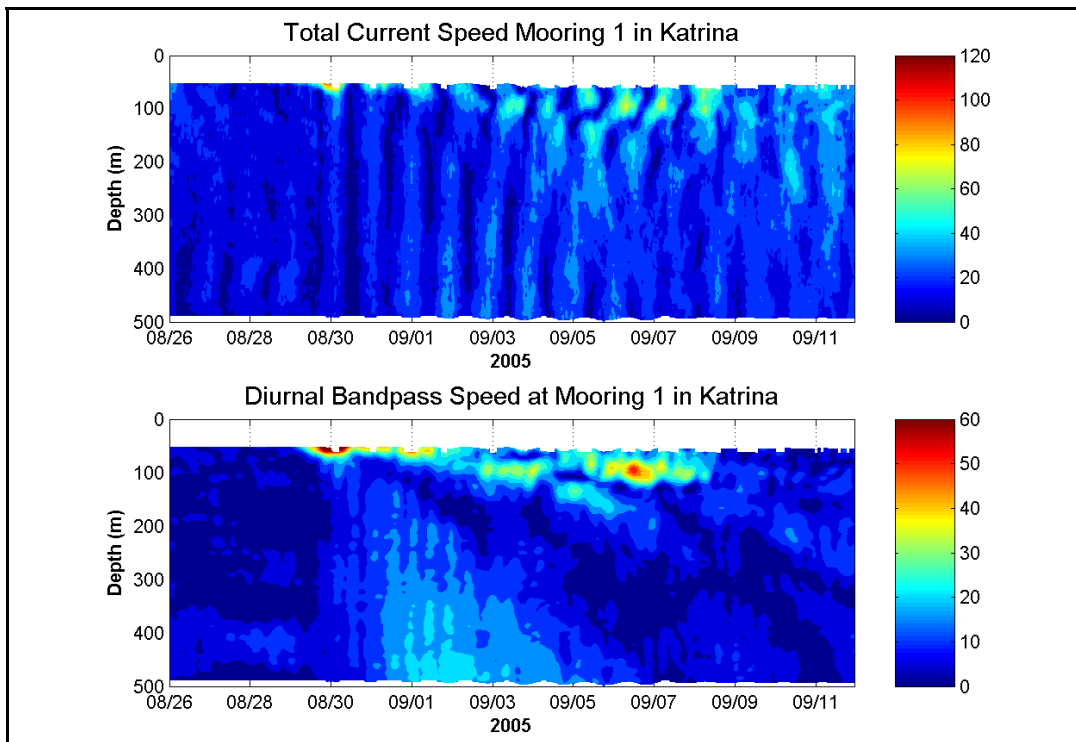


Figure 5.1-28. Total current speed and diurnal bandpass current speed during Hurricane Katrina at mooring 1.

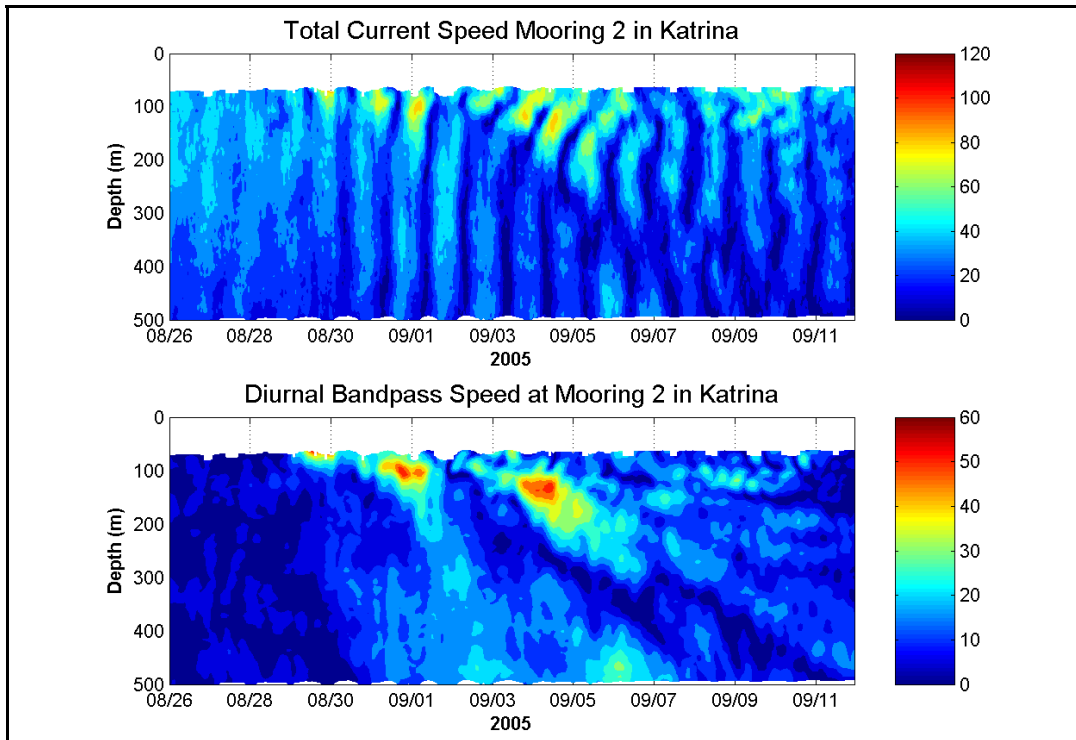


Figure 5.1-29. Total current speed and diurnal bandpass current speed during Hurricane Katrina at mooring 2.

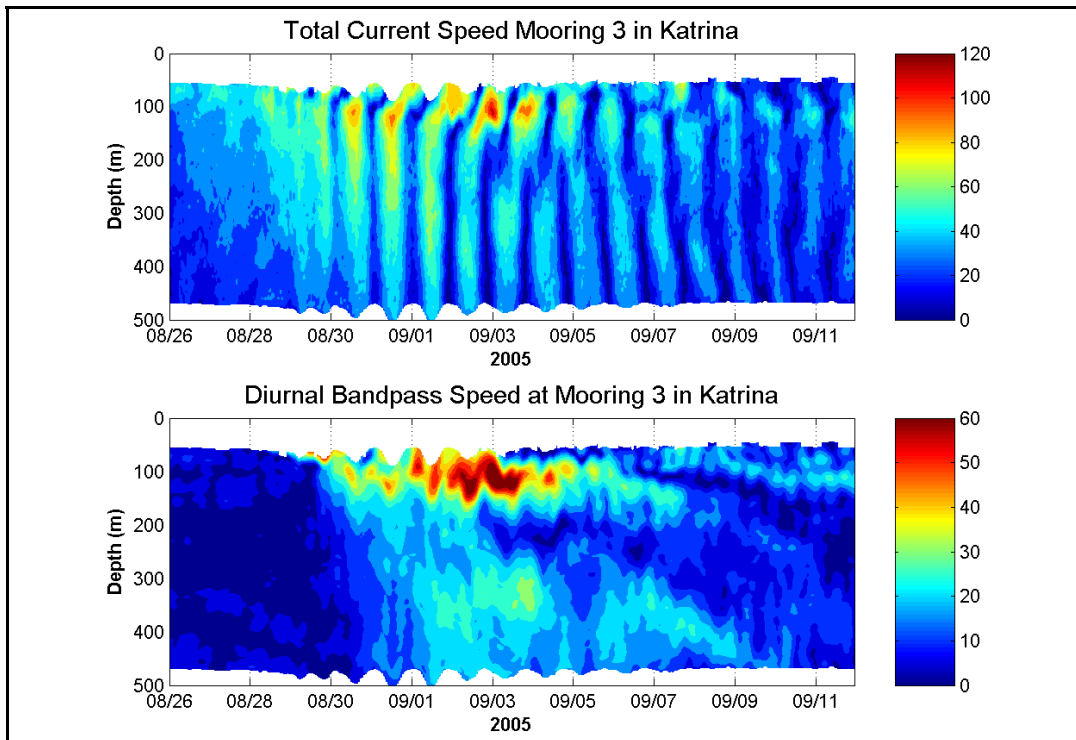


Figure 5.1-30. Total current speed and diurnal bandpass current speed during Hurricane Katrina at mooring 3.

Figures 5.1-31 – 5.1-33 show the total and band-passed current speeds during Hurricane Rita. Again, the only significant total currents and inertial oscillations were at M3. The track of Rita was farther to the south of the moorings than the track of Katrina. Moorings M2 and M3 were just inside the extent of tropical storm winds while M1 was outside. In addition, M3 was very near the northern edge of the Loop Current. Again, the combination of strong winds and a pre-existing feature lead to the strongest inertial oscillations.

Figures 5.1-34 – 5.1-37 are scatter plots comparing the magnitude of the band passed currents to the total current magnitude at several depths. It was apparent that there was no correlation between the total current speed and the band passed speed. This was reasonable, because most of the strong currents were due to the LC or eddies. Strong inertial oscillations only occur under strong clockwise rotating winds, and the wind events were statistically independent from the LC and eddy events.

The statistics in Figure 5.1-38 show a more interesting pattern. The ratio of the band passed speed to the total current speed is plotted as a function of depth. All ADCP measurements from the three moorings were combined. The small circles show the mean band passed speed divided by the mean total current speed at the same time. The lines show various percentiles of band passed speed divided by the same percentiles of the total current speed. All of the curves are very similar. They show that the inertial oscillations become an increasingly large fraction of the total current speed as the depth increases. Inertial oscillations penetrated with less attenuation than the total currents.

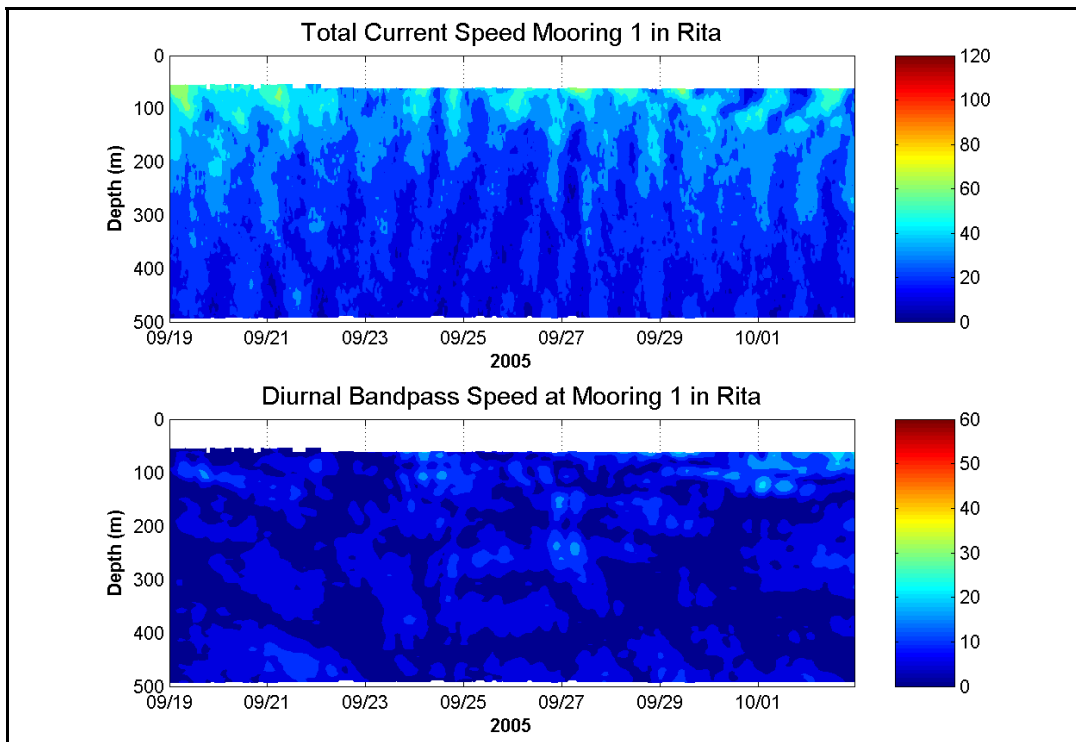


Figure 5.1-31. Total current speed and diurnal bandpass current speed during Hurricane Rita at mooring 1.

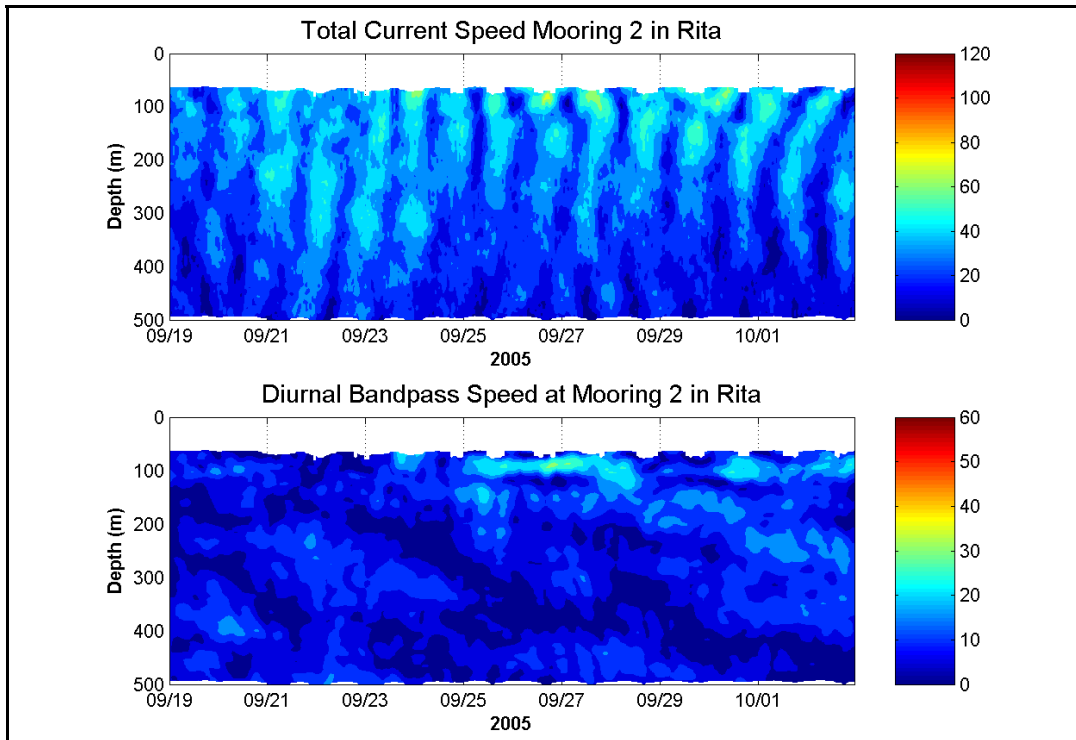


Figure 5.1-32. Total current speed and diurnal bandpass current speed during Hurricane Rita at mooring 2.

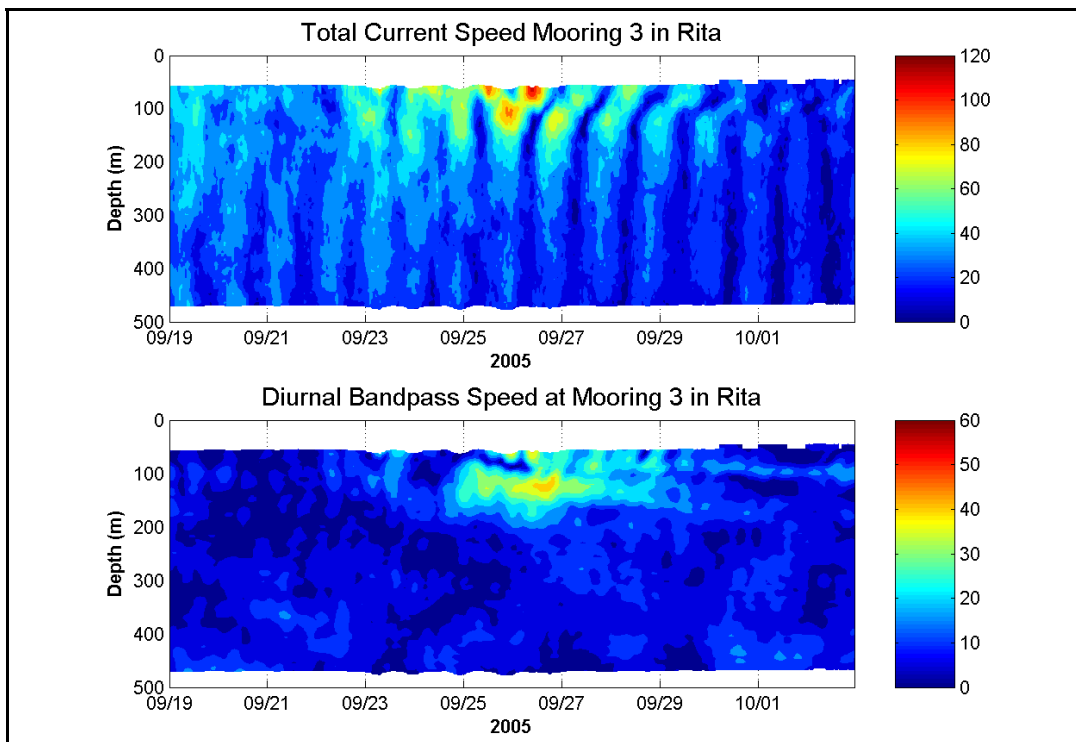


Figure 5.1-33. Total current speed and diurnal bandpass current speed during Hurricane Rita at mooring 3.

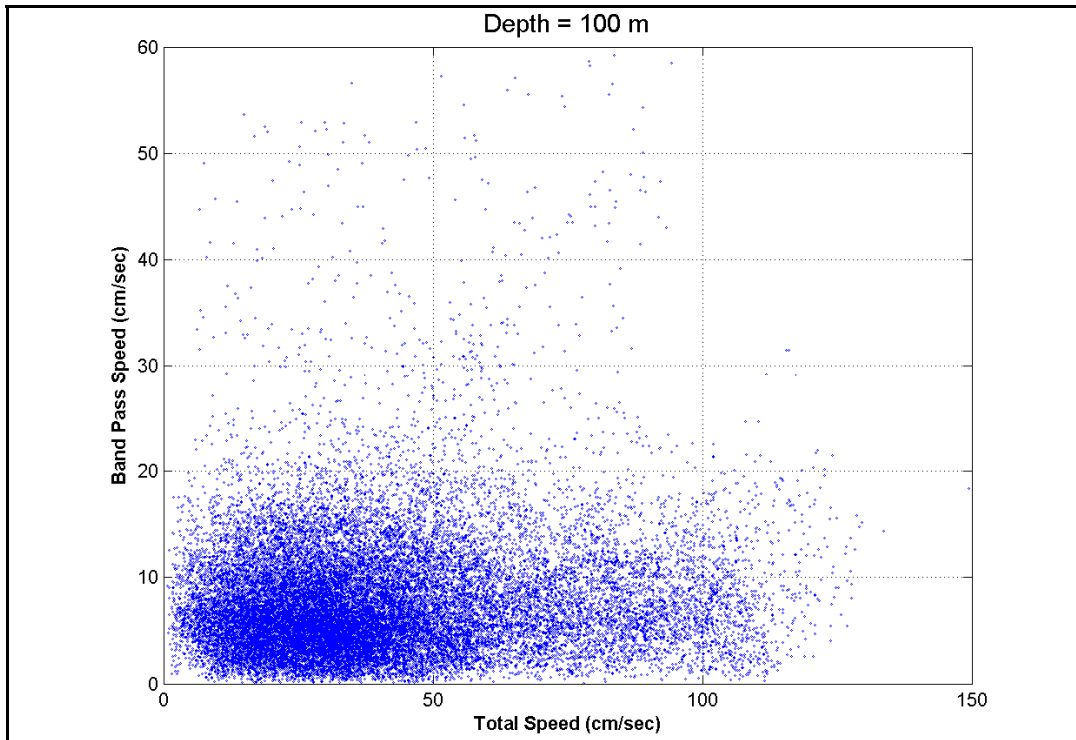


Figure 5.1-34. Scatter plot of band passed current speed vs. total current speed at 100 m depth.

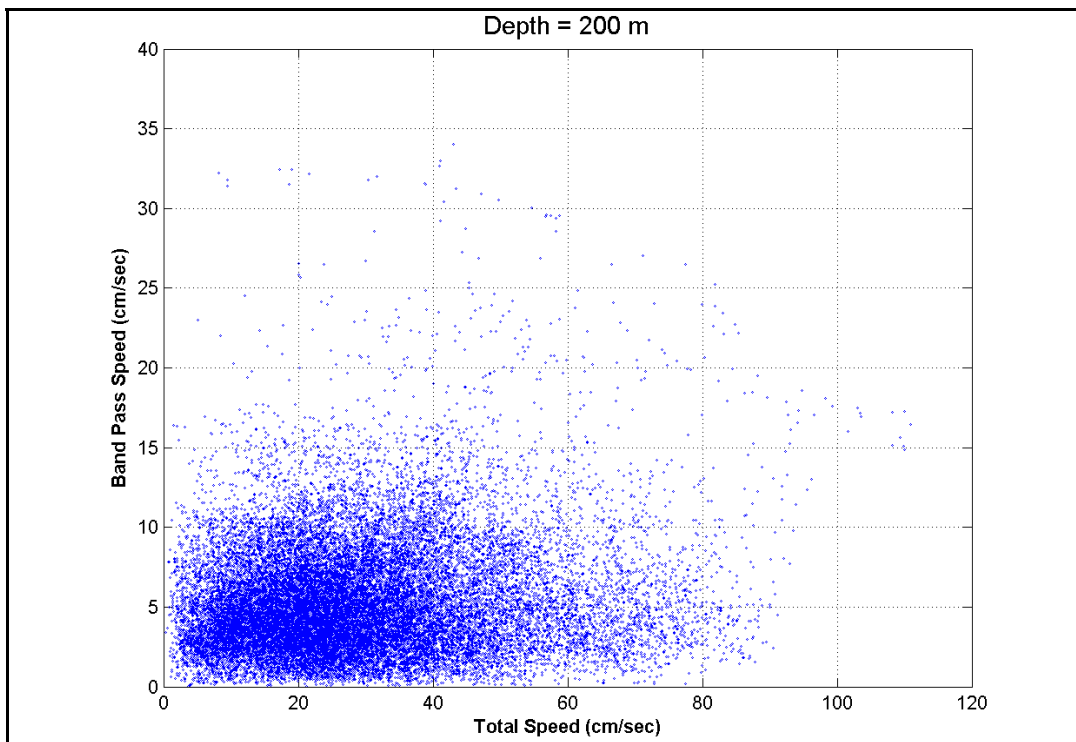


Figure 5.1-35. Scatter plot of band passed current speed vs. total current speed at 200 m depth.

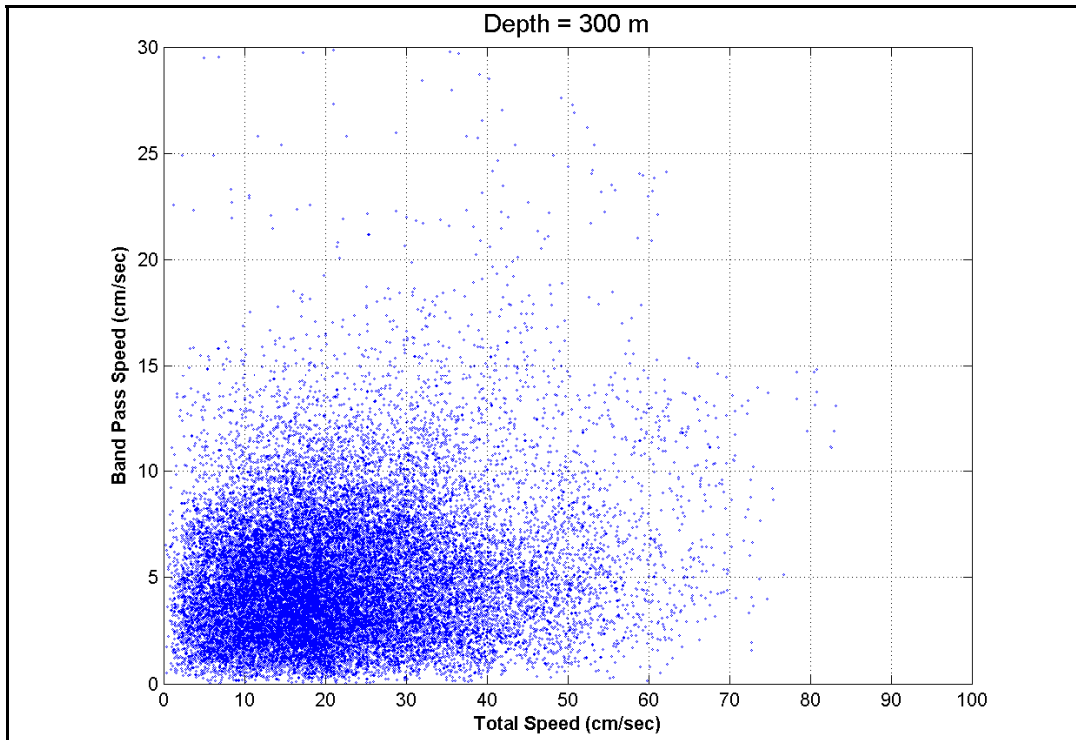


Figure 5.1-36. Scatter plot of band passed current speed vs. total current speed at 300 m depth.

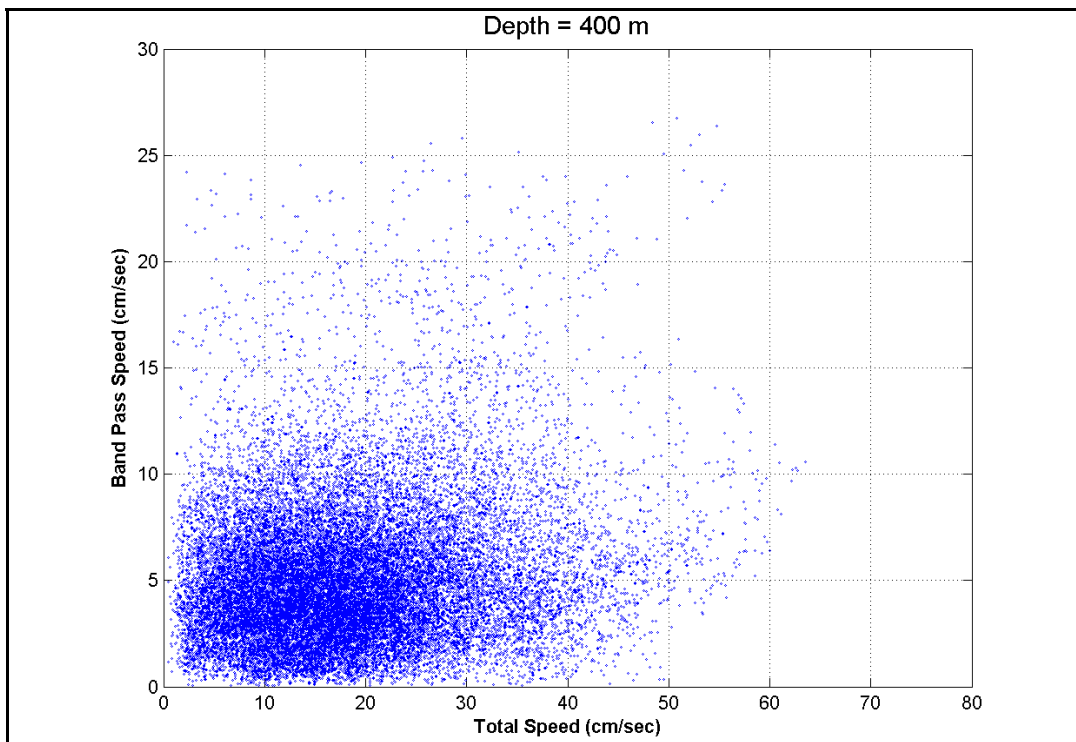


Figure 5.1-37. Scatter plot of band passed current speed vs. total current speed at 400 m depth.

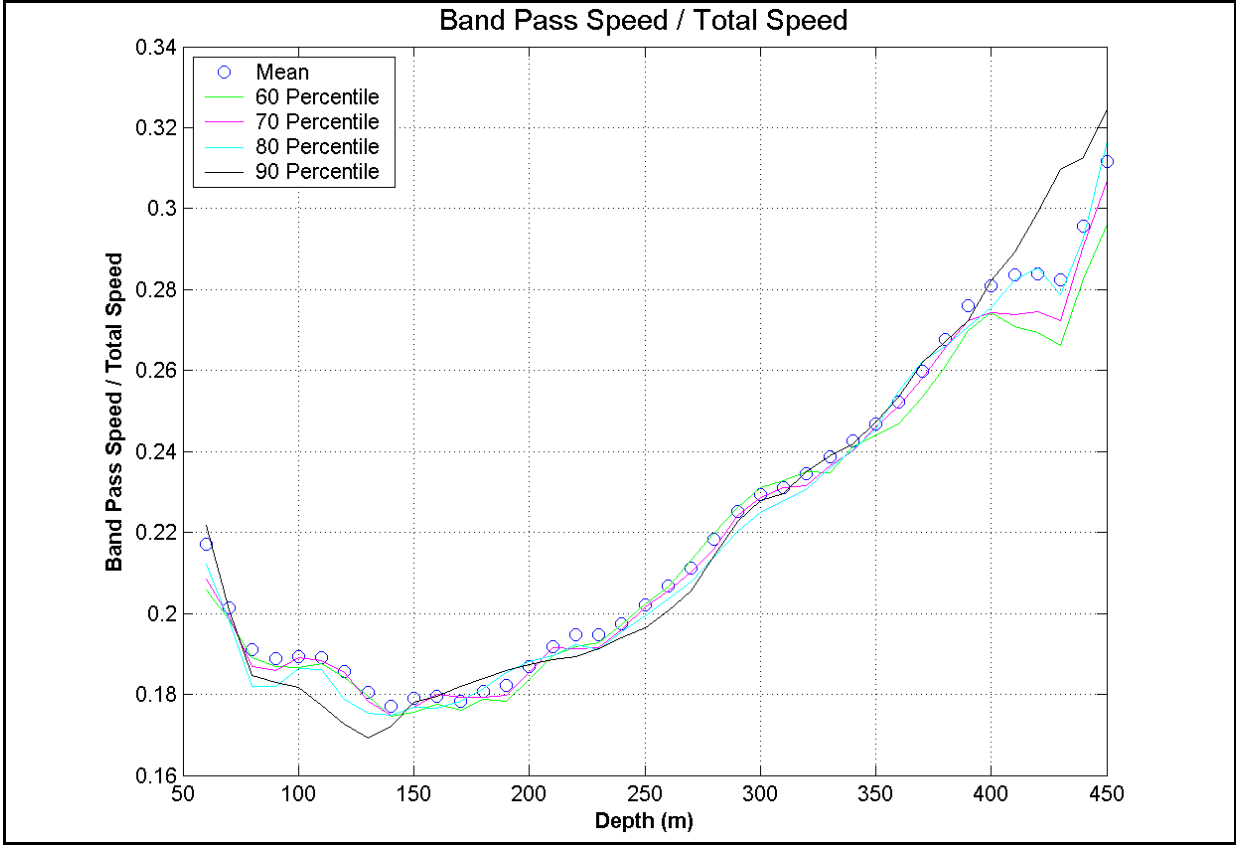


Figure 5.1-38. Ratio of band passed speed to total current speed.

5.1.8.2 Wavelet Analysis of the Inertial Oscillations

These inertial motions generated by the passage of Hurricane Katrina and Rita were also investigated using the wavelet transform. This method estimates the temporal variability of energy in specified frequency bands. Wavelet power spectra were generated for all detided, gap-filled, gridded ADCP and current meter records using a Morlet basis function. We used the method described in Torrence and Compo (1998) to transform observed time-series into Fourier space.

The wavelet power spectrum of the normalized east-west velocity component at ~80 m at mooring M3 during deployment 2 is presented in Figure 5.1-39, along with the global wavelet spectrum and average variance in the inertial band (0.5 – 2 day period). As seen previously using the Fourier-derived spectrum, the wavelet power spectrum illustrated a red spectrum throughout deployment, with minimal energy in the 2 – 4 day period range and a clear diurnal peak. The inertial energy was best represented by the peak around 1 cpd in the global wavelet spectrum, which is the integration of the wavelet power spectrum through time. Looking at the wavelet power spectrum, it was clear that inertial motions were excited immediately following hurricanes Katrina and Rita and persisted for around 2 weeks at this depth. Not only did the storms amplify inertial motions; energy was elevated throughout the sub-inertial frequency domain. There was also a local maximum of sub-inertial energy at ~ 4 – 6 day period that started in mid November and continued through early December that can be attributed to the presence of the Loop Current extending into the study region. The average variance in the inertial band time-series was constructed by integration of the wavelet power spectrum in the period band 0.5 – 2 days throughout the observational period. This panel illustrated the variance in the inertial band caused by storms as well, indicated by the significant peaks in August and September.

Contours of the average variance in the inertial band for time-series in the upper water column at each mooring are given in Figure 5.1-40. The downward propagation of inertial energy after Katrina and Rita to 500 m is indicated in this figure. The strongest response to the storms was seen at moorings M2 and M3, as the storm track was just south of the moorings. Note that there were generally two subsurface maxima of energy present after the storms and two paths for inertial energy were revealed. There was a direct influence on the entire water column that occurred during or immediately after the storm due to the storm's intensity, evidenced by the nearly vertical column of high inertial energy around September 1, 2005. There was also the downward propagation of inertial energy, evidenced by the diagonal streak of high energy following the storm. It seemed that the initial response to the storms was strongest at M3, while the propagation response was strongest at M2. Inertial waves after Katrina were present more than 2 weeks after the storm and penetrated quickly to the base of the upper layer. It was interesting to note that the energy minimum between 200 and 300 m at mooring M3 may have represented the effect of the pycnocline on the downward energy propagation. The amplitudes of the inertial oscillations after Hurricane Rita were not as large as the motions excited by Hurricane Katrina and didn't penetrate as deep, but appeared to persist at the surface longer. The presence of a cold core eddy in the study region during the passage of these storms likely affected the inertial motions greatly. The rate of downward inertial energy propagation was roughly 30 m day^{-1} .

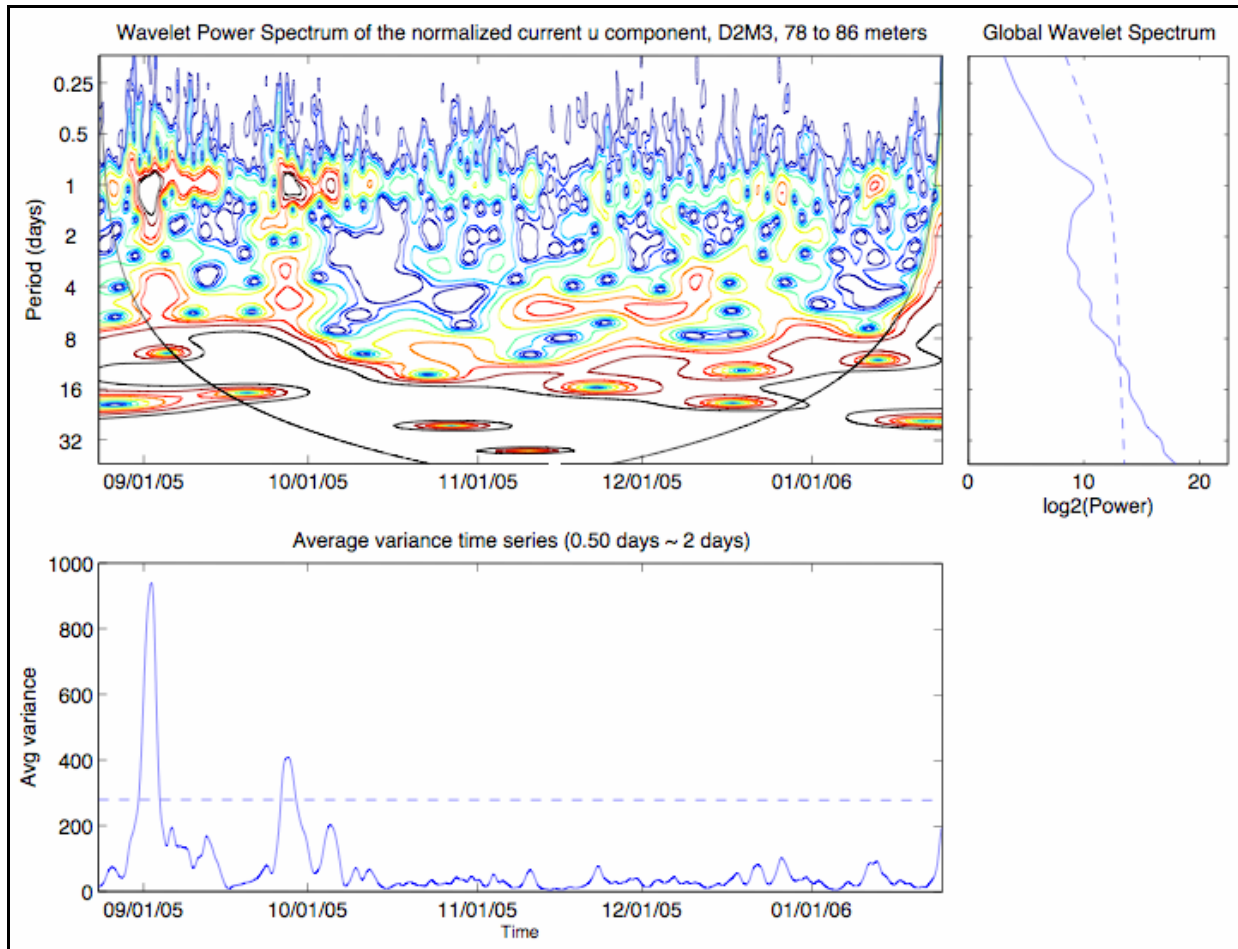


Figure 5.1-39. (Top left) Wavelet power spectrum of the hourly east-west current time-series at ~ 80 m depth at mooring 3 during deployment 2. The contours are at normalized variances of 0.062, 0.125, 0.25, 0.5, 1, 2, 3, and 6, with red being the highest and blue being the lowest variance. The black semicircle at the bottom of the figure indicates the cone of influence, where the ends of the time-series contaminate the signal. (Top right) The global wavelet spectrum gives the time-averaged wavelet power over the frequency domain. The blue dashed line is the 90% confidence level. (Bottom) The average variance time series gives the frequency-averaged wavelet power in the inertial band (0.5 – 2 day period) during the observational period. The blue dashed line is the 90% confidence level.

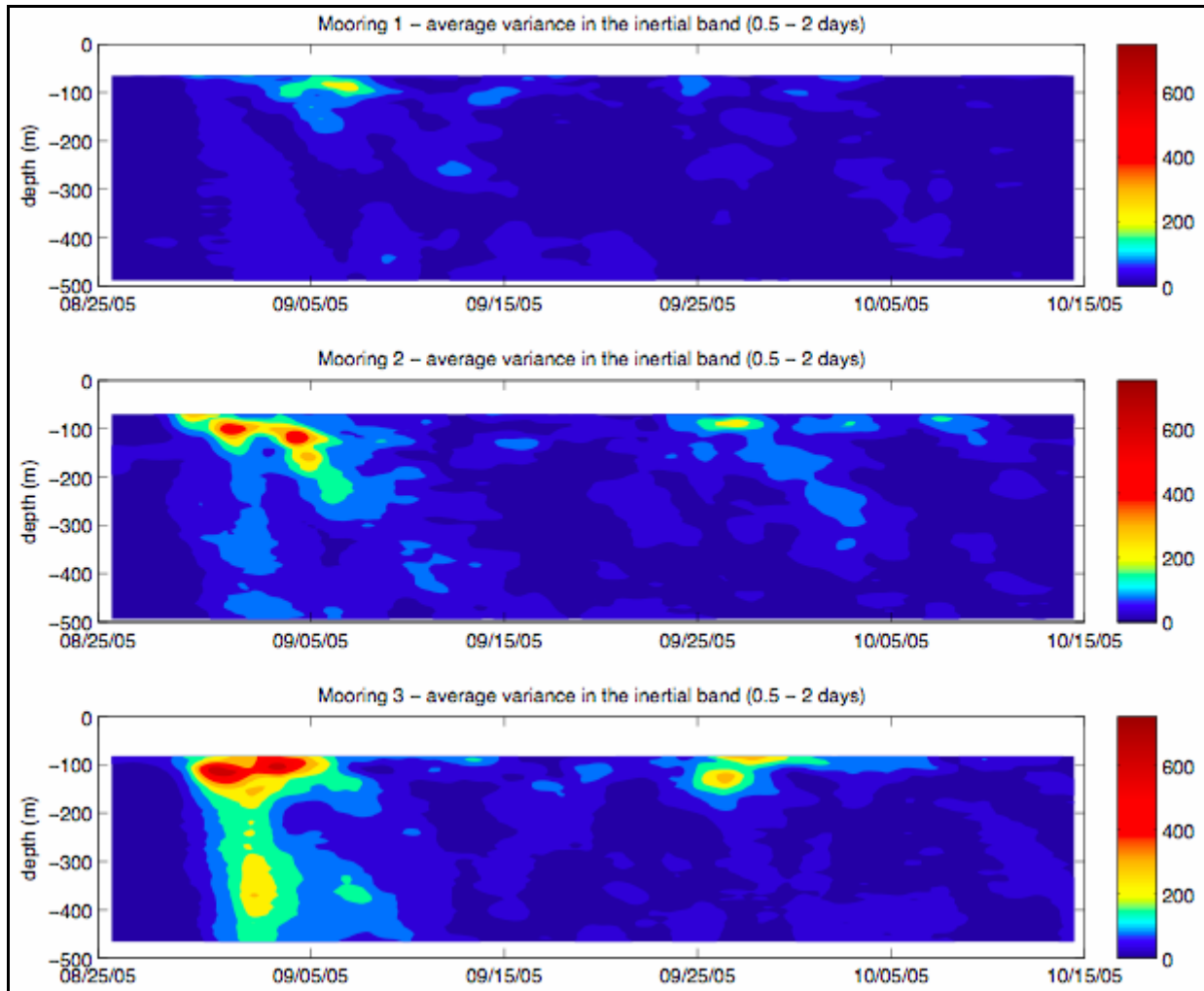


Figure 5.1-40. Contours of the frequency-averaged wavelet power in the inertial band (0.5 – 2 day period) during the weeks after Hurricanes Katrina and Rita in the upper 500 m of the water column at moorings M1 (top), M2 (middle), and M3 (bottom).

A full water column vertical EOF of the average variance in the inertial band was executed using ADCP and current meter speed records from the three moorings. Figures 5.1-41 and 5.1-42 show the Principal Component (PC) time series and the vertical amplitudes for the three leading EOF modes. Modes 1, 2, and 3 explain ~71%, ~8%, and ~4% respectively of the variance in the inertial band energy. It was clear from the timing of the peak values in the PC time series that the three modes were related to the tropical storms in the GOM. Mode 1 was closely associated with the envelope of inertial energy following Hurricanes Katrina and Rita. Amplitudes of this mode decreased away from the storm tracks from M3 to M2 to M1. At mooring M3, the inhibiting effect of the thermocline on inertial oscillations was evident, as seen in the minimum amplitudes of the first mode around 200 m. Mode 2 had the opposite amplitude for M1 and M2 compared with M3. Mode 3 was mostly driven by mooring M3 particularly at depths between 200-500 m.

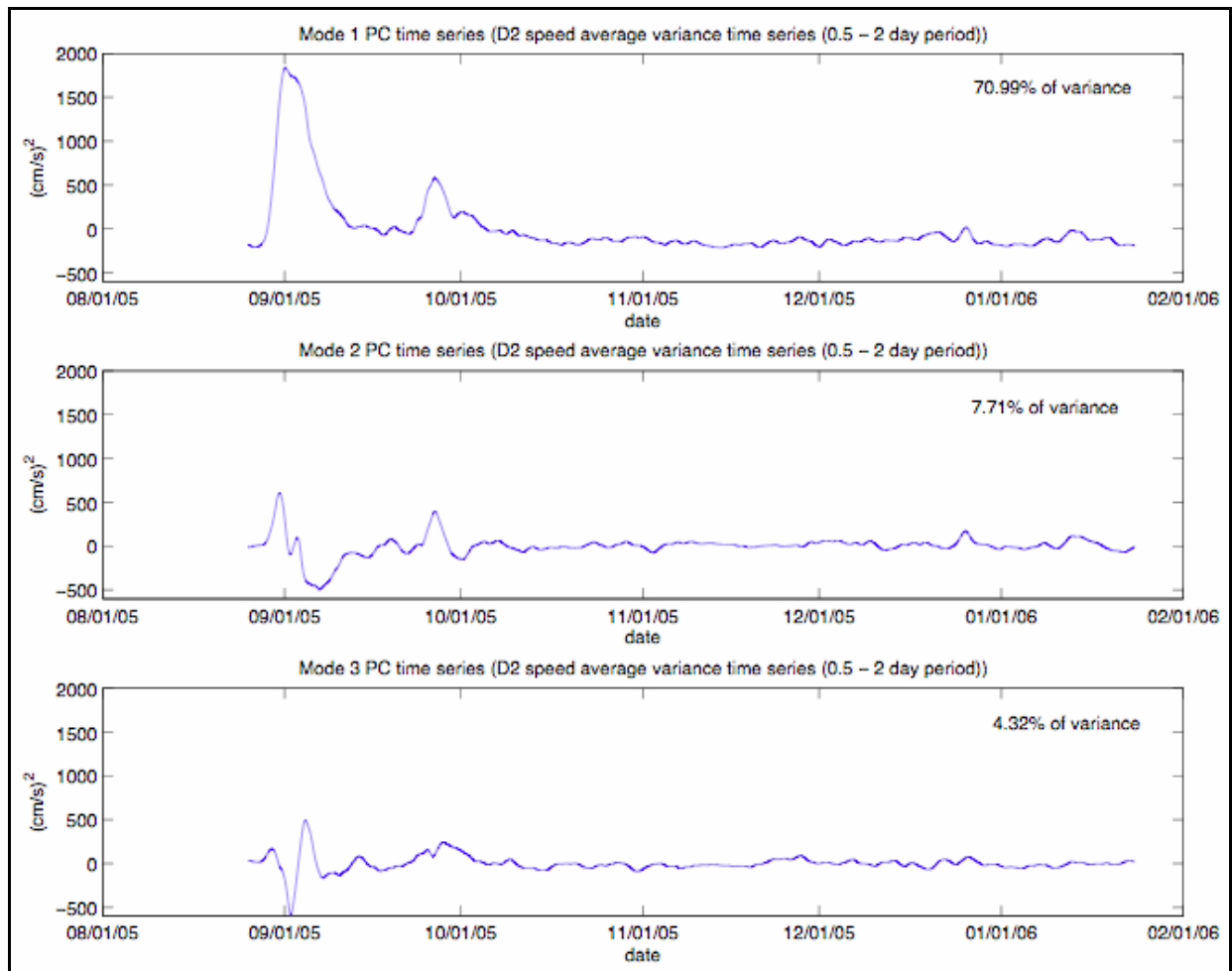


Figure 5.1-41. Principal component time-series for the leading modes from the combined three-mooring, full water column vertical EOF analysis of the frequency-averaged wavelet power in the inertial band (0.5 – 2 day period) during deployment 2. Mode one: 71 % of variance (top), mode two: 7.7% of variance (middle), mode three: 4.3% of variance (bottom).

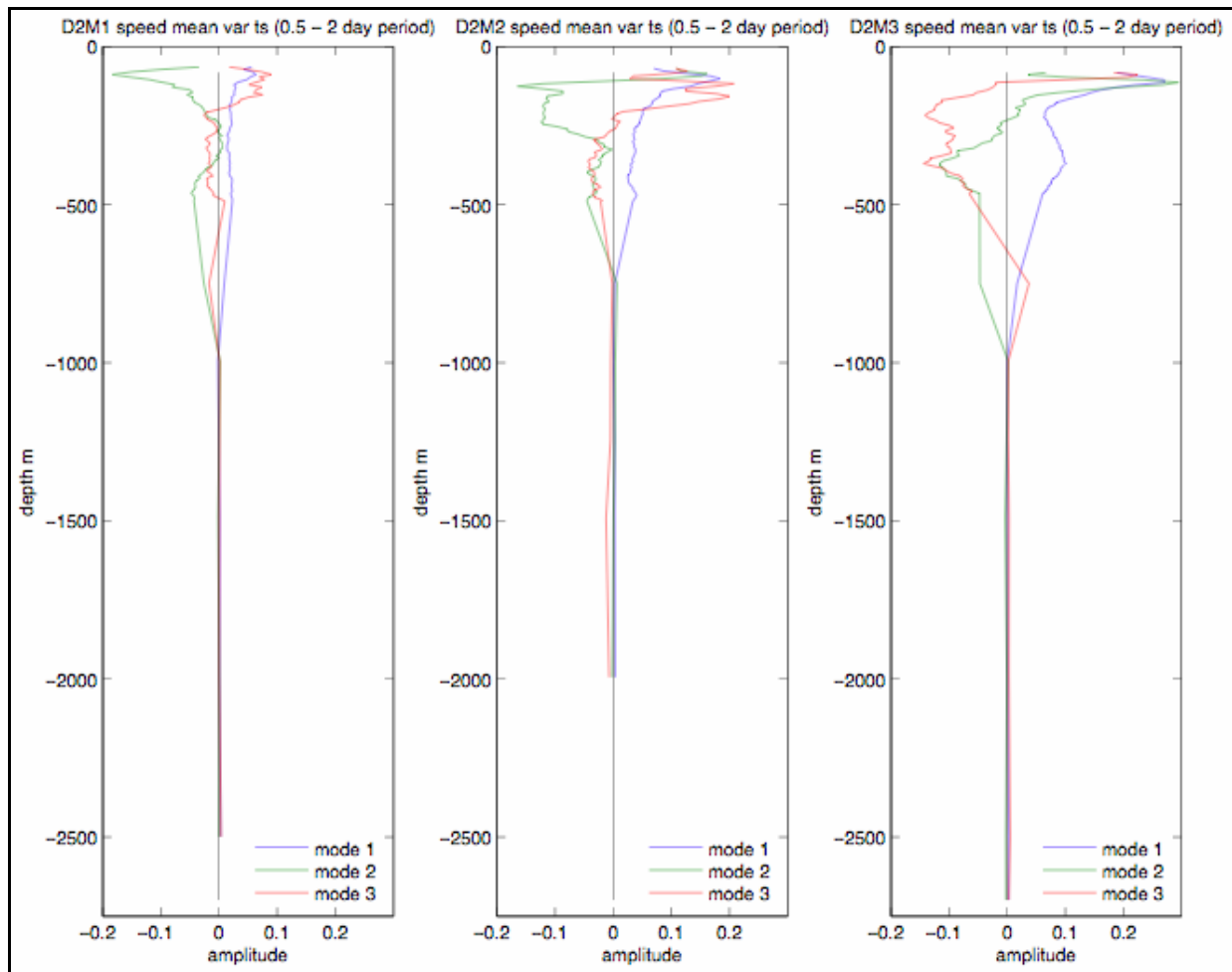


Figure 5.1-42. Amplitudes of leading modes for moorings M1 (left), M2 (center), M3 (right), for combined three-mooring full water-column vertical EOF analysis of the frequency-averaged wavelet power in the inertial band (0.5 – 2 day period) during deployment 2.

5.1.8.3 1-D Turbulence Closure Model

The oil industry uses current measurements to design facilities and plan for operations. Strong currents are the main concern. Similar to what was experienced during the Eastern GOM Study, historical measurements have shown that the main sources of strong currents in the GOM are:

- The LC and its eddies
- Hurricanes
- Bottom currents enhanced by topography (TRWs)

These phenomena are generally considered in isolation, but operations are now far enough out in the GOM that attention is being paid to the possibility that a hurricane and eddy could affect a location at the same time. This in fact occurred in the study area during the passage of Hurricane Katrina.

Hurricane Katrina passed near the Eastern GOM moorings while a cold core eddy was sitting over the southern portion of the study area, plus was located on the periphery of a strong LCE, Eddy Vortex. Figure 5.1-43 shows the locations of Eddy Vortex, as well as the location of a cold core eddy sitting over the southern portion of the study area, and their positions relative moorings M1, M2, and M3 just prior to the passage of Hurricane Katrina. Figure 5.1-44 shows the current speed measured at mooring M3 during Katrina. The measurements were compared to the results of a one dimensional turbulence closure model. The initial response on August 29 was modeled rather well, but the one dimensional model cannot represent the inertial oscillations after the storm passage.

The inertial oscillations are shown in more detail in Figure 5.1-45. The pass band was from 12 to 48 hours. As expected, the oscillations had an upward phase propagation and downward energy propagation. Figure 5.1-46 shows the oscillations at Mooring 1, just a few miles north of M3. The initial response was about the same, but the oscillations were much stronger at M3 than at M1. Hurricane Katrina passed about the same distance from the two moorings, but they were in a different situation with respect to Eddy Vortex and the cold core eddy shown in Figure 5.1-43, as M3 was in the middle of the cold core eddy. The measurements from M3 show that the site experienced enhanced inertial oscillations which were likely caused by non-linear interaction between the eddy and the hurricane. Figure 5.1-47 shows the lowpass and bandpass speeds at M3 for the entire second deployment. The lowpass currents were dominated by several intrusions of the LC or eddies, but strong diurnal currents only appeared with the combination of an eddy and a hurricane.

The concept that the interaction of the hurricane with the cold core eddy resulted in enhanced inertial oscillations was of high interest to the oil and gas industry's CASE joint industry project. With the permission of BOEMRE and the authors, current measurements from the moorings during the period of inertial oscillations generated by Hurricane Katrina were provided to researchers for that program. In return, their analysis was made available to this study team. The analysis is presented in a report (Accurate Environmental Forecasting, Inc. 2007) which is contained herein in Appendix F.

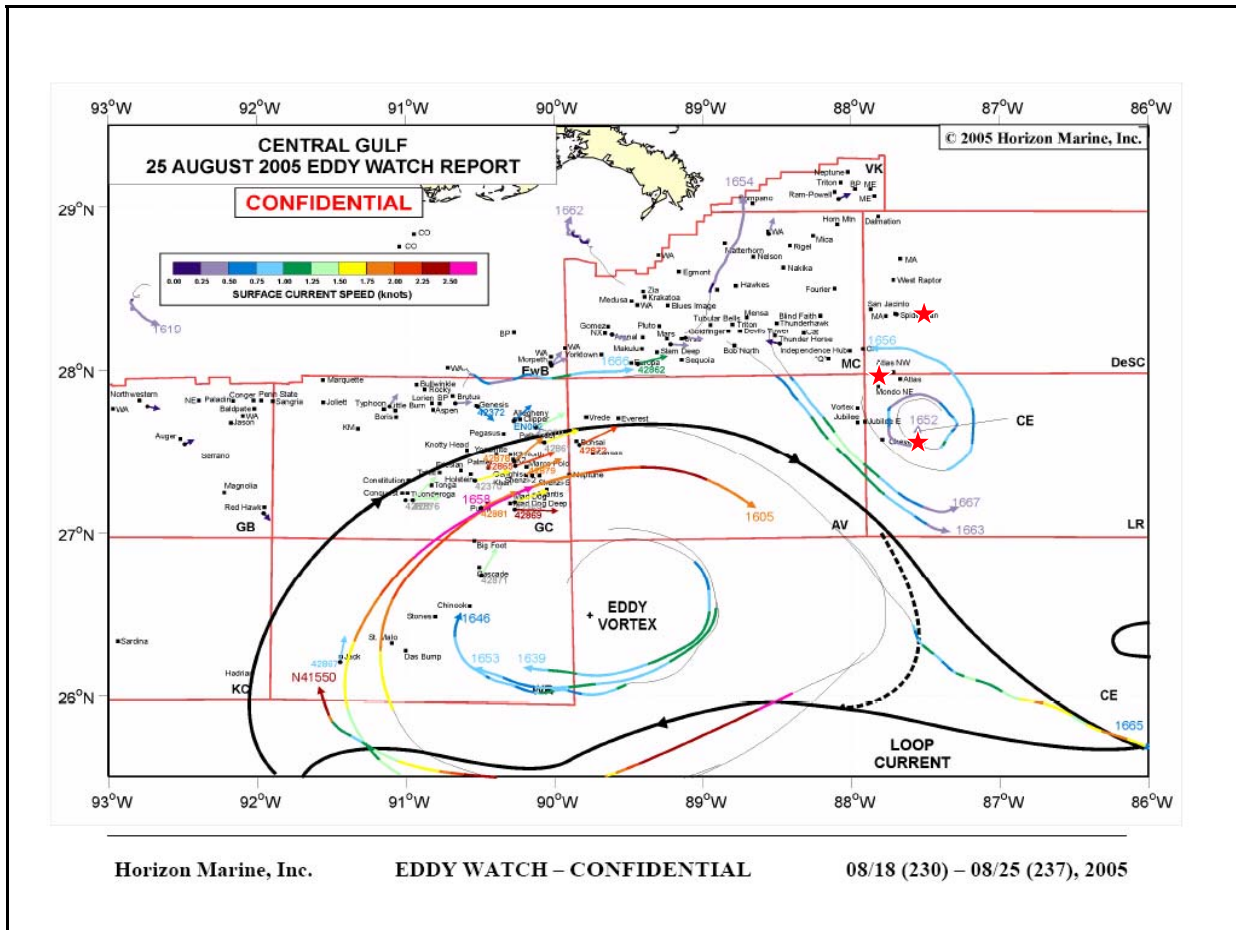


Figure 5.1-43. Eddy Vortex just before Hurricane Katrina. Mooring 1 is the northern red star and Mooring 3 is the southern red star.

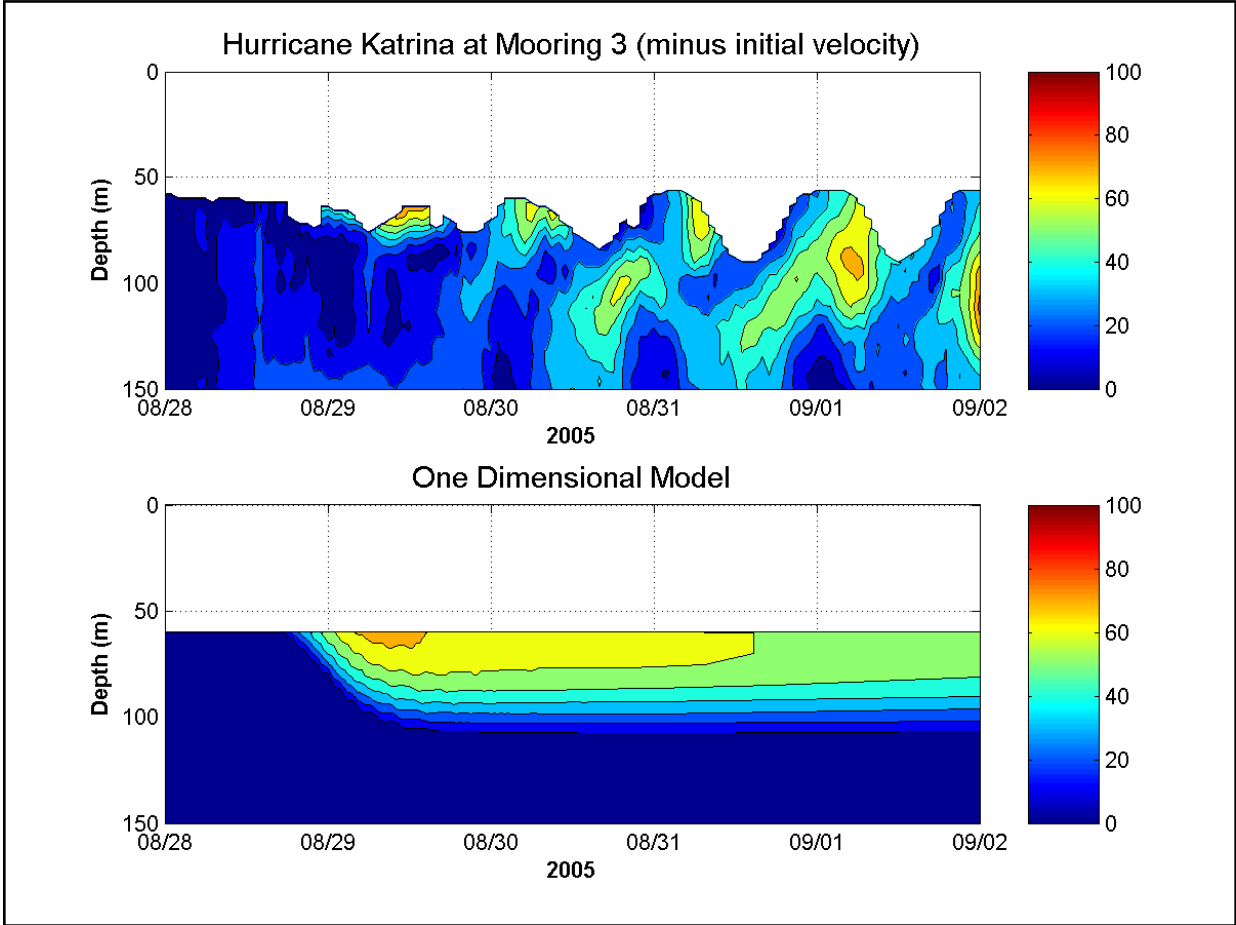


Figure 5.1-44. Measurements at Mooring 3 compared to a one dimensional turbulence model.

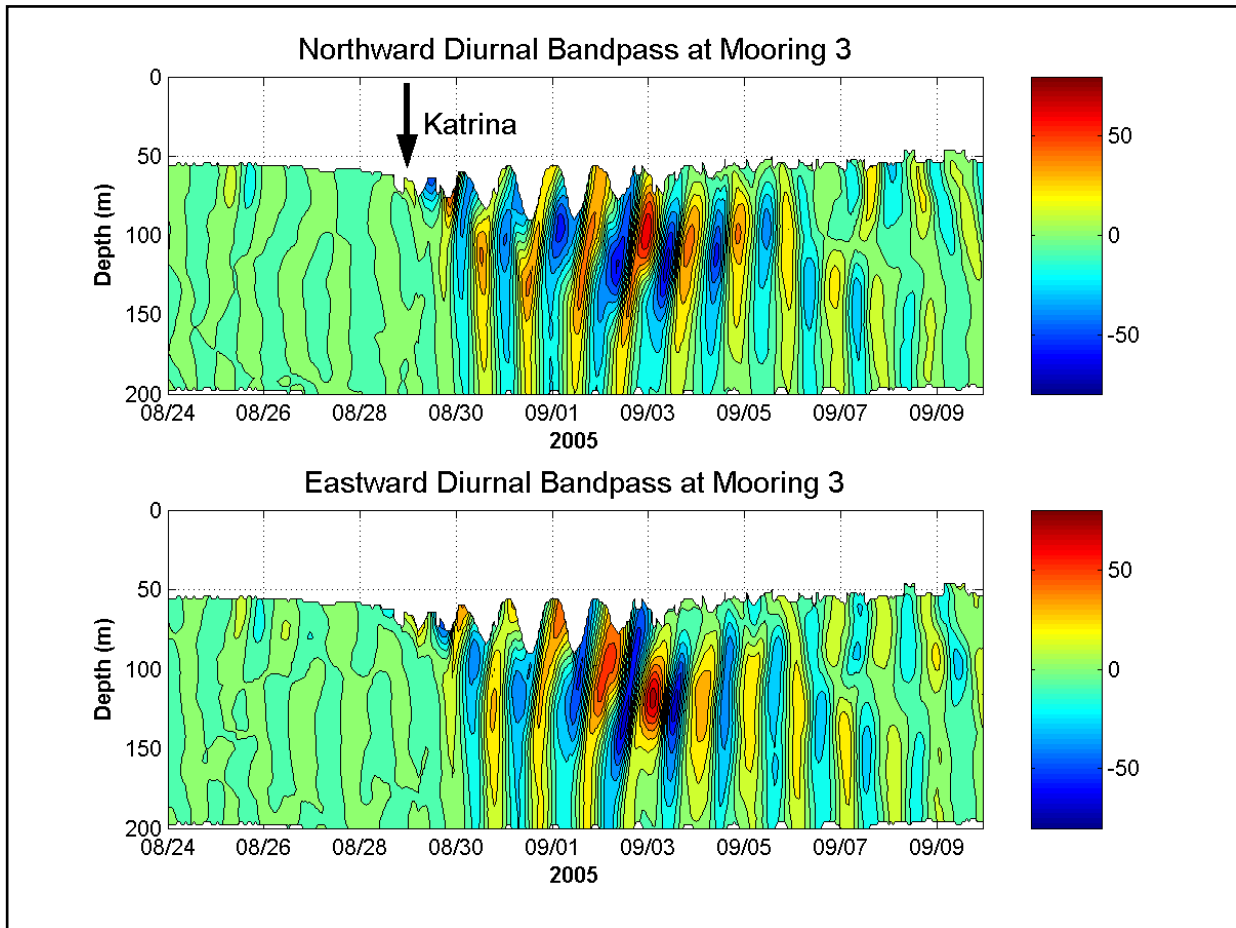


Figure 5.1-45. Diurnal bandpass currents at Mooring 3.

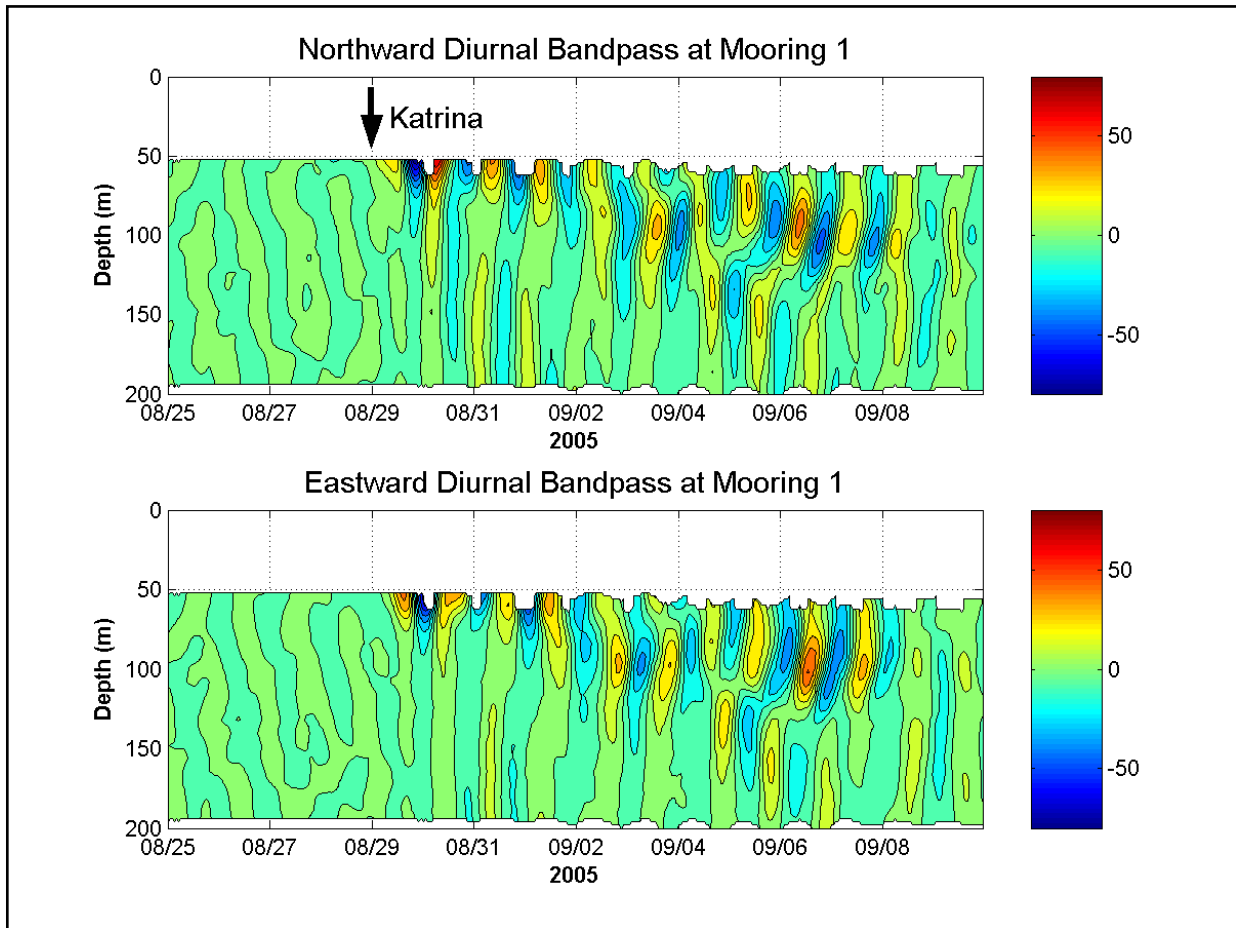


Figure 5.1-46. Diurnal bandpass currents at Mooring 1.

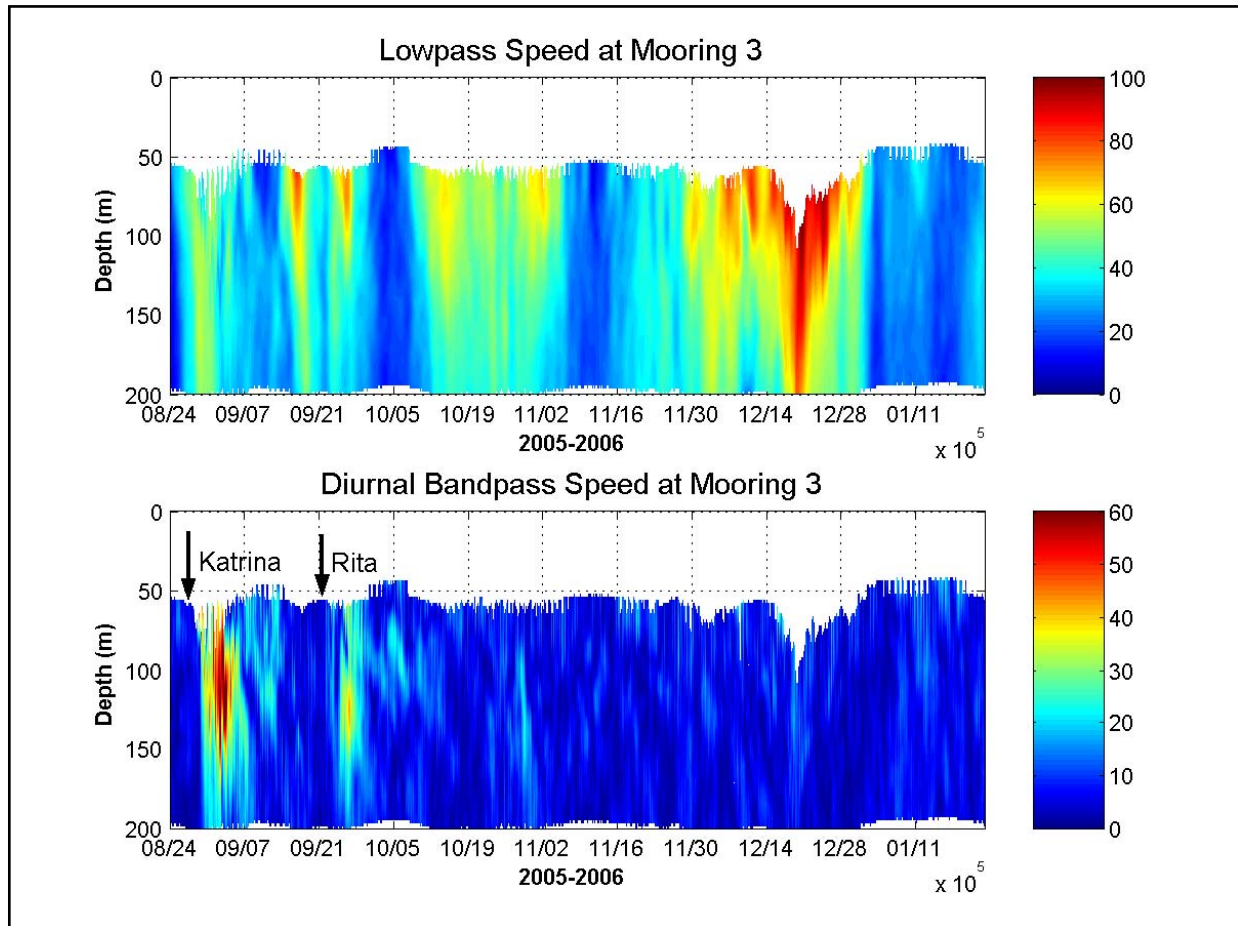


Figure 5.1-47. Lowpass current speed at Mooring 3 compared to the diurnal bandpass speed.

5.2 Hydrography Measurements

As discussed earlier, the LC and Eddy Vortex impacted the study area and surrounding water several times during the measurement period. The impact on the currents in this area have been presented earlier. In this section, we discuss evidence of these LC and LCE features on the hydrography when the warm surface waters extend below 100m.

During all three hydrography cruises, the presence of the LC or mesoscale eddy features were evident by the depth of the 20° isotherm. These features were discernable when the 20° isotherm reached 150-200m depth. During Hydrography Cruise 1 (17-23 January 2005) the southwest section of the study area was impacted by a warm water mesoscale feature (Figure 5.2-1). During Hydrographic Cruise 2 (18-25 August 2005) the 20° isotherm remained fairly shallow (~ 100 m) throughout much of the study area until the conclusion of the cruise. However, as the ship steamed toward the northwest, it appeared to have passed near the edge of Eddy Vortex (Figure 5.2-2). Here the 20° isotherm reaches to approximately 150m depth.

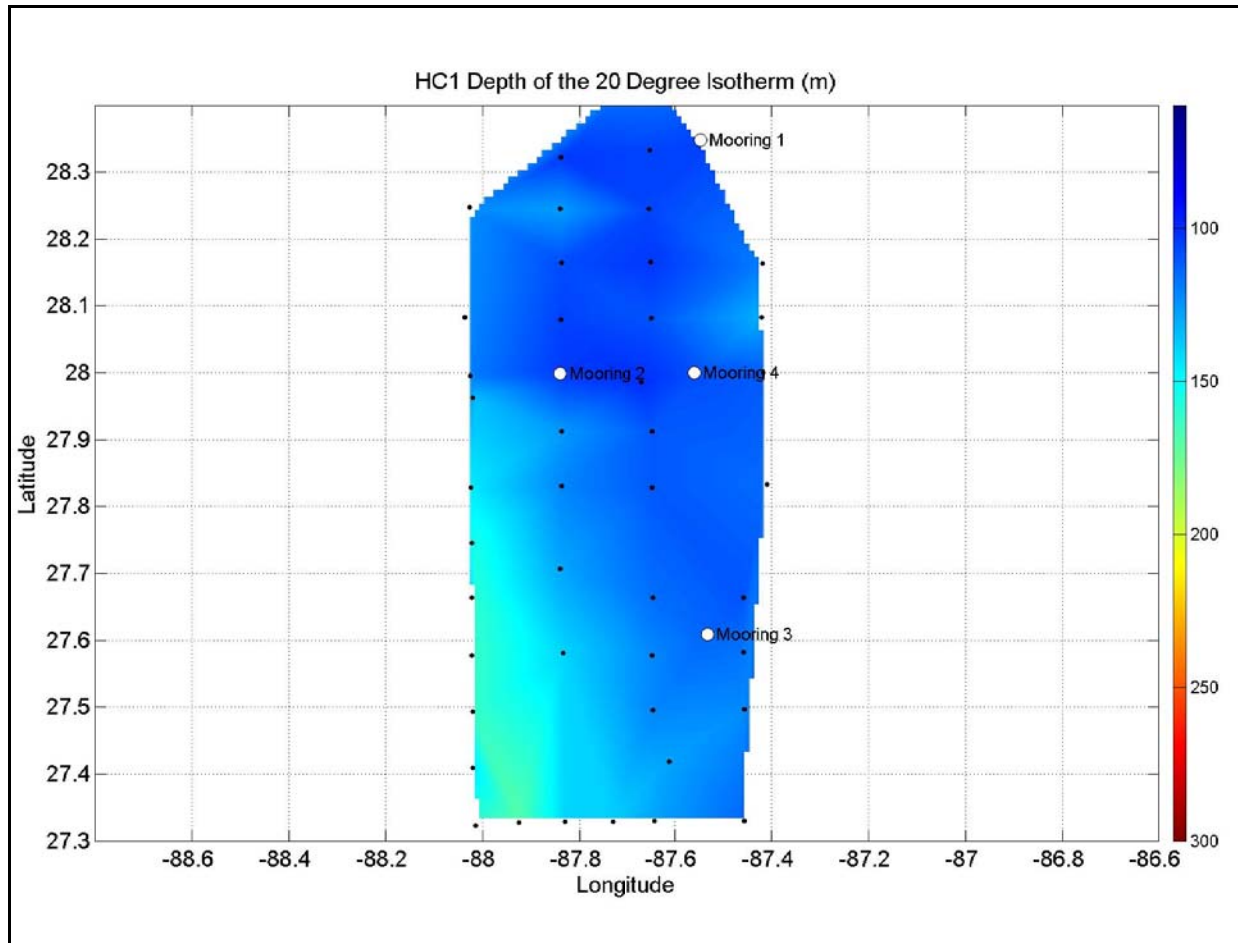


Figure 5.2-1. Color contour of the depth of the 20° isotherm during Hydrographic Cruise 1 in January 2005. Depth scale ranges from near surface (deep blue) to 300 m (dark red).

Hydrographic Cruise 3 (20-28 January) saw the most dramatic and intensive influence from the LC (Figure 5.2-3). The same transect line was sampled as the vessel transited into and out of the study area (Transects 1 and 2, respectively). These transects gave an indication of how far the edge of the LC had migrated north during the cruise. Comparing vertical profiles of these two transects further illustrated the presence of the LC. Figure 5.2-4 shows the contour along transect 1. The 20° isotherm remains at 100 m and above. Figure 5.2-5 shows the contour along transect 2. Here the 20° isotherm is deep at 150 m at the start of the transect (SE) and rises to above 100 m going northwestward. Most of the area south of a line bisecting the study area along these two transects was sampled in the later part of the cruise. The 20° isotherm has deepened to 150-250 m, a clear indication of the LC migrating into the study area.

In the eastern section of the study area (center to east edge) there may have been an indication of a possible cold core eddy (Figure 5.2-6). The 15° isotherm rose in the water column as the transect moved from the center to the eastern edge of the study area. However, the 15° isotherm never rose above 150m.

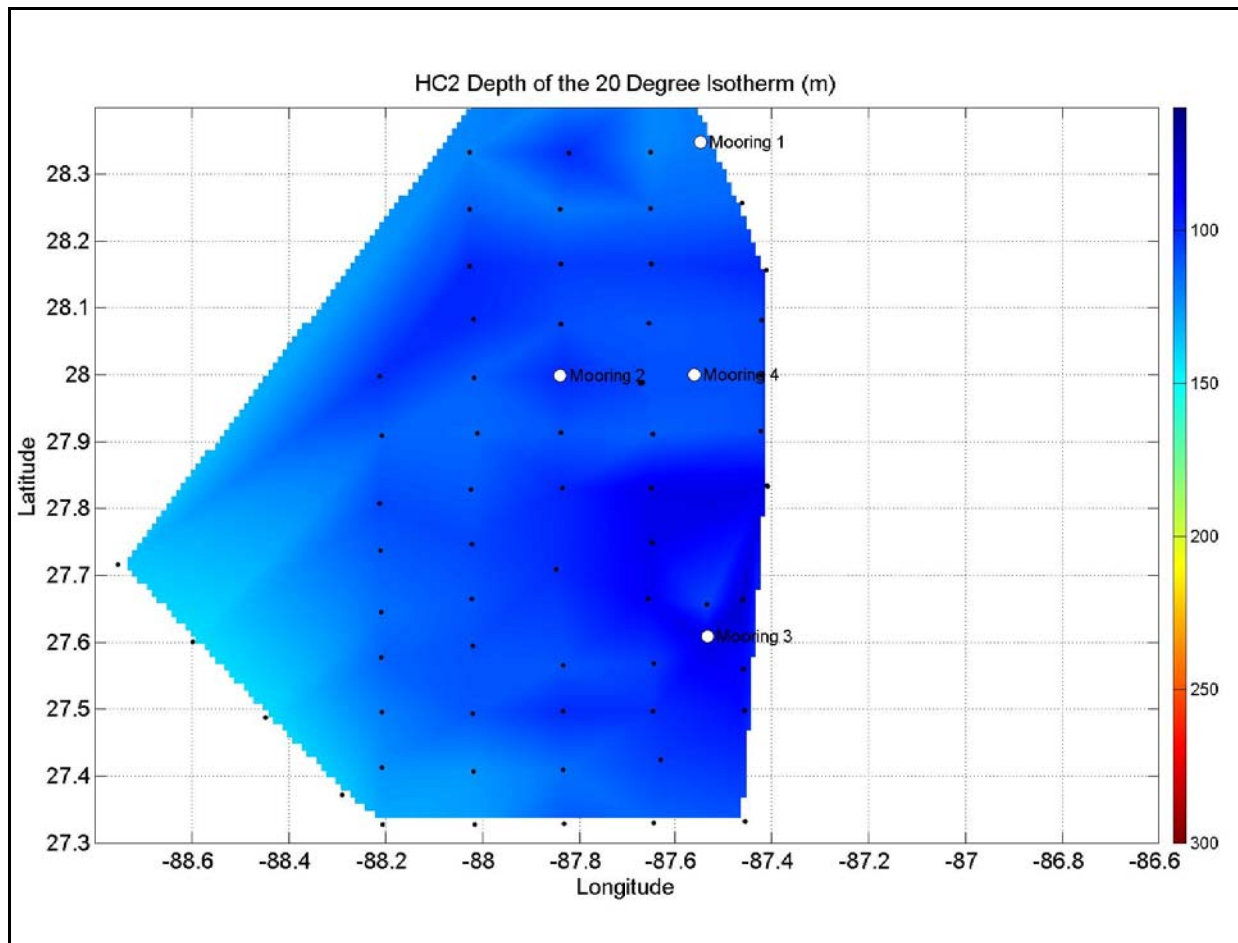


Figure 5.2-2. Color contour of the depth of the 20° isotherm during Hydrographic Cruise 2 in August 2005. Depth scale ranges from near surface (deep blue) to 300 m (dark red).

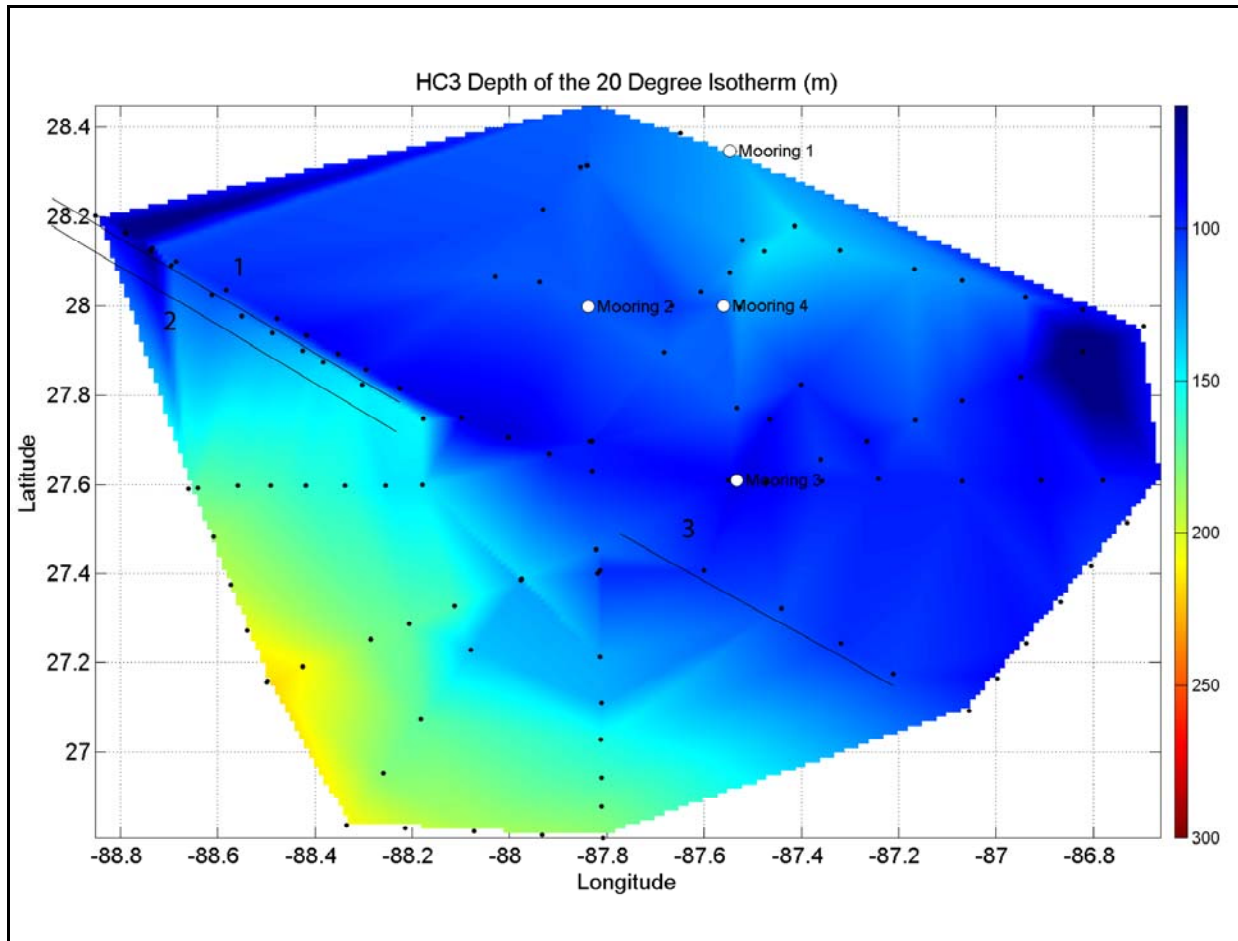


Figure 5.2-3. Color contour of the depth of the 20° isotherm during Hydrographic Cruise 3 in January 2006. Depth scale ranges from near surface (deep blue) to 300 m (dark red). Transect lines (1 through 3) indicate locations of the vertical color contours of temperature.

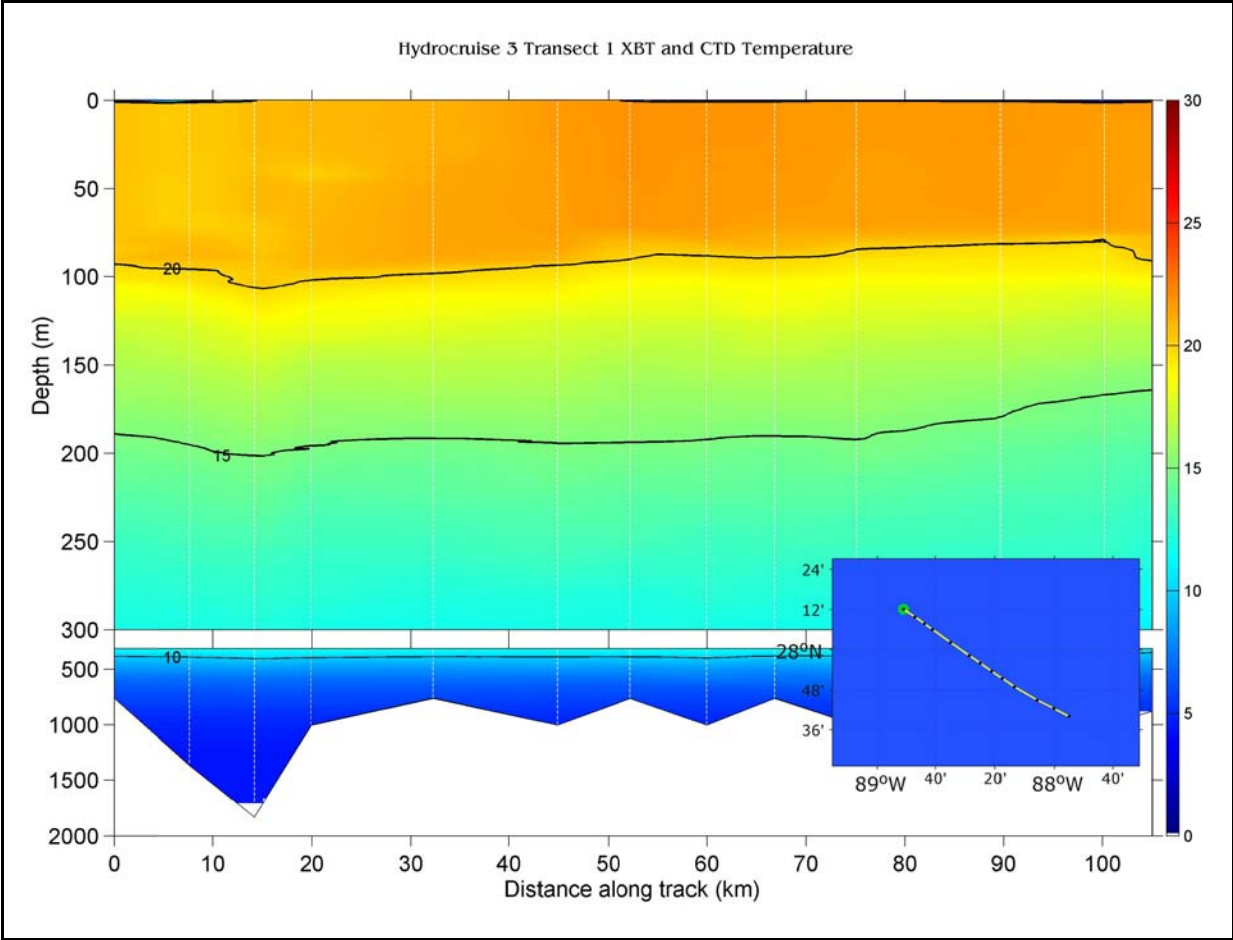


Figure 5.2-4. Hydrocruise 3 Transect 1 temperature from XBT and CTD casts. Inset shows the transect path.

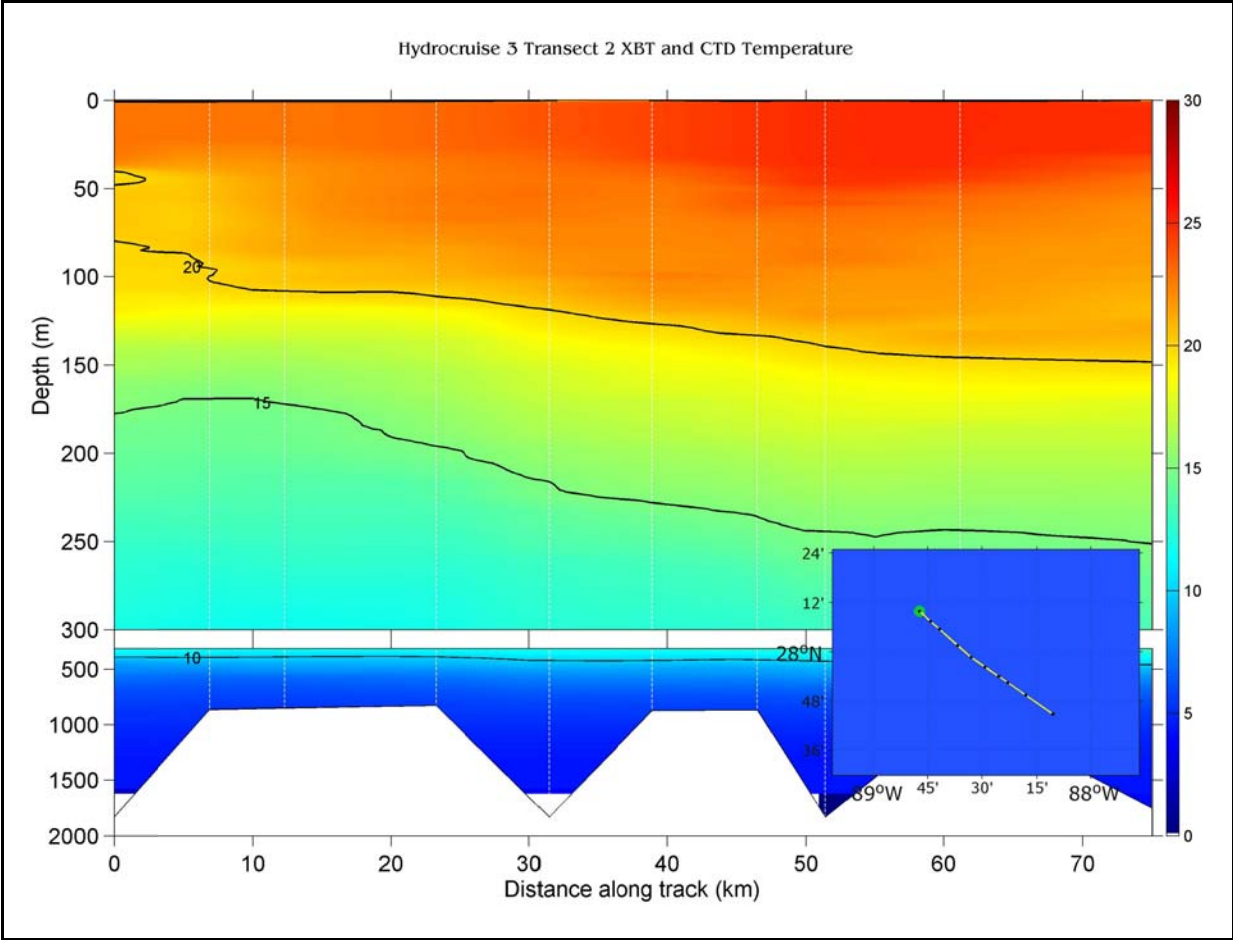


Figure 5.2-5. Hydrocruise 3 Transect 2 temperature from XBT and CTD casts. Inset shows the transect path.

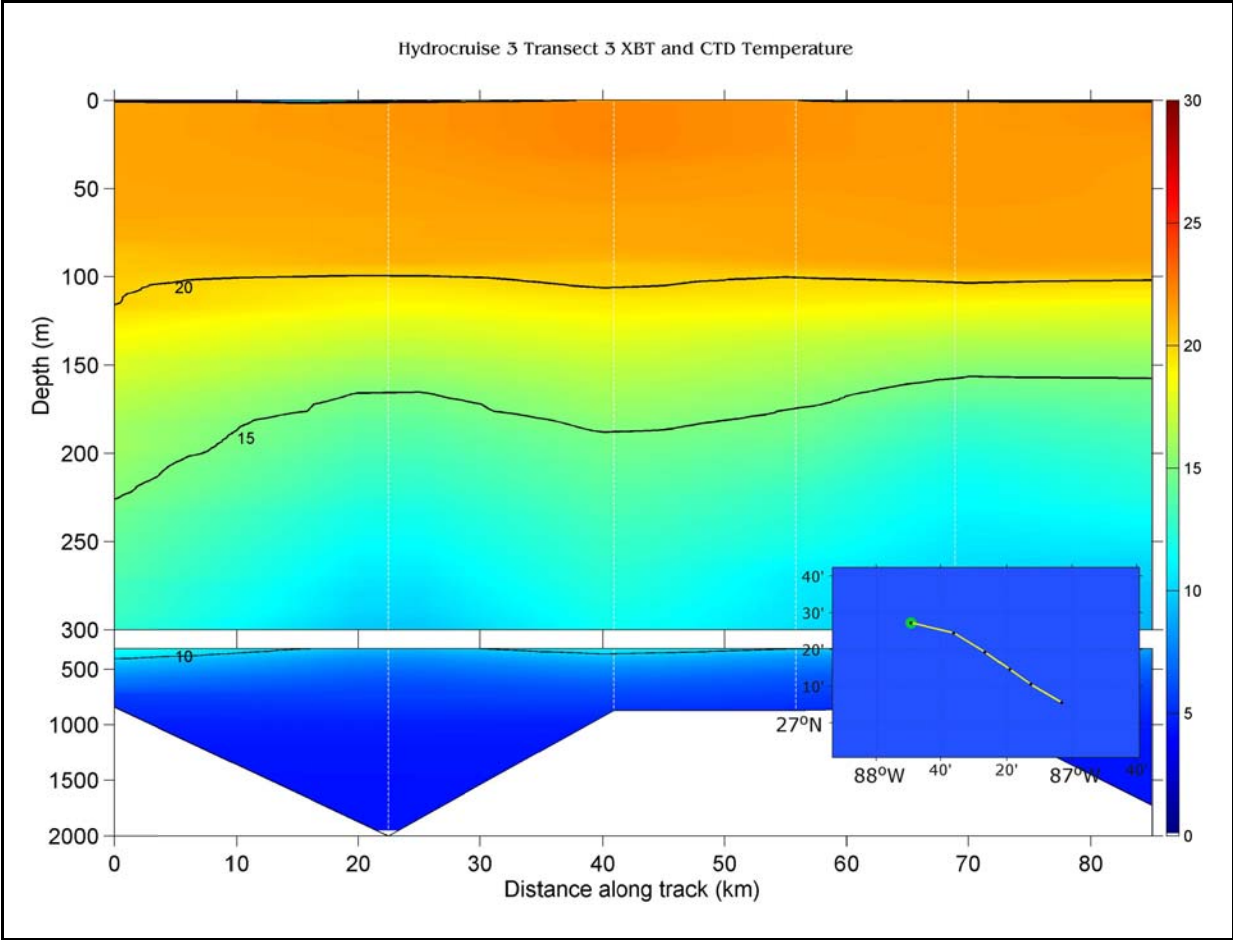


Figure 5.2-6. Hydrocruise 3 Transect 3 temperature from XBT and CTD casts. Inset shows the transect path.

6.0 DEEP CIRCULATION

6.1 *Overview of Observations of Topographic Rossby Waves in the Deep Gulf*

6.1.1 Background

Comprehensive long-term deep current measurements from moorings in the GOM were not made until the 1980's. These were analyzed by Hamilton (1990) who showed that the variability under the LC, in the north-central and northwest Gulf had the characteristics of topographic Rossby waves (TRWs) including high coherence through the lower water column, bottom intensification, and period and wavevector agreements with the dispersion relation as given by Rhines (1970). Hamilton (1990) speculated that pulsations of the LC were the primary source of the lower-layer TRWs, and evoked the Malanotte-Rizzoli et al. (1987) model of broad-band radiation from a pulsating meander in a channel over a sloping bottom as an explanation of the observations. A significant correlation, with a lag of 106 days, was found between deep currents under the east side of the LC and a mooring in the northwest GOM that implied a minimum group speed of $\sim 9 \text{ km d}^{-1}$ in rough agreement with group speeds estimated from the dispersion relation (Hamilton 1990). The dispersion relation indicated that TRW-trains propagate generally westward at higher group speeds than LC anticyclonic eddies, which translate westward and southwestward, at ~ 3 to 6 km d^{-1} , into the western GOM (Elliott 1982; Kirwan et al. 1984). Therefore, motions in the lower layer are largely decoupled from the eddy currents in the upper layer. Numerical modeling studies of Oey (1996) and Oey and Lee (2002) showed that simulated deep currents could be interpreted as TRWs, and the results suggested that TRWs radiated towards the northern slope as LC eddies translated across the western basin. Oey and Lee (2002) also suggested that the topography and the anticlockwise deep mean flows along the northern slope provided sufficient refraction of the TRWs that most energetic deep waves were confined to the deep basin.

Deep currents were previously measured due south of the Mississippi delta at the base of a steep 500-m escarpment (the Sigsbee escarpment) in 2000 m water depth (I1 in Figure 6.1-1) between September 1999 and September 2001 (Hamilton 2007). The flows were highly energetic; a maximum speed of 90 cm s^{-1} was observed 100 m above the bottom (Hamilton and Lugo-Fernandez 2001) with characteristic periods of ~ 10 to 20 days, which were much shorter than the previously observed ~ 20 to 100 days (Hamilton 1990). Moreover, a characteristic of these currents were that 4 to 5 wave trains were observed over the 2-year interval generally beginning with a high-energy burst (speeds $> 50 \text{ cm s}^{-1}$) and decaying over the next 3 to 4 months. Each wave train had slightly different characteristic wavelengths and periods, indicating different geographical source regions. Some could be associated with the presence of LC eddies; however, at least one occurred when upper layer eddy activity was weak. Hamilton (2007) speculated that these short period waves were being reflected from the steep escarpment rather than refracted by the changing bottom slopes, and suggested that the TRWs were locally generated and possibly trapped by the bathymetry. Mizuta and Hogg (2004) theoretically modeled TRWs propagating onto a shoaling slope. The shoaling slope induced a reflected wave component and a principal result was that a mean flow developed over the slope, forced by convergence of boundary layer Reynolds' stresses. DeHaan and Sturges (2005) came to similar conclusions in that they attributed the observed anticlockwise (i.e. westward) deep mean flow along the base of the northern slope to rectification of incident TRWs.

Malanotte-Rizzoli et al. (1995) proposed wavenumber coupling between a propagating surface feature, such as a frontal eddy, and deep flows as an alternate generation mechanism for TRWs. Pickart (1995) showed that this mechanism could account for the generation of 40-day TRWs that are observed at Cape Hatteras by 40-day eastward propagating meanders of the Gulf Stream. Wave trains of TRWs propagate westward and southwestward along the slope in the northwest Atlantic, with phase propagation southeastwards toward deeper water. The coupling to eastward propagating meanders requires that the bottom slope have a direction such that a 40-day TRW wavenumber has an eastward component that matches the eastward wavenumber of the meanders. This coupling mechanism may be important for short period TRWs in the GOM because energetic cyclonic eddies are observed on the LC front and on the edges of LC eddies (Vukovich 1986; Zavala-Hidalgo et al. 2003). However, because waves are observed to have wide range of periods between ~ 10 and 100 days, the generation of broadband TRW radiation by the large scale movements of the LC and LC eddies (Malanotte-Rizzoli et al. 1987) should not be discounted. Hogg (2000) indicated that energetic near bottom currents, with TRW characteristics, observed over the tail of the Grand Banks seemed to better agree with broadband radiation by the Gulf Stream and warm rings, rather than through meander coupling.

As noted previously, over the past several years, three major observational programs have taken place in the deep waters of the north-central, northwest and the northeast GOM. These studies deployed closely spaced arrays of current meter moorings and inverted echo sounders with pressure sensors (PIES). The central Gulf study also deployed 36 RAFOS floats at depths between 1000 m and the bottom. These observations allow a more comprehensive analysis of deep-water circulations, and an extended and refined description of the lower-layer TRW regime in the GOM. Thus, the aim of this overview is to review these new data as they pertain to the lower-layer below 1000 m, particularly in regard to the generation, propagation and dissipation of TRWs, deep mean flows, and possible couplings to upper-layer LC and LCE circulations.

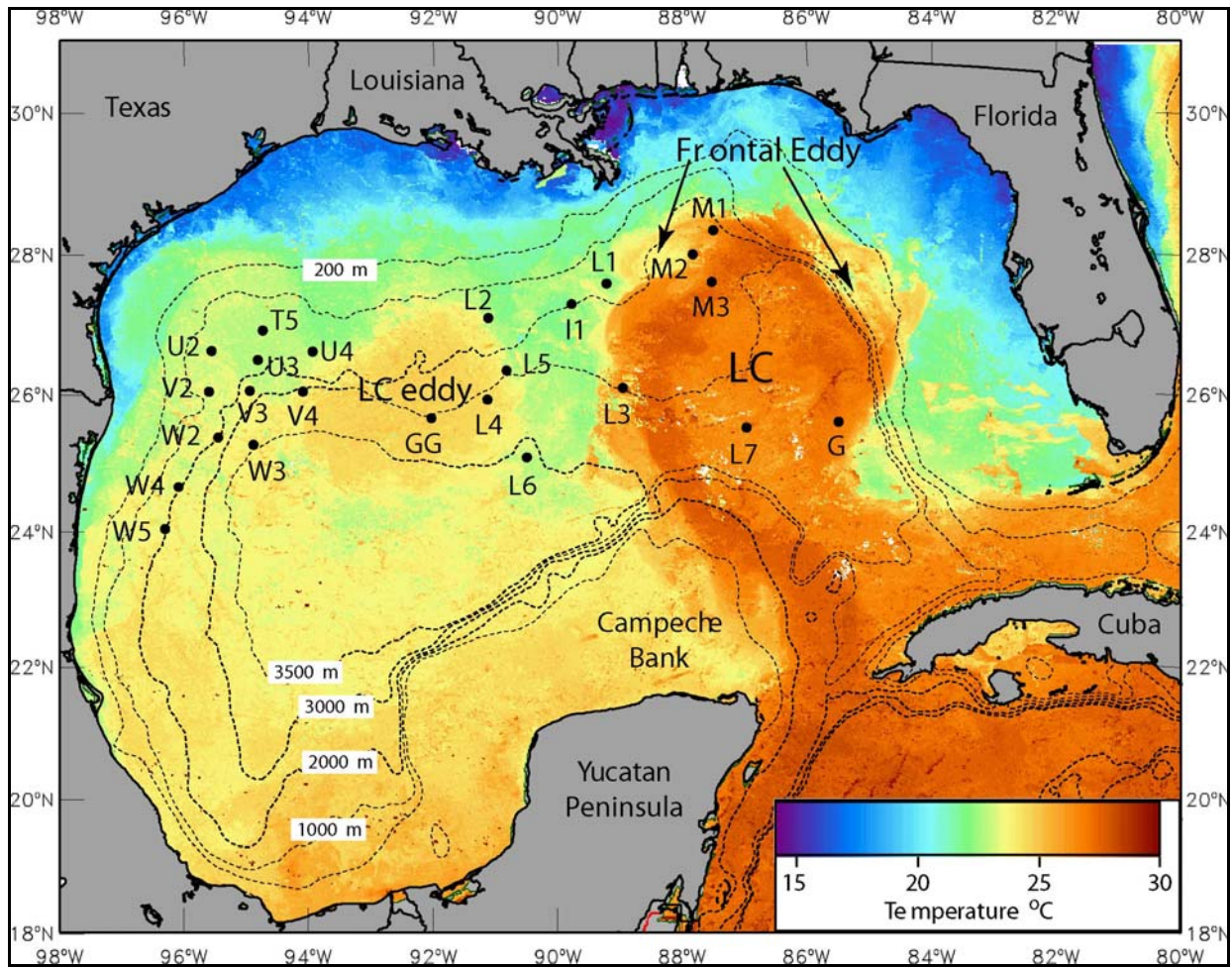


Figure 6.1-1. Locations of the principal full-depth moorings used in the analyses. The SST image is a 3-day composite centered on February 5, 1998, and shows an extended LC and a detached LCE (named eddy El Dorado). Image courtesy of John Hopkins University Applied Physics Laboratory.

6.1.2 Data

Because this overview uses observations from a number of recent MMS studies, as well as from this eastern GOM study, the databases will be briefly reviewed here.

6.1.2.1 Moorings

The majority of recent full-depth sub-surface, taut-line moorings deployed in the GOM have been instrumented with combinations of ADCPs, single point current meters, and temperature and salinity sensors. Generally ADCPs are deployed in the upper layer with a common configuration being an upward-looking 75 kHz at 450 to 500 m, and below this, point current measurements at fixed intervals of 250 m and 500 m above and below 1000 m, respectively. Moorings in Mexican waters (W2, W3, W4, W5 and L6: Figure 6.1-1) were also instrumented with upward-looking 75 and 300 kHz ADCPs at ~1200 m and ~10 m above bottom, respectively. Table 6.1-1 lists the observational studies, their originating institutions, and a subset of these moorings are located in Figure 6.1-1. Some of these studies also deployed bottom moorings with either 1 or 2 current meters at 500 and/or 100 m above the seabed (MAB) and PIES as part of their array designs. Moorings G and GG (Figure 6.1-1) were deployed prior to 1990, and were previously analyzed by Hamilton (1990).

All these records were treated in a uniform manner, similar to the methodologies discussed in Chapter 2. In this chapter, current meter moorings will be referred to by a 2 character ID, where the first letter is a transect or group identifier, and the second character is the mooring number within the group (Figure 6.1-1 and Table 6.1-1). Groups with the same first letter were deployed at similar times. Because various subsets of the observations are used in the following sections, the depth levels will be identified as they are employed.

6.1.2.2 RAFOS Floats

RAFOS floats were deployed in the Exploratory program, and this was the first time such instruments had been used in the GOM. RAFOS floats (Rossby et al. 1986) are neutrally buoyant glass-tube floats that can be ballasted in the laboratory to drift with the currents below the surface at a user selected pressure (roughly depth) or density for extended periods. The floats are equipped with temperature and pressure sensors, and with an acoustic hydrophone that listens to the arrival times of acoustic signals sent from pre-deployed sound sources. In the Exploratory study, the floats received acoustic signals from three sound sources deployed at the sites shown in Figure 6.1-2. The sound sources were programmed to transmit every 8 hours. At the end of the deployment, the floats surfaced and transmitted their data to shore via satellite. The focus of the study was on deep currents, so all the floats were configured to follow pressure as opposed to density surfaces. The initial deployment of 30 floats was in April 2003, followed by 6 more in October 2003. The former surfaced in April 2004, and the latter at the end of May 2004. The floats were launched on a grid pattern over the lower slope in the region encompassed by the L1 to L4 moorings (Figure 6.1-1). Nominal launch depths were at 500-m intervals between 1000 and 3000 m, with the majority (15 out of 36) at 1500 m.

During the course of the Exploratory study, monitoring showed that two of the sound sources were failing after 3 months in the water. They were replaced about 6 months into the study. Therefore, most of the float tracks have two sections, the first 3 months and the last 6 months of the one-year deployments. Again, more details of the RAFOS float part of the Exploratory program can be found in Donohue et al. (2006).

Table 6.1-1

Moorings Deployed by Observational Studies in the Deep GOM.

Name Reference	Institution	Dates	Locations (Fig. 6.1-1)	Numbers		
				Full-Depth	Bottom	PIES
DeSoto Extn. Hamilton et al., (2003)	SAIC	8/99-8/01	I1	1	4	3
Exploratory Donohue et al., (2006)	SAIC	4/03-4/04	L1 to L4	4	15	27
Exploratory	LSU	4/03-6/04	L5	1	-	-
Canekito Sheinbaum et al., (2007)	CICESE	5/03-8/04	L6	1	-	-
SEBSEP Donohue et al., (2006)	Industry	4/03-5/04	Escarpment Transect North of L4	-	6	-
LSU Long-Term	LSU	4/03-6/04	L7	1	-	-
NW GOM Donohue et al., (2008)	SAIC	4/04-7/05	T5 to V4	13	-	10
W GOM	CICESE	8/04-11/05	W2 to W5	5	-	-
NE GOM	EHI	1/05-1/06	M1 to M3	3	1	8

Institutions listed above:

SAIC – Science Applications International Corporation, Raleigh, NC

EHI – Evans Hamilton Inc., Seattle, WA

LSU – Louisiana State University, Baton Rouge, LA

CICESE – Centro de Investigación Científica Y Educación Superior de Ensenada, Ensenada, Mexico

Industry – DEEPSTAR Oil Industry Consortium

After the travel times were converted to geographical positions, individual float tracks were smoothed using the successive corrections method of Pedder (1993) using a time scale of 1 day, and resampled at 6 hour intervals. This was the same as the procedures used by Hamilton et al. (1999) for near-surface drifters in the GOM. A spaghetti diagram of all the smoothed tracks produced by the 36 floats is given in Figure 6.1-2.

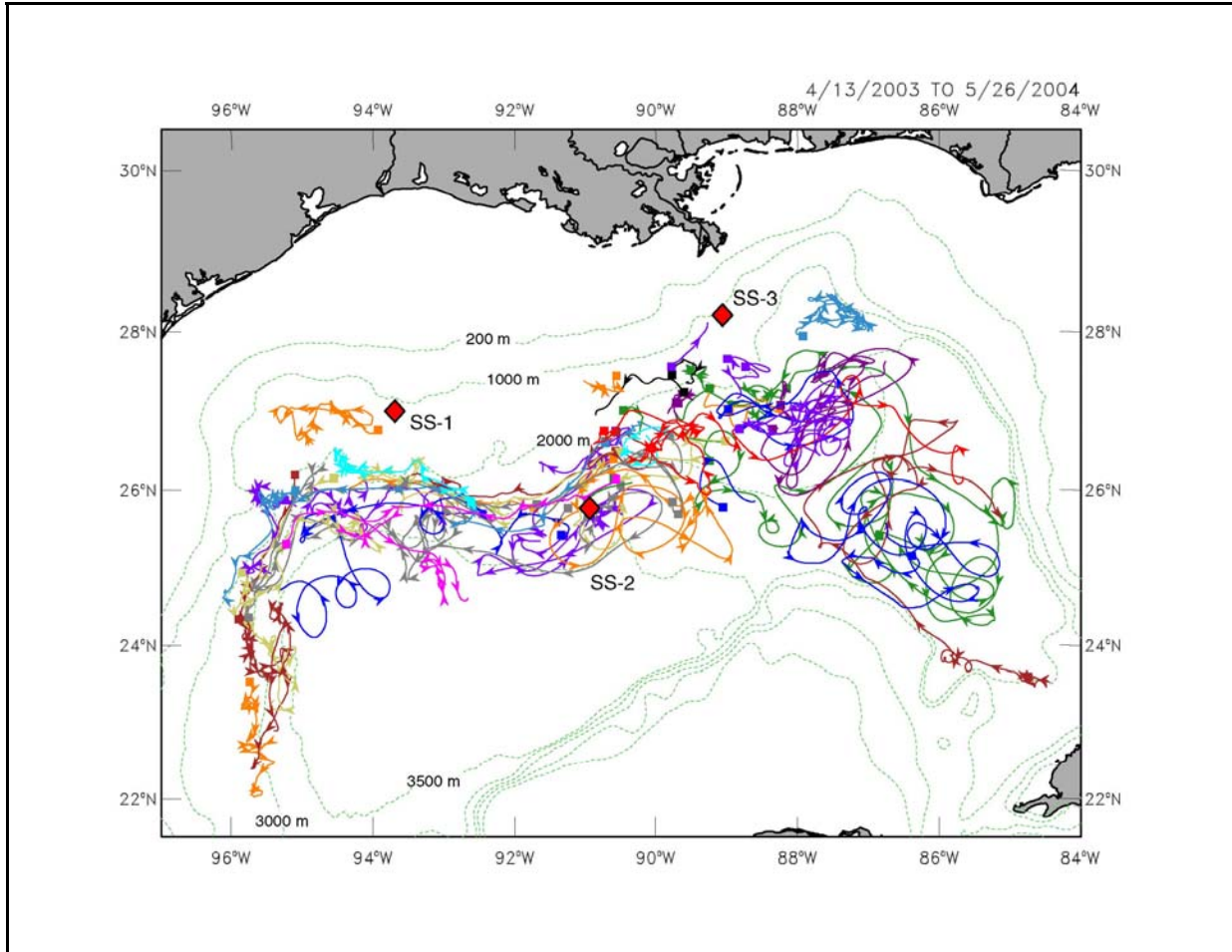


Figure 6.1-2. Spaghetti plot of all 36 RAFOS float smoothed trajectories at all depths (1000 to 2500 m) in the Exploratory Study. Sound sources are given by the large diamonds, and the beginning of each track is indicated by a square. Arrow heads are at 10-day intervals. Most floats have two tracks because of sound source failures in the first 3 months of the program (from Donohue et al. 2006).

6.1.3 Gulf-Wide Overview of Deep Currents

Generally, in the GOM, the current velocity variability is highly coherent through the lower water column at depths greater than 1000 m. One of the fundamental questions is the spatial distribution of the depth-integrated eddy kinetic energy (EKE) over the lower water column that can be attributed to TRWs. This quantity is a more complete measure of wave EKE than using EKE at a single depth level. The former was estimated for each full-depth mooring that was deployed in water depths of 2000 m or greater, by calculating the first complex empirical orthogonal function (CEOF) using the available velocities from depth levels in the lower part of the water column (Table 6.1-2). Thus,

$$U(z,t) = \sum_n A_n(t) \cdot e_n(z), \quad (6.1.1)$$

where all quantities are complex and the mode amplitude, A_n , is normalized to unit variance. The record means of U were removed before the analysis. The mode amplitudes and eigenvectors, e_n , are relative to an arbitrary reference, and the usual practice (Merrifield and Winant 1989) is to rotate the spatial eigenvector into the frame of the semi-major principal axis of the corresponding amplitude time series. The depth-integrated EKE between 1000 m and 50 meters above bottom (MAB) is given by:

$$EKE_H = \frac{1}{2} \int U^* U dz = \frac{1}{2} \sum_n A_n^*(t) A(t) \int_{1000}^{H-50} e_n^*(z) e_n(z) dz \quad (6.1.2)$$

where the integral was approximated by using the trapezium rule for the discrete measurement levels. The integral was terminated 50 m above bottom (H) so as to exclude the bottom boundary layer, and for the practical reason that the majority of moorings had no measurements there. In the following analysis, only the first mode ($n = 1$) was used because for most moorings, this accounted for a high percentage of the total variance of the input records (Table 6.1-2). The first mode also has the characteristics of TRWs with bottom intensification, vertically coherent fluctuations (guaranteed by the use of a single CEOF mode), and principal axes that are at a small angle to the general trend of the local isobaths. The use of depth levels above 1000 m was sometimes necessary to properly characterize the lower-layer velocity profile. In these cases, the percent of total variance accounted for by the mode was reduced somewhat over other similar locations, because these upper-levels contain some surface layer eddy signals (e.g., GG and L7 in Table 6.1-2).

The lower-layer depth-integrated EKE_H for the locations in Table 6.1-2 are given in Figure 6.1-3, which also shows the depth-mean standard deviation ellipses obtained from the eigenvectors. The highest EKE_H was under the LC at G and L7, with the west side having the maximum observed energy. Energy levels reduced towards the west and also north of L7; however, relatively higher energy levels were observed moving into the escarpment from L7 through L3 and L5, suggesting a wave propagation path with lower EKE_H to the north (M3) and south (L6). The base of the escarpment was approximately delineated by I1, L5, L4, GG and V4. It was somewhat surprising that the energy level at M3, which was close to the northern LC front for most of 2005, was less than at the escarpment further to the west. Moreover M1, which was near the steep west Florida escarpment, had essentially negligible lower-layer EKE_H . In the west, the two deeper locations at V4 and W2 had EKE_H comparable to that at 92°W (GG), but again the moorings at the base of the steep Mexican slope had small variances with W5 also being essentially negligible. Oey and Lee's (2002) numerical model studies had the result that 20 to 100 day deep energy was primarily restricted to a band across the northern GOM between the ~ 3000 and 3500 m isobaths, which had some correspondence to Figure 6.1-3. Radiation by the model LC and westward translating LCEs was the attributed source of this deep energy. The standard deviation ellipses (Figure 6.1-3) tend to show major principal axes approximately aligned with the isobaths near the escarpment and steep topography. On the abyssal plain the fluctuations were less rectilinear and the principal axes were at small angles to the isobaths. This was particularly evident at L3.

The normalized amplitude time series for each location are given in Figure 6.1-4. TRW theory (Rhines 1970) defines a cut-off frequency, $N\alpha$, where N is the lower-layer Brunt-Vaisala frequency and α , the local bottom slope, above which waves are not supported by these dynamics. The deep GOM topography is roughly bowl shaped; therefore, locations with the deeper water depths should tend to have the largest fluctuations at longer periods. This rule holds quite well in both the eastern and western parts of the GOM basin, with the dominant periods being shorter closer to the continental slope (e.g. W2, M2 and I1) and longer in deeper water (e.g., L7, L6, M3 and W3). The spectra of the normalized amplitudes are given in Figure 6.1-5, where the relative contributions to the variance clearly show that longer periods tend to dominate in deeper water. Two dominant peaks of 50 to 60 days, and 25 to 30 days can be identified with water depths of $> \sim 3000$ m, and ~ 2500 to 3000 m, respectively. The latter peak was prominent in the early central and western GOM deep current data (Hamilton 1990), and clearly the yearlong records resolve most of the variance at these sites. This was not the case for the very deep locations, including the site in the western GOM (W3), where the low frequency tails, with periods longer than 100-days, were not resolved. Some of these deep records (W3 and L6) had energy also at the 25 to 30 day period peak. In the eastern GOM, the LC pulsation and eddy shedding had irregular intervals ranging from about 3 to 18 months (Sturges and Leben 2000), and it would be expected that some of this variability would be transferred to the lower-layer. The amplitudes at I1, M2 and L3 did not fit into these frequency band classifications. I1 and M2 had prominent peaks shorter than 30 days. The short period waves at I1, and associated near bottom moorings, had been previously analyzed by Hamilton (2007) who suggested that wave trains with periods of ~ 8 to 12 days were generated fairly local to the eastern Sigsbee escarpment and were trapped there by the topography. The amplitude at L3 is the only one that shows fairly uniform energy over a broad band with periods from 10 to ~ 100 days.

Based on this analysis, frequency domain EOFs were calculated, in a similar manner to the CEOFs above, for some or all of three frequency bands, 0.01 – 0.03, 0.024 – 0.05, and 0.05 – 0.2 cpd based on the spectral content at each location (Figure 6.1-5). Table 6.1-2 gives the percentages of total variance in each frequency band, accounted for by the modes, for each mooring. In most cases one mode sufficed, but in a few cases two modes were significant according to the eigenvalue criteria of North et al. (1982). The depth integrated EKE_H and depth mean standard deviation ellipses were calculated using similar formulae to those used for the time domain CEOF analyses, and are given in Figure 6.1-6. The distribution of EKE_H confirmed the qualitative evaluation of dominant periodicities from Figure 6.1-4 with the lowest frequency (52-day) band tending to have the most energy at 3000 m depth or more with decay towards the west from the west side of the LC (L7). The center frequency band (29-day) also had some power at L7 and had a more uneven distribution with most of the larger relative contributions to the total energy being near the escarpment (e.g., L5, GG and V4, but not L4). The shortest period (10-day) band was mainly significant in a small region south of the delta (L3, I1, and L5).

Table 6.1-2

Lower-Layer EOF Analysis of Currents by Mooring.

Mooring	Depth Levels (m)	Mode 1 Percent of Total Variance				Start Date (yy-mm-dd)	Length (days)
		CEOF	Frequency Bands (cpd)				
			0.01-0.03	0.024-0.05	0.05-0.2		
G	1565, 2364, 3174	97.7	63.2/ 35.3a	77.3/ 20.9a	-	84-07-24	552
GG	725, 1650	71.8	71.6	80.8		87-11-15	346
I1	1000, 1200, 1600, 1800	88.9	83.7	87.9	84.8	99-09-02	525
L3	1000, 1500, 2000, 2500, 2900	97.7	94.0	83.2	73.5	03-04-09	363
L4	1000, 2000, 2500, 2900, 3250	97.0	97.8	77.0	-	03-04-05	365
L5	1165, 1415, 1677, 1925, 2175, 2625, 2925	95.0	96.1	96.7	84.4	03-04-22	411
L6	1005, 1479, 1985, 2490, 2995, 3308	97.2	80.6	87.9	-	03-05-16	465
L7	500, 2000, 3000, 3187, 3256	85.5	70.4/23.6a	69.9/21/6a	-	03-04-24	410
V3	1000, 1500, 2000, 2400	77.3	79.9	92.8	-	04-03-25	456
V4	1000, 1500, 2000, 2500, 3000	92.5	84.5	92.4	-	04-03-24	456
W2	1000, 1110, 1544, 1965	76.4	83.0	83.3	-	04-08-31	431
W3	1007, 1541, 2048, 3038, 3518	90.9	89.9	62.4/33.4a	-	04-08-31	431
W4	1572, 1941	84.4	-	-	-	04-08-30	433
W5	1025, 1125, 1572, 1998	61.8	-	-	-	04-08-30	434
M1	729, 1224, 1472, 2479	84.5	-	-	-	05-01-26	276
M2	1037, 1284, 1532, 2035	81.0	66.6/20.0a	76.9/14.0a	53.3/28.4a	05-01-25	359
M3	987, 1234, 1482, 1985, 2489, 2689	92.7	89.2	78.8	-	05-01-24	361

^a = Mode 2

The depth-average modes (Figure 6.1-6b) contained a great deal of information on rms particle displacements as a function of frequency. The hodograph ellipses were much more rectilinear than their equivalent CEOF modes (Figure 6.1-3), and this is to be expected as TRWs are frequency dependant transverse waves (Rhines 1970). Other properties were obtained from the dispersion relation under the assumption that $f\alpha/H \gg \beta$, where β is the gradient of the Coriolis parameter, f . For the wavevector, K , with components (k, l) , directed parallel and perpendicular to the bottom isobaths ($\alpha = dH/dy$), the wave frequency, ω , is given by:

$$\omega = -k\alpha N/K \coth(NHK/f), \quad (6.1.3)$$

The along-isobath wavenumber, k , must be negative, so the wavevector must point into the 2nd or 3rd quadrants with the y-axis directed up-slope. It can be shown that the wavevector is perpendicular to the transverse velocities and therefore perpendicular to the major axes of the ellipses in Figure 6.1-6b. The group velocity, cg ($= \partial\omega/\partial k, \partial\omega/\partial l$) is directed normal to the wavevector, such that cg is directed clockwise (upslope) or anticlockwise (downslope) with respect to K when the latter points downslope (i.e., into the 3rd quadrant) or upslope (i.e., into the 2nd quadrant), respectively. Therefore, the energy propagates along rays that coincide with the direction of the major axes of the ellipses in Figure 6.1-6b such that shallower water is to the right (Oey and Lee 2002). Another consequence of equation 6.1.3 is that the wavevector rotates such that it becomes more perpendicular to the isobaths as the frequency decreases. At the cut-off frequency, $N\alpha$, the wavevector points along the negative x-axis and the wave velocities are normal to the isobaths. This rotation of the wavevector with frequency is one of the diagnostics of TRWs and occurred at locations with gentle bottom slopes such as L3, L6, and L7 (Figure 6.1-6b). Closer to the escarpment, the ellipse major axes were more constrained to be along the trend of the steep slope, as has been noted in previous studies (Hamilton 2007). This implied that the wave energy propagated along, rather than across, the escarpment slope.

Unlike the CEOF modes, some locations, particularly under the LC at G and L7, had more than one significant mode (Table 6.1-2) in some of the frequency bands. The inclination of the ellipses at L3 implied energy flux towards the northwest and the escarpment at 52 and 29 days. At 52 days this was compatible with the mode 2 ellipse at L7, and this mode had about the same EKE_H as the 52-day mode 1 at L3. Therefore, part of the L7 fluctuations at this period could be contributing to the northwest propagation of TRWs towards the escarpment. However, the larger proportion of the 52-day energy was in mode 1, and this ellipse and the 29-day mode 1 ellipse implied energy flux towards the Campeche Bank, where the topography slopes up to the south and TRWs would presumably refract into the southeast corner of the eastern basin. It is possible that the lower magnitude northeastward 52-day and the northwestward 29-day fluxes at G may have originated from such TRWs on the west-side of the LC, propagating anticlockwise around the deep southern half of the eastern basin. If the direction of cg at L3 was towards the escarpment, then the direction at L6 of the much weaker fluctuations was southwestward towards the center of the western basin and therefore may be a manifestation of reflected TRWs from the northward shoaling topography (Mizuta and Hogg 2004).

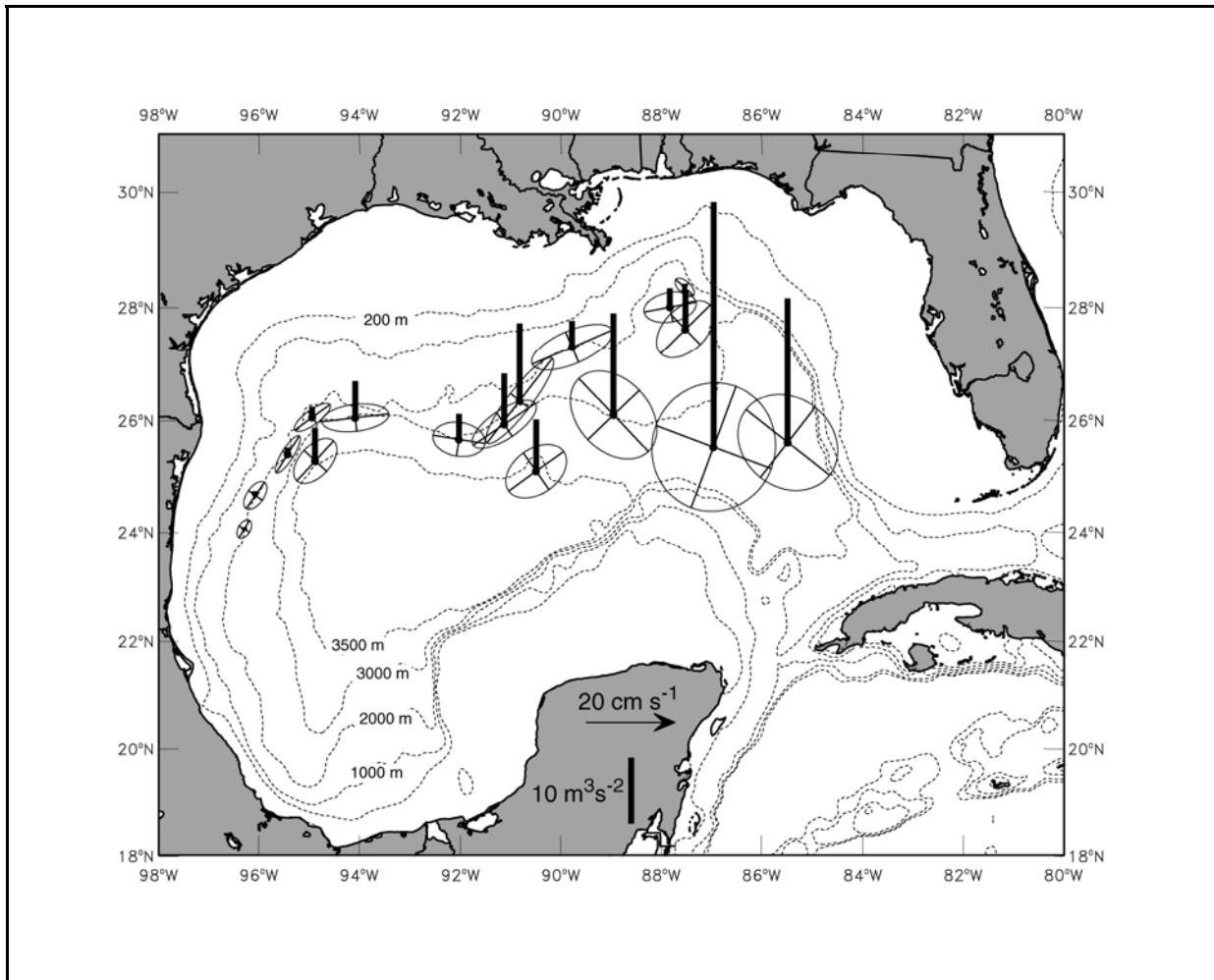


Figure 6.1-3. Depth-integrated EKE for the CEOF mode 1 lower-layer currents at the locations identified in Table 6.1-2 (thick vertical bars). The standard deviation ellipses are representations of the depth-average lower-layer mode 1 currents (scale given by the arrow).

The overall view of TRWs in Figure 6.1-6 suggests considerable complexity in both the frequency and energy content of the fluctuations, and it also suggests possible propagation paths of wave packets. The indication from the available observations is that the deepwater region on the west side of the LC, just north of the Campeche Bank, had very high lower-layer kinetic energy which may be radiating towards both the west and south. The escarpment between 90 and 92°W turned the northwestward propagating waves into along-slope fluctuations. In the northwest corner, energy levels were small compared to the eastern GOM and the central parts of the escarpment.

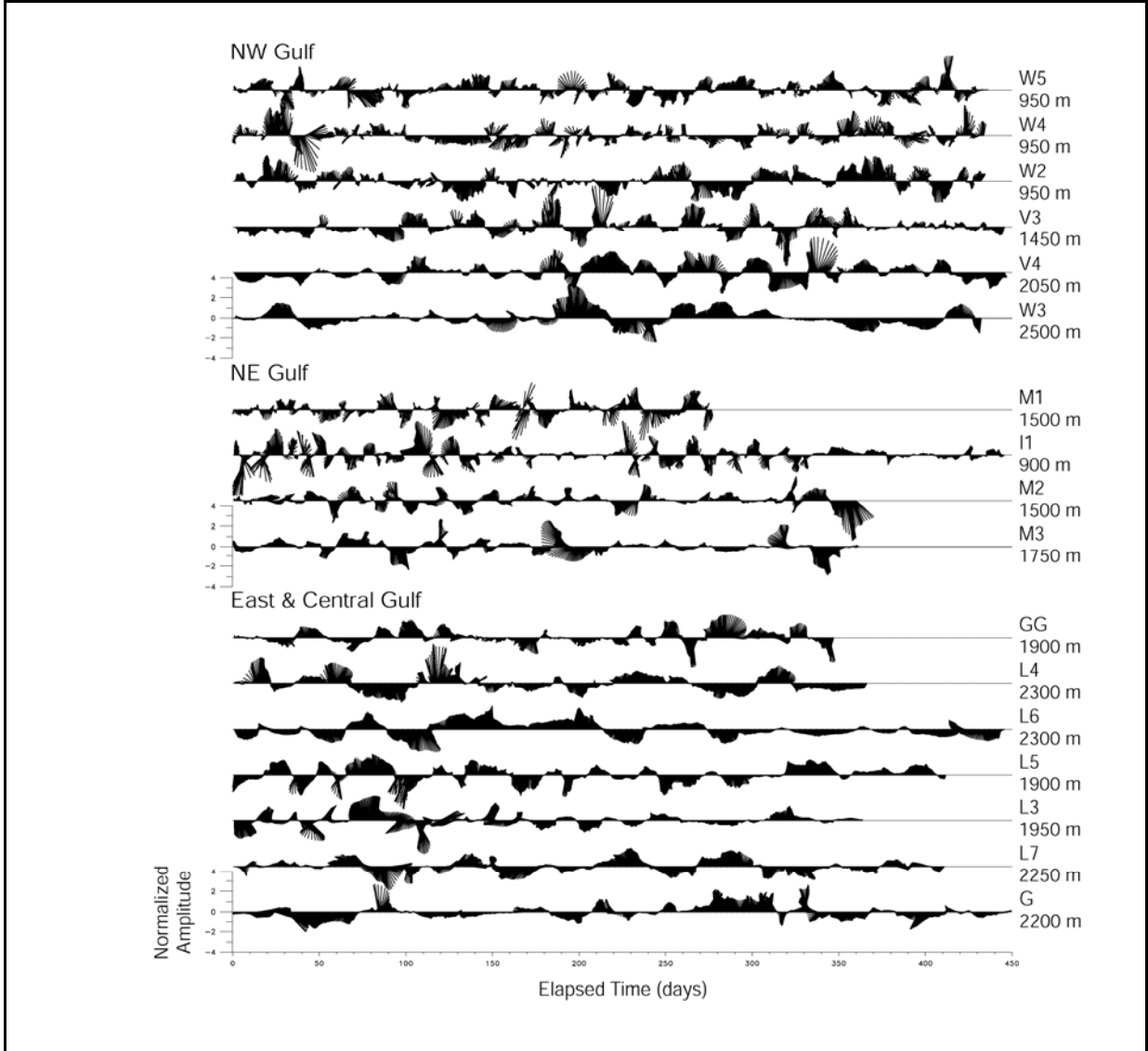


Figure 6.1-4. CEOF mode 1 normalized amplitudes for lower-layer currents. The abscissa is elapsed time in days from the beginning of each time series. The depths below the mooring IDs are the lower-layer integration depths below 1000 m.

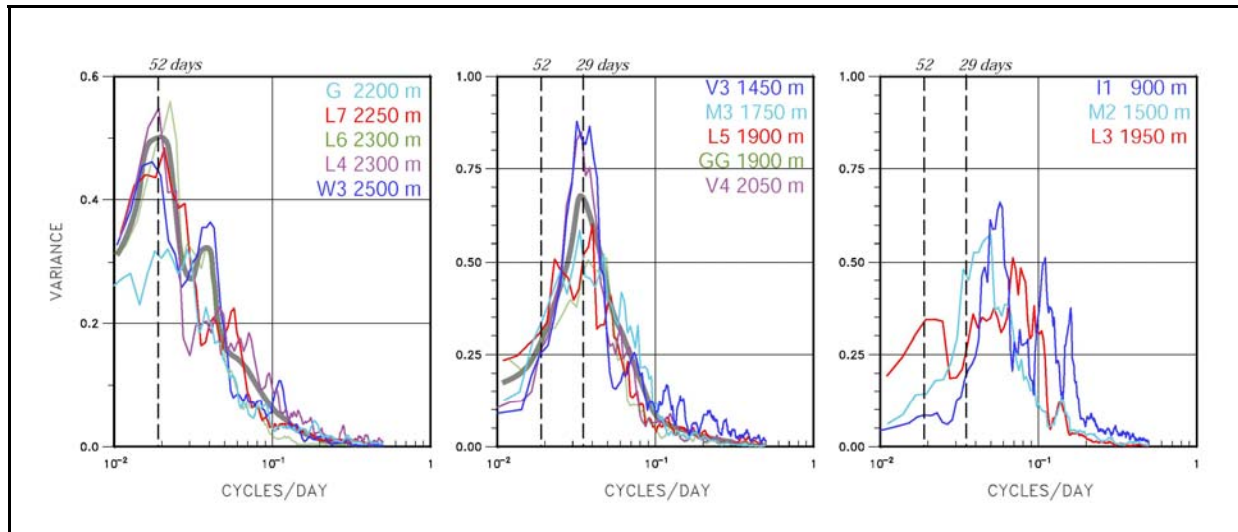


Figure 6.1-5. Spectra, in variance preserving form, for the normalized CEOF mode 1 amplitudes of the lower-layer currents. The color codes give the mooring location and lower-layer thickness, and red is used for the largest depth-integrated EKE in each group. The thick gray lines are the subjectively averaged spectra.

Further evidence for the dominance of TRWs in the lower-layer came from the deep Lagrangian float tracks of the Exploratory Study. If linear TRWs were the only process operating in the lower-layer, then to first order, floats placed in such a field would simply oscillate in a rectilinear fashion about their deployment point with the direction and amplitude of the displacements changing with changing period of the waves propagating through the area. This would be a completely different pattern to that shown by near-surface drifters deployed in the cores of upper-layer eddies, which had the characteristics of translating loops (e.g., Kirwan et al. 1984; Hamilton et al. 1999). Examination of Figure 6.1-2 shows that the deep float tracks more closely resembled the former rather than the latter. This was most noticeable in the eastern basin, under the LC, where the large amplitude displacements had both clockwise and anticlockwise motions that were often adjacent in time. There are several tracks that began less than half a degree apart, and after six months, ended in the same vicinity, still less than half a degree apart. Of the 36 floats deployed, only one had a section of track that was consistent with a translating cyclonic eddy. In Figure 6.1-2, three anticlockwise loops were observed moving in towards the western slope between 24 and 25°N, and 93 to 96°W. This apparent deep eddy is discussed in Donohue et al. (2008). The other exceptions to the general meandering over the same region were the tracks that moved close to the escarpment where they were transported westwards in a relatively narrow stream. This appeared to be the main route by which floats, initially deployed around 91°W, get to the western part of the basin. It was also noteworthy that almost no floats crossed the escarpment from the abyssal plain to the northern slope. The 4 tracks north of the escarpment in Figure 6.1-2 were all at 1000 m and therefore were more likely to be influenced by the lower circulations of surface-layer eddies.

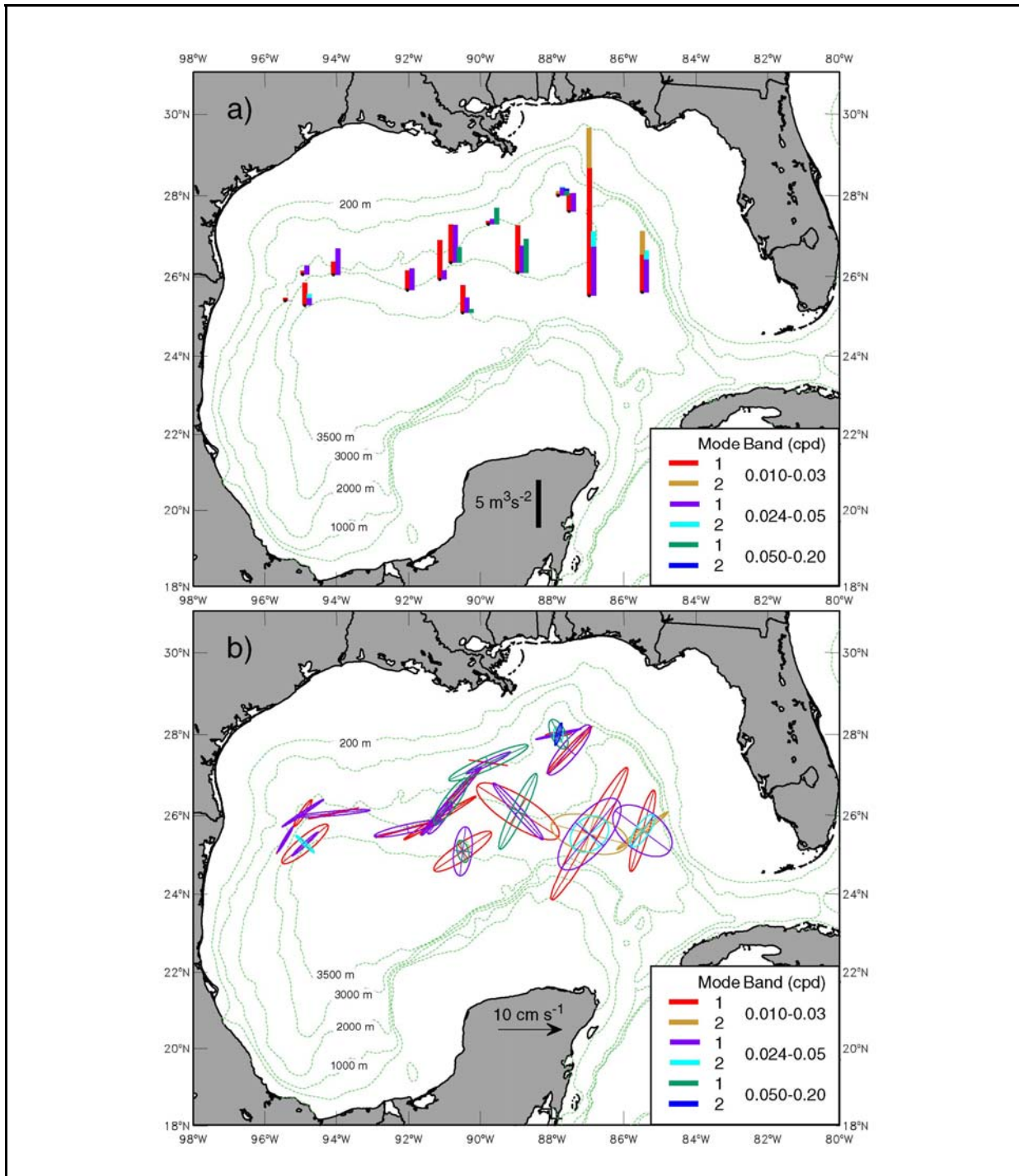


Figure 6.1-6. a) Depth-integrated EKE as a function of frequency band. Where more than 1 mode is present, the height of the bar represents the total EKE, and the colors show the split between the modes. b) Depth average mode eigenvectors represented as hodographs for each frequency band. Mode and band colors are the same as for a).

Mizuta and Hogg (2004) modeled the refraction and reflection of upslope propagating TRWs onto uniform shoaling topography. Their principal result was that incident and reflected waves produced a convergence of Reynold's stresses in the bottom boundary layer that forced an along-slope mean current that would be concentrated where the bottom slope (α) began to increase. The depth structure of this mean flow was similar to, but not necessarily exactly the same as the incident TRWs. DeHaan and Sturges (2005) used more heuristic arguments on the rectification of TRWs by a topographic slope to explain the limited observations of cyclonic mean flow along the base of the northern slope in the GOM. The present expanded currents database, including the deep Lagrangian floats, can be used to extend and further confirm the existence of substantial westward mean flows along the Sigsbee escarpment.

Means and standard deviations of float velocities were calculated by defining rectangular areas that were adjacent to and aligned along the escarpment. The sections of all smoothed float tracks which passed through and were within the rectangle, excluding the two deployed at 1000 m, were used to calculate velocities using centered finite differences. The ensemble average of these velocity estimates produced the statistics for the box location. The method is similar to DiMarco et al.'s (2005) estimation of gulf-wide velocity statistics using near-surface drifters. In addition, Lagrangian velocity statistics were estimated for 1° latitude-longitude squares centered on selected mooring locations for the purpose of forming a comparison with Eulerian estimates using current meter measurements. The nearly barotropic nature of the flows below 1000 m meant that mixing floats from 1500, 2000, 2500 and 3000 m depth, into a single lower-layer estimate, was unlikely to bias the results. The means and standard deviation ellipses from both floats and moorings are shown in Figure 6.1-7, with supporting data in Table 6.1-3. The degrees of freedom (*dof*) were estimated using velocity time series from nearby moorings to calculate the autocorrelation time scales. Given the varying dominant periodicities with location, the estimates were less reliable at deeper water depths. The standard error of the mean is given by:

$$S_E = \sigma_v / \sqrt{dof}, \quad (6.1.4)$$

where σ_v is the standard deviation along the principal major axis of the ellipse. For the western boxes 1 and 2, the time scale was interpolated from moorings W2 and W3 to the 3000 m isobath (Figure 6.1-7).

Mean currents from both moorings and floats showed consistent westward flows along the escarpment that seemed to form a continuous current from around 89°W to below 24°N on the Mexican slope. The variances were also reasonably consistent between floats and moorings even where the measurements were taken in different years. In the western GOM, the float mean for box 2 was in the same direction (SSW) as that at W2, but had a smaller magnitude, which was either a consequence of different measurement periods or the mean flows were concentrated close to the base of the slope. Jet-like mean flows over the steepest part of the escarpment were analyzed in Donohue et al. (2006) for a transect around 91°W . Of interest is that floats that moved southwards from the northwest corner near 26°N followed the 3000 m isobath (Figure 6.1-2). This helps to explain why the EKE at W5 was so weak since the source of the energy was in the northwest corner and also followed the general direction of the 3000 m isobath leaving shallower areas of the lower western slope in a shadow zone.

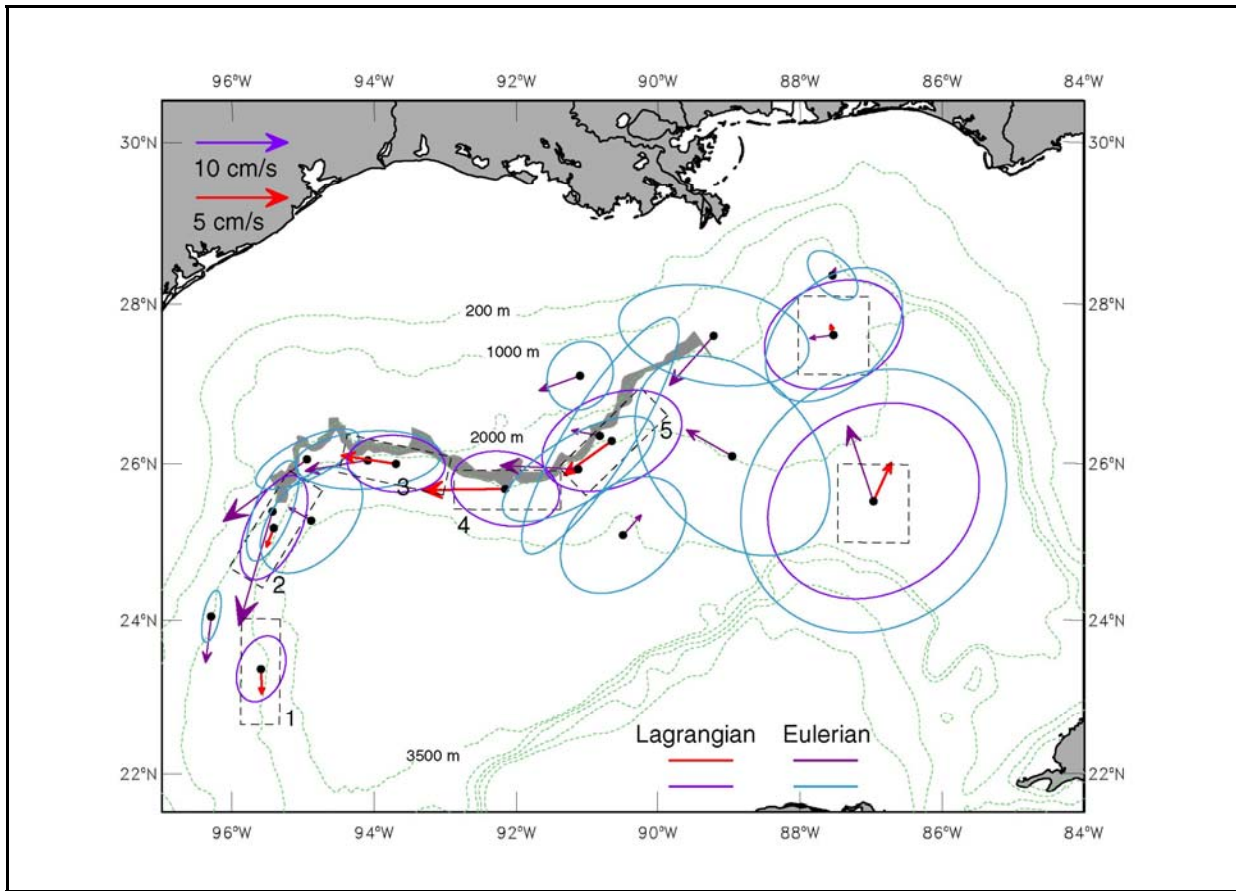


Figure 6.1-7. Lower-layer mean currents from RAFOS floats (red) and lower-layer current meters (purple). Mean velocity scale is 5 cm s^{-1} . The dashed boxes are the averaging areas for the floats, and the escarpment box location numbers refer to Table 6.1-3. The float (blue) and current meter (cyan) standard deviation ellipses use a scale of 10 cm s^{-1} . The light gray shaded area shows the steepest slope (500 m descent) of the Sigsbee escarpment.

Table 6.1-3

Time Scales and Degrees of Freedom for Lagrangian and Eulerian Velocity Statistics

Location	Longitude Latitude	Box Size	Number Tracks in Box	Mean Float/CM Depth (m)	Number 6-h Velocity Estimates	Auto- correlation Time Scale (hours)	dof	S_E (cm s^{-1})
1-L	95.60°N 23.37°W	1.5° x.5°	23	2053	2810	60	28 1	0.2
2-L	95.42°W 25.18°N	1.5° x.5°	15	1796	1577	60	15 8	0.5
3-L	93.70°W 25.99°N	1.5° x.5°	25	2108	1468	95	93	0.5
4-L	92.16°W 25.67°N	1.5° x.5°	22	1810	1151	100	69	0.7
5-L	90.66°W 26.28°N	1.5° x.5°	34	1761	1375	122	68	0.9
L5-E	90.82°W 26.34°N			2625	1644	122	81	1.5
L7-L	86.97°N	1°x1 °	29	1656	1465	240	37	1.8
L7-E	25.52°N			3187	1642		41	2.2
M3-L	87.53°W	1°x1 °	12	1856	1071	140	46	1.1
M3-E	27.61°N			2689	1436		62	1.0
M1-E	87.55°W 28.35°N			2479	1444	79	11 0	0.3
L1-E	89.22°W 27.60°N			1400	1523	62	14 7	0.8
L2-E	91.11°W 27.10°N			1650	1485	45	19 8	0.3
L3-E	88.96°W 26..09°N			2900	1451	61	14 3	1.0
L4-E	91.13°W 25.92°N			3250	1462	100	88	0.9
L6-E	90.50°W 25..09°N			2995	1861	190	59	0.9
V3-E	94.95°W 26.05°N			2400	1823	90	12 2	0.5
V4-E	94.09°W 26.04°N			3000	1823	95	11 5	0.7
W2-E	95.44°W 25.39°N			1965	1725	40	25 9	0.3
W3-E	94.89°W 25.27°N			3518	1727	175	59	0.8
W5-E	96.30°W 24.04°N			1998	1735	35	29 7	0.2

-L = Estimated from Lagrangian floats.

-E = Estimated from moored current measurements.

6.2 Basic Statistics from Moorings

The basic statistics of the deep moored 40-HLP currents for the Eastern GOM Study are presented in Figure 6.2-1. This figure includes the nine-month records (May 2005 to January 2006) from the LSU mooring at L7, and two deep 6 month long (July 2005 to January 2006) records from bottom mounted 37.5 kHz ADCPs on the Alabama – Mississippi lower slope. The latter were from the MMS Notice to Lessee's (NTL) program and were collected by industry at drilling platform locations as reported to NDBC. The data were archived by NDBC, who performed the initial QA/QC. The data are for NDBC platform numbers 42374 and 42375, in 1670 and 1950 m water depths, respectively. No useable upper-layer currents were available from these platforms. The L7 LSU mooring was deployed at the same site, and was similarly configured to the earlier mooring discussed in Section 6.1. The statistics for L7 and the NTL ADCPs were calculated for the longest possible records that overlap the Eastern GOM Study deployments (January 2005 to January 2006).

Because of the high vertical coherence in the lower water column, only two levels are given in Figure 6.2-1. The upper level was at a nominal 1200 m depth and is just below any direct influence of upper-layer LC flows. The near-bottom vectors were from the closest measurement from the seabed that would not be influenced by the frictional bottom boundary layer, i.e., at least ~ 100 m above bottom. In some cases (e.g., at M2) the instrument at 500 m from the bottom was used because of instrument problems with the bottom-most level.

The deep mean flows were northward at L7, and were similar to the 2003-2004 results for this same location (Figure 6.1-7). This implies fairly consistent mean flows occurred at this location during the two study periods. However, the LC was similar in its location during both studies, being in a generally extended state while these moorings were deployed. The fluctuations, however, had less variance than for the earlier interval, though they were still more energetic than the M locations further north. The lower water column still contained considerably more EKE_H because of the approximate doubling of the thickness of the lower water column between M3 and L7. The L7 fluctuations were also bottom intensified between 1200 and 3000 m. Near-bottom mean flows at M3 and M4 were westward towards the escarpment south of the delta. At M3, and to a lesser extent at M2, the mean currents at 1200 m were essentially negligible, which was a contrast to the more depth independent means at L7. Where the slope was steeper (M1, 42374 and 42375), the means tended to follow the isobaths.

The standard deviation ellipses at M2 and M3 clearly showed evidence of bottom intensification, with principal axes directed westward and southwestward, respectively, across the isobaths into shallower water, which is characteristic of TRW motions. The moorings on the steep slope had low energy, except that 42374 was slightly more energetic; however, this site seemed to be in a different slope regime than the lower slope moorings M1 and 42375 (see below). Previous deep measurements on the lower Alabama – Mississippi slope, between the 1500 and 2000 m isobaths, have shown very weak currents there.

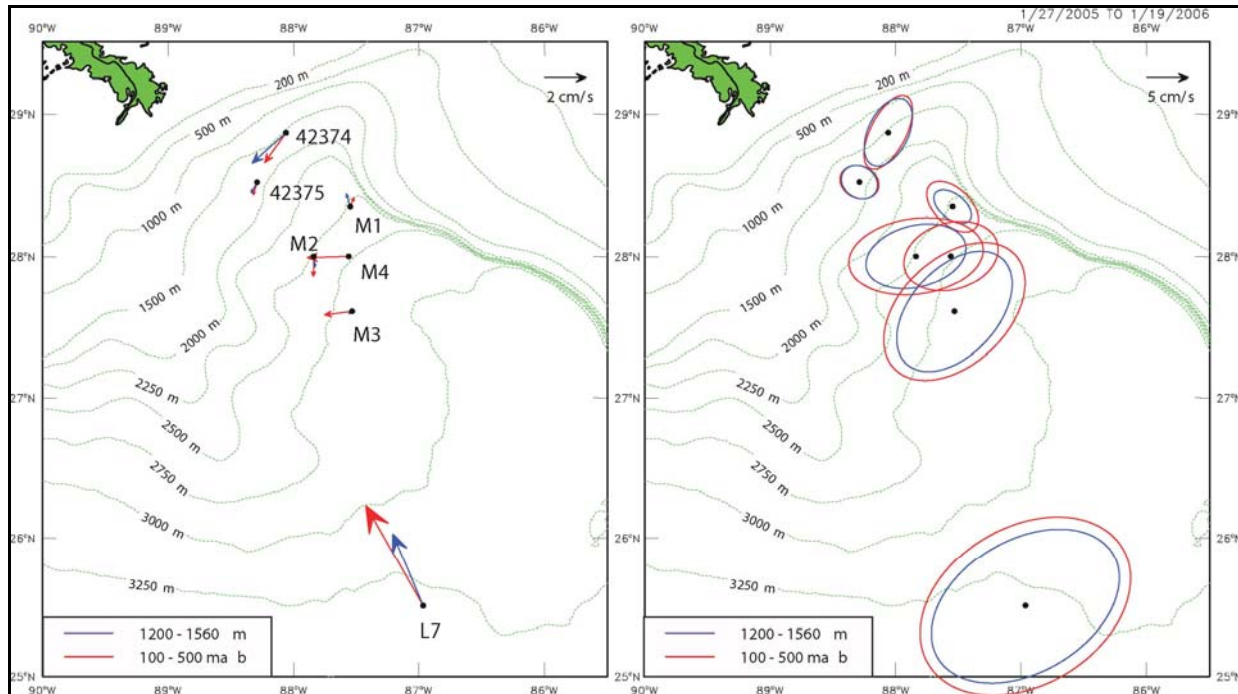


Figure 6.2-1. Mean (LH panel) and standard deviation ellipses (RH panel) for currents 100 to 500 m above bottom (red) and ~ 1200 m depth (blue) except for 42375 where the upper level is at 1560 m. Note the change in velocity scales between the panels.

6.2.1 Event Analysis

The stick plots of the low-frequency deep velocities for the moorings in Figure 6.2-1 are given in Figure 6.2-2. Only two or three depths below 1200 m are plotted because of the very high coherence of the observations in the lower water column. Under the LC at L7, the fluctuations of the currents were predominantly northwards with few reversals, were depth independent from 1200 to 3200 m, had relatively long periods (~ 30 days or more), and had the maximum speeds (~ 30 cm s⁻¹ in late December 2005) of all these measurements. For the M2, M3 and M4 moorings, the fluctuations were more variable in amplitude, had more frequent reversals, and had somewhat shorter characteristic periods. There was clearly a decrease in energy moving from south to north over the 45 km spacing from M3 to M4 and M2. On and near the slope, at M1, 42374 and 42375, the fluctuations were much less energetic, with amplitudes mostly less than 5 cm s⁻¹, and their characteristic periods were much shorter, generally less than ~ 20 days.

The summer and fall of 2005 was one of the most active hurricane seasons on record. A number of very strong hurricanes passed fairly close to the moorings as shown in Appendix A and in Figure 6.2-3. The center of Hurricane Katrina passed close to L7 on August 28, 2005 at which time it was classified as a category 4 hurricane. In the deep current records, there was evidence of low-frequency pulses at some of the deep-water moorings when the storms were intense and passed fairly close to the moorings. A short-lived northward pulse of ~ 20 cm s⁻¹ was observed in the lower water column at L7, which stood out from the background flows. A month later, a similarly intense Rita passed by L7 at a greater distance, but there was no obvious pulse from the hurricane.

In contrast, moorings M2, M3 and M4 on the abyssal rise showed no discernable response to the passage of these major storms. However, the continental slope near-bottom currents at M1, 42374 and 42375, did show consistent short period pulses or rotary fluctuations (e.g., at 42375) at the times of the closest approaches of the major hurricanes Dennis, Katrina and Rita. The strongest response was at the shallowest site 42374, and here the initial amplitude was clearly proportional to the distance of the paths from the location. Previous measurements by Teague et al. (2007) on the upper Alabama – Mississippi slope during the passage of hurricane Ivan in 2004 had shown a short period (2 to 5 days) TRW wave response of the slope to this storm. It is reasonable that the lower slope could be part of the same slope wave-guide that facilitates a low-frequency response to these intense storms. It is noteworthy that all three of the 2005 hurricanes that generated slope TRWs passed over the edge of the west Florida shelf break near the dry Tortugas where the slope turns eastward into the Florida Straits entrance. Thus, short period disturbances could propagate along the slope to the measurement sites on the Alabama – Mississippi slope as suggested by Hetland et al. (1999).

Deep circulation was punctuated by a number of energetic low-frequency events. Figure 6.2-4 shows deep EKE and variance ellipses from the combined PIES and deep current meters. As noted above, EKE within the array increased to the south. The lower panel of Figure 6.2-4 shows the array-averaged EKE as a function of time. The six largest EKE peaks identified six deep events referred to here as events a through f. Figure 6.2-2 also shows these energetic low-frequency events. Maps of altimeter-derived SSH for the eastern basin put the measurements in context of the larger-scale LC, and the high resolution lower-layer streamlines and geostrophic bottom currents overlaid with PIES derived SSH showed the local relation of the bottom flows to the upper-layer. These maps are provided (Figures 6.2-5a-f) for each event indicated in Figures 6.2-4 and 6.2-2, generally centered about the middle of the local EKE maxima. In addition, Figure 6.2-6 presents a hovmuller plot of lower-layer streamfunction and upper-layer geopotential height along a transect that coincided with a deep eddy propagation route within the array. In the discussion below of the deep events, references will be made to deep cyclones and anticyclones. This is just shorthand for deep cyclonic and anticyclonic circulations for which there is little evidence that they contain translating closed cores in the same sense that upper layer eddies do. As discussed extensively in Donohue et al. (2008), the present view is that apparent deep cyclones and anticyclones are primarily the result of packets of dispersive TRWs.

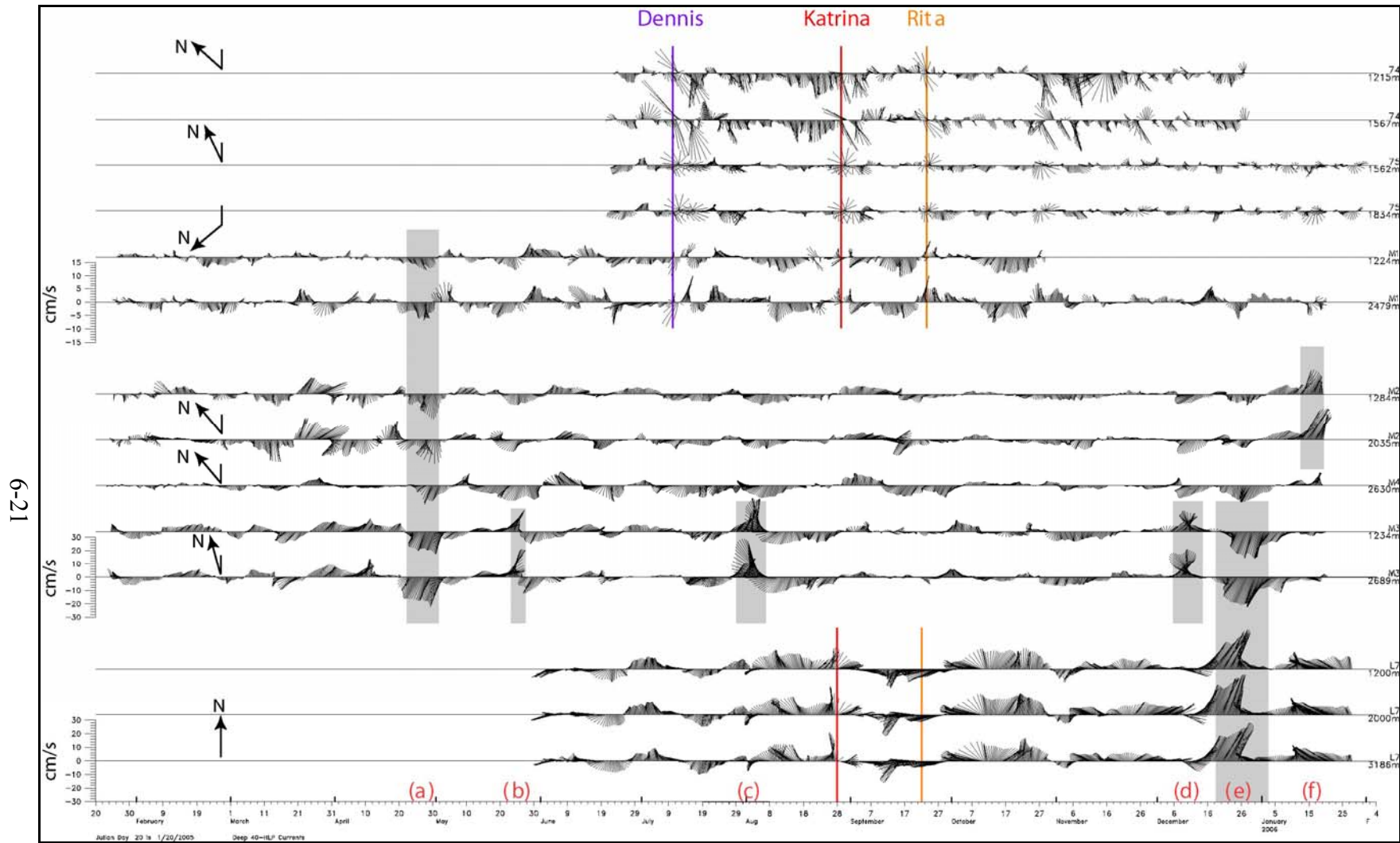


Figure 6.2-2. Stick plots of the 40-HLP currents for the indicated moorings and depths. The event lines (colored for the tropical storms and shaded for strong low frequency fluctuations) are discussed in the text. The labeled (a through f) events correspond to the events marked in Figure 6.2-4, and are further illustrated in Figures 6.2-5a-f. The speed scale for moorings 74, 75, and M1 is at 15 cm s^{-1} (top) and the other moorings are at a speed scale of 30 cm s^{-1} (bottom).

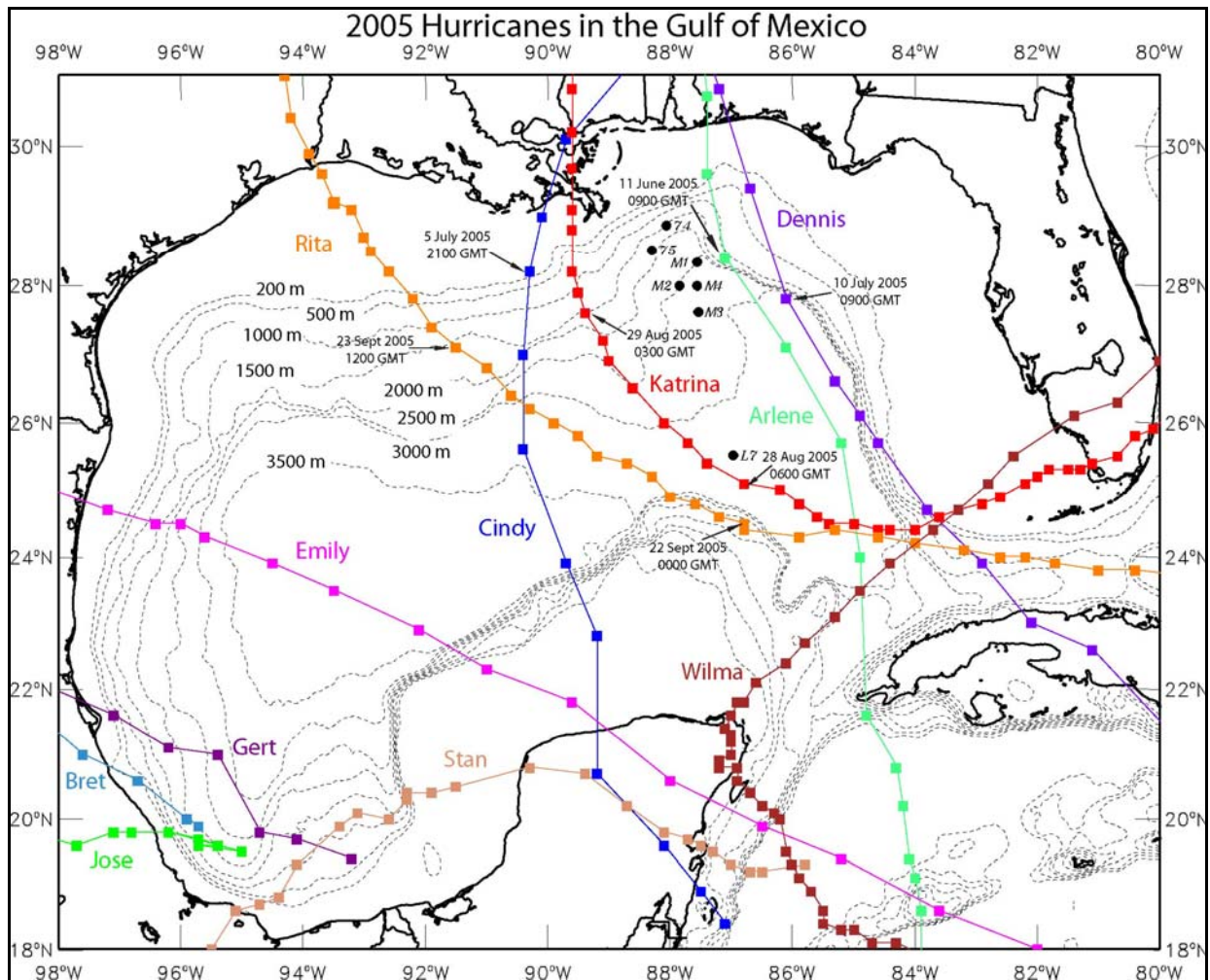


Figure 6.2-3. Tracks of the center low pressures of tropical storms and hurricanes that passed over the Gulf of Mexico in 2005.

The late April 2005 event, with south or southwestward flows over the main part of the array and northwest flows at M1, occurred when the LC was extended well towards the delta. During this time the study region was dominated by a LCFE with southeastward flows at M2 and M3 along the LC front and reversed flows on the north side of the cyclone at M1 (Figure 6.2-4a). The lower layer streamlines were approximately normal to the upper-layer flows and the strong currents are caused by a deep cyclone in the southern part of the array. The LC remained in this configuration for most of April, May and June, though the cyclonic LCFE propagated along the front towards the southeast and possibly merged with another cyclone during this interval. The persistence of the upper-layer flows at M3 through this interval is shown in Figure 6.2-7 and as the LC front moved further over the site in May, the southeastward currents at M3 strengthened. M3 was within the LC when the salinity at 125 or 200 m depth was greater than 36.7 indicating the presence of subtropical underwater (SUW) that constitutes the core of the LC and LC eddies. In the lower-layer, the deep anticyclone in the northeast part of the study area strengthened and moved southeastward. The cyclone decayed in early May or possibly moved out of the study area towards the southeast, which was approximately in the direction of the surface LC front. The deep cyclone either moved into the study area from the east at the beginning of the event or intensified in place. The apparent growth and decay of deep vortices without any direct connection to upper-layer forcing could be considered evidence for the planetary wave-like nature of lower-layer circulations.

The three following events, in May, August and early December, at M3 had similar behavior to each other (Figure 6.2-2) which was a northward pulse accompanied by a cyclonic rotation of the velocity vectors. This was very similar to the characteristic velocity signal produced by a Gulf Stream cyclonic frontal eddy at the shelf break in the south Atlantic Bight (Lee and Atkinson 1983; Bane et al. 1981). The corresponding spatial maps are given in Figures 6.2-5b, c and d, respectively. In all three cases the events' cyclonically rotating velocity vectors were caused by an anticyclone-cyclone pair translating fairly rapidly southeastward through the array (Figure 6.2-6). This was again the general direction of the surface LC front, and the M moorings were on the northeast edge of this front. In all these three cases the cyclone – anticyclone pair appeared to propagate southeastward, intensify in the southeast corner of the array and possibly decay in place. There was an intriguing consistency with the surface layer LC flows, because the deep cyclone tended to follow and remain locked to an upper-ocean high (Figure 6.2-6 and Figure 6.2-5b through d). Note that in each case the PIES maps revealed a richer structure (more curvature) along the cyclonic edge of the LC than the satellite SSH maps. The connection to the upper-layer flow was difficult to discern due to the limited window of the array and the inability of the satellite SSH product to resolve the small spatial and rapid time scales associated with frontal perturbations and/or instabilities of the LCFE flows.

The event at the end of December (Figure 6.2-2) had very similar characteristics, for both upper and lower layer flows, to the event in April (compare Figures 6.2-5e with 6.2-5a and note the lack of southwestward propagation of these features in Figure 6.2-6). The LC and an incipient LC eddy extended to the northwest, and a fairly stationary cyclonic frontal eddy dominated the upper-layer flows in the study area (Note the presence of cold, less saline water at M3 in Figure 6.2-7). This cyclone was larger and more vigorous than the one in April-May. The lower layer flows at M3 and M4, and to a lesser extent at M2 were dominated by a cyclone, which, similar to the event in April, intensified in place and then decayed while moving out of the study area towards the southeast. At the same time, the deep anticyclone to the north began to strengthen. The deep strong northward flows at L7 that began in the middle of December, appeared to be unrelated to the deep circulations in the study area. The upper layer at L7 was clearly within the main part of the LC front (Figure 6.2-5e). By the middle of January 2006, the upper-layer circulation had not changed much (Figure 6.2-5f); the LC eddy was still attached but had moved westward, and the LC front was further north and the study area moorings were primarily on the northern side of the cyclonic frontal eddy. In the lower-layer however, the cyclone and anticyclone were in the reversed positions with the cyclone to the northeast of the anticyclone, which produced the large northeast flows at M2 (Figure 6.2-2). The deep cyclone may have moved in from the west and intensified. The deep eddy pair began to move southwards just before the end of the data records.

The common characteristics of these events were the presence of deep high and low pressure centers with separation length scales of ~ 50 to 100 km that intensified and decayed while propagating south or southeastwards in the general direction of the overlying front of the east-side of the LC. Lower and upper layer streamlines invariably crossed at right angles during the more energetic lower-layer events. The significance of this is not clear at present; however, a more quantitative analysis of possible upper-lower layer connections is given in Chapter 7.

6.3 Topographic Rossby Waves North of the Loop Current

Kinetic energy spectra for the lower-layer currents from the study area moorings (M1-M4) plus L7 are given in Figure 6.3-1. The latter had an 8-month record compared to the 12-month records of the M moorings, so spectral resolution was not as good at L7. For the analysis, 3 or 4 depth levels were used beginning at ~ 750 m, which was likely to be influenced by upper-layer LC currents. However, most of these 750 m spectra showed energy at the same frequencies as the deeper spectral peaks, indicating that there may be connections between upper and lower layer regimes. The M1 spectra showed very low energy and have very little in common with the moorings further south. M2, M3, and M4 had a prominent peak at 20 days; M3 and L7 had energy at longer periods with peaks at 30 to 35 days. M2, M3 and L7 showed bottom intensification at depths below 1000 m, whereas at M4 the fluctuations were essentially depth independent through the 100 m separation of the measurements. Therefore, except for M1, the lower layer signals had spectra characteristic of TRWs. Low frequency near-bottom EKE increased towards the west and south from M4, which was noted also in the overview analysis. This is made clearer in Figure 6.3-2, where the highest energy near-bottom spectra from each mooring are plotted on one graph and common peaks at ~ 30 , 25 and 20 days are highlighted.

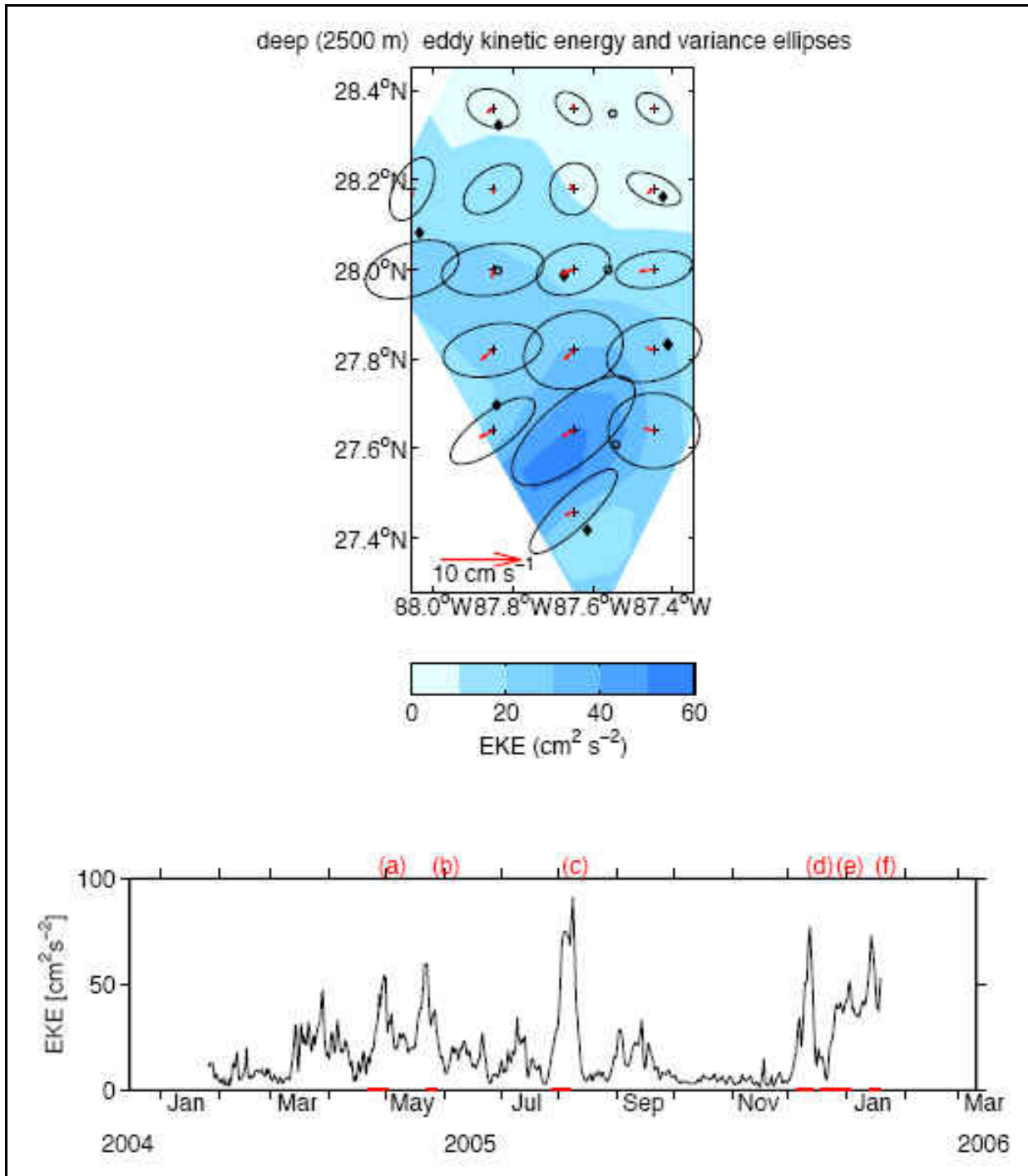


Figure 6.2-4. Upper panel: Mean lower-layer (2500 m) eddy kinetic energy averaged between 27 January to 19 January 2006 contoured every 20 cm²s⁻². Bathymetry contoured every 500 m depth with gray lines. PIES sites are indicated by diamonds, and current meters denoted by circles. Bottom panel: Array-average mean lower-layer eddy kinetic energy. The six strongest events are highlighted by the red line along the bottom x-axis and labeled consistently with Figures 6.2-5a-f.

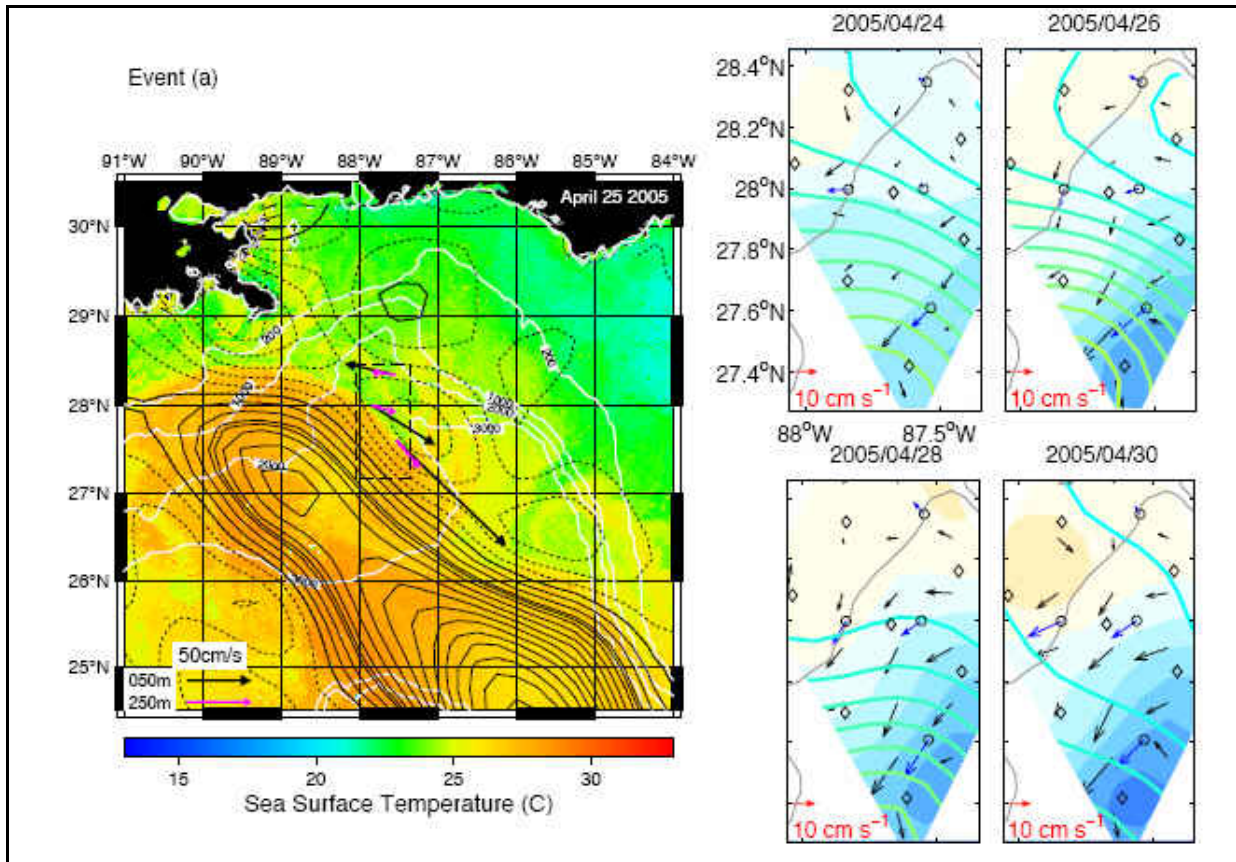


Figure 6.2-5a. The LH panel shows the 3-day composite SST overlaid with CCAR altimeter-derived SSH for April 25, 2005. Upper layer 1-day averaged currents at 50 and 250 m depth are given for the moorings. The RH panels show PIES-derived SSH (thick lines) and the stream function (solid color; blue shades cyclonic, pink shades anticyclonic) and currents at 2500 m. The blue and black arrows are observed and mapped geostrophic currents, respectively.

TRW wavelengths were estimated by calculating the frequency domain EOF modes for the records at 100 to 500 m above bottom (MAB) on moorings M2, M3 and M4. The horizontal wavenumbers were found by least-square fits to the mode phase angle differences across the array in the same manner as Hamilton (1990). Based on the spectra, two frequency bands were analyzed, and the results are given in Table 6.3-1. Also in Table 6.3-1, the results of the vertical analysis of the 2005 - 2006 L7 lower-layer velocities are given, and for convenience, the similar results are repeated, from Table 6.1-2, for L7 from the 2003 - 2004 interval.

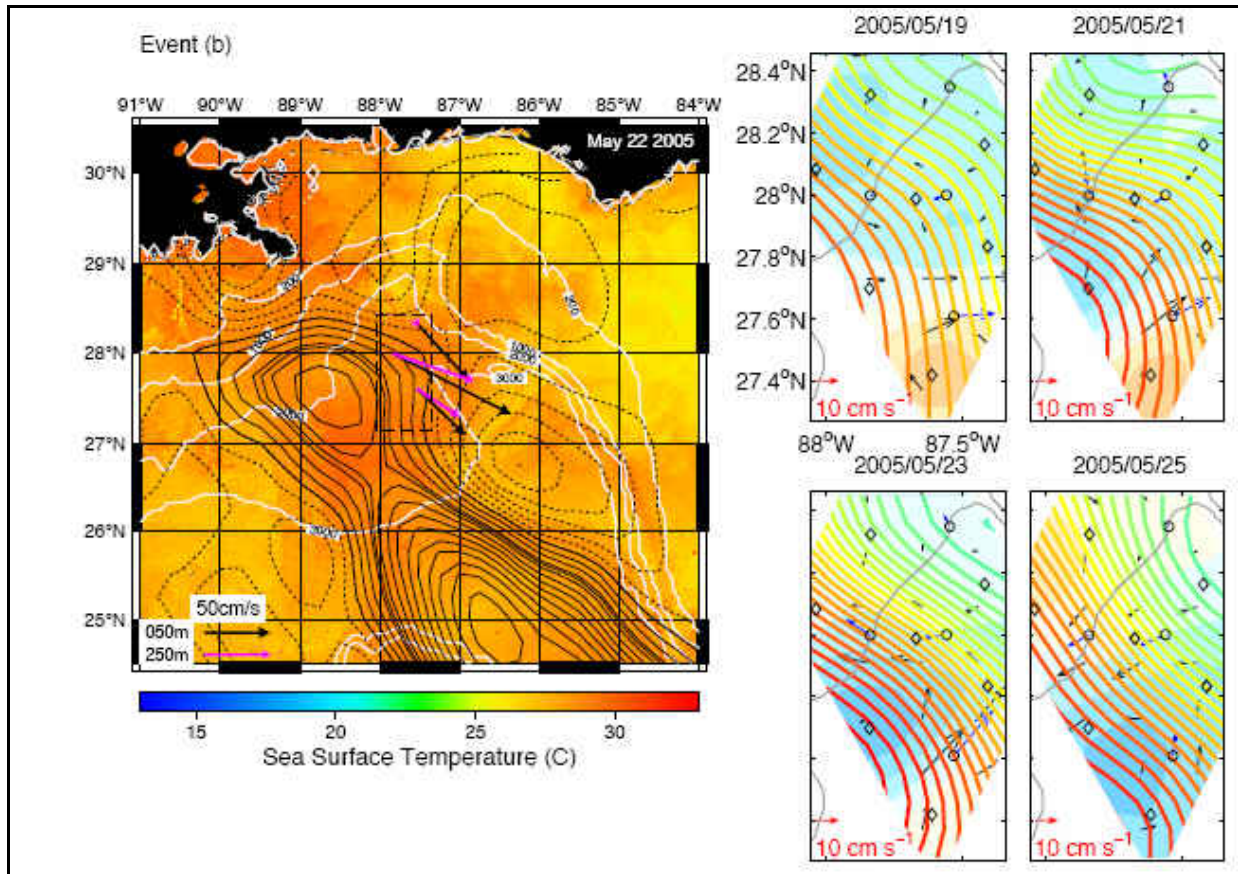


Figure 6.2-5b. The LH panel shows the 3-day composite SST overlaid with CCAR altimeter-derived SSH for May 22, 2005. Upper layer 1-day averaged currents at 50 and 250 m depth are given for the moorings. The RH panels show PIES-derived SSH (thick lines) and the stream function (solid color; blue shades cyclonic, pink shades anticyclonic) and currents at 2500 m. The blue and black arrows are observed and mapped geostrophic currents, respectively.

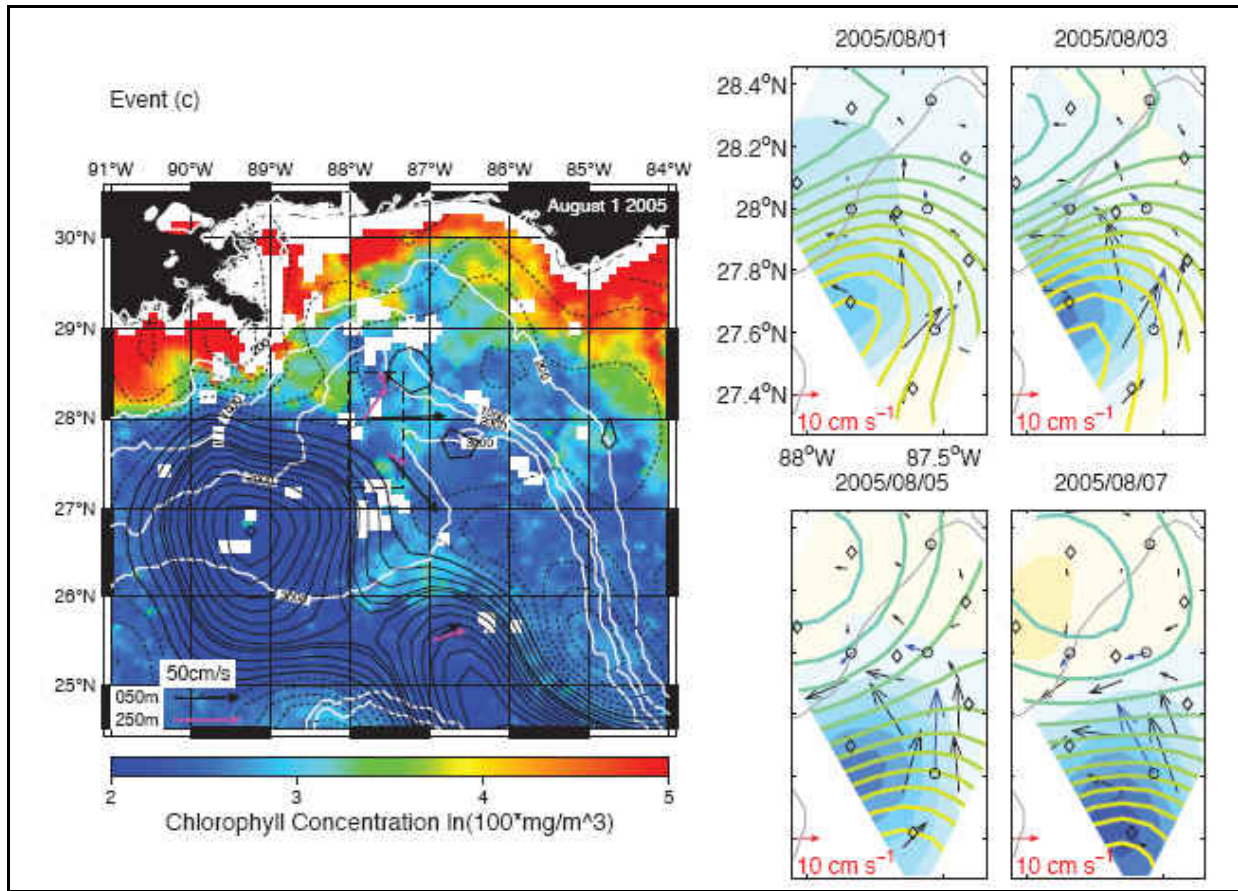


Figure 6.2-5c. The LH panel shows the 3-day composite chlorophyll concentration overlaid with CCAR altimeter-derived SSH for August 1, 2005. Upper layer 1-day averaged currents at 50 and 250 m depth are given for the moorings. The RH panels show PIES-derived SSH (thick lines) and the stream function (solid color; blue shades cyclonic, pink shades anticyclonic) and currents at 2500 m. The blue and black arrows are observed and mapped geostrophic currents, respectively.

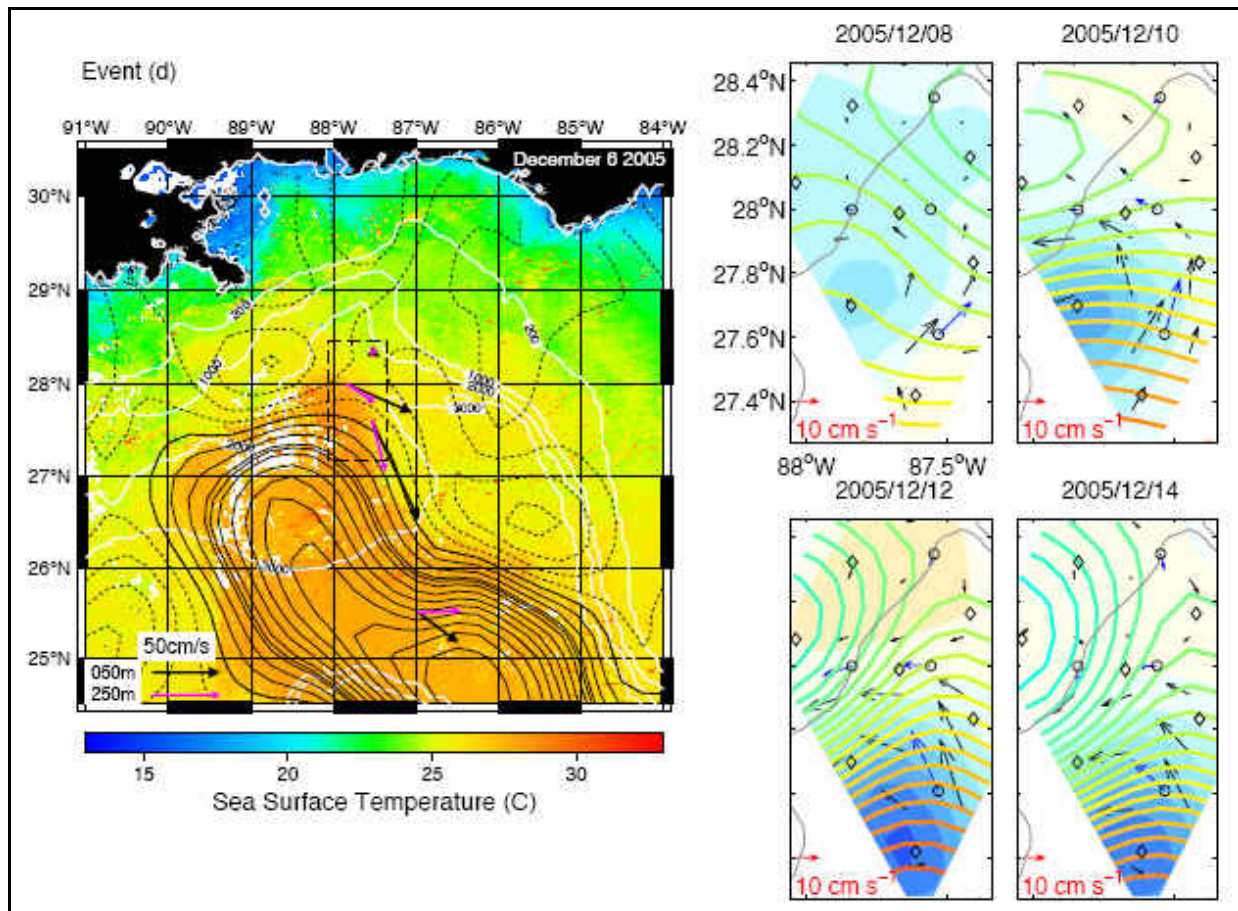


Figure 6.2-5d. The LH panel shows the 3-day composite SST overlaid with CCAR altimeter-derived SSH for December 6, 2005. Upper layer 1-day averaged currents at 50 and 250 m depth are given for the moorings. The RH panels show PIES-derived SSH (thick lines) and the stream function (solid color; blue shades cyclonic, pink shades anticyclonic) and currents at 2500 m. The blue and black arrows are observed and mapped geostrophic currents, respectively.

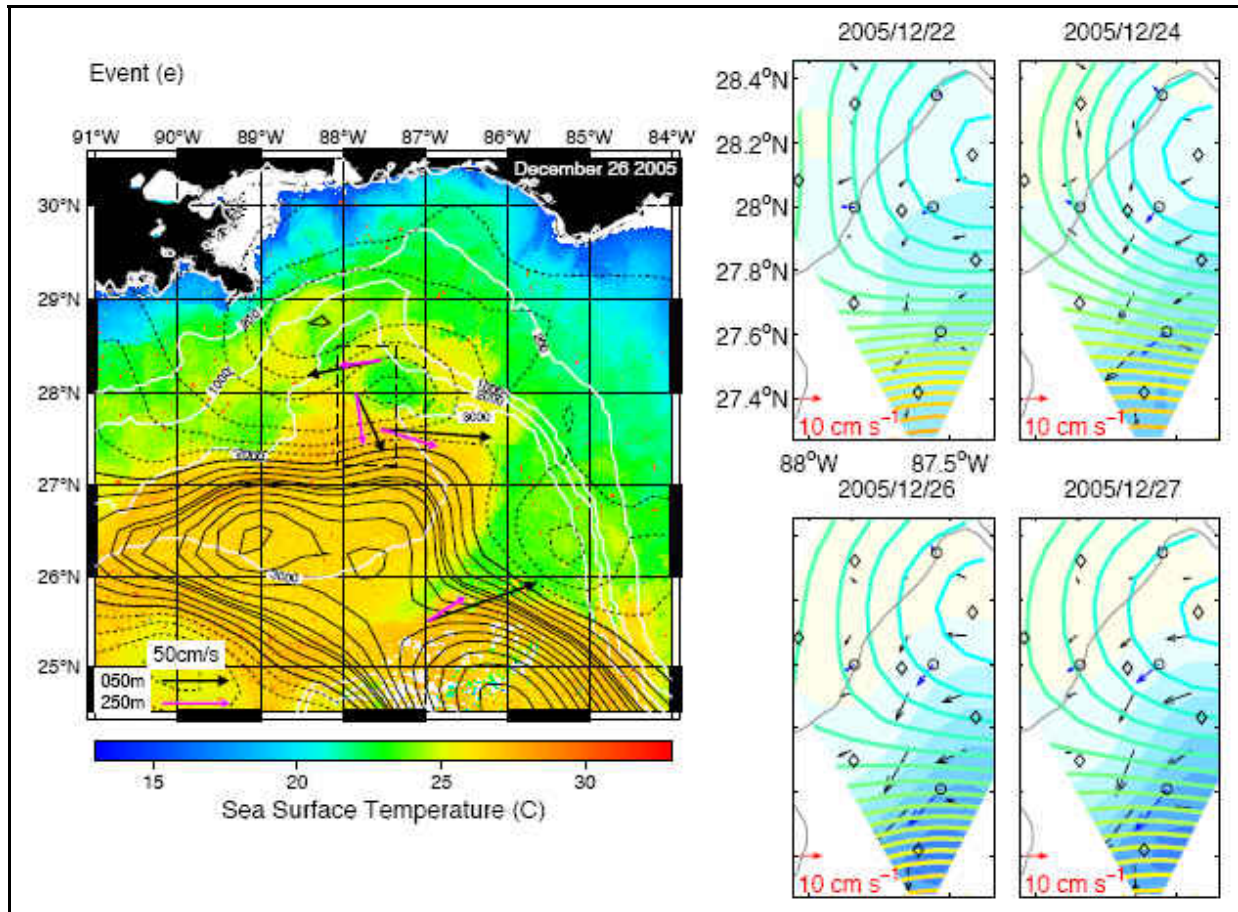


Figure 6.2-5e. The LH panel shows the 3-day composite SST overlaid with CCAR altimeter-derived SSH for December 26, 2005. Upper layer 1-day averaged currents at 50 and 250 m depth are given for the moorings. The RH panels show PIES-derived SSH (thick lines) and the stream function (solid color; blue shades cyclonic, pink shades anticyclonic) and currents at 2500 m. The blue and black arrows are observed and mapped geostrophic currents, respectively.

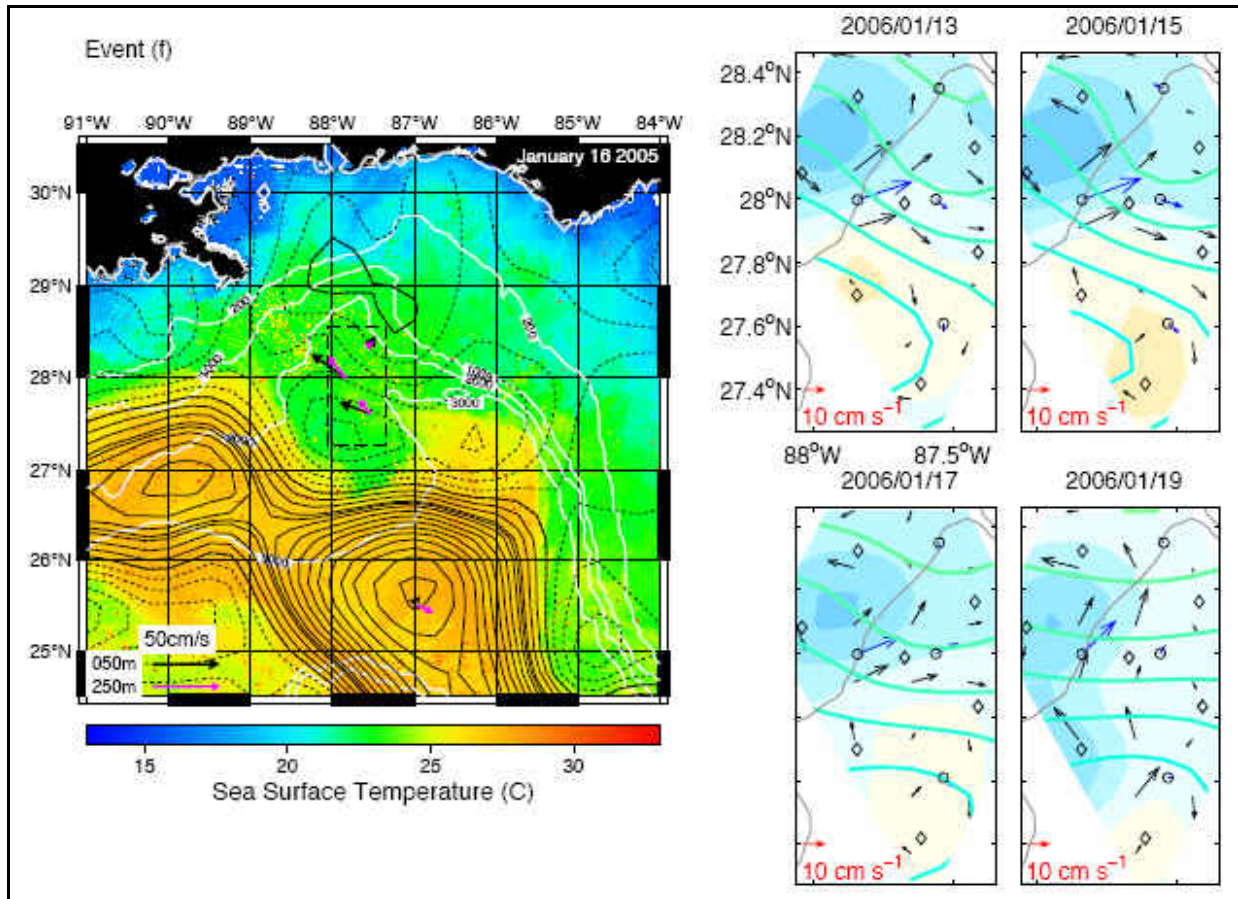


Figure 6.2-5f. The LH panel shows the 3-day composite SST overlaid with CCAR altimeter-derived SSH for January 16, 2006. Upper layer 1-day averaged currents at 50 and 250 m depth are given for the moorings. The RH panels show PIES-derived SSH (thick lines) and the stream function (solid color; blue shades cyclonic, pink shades anticyclonic) and currents at 2500 m. The blue and black arrows are observed and mapped geostrophic currents, respectively.

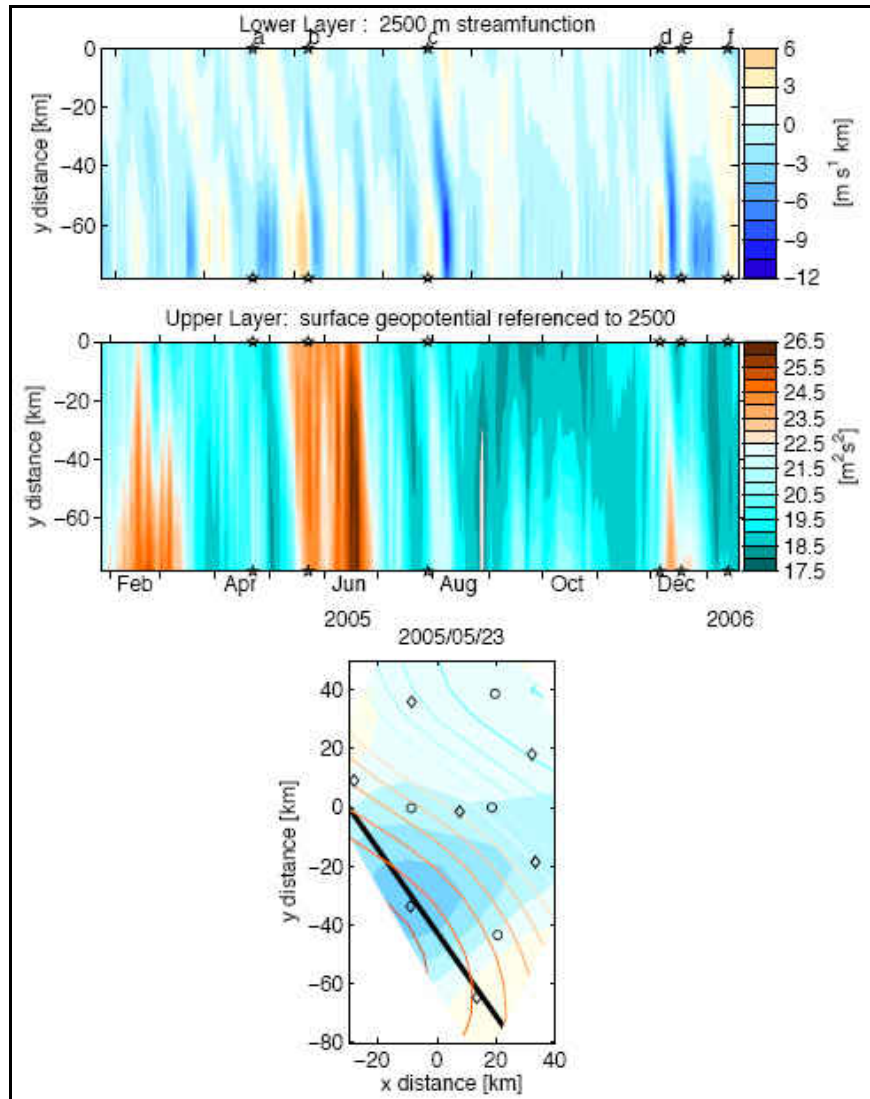


Figure 6.2-6. Snapshot of upper and lower layer circulation on May 23 (bottom panel) with surface geopotential referenced to 2500 m denoted by colored lines and bottom streamfunction indicated by filled colored contours. PIES sites are diamonds, current meters are circles. The thick black line represents the frequent translation route of deep cyclones. Upper (middle) panel: Hovmuller plot of lower-layer streamfunction (surface geopotential) along the transect shown in the circulation map (bottom panel). Six strong lower-layer events (a through f) labeled and denoted by black stars correspond to the strongest EKE events shown in Figure 6.2-4. Contour intervals and color scales for upper and lower layer circulation are consistent between the Hovmuller plots and the circulation map.

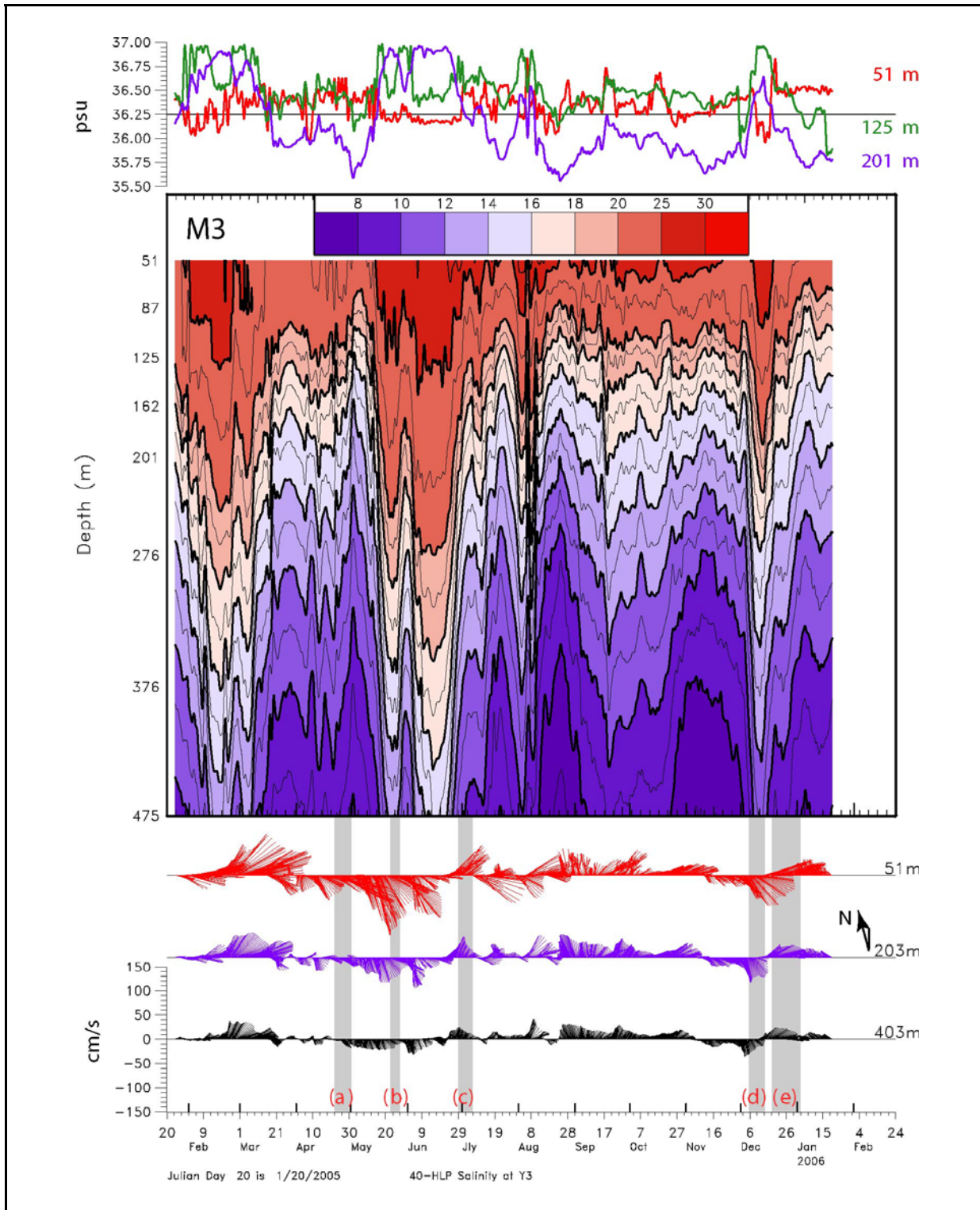


Figure 6.2-7. Upper layer 40-HLP currents, temperatures (solid contours) and salinities from mooring M3. The gray shading corresponds to the deep current events (a through e) marked in Figures 6.2-2 and 6.2-4.

Table 6.3-1

EOF and Wavenumber Analysis of Eastern GOM Deep Currents

Mooring Group (with depths (m))	Analysis Interval Dates	Frequency Band (cpd)	Center Period (days)	Mode Number	% Total Variance	Wavelength (km)
M2 (2035), M3 (2489), &M4 (2530)	2005-01-27 2006-01-19	0.033-0.045	25	1	64.1	222
				2	30.0	146
		0.010-0.033	60	1	62.7	162
				2	17.6	338
L7 (875,1200,1500, 2000,2500,3000)	2005-06-03 2006-01-28	0.033-0.045	25	1	78.9	
				1	72.7	
		0.010-0.033	60	2	25.1	
L7 (500,2000,3000, 3187,3256)	2003-04-24 2004-06-07	0.024-0.050	27	1	69.9	
				1	70.4	
		0.010-0.030	61	1	70.4	
				2	23.6	300†

†Estimated from backward ray trace given in Figure 6.3-3.

The results of the Eastern GOM Study analysis for the 60-day period band are shown in Figure 6.3-3. This figure also shows the EKE and the velocity hodographs for the mode 1 EOF analysis of the near-bottom currents in the Exploratory array (redrawn from Donohue et al. 2006). In the M2, M3 and M4 moorings, the highest 60-day energy was at M3 and mode 1 reflected this. The wavelength calculated from the phase differences was 162 km, which was within the range of previously derived estimates in the deep GOM (Hamilton 1990; 2007). The direction of the major axes of the 1st mode ellipses indicated that phase propagation was south or southeastwards and thus corresponded to the propagation direction of the deep eddies described in Section 6.2.1. The second mode was barely significant and the derived wavelength was larger than expected, suggesting that this weak signal was not a propagating wave. TRW ray tracing from the full dispersion relation, employing the same methods described in Donohue et al. (2006) and Hamilton (2007) and using the 162 km initial wavelength and a 60-day period, showed that a TRW could reach the upper escarpment in about 40 to 45 days, but the region of impact was an area of low energy as measured by the earlier study. However, if the ray is moved slightly southward so that it favors the larger fluctuations at M3, then it is apparent that this northeastern OMf region could potentially supply some energy to the northern part of the high EKE region below the escarpment. Southward displacement of the ray could also be caused by the westward mean flow along the escarpment as discussed by Oey and Lee (2002). This effect was not included in the ray tracing calculations given here. Hamilton (2007) did attempt to crudely model a mean escarpment current and found some displacement of the rays near the escarpment; however, not including this effect did not significantly change the results. The long transit times and the relatively low energy compared to the southern edge of the exploratory array probably favored dissipation of these 60-day TRWs before they impacted the escarpment region. Backward ray tracing of this 60-day wave indicated that the source region was probably between the 3000 and 2500-m isobaths, because at depths deeper than 3000 m the group velocities become very small which caused the ray to be terminated. The direction of this backward ray was similar to the direction of the eastern LC front as described in Section 6.2.1.

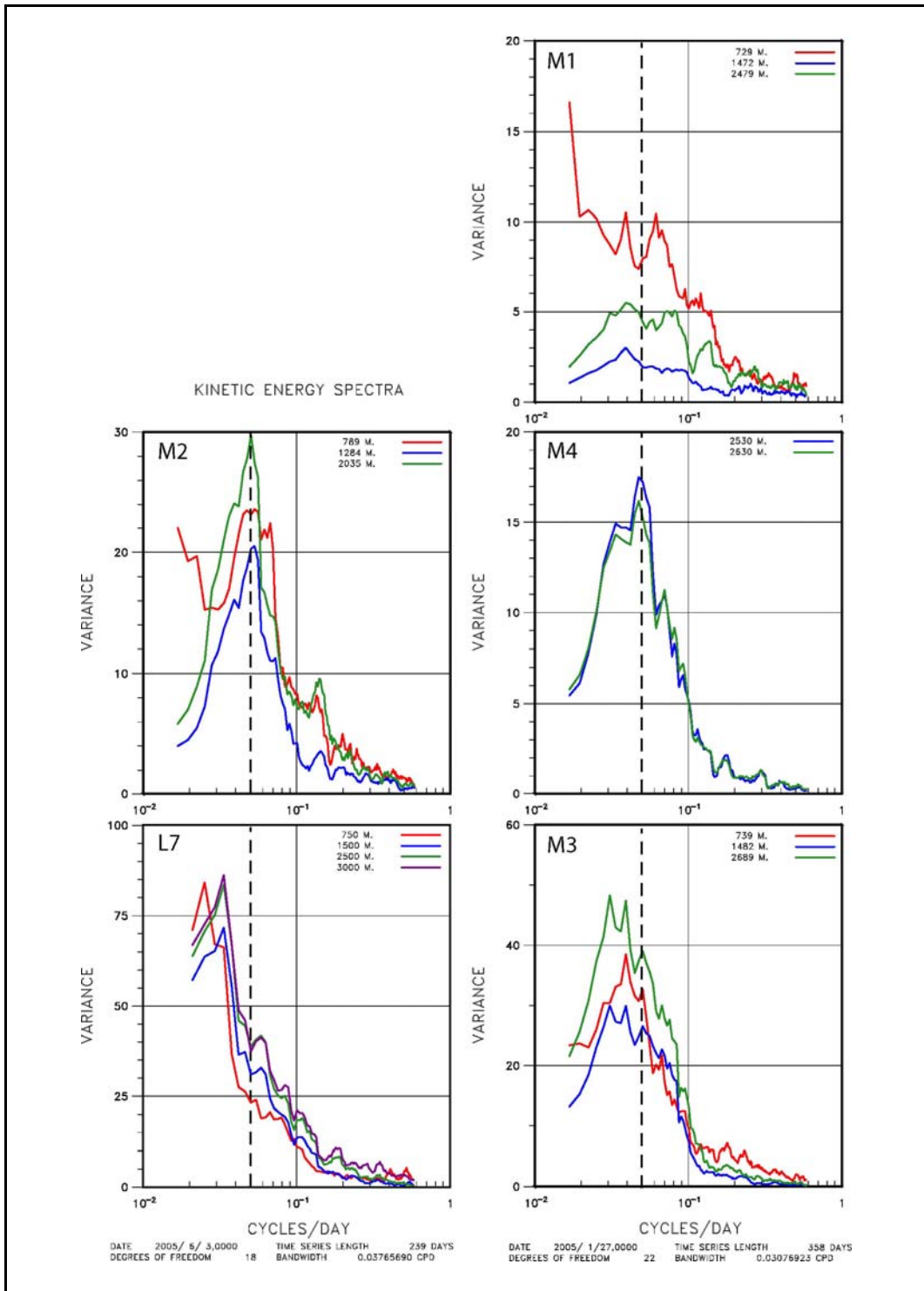


Figure 6.3-1. Variance preserving kinetic energy spectra for selected lower-layer velocity observations at moorings M1-M4 and L7.

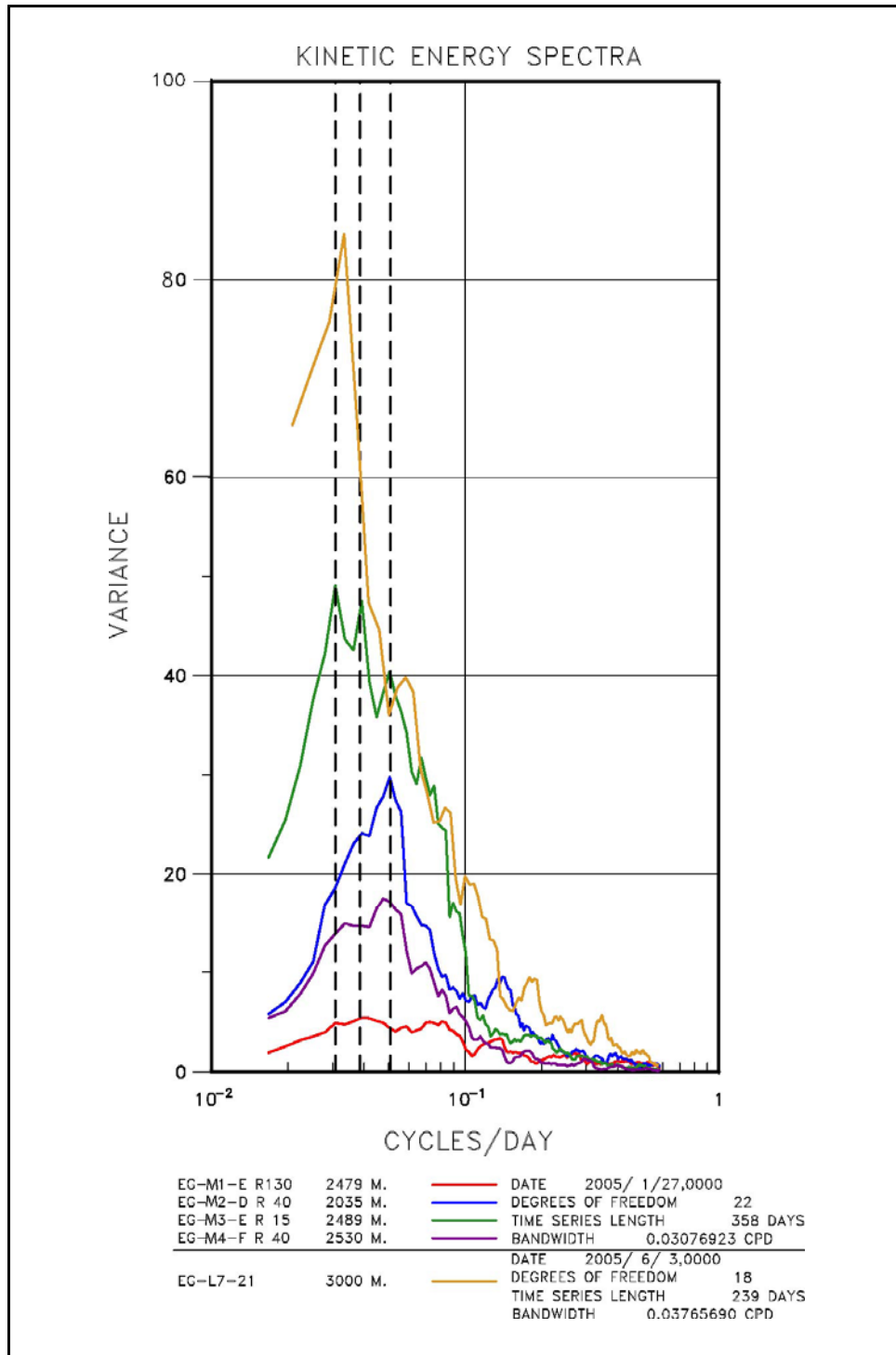


Figure 6.3-2. Variance preserving kinetic energy spectra for near-bottom velocity observations on the indicated moorings. Note the L7 spectra is for a different time interval than those for the M moorings.

In the Exploratory program, a wavelength of 203 km was determined for a 61 day TRW originating in the southeast corner of the array where the 1st mode signal was large (Figure 6.3-3). The path of the forward ray corresponded nicely to the high-energy region below the escarpment, particularly if reflection is assumed at the point where the ray encounters the steep slope. The 60-day period energy above the escarpment was essentially negligible and the energy along the transmitted forward ray was rapidly attenuated to the west. A backward ray-trace showed that L7 lied on the energy propagation path, and the mode 2 oscillations from the L7 lower layer analysis from the same interval as the Exploratory program (Table 6.3-1 and Figure 6.3-3) lined up with ray quite closely. The wavelength at L7 from the backward ray path was 300 km, and this was consistent with the almost depth independent nature of the fluctuations of both modes, which implied a trapping depth ($1/\lambda$) on the order of the water depth (3340 m). The trapping depth is related to the wavelength for constant N by:

$$\lambda = NK/f, \quad (6.3.1)$$

Using a wavelength of 300 km, and $N = 10^{-3} \text{ s}^{-1}$, gave an estimated $1/\lambda$ of ~ 3000 m. The transit time from L7 to the escarpment was ~ 25 days, which was much less than the transit time from the northern M array.

A similar EOF analysis for the 2005-2006 interval at L7 also showed two modes with the major axes of the ellipses normal to each other, but at approximately 45° to the modes of the earlier interval. In 2003 and 2004, the LC axis was more northerly directed (Donohue et al. 2006) than the more northwesterly trend in 2005, and this perhaps had an influence on the genesis of the TRW modes along the west side of the LC. The slightly differing results at L7 suggested, not surprisingly, that there was inter-annual variability in the deep TRW regime. If the west side of the LC is the primary generation zone for longer period TRWs then the northern and southern rays in Figure 6.3-3 implied a reduction in horizontal area between the rays as they approached the escarpment. This would indicate an increase in energy if dissipation is disregarded and could account for the large amplitude 60-day fluctuations observed next to the escarpment in Figure 6.3-3.

The EOF analysis of wavelengths were also conducted for 20 to 25 day periods (Table 6.3-1 and Figure 6.3-4). In the horizontal EOF analysis of the three M moorings, the first two modes were significant and the directions of the major axes of the ellipses at M3 and M4 implied that energy was propagating up-slope (mode 1) and down-slope (mode 2). With the estimated wavelengths from the phase analysis, the ray tracing produced two similar ray paths towards the escarpment because the down-slope ray was reversed by the topography. The backward ray paths were also similar and pointed to the M1 location, which had very low energy in this frequency band (Figure 6.3-2). This implied again that the generation zone was fairly local to the deeper parts of the study area. The 25-day forward ray paths implied that the M moorings could be an upstream source for the relatively weak fluctuations at the shallower eastern end of the escarpment. Transit times would be in the range of ~ 12 to 15 days. The mode 1 EKE and hodograph ellipses for the Exploratory program (Figure 6.3-4) again showed that the largest amplitude fluctuations were below the escarpment between 90 and 91.5°W. The 22.4-day ray paths initiated in the southeast corner of the Exploratory array aligned nicely with the more energetic ellipses, with an indication that both reflected and transmitted rays contributed to the variance in the west. Again the effects of persistent mean flows near the escarpment have been neglected. The rapid damping of the fluctuations above the escarpment seemed to show that the transmitted ray was dissipated by the rough topography there. The backward ray path implied that the L7 site was too far east to contribute to the 20 to 25-day energy at the escarpment. At L7 during 2005 mode 1 dominated, and the direction of the ellipse major axis implied that TRWs with this period at this location were primarily propagating towards the Campeche Bank and were likely to be refracted into the southern part of the eastern basin as discussed in Section 6.1. Therefore, these shorter period TRWs in the Exploratory region appeared to have more than one source with the shallower part of the escarpment most likely influenced by the northeast, and the deeper part seemed to have source regions further south but not under the LC, as seemed to be the case for the longer period waves.

6.3.1 Wavelet Analysis

Wavelet transforms are localized functions of time-scale and frequency that are used to expand time series into time-frequency space, and therefore, can find localized intermittent periodicities. In this investigation, Continuous Wavelet Transforms (CWT), specifically the complex Morlet transform, were used because they are better for feature extraction and revealing patterns. The time-scale of a Morlet wavelet very nearly equates to its equivalent Fourier period. The analysis follows Torrence and Compo (1998), where the significance levels for the wavelet power spectrum are calculated using the theoretical red-noise spectrum for a univariate lag-1 autoregressive process. The lag-1 autocorrelation coefficient (α) in this study was estimated by the non-linear least-square fit of the Fourier spectrum of the time series to the theoretical red-noise spectrum. The time-averaged or global wavelet spectrum has been shown to provide an unbiased and consistent estimation of the true Fourier power spectrum of a time series. Torrence and Compo (1998) also define a “cone of influence” where end of time series effects can distort the analysis, and the regions of the time-frequency space where this occurs increase with the time scale of the wavelet.

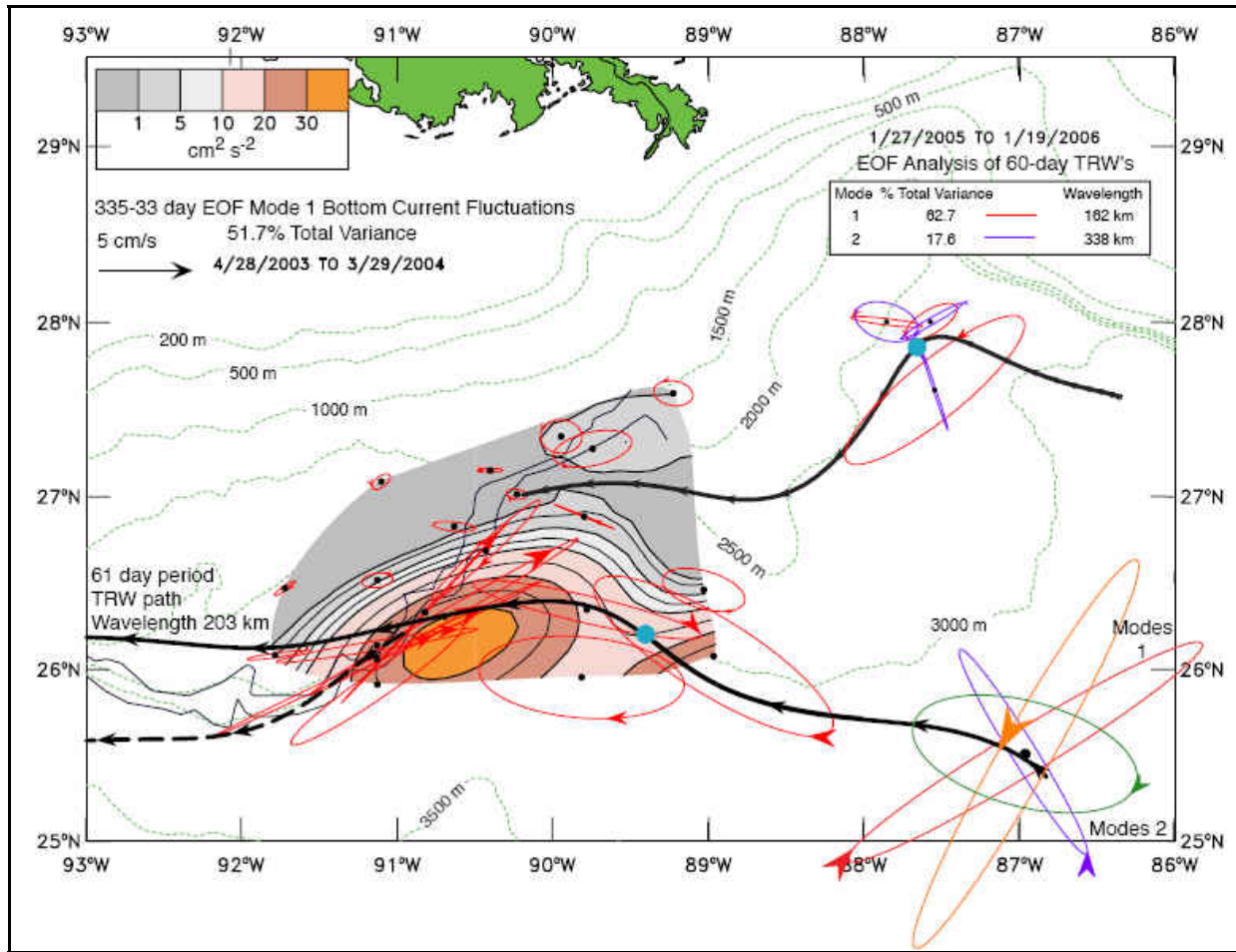


Figure 6.3-3. West of 89°W, the near-bottom (100 to 500 MAB) EKE is contoured for the 335-33 day EOF mode 1 velocities from the Exploratory Program. The elliptical hodographs show the mode 1 currents at each mooring with arrow heads giving relative phase. The EOF modes for similar near-bottom currents at the M moorings in the eastern GOM are also shown. At L7, the red and orange modes 1, and the blue and green modes 2 ellipses are for the lower-layer velocities for the Eastern GOM Study and Exploratory Study time intervals, respectively. The thick black lines are TRW ray traces initiated at the blue dots with the indicated periods and wavelengths. The reflected ray is given by the dashed line. Arrow heads are every 5 days.

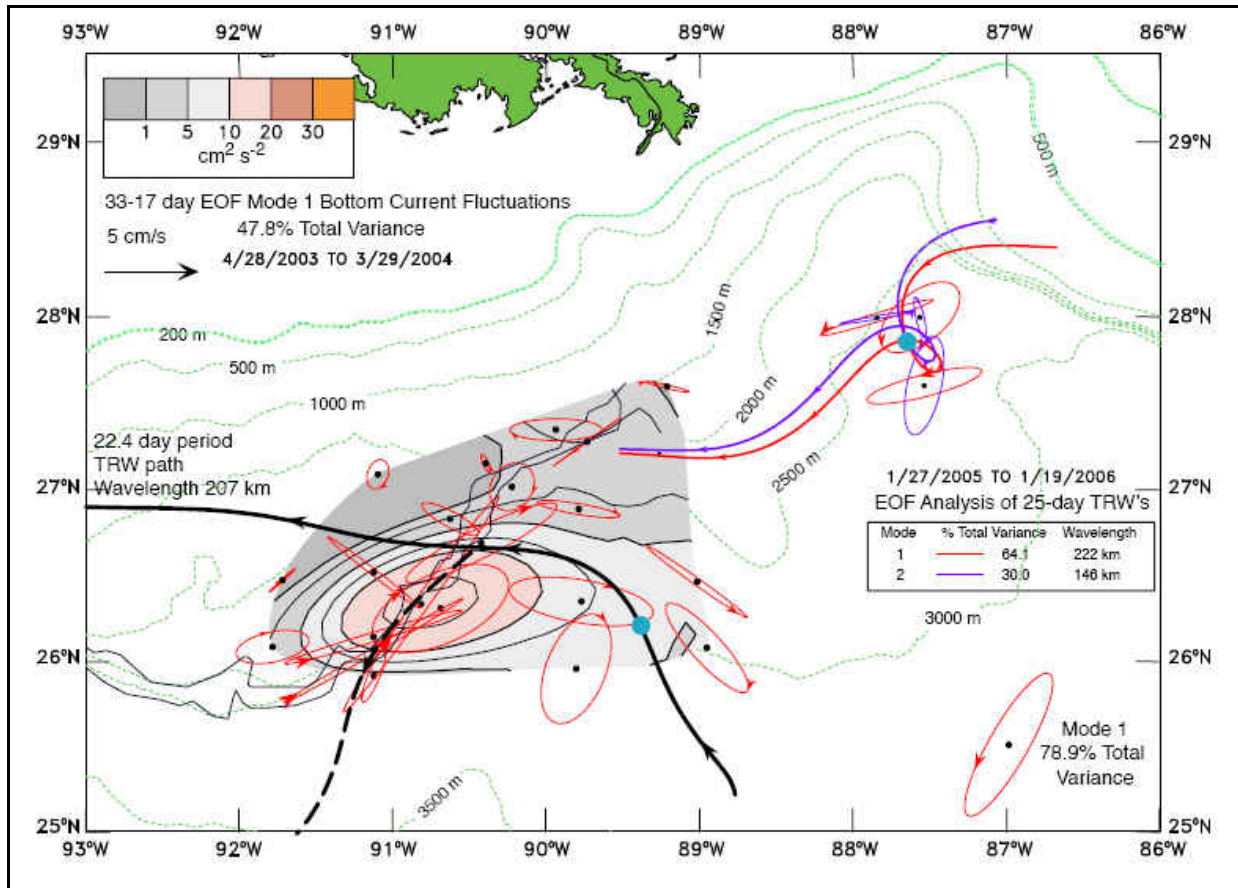


Figure 6.3-4. West of 89°W, the near-bottom (100 to 500 MAB) EKE is contoured for the 33-17 day EOF mode 1 velocities from the Exploratory Program. The elliptical hodographs show the mode 1 currents at each mooring with arrow heads giving relative phase. The EOF modes for similar near-bottom currents at the Y moorings in the eastern GOM are also shown. At L7, the 3000-m ellipse is from the 25-day EOF analysis of the lower-layer currents using the Eastern GOM Study time interval. The thick lines are TRW ray traces initiated at the blue dots with the indicated periods and wavelengths. The reflected ray is given by the dashed line. Arrow heads are every 5 days.

The wavelet power spectra were calculated for the cross (u) and along (v) isobath components of the 2500 m currents at M3 (Figure 6.3-5). The distribution of power with time and frequency showed that there was more significant variance at shorter periods in the u- than the v- component, and that the v-component dominated at longer periods. This was expected from the dispersion relation (6.1.3) for TRWs, because the principal major axis of the fluctuations rotates from across- to along-isobath as the wave period increases. This further confirmed that the lower-layer motions in the study area were dominated by TRWs as such a pattern would not be expected from translating eddies. The global spectra showed little significant power at periods longer than 80 days and the ~ 60 and 25-day peaks corresponded to the Fourier spectra in Figure 6.3-1 and the ray tracing given above. Figure 6.3-5 also shows that the fluctuations were intermittent but that times of significant power occurred throughout the summer (May through August, 2005) when the LC was extended to the northwest and Eddy Vortex was undergoing a sequence of detachments and reattachments. After the final separation and the rapid translation of Eddy Vortex to the west at the beginning of September, the power decreased below the 95% significance levels, particularly at shorter periods. This suggested that the presence of the LC or a LCE over the study area had a direct influence on the amplitudes of the lower-layer TRWs.

A similar wavelet analysis was performed for the 2500 m currents at L3 for the Exploratory Study. As shown by Figure 6.3-3, L3 can be considered to be downstream of the LC, and it was of interest to see if similar patterns were observed there as compared to the northeast side of the LC front where M3 was situated for much of 2005. The u and v-component wavelet power spectra for L3 are given in Figure 6.3-6. The cross-isobath u-component had significant power at shorter periods compared with the along isobath component. The EKE spectrum for L3 (Figure 6.1-5) was noteworthy in that it had fairly broad power over periods from 10 to 100 days. The global power in Figure 6.3-6 shows that the u- and v-components dominated at periods of 10 to 30 days and 40 to 100 days, respectively. The power in both period bands had higher amplitudes from June to September 2003, while Eddy Sargassum formed and separated. Eddy Sargassum was similar to Eddy Vortex in that its initial location, before translating into the western GOM, was in the northern part of the eastern basin. Eddy Titanic on the other hand, detached in January 2004 much closer to the Campeche Bank, and its initial southwestward path was close to and parallel to the steep southern slope. The wavelet power at L3 showed some increase around the time of Titanic's separation, particularly in the u-component, but the amplitudes were not significant at the 95% level. Therefore, there were some indications that TRW activity north and west of the LC increases during LC extensions and LCE separations as would be expected from the models of TRW generation by a pulsating meander over a uniform sloping bottom (Malanotte-Rizzoli et al. 1987). It is however, by no means conclusive because of the limited number of events observed by these studies.

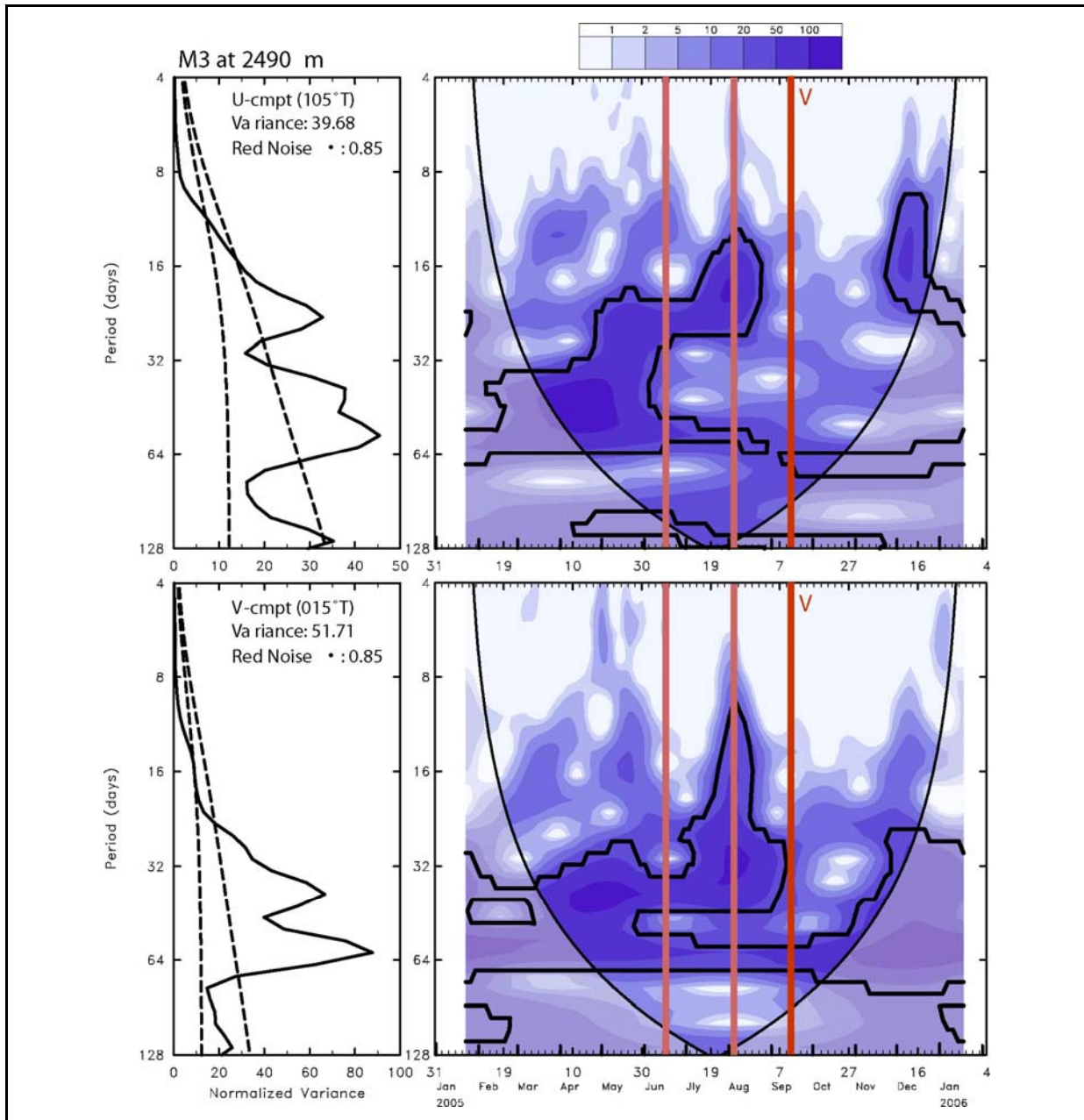


Figure 6.3-5. RH panels show the local wavelet power spectrum of the velocity components from M3 at 2490 m for the indicated time interval using the Morlet wavelet normalized by the variances of the respective series. The thick solid contours encloses regions of greater than 95% confidence for a red-noise process with the indicated lag-1 (α) coefficients. The lighter shades indicate the “cone of influence” where edge effects become important. Separation events for LCE Vortex are shown by thick vertical lines, with final detachment in red. The LH panels show the respective global (time-averaged) wavelet spectrum (solid lines). The dashed lines show the mean red noise spectrum (lower), and the 95% confidence levels (upper) for the global wavelet spectra, given their respective α 's.

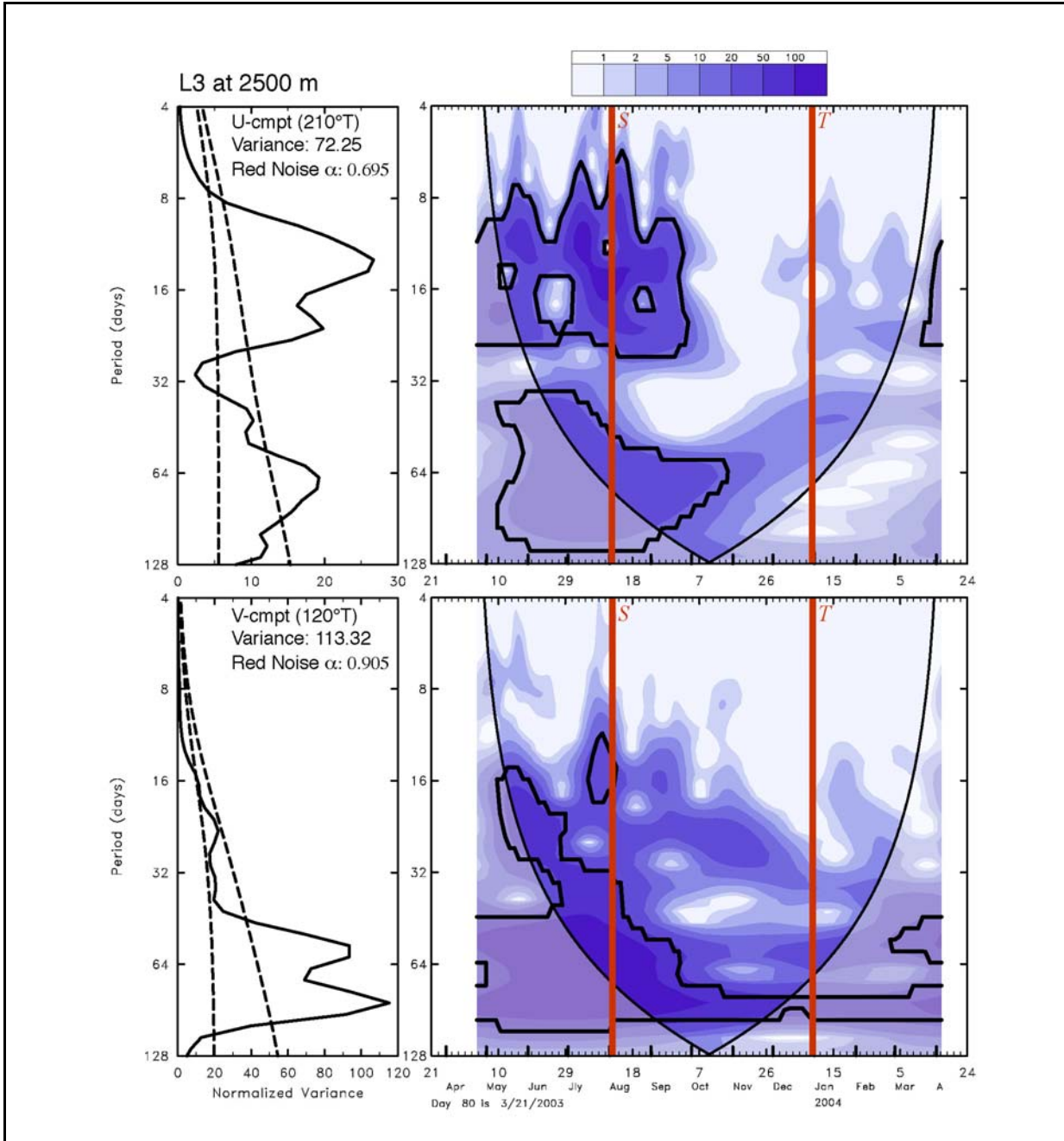


Figure 6.3-6. RH panels show the local wavelet power spectrum of the velocity components from L3 at 2500 m for the indicated time interval using the Morlet wavelet normalized by the variances of the respective series. The thick solid contours encloses regions of greater than 95% confidence for a red-noise process with the indicated lag-1 (α) coefficients. The lighter shades indicate the “cone of influence” where edge effects become important. The red event lines show the detachment dates of LCE’s Sargassum and Titanic. The LH panels show the respective global (time averaged) wavelet spectrum (solid lines). The dashed lines show the mean red noise spectrum (lower), and the 95% confidence levels (upper) for the global wavelet spectra, given their respective α ’s.

7.0 VERTICAL COUPLING

Establishing relationships between observations of upper and lower circulations in the deep GOM has proved to be difficult over the years. Generally, currents above 800 m and below 1200 m have not been correlated at significant time scales. There have been intriguing events where flows appear to be similar through the whole water column; however, they were not long lasting and generally quite rare. A few examples of these events are noted for the I1 mooring in Hamilton (2007), where they were mostly associated with peripheral cyclones or frontal eddies on LCEs. To further evaluate potential vertical coupling between the upper and lower layers, an approach was taken to use CEOF analysis in the time domain of the depth profiles of currents, which further established the two-layered nature of the flows, followed by an examination of relative vorticity, ζ , and potential vorticity (PV) in these layers.

7.1 CEOFs

The CEOF analysis is similar to that employed for the lower-layer currents in Chapter 6. Time domain CEOFs are used rather than frequency domain EOFs because the 1-year time series of upper-layer currents do not resolve the ~ 6 to 18 month fluctuations of the LCE shedding cycle. Another approach using dynamical normal modes, which are a theoretical decomposition of current profiles based on the vertical profiles of the Brunt-Vaisala (buoyancy) frequency, is also used. This analysis has many similarities to the purely statistical CEOFs. A limitation of dynamic modes is that the bottom is assumed to be level, and this precludes any bottom intensification of the currents.

The analysis of the vertical currents profiles concentrates on the M3 mooring, because it had the best one-year coverage of all the full-depth moorings in the Eastern GOM Study area. Similar analyses for the M1 and M2 moorings were qualitatively the same as for M3. Initially upper and lower layer CEOFs were calculated for 6 levels of demeaned currents in each layer with the 987 m level being common to both. The results are given in Figure 7.1-1a and the first mode for each layer accounted for $> 90\%$ of the total variance of each set of 6 records. The upper-layer mode was strongly sheared, and approximately unidirectional with the principal axis directed approximately north – south. Clearly the 987 m level currents were only weakly coherent with the mode. The lower-layer currents were highly coherent with the lower-layer mode 1 from 1000 m to the bottom. The mode CEOFs were again unidirectional, with the principal axes being more along the isobaths trending southwest to northeast and showed an increase in amplitude towards the bottom. Therefore, it was reasonable to associate the upper-layer mode 1 fluctuations with the LC and its peripheral cyclones, and the lower-layer mode 1 with TRWs.

The complex amplitude time series of the modes (normalized to unit variance) are given in Figure 7.1-2, which also shows the observed 40-HLP currents at M3. Apart from visual differences arising from the different axis rotations, it can be seen that the upper and lower layer modes closely resembled the observed currents from the upper layer (179 m) and lower layer (987 and 1985 m), respectively. Correlations between the modes were not significant for the v-component at any lag and barely significant (-0.26 : 99% significance level = 0.16) at zero lag for the u-component.

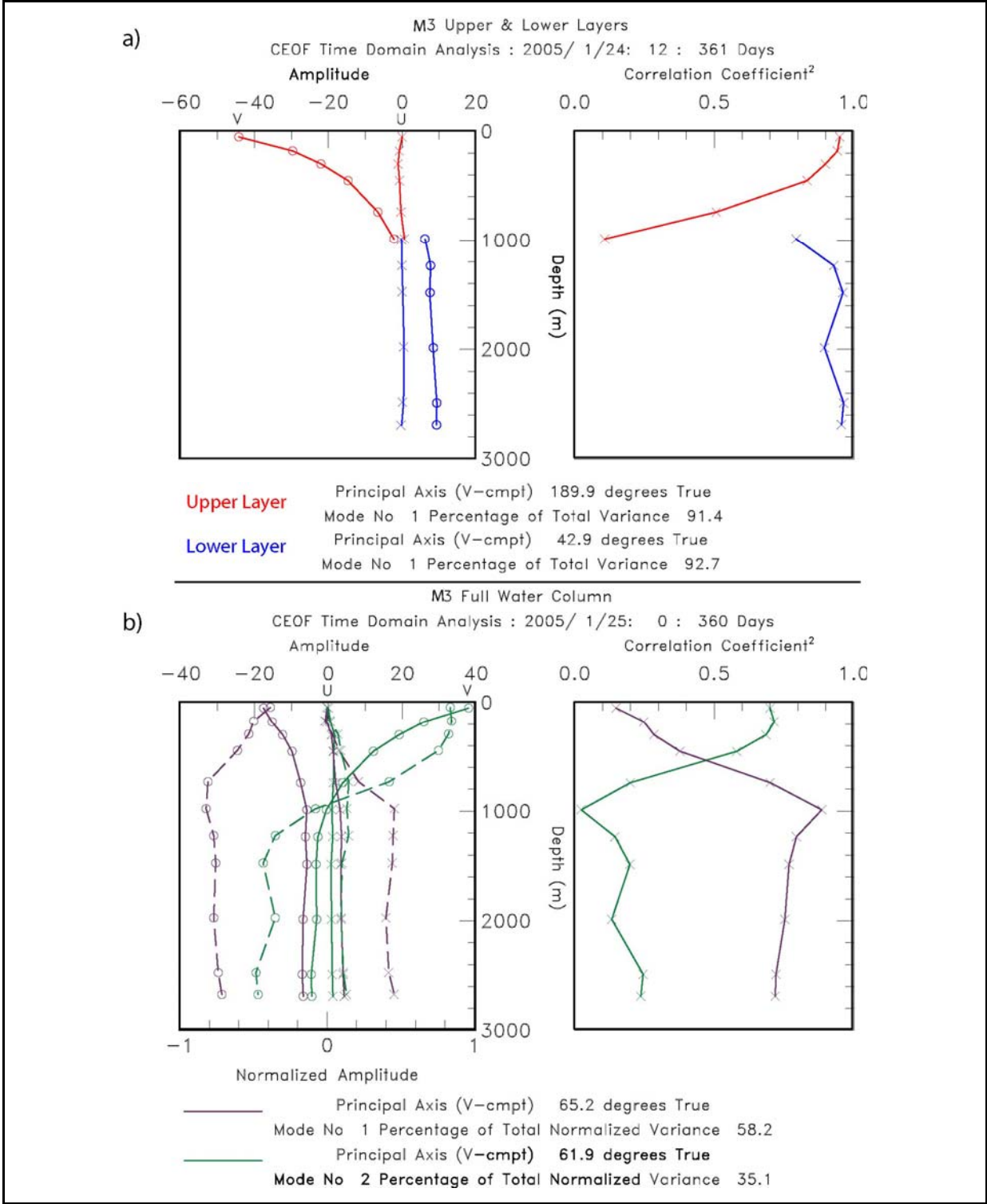


Figure 7.1-1. Depth profiles of CEOF amplitudes (cm/s) from a) separate analyses of upper and lower layer currents at M3, and b) full water column analysis of normalized currents at M3. The solid and dashed lines are the denormalized and normalized amplitudes, respectively.

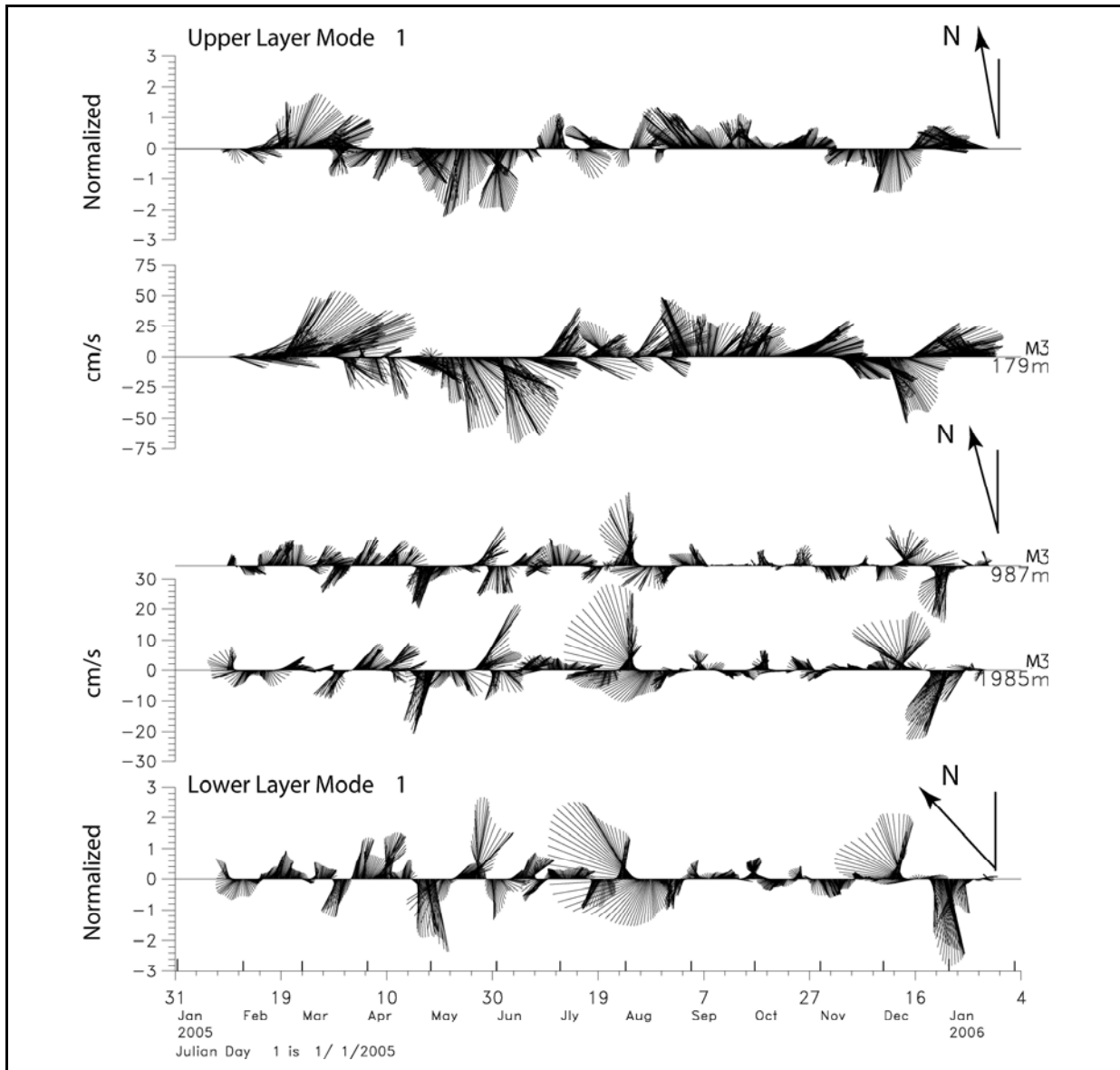


Figure 7.1-2. Mode 1 amplitude vector time series (top panel: upper-layer; bottom panel: lower-layer) from the M3 CEOF layer analysis. The middle panels show 40-HLP current observations from 3 depths on M3.

This two-layer analysis indicated that there was minimal connection between the modes that accounted for > 90% of the variance in each layer. To analyze the total water column at M3, the CEOFs were calculated for 5 levels in each layer and at the 987 m level. Because the velocity variances were an order of magnitude larger in the upper water column than near the bottom, the complex velocities were normalized to unit variance, so that each level was equally weighted and the parts of the water column above and below 1000 m had the same number of records. Two modes accounted for 93.3% of the total normalized variance of the 11 velocity records (Figure 7.1-1b). The mode velocity profiles were plotted with normalized magnitudes and also “denormalized” by multiplying by the standard deviation of each velocity record. Currents at 983 m and below were highly coherent with mode 1. The correlations then decayed towards the surface. Therefore, this was essentially the bottom trapped TRW signal, even though the upper-layer denormalized magnitudes increased towards the surface. The latter was not significant and was a result of weighting by the much larger upper layer variances. However, this mode did indicate that some of the signal above 1000 m was attributable to TRW motions.

Mode 2 was primarily surface intensified and was clearly similar to the upper-layer mode 1 in Figure 7.1-1a. However, it also had a weak almost depth-independent expression, in the opposite direction below 1000 m, that had small, barely significant correlation coefficients. The zero crossover point was at about 800 m, and this mode closely resembled the dynamical normal mode 1, discussed in Section 7.2. The lower layer had a small contribution from upper-layer LC or eddy fluctuations through dynamical coupling, just as the upper layer had a small contribution from TRW flows decaying upwards through the water column. Therefore, the separate layer and full water column CEOF velocity modes were essentially equivalent and indicated only very weak interactions.

7.1.1 Potential Vorticity

The measurements on the three full-depth moorings allowed for calculations of layer potential vorticity. The Ertel potential vorticity (PV) for a layer bounded by isopycnals is conserved in the absence of dissipation, and is defined as:

$$PV = \frac{\zeta + f}{h}, \quad (7.1-1)$$

where $\zeta = \partial v / \partial x - \partial u / \partial y$ is the relative vorticity, f is the Coriolis parameter, and h is the layer thickness, bounded by isopycnal surfaces. The relative vorticity, ζ , is calculated for fixed depth levels from current measurements by fitting planes to the three measurements. Thus,

$$\begin{aligned} u(x, y, z, t) &= u_0 + x \partial u / \partial x + y \partial u / \partial y \\ v(x, y, z, t) &= v_0 + x \partial v / \partial x + y \partial v / \partial y, \end{aligned} \quad (7.1-2)$$

where (x, y) are measured from the center position of the subset of the array used for the estimates. The results are normalized by the local Coriolis parameter ($f = \sim 6.5 \cdot 10^{-5} \text{ s}^{-1}$). The north-south and east-west extents of the array are 82 and 30 km respectively, and therefore the calculation of ζ has these implicit scales that are appropriate for the larger frontal or peripheral eddies. The potential vorticity anomaly is defined as:

$$PVA = \frac{\zeta + f}{h} - \frac{f}{H}, \quad (7.1-3)$$

where H is a constant and represents the thickness of the layer at rest. Normalizing by H/f ,

$$PVA = \frac{H}{h} \frac{\zeta}{f} + \left(\frac{H}{h} - 1 \right), \quad (7.1-4)$$

where the term in parentheses represents the stretching effect (sometimes defined as the Sverdrup PVA) as a fraction of f/H . PVA is a linear function of PV and is therefore also a conserved quantity.

Layer thicknesses, h , were estimated by averaging isotherm depths, calculated by linear interpolation between temperature sensors at the M1, M2 and M3 locations, and the appropriate ζ was found by vertically averaging $\zeta(x,y,z,t)$ between delineating isotherms, using common depths for the three moorings and equation 7.1-2 for the horizontal velocity gradient estimates. Common velocity depths were between 76 and 428 m with 8 m spacing, and at a nominal 750, 1500 and 2300 m. In the calculations below, only two layers were considered: between the surface and the 8 °C isotherm, and between the 8 °C isotherm and the bottom. The statistics for the two layers are given in Table 7.1-1.

Time series of ζ , for the upper and lower layers, along with the depths of the 15 and 8 °C isotherms are given in Figure 7.1-3, where the color shading differentiates between cyclonic (cold) and anticyclonic (warm) eddies ($\zeta >$ and $<$ 0, respectively). These time series were compared with the surface relative vorticity calculated from the PIES array, which put the major events in a larger scale context (Note that the opposite sign convention was used here than for ω calculated from the PIES. The PIES derived ζ resolved smaller horizontal scales, but were calculated using surface geostrophic velocities rather than observed sub-inertial velocities as was done here. However, the results were quite similar. The relative vorticity was at a maximum near the surface and decreased with depth through the upper layer. It then showed a slight increase towards the bottom, similar to the vertical profile of velocity variances. There was some correspondence between the lower and upper layer peaks in ζ , indicating a connection that was not apparent in the velocity fluctuations. The depth of the 8 °C isotherm had been used to delineate the lower parts of LC eddies, and here it was a reasonable choice for the interface between the upper and lower layers, given the vertical distribution of temperature observations on the three moorings. A slightly better choice would have been the 6 °C isotherm depth, which was used for the layer PV analysis from the PIES given below. However, in the moored temperature measurements, the depth of the 6 °C isotherm was not as well resolved as the 8 °C. For the most part the 8 °C isotherm lies between 400 and 750 m where ζ has smaller magnitudes, and showed the expected relations with deep and shallow excursions corresponding to anticyclonic and cyclonic flows, respectively. Mean relative vorticity in both layers was positive. In the upper layer the relatively large mean value (5% of f) was a consequence of the array being on the east and cyclonic side of the LC front for most of the study interval, as well as from the frequent passage of cyclonic frontal eddies.

Table 7.1-1

Potential Vorticity Parameters

Layers	Mean Thickness H (m)	Depths of 8 °C Isotherm (m)	Layer Mean $\langle \zeta/f \rangle$	Layer Std. Dev. $\langle (\zeta^2/f^2) \rangle^{1/2}$	Maximum Correlation Coefficient	Lag (days)
Surface to 8°C	550	Minimum 428	0.052	0.103	0.42 (0.16)†	1 (Surface Lags)
8°C to Bottom	2150	Maximum 758	0.008	0.021		

†99% Significance Level

The upper and lower layer vertically averaged relative vorticities were significantly correlated (Table 7.1-1), though some of the correlation was caused by the upper layer ζ leaking below the 8 °C isotherm depth (Figure 7.1-3). The coherence squared and phase differences between the upper and lower layer averaged ζ , as well as ζ at the 300 and 2300 m depth levels, are given in Figure 7.1-4. There was significant coherence at TRW frequencies in the 20 to 35 day period band, with the upper layer lagging the lower layer by $\sim 90^\circ$, that was suggestive of baroclinic instability mechanisms (McWilliams 2006).

Time series of *PVA* (Equation 7.1-4) and its constituent terms (ζ and stretching: $H/h-1$) are given for both layers in Figure 7.1-5, which showed that for many events the stretching term dominated (e.g., the warm and cold eddy events in May-June and October-November, respectively), and because the stretching terms were inversely correlated in the two layers, this contributed to the overall coherence of the total *PVA* of the layers. However, there were other events when the stretching was weak and ζ dominated the total *PVA* (e.g., the events in March-April, and at the beginning of August and the middle of December).

The coherence squared and phase differences between the layer *PVA*, and for each layer between ζ and the stretching term (Figure 7.1-5) showed that, for the upper layer, ζ correlated quite well with stretching, as can be visually ascertained in Figure 7.1-3. In the lower layer, only the 25-30 day period band was coherent, which corresponded to the same frequencies for which ζ was coherent between the layers (Figure 7.1-4). The relation between lower layer stretching and relative vorticity at 25 to 30 days indicated active TRW generation by the upper layer, because the total layer *PVAs* were coherent at these frequencies (Figure 7.1-5). In the Chapter 6 analysis of lower layer currents at M3, the wavelet power (Figure 6.3-5) showed that 16 to 32 day period fluctuations were prevalent and significant during June to August when Eddy Vortex was attaching and detaching from the extended LC. Therefore, there is some evidence that eddies, and their local upper-layer *PV* fluctuations that have a substantial stretching component, have a relation to 25-30 day TRWs in the lower layer. The latter will radiate westward towards the escarpment as indicated by the ray paths in Figure 6.3-4.

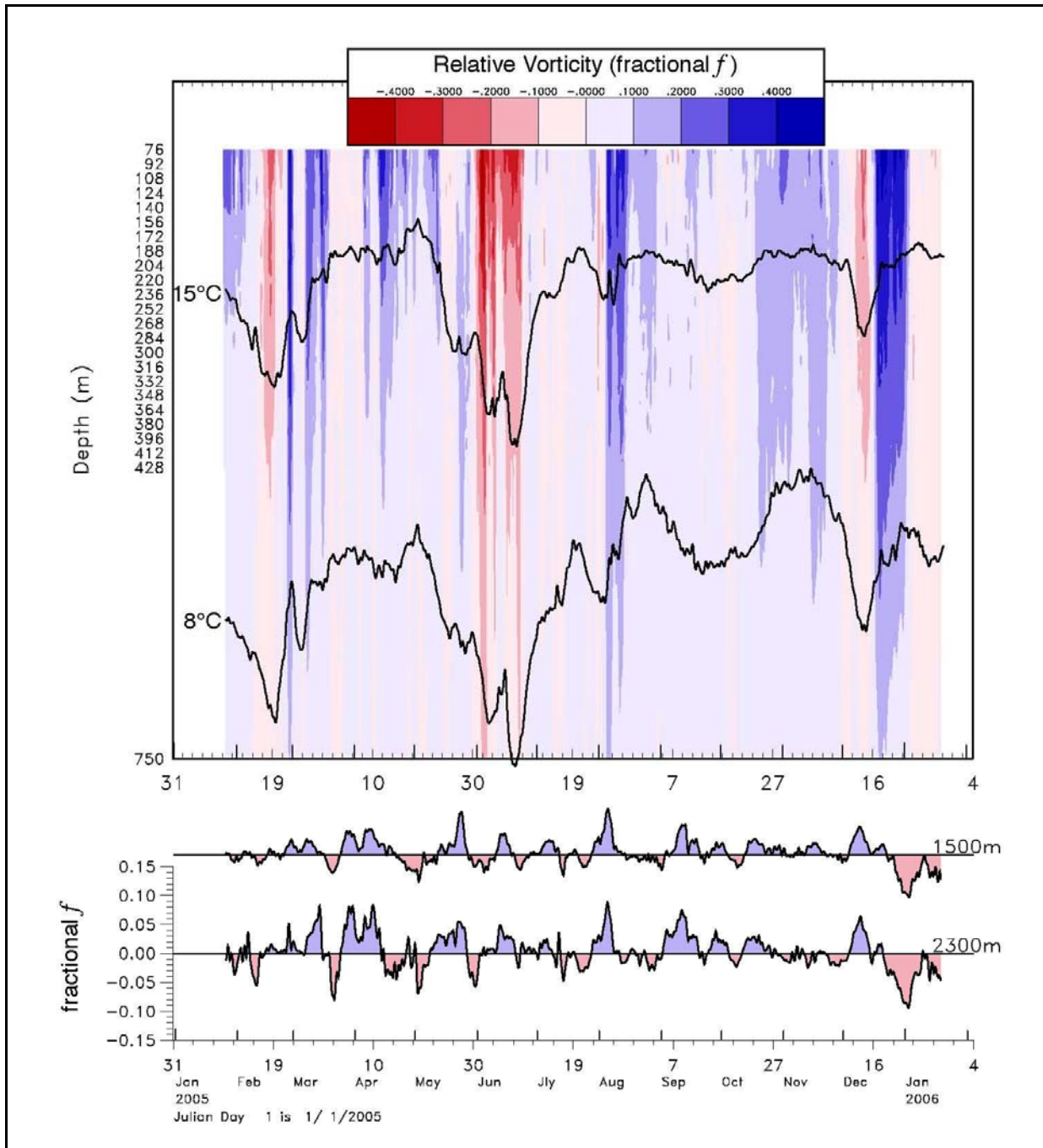


Figure 7.1-3. Relative vorticity (as a fraction of f) contoured for the upper layer, and as time series for the lower layer (1500 and 2300 m) calculated for the M1, M2 and M3 moorings. The upper layer contour plot is overlaid with the depths of the 15 and 8°C isotherms.

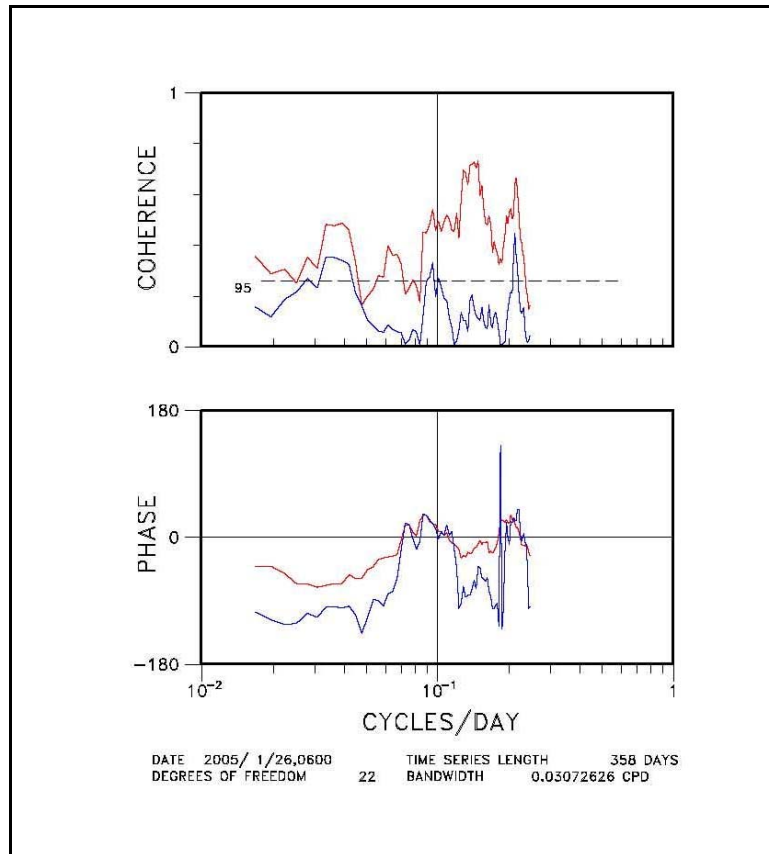


Figure 7.1-4. Coherence squared and phase differences between upper and lower layer averaged ζ (red lines), and ζ at 300 and 2300 m (blue lines).

7.2 *Dynamic Modes*

7.2.1 Vertical Structure of Low-Frequency Variability

7.2.1.1 Empirical Orthogonal Function (EOF) Analysis

Empirical orthogonal function (EOF) analysis, also known as principal component analysis is an accepted tool to quantify patterns of variability in large sets of time-series data that are of sufficient spatial distribution (Emery and Thomson 2001; Preisendorfer 1988). We employed an EOF analysis to the Eastern GOM Study current meter data in a manner consistent with previous studies in the GOM (Nowlin et al. 2001). In those previous studies, mooring locations which had at least 5 depth levels distributed throughout the water column were chosen for analysis. At the time, only one mooring containing high vertical resolution from a moored current profiler was publicly available. EOF analysis was also performed on current output from a three-dimensional general circulation model of the full GOM basin (Kantha et al. 2005). The general conclusion of the previous studies showed consistent vertical modal structure at several locations across the northern slopes of the GOM. The structure was consistent for coarse and fine vertically resolved current observations.

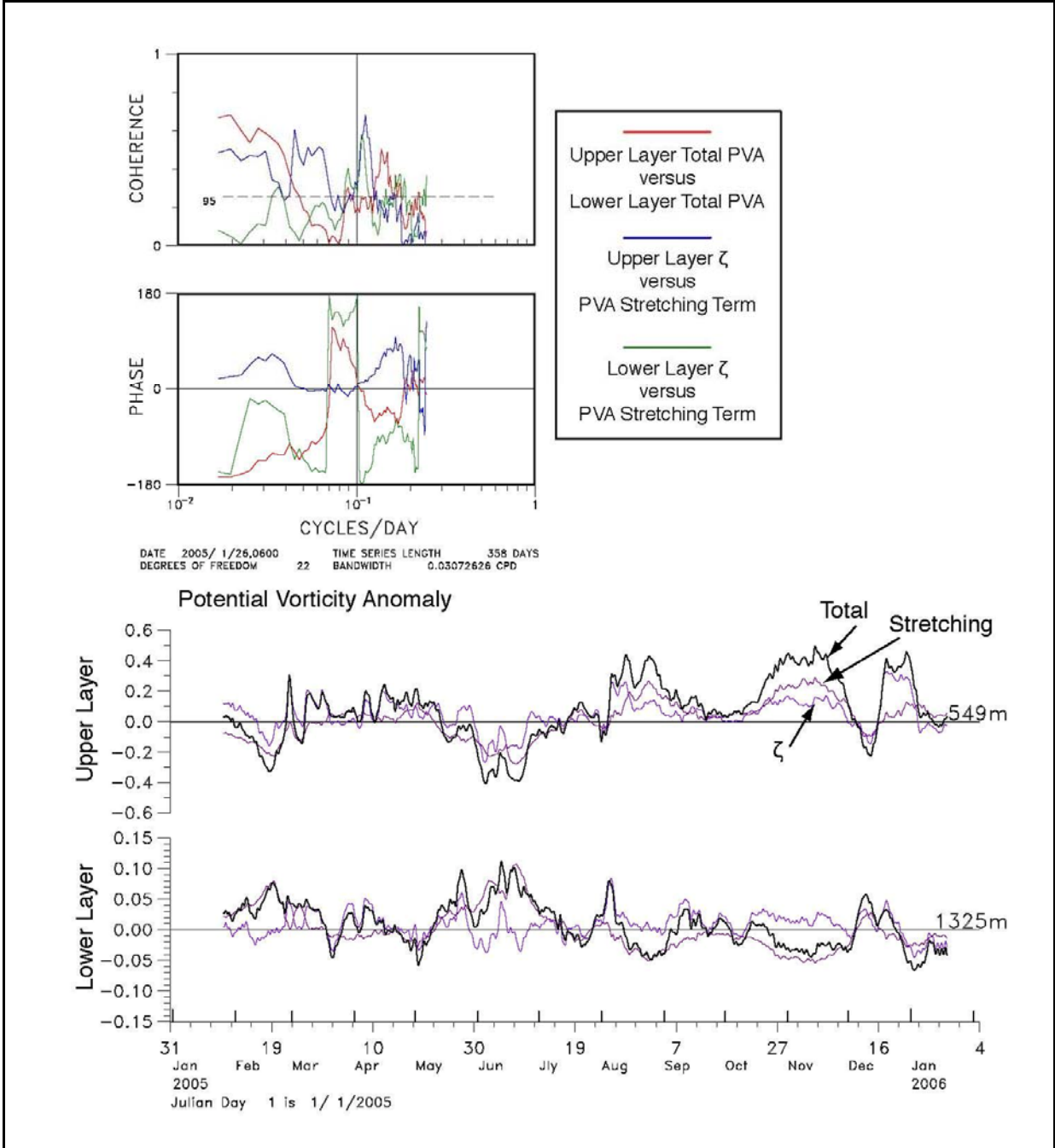


Figure 7.1-5. Potential vorticity anomalies and their component relative vorticity and stretching terms for the upper and lower layers with interface defined by the 8 °C isotherm (lower panel). The upper panel shows coherence squared and phase differences for the indicated upper and lower layer quantities.

Nowlin et al. (2001) found that the first mode, Mode 1, defined as the mode with the greatest percentage of variance, had a surface maximum that decreased exponentially with depth. Mode 2, containing the second largest percentage of variance, was bottom intensified with a zero-crossing or minimum in the upper 500 meters and barotropic (nearly constant) at depth. The interpretation of these previous results concluded that the dynamics of the low-frequency variability of the GOM can be interpreted as a two-layer system. The dynamics of the upper layer were associated with the exponentially decaying with depth motions of the LC and LCEs. The depth defining the transition to the lower layer was coincident with the sill depth of the Florida Straits. The bottom intensification for these analysis was attributed to the influence of the sloping topography on available normal dynamic modes estimated from stability theory (Charney and Flierl 1981). This interpretation was supported by the conclusion drawn from the spectral character and vertical profiles of the basic statistical parameters presented in Chapter 5 of this report.

It is important to recall however, that EOF modes are purely statistical constructs and in themselves do not represent physical processes. Therefore, the decomposition of statistically derived EOF modes are typically regressed onto dynamic modes to refine their interpretation. We begin this section by describing the EOF calculation performed for this study. Then, a description of the dynamic mode analysis of the Eastern GOM Study hydrographic data is given. Next, time series of dynamic modal amplitudes are estimated by regressing dynamic modes onto vertical profiles of current observations. Finally, correlations of sea surface height gradient and dynamic mode time series are estimated and presented.

The vertical EOF decomposition of east-west and north-south velocity component data was performed at each mooring, for each deployment, using data at approximately 12 depth levels that were distributed throughout the water column. Due to computation considerations of memory and computing time, data from each gap-filled single point current meter and five depth levels of the ADCP data were used in the calculation. All current data were 40-hr low-passed filtered and decimated to daily values to remove tidal, inertial, and other high frequency motions. The sequence of plots shown in Figures 7.2-1 – 7.2-6 shows the results of the EOF. These plots affirmed that the horizontal current structure in this region of the GOM resembles a 2-layer system. The eddy field caused intensification of the surface currents, which exponentially decayed in magnitude with depth to ~ 800 m. This structure was observed in the Mode 1 amplitudes, which contained the largest percentage of variance (~ 80 - 95 %) (Table 7.2-1). This mode showed maximum amplitudes at the surface that decreased with depth to nearly zero below 1000 m. The dynamic effect of eddies were rarely seen below 800 m; the sill depth of the Florida Straits. An energy minimum was present at 800-1000 m, evidenced by the small amplitudes of the prevalent first mode at this depth.

Table 7.2-1

EOF Mode Variance

Percentage of variance in EOF Modes 1, 2, and 3 for mooring M1, M2, and M3 for velocity components during deployment 1 and deployment 2 (in parentheses).

	Mode 1	Mode 2	Mode 3
M1			
u-component	96.51 (88.12)	2.33 (6.38)	0.47 (2.62)
v-component	95.43 (88.37)	2.80 (6.44)	0.72 (2.21)
M2			
u-component	93.53 (79.48)	3.24 (12.77)	1.81 (5.82)
v-component	95.58 (96.06)	2.52 (1.98)	0.86 (1.24)
M3			
u-component	84.67 (88.47)	10.36 (6.83)	3.23 (3.18)
v-component	87.66 (85.96)	8.09 (11.49)	2.85 (1.43)

The second mode, Mode 2, explained the second largest percentage of variance. In general, the amplitude crossed zero near 200 m depth and was nearly constant or gradually increasing with increasing depth. During deployment 1, the amplitude of Mode 2 at mooring M1 showed a mid-water maximum at 300 and 1000 m. The structure of this mode however, was more similar to the vertical structure found in Mode 3 at moorings M2 and M3. Further, the percentage of variance in the second and third modes increased from M1 to M3, indicating more variance in the higher order modes closer to the Loop Current. During the second deployment, Mode 2 at mooring M1 again resembled higher order modes at M2 and M3. However, the percentage of variance in modes 2 and greater was a maximum in the east-west velocity component of mooring M2 and was generally greater during deployment 2 than for deployment 1.

The vertical structure of Mode 3 was more complex, with two zero crossings typically in the upper 1000 m and relatively constant in water depths below 1000 m. The amount of variance contained in this mode was a small fraction of the current variance (< 4 %).

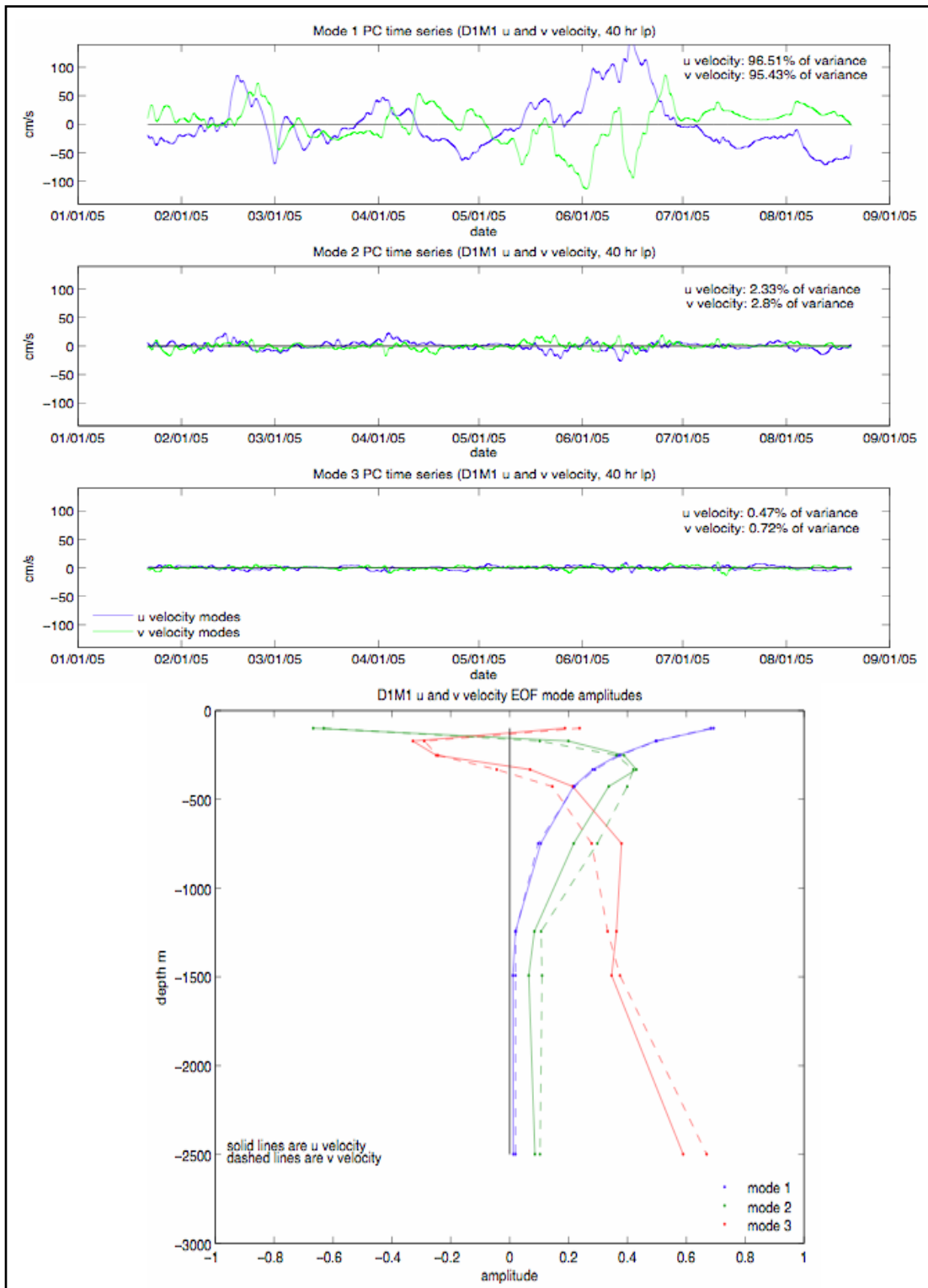


Figure 7.2-1. Vertical EOFs of east-west and north-south current velocity at mooring M1 during deployment 1. Top three panels: Principal component (PC) time series of first three empirical modes. Bottom panel: Amplitudes of empirical modes corresponding to PC time series.

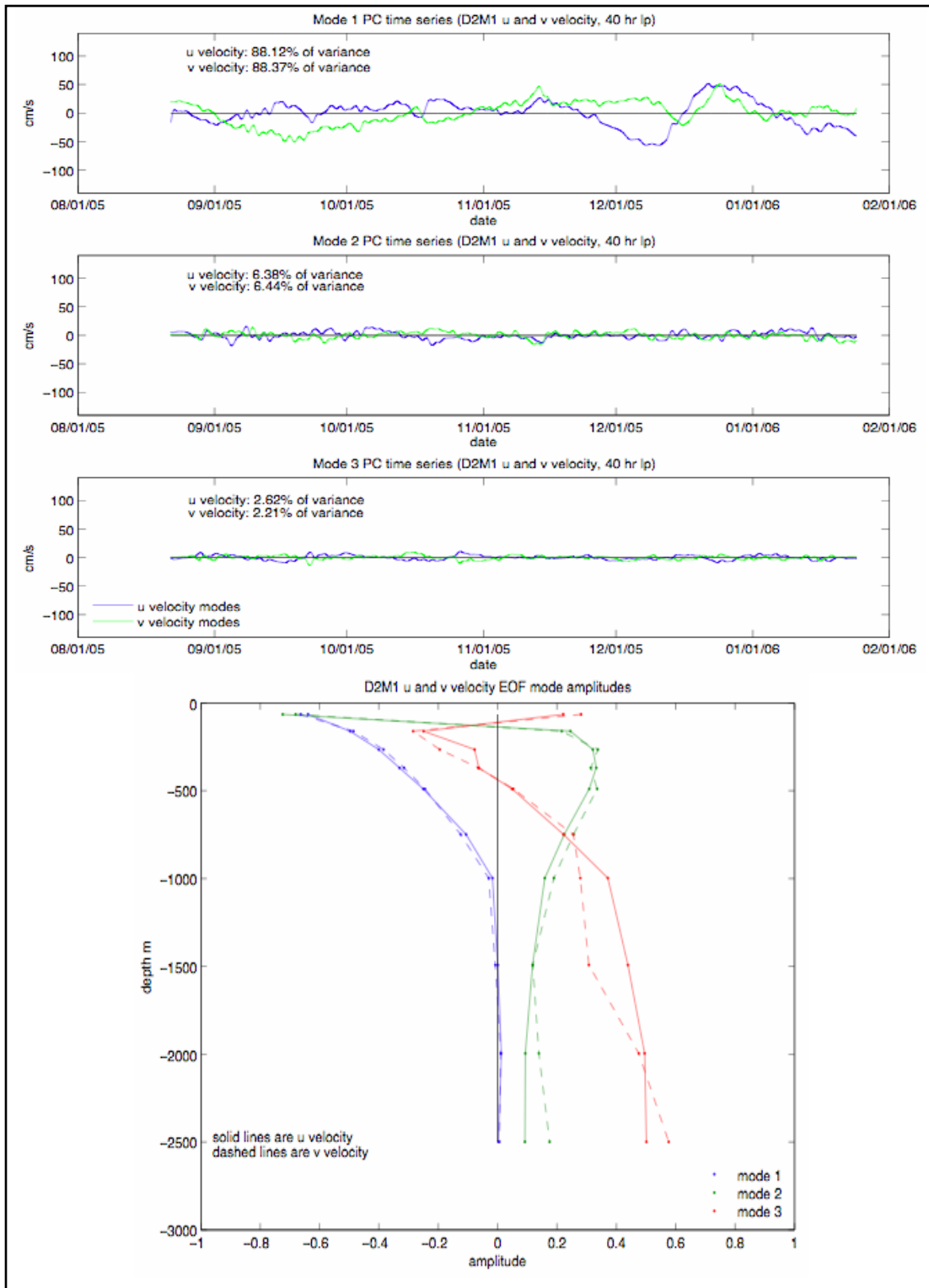


Figure 7.2-2. Vertical EOFs of east-west and north-south current velocity at mooring M1 during deployment 2. Top three panels: Principal component (PC) time series of first three empirical modes. Bottom panel: Amplitudes of empirical modes corresponding to PC time series.

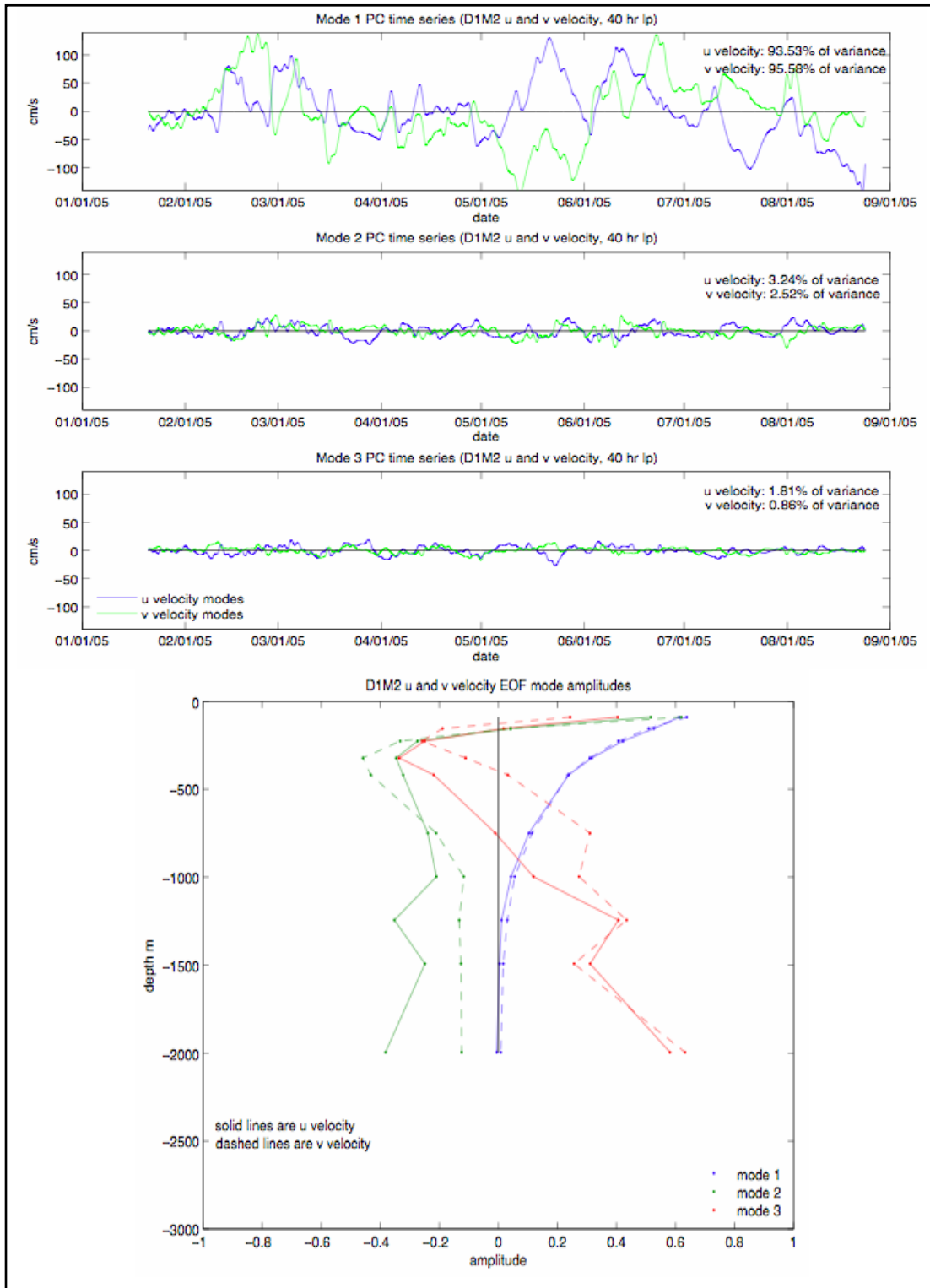


Figure 7.2-3. Vertical EOFs of east-west and north-south current velocity at mooring M2 during deployment 1. Top three panels: Principal component (PC) time series of first three empirical modes. Bottom panel: Amplitudes of empirical modes corresponding to PC time series.

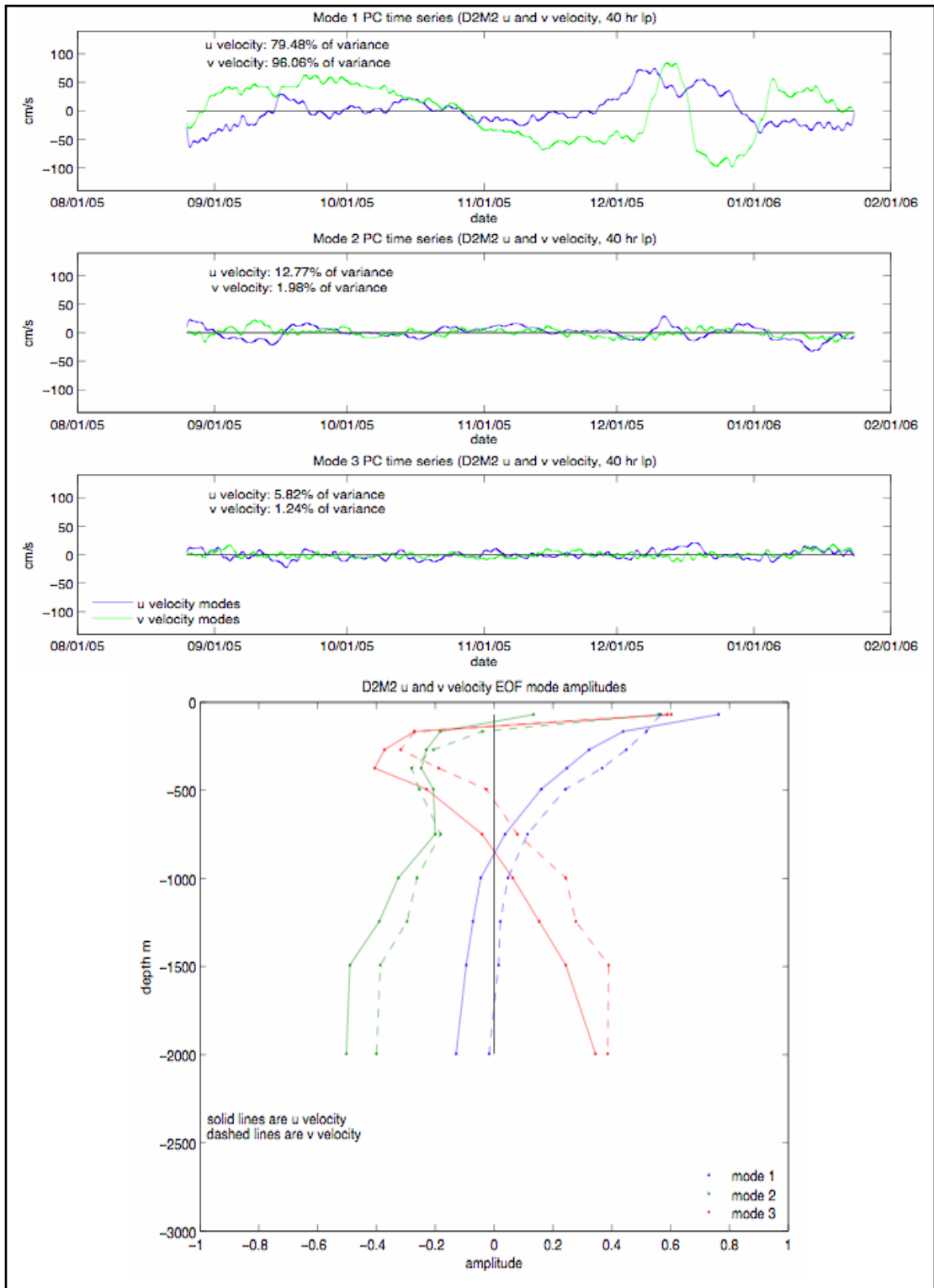


Figure 7.2-4. Vertical EOFs of east-west and north-south current velocity at mooring M2 during deployment 2. Top three panels: Principal component (PC) time series of first three empirical modes. Bottom panel: Amplitudes of empirical modes corresponding to PC time series.

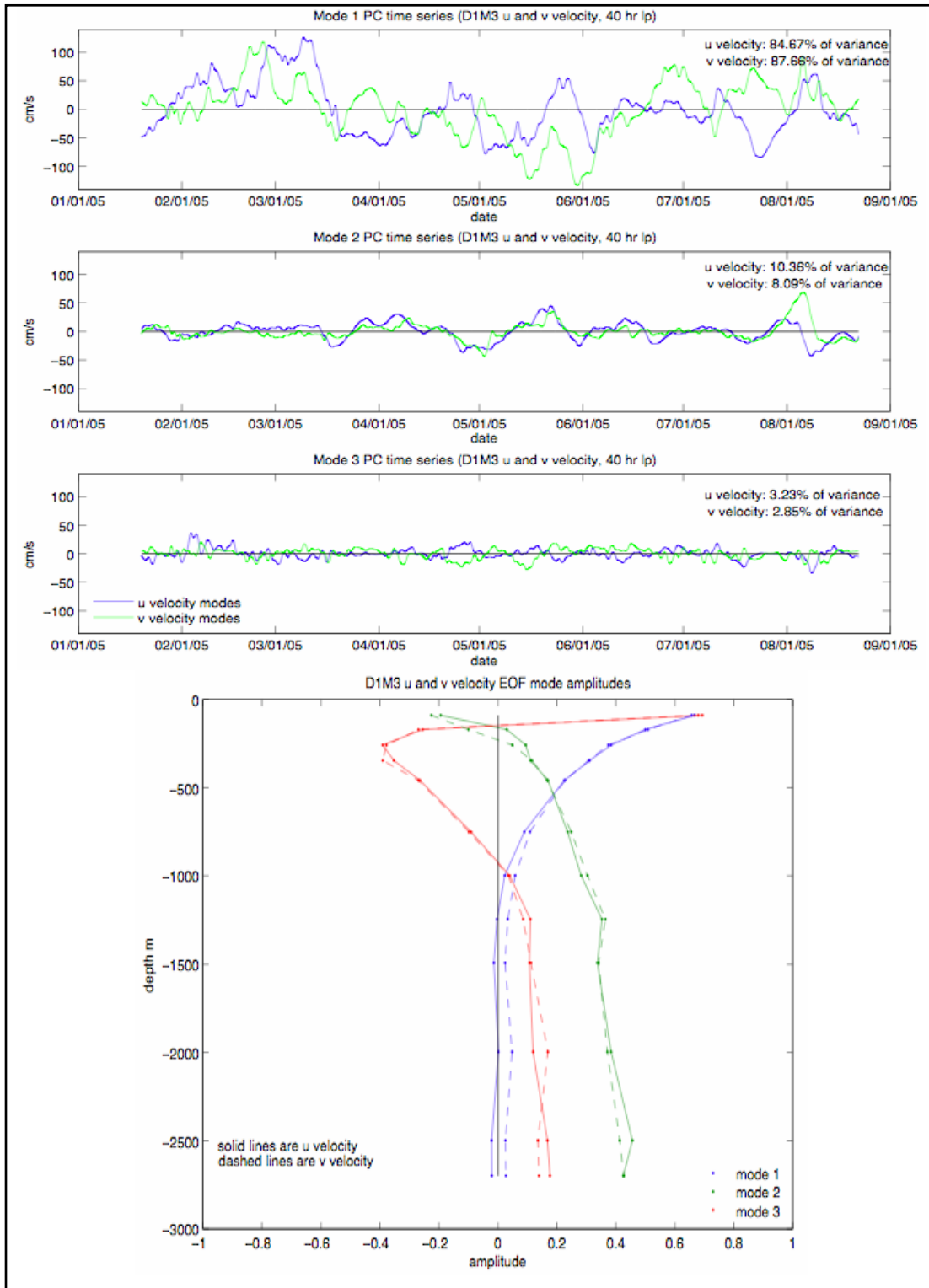


Figure 7.2-5. Vertical EOFs of east-west and north-south current velocity at mooring M3 during deployment 1. Top three panels: Principal component (PC) time series of first three empirical modes. Bottom panel: Amplitudes of empirical modes corresponding to PC time series.

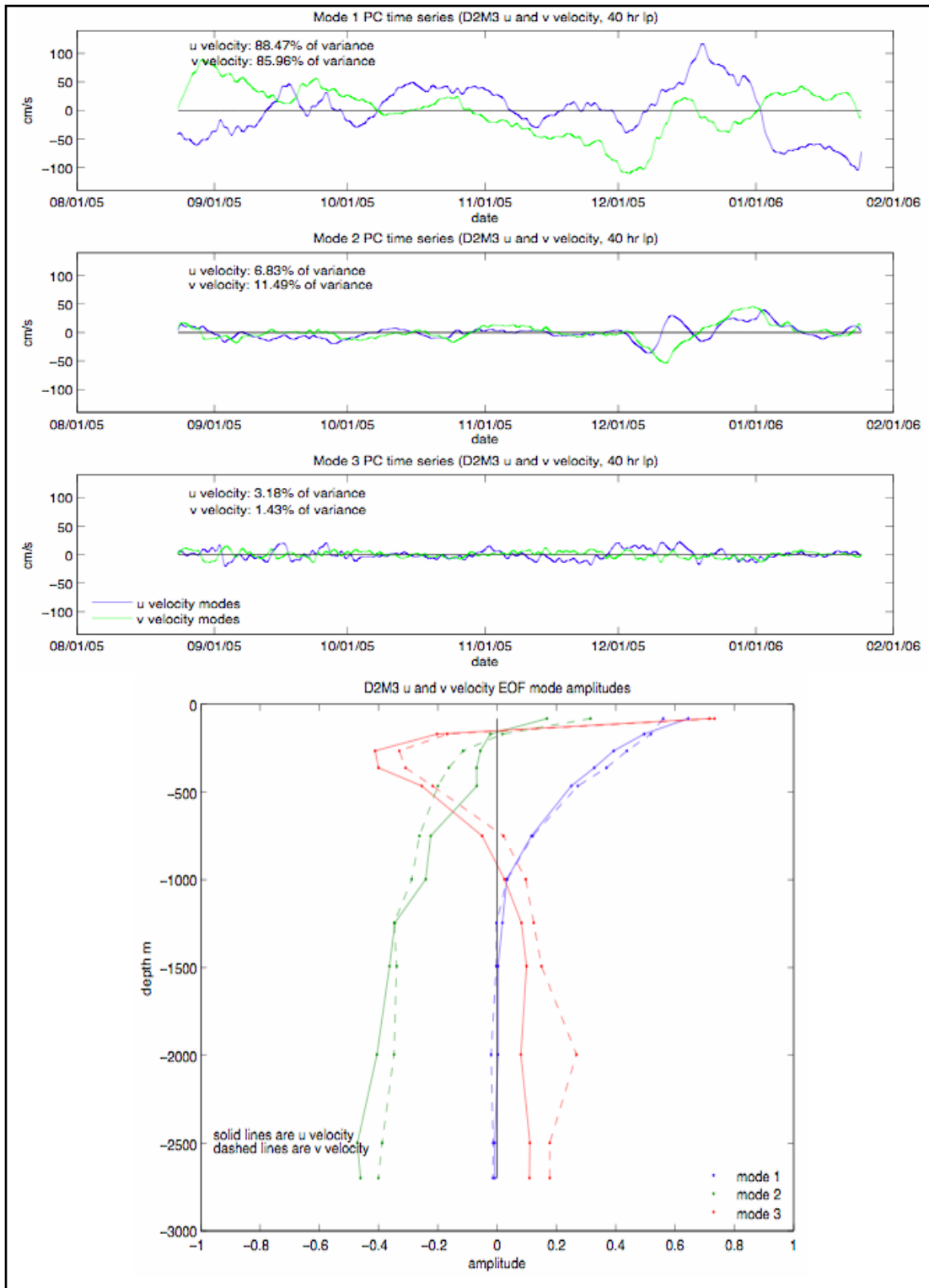


Figure 7.2-6. Vertical EOFs of east-west and north-south current velocity at mooring M3 during deployment 2. Top three panels: Principal component (PC) time series of first three empirical modes. Bottom panel: Amplitudes of empirical modes corresponding to PC time series.

7.2.1.2 Dynamical Mode Analysis

The estimation of dynamic modes was motivated by the desire to identify horizontally propagating wave solutions under the Boussinesq approximation for a rotating fluid (LeBlond and Mysak 1978). The method solves an eigenvalue equation for a prescribed stability profile, $N(z)$. The resulting vertical eigenfunctions are the allowable structures for that stability. “The eigenfunctions are real, orthogonal with real eigenvalues. The gravest mode is identified as the barotropic mode, and the modes $n=1,2,3,\dots$ are the sequence of baroclinic modes” (LeBlond and Mysak 1978). The calculations which follow presumed a flat ocean bottom.

Stability profiles were derived from temperature and salinity (CTD) data from hydrographic data collected adjacent to mooring sites M1, M2, and M3 during the Eastern GOM Study. The CTD data were used to calculate vertical buoyancy modes that represent the mean horizontal current structure at the three mooring locations. Note that the modes were calculated using a discretized version of the Taylor-Goldstein equation for a linear, flat-bottomed ocean (Klinck 1999). Temporal and spatial means were not removed from the CTD data prior to mode calculation. Although the theoretical modes are based on a resting ocean, neutral modes of an ocean with a surface-intensified mean flow are important for studies of baroclinic instability. The results should vary significantly when mean flow is included in the model, as the modes in this case become dependent on lateral scales of motion (Gill et al. 1974; Wunsch 1997). The density field in the upper 500 m is vital to the determination of mode structure (Wunsch 1997). Because hydrographic data was only available from three Eastern GOM Study cruises at two different times of the year in a region where the LC is constantly altering the density field, hydrographic cruise data evaluated in the MMS Deepwater Physical Oceanography Reanalysis and Synthesis of Historical Data Study (Nowlin et al. 2001) were also analyzed for comparison, and yielded similar results.

Figure 7.2-7 shows locations of the Eastern GOM Study mooring sites and the locations of historical casts that were averaged to create mean temperature and salinity profiles for the Eastern Gulf (east of 89° W). Figure 7.2-8 shows the temperature and salinity relationship in the waters of the eastern GOM, and clearly indicates water masses of Caribbean origin. Subtropical Under Water (SUW), is identified by salinity values greater than 36.5 at depths of ~ 200 m (sigma-theta between 25 and 26 kg/m^3), and is associated with the presence of the Loop Current and young warm core eddies in the study region. Vertical profiles of Brunt-Vaisala frequency, shown in Figure 7.2-9, were found to be a maximum between 100 - 200 m during the winter and near the surface (< 20 m depth) during the summer. Dynamic modes calculated from CTD casts at (or closest to) the mooring sites during deployment, maintenance, and recovery cruises were used to create an average set of modes to fit to the velocity data collected during mooring deployment.

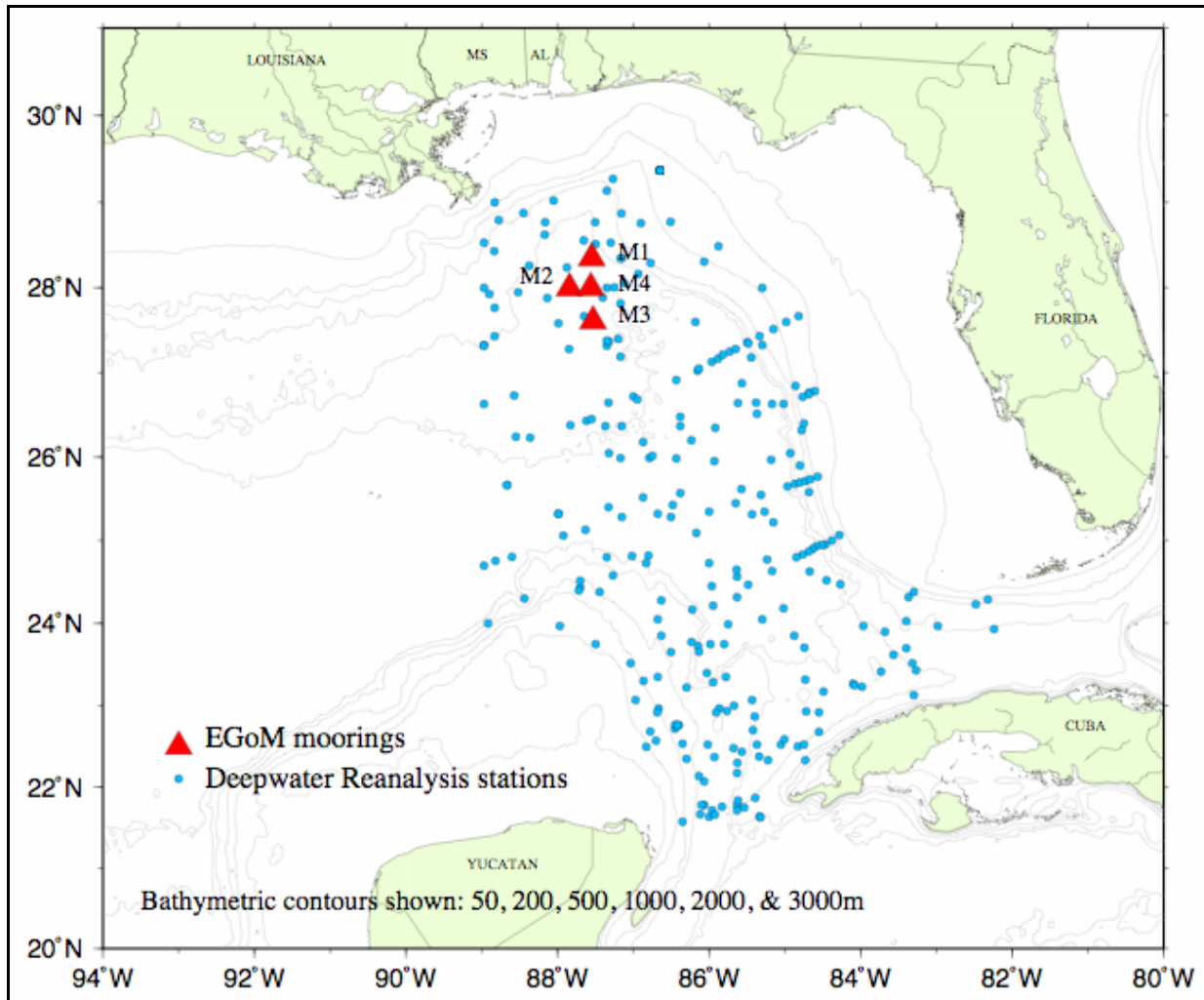


Figure 7.2-7. Location of BOEMRE Eastern Gulf of Mexico Circulation Study (EGOM) moorings and MMS Deepwater Physical Oceanography Reanalysis and Synthesis of Historical Data stations in the eastern Gulf of Mexico (east of 89° W) that were used to estimate dynamic modes.

Figures 7.2-10 – 7.2-15 give the normalized dynamic modes constructed from the casts at each mooring deployment. The barotropic mode was simply equal to one throughout the water column. First and second baroclinic modes had similar shapes at each mooring. The first mode crossed zero around 600 m; the second mode crossed zero twice, around 200 and 900 m. Below 1200 m all modes were barotropic, i.e., nearly constant with increasing depth. As can be seen, the general shape of these modes was the same for each deployment. The relative amplitudes were nearly identical; the principal difference between casts was the depth of zero-crossing of the modes.

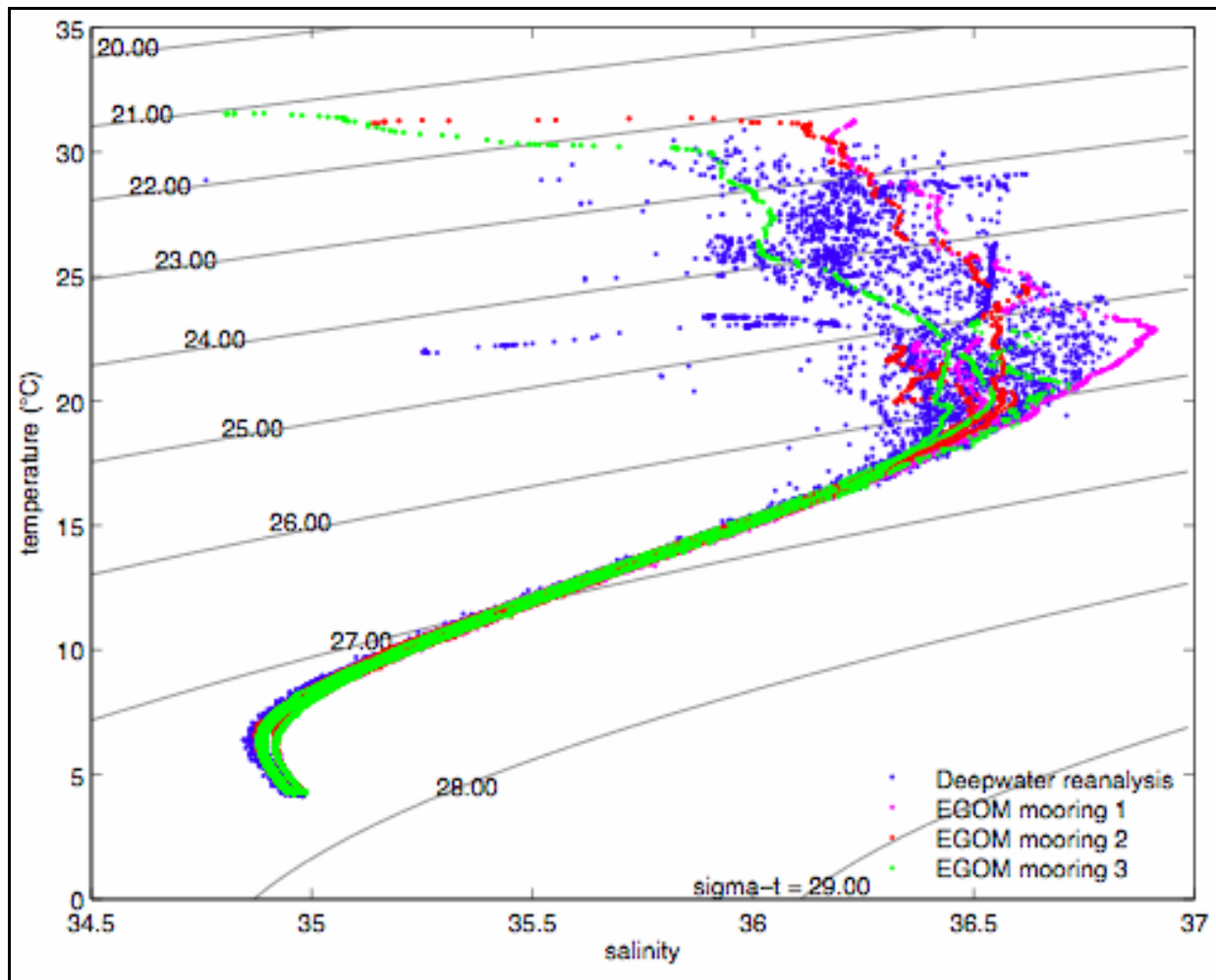


Figure 7.2-8. T-S plot of CTD, XBT, and Nansen/Niskin bottle data collected between 1915 and 2000 and analyzed in the MMS-funded Physical Oceanography Reanalysis and Synthesis of Historical Data Report (Nowlin et al. 2001) and CTD cast data from three EGOM cruises taken near each of the three EGOM mooring sites. Density as sigma-theta (kg m^{-3}) is also depicted on this plot.

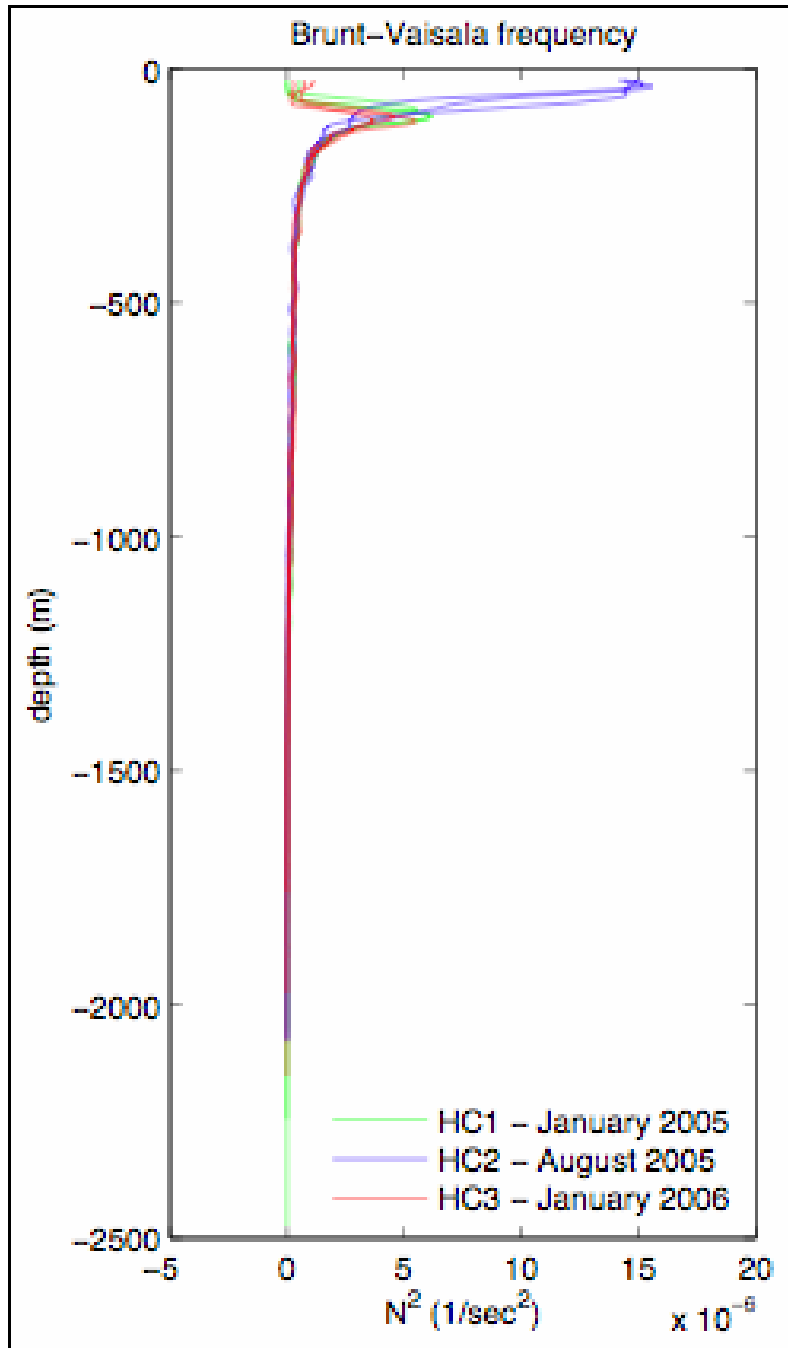


Figure 7.2-9. Vertical profiles of Brunt-Vaisala frequency at or nearest to each mooring site based on three EGOM hydrographic cruises in January 2005, August 2005, and January 2006.

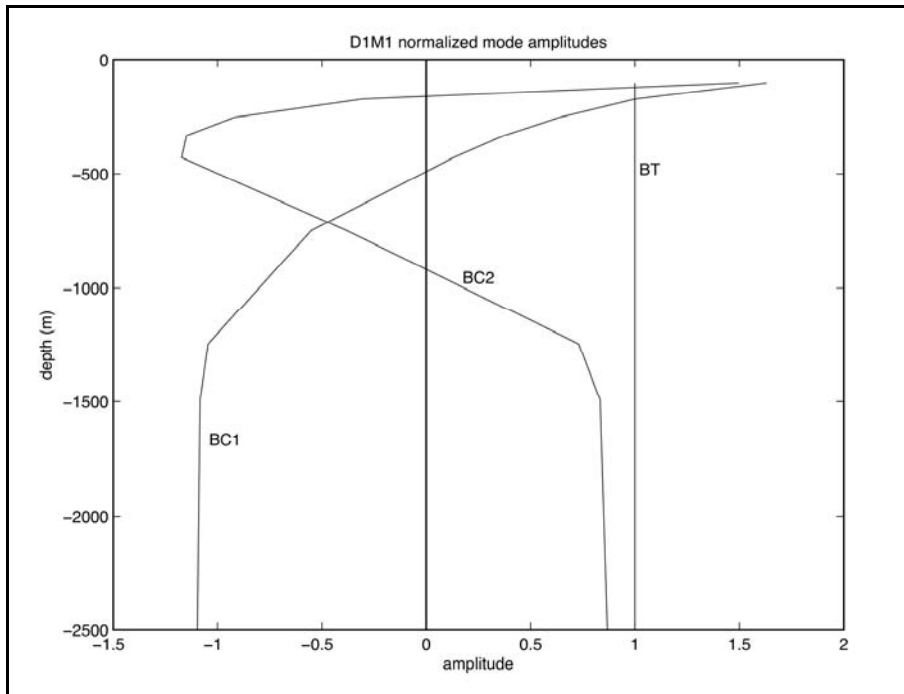


Figure 7.2-10. Normalized barotropic and first two baroclinic modes calculated with averaged casts at mooring M1 from cruises in January and August of 2005.

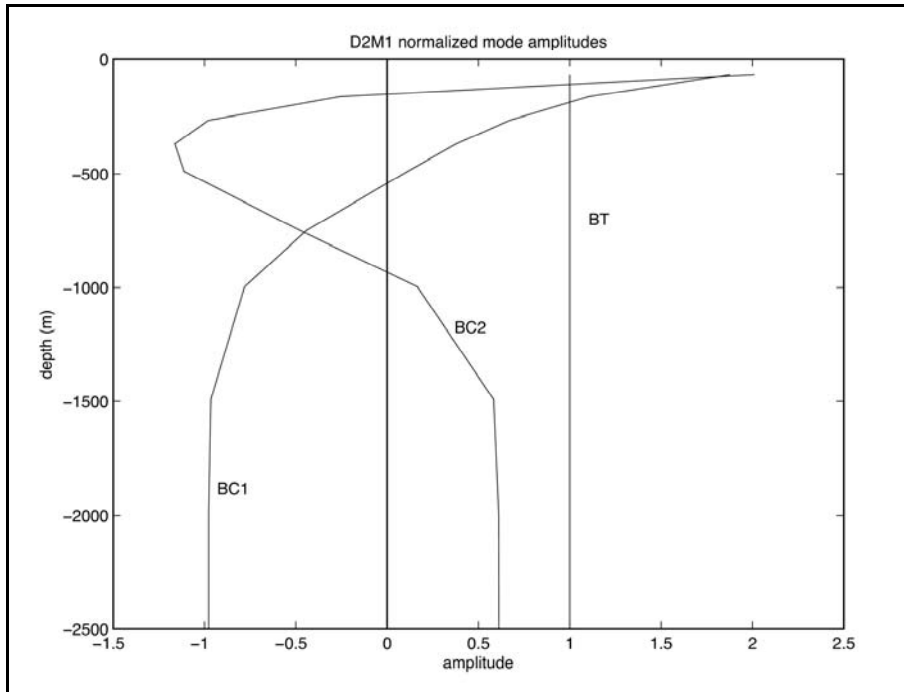


Figure 7.2-11. Normalized barotropic and first two baroclinic modes calculated with averaged casts at mooring M1 from cruises in August 2005 and January 2006.

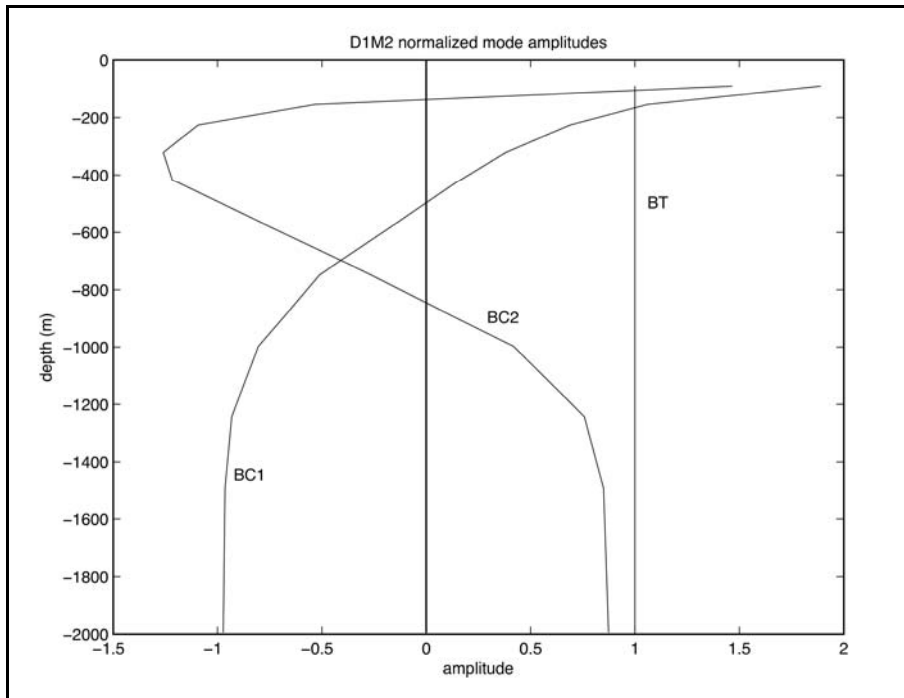


Figure 7.2-12. Normalized barotropic and first two baroclinic modes calculated with averaged casts at mooring M2 from cruises in January and August of 2005.

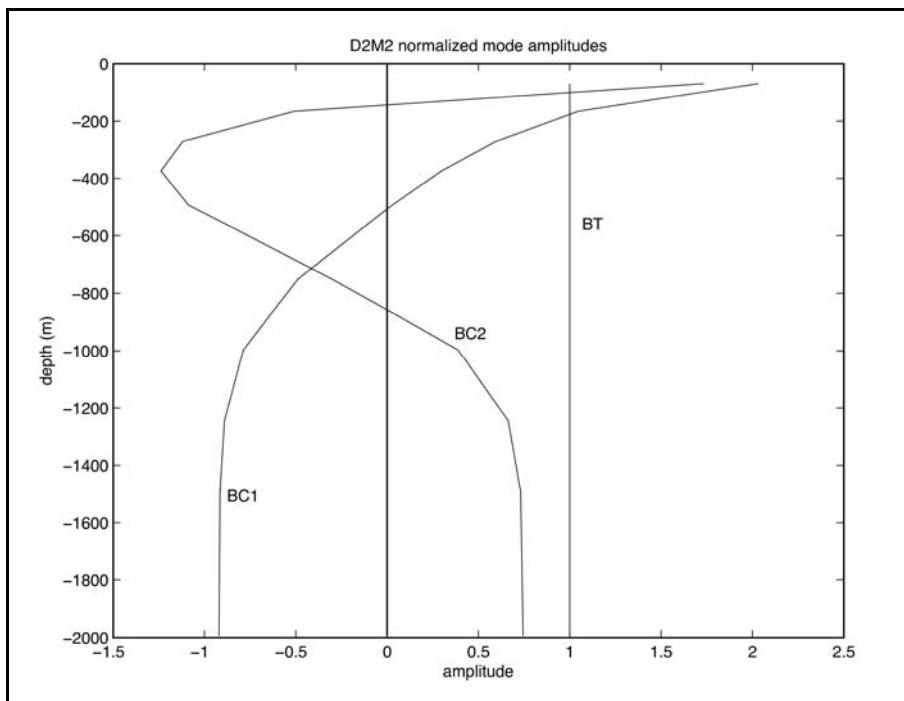


Figure 7.2-13. Normalized barotropic and first two baroclinic modes calculated with averaged casts at mooring M2 from cruises in August 2005 and January 2006.

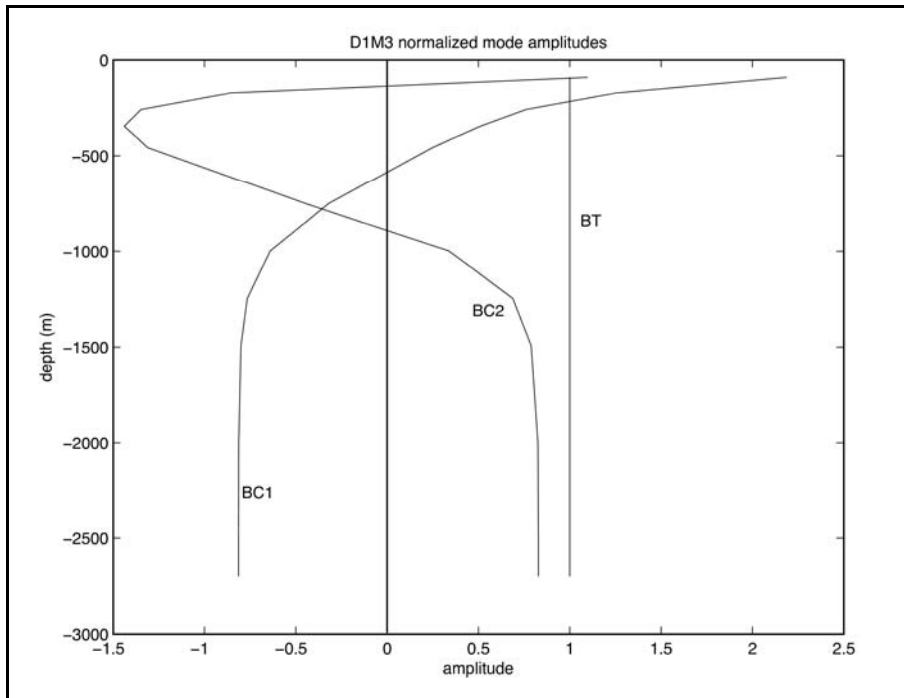


Figure 7.2-14. Normalized barotropic and first two baroclinic modes calculated with averaged casts at M3 from cruises in January and August of 2005.

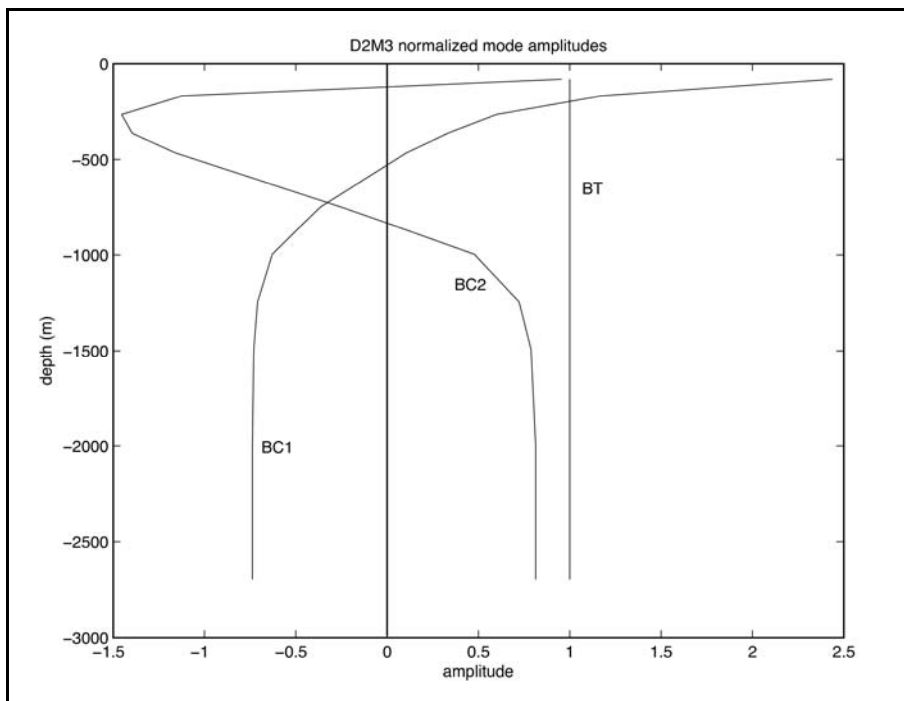


Figure 7.2-15. Normalized barotropic and first two baroclinic modes calculated with averaged casts at M3 from cruises in August 2005 and January 2006.

The temporal variation of the barotropic and first two baroclinic modes were estimated using a least squares minimization that fits the calculated set of vertical modes to synoptic vertical profiles of the moored ADCP and single-point current meter data. Three modes were used in the least squares fit. The modes were not normalized prior to the fitting. The sequence of Figures 7.2-16 – 7.2-27 shows a three-panel representation of the results of the least squares fit of the first three dynamic modes to the current profiles. Each figure corresponds to a single deployment, mooring, and velocity component. The top panel represents the spatial (vertical) correlation of the fit with the observed profile. Correlations of one indicated a perfect fit with no residual error, less than one indicated higher order ($n > 2$) modal variability. The bottom panel shows the time-series of the first three dynamic mode amplitudes resulting from the fitting procedure. The right panel shows the time correlation between the observed and modeled time series at a particular depth. This was an indication of the vertical structure of the goodness of fit. Generally, the barotropic time series amplitudes were significantly smaller than the baroclinic amplitudes at all moorings, both deployments, and both velocity components. As found previously in the EOF analysis, most of the variance in the observed velocity data can be explained by a surface trapped mode that decays exponentially with depth. Therefore, we expect that the temporal amplitudes of the first baroclinic mode to be large and to indicate the presence of surface trapped, i.e., eddy related, motions. The amplitudes of the second dynamic mode were more variable, i.e., possessed higher frequency motions, than the first baroclinic mode and were small relative to the amplitudes of the first baroclinic mode. During the first deployment, the east-west velocity amplitudes were mostly positive, i.e., eastward, because of the location of the mooring relative to the location of the northeastern edge of the LC. In general, mode amplitudes were greater during the first deployment, as more surface intensified, high-speed current eddy events were encountered in the spring and summer of 2005 than during the fall and winter of 2005–2006. The high correlation between mode 1 amplitudes and CTD pressure records, which fluctuated due to mooring draw down, were also validation of the first baroclinic mode amplitudes as indicators of eddy activity in the eastern GOM.

Spatial correlation at every sample time between observed and modeled velocity from the least squared fit of dynamic modes showed that when the first baroclinic mode amplitudes were close to zero, the correlation was poor. The low correlation could possibly indicate times of relative quiescence in the wake of eddies, that higher-order modes characterize the vertical structure.

Correlations in the time domain were determined between record length velocity data and modeled velocity at every current meter depth and five ADCP layer depths. The model fits well above 500 m, and below 500 m, the correlation decreased. In some cases, e.g., the fit to velocity components collected during the second deployment, the correlation was a minimum between 800 – 1000 m, and may be associated with the kinetic energy minimum at this level in the GOM.

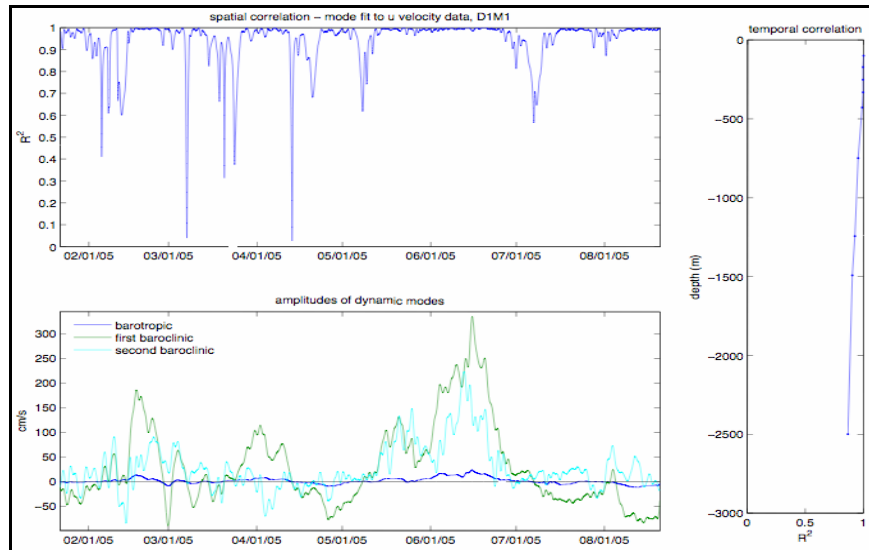


Figure 7.2-16. (Top) Spatial correlation between observed u velocity at mooring M1 from deployment 1 and the modeled u velocity from CTD cast data on the EGOM hydrographic cruises. (Bottom) Amplitudes of the first three theoretical modes based on the least squares regression. (Right) Temporal correlation between modeled and observed velocity.

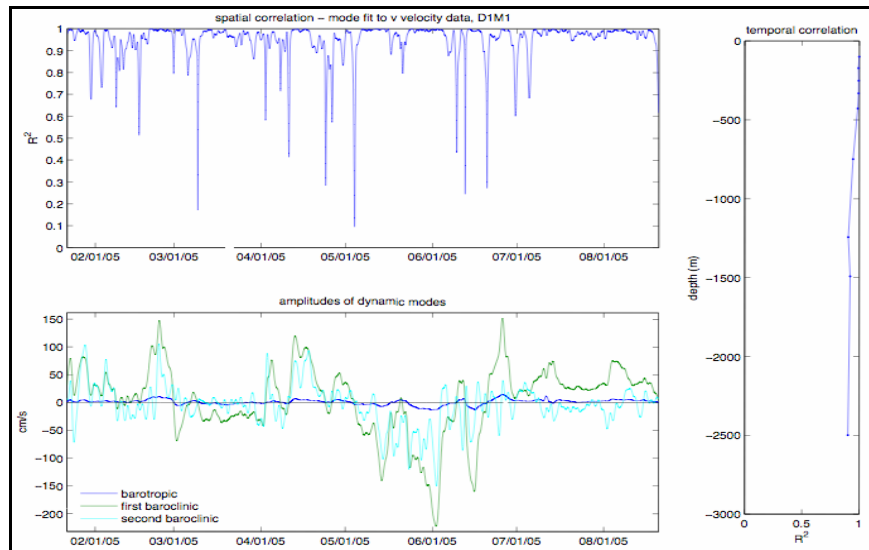


Figure 7.2-17. (Top) Spatial correlation between observed v velocity at mooring M1 from deployment 1 and the modeled v velocity from CTD cast data on the EGOM hydrographic cruises. (Bottom) Amplitudes of the first three theoretical modes based on the least squares regression. (Right) Temporal correlation between the modeled and observed velocity.

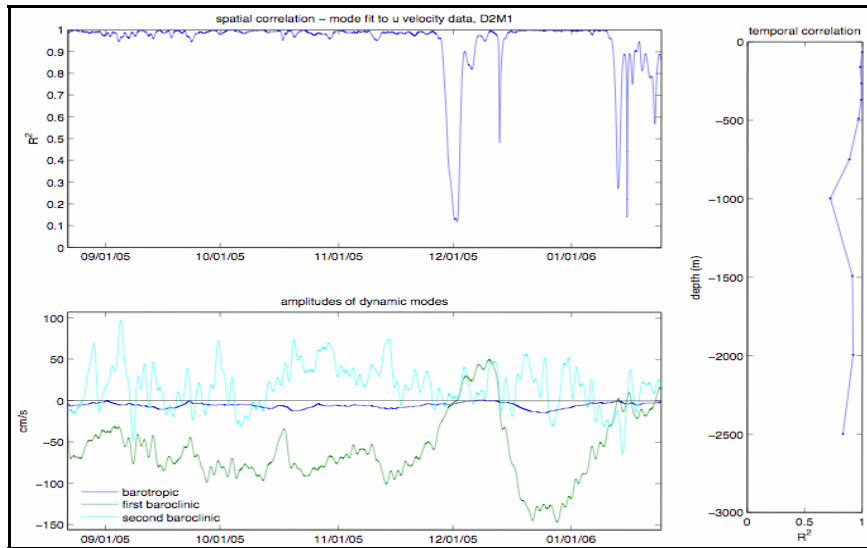


Figure 7.2-18. (Top) Spatial correlation between observed u velocity at mooring M1 from deployment 2 and the modeled u velocity from CTD cast data on the EGOM hydrographic cruises. (Bottom) Amplitudes of the first three theoretical modes based on the least squares regression. (Right) Temporal correlation between the modeled and observed velocity.

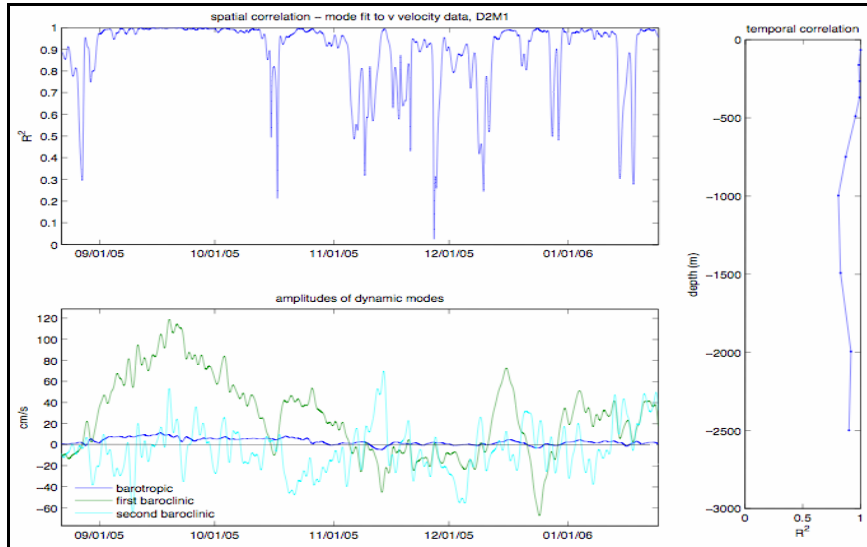


Figure 7.2-19. (Top) Spatial correlation between observed v velocity at mooring M1 from deployment 2 and the modeled v velocity from CTD cast data on the EGOM hydrographic cruises. (Bottom) Amplitudes of the first three theoretical modes based on the least squares regression. (Right) Temporal correlation between the modeled and observed velocity.

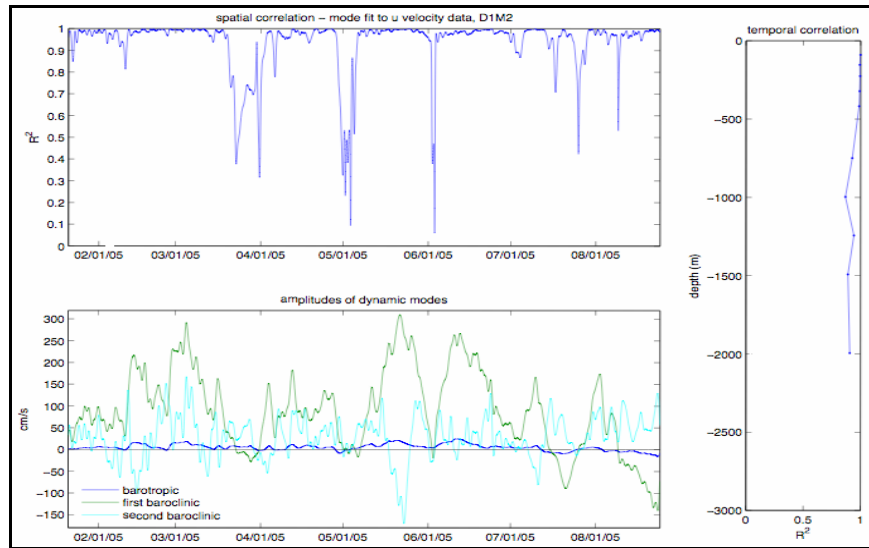


Figure 7.2-20. (Top) Spatial correlation between observed u velocity at mooring M2 from deployment 1 and the modeled u velocity from CTD cast data on the EGOM hydrographic cruises. (Bottom) Amplitudes of the first three theoretical modes based on the least squares regression. (Right) Temporal correlation between the modeled and observed velocity.

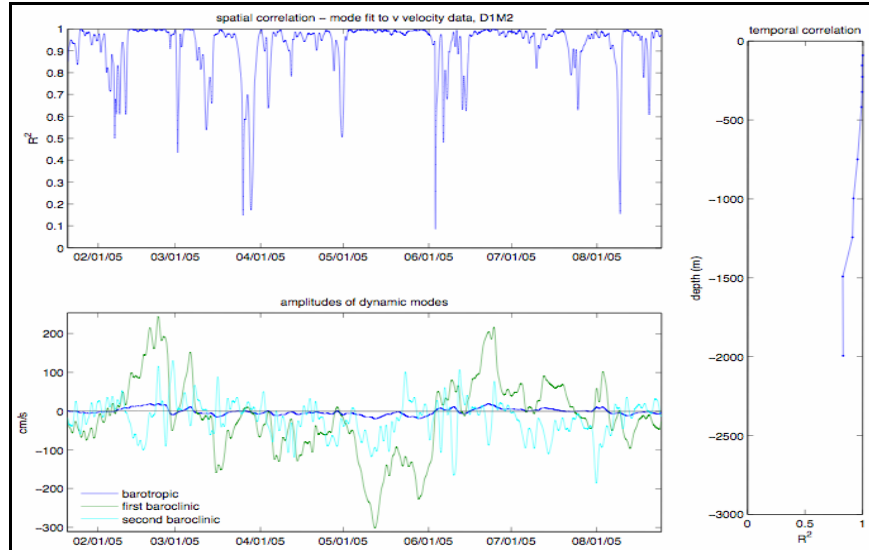


Figure 7.2-21. (Top) Spatial correlation between observed v velocity at mooring M2 from deployment 1 and the modeled v velocity from CTD cast data on the EGOM hydrographic cruises. (Bottom) Amplitudes of the first three theoretical modes based on the least squares regression. (Right) Temporal correlation between the modeled and observed velocity.

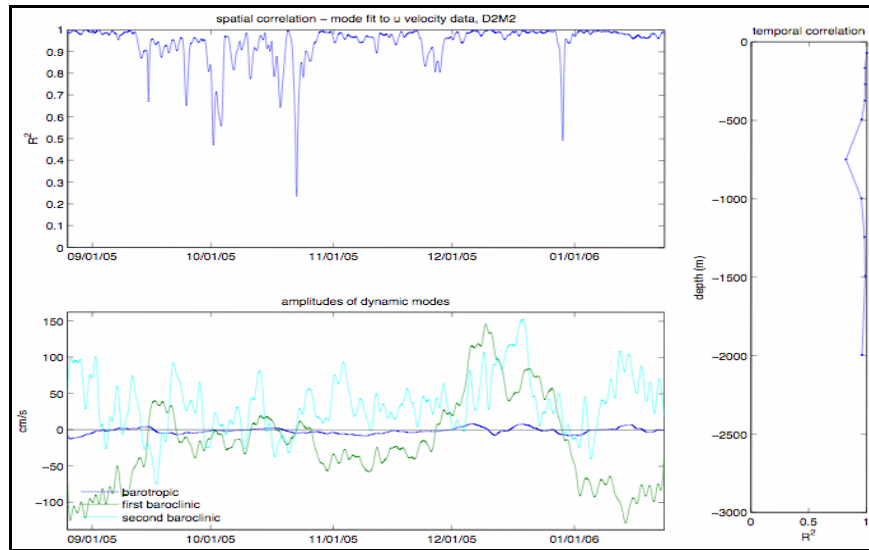


Figure 7.2-22. (Top) Spatial correlation between observed u velocity at mooring M2 from deployment 2 and the modeled u velocity from CTD cast data on the EGOM hydrographic cruises. (Bottom) Amplitudes of the first three theoretical modes based on the least squares regression. (Right) Temporal correlation between the modeled and observed velocity.

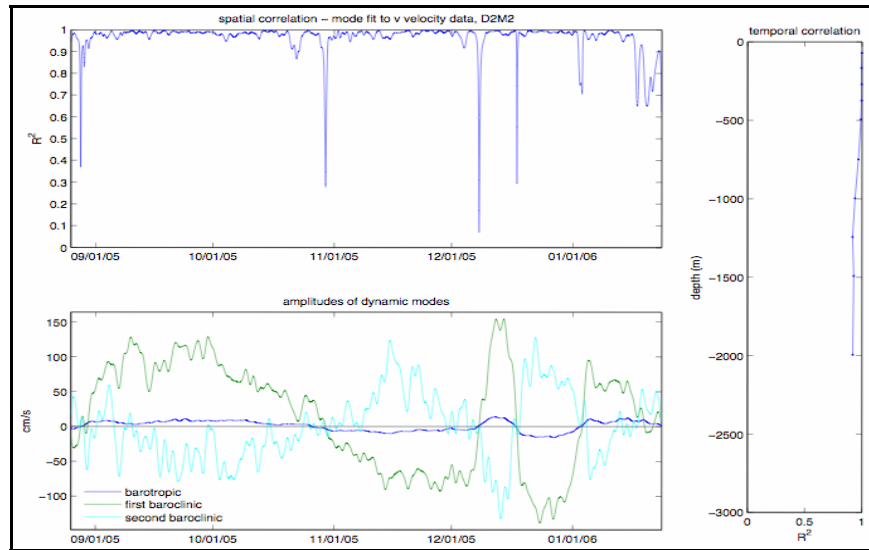


Figure 7.2-23. (Top) Spatial correlation between observed v velocity at mooring M2 from deployment 2 and the modeled v velocity from CTD cast data on the EGOM hydrographic cruises. (Bottom) Amplitudes of the first three theoretical modes based on the least squares regression. (Right) Temporal correlation between the modeled and observed velocity.

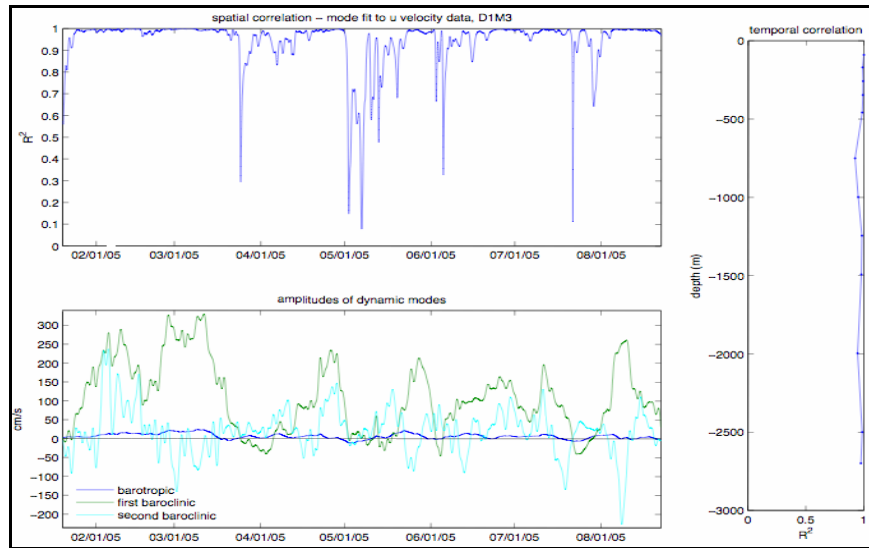


Figure 7.2-24. (Top) Spatial correlation between observed u velocity at mooring M3 from deployment 1 and the modeled u velocity from CTD cast data on the EGOM hydrographic cruises. (Bottom) Amplitudes of the first three theoretical modes based on the least squares regression. (Right) Temporal correlation between the modeled and observed velocity.

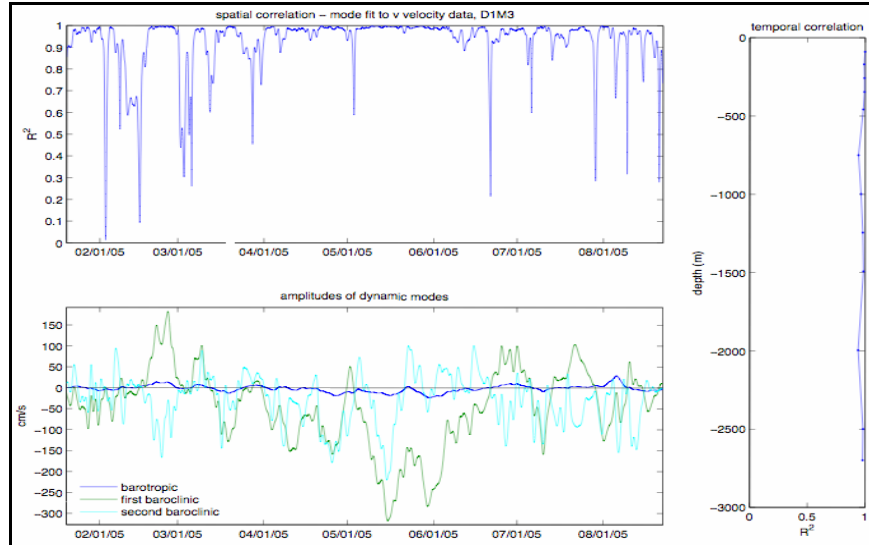


Figure 7.2-25. (Top) Spatial correlation between observed v velocity at mooring M3 from deployment 1 and the modeled v velocity from CTD cast data on the EGOM hydrographic cruises. (Bottom) Amplitudes of the first three theoretical modes based on the least squares regression. (Right) Temporal correlation between the modeled and observed velocity.

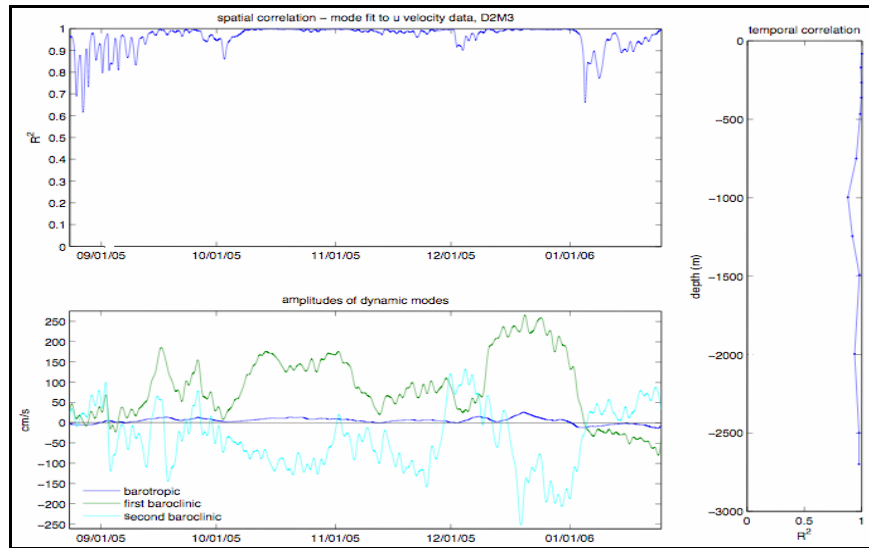


Figure 7.2-26. (Top) Spatial correlation between observed u velocity at mooring M3 from deployment 2 and the modeled u velocity from CTD cast data on the EGOM hydrographic cruises. (Bottom) Amplitudes of the first three theoretical modes based on the least squares regression. (Right) Temporal correlation between the modeled and observed velocity.

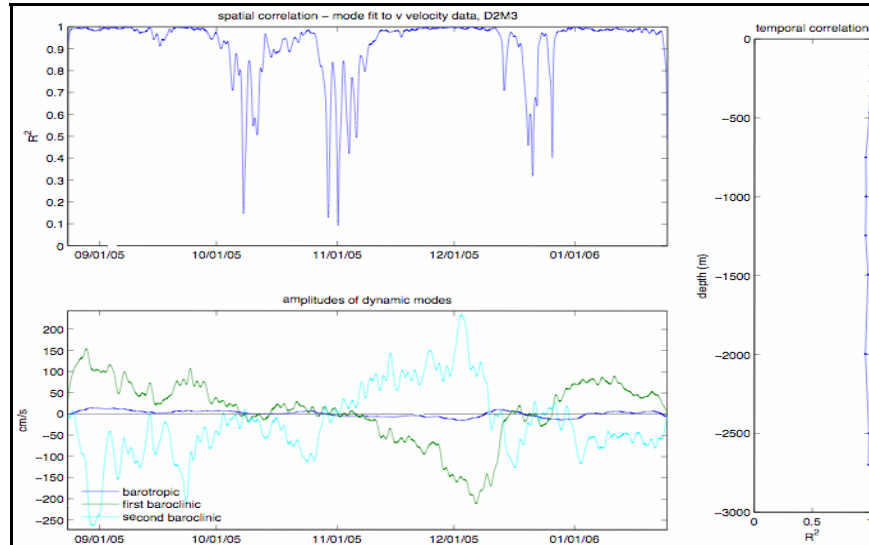


Figure 7.2-27. (Top) Spatial correlation between observed v velocity at mooring M3 from deployment 2 and the modeled v velocity from CTD cast data on the EGOM hydrographic cruises. (Bottom) Amplitudes of the first three theoretical modes based on the least squares regression. (Right) Temporal correlation between the modeled and observed velocity.

7.2.1.3 Model Utility Test for Dynamic Modes

Two types of model utility tests were performed on the modal fit to the observed currents in the space domain. The first test utilized the F statistic to assess whether a useful relationship between the observed data and any of the modal predictors existed. The null hypothesis for this test was that the coefficient of all modes included in the model equals zero was to be rejected if the test statistic, which is a function of the degrees of freedom, the number of modes included in the fit, and spatial correlation, is greater than or equal to the F critical value found in an F distribution table, determined by the degrees of freedom, the number of modes included in the fit, and the significance level, α . For these data, the significance level of $\alpha = 0.05$ was chosen. The goodness of fit test confirmed that the barotropic and at least one of the baroclinic modes are necessary to the regression approximately 80 – 90 % of the time.

The second statistical test is an inference for a single mode coefficient, which determines if a certain mode needs to be included in the fit. This test is a two-tailed test using the t statistic to reject or accept the null hypothesis that the targeted mode coefficient is equal to zero, i.e., it is not necessary in the multiple regression. The null hypothesis is rejected if the test statistic, calculated from the amplitude of the mode, the error sum of squares, and the error degrees of freedom, falls outside of the rejection region determined by the critical values, which are given in a t table, determined by the degrees of freedom and the significance level α . This test indicated that the first baroclinic mode was the only mode necessary to explain the current structure at moorings M1, M2, and M3 during most of their deployment; however, the second baroclinic mode was necessary to the fit of velocity data during portions of the deployments, and particularly to the data collected at mooring M3 during periods within its second deployment.

7.2.1.3.1 *Temporal Correlation of First Baroclinic Mode and Sea Surface Height Gradient*

This section investigates potential causes of the observed current structure. Since geostrophic current velocity should be perpendicular to the sea surface height gradient we expected a relationship between the sea surface height gradient and the first baroclinic mode. We calculated the time series of sea surface height gradient in the north-south and east-west directions in the vicinity of each mooring and correlated that with the time series of the first baroclinic mode for the perpendicularly oriented velocity component. In general, a significantly large correlation was found between the orthogonal SSH gradient and the first baroclinic mode amplitudes. East-west velocity mode 1 amplitudes were compared to the sea surface height gradient in the north-south direction (even numbered Figures 7.2-28 – 7.2-50), and the north-south velocity mode 1 amplitudes were compared to sea surface height gradient in the east-west direction (odd numbered Figures 7.2-29 – 7.2-51). The coherency spectra showed that the coherency was significant only at low frequencies, thus reinforcing that mode 1 amplitudes are related to the pressure gradient, indicating geostrophic currents.

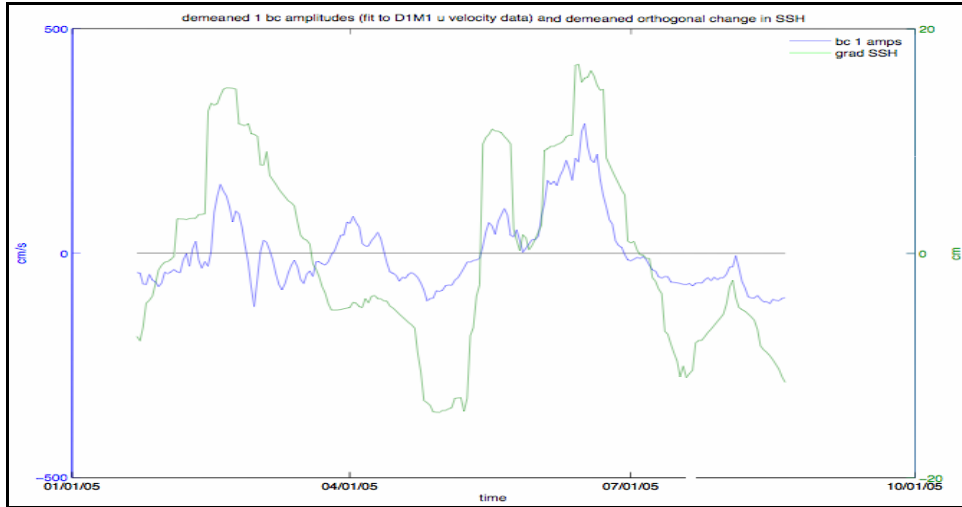


Figure 7.2-28. Temporal amplitudes of first baroclinic (bc) mode of the east-west velocity at M1 during deployment 1 (blue) and the SSH gradient in the north-south direction (green).

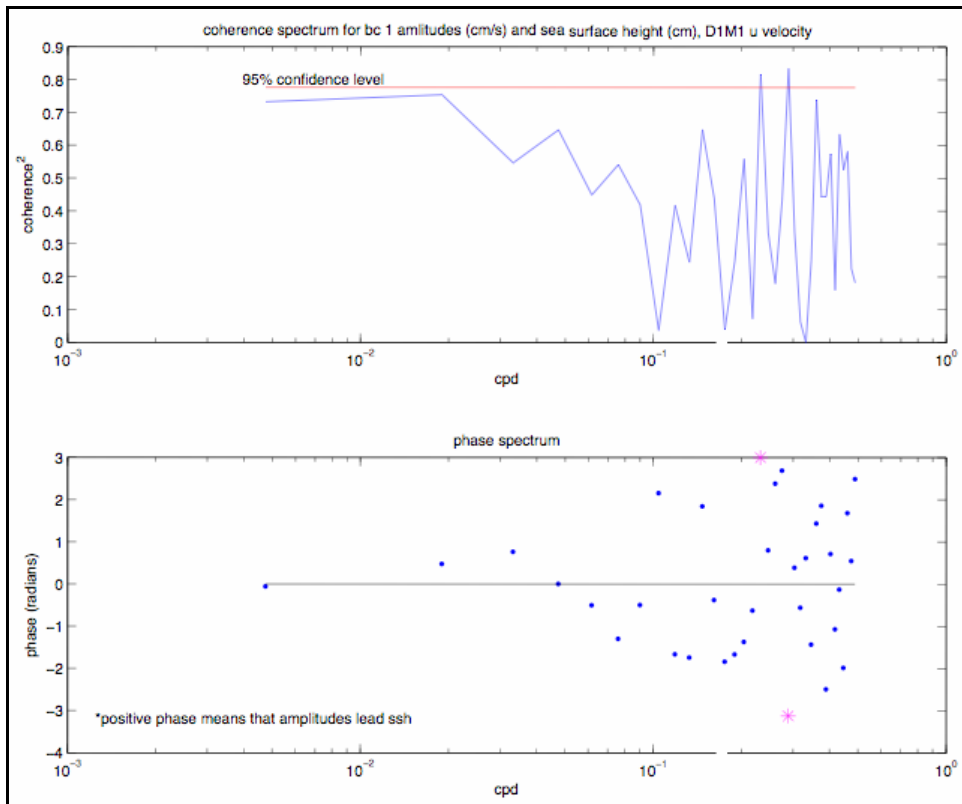


Figure 7.2-29. Coherency (top) and phase (bottom) spectra of the temporal amplitudes of the first baroclinic mode for the east-west velocity at M1 during deployment 1 and the SSH gradient in the north-south direction.

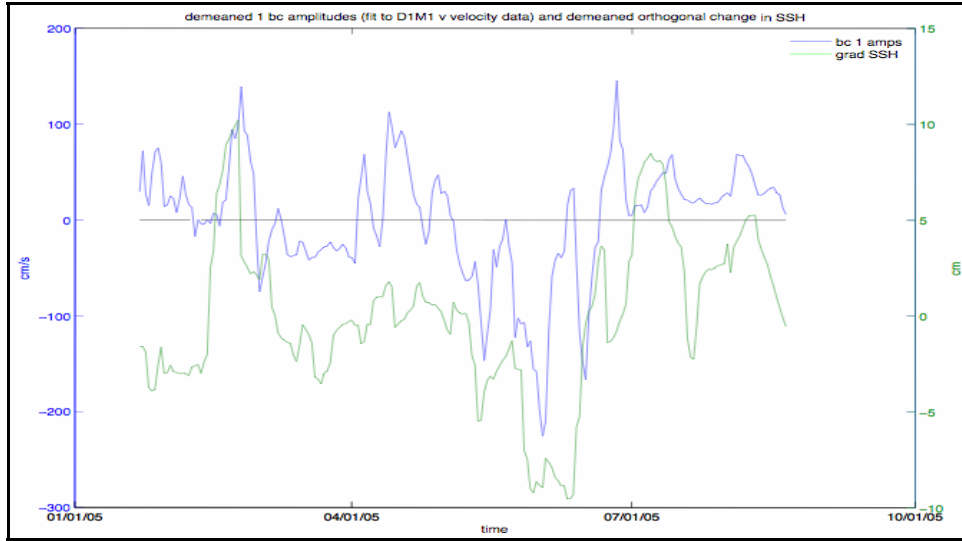


Figure 7.2-30. Temporal amplitudes of first baroclinic mode of the north-south velocity at mooring M1 during deployment 1 (blue) and the SSH gradient in the east-west direction (green).

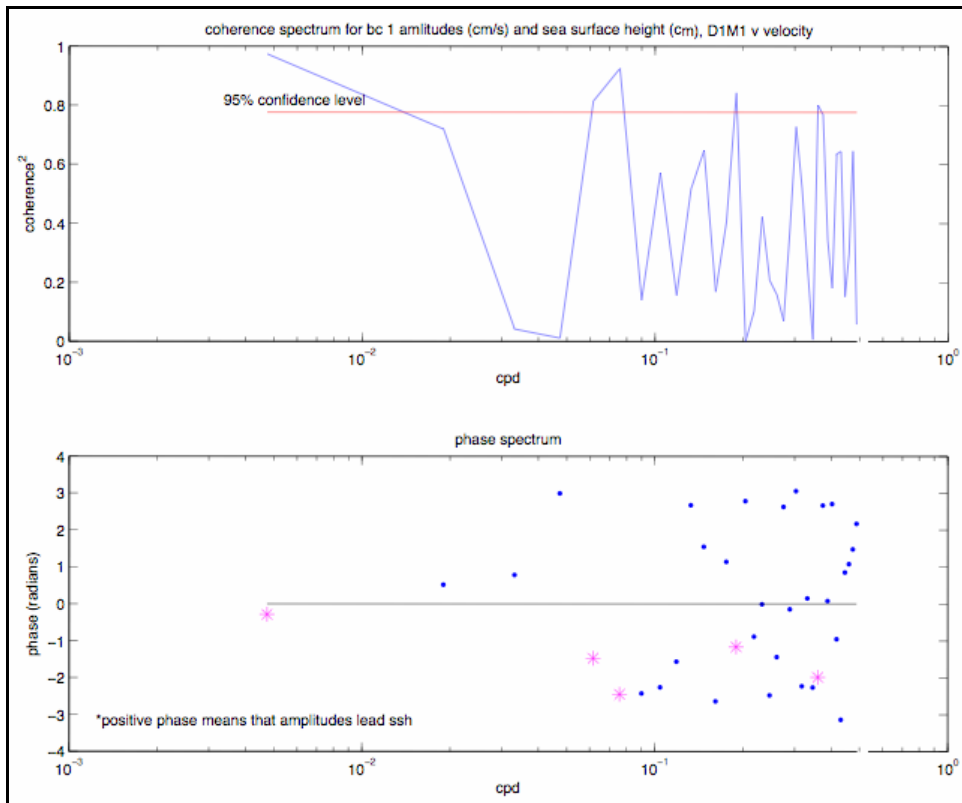


Figure 7.2-31. Coherency (top) and phase (bottom) spectra of the temporal amplitudes of the first baroclinic mode for the north-south velocity component at mooring M1 during deployment 1 and the SSH gradient in the east-west direction.

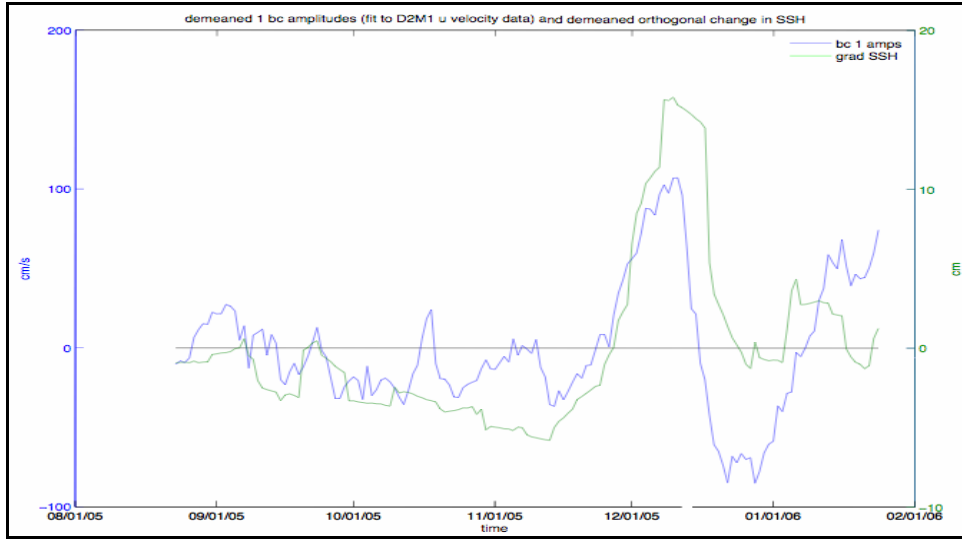


Figure 7.2-32. Temporal amplitudes of first baroclinic mode of the east-west velocity at mooring M1 during deployment 2 (blue) and the SSH gradient in the north-south direction (green).

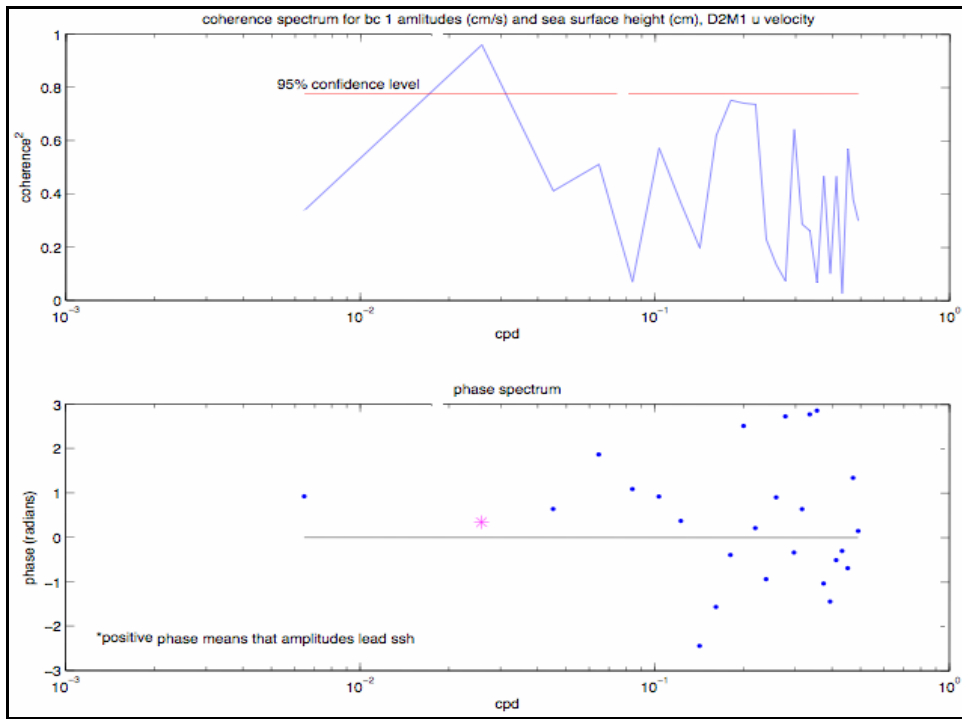


Figure 7.2-33. Coherency (top) and phase (bottom) spectra of the temporal amplitudes of the first baroclinic mode for the east-west velocity component at mooring M1 during deployment 2 and the SSH gradient in the north-south direction.

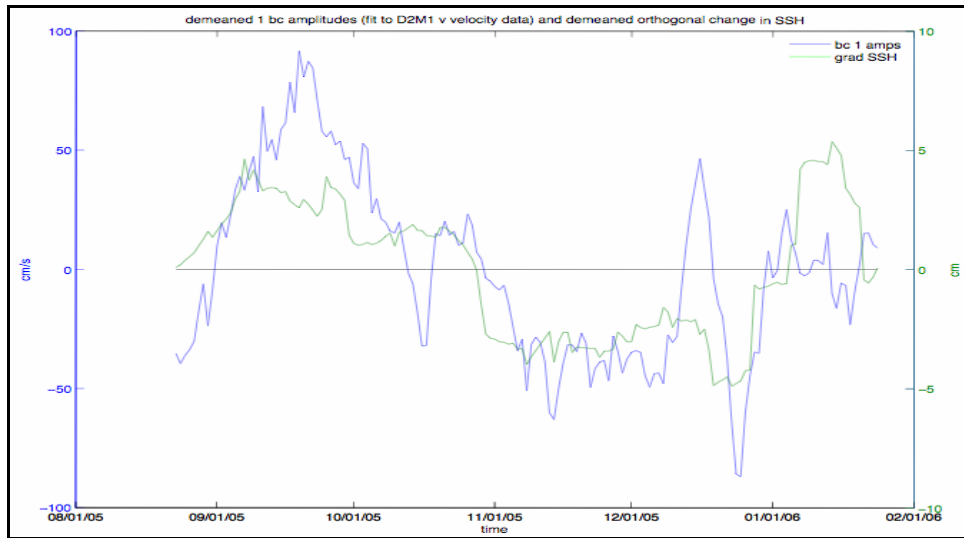


Figure 7.2-34. Temporal amplitudes of first baroclinic mode of the north-south velocity at mooring M1 during deployment 2 (blue) and the SSH gradient in the east-west direction (green).

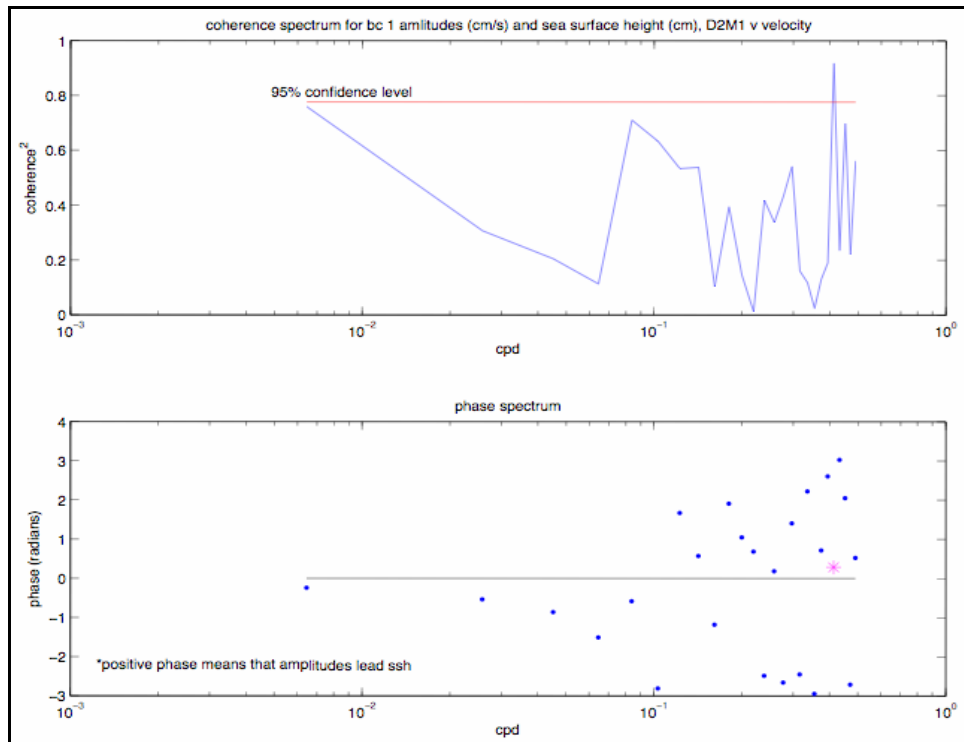


Figure 7.2-35. Coherency (top) and phase (bottom) spectra of the temporal amplitudes of the north-south velocity first baroclinic mode at M1 during deployment 2 and the SSH gradient in the east-west direction.

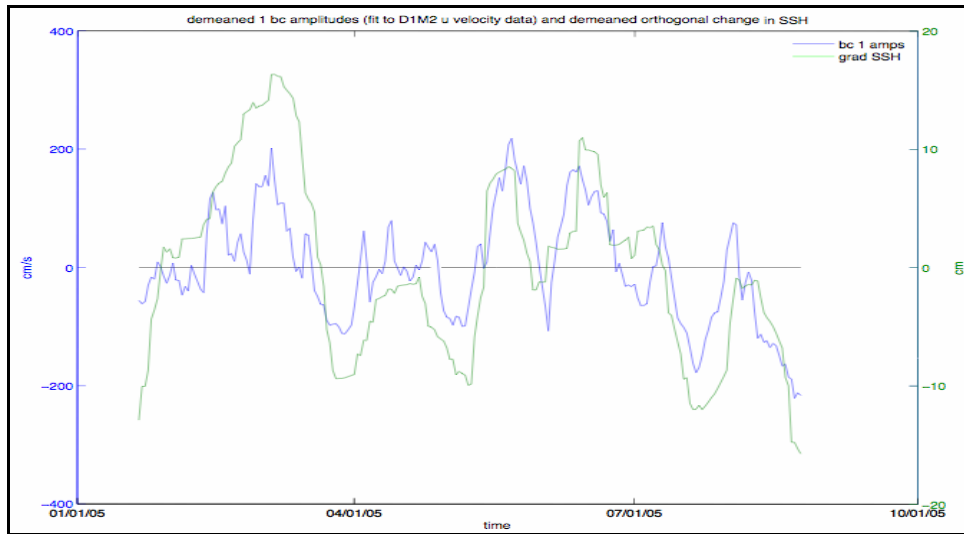


Figure 7.2-36. Temporal amplitudes of first baroclinic for the east-west velocity mode at mooring M2 during deployment 1 (blue) and the SSH gradient in the north-south direction (green).

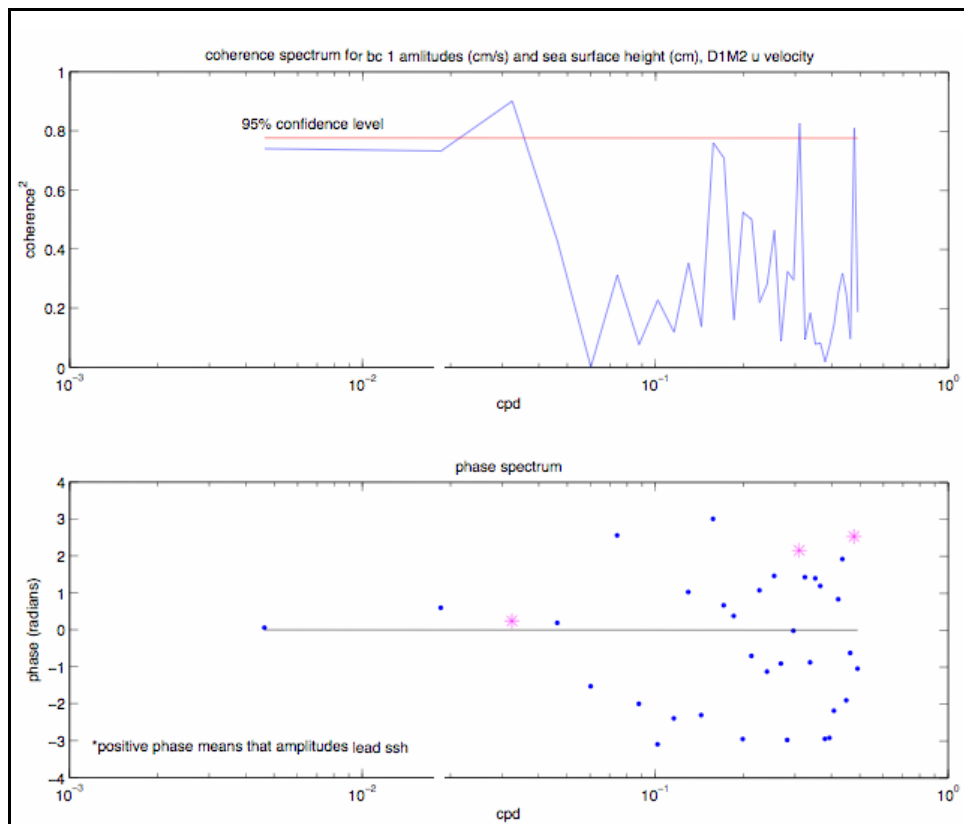


Figure 7.2-37. Coherency (top) and phase (bottom) spectra of the temporal amplitudes of the first baroclinic mode of the east-west velocity component at mooring M2 during deployment 1 and the SSH gradient in the north-south direction.

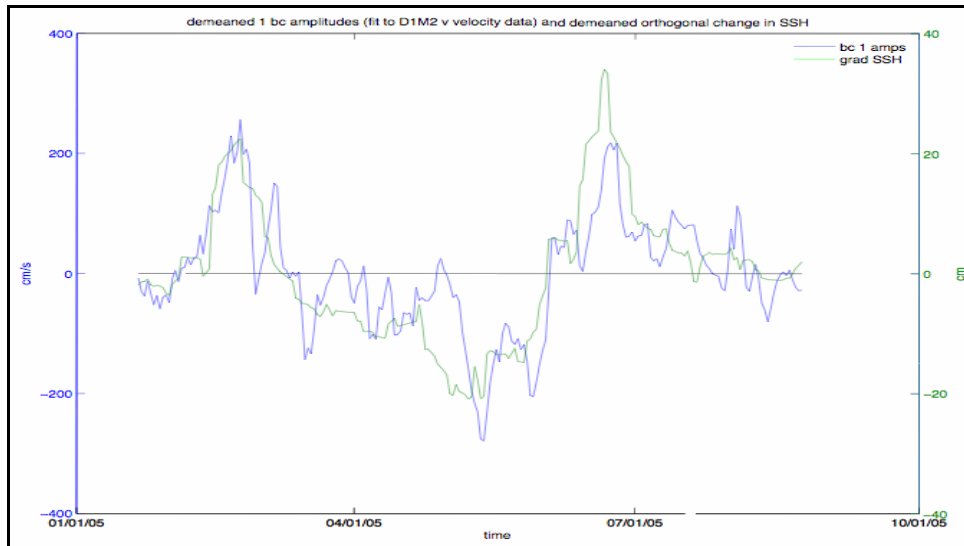


Figure 7.2-38. Temporal amplitudes of first baroclinic mode of the north-south velocity at mooring M2 during deployment 1 (blue) and the SSH gradient in the east-west direction (green).

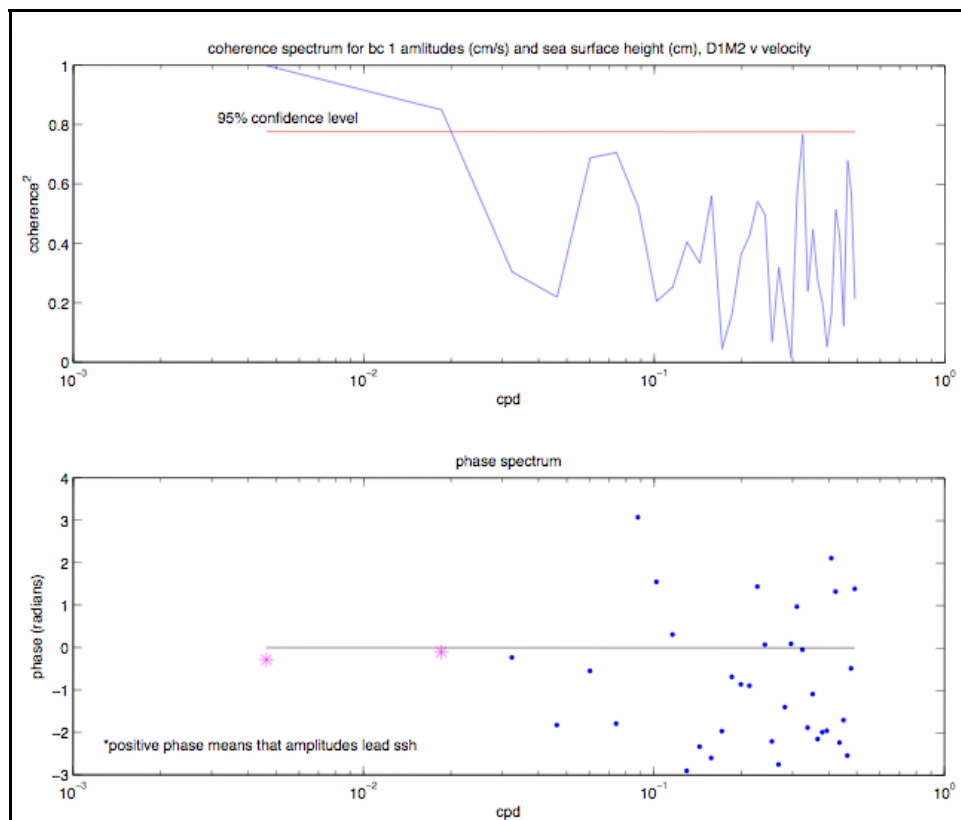


Figure 7.2-39. Coherency (top) and phase (bottom) spectra of the temporal amplitudes of the first baroclinic mode for the north-south velocity component at mooring M2 during deployment 1 and the SSH gradient in the east-west direction.

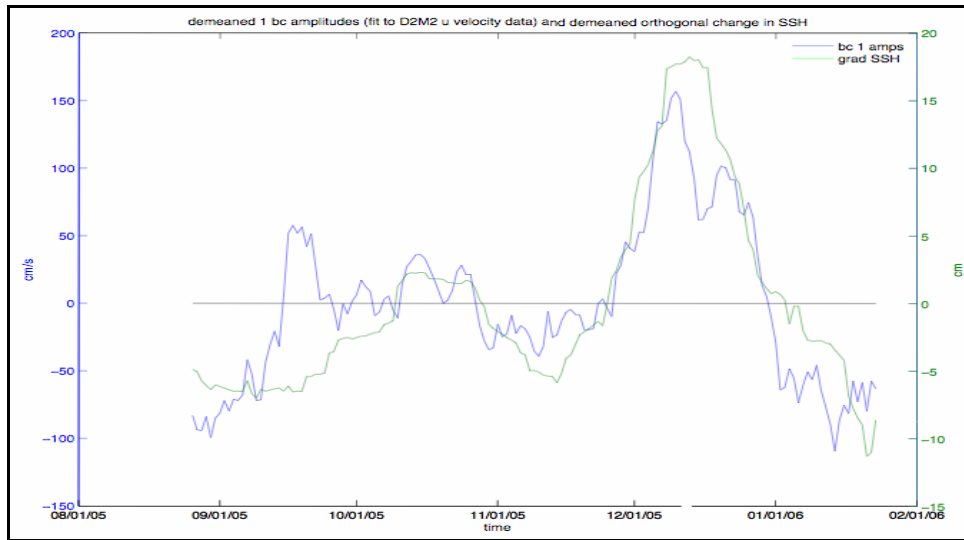


Figure 7.2-40. Temporal amplitudes of first baroclinic mode for the east-west velocity at mooring M2 during deployment 2 (blue) and the SSH gradient in the north-south direction (green).

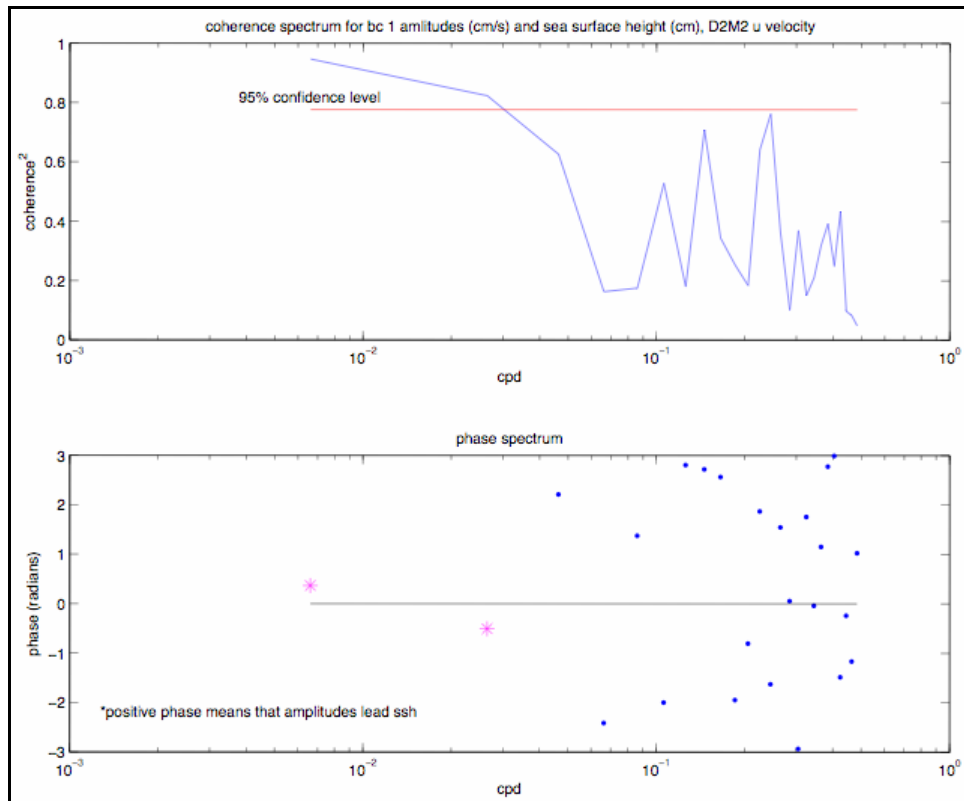


Figure 7.2-41. Coherency (top) and phase (bottom) spectra of the temporal amplitudes of the first baroclinic mode for the east-west velocity component at mooring M2 during deployment 2 and the SSH gradient in the north-south direction.

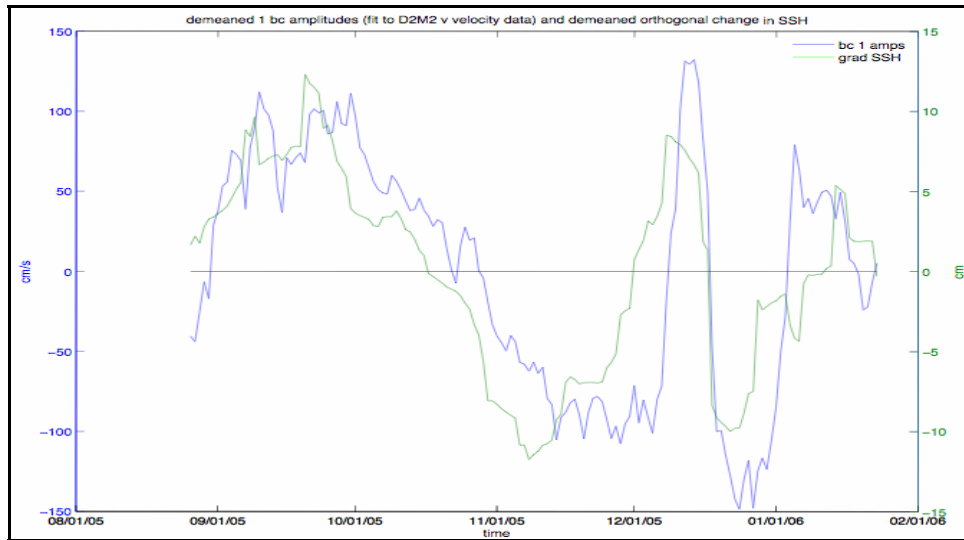


Figure 7.2-42. Temporal amplitudes of first baroclinic mode for the north-south velocity at mooring M2 during deployment 2 (blue) and the SSH gradient in the east-west direction (green).

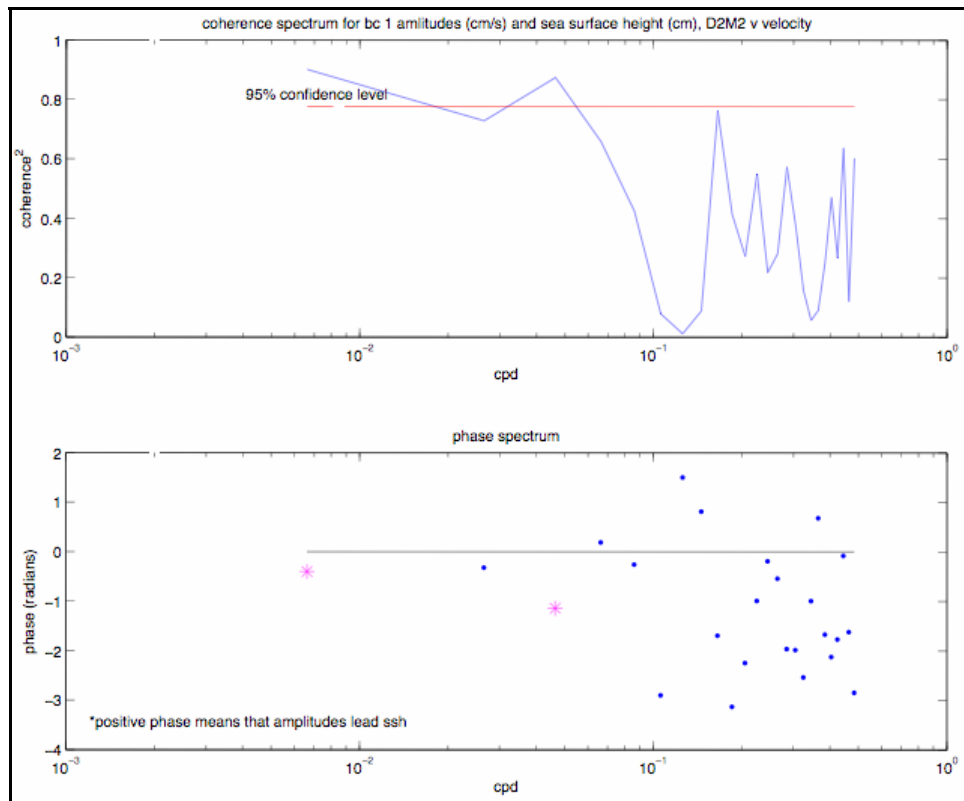


Figure 7.2-43. Coherency (top) and phase (bottom) spectra of the temporal amplitudes of the first baroclinic mode for the north-south velocity component at mooring M2 during deployment 2 and the SSH gradient in the east-west direction.

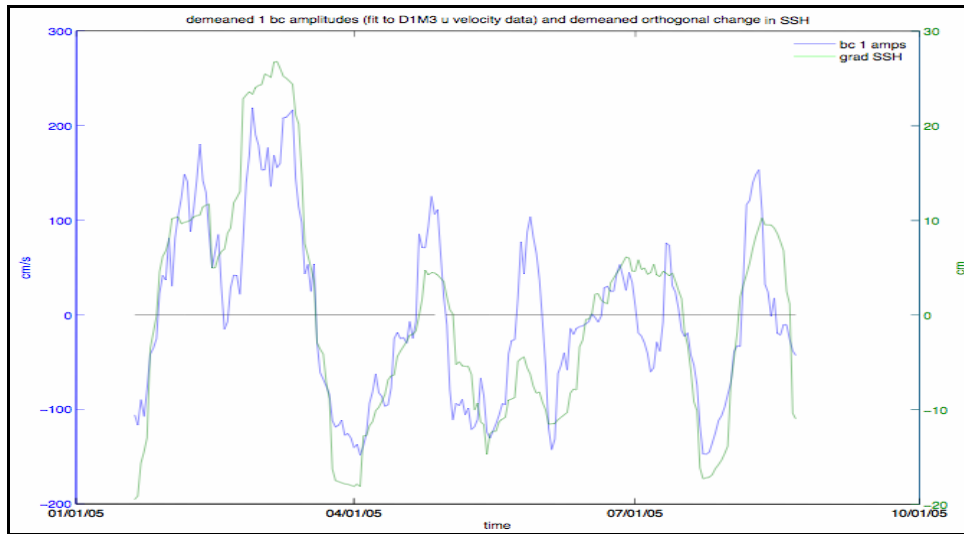


Figure 7.2-44. Temporal amplitudes of first baroclinic mode for the east-west velocity at mooring M3 during deployment 1 (blue) and the SSH gradient in the north-south direction (green).

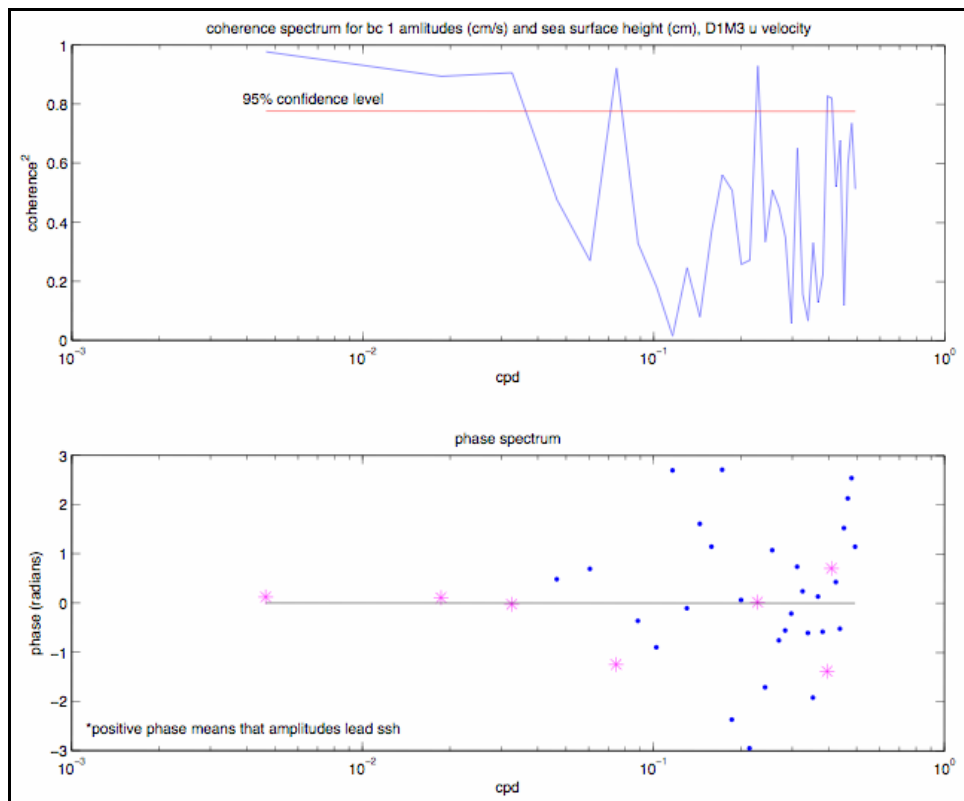


Figure 7.2-45. Coherency (top) and phase (bottom) spectra of the temporal amplitudes of the first baroclinic mode for the east-west velocity component at mooring M3 during deployment 1 and the SSH gradient in the north-south direction.

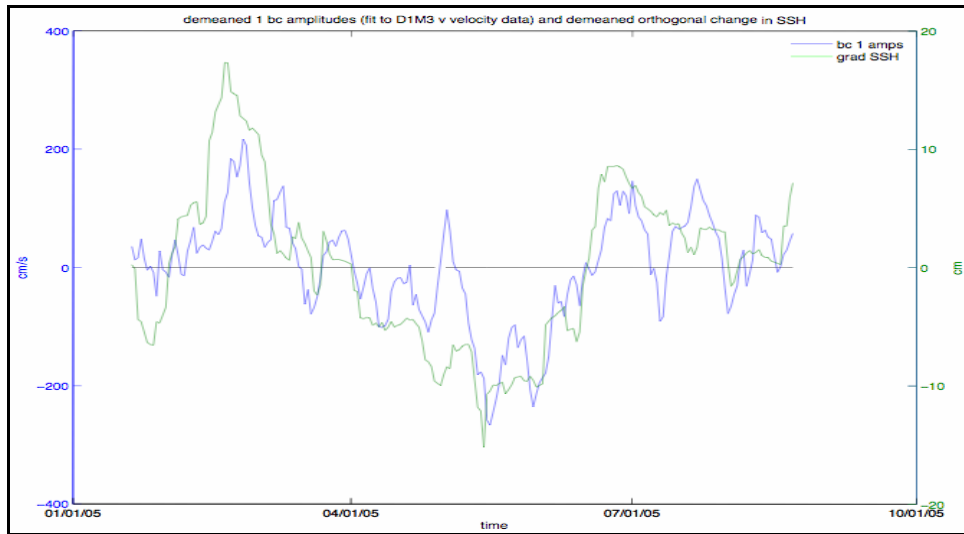


Figure 7.2-46. Temporal amplitudes of first baroclinic mode for the north-south velocity at M3 during deployment 1 (blue) and the SSH gradient in the east-west direction (green).

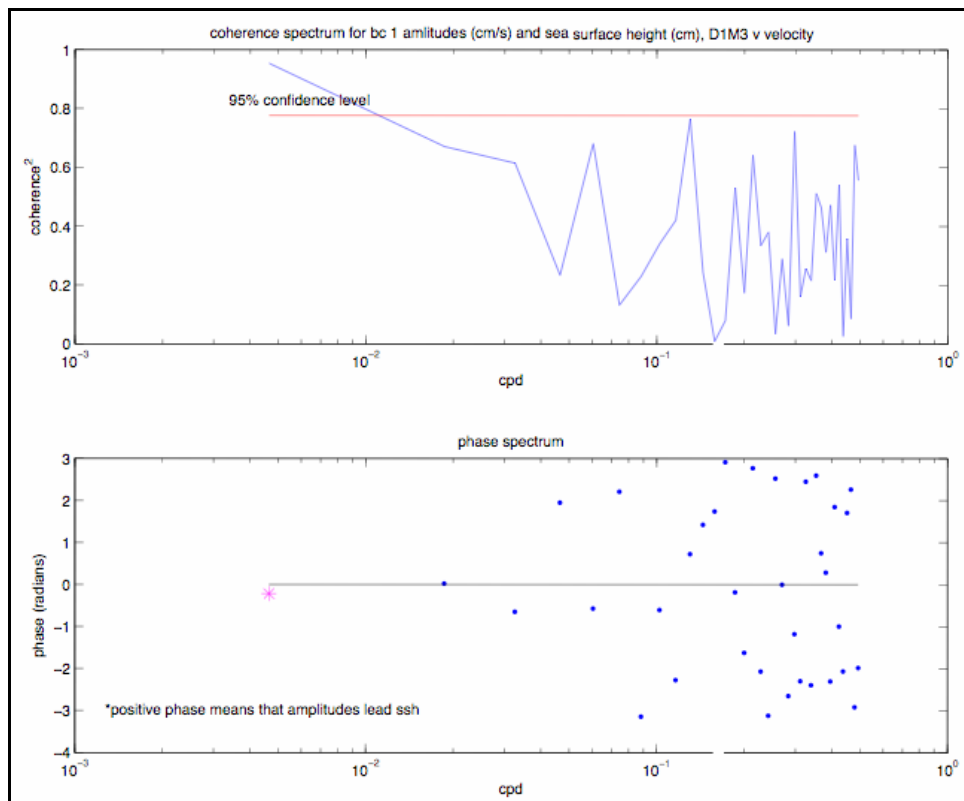


Figure 7.2-47. Coherency (top) and phase (bottom) spectra of the temporal amplitudes of the first baroclinic mode for the north-south velocity at M3 during deployment 1 and the SSH gradient in the east-west direction.

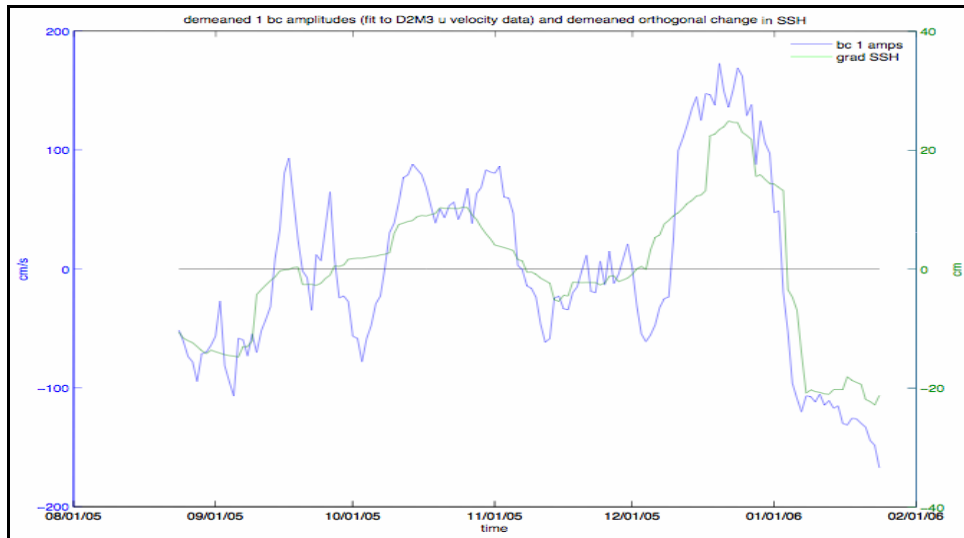


Figure 7.2-48. Temporal amplitudes of first baroclinic mode for the east-west velocity at M3 during deployment 2 (blue) and the SSH gradient in the north-south direction (green).

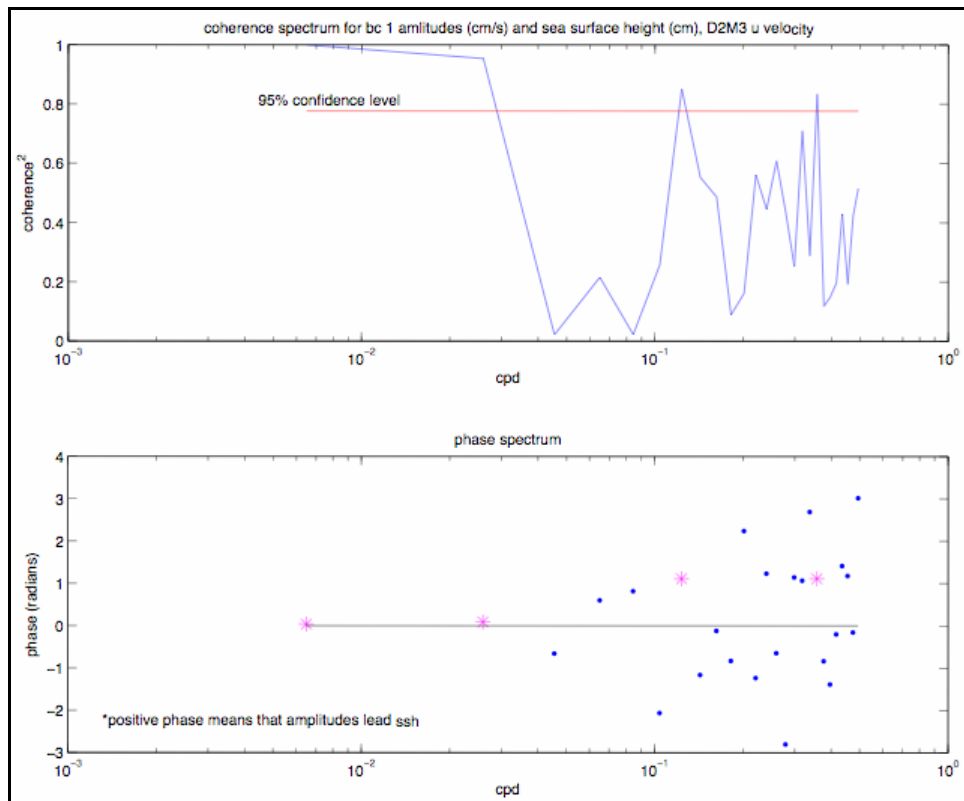


Figure 7.2-49. Coherency (top) and phase (bottom) spectra of the temporal amplitudes of the first baroclinic mode for the east-west velocity at M3 during deployment 2 and the SSH gradient in the north-south direction.

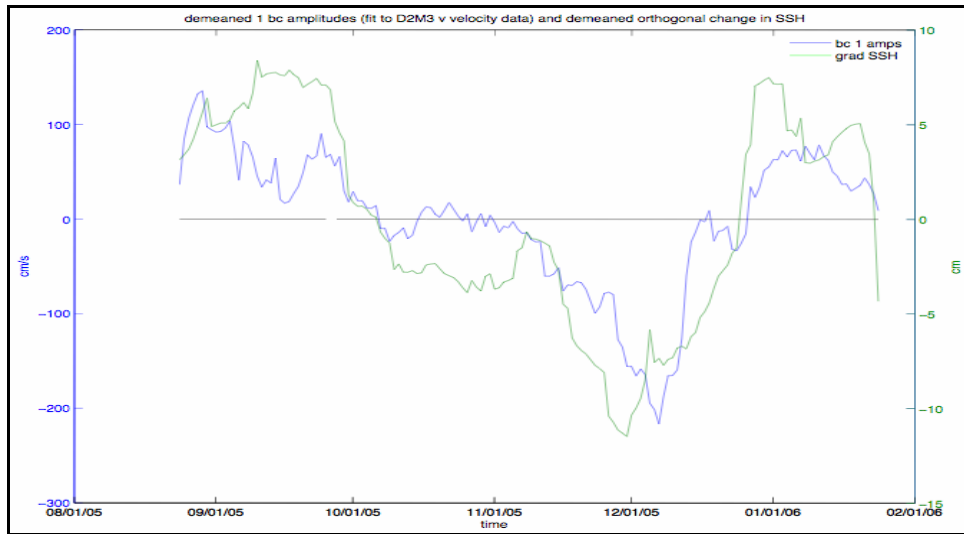


Figure 7.2-50. Temporal amplitudes of first baroclinic (bc) mode for the north-south velocity at M3 during deployment 2 (blue) and the SSH gradient in the east-west direction (green).

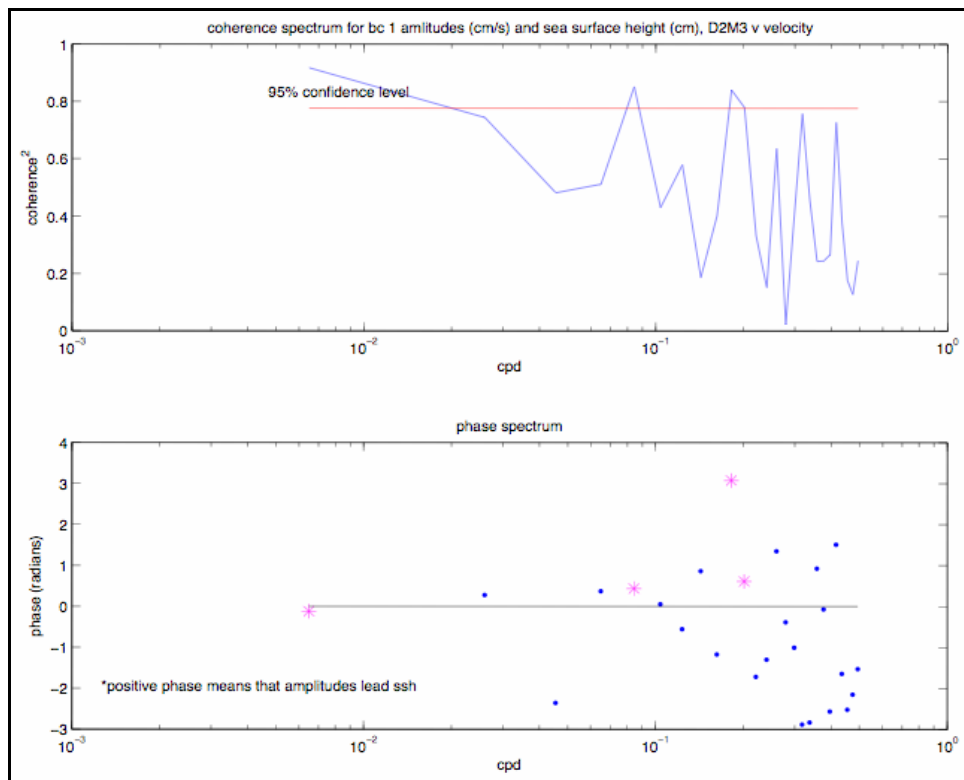


Figure 7.2-51. Coherency (top) and phase (bottom) spectra of the temporal amplitudes of the first baroclinic (bc) mode for the north-south velocity at M3 during deployment 2 and time series of the SSH gradient in the east-west direction.

7.2.1.3.2 Spectra and Temporal Scales of Modes

Power spectra and autocorrelation functions were generated for the dynamic mode time series using FFT methods as discussed previously. The results from these analyses were consistent between data from each mooring deployment. An example of this calculation for the mode fit to mooring M3 velocity data during deployment 1 are presented in Figure 7.2-52. Spectra for mode fits to u and v velocity exemplified a typical energy and enstrophy-conserving velocity spectrum, with an energy cascade in the red direction, i.e., from high to low frequencies. The barotropic amplitudes exhibited less energy than the first baroclinic modes at low frequencies. Also recall that variance at frequencies greater than 1 cpd was small because 40-hour low-passed filtered versions of the data were used in these calculations. The second baroclinic mode spectra are nearly white (constant) at frequencies less than 1 cpd.

A scales analysis was performed by estimating the first zero-crossing of the normalized autocovariance function (NACF) derived for each modal time series. This calculation quantifies the temporal lag in which the data becomes decorrelated from previous observations. Results showing the NACF for the fit to the velocity data from mooring M3 during deployment 1 are presented in Figure 7.2-53. The first baroclinic mode amplitudes had the longest time scales (13-39 days), and the second baroclinic mode amplitudes have the shortest time scales (6-7 days). For most of the moored data, the barotropic and first baroclinic mode time series displayed eddy time scales (~ 25 days), which was expected because of the active eddy regime in the East Gulf.

7.3 Upper/Lower-Layer Coupling Analysis Using PIES Data

An analysis of upper and lower layer potential coupling was also performed using primarily the PIES data. The array-averaged EKE for the upper (surface) and deep (2500 m) levels are shown in Figure 7.3-1. The upper and lower layer EKE did not indicate a direct one-to-one correspondence between the surface and deep energetic current events. During the measurement period, the variability in both layers appeared to be associated with features that propagated into the region from outside, i.e., much of the variability was remotely generated. Recall that the upper EKE reflects primarily the propagation of LC, LCEs and frontal cyclones into and out of the array area.

The mix of locally and remotely generated variability, each with similar magnitudes, can obscure the evidence of upper and lower-layer interactions. Therefore, the lower-layer potential vorticity was analyzed to help elucidate potential vertical coupling. The resolution of the PIES and moorings array allowed investigation of both the advective and tendency terms in the deep potential vorticity budget. In addition, a potential vorticity case study is presented of a deep cyclone (event c) where the production of relative vorticity was balanced by lower-layer stretching as the cyclone propagated southeastward into deeper water.

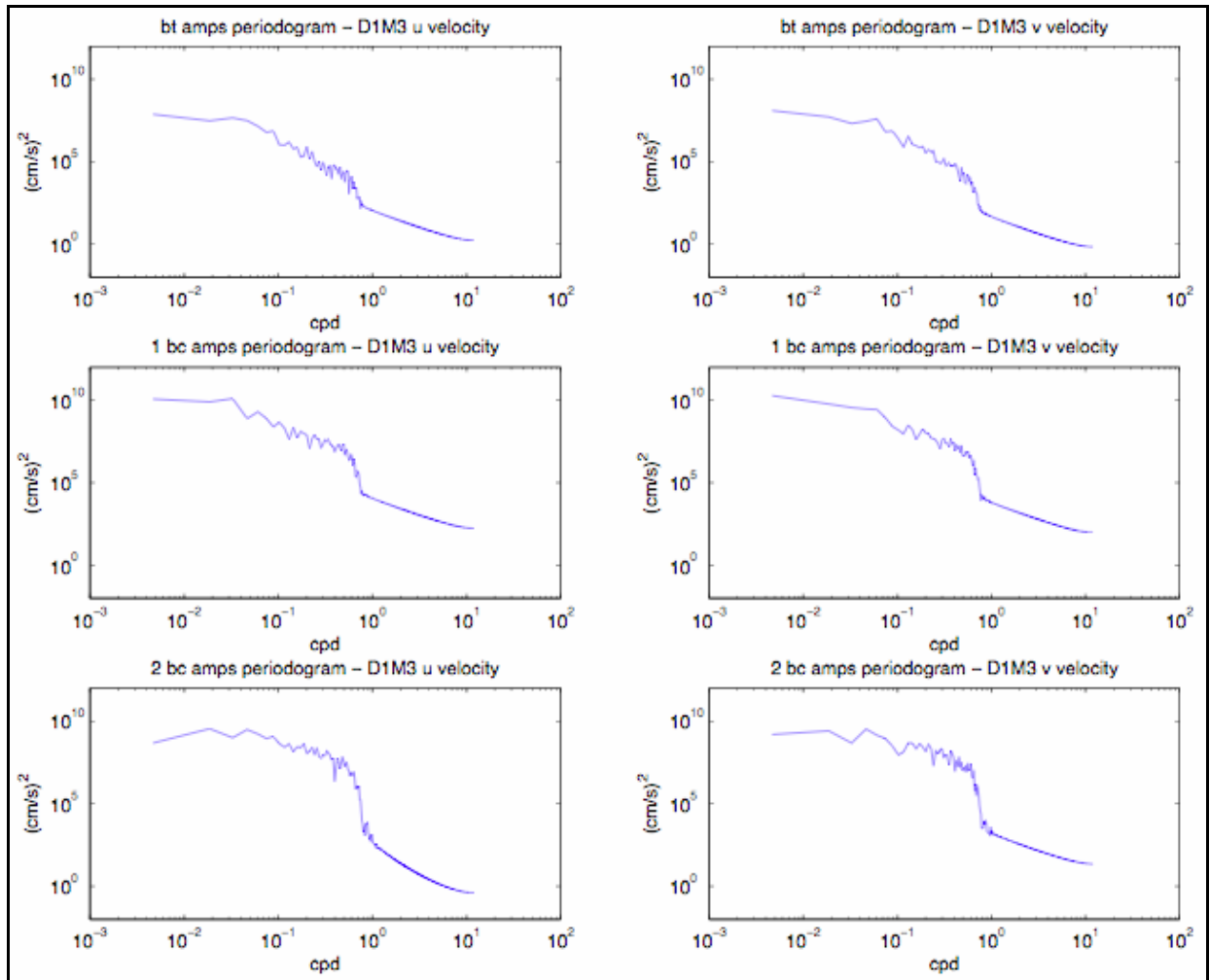


Figure 7.2-52. Power spectra of the time-series amplitudes of the first three theoretical modes (top: barotropic mode; middle: first baroclinic mode; bottom: second baroclinic mode) time-series for fits to the east-west (left) and north-south (right) velocity data at mooring M3 during deployment 1.

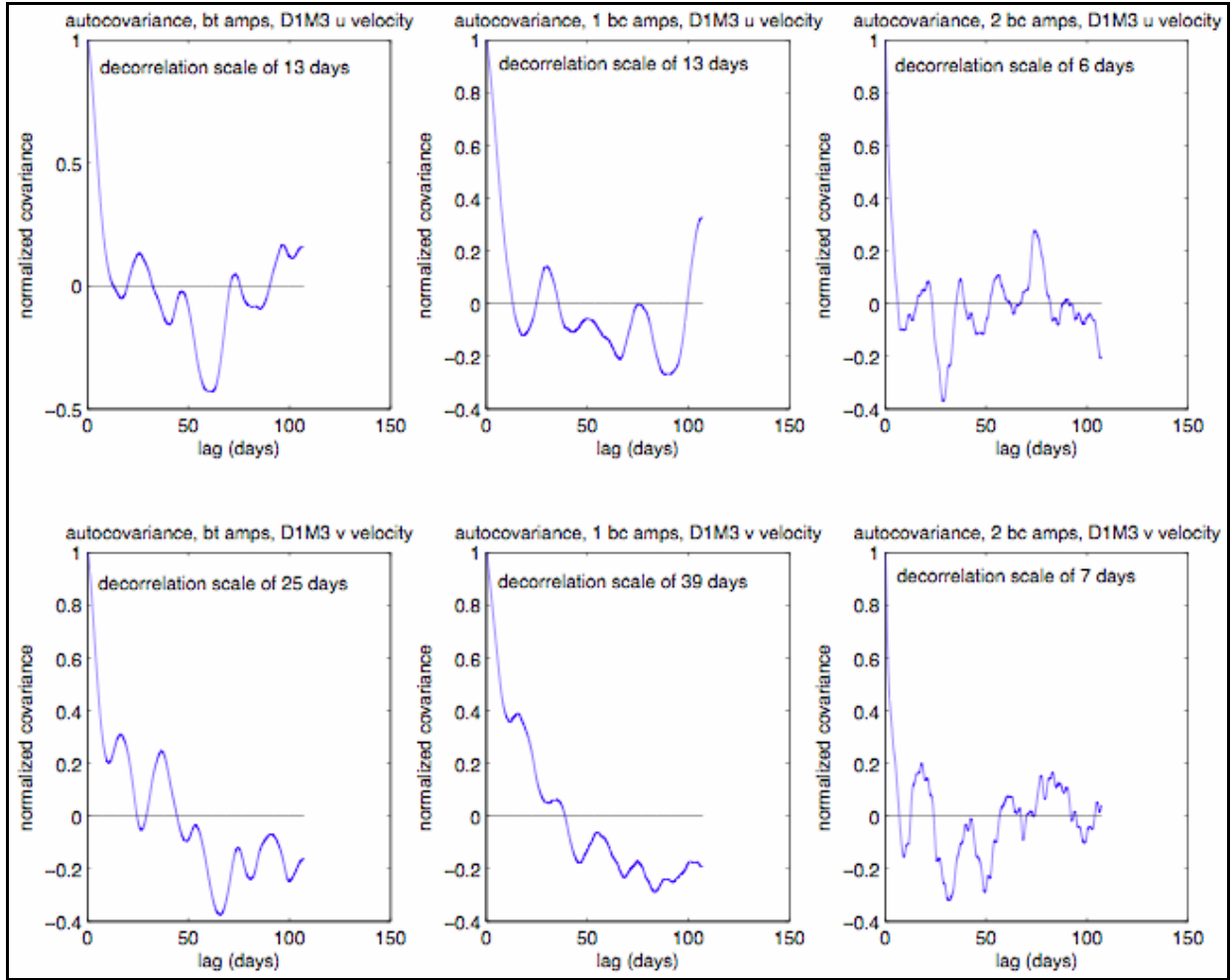


Figure 7.2-53. Normalized autocovariance function (NACF) of mode amplitudes from the fit to east-west and north-south velocity component data at mooring M3 during deployment 1.

Lower-layer potential vorticity q was calculated as the sum of the Coriolis parameter f and relative vorticity, $\zeta = \partial v / \partial x - \partial u / \partial y$, divided by lower layer thickness h :

$$q = \frac{f + \zeta}{h}, \quad (7.3.1)$$

The distance between the ocean bottom H and the 6°C isotherm depth h_6 defines lower-layer thickness. In the absence of external torques, lower-layer potential vorticity will be conserved:

$$\frac{Dq}{Dt} = \frac{\partial q}{\partial t} + u \frac{\partial q}{\partial x} + v \frac{\partial q}{\partial y} + w \frac{\partial q}{\partial z} = 0, \quad (7.3.2)$$

The advective terms can present a challenge because they require a highly-resolved array of measurements to determine the spatial gradients of a second-order term q . The measurement array contained the resolution required to calculate these terms.

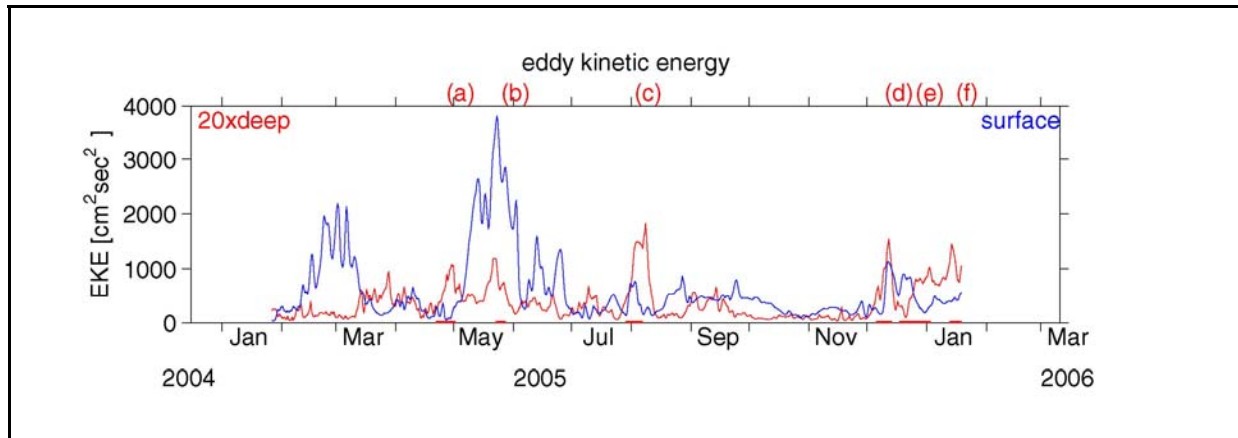


Figure 7.3-1. Measurement array mean eddy kinetic energy (EKE) at the surface (blue) and at 2500 m (red). The six major deep events are denoted by letters along the top of the time axis.

Figures 7.3-2, 7.3-3, and 7.3-4 show the mean and standard deviation of lower-layer potential vorticity, thickness, and relative vorticity, respectively, calculated from the PIES data. Topography greatly influenced the mean potential vorticity. The largest contribution to mean lower-layer thickness derived from H rather than h_6 . Mean relative vorticity was weak. Scaled by the Coriolis parameter, ζ/f expressed the Rossby number and had an absolute range near 0.02 within the array with negative (anticyclonic) values mainly in the northwest and the most positive (cyclonic) values in the southern portion of the array. Lower-layer potential vorticity was calculated as the Laplacian of the lower-layer streamfunction through optimal interpolation using a Gaussian correlation scale of 60 km.

Lower-layer potential vorticity exhibited the largest fluctuations along the southwestern edge of the array and was coincident with large fluctuations in lower-layer thickness. Temporal variability in lower-layer thickness at any site was due to changes in the thermocline depth. In the southern portion of the array, thermocline depth varied by 470 m (peak-to-peak in the bottom panel of Figure 7.3-3). Lower layer relative vorticity exhibited the largest variability in the southern portion of the array where the Rossby number reached maximum values near 0.28 in the strong cyclonic events and varied from -0.12 to 0.28.

In order to separate the contributions of lower-layer stretching and vorticity, we expanded q using a binomial series expansion,

$$\begin{aligned}
q &= \frac{f + \zeta}{H - h\delta} \\
q &= \frac{f(1 + \frac{\zeta}{f})}{H - h\delta} \\
q &= f(1 + \frac{\zeta}{f})(\frac{1}{H} + \frac{h\delta}{H^2} + \frac{h\delta^2}{H^3} + \dots) \\
q &= \frac{f}{H} + \frac{\zeta}{H} + \frac{h\delta f}{H^2} + \frac{\zeta h\delta}{H^2} + \frac{h\delta^2 f}{H^3} + \frac{\zeta h\delta^2}{H^3} + \dots \\
\tilde{q} &= \frac{f}{H} + \frac{\zeta}{H} + H\text{terms} \\
H\text{terms} &= \frac{h\delta f}{H^2} + \frac{h\delta^2 f}{H^3} + \dots + \frac{h\delta^{10} f}{H^{11}}.
\end{aligned}$$

In the bottom two lines we define a modified lower-layer potential vorticity, \tilde{q} , which approximates q and does not contain any joint $h\delta$ and ζ terms. Interestingly, while these terms were found to be small, they were not insignificant; see for example the difference between q (red line) and \tilde{q} (blue line) shown in the middle panel of Figure 7.3-5.

The experimental design allowed us to calculate the terms in the lower-layer potential vorticity equation. Here we show the results for the location shown as the orange diamond in Figures 7.3-3 and 7.3-4 and the red star in Figures 7.3-5 and 7.3-6. Both thickness and relative vorticity variability contributed to the local rate of change in total potential vorticity. The bottom panel of Figure 7.3-6 shows that the tendency term and the advective terms nearly balanced. This kind of analysis lends itself to parallel diagnostics between model and observational data sets. A next step is to decompose the potential vorticity into mean and eddy components for further diagnosis.

The deep cyclone events discussed in Chapter 6 shared similar characteristics. First, they propagated across the southwestern portion of the array from west to east. Second, they appeared to be locked behind an eastward propagating upper-ocean anticyclone. Third, the deep cyclones intensified as they moved eastward. Here we investigate the potential vorticity associated with the deep cyclone of event c as a case study. Again, a binomial expansion was used to separate stretching and relative vorticity. We define H_L as the cyclones mean lower-layer thickness and h' as the deviation of lower-layer thickness from H_L . The potential vorticity of the cyclone, q_L , and its binomial expansion from H_L is

$$\begin{aligned}
q_L &= \frac{f + \zeta_L}{H_L - h'} \\
q_L &= \frac{f}{H_L} + \frac{\zeta_L}{H_L} - \frac{fh'}{H_L^2} + \dots
\end{aligned}$$

and we retain the first three terms to define an approximate potential vorticity,

$$\tilde{q}_L = \frac{f}{H_L} + \frac{\zeta_L}{H_L} - \frac{fh'}{H_L^2}.$$

In order to view the cyclone's potential vorticity in a Lagrangian framework the local minimum associated with the cyclone for each half-day map was determined and then the thickness and relative vorticity values were interpolated to the cyclone position. The cyclone's potential vorticity was nearly constant as expected (Figure 7.3-7, panel A); its relative vorticity (panel B) and thickness (panel B) increased over time. The thickness increase was due almost entirely to the change in ocean depth as the eddy propagated to the southeast. The depth of the thermocline showed no discernable increase over time (panel C). The cyclone spun up over time as a consequence of its propagation into deeper ocean depths. This result was similar to the other two cyclone events, not shown.

These results provide an intriguing but limited view of the dynamics and potential vorticity development in upper layer and deep features propagating around the edges of the LC. The results are highly suggestive of upper and deep layer coupling under certain conditions not yet well understood. The results also demonstrated that a measurement array with the resolution and site-spacings utilized in the Eastern GOM Study is both necessary and well-suited to diagnose these types of events. However, to develop a much broader and in-depth understanding of the development and life of such couplings, the region covered by future measurement arrays would need to be much larger.

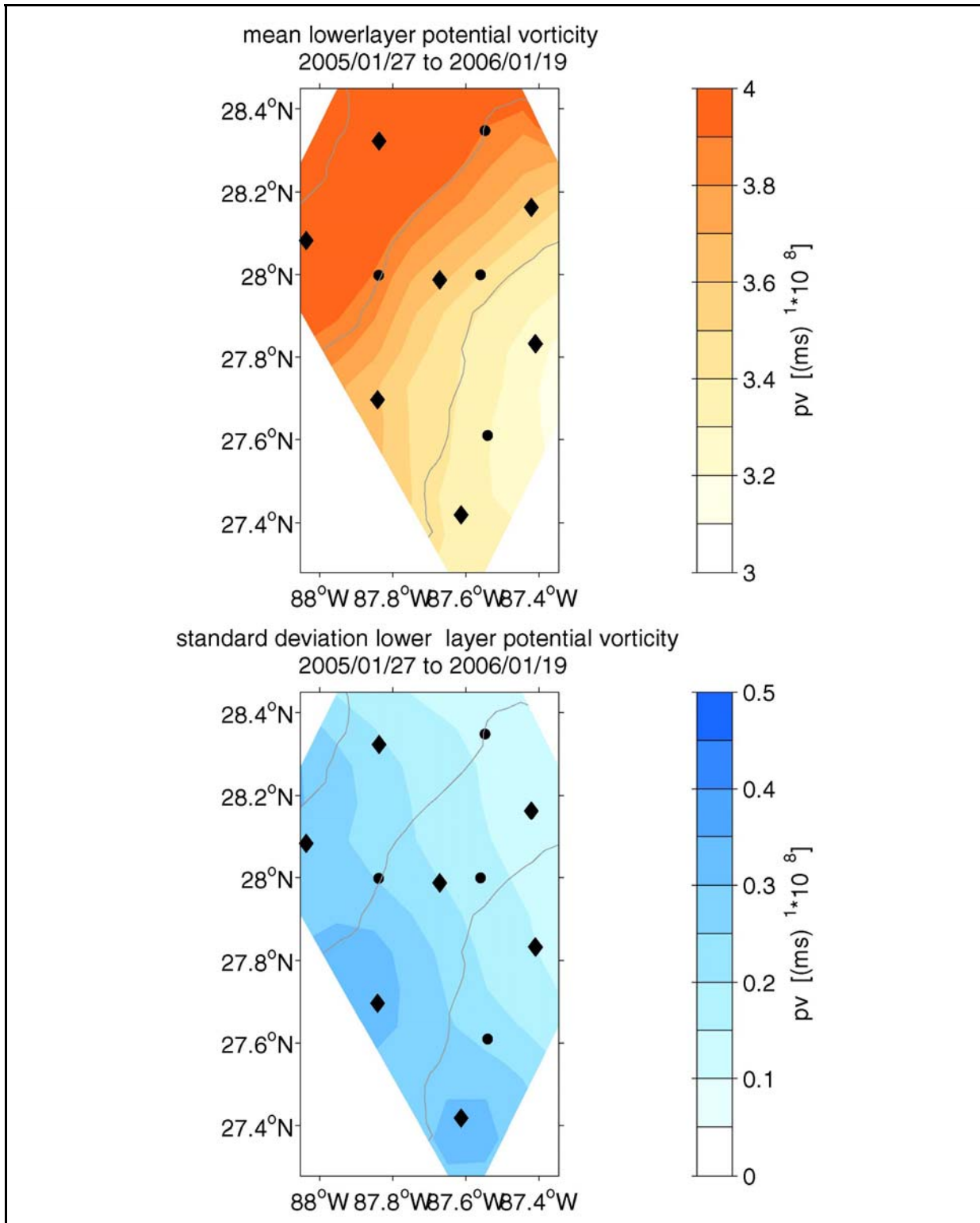


Figure 7.3-2. Top (bottom) panel: Mean (standard deviation) lower-layer potential vorticity. Topography contoured every 250 m depth denoted by gray lines in each panel. PIES denoted by diamonds, current meter moorings denoted by circles.

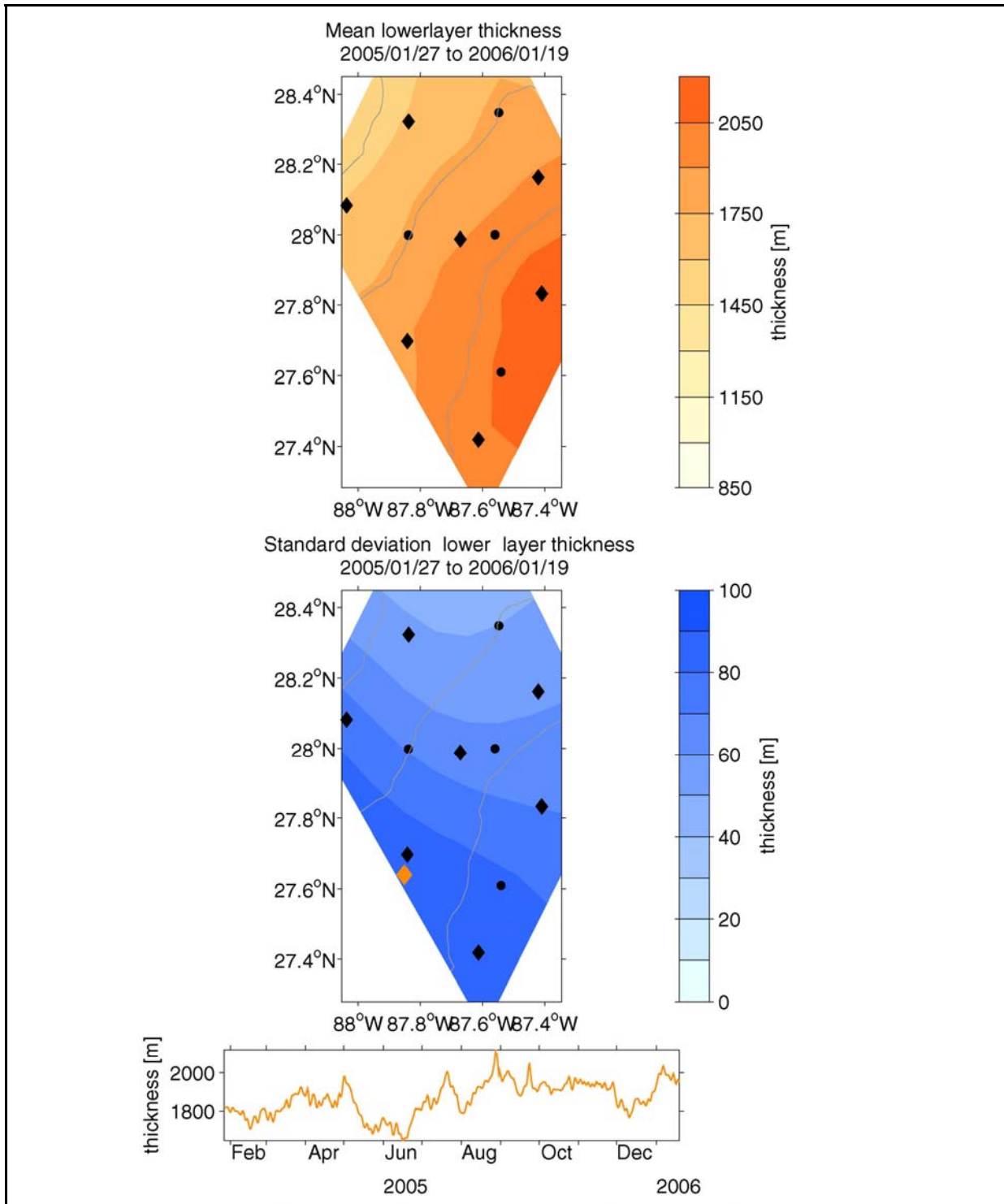


Figure 7.3-3. Top (middle) panel: Mean (standard deviation) of lower-layer thickness. Topography contoured every 250 m depth denoted by gray lines in each panel. PIES denoted by diamonds, current meter moorings denoted by circles. Bottom panel: Time series of lower-layer thickness at the site shown with the orange diamond in the middle panel.

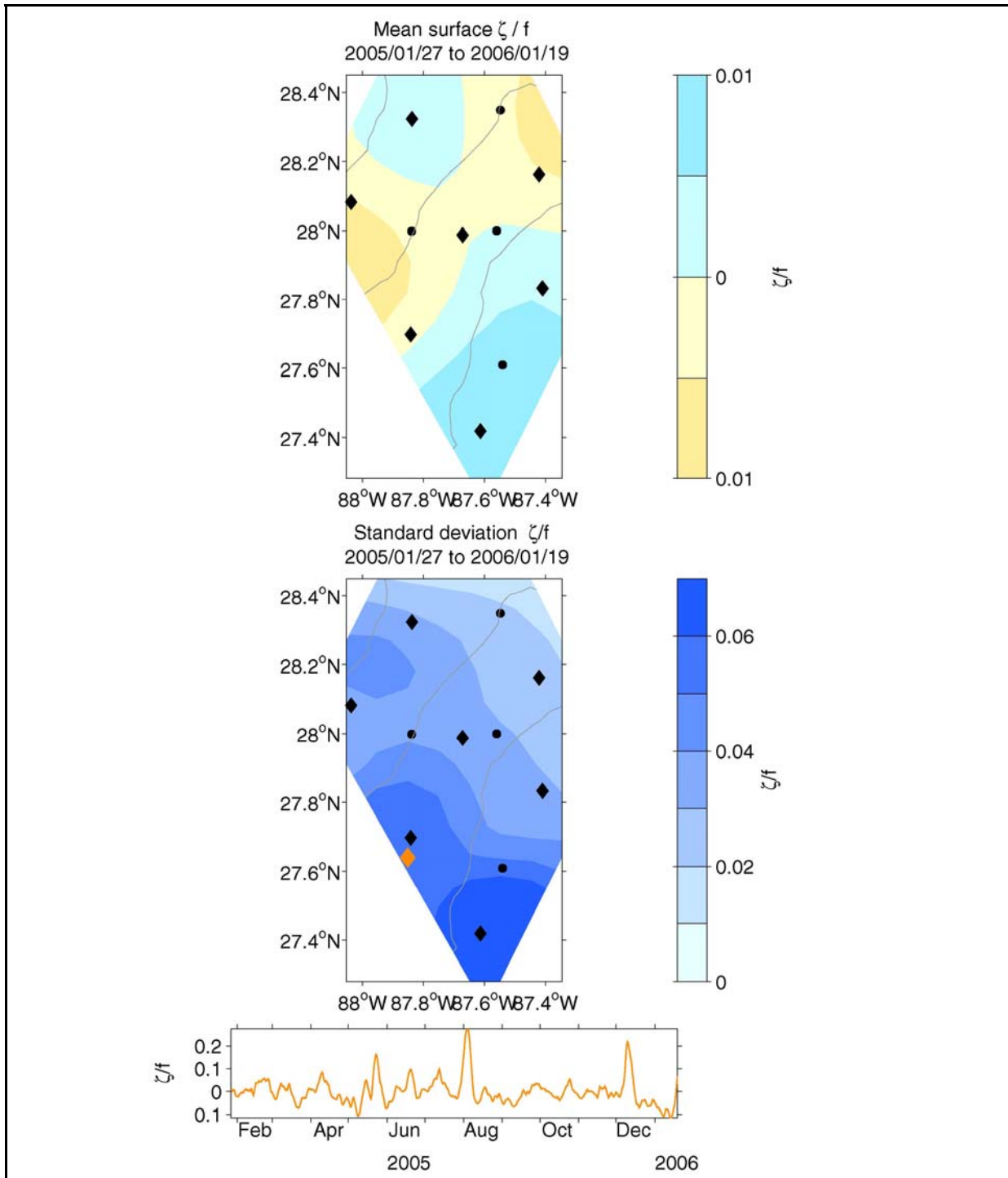


Figure 7.3-4. Top (middle) panel: Mean (standard deviation) of lower-layer relative vorticity divided by the local Coriolis parameter (f). Topography contoured every 250 m depth denoted by gray lines in each panel. PIES denoted by diamonds, current meter moorings denoted by circles. Bottom panel: Time series of lower-layer thickness at the site shown with the orange diamond in the middle panel.

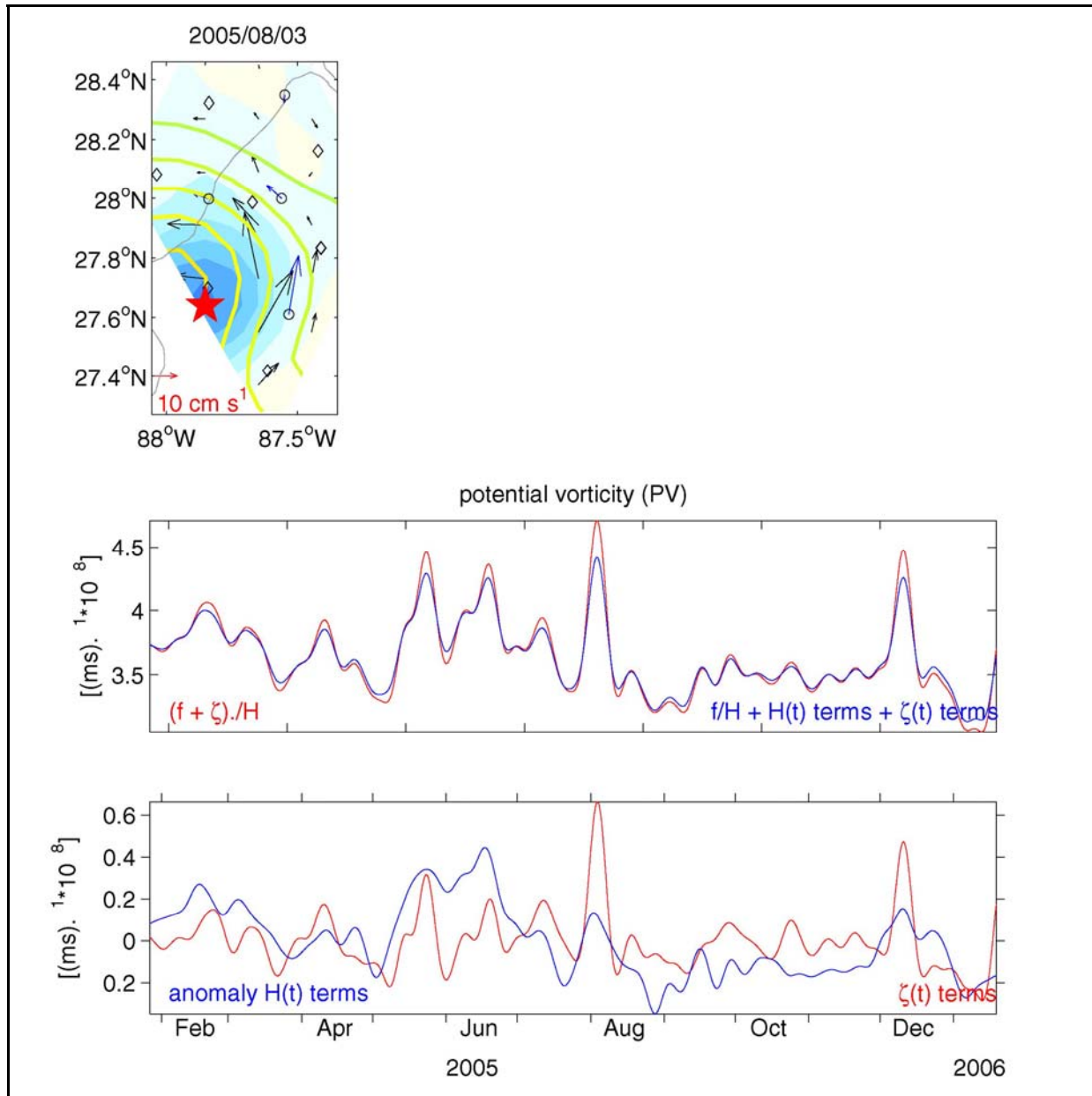


Figure 7.3-5. Top panel: Snapshot of upper and deep circulation on August 3, 2005. PIES derived SSH (thick lines) and 2500 m streamfunction (solid color; blue shades cyclonic, pink shades anticyclonic). The blue and black arrows are observed and mapped geostrophic currents, respectively. Topography contoured every 500 m in gray. Middle panel: Time series of total lower layer potential vorticity (red) and approximated lower layer potential vorticity (blue) as described in the text for the red star in the top panel. Bottom panel: Contribution of thickness (blue) and relative vorticity variability to total lower-layer potential vorticity for the red star in the top panel.

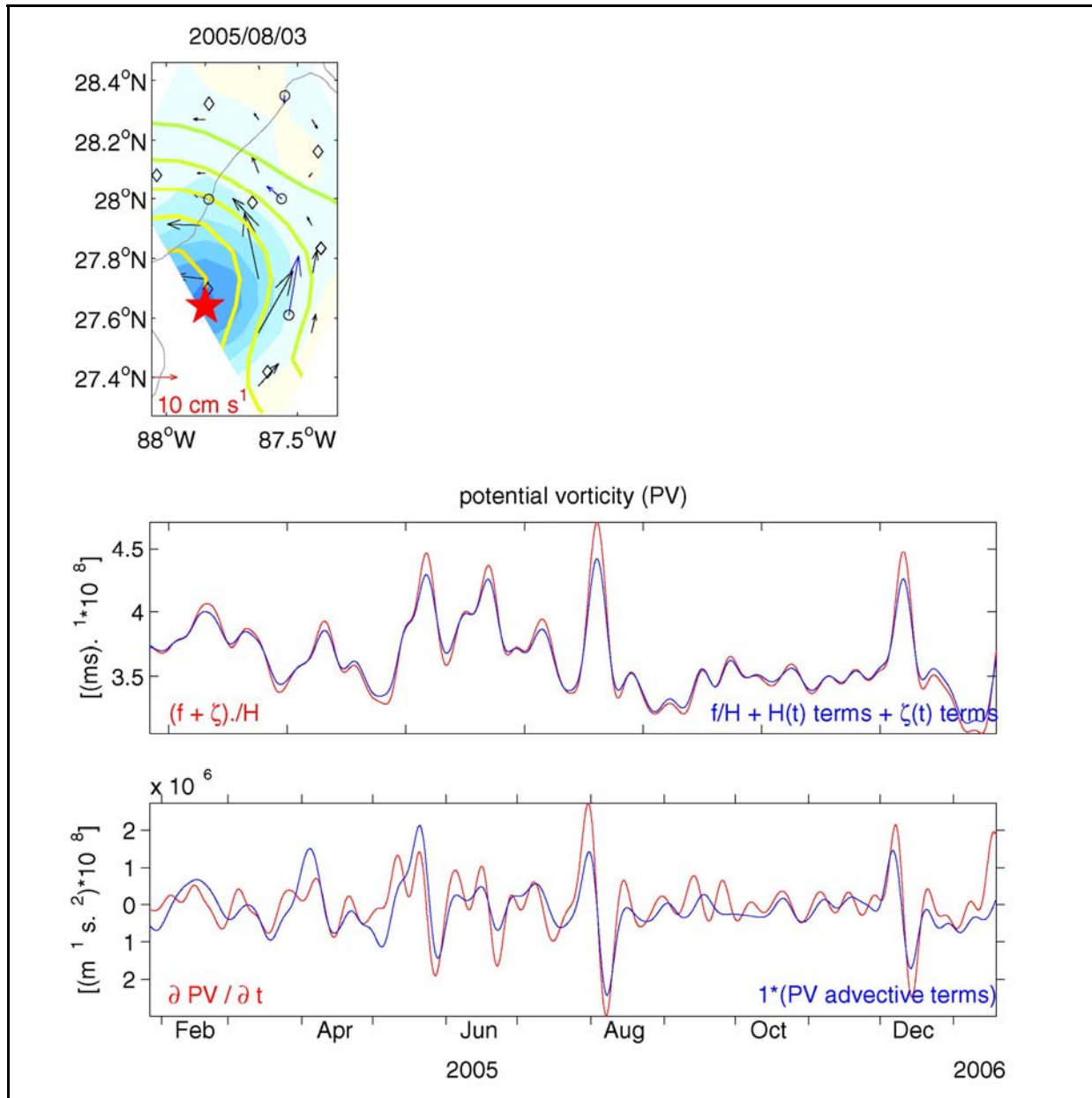


Figure 7.3-6. Top panel: Snapshot of upper and deep circulation on August 3, 2005. PIES derived SSH (thick lines) and 2500 m streamfunction (solid color; blue shades cyclonic, pink shades anticyclonic). The blue and black arrows are observed and mapped geostrophic currents, respectively. Topography contoured every 500 m in gray. Middle panel: Time series of total lower layer potential vorticity (red) and approximated lower layer potential vorticity (blue) as described in the text for the red star in the top panel. Bottom panel: Contribution of tendency (red) and advective terms multiplied by -1 (blue) to the total rate of change in potential vorticity at the red star in the top panel.

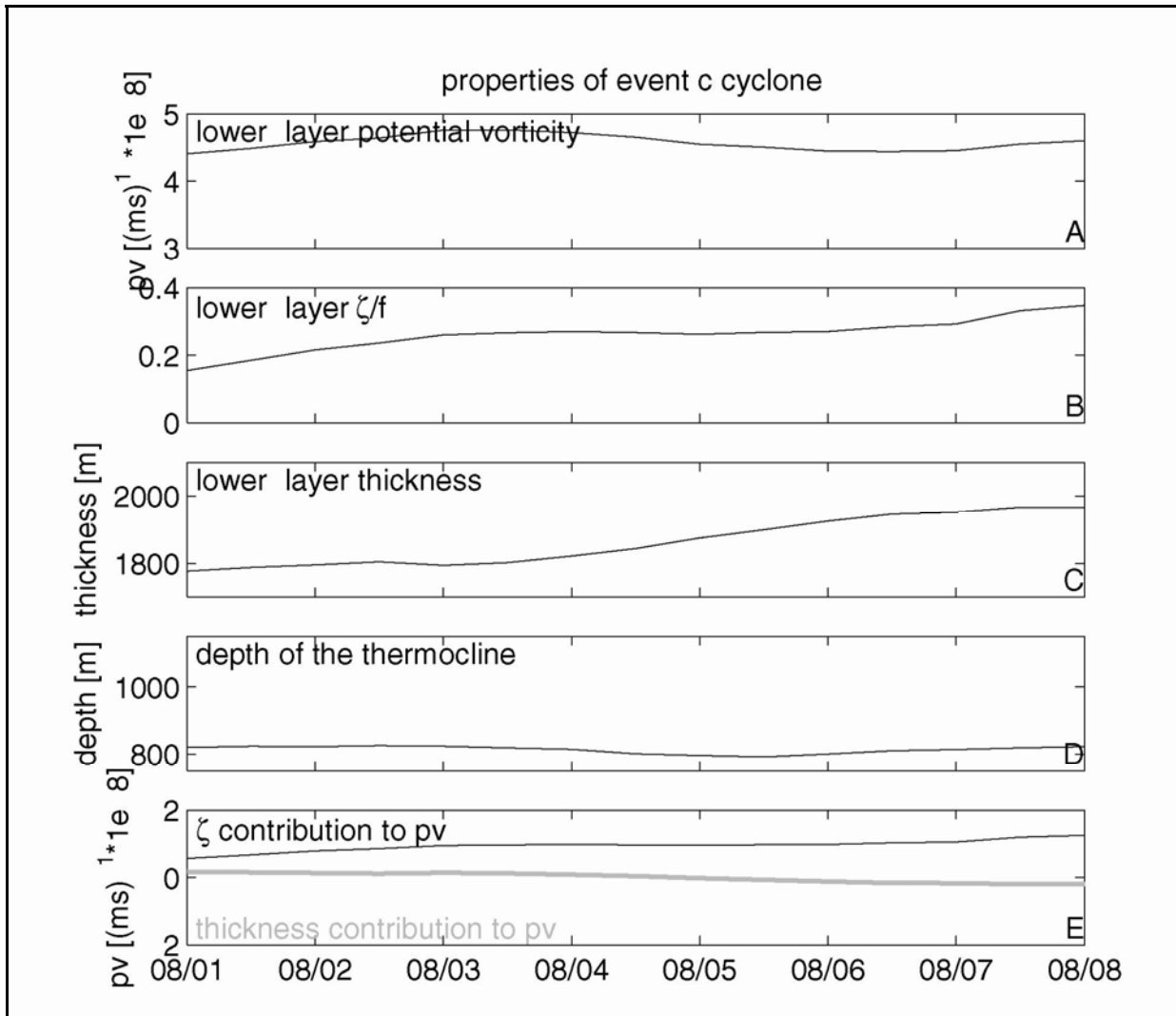


Figure 7.3-7. Properties of event c cyclone. Panel A: Lower layer potential vorticity. Panel B: Lower-layer relative vorticity scaled by the Coriolis parameter. Panel C: Lower-layer thickness. Panel D: Depth of the thermocline. Panel E: Relative vorticity (thickness) contribution to potential vorticity in black (gray).

8.0 SUMMARY AND CONCLUSIONS

Prior to this study, few deep water current measurements had been collected in the eastern GOM, especially in the area of the BOEMRE Eastern Gulf Lease Sale 181. To further the understanding of the circulation and its drivers in this region, BOEMRE commissioned the present *Survey of Deepwater Currents in the Eastern Gulf of Mexico*. The study consisted of a collection and analysis of a suite of both in-situ and remote sensing measurements. Measurements from PIES spanned December 2004 – January 2006. Measurements from three tall and one near-bottom current meter moorings spanned January 2005 – January 2006. Satellite remote sensing measurements spanned the entire field measurement period. Additional ancillary data such as coastal winds, runoff, and tides, Eddy Watch maps and drifting buoy tracks, and measurements available from other researchers or historical data sets, were all utilized to help analyze the new measurements and place them in historical perspective.

8.1 Summary of the Results

Prior to the study, the deep water portion of the eastern GOM was thought to be impacted less frequently by the LC and LCEs or their frontal features, resulting in less energetic circulation than is found in the north-central GOM where the LC and LCE's often penetrate. On a quasi-annual basis, the northern edge of the Loop Current reaches between 24° and 28° N into the Gulf of Mexico (Sturges and Evans 1983), yet for the majority of the field measurement period, the northern edge (as the LC or Eddy Vortex) remained between 27° and 28° N, and impacted the study area for much of the measurement period.

During the study, the LC spawned Eddy Vortex. Using metrics applied to historical altimetry data to evaluate eddy separations (Leben, 2005), Eddy Vortex detached and reattached from the LC a total of four times, prior to final separation. This was the largest number of detachment/reattachment events observed during a single LC intrusion cycle within the historical altimeter record. Final detachment occurred on 13 September 2005. During this period of detachment and reattachment, the extended intrusion of the LC and an associated eddy was one of the most northerly intrusions on record. It was only exceeded by the intrusion that generated Eddy Sargassum during the Exploratory Study. As a result of the detachment and reattachment process, Eddy Vortex resided in the northern GOM, and impacted the circulation in the study area, for much of the field measurement period. The greatest influence was observed during deployment 1, with less but still significant influence, especially to the southernmost mooring M3 during deployment 2.

In addition, during the mooring deployments, five hurricanes and one tropical storm traversed the Gulf; the most severe being Hurricanes Katrina and Rita. Hurricane Katrina entered the Gulf of Mexico on August 26, 2005 and was nearest to the study area on August 28, 2005; Hurricane Rita entered the Gulf of Mexico on September 20, 2005 and was nearest to the study region on September 22, 2005.

The combination of the extended stay of the LC and Eddy Vortex in the northern GOM, and the number of severe storms passing near the study area, resulted in extensive periods of energetic currents within the study area during the measurement period.

In Chapter 3, details of the metrics of the LC and Eddy Vortex are provided. These metrics are also placed in perspective based on the historical altimetry record that now spans 13.5 years from 1 January 1993 through 15 January 2006. During the study period, the LC year-long area and latitude of northern extent were maximums for the entire period of the altimeter record. The average LC length and westward longitude were only exceeded by one prior intrusion that formed, Eddy Millennium. The LC statistics concerning LC volume and circulation were near the upper historical ranges. The metrics also calculated that the LC or Eddy Vortex intruded into the PIES array for this study a total of 52 days during 2005, which is quite an extensive visit as the historical average is 22 days per year.

In Chapter 4, the dynamics of Eddy Vortex and some cold core eddies were examined using both a kinematic and a dynamic approach. These analyses provided some guidance on the formation and characteristics of Eddy Vortex and some of its frontal features. Mean surface circulation over the first six months of measurements shows southeast flow resulting from the presence of Eddy Vortex. Three episodes of high EKE lasting 15-30 days occurred during Eddy Vortex detachment and reattachment. Mean flow during the last six months has weaker currents due to several frontal cyclones. Only one episode of high EKE occurred during a strong frontal cyclone.

Chapter 5 presented a basic overview of the measurement results from the moorings. A variety of analyses were performed to provide perspectives on the basic structure, vorticity, and dynamics of the currents that were measured. Due to the significant presence of the LC and Eddy Vortex, along with cold core eddies and other frontal features, a significant portion of the entire measurement record contains very energetic currents in the upper layer. This was more prevalent during the first deployment. However, during the second deployment, the passage of both Hurricane Katrina and Hurricane Rita created energetic inertial oscillations. The passage of Hurricane Katrina coincided with the presence of a cold core eddy situated over the southern portion of the study area, and the resulting current measurements show an enhanced inertial oscillation strength. This provided a rare opportunity to view the effects of combined forces of a cold core eddy and a hurricane on exciting the circulation.

Chapter 6 focuses on the deep circulation seen in the eastern GOM during the study, and compares it to the historical knowledge of deep circulation in the GOM. Much of the focus is on TRWs and their potential generation and translation from the study area. The deep currents at moorings M2 and M3 showed evidence of bottom intensification of the currents, with principal axes of standard deviation ellipses directed westward and southwestward, respectively. These directions are across the isobaths towards shallower water, which is characteristic of TRW motions. The deep circulation was punctuated by a number of energetic low-frequency events that were typical of TRW presence.

In Chapter 7, potential vertical coupling of the upper and lower layers of the GOM in the study area were investigated. Some sophisticated analyses were performed to assess the dominant modes controlling the circulation, and to evaluate the extent of coupling. Specific short duration periods of similar flow through a majority of the water column have been previously seen (Hamilton 2007), and were again seen in this study's measurements. While the analyses showed there was minimal connection between the upper and lower layers, it also showed that the lower layer had a small contribution from upper-layer LC or LCE dynamics through dynamic coupling, and the upper layer had a small contribution from TRW flows decaying upwards through the water column.

8.2 Conclusions

Prior to the study, the study team had a significant concern if the eastern GOM would experience any sizable current energetics. The primary conclusion from the study is that the eastern GOM is a very active region in terms of circulation, especially when the LC or an LCE is present. The circulation characteristics of the region are very similar to those in the north-central GOM when similar processes are at work, whether they be the presence of the LC, and LCE, frontal features, or major storms. Significant advancement in the understanding of the circulation in the eastern GOM was achieved including:

- Extended LC intrusion significantly impacted the study area upper ocean circulation during the first half of the EGOM program. Once Eddy Vortex finally separated, fewer LC or frontal features impacted the circulation and the character of the circulation returned to conditions more typical for this region.
- Cyclones are an important dynamical component of the general circulation of the GOM and significantly impacted the study region during the program.
- Comparisons were drawn between the mean surface circulation over the first six months of measurements versus the last six months. The mean for the first six months revealed southeast flow from the presence of Eddy Vortex while the last six months had comparatively weak circulation.
- The PIES array captured the mesoscale frontal meanders along the periphery of the LC and while well resolved provided a limited window.
- Cyclonic events occurred more frequently than anticyclonic events in the EGOM vorticity record.
- Currents during both deployments at all three tall moorings showed a high degree of coherency at water depths above 500 m, with weaker coherence extending down to 750 m, and with only occasional coherence at deeper depths.
- Large amplitude inertial oscillations are evident immediately after the passages of Hurricanes Katrina and Rita. These current oscillations persisted for at least two weeks after the passage of these storms.
- The passage of Hurricane Katrina near the study's moorings while a cyclonic (cold core) eddy was sitting over the southern portion of the study area, is believed to have generated stronger than normal currents.

- In general, spectral energy was greatest in the shallow ocean depth (<300 m). Surface records (~ 50 m) contained larger weather-band variance than deeper records.
- The extrapolated near-bottom current speeds at M1 near the Florida Escarpment were no larger than those at M3 on the abyssal plane. This was an interesting contrast to near-bottom currents near the Sigsbee Escarpment farther west, where bottom currents were much stronger in proximity to the Escarpment.
- The lower-layer motions in the study area are dominated by TRWs. The presence of the LC or LCE over the study area had a direct influence on the amplitudes of the lower-layer TRWs.
- Deep circulation experiences TRW packets, though generation of TRWs that translate into the north-central GOM do not appear to be generated in this region. TRW generated currents are also not affected significantly by steep bathymetry in this region.
- The lower layer had a small contribution from upper LC or eddy fluctuations through dynamical coupling, just as the upper layer had a small contribution from TRW flows decaying upwards through the water column.
- The horizontal current structure in this region of the Gulf resembles a 2-layer system. The eddy field causes intensification of the surface currents, which exponentially decay in magnitude with depth to ~ 800 m., while the lower layer was influenced primarily by TRWs propagating through the region.

8.3 Recommendations

The one year measurement program in the eastern GOM was judicious in timing in that it caught significant penetrations of the LC and an LCE into the region, as well as multiple large storms. The study region, however, was actually fairly small, and fairly limited in measurement locations, to extrapolate the study results to a much larger portion of the eastern GOM. The primary recommendations for future studies to further assess the larger eastern GOM circulation features, and to better explore the dynamics and interactions of the water column with the LC and its eddies, are as follows:

- Conduct a larger-scale circulation study of the eastern GOM spanning more of this area to better assess the geographic extent of the circulation and processes found during this study.
- Conduct in-situ measurements at both small (25km) and large (50-100km) scales so as to observe currents over a wider area, yet maintain the ability to calculate vorticity, coherence between measurement sites, and to assess the small scale interactions at the edges of the LC and LCEs which are imparting significant energy into the water column.

- Add gliders so as to better map hydrography changes in critical areas, such as the LC and LCE edges, and so as to provide hydrography measurements over much longer time scales than can be achieved by hydrography cruises using CTDs and XBTs.
- Concentrate a set of moorings in the path of, and at the boundaries of, the LC and LCEs, as best as they can be positioned, to improve understanding of the frontal features and how they affect and control LC movements and eddy shedding.
- Continue to employ remote sensing (satellite measurements) in future studies, as these provide such a great basis of understanding of the features that affect specific in-situ measurement sites.
- Conduct coordinated programs geographically to obtain measurements in the southern portion of the LC as well as the northern portion so as to better understand what drives and controls its northward intrusions and southward retractions.
- Conduct coordinated programs with other institutions, in particular those institutions conducting oceanographic measurements of major storms, so as to make use of their fast response measurement capabilities in front of the storms.
- Finally, keep funding quality research in the GOM.

9.0 LITERATURE CITED

- Accurate Environmental Forecasting, Inc. 2007. Ocean response to hurricane Katrina in presence of a cyclone Ocean model validation study Preliminary report. Unpublished.
- Bane, J.M., Jr., D.A. Brooks, and K.R. Lorenson. 1981. Synoptic observations of the three-dimensional structure and propagation of Gulf Stream meanders along the Carolina continental margin. *J. Geophys. Res.* 86:6411-6425.
- Berger, T. 1993. Loop Current eddy shedding cycle. LATEX Program Newsletter. College of Geosciences, Texas A&M University. 2(24).
- Bloomfield, P. 1976. Fourier analysis of time series: an introduction. New York: J. Wiley.
- Bretherton, F.P., R.E. Davis, and C.B. Fandry. 1976. A technique for objective analysis and design of oceanographic experiments applied to MODE-73. *Deep Sea Research* 23:559-582.
- Briggs, W.L. 1987. A multigrid tutorial. *Soc. Ind. and Appl. Math.*:88.
- Charney, J.G. and G.R. Flierl. 1981. Oceanic analogues of large-scale atmospheric motions. *Evolution of Physical Oceanography*. Edited by B.A. Warren and C. Wunsch. Cambridge, MA: MIT Press. 504–548 pp.
- Cressman, G.P. 1959. An operational objective analysis system. *Mon. Weather Rev.* 87:367-374.
- Cushman-Roisin, B., W.H. Heil, and D. Nof. 1985. Oscillations and rotation of elliptical warm-core rings. *J. Geophys. Res.* 91:11756-11764.
- DeHaan, C.J. and W. Sturges. 2005. Deep cyclonic circulation in the Gulf of Mexico. *J. Phys. Oceanogr.* 35:1801-1812.
- DiMarco, S.F., W.D. Nowlin, Jr., and R.O. Reid. 2005. A statistical description of the velocity fields from upper ocean drifters in the Gulf of Mexico. In: Sturges, W. and A. Lugo-Fernandez. *Circulation in the Gulf of Mexico: observations and models*. Washington, DC.: American Geophysical Union. Pp. 101-110.
- Donohue, K., P. Hamilton, K. Leaman, R. Leben, M. Prater, D.R. Watts, and E. Waddell. 2006. Exploratory study of deepwater currents in the Gulf of Mexico. Volume II: Technical report. U.S. Dept. of the Interior, Minerals Management Service, Gulf of Mexico OCS Region, New Orleans, LA. OCS Study MMS 2006-074. 430 pp.
- Donohue, K., P. Hamilton, R.R. Leben, D.R. Watts, and E. Waddell. 2008. Survey of deepwater currents in the northwestern Gulf of Mexico. Volume II: Technical Report. U.S. Dept. of the Interior, Minerals Management Service, Gulf of Mexico OCS Region, New Orleans, LA. OCS Study MMS 2008-031. 375 pp.

- Elliott, B.A. 1982. Anticyclonic rings in the Gulf of Mexico. *J. Phys. Oceanogr.* 12:1292-1309.
- Emery, W.J. and R.E. Thompson. 2001. *Data Analysis Methods in Physical Oceanography*. Amsterdam: Elsevier.
- Fofonoff, N.P. and R.M. Hendry. 1985. Current variability near the southeast Newfoundland Ridge. *J. Phys. Oceanogr.* 15:963-984.
- Fratantoni, P.S., T.N. Lee, G. Podesta, and F. Muller-Karger. 1998. The influence of Loop Current perturbations on the formation and evolution of Tortugas eddies in the southern Straits of Florida. *J. Geophys. Res.* 103:24759-24779.
- Fu, L.-L., D. Stammer, R.R. Leben, and D.B. Chelton. 2003. Improved spatial resolution of ocean surface topography from the T/P–Jason-1 altimeter mission. *EOS, Transactions, American Geophysical Union.* 84:241,247-249.
- Gill, A.E., J.S.A. Green, and A.J. Simmons. 1974. Energy partition in the large-scale ocean circulation and the production of mid-ocean eddies. *Deep-Sea Res.* 21(7):499-528.
- Gille, S.T. and C.W. Hughes. 2001. Aliasing of high-frequency variability by altimetry: evaluation from bottom pressure records. *Geophys. Res. Lett.* 28:1755-1758.
- Glenn, S.M., G.Z. Forristall, P. Cornillon, and G. Milkowski. 1990. Observations of Gulf Stream Ring 83-E and their interpretation using feature models. *J. Geophys. Res.* 95:13043-13063.
- Greenslade, D.J.M., D.B. Chelton, and M.G. Schlax. 1997. The midlatitude resolution capability of sea level fields constructed from single and multiple altimeter datasets. *J. Atmos. Oceanic Technol.* 14:849-870.
- Hamilton, P. 1990. Deep currents in the Gulf of Mexico. *J. Phys. Oceanogr.* 20:1087-1104.
- Hamilton, P. 2007. Deep-current variability near the Sigsbee Escarpment in the Gulf of Mexico. *J. Phys. Oceanogr.* 37:708-726.
- Hamilton, P. and A. Lugo-Fernandez. 2001. Observations of high speed deep currents in the northern Gulf of Mexico. *Geophys. Res. Lett.* 28:2867-2870.
- Hamilton, P., G.S. Fargion, and D.C. Biggs. 1999. Loop Current eddy paths in the western Gulf of Mexico. *J. Phys. Oceanogr.* 29:1180-1207.
- Hamilton P., T.J. Berger, J.H. Churchill, R.R. Leben, T.N. Lee, J.J. Singer, W. Sturges, and E. Waddell. 2000. DeSoto Canyon eddy intrusion study: Final report. Volume II: Technical report. U.S. Dept. of the Interior, Minerals Management Service, Gulf of Mexico OCS Region, New Orleans, LA. OCS Study MMS 2000-080. 269 pp.

- Hamilton, P., K. Donohue, J.J. Singer, and E. Waddell. 2003. Deepwater Observations in the Northern Gulf of Mexico from In-situ Current Meters and PIES, Final Report. Volume II: Technical Report. U.S. Dept. of the Interior, Minerals Management Service, Gulf of Mexico OCS Region, New Orleans, LA. OCS Study MMS 2003-049. 100 pp.
- Harris, F.J. 1978. Use of windows for harmonic-analysis with discrete Fourier-transform. *Proceedings of the IEEE* 66(1):51-83.
- Hendricks, J.R., G.H. Born, C. Koblinsky, and R.R. Leben. 1996. EOF analysis of global TOPEX/POSEIDON data and implications for detection of global sea level rise. *J. Geophys. Res.* 101:14131-14146.
- Hendry, R.M., D.R. Watts, and C.S. Meinen. 2002. Newfoundland Basin sea-level variability from TOPEX/POSEIDON altimetry and inverted echo sounder - bottom pressure measurements. *Can. J. Remote Sensing* 28:544-555.
- Hetland, R.D., Y. Hsueh, R.R. Leben, and P.P. Niiler. 1999. A Loop Current-induced jet along the edge of the west Florida shelf. *Geophys. Res. Lett.* 26:2239-2242.
- Hogg, N.G. 2000. Low-frequency variability on the western flanks of the grand banks. *J. Mar. Res.* 58:523-545.
- Hooker, S.B., E.R. Firestone, J.G. Acker, J.W. Campbell, J.M. Blaisdell, and M. Darzi. 1995. Level-3 SeaWiFS data products: Spatial and temporal binning algorithms. In: SeaWiFS Technical Report Series. Vol. 32. NASA Tech. Memorandum 104566. Greenbelt, MD. NASA Goddard Space Flight Center.
- Inoue, M. and S.E. Welsh. 1997. Numerical simulation of Gulf of Mexico circulation under present and glacial climatic conditions. U. S. Dept. of the Interior, Minerals Management Service, Gulf of Mexico OCS Region, New Orleans, La. OCS Study MMS 96-0067. Pp146.
- Kantha, L., J.-K. Choi, K.J. Schaudt, and C.K. Cooper. 2005. A regional data assimilation model for operational use in the Gulf of Mexico. In: Sturges, W. and A. Lugo-Fernandez, eds. *Circulation in the Gulf of Mexico: Observations and models*. Washington, DC.: American Geophysical Union.
- Kirwan, A.D., Jr., W.J. Merrell Jr., J.K. Lewis, and R.E. Whitaker. 1984. Lagrangian observations of an anticyclonic ring in the western Gulf of Mexico. *J. Geophys. Res.* 89:3417-3424.
- Klink, J. 1999. *dynmodes.m*. Matlab script. klinck@ccpo.odu.edu.
- Koblinsky, C.J., B.D. Beckley, R.D. Ray, Y.-M. Wang, and A. Brenner. 1999. NASA Ocean altimeter pathfinder project. Report 1: Data processing handbook. NASA/TM-1998-208605.
- LeBlond, P.H. and L.A. Mysak. 1978. *Waves in the Ocean*. New York: Elsevier.

- Leben, R.R. 2005. Altimeter-derived Loop Current metrics. In: Sturges, W., and A. Lugo-Fernández, eds. *Circulation in the Gulf of Mexico: Observations and Models*. Washington, DC.: American Geophysical Union. Pp. 181-201.
- Leben R.R., G.H. Born, and B.R. Engebret. 2002. Operational altimeter data processing for mesoscale monitoring. *Marine Geodesy* 25:3-18.
- Lee, T.N. and L.P. Atkinson. 1983. Low-frequency current and temperature variability from Gulf Stream frontal eddies and atmospheric forcing along the southeast U.S. outer continental shelf. *J. Geophys. Res.* 88:4541-4567.
- Lee, T.N., K. Leaman, E. Williams, T. Berger, and L. Atkinson. 1995. Florida Current meanders and gyre formation in the southern Straits of Florida. *J. Geophys. Res.* 100:8607-8620.
- McWilliams, J.C. 2006. *Fundamentals of Geophysical Fluid Dynamics*. Cambridge, U.K.: Cambridge University Press.
- Malanotte-Rizzoli, P., D.B. Haidvogel, and R.E. Young. 1987. Numerical simulation of transient boundary-forced radiation, Part I: The linear regime. *J. Phys. Oceanogr.* 17:1439-1457.
- Malanotte-Rizzoli, P., N.G. Hogg, and R.E. Young. 1995. Stochastic wave radiation by the Gulf Stream: numerical experiments. *Deep Sea Res.* 42:389-423.
- Meinen, C.S. and D.R. Watts. 1998. Calibrating inverted echo sounders equipped with pressure sensors. *J. Atmos. Oceanic Technol.* 15:1339-1345.
- Meinen, C.S. and D.R. Watts. 2000. Vertical structure and transport on a transect across the North Atlantic Current near 42 degree N: Time series and mean. *Journal of Geophysical Research.* 105(C9):21869-21891.
- Merrifield, M.A. and C.D. Winant. 1989. Shelf circulation in the Gulf of California: A description of the variability. *J. Geophys. Res.* 94:18133-18160.
- Mizuta, G. and N.G. Hogg. 2004. Structure of the circulation induced by a shoaling topographic wave. *J. Phys. Oceanogr.* 34:1793-1810.
- Munk, W.H. and D.E. Cartwright. 1966. Tidal spectroscopy and prediction. *Philosophical Transactions of the Royal Society of London* 259(A):533-581.
- North, G.R., T.L. Bell, R.F. Calahan, and F.J. Moeng. 1982. Sampling errors in the estimation of empirical orthogonal functions. *Mon. Weather Rev.* 110:699-706.
- Nowlin, W.D., J.S. Bottero, and R.D. Pillsbury. 1982. Observations of the principal tidal currents at Drake Passage. *Journal of Geophysical Research – Oceans and Atmospheres* 87(NC8):5752-5770.

- Nowlin, W.D. Jr., A.E. Jochens, R.O. Reid, and S.F. DiMarco. 1998a. Texas-Louisiana Shelf Circulation and Transport Processes Study. Synthesis Report. Volume I: Technical Report. U.S. Dept. of the Interior, Minerals Management Service, Gulf of Mexico OCS Region, New Orleans, LA. OCS Study MMS 98-0035. 502 pp.
- Nowlin, W.D. Jr., A.E. Jochens, R.O. Reid, and S.F. DiMarco. 1998b. Texas-Louisiana Shelf Circulation and Transport Processes Study: Synthesis Report, Volume II: Appendices. U.S. Dept. of the Interior, Minerals Management Service, Gulf of Mexico OCS Region, New Orleans, LA. OCS Study MMS 98-0036. 288 pp.
- Nowlin, W.D., Jr., A.E. Jochens, S.F. DiMarco, R.O. Reid, and M.K. Howard. 2001. Deepwater physical oceanography reanalysis and synthesis of historical data. Synthesis Report. U.S. Dept. of the Interior, Minerals Management Service, Gulf of Mexico OCS Region, New Orleans, LA. OCS Study MMS 2001-064. 528 pp.
- O'Reilly, J.E., S. Maritorena, B.G. Mitchell, D. Siegel, K. Carder, S. Garver, M. Kahru, and C. McClain. 1998. Ocean color chlorophyll algorithms for SeaWiFS. *J. Geophys. Res.* 103:24937-24953.
- Oey, L.-Y. 1996. Simulation of mesoscale variability in the Gulf of Mexico: sensitivity studies, comparison with observations, and trapped wave propagation. *J. Phys. Oceanogr.* 26:145-175.
- Oey, L.-Y. and H.-C. Lee. 2002. Deep eddy energy and topographic Rossby waves in the Gulf of Mexico. *J. Phys. Oceanogr.* 32:3499-3527.
- Park, J.-H. and D.R. Watts. 2006. Near 5-day nonisostatic response of the Atlantic Ocean to atmospheric surface pressure deduced from sub-surface and bottom pressure measurements. *Geophysical Research Letters* 33:L12610. doi:10.1029/2006GL026304.
- Parke, M.E., R.H. Stewart, D.L. Farless, and D.E. Cartwright. 1987. On the choice of orbits for an altimetric satellite to study ocean circulation and tides. *J. Geophys. Res.* 92:11693-11707.
- Parke, M.E., G. Born, R. Leben, C. McLaughlin, and C. Tierney. 1998. Altimeter sampling characteristics using a single satellite. *J. Geophys. Res.* 103:10513-10526.
- Pedder, M.A. 1993. Interpolation and filtering of spatial observations using successive corrections and Gaussian filters. *Mon. Weather Rev.* 121:2889-2902.
- Pickart, R.S. 1995. Gulf Stream-generated topographic Rossby waves. *J. Phys. Oceanogr.* 25:574-586.
- Preisendorfer, R.W. 1988. *Principal Component Analysis in Meteorology and Oceanography*. Amsterdam: Elsevier.

- Press, W.H., S.A. Teukolsky, W.T. Vettering, and B.P. Flannery. 1992. Numerical recipes in FORTRAN, the art of scientific computing. New York: Cambridge University Press. 963 pp.
- Rhines, P.B. 1970. Edge-, bottom-, and Rossby waves in a rotating stratified fluid. *Geophys. Fluid Dyn.* 1:273-302.
- Rossby, T., D. Dorson, and J. Fontaine. 1986. The RAFOS system. *J. Atmos. Oceanic Technol.* 3:672-679.
- Sheinbaum, J., A. Badan, J. Ochoa, J. Candela, D. Rivas, and J.I. González. 2007. Full-water column current observations in the central Gulf of Mexico: Final Report. U.S. Dept. of the Interior, Minerals Management Service, Gulf of Mexico, OCS Region. New Orleans, LA. OCS Study MMS 2007-022. 58 pp.
- Schlax, M.G. and D.B. Chelton. 1994. Detecting aliased tidal errors in altimeter height measurements. *J. Geophys. Res.* 99:12603-12612.
- Sturges, W. 1994. The frequency of ring separations from the Loop Current. *J. Geophys. Oceanogr.* 24:1647-1651.
- Sturges, W. and J.C. Evans. 1983. On the variability of the Loop Current in the Gulf of Mexico. *J. Mar. Res.* 41:639-653.
- Sturges, W. and R. Leben. 2000. Frequency of ring separations from the Loop Current in the Gulf of Mexico: a revised estimate. *J. Phys. Oceanogr.* 30:1814-1819.
- Sturges, W., J.C. Evans, S. Welsh, and W. Holland. 1993. Separation of warm core rings in the Gulf of Mexico. *J. Phys. Oceanogr.* 23(2):250-286.
- Teague, W.J., E. Jarosz, D.W. Wang, and D.A. Mitchell. 2007. Observed Oceanic Response over the Upper Continental Slope and Outer Shelf during Hurricane Ivan. *J. Phys. Oceanogr.* 37:2181-2206.
- Tierney, C.C., M.E. Parke, and G.H. Born. 1998. An investigation of ocean tides derived from along-track altimetry. *J. Geophys. Res.* 103:10273-10287.
- Torrence, C. and G.P. Compo. 1998. A Practical Guide to Wavelet Analysis. *Bulletin American Meteorological Society* 79:61-78.
- Vukovich, F.M. 1986. Aspects of the behavior of cold perturbations in the eastern Gulf of Mexico: A case study. *J. Phys. Oceanogr.* 16:175-188.
- Vukovich, F.M. 1988. On the formation of elongated cold perturbations off the Dry Tortugas. *J. Phys. Oceanogr.* 18:1051-1059.
- Vukovich, F.M. and G.A. Maul. 1985. Cyclonic eddies in the eastern Gulf of Mexico. *J. Phys. Oceanogr.* 15:105-117.

- Walker, N.D., R.R. Leben, and S. Balasubramanian. 2005. Hurricane-forced upwelling and chlorophyll a enhancement within cold-core cyclones in the Gulf of Mexico. *Geophys. Res. Lett.* 32(L18610):1-5.
- Wang, Y.M. 2001. GSFC00 mean sea surface, gravity anomaly and vertical gravity gradient from satellite altimeter data. *J. Geophys. Res.* 106:31167-31174.
- Watts, D.R. and H. Kontoyiannis. 1990. Deep-ocean bottom pressure measurement: Drift removal and performance. *Journal of Atmospheric and Oceanic Technology* 7:296-306.
- Watts, D.R., K.L. Tracey, and A.I. Friedlander. 1989. Producing accurate maps of the Gulf Stream thermal front using objective analysis. *Journal of Geophysical Research* 94(C6):8040-8052.
- Watts, D.R., X. Qian, and K.L. Tracey. 2001. Mapping abyssal current and pressure fields under the meandering Gulf Stream. *Journal of Atmospheric and Oceanic Technology* 18:1052-1067.
- Welsh, S.E. and M. Inoue. 2000. Loop Current rings and the deep circulation in the Gulf of Mexico. *J. Geophys. Res.* 105(C7):16951-16959.
- Wunsch, C. 1997. The vertical partition of oceanic horizontal kinetic energy. *J. Phys. Oceanogr.* 27(8):1770-1794.
- Zavala-Hidalgo, J., S.L. Morey, and J.J. O'Brien. 2003. Cyclonic eddies northeast of the Campeche Bank from altimetry data. *J. Phys. Oceanogr.* 33:623-629.

APPENDIX A
Hurricanes and Tropical Storm Events

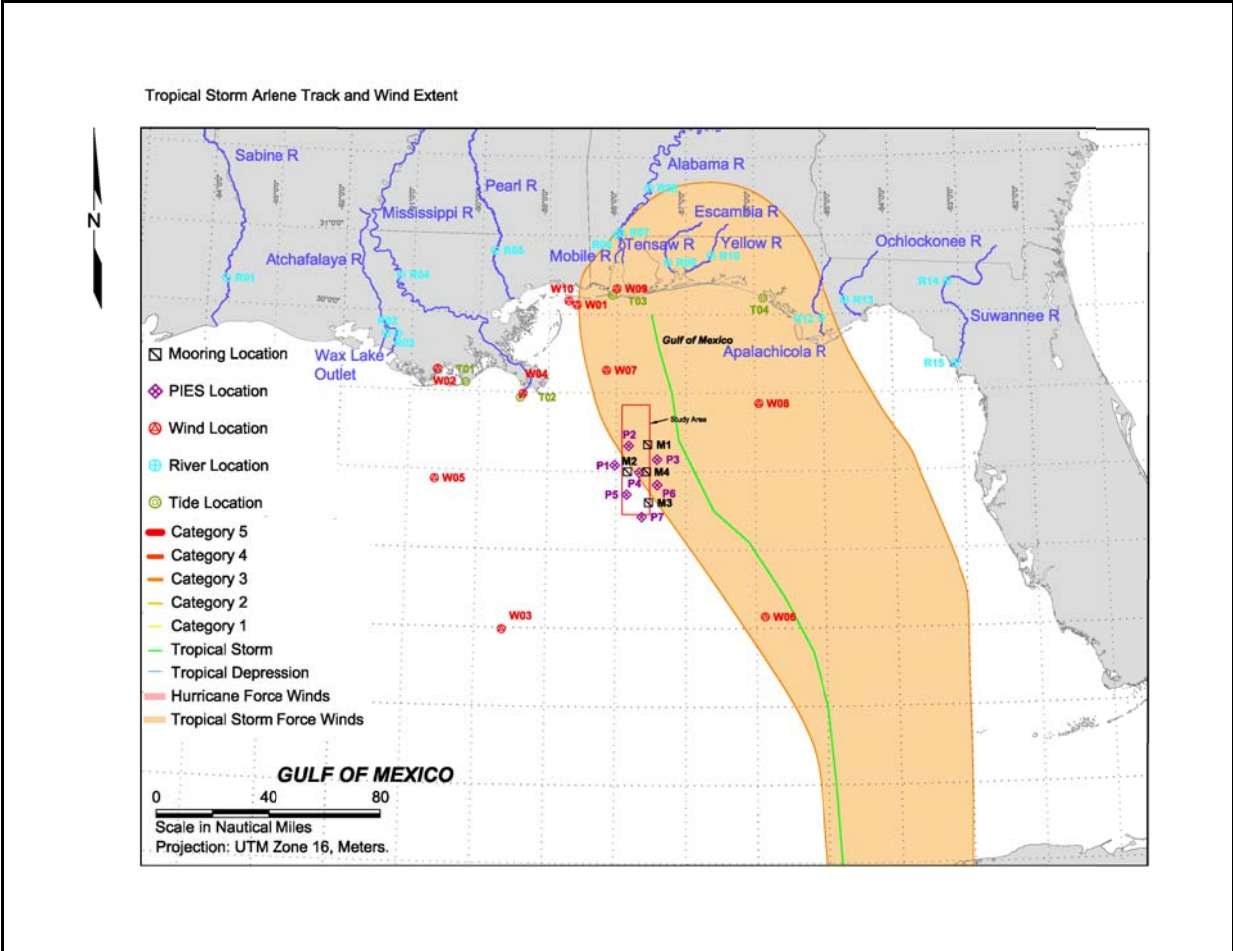


Figure A-1. Storm track and wind extent of tropical storm Arlene.

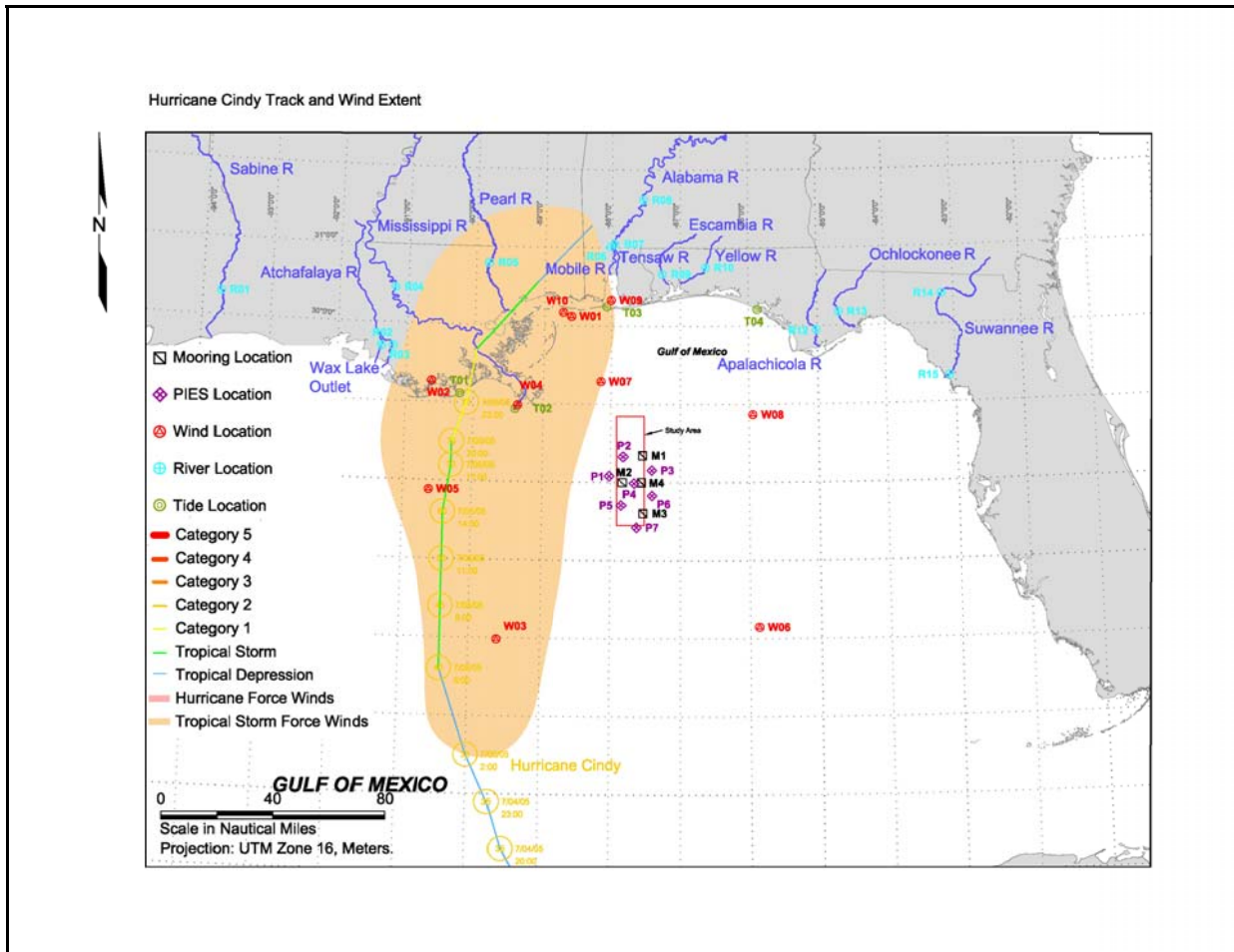


Figure A-2. Storm track and wind extent of hurricane Cindy.

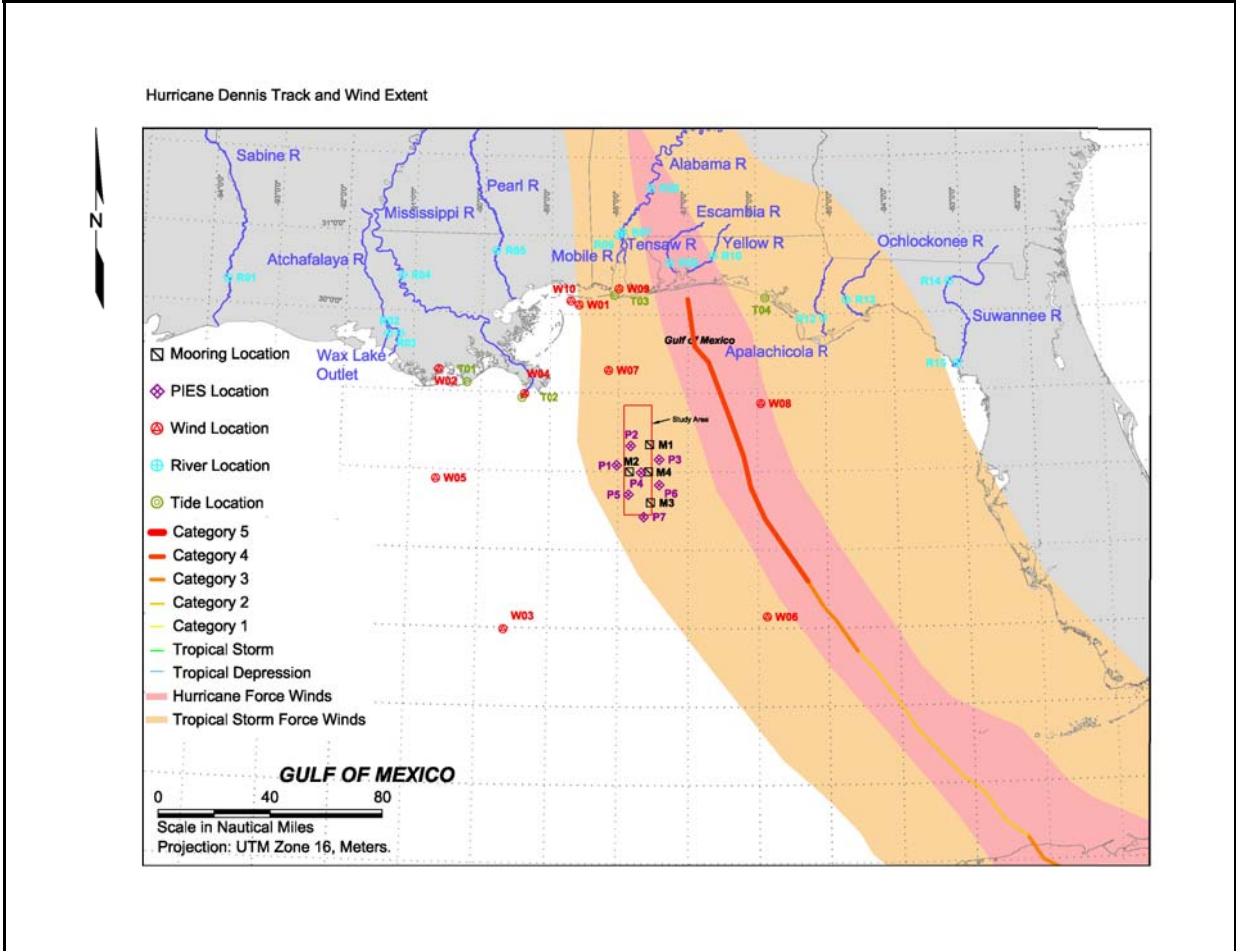


Figure A-3. Storm track and wind extent of hurricane Dennis.

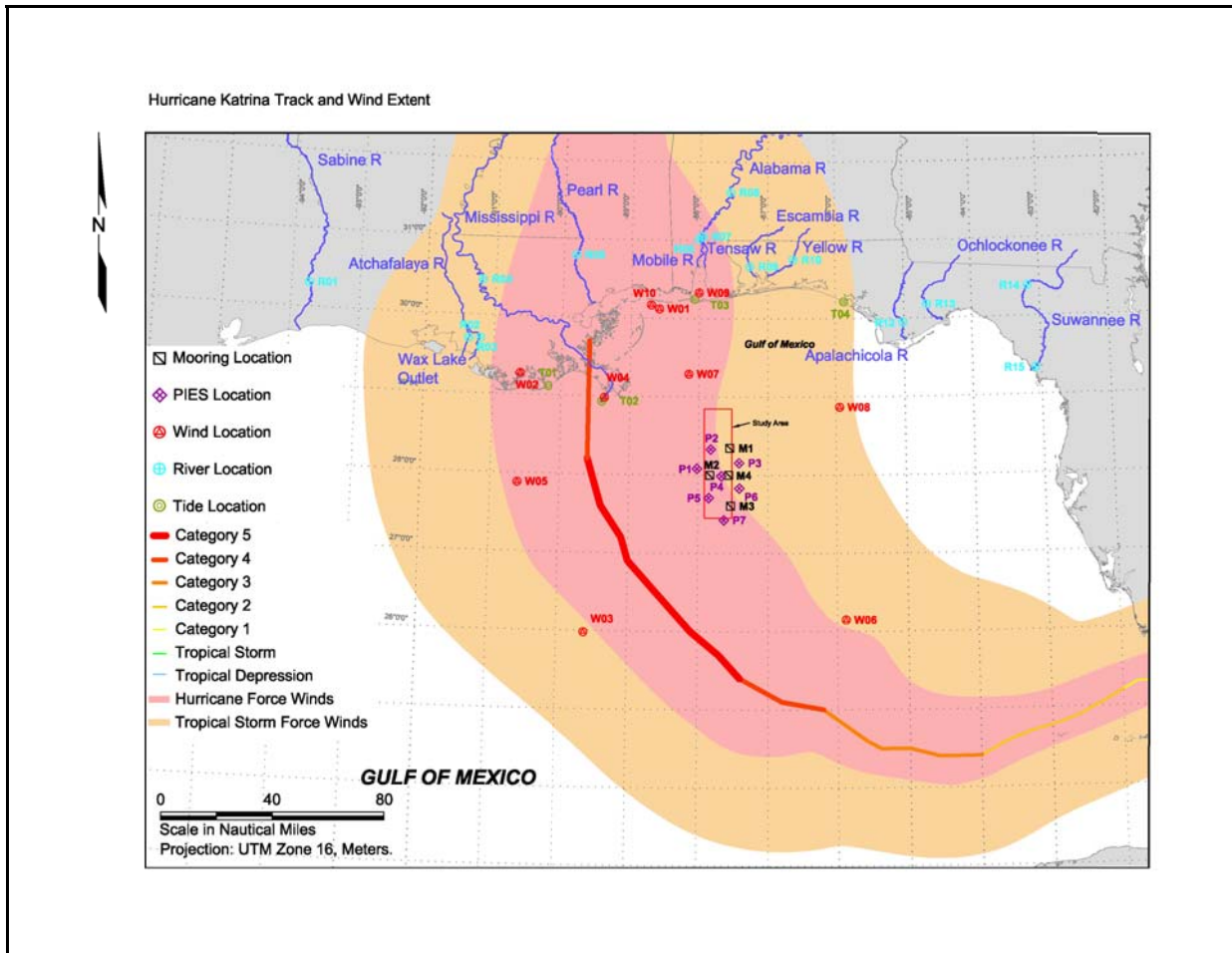


Figure A-4. Storm track and wind extent of hurricane Katrina.

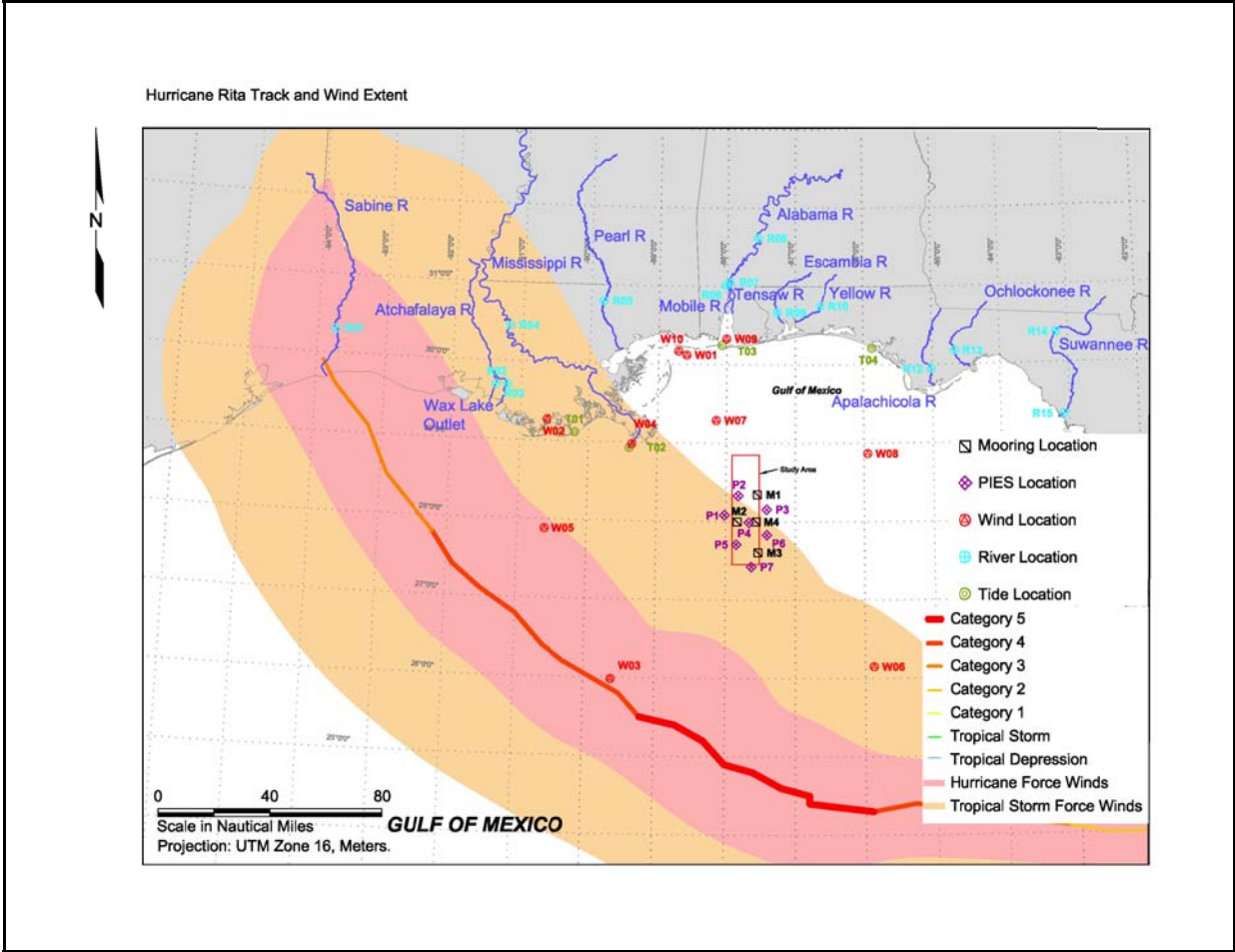


Figure A-5. Storm track and wind extent of hurricane Rita.

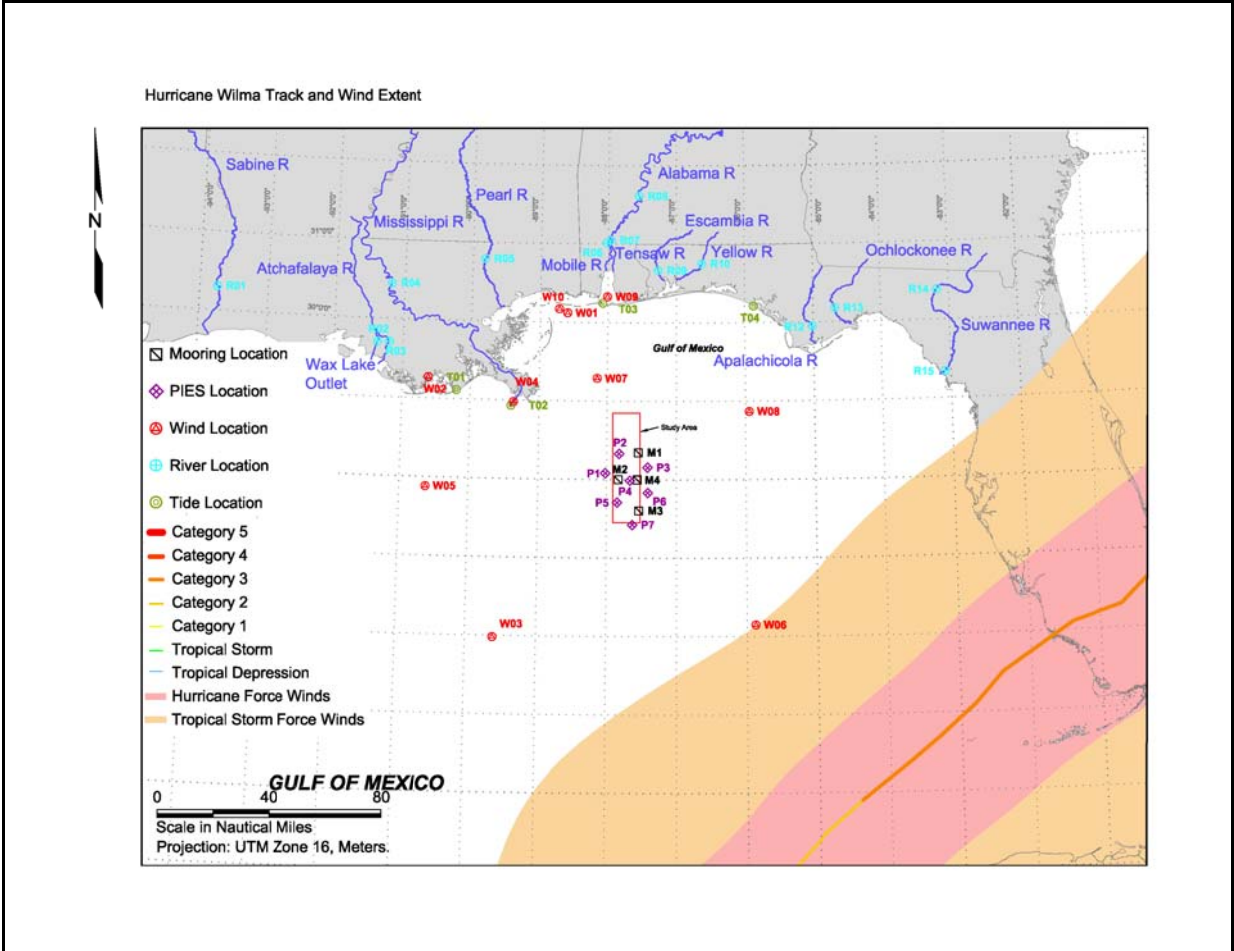


Figure A-6. Storm track and wind extent of hurricane Wilma.

APPENDIX B
Color Vector Plots of Current Magnitude and Direction

Currents as measured from the ADCP and single point current meters are displayed as vector plots of current speed (cm s^{-1}) and direction. This displays the magnitude and direction the current is going toward from both the ADCP and single point instruments on Moorings 1-4. These plots cover the entire length of the mooring. The bins selected for display are referenced to meters depth.

Grey lines in the figures show the closest passing of storms and loop current events. A list of the events can be found in Table 3.1-3. Abbreviations used in the figure annotations are as follows: E for Eddy, D for detachment, R for reattachment, FD for final detachment, LC for Loop Current, and LCFE for Loop Current Frontal Eddy. Multiple events of the same type are numbered in chronological order (i.e. LC1 is Loop Current event 1).

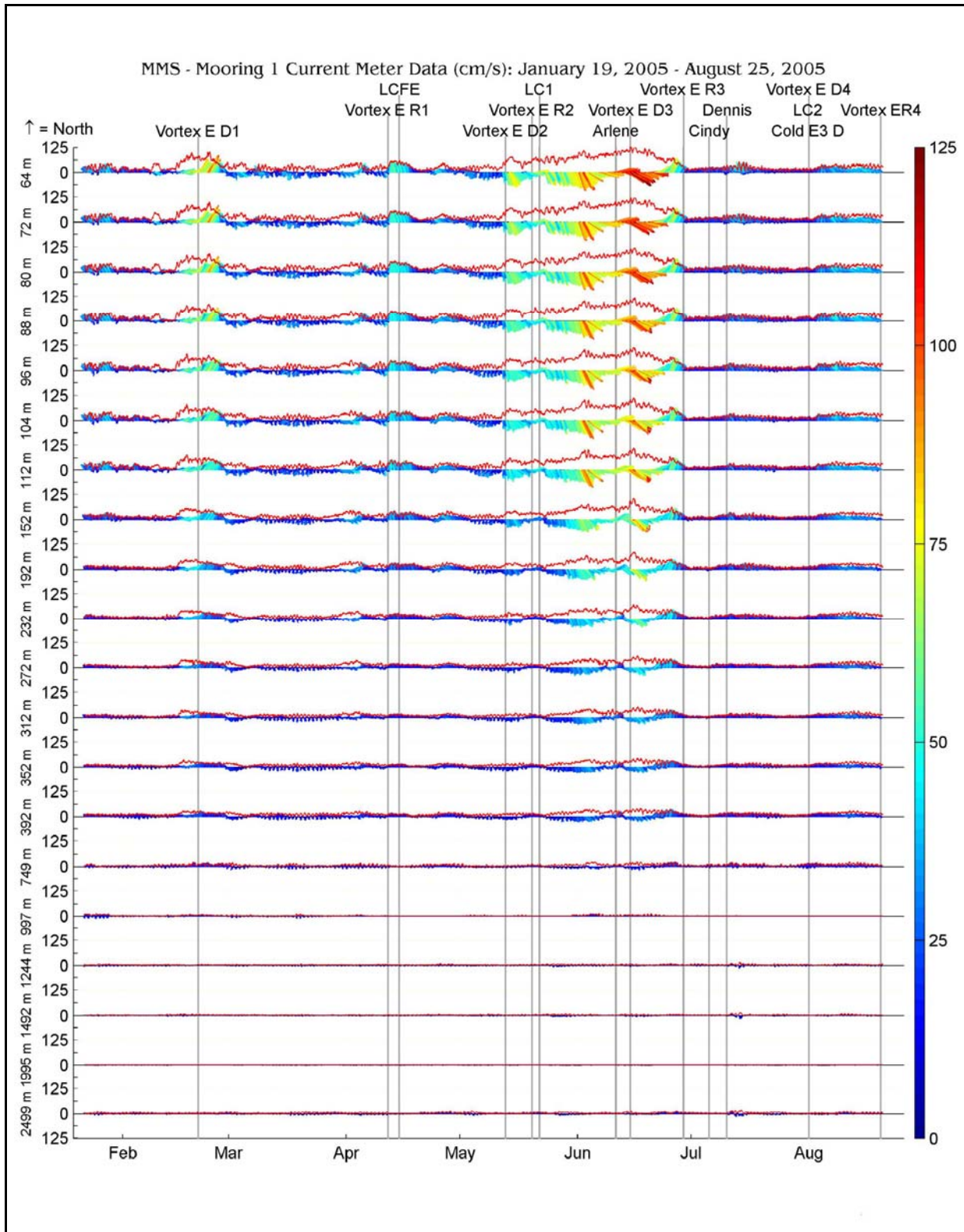


Figure B-1. Mooring 1 current vectors for Deployment 1.

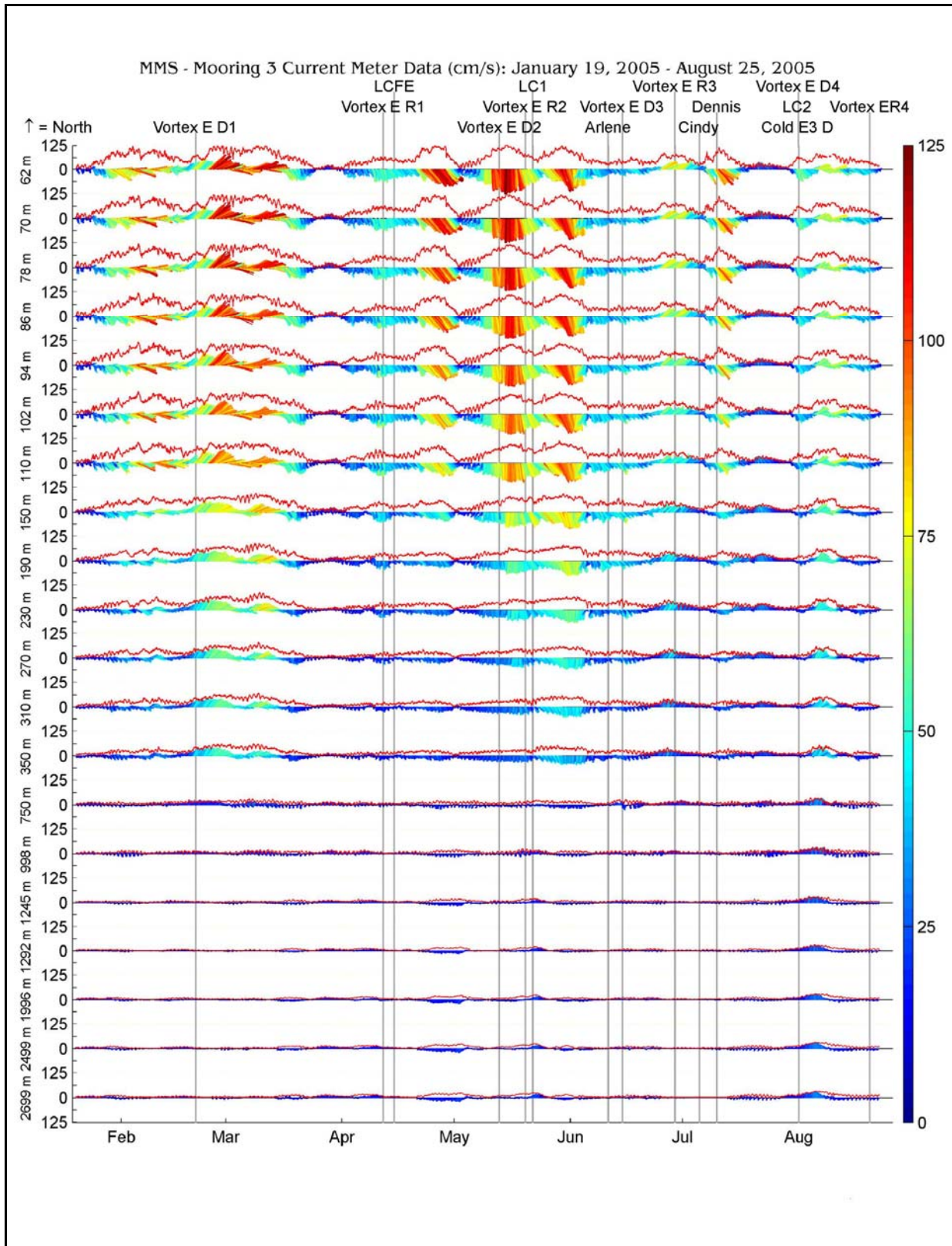


Figure B-5. Mooring 3 current vectors for Deployment 1.

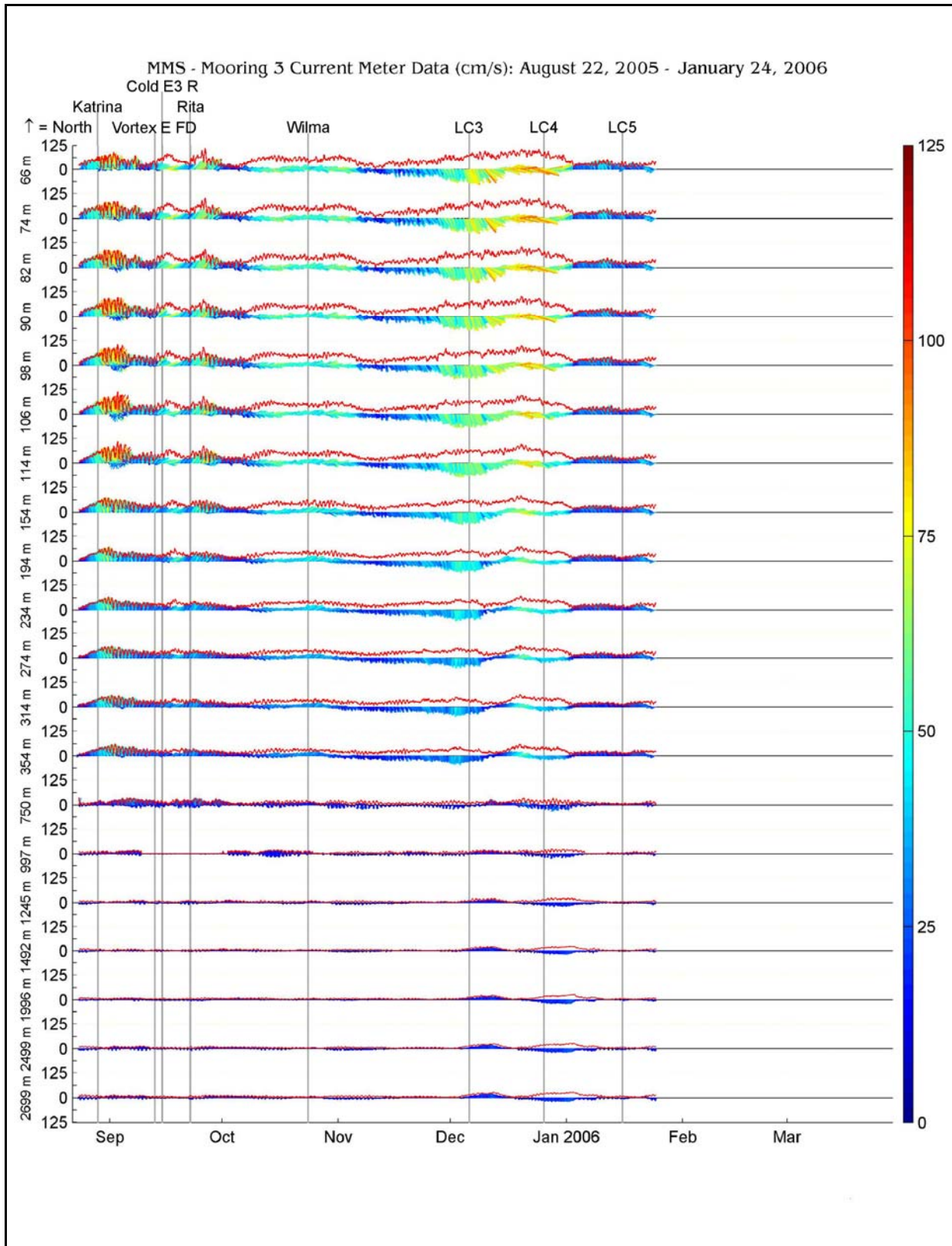


Figure B-6. Mooring 3 current vectors for Deployment 2.

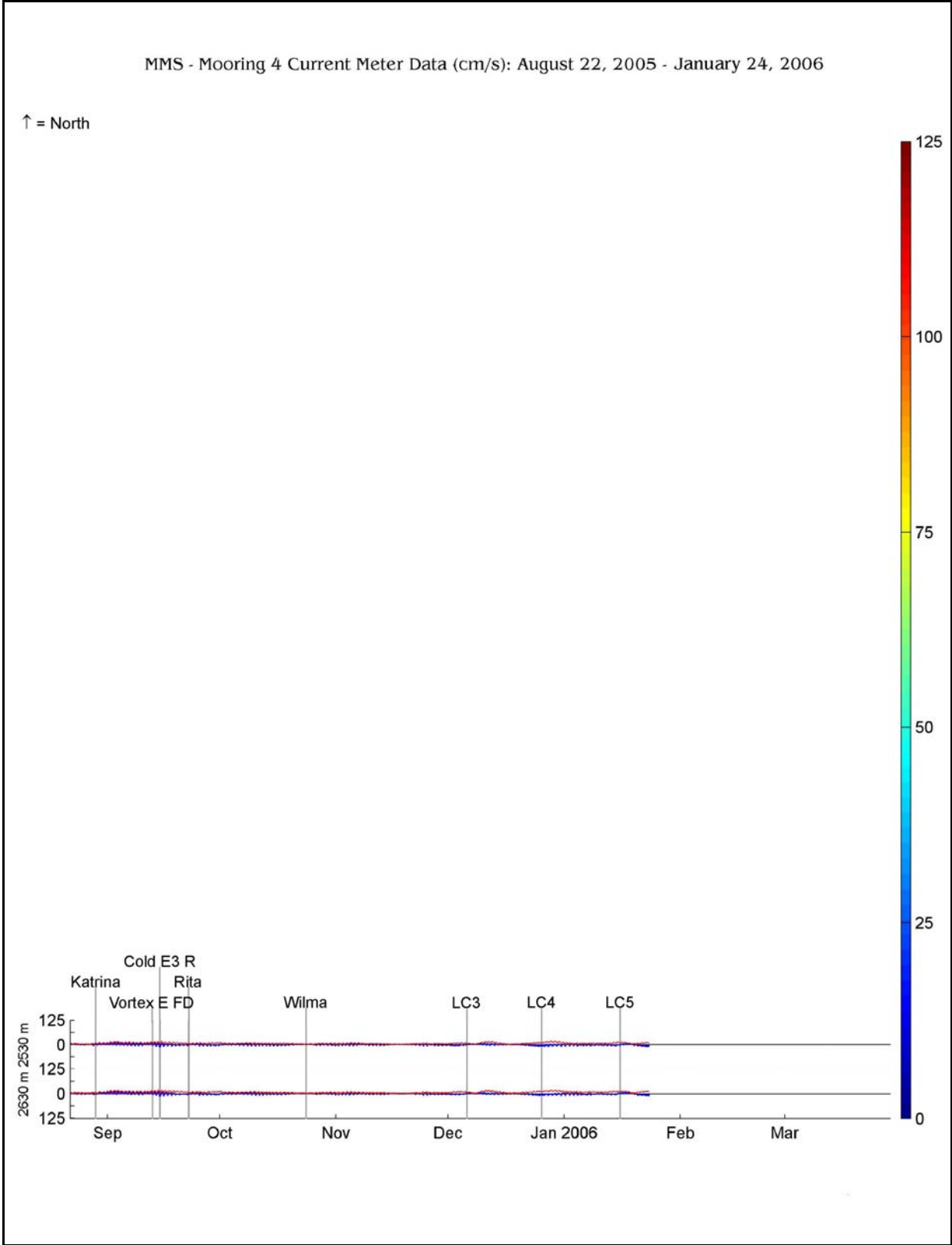


Figure B-8. Mooring 4 current vectors for Deployment 2.

APPENDIX C
Basic Statistics for Current Measurements

Statistics for the u and v components of the current speed are presented as tables for Moorings 1-4. The statistics calculated were minimum, maximum, mean and standard deviation.

Table C-1

Statistics from Mooring 1 Deployment 1 ADCP for the u and v components of the currents measured.

Instrument	Serial Number	Bin Depth	N	Parameter	Minimum	Maximum	Mean	Standard Deviation
RDI Broadband 75 kHz Long-Ranger ADCP	1307	40 - 48 m	0	u (cm/s)	*****	*****	*****	*****
				v (cm/s)	*****	*****	*****	*****
RDI Broadband 75 kHz Long-Ranger ADCP	1307	48 - 56 m	4059	u (cm/s)	-50.06	74.82	1.831	21.676
				v (cm/s)	-63.05	62.8	5.92	20.839
RDI Broadband 75 kHz Long-Ranger ADCP	1307	56 - 64 m	4392	u (cm/s)	-49.25	94.02	4.807	24.208
				v (cm/s)	-86.03	77.1	5.185	23.211
RDI Broadband 75 kHz Long-Ranger ADCP	1307	64 - 72 m	4646	u (cm/s)	-44.7	113.22	8.177	28.235
				v (cm/s)	-75.97	78.52	4.981	23.86
RDI Broadband 75 kHz Long-Ranger ADCP	1307	72 - 80 m	4893	u (cm/s)	-44.51	119.95	11.01	31.34
				v (cm/s)	-96.34	87.13	3.582	25.041
RDI Broadband 75 kHz Long-Ranger ADCP	1307	80 - 88 m	4965	u (cm/s)	-43.14	119.57	11.35	31.686
				v (cm/s)	-92.42	86.6	3.187	24.839
RDI Broadband 75 kHz Long-Ranger ADCP	1307	88 - 96 m	5001	u (cm/s)	-44.55	120.15	11.292	31.536
				v (cm/s)	-92	80.83	2.939	24.13
RDI Broadband 75 kHz Long-Ranger ADCP	1307	96 - 104 m	5019	u (cm/s)	-40.68	135.86	10.89	30.863
				v (cm/s)	-90.71	69.06	2.836	23.45
RDI Broadband 75 kHz Long-Ranger ADCP	1307	104 - 112 m	5039	u (cm/s)	-41.13	131.67	10.367	30.35
				v (cm/s)	-90.28	67.62	2.823	22.907
RDI Broadband 75 kHz Long-Ranger ADCP	1307	112 - 120 m	5050	u (cm/s)	-37.33	130.51	9.816	29.561
				v (cm/s)	-92.16	63.62	2.886	22.178
RDI Broadband 75 kHz Long-Ranger ADCP	1307	120 - 128 m	5057	u (cm/s)	-39.68	129.23	9.326	28.642
				v (cm/s)	-95.15	63.54	2.802	21.324
RDI Broadband 75 kHz Long-Ranger ADCP	1307	128 - 136 m	5057	u (cm/s)	-45.89	121.9	8.771	27.45
				v (cm/s)	-92.6	60.73	2.717	20.526
RDI Broadband 75 kHz Long-Ranger ADCP	1307	136 - 144 m	5057	u (cm/s)	-41.06	116.53	8.22	26.309
				v (cm/s)	-89.56	60.85	2.707	19.892
RDI Broadband 75 kHz Long-Ranger ADCP	1307	144 - 152 m	5057	u (cm/s)	-41.35	114.15	7.642	25.222
				v (cm/s)	-83.49	60.05	2.682	19.231
RDI Broadband 75 kHz Long-Ranger ADCP	1307	152 - 160 m	5057	u (cm/s)	-42.7	109.83	7.145	24.324
				v (cm/s)	-71.8	59.7	2.727	18.462
RDI Broadband 75 kHz Long-Ranger ADCP	1307	160 - 168 m	5057	u (cm/s)	-38.36	109.37	6.755	23.474
				v (cm/s)	-68.52	53.92	2.754	17.811
RDI Broadband 75 kHz Long-Ranger ADCP	1307	168 - 176 m	5057	u (cm/s)	-37.66	112.45	6.526	22.901
				v (cm/s)	-64.92	52.27	2.725	17.429
RDI Broadband 75 kHz Long-Ranger ADCP	1307	176 - 184 m	5057	u (cm/s)	-37.17	106.98	6.136	22.196
				v (cm/s)	-62.19	51.35	2.68	17.018
RDI Broadband 75 kHz Long-Ranger ADCP	1307	184 - 192 m	5057	u (cm/s)	-34.95	103.96	5.823	21.534
				v (cm/s)	-61.25	51.21	2.635	16.633
RDI Broadband 75 kHz Long-Ranger ADCP	1307	192 - 200 m	5057	u (cm/s)	-35.8	105.98	5.573	21.032
				v (cm/s)	-63.71	50.31	2.636	16.178
RDI Broadband 75 kHz Long-Ranger ADCP	1307	200 - 208 m	5057	u (cm/s)	-34.05	106.51	5.39	20.36
				v (cm/s)	-62.78	51.43	2.575	15.749
RDI Broadband 75 kHz Long-Ranger ADCP	1307	208 - 216 m	5057	u (cm/s)	-35.2	102.85	5.167	19.568
				v (cm/s)	-63.39	50.51	2.426	15.151
RDI Broadband 75 kHz Long-Ranger ADCP	1307	216 - 224 m	5057	u (cm/s)	-37.75	102.11	4.776	19.257
				v (cm/s)	-61.48	47.97	2.472	14.956
RDI Broadband 75 kHz Long-Ranger ADCP	1307	224 - 232 m	5057	u (cm/s)	-39.3	100.7	4.589	18.838
				v (cm/s)	-60.27	48.58	2.469	14.691
RDI Broadband 75 kHz Long-Ranger ADCP	1307	232 - 240 m	5057	u (cm/s)	-41.37	97.11	4.361	18.309
				v (cm/s)	-58.69	46.31	2.497	14.353
RDI Broadband 75 kHz Long-Ranger ADCP	1307	240 - 248 m	5057	u (cm/s)	-36.94	94.81	4.194	17.824
				v (cm/s)	-55.2	48.98	2.467	13.94

Table C-1. Statistics from Mooring 1 Deployment 1 ADCP for the u and v components of the currents measured (continued).

Instrument	Serial Number	Bin Depth	N	Parameter	Minimum	Maximum	Mean	Standard Deviation
RDI Broadband 75 kHz Long-Ranger ADCP	1307	248 - 256 m	5057	u (cm/s)	-36.99	90.21	3.945	17.346
				v (cm/s)	-53.56	46.22	2.392	13.417
RDI Broadband 75 kHz Long-Ranger ADCP	1307	256 - 264 m	5057	u (cm/s)	-36.79	90.7	3.797	16.812
				v (cm/s)	-55.87	49.83	2.408	13.011
RDI Broadband 75 kHz Long-Ranger ADCP	1307	264 - 272 m	5057	u (cm/s)	-32.93	80.5	3.539	16.211
				v (cm/s)	-50.14	47.41	2.399	12.639
RDI Broadband 75 kHz Long-Ranger ADCP	1307	272 - 280 m	5057	u (cm/s)	-33.29	80.12	3.475	15.786
				v (cm/s)	-50.48	47.33	2.38	12.307
RDI Broadband 75 kHz Long-Ranger ADCP	1307	280 - 288 m	5057	u (cm/s)	-33.86	75.3	3.233	15.397
				v (cm/s)	-49.64	43.1	2.31	12.004
RDI Broadband 75 kHz Long-Ranger ADCP	1307	288 - 296 m	5057	u (cm/s)	-34.41	73.89	3.018	15.013
				v (cm/s)	-46.45	41.99	2.238	11.739
RDI Broadband 75 kHz Long-Ranger ADCP	1307	296 - 304 m	5057	u (cm/s)	-33.23	68.6	2.895	14.724
				v (cm/s)	-45.32	40.37	2.236	11.585
RDI Broadband 75 kHz Long-Ranger ADCP	1307	304 - 312 m	5057	u (cm/s)	-32.98	66.55	2.774	14.401
				v (cm/s)	-43.03	38.64	2.218	11.423
RDI Broadband 75 kHz Long-Ranger ADCP	1307	312 - 320 m	5057	u (cm/s)	-32.55	64.42	2.654	14.219
				v (cm/s)	-41.48	39.11	2.198	11.246
RDI Broadband 75 kHz Long-Ranger ADCP	1307	320 - 328 m	5057	u (cm/s)	-32.56	59.84	2.575	13.934
				v (cm/s)	-39.08	40.02	2.202	11.033
RDI Broadband 75 kHz Long-Ranger ADCP	1307	328 - 336 m	5057	u (cm/s)	-32.47	56.88	2.422	13.751
				v (cm/s)	-37.32	38.75	2.187	10.896
RDI Broadband 75 kHz Long-Ranger ADCP	1307	336 - 344 m	5057	u (cm/s)	-31.84	52.66	2.304	13.502
				v (cm/s)	-35.29	37.27	2.196	10.759
RDI Broadband 75 kHz Long-Ranger ADCP	1307	344 - 352 m	5057	u (cm/s)	-32.41	49.6	2.243	13.275
				v (cm/s)	-35.9	37.94	2.142	10.605
RDI Broadband 75 kHz Long-Ranger ADCP	1307	352 - 360 m	5057	u (cm/s)	-30.42	49.42	2.169	13.129
				v (cm/s)	-36.29	36.61	2.084	10.329
RDI Broadband 75 kHz Long-Ranger ADCP	1307	360 - 368 m	5057	u (cm/s)	-28.11	48.04	2.17	13.002
				v (cm/s)	-36.84	34.66	2.088	10.18
RDI Broadband 75 kHz Long-Ranger ADCP	1307	368 - 376 m	5057	u (cm/s)	-29.21	49.54	2.11	12.792
				v (cm/s)	-33.91	34.87	1.932	10.049
RDI Broadband 75 kHz Long-Ranger ADCP	1307	376 - 384 m	5057	u (cm/s)	-28.81	47.91	2.079	12.497
				v (cm/s)	-35.42	35.2	1.917	9.893
RDI Broadband 75 kHz Long-Ranger ADCP	1307	384 - 392 m	5057	u (cm/s)	-28.43	48.1	1.939	12.173
				v (cm/s)	-32.73	36.5	1.882	9.775
RDI Broadband 75 kHz Long-Ranger ADCP	1307	392 - 400 m	5057	u (cm/s)	-28.7	43.25	1.795	11.926
				v (cm/s)	-31.67	41.09	1.949	9.642
RDI Broadband 75 kHz Long-Ranger ADCP	1307	400 - 408 m	5057	u (cm/s)	-27.88	44.33	1.717	11.669
				v (cm/s)	-30.03	37.8	1.915	9.495
RDI Broadband 75 kHz Long-Ranger ADCP	1307	408 - 416 m	5057	u (cm/s)	-28.66	41.64	1.636	11.455
				v (cm/s)	-27.66	38.81	1.852	9.324
RDI Broadband 75 kHz Long-Ranger ADCP	1307	416 - 424 m	5057	u (cm/s)	-30.18	41.37	1.591	11.209
				v (cm/s)	-26.74	38.87	1.849	9.041
RDI Broadband 75 kHz Long-Ranger ADCP	1307	424 - 432 m	5057	u (cm/s)	-29.35	41.27	1.542	10.982
				v (cm/s)	-28.26	34.95	1.782	8.844

Table C-2

Statistics from Mooring 1 Deployment 1 single point current meters for the u and v components of the currents measured.

Instrument	Serial Number	Depth	N	Parameter	Minimum	Maximum	Mean	Standard Deviation
S4	78017	0749 m	5056	u (cm/s)	-22.28	22.87	-0.201	6.552
				v (cm/s)	-19.62	24.3	1.222	5.561
Aanderaa RCM 7	7223	0997 m	1563	u (cm/s)	-12.52	10.35	0.218	2.755
				v (cm/s)	-13.08	10.5	0.569	3.467
Aanderaa RCM 7	7692	1244 m	5056	u (cm/s)	-11.56	9.16	-0.141	2.693
				v (cm/s)	-16.06	10.22	0.553	2.618
Aanderaa RCM 7	9722	1492 m	5056	u (cm/s)	-9.66	8.36	-0.022	2.159
				v (cm/s)	-14.27	10.56	0.378	2.209
Aanderaa RCM 8s	10053	1995 m	0	u (cm/s)	*****	*****	*****	*****
				v (cm/s)	*****	*****	*****	*****
Aanderaa RCM 8	12085	2499 m	5056	u (cm/s)	-9.46	12.85	0.047	2.965
				v (cm/s)	-14.97	12.82	0.479	2.97

Table C-3

Statistics from Mooring 2 Deployment 1 ADCP for the u and v components of the currents measured.

Instrument	Serial Number	Bin Depth	N	Parameter	Minimum	Maximum	Mean	Standard Deviation
RDI Broadband 75 kHz Long-Ranger ADCP	5165	30 - 38 m	0	u (cm/s) v (cm/s)	***** *****	***** *****	***** *****	***** *****
RDI Broadband 75 kHz Long-Ranger ADCP	5165	38 - 46 m	2882	u (cm/s) v (cm/s)	-47.66 -105.29	84.31 41.58	19.744 -12.678	21.21 21.955
RDI Broadband 75 kHz Long-Ranger ADCP	5165	46 - 54 m	3721	u (cm/s) v (cm/s)	-51.21 -123.75	93.53 95.71	25.216 -11.723	25.831 27.366
RDI Broadband 75 kHz Long-Ranger ADCP	5165	54 - 62 m	4172	u (cm/s) v (cm/s)	-52.68 -126.53	106.22 110.94	27.551 -10.742	28.372 32.463
RDI Broadband 75 kHz Long-Ranger ADCP	5165	62 - 70 m	4591	u (cm/s) v (cm/s)	-55.98 -125.61	107.04 107.09	29.754 -10.358	29.91 36.158
RDI Broadband 75 kHz Long-Ranger ADCP	5165	70 - 78 m	4904	u (cm/s) v (cm/s)	-55.16 -129.13	125.15 111.76	31.772 -8.007	31.296 37.525
RDI Broadband 75 kHz Long-Ranger ADCP	5165	78 - 86 m	5065	u (cm/s) v (cm/s)	-57.06 -122.63	131.02 114.81	32.438 -6.601	32.219 37.167
RDI Broadband 75 kHz Long-Ranger ADCP	5165	86 - 94 m	5111	u (cm/s) v (cm/s)	-55.65 -114.28	122.53 111.91	31.853 -6.361	32.254 36.117
RDI Broadband 75 kHz Long-Ranger ADCP	5165	94 - 102 m	5153	u (cm/s) v (cm/s)	-57.02 -111.58	121.34 103.08	31.285 -5.986	32.434 35.1
RDI Broadband 75 kHz Long-Ranger ADCP	5165	102 - 110 m	5174	u (cm/s) v (cm/s)	-55.47 -106.3	116.12 98.3	30.363 -5.565	32.232 34.137
RDI Broadband 75 kHz Long-Ranger ADCP	5165	110 - 118 m	5174	u (cm/s) v (cm/s)	-53.86 -102.82	110.87 92.26	29.159 -5.089	31.708 33.269
RDI Broadband 75 kHz Long-Ranger ADCP	5165	118 - 126 m	5174	u (cm/s) v (cm/s)	-52.56 -99.94	107.58 89.98	27.826 -4.691	31.058 32.393
RDI Broadband 75 kHz Long-Ranger ADCP	5165	126 - 134 m	5174	u (cm/s) v (cm/s)	-54.93 -93.31	107.25 80.66	26.621 -4.226	30.284 31.46
RDI Broadband 75 kHz Long-Ranger ADCP	5165	134 - 142 m	5174	u (cm/s) v (cm/s)	-54.53 -89.29	106.64 74.32	25.349 -4.008	29.441 30.457
RDI Broadband 75 kHz Long-Ranger ADCP	5165	142 - 150 m	5174	u (cm/s) v (cm/s)	-53.41 -87.27	102.33 73.18	24.07 -3.675	28.627 29.373
RDI Broadband 75 kHz Long-Ranger ADCP	5165	150 - 158 m	5174	u (cm/s) v (cm/s)	-54.28 -85.75	96.34 70.41	22.912 -3.366	27.735 28.525
RDI Broadband 75 kHz Long-Ranger ADCP	5165	158 - 166 m	5174	u (cm/s) v (cm/s)	-52.23 -83.23	93.77 70.02	21.776 -3.107	26.843 27.851
RDI Broadband 75 kHz Long-Ranger ADCP	5165	166 - 174 m	5174	u (cm/s) v (cm/s)	-51.85 -80.45	96.05 70.84	20.722 -2.797	26.101 27.213
RDI Broadband 75 kHz Long-Ranger ADCP	5165	174 - 182 m	5174	u (cm/s) v (cm/s)	-53.6 -81.96	89.31 72.89	19.852 -2.53	25.426 26.583
RDI Broadband 75 kHz Long-Ranger ADCP	5165	182 - 190 m	5174	u (cm/s) v (cm/s)	-51.74 -81.67	88.31 75.46	18.997 -2.304	24.793 25.966
RDI Broadband 75 kHz Long-Ranger ADCP	5165	190 - 198 m	5174	u (cm/s) v (cm/s)	-52.55 -80.54	89.27 76.95	18.162 -2.141	24.229 25.349
RDI Broadband 75 kHz Long-Ranger ADCP	5165	198 - 206 m	5174	u (cm/s) v (cm/s)	-53.69 -78.12	90.06 73.46	17.424 -2.082	23.713 24.764
RDI Broadband 75 kHz Long-Ranger ADCP	5165	206 - 214 m	5174	u (cm/s) v (cm/s)	-52.66 -74.46	90.13 70.5	16.856 -2.006	23.323 24.227
RDI Broadband 75 kHz Long-Ranger ADCP	5165	214 - 222 m	5174	u (cm/s) v (cm/s)	-50.27 -72.57	85.9 69.32	16.161 -1.884	22.952 23.641
RDI Broadband 75 kHz Long-Ranger ADCP	5165	222 - 230 m	5174	u (cm/s) v (cm/s)	-50.8 -70.41	85.68 74.87	15.529 -1.758	22.478 23.019
RDI Broadband 75 kHz Long-Ranger ADCP	5165	230 - 238 m	5174	u (cm/s) v (cm/s)	-48.38 -67.4	81.99 77.66	15.09 -1.649	21.995 22.529

Table C-3. Statistics from Mooring 2 Deployment 1 ADCP for the u and v components of the currents measured (continued).

Instrument	Serial Number	Bin Depth	N	Parameter	Minimum	Maximum	Mean	Standard Deviation
RDI Broadband 75 kHz Long-Ranger ADCP	5165	238 - 246 m	5174	u (cm/s)	-47.1	83.03	14.599	21.489
				v (cm/s)	-64.3	73.06	-1.563	22.018
RDI Broadband 75 kHz Long-Ranger ADCP	5165	246 - 254 m	5174	u (cm/s)	-47.56	81.43	14.099	21.012
				v (cm/s)	-62.11	75.14	-1.388	21.715
RDI Broadband 75 kHz Long-Ranger ADCP	5165	254 - 262 m	5174	u (cm/s)	-46.75	81.69	13.709	20.758
				v (cm/s)	-61.1	76.72	-1.198	21.475
RDI Broadband 75 kHz Long-Ranger ADCP	5165	262 - 270 m	5169	u (cm/s)	-49.15	80.23	13.355	20.719
				v (cm/s)	-57.44	76	-1.108	21.053
RDI Broadband 75 kHz Long-Ranger ADCP	5165	270 - 278 m	5113	u (cm/s)	-48.43	84.75	12.617	20.252
				v (cm/s)	-57.09	67.4	-0.86	20.283
RDI Broadband 75 kHz Long-Ranger ADCP	5165	278 - 286 m	4915	u (cm/s)	-45.14	78.17	11.075	18.791
				v (cm/s)	-52.51	67.02	-0.541	19.44
RDI Broadband 75 kHz Long-Ranger ADCP	5165	286 - 294 m	4800	u (cm/s)	-48.4	76.2	10.449	17.585
				v (cm/s)	-51.69	65.34	-0.492	18.927
RDI Broadband 75 kHz Long-Ranger ADCP	5165	294 - 302 m	4899	u (cm/s)	-45.76	71.8	10.937	17.607
				v (cm/s)	-51.51	64.56	-0.812	18.94
RDI Broadband 75 kHz Long-Ranger ADCP	5165	302 - 310 m	5009	u (cm/s)	-45.23	74.14	11.089	18.042
				v (cm/s)	-51.46	60.97	-1.156	18.801
RDI Broadband 75 kHz Long-Ranger ADCP	5165	310 - 318 m	5042	u (cm/s)	-43.86	73.88	11.098	17.917
				v (cm/s)	-48.96	58.12	-1.17	18.607
RDI Broadband 75 kHz Long-Ranger ADCP	5165	318 - 326 m	5087	u (cm/s)	-45.24	70.87	10.774	17.561
				v (cm/s)	-51.13	56.33	-1.049	18.235
RDI Broadband 75 kHz Long-Ranger ADCP	5165	326 - 334 m	5158	u (cm/s)	-44.96	68.6	10.413	17.447
				v (cm/s)	-47.29	55.09	-0.881	18.045
RDI Broadband 75 kHz Long-Ranger ADCP	5165	334 - 342 m	5171	u (cm/s)	-42.44	65.95	10.062	17.133
				v (cm/s)	-48.19	53	-0.735	17.816
RDI Broadband 75 kHz Long-Ranger ADCP	5165	342 - 350 m	5173	u (cm/s)	-45.77	63.7	9.806	16.745
				v (cm/s)	-46.05	54.45	-0.661	17.455
RDI Broadband 75 kHz Long-Ranger ADCP	5165	350 - 358 m	5174	u (cm/s)	-45.79	63.17	9.568	16.405
				v (cm/s)	-45.69	51.2	-0.613	17.195
RDI Broadband 75 kHz Long-Ranger ADCP	5165	358 - 366 m	5174	u (cm/s)	-47.57	59.74	9.348	15.995
				v (cm/s)	-44.98	50.77	-0.581	16.918
RDI Broadband 75 kHz Long-Ranger ADCP	5165	366 - 374 m	5174	u (cm/s)	-44.17	59.41	9.116	15.733
				v (cm/s)	-45.25	49.29	-0.594	16.565
RDI Broadband 75 kHz Long-Ranger ADCP	5165	374 - 382 m	5174	u (cm/s)	-40.45	56.81	8.788	15.38
				v (cm/s)	-44.69	49.56	-0.535	16.2
RDI Broadband 75 kHz Long-Ranger ADCP	5165	382 - 390 m	5174	u (cm/s)	-38.94	56.09	8.467	15.008
				v (cm/s)	-42.39	45.61	-0.457	15.911
RDI Broadband 75 kHz Long-Ranger ADCP	5165	390 - 398 m	5174	u (cm/s)	-39.43	58.12	8.287	14.719
				v (cm/s)	-44.04	45.39	-0.396	15.529
RDI Broadband 75 kHz Long-Ranger ADCP	5165	398 - 406 m	5174	u (cm/s)	-37.77	53.73	8.027	14.417
				v (cm/s)	-39.66	42.74	-0.359	15.131
RDI Broadband 75 kHz Long-Ranger ADCP	5165	406 - 414 m	5174	u (cm/s)	-39.19	54.22	7.755	14.053
				v (cm/s)	-39.73	43.59	-0.355	14.736
RDI Broadband 75 kHz Long-Ranger ADCP	5165	414 - 422 m	5174	u (cm/s)	-38.8	54.25	7.485	13.554
				v (cm/s)	-37.05	43.26	-0.385	14.253

Table C-4

Statistics from Mooring 2 Deployment 1 single point current meters for the u and v components of the currents measured.

Instrument	Serial Number	Depth	N	Parameter	Minimum	Maximum	Mean	Standard Deviation
S4	81617	0749 m	5174	u (cm/s)	-23.48	27.26	2.601	7.574
				v (cm/s)	-27.22	35.52	-0.062	8.115
Aanderaa RCM 7	7507	0997 m	5174	u (cm/s)	-16.55	16.41	0.579	5.071
				v (cm/s)	-13.27	22.48	-0.055	5.161
Aanderaa RCM 8s	7771	1244 m	5174	u (cm/s)	-21.81	21.18	-0.205	6.658
				v (cm/s)	-20.17	20.34	-0.783	5.929
Aanderaa RCM 8	12803	1492 m	5174	u (cm/s)	-14.54	14.39	-0.449	4.13
				v (cm/s)	-10.46	9.77	-0.419	2.955
Aanderaa RCM 8s	9807	1995 m	5174	u (cm/s)	-20.3	21.97	-1.053	6.675
				v (cm/s)	-19.6	20.92	-0.91	5.301
Aanderaa RCM 8	12807	2499 m	2240	u (cm/s)	-10.73	13.53	-0.335	3.546
				v (cm/s)	-9.57	7.62	-0.043	2.734

Table C-5

Statistics from Mooring 3 Deployment 1 ADCP for the u and v components of the currents measured.

Instrument	Serial Number	Bin Depth	N	Parameter	Minimum	Maximum	Mean	Standard Deviation
RDI Broadband 75 kHz Long-Ranger ADCP	5699	38 - 46 m	1737	u (cm/s)	-34.55	64.43	15.652	18.119
				v (cm/s)	-70.26	33.84	-11.52	20.988
RDI Broadband 75 kHz Long-Ranger ADCP	5699	46 - 54 m	2688	u (cm/s)	-28.22	78.65	23.931	21.669
				v (cm/s)	-89.47	44.84	-13.777	22.557
RDI Broadband 75 kHz Long-Ranger ADCP	5699	54 - 62 m	3702	u (cm/s)	-33.58	110.63	31.145	25.578
				v (cm/s)	-103.9	50.61	-14.957	25.284
RDI Broadband 75 kHz Long-Ranger ADCP	5699	62 - 70 m	4278	u (cm/s)	-34.22	119.15	34.292	28.156
				v (cm/s)	-122.83	56.78	-17.844	29.467
RDI Broadband 75 kHz Long-Ranger ADCP	5699	70 - 78 m	4703	u (cm/s)	-32.71	113.44	35.223	29.021
				v (cm/s)	-135.97	58.59	-19.13	32.147
RDI Broadband 75 kHz Long-Ranger ADCP	5699	78 - 86 m	4902	u (cm/s)	-27.86	118.95	36.288	30.052
				v (cm/s)	-124.66	64.97	-18.191	32.421
RDI Broadband 75 kHz Long-Ranger ADCP	5699	86 - 94 m	5063	u (cm/s)	-28.23	128.35	37.155	31.023
				v (cm/s)	-119.43	83.82	-17.094	33.028
RDI Broadband 75 kHz Long-Ranger ADCP	5699	94 - 102 m	5125	u (cm/s)	-32.3	133.1	37	31.544
				v (cm/s)	-115.73	80.95	-16.095	32.733
RDI Broadband 75 kHz Long-Ranger ADCP	5699	102 - 110 m	5149	u (cm/s)	-36.5	131.53	36.32	31.468
				v (cm/s)	-109.92	78.81	-15.138	32.006
RDI Broadband 75 kHz Long-Ranger ADCP	5699	110 - 118 m	5149	u (cm/s)	-31.94	128.44	35.127	30.821
				v (cm/s)	-104.49	81.45	-14.241	31.33
RDI Broadband 75 kHz Long-Ranger ADCP	5699	118 - 126 m	5149	u (cm/s)	-33.63	128.89	33.918	30.076
				v (cm/s)	-102.7	85.1	-13.318	30.466
RDI Broadband 75 kHz Long-Ranger ADCP	5699	126 - 134 m	5149	u (cm/s)	-30.72	124.54	32.727	29.179
				v (cm/s)	-102.21	82.61	-12.538	29.482
RDI Broadband 75 kHz Long-Ranger ADCP	5699	134 - 142 m	5149	u (cm/s)	-33.26	122.61	31.609	28.138
				v (cm/s)	-100.4	80.34	-11.966	28.627
RDI Broadband 75 kHz Long-Ranger ADCP	5699	142 - 150 m	5149	u (cm/s)	-33.5	114.78	30.36	26.873
				v (cm/s)	-98.48	73.52	-11.495	27.828
RDI Broadband 75 kHz Long-Ranger ADCP	5699	150 - 158 m	5149	u (cm/s)	-35.6	108.5	29.02	25.645
				v (cm/s)	-96.42	70.86	-10.886	27.089
RDI Broadband 75 kHz Long-Ranger ADCP	5699	158 - 166 m	5149	u (cm/s)	-31.45	99.45	27.758	24.63
				v (cm/s)	-90.1	66.3	-10.186	26.34
RDI Broadband 75 kHz Long-Ranger ADCP	5699	166 - 174 m	5149	u (cm/s)	-36.76	97.37	26.534	23.841
				v (cm/s)	-87.04	55.83	-9.572	25.603
RDI Broadband 75 kHz Long-Ranger ADCP	5699	174 - 182 m	5149	u (cm/s)	-35.13	100.09	25.442	23.213
				v (cm/s)	-87.71	51.23	-9.058	24.818
RDI Broadband 75 kHz Long-Ranger ADCP	5699	182 - 190 m	5149	u (cm/s)	-32.06	102.82	24.541	22.616
				v (cm/s)	-86.64	50.4	-8.611	24.047
RDI Broadband 75 kHz Long-Ranger ADCP	5699	190 - 198 m	5149	u (cm/s)	-24.09	97.67	23.554	21.982
				v (cm/s)	-84.7	49.07	-8.055	23.508
RDI Broadband 75 kHz Long-Ranger ADCP	5699	198 - 206 m	5149	u (cm/s)	-27.75	94.2	22.624	21.457
				v (cm/s)	-82.75	51.38	-7.52	22.971
RDI Broadband 75 kHz Long-Ranger ADCP	5699	206 - 214 m	5149	u (cm/s)	-31.02	96.86	21.858	21.092
				v (cm/s)	-80.29	54.85	-7.15	22.396
RDI Broadband 75 kHz Long-Ranger ADCP	5699	214 - 222 m	5149	u (cm/s)	-31	98.76	21.185	20.683
				v (cm/s)	-77.79	54.63	-6.787	21.819
RDI Broadband 75 kHz Long-Ranger ADCP	5699	222 - 230 m	5149	u (cm/s)	-32.73	94.34	20.658	20.264
				v (cm/s)	-73.43	54.34	-6.557	21.336
RDI Broadband 75 kHz Long-Ranger ADCP	5699	230 - 238 m	5149	u (cm/s)	-30.04	91.71	20.032	19.839
				v (cm/s)	-73.36	53.17	-6.235	20.865
RDI Broadband 75 kHz Long-Ranger ADCP	5699	238 - 246 m	5149	u (cm/s)	-24.15	91.98	19.392	19.395
				v (cm/s)	-73.56	52.15	-6.025	20.272

Table C-5. Statistics from Mooring 3 Deployment 1 ADCP for the u and v components of the currents measured (continued).

Instrument	Serial Number	Bin Depth	N	Parameter	Minimum	Maximum	Mean	Standard Deviation
RDI Broadband 75 kHz Long-Ranger ADCP	5699	246 - 254 m	5149	u (cm/s)	-23.08	91.66	18.913	19.066
				v (cm/s)	-68.89	51.43	-5.76	19.686
RDI Broadband 75 kHz Long-Ranger ADCP	5699	254 - 262 m	5149	u (cm/s)	-22.65	91	18.477	18.664
				v (cm/s)	-70.34	50.95	-5.424	19.204
RDI Broadband 75 kHz Long-Ranger ADCP	5699	262 - 270 m	5149	u (cm/s)	-22.13	92.32	18.071	18.348
				v (cm/s)	-64.12	50.71	-5.105	18.806
RDI Broadband 75 kHz Long-Ranger ADCP	5699	270 - 278 m	5149	u (cm/s)	-20.79	89.76	17.699	18.003
				v (cm/s)	-63.25	49.79	-4.833	18.444
RDI Broadband 75 kHz Long-Ranger ADCP	5699	278 - 286 m	5149	u (cm/s)	-21.51	87.63	17.273	17.708
				v (cm/s)	-63.14	49.32	-4.591	18.138
RDI Broadband 75 kHz Long-Ranger ADCP	5699	286 - 294 m	5149	u (cm/s)	-21.19	86.92	16.778	17.371
				v (cm/s)	-60.69	51.91	-4.432	17.888
RDI Broadband 75 kHz Long-Ranger ADCP	5699	294 - 302 m	5149	u (cm/s)	-23.24	82.2	16.358	17.082
				v (cm/s)	-58.36	50.85	-4.268	17.624
RDI Broadband 75 kHz Long-Ranger ADCP	5699	302 - 310 m	5149	u (cm/s)	-23.65	83.86	16.033	16.824
				v (cm/s)	-60.06	49.79	-4.143	17.303
RDI Broadband 75 kHz Long-Ranger ADCP	5699	310 - 318 m	5149	u (cm/s)	-19.82	81.8	15.8	16.554
				v (cm/s)	-57.33	47.39	-4.012	17.071
RDI Broadband 75 kHz Long-Ranger ADCP	5699	318 - 326 m	5149	u (cm/s)	-20.84	80.55	15.434	16.251
				v (cm/s)	-56.54	47.47	-3.937	16.887
RDI Broadband 75 kHz Long-Ranger ADCP	5699	326 - 334 m	5149	u (cm/s)	-19.22	78.08	15.115	15.981
				v (cm/s)	-55.15	46.75	-3.867	16.698
RDI Broadband 75 kHz Long-Ranger ADCP	5699	334 - 342 m	5149	u (cm/s)	-20.41	75.89	14.893	15.657
				v (cm/s)	-55.53	46.46	-3.724	16.365
RDI Broadband 75 kHz Long-Ranger ADCP	5699	342 - 350 m	5149	u (cm/s)	-22.19	74.85	14.572	15.499
				v (cm/s)	-55.49	45.56	-3.547	16.154
RDI Broadband 75 kHz Long-Ranger ADCP	5699	350 - 358 m	5149	u (cm/s)	-22.13	73.36	14.278	15.285
				v (cm/s)	-53.66	43.81	-3.4	15.987
RDI Broadband 75 kHz Long-Ranger ADCP	5699	358 - 366 m	5149	u (cm/s)	-23.72	76.1	14.005	15.084
				v (cm/s)	-48.75	45.39	-3.251	15.712
RDI Broadband 75 kHz Long-Ranger ADCP	5699	366 - 374 m	5149	u (cm/s)	-21.88	72.26	13.744	14.804
				v (cm/s)	-50.05	44.79	-3.148	15.453
RDI Broadband 75 kHz Long-Ranger ADCP	5699	374 - 382 m	5149	u (cm/s)	-24.33	68.83	13.496	14.549
				v (cm/s)	-46.35	47.43	-2.975	15.209
RDI Broadband 75 kHz Long-Ranger ADCP	5699	382 - 390 m	5149	u (cm/s)	-22.18	69.19	13.275	14.247
				v (cm/s)	-45.47	47.88	-2.955	14.887
RDI Broadband 75 kHz Long-Ranger ADCP	5699	390 - 398 m	5149	u (cm/s)	-22.22	63.47	12.951	13.893
				v (cm/s)	-45.9	46.74	-2.842	14.7
RDI Broadband 75 kHz Long-Ranger ADCP	5699	398 - 406 m	5149	u (cm/s)	-20.63	64.46	12.698	13.612
				v (cm/s)	-46.45	46.3	-2.665	14.368
RDI Broadband 75 kHz Long-Ranger ADCP	5699	406 - 414 m	5149	u (cm/s)	-21.58	61	12.469	13.417
				v (cm/s)	-47.99	46.11	-2.551	14.035
RDI Broadband 75 kHz Long-Ranger ADCP	5699	414 - 422 m	5149	u (cm/s)	-19.41	61.68	12.151	13.191
				v (cm/s)	-41.19	49.3	-2.424	13.777
RDI Broadband 75 kHz Long-Ranger ADCP	5699	422 - 430 m	5149	u (cm/s)	-22.38	60.91	11.867	12.978
				v (cm/s)	-39.28	45.88	-2.338	13.556
RDI Broadband 75 kHz Long-Ranger ADCP	5699	430 - 438 m	5149	u (cm/s)	-20.47	58.54	11.585	12.665
				v (cm/s)	-41.57	44.08	-2.342	13.301
RDI Broadband 75 kHz Long-Ranger ADCP	5699	438 - 446 m	5149	u (cm/s)	-19.79	57.9	11.304	12.388
				v (cm/s)	-37.68	50.19	-2.249	13.088
RDI Broadband 75 kHz Long-Ranger ADCP	5699	446 - 454 m	5149	u (cm/s)	-19.17	60.67	10.99	12.148
				v (cm/s)	-35.98	48.89	-2.158	12.78
RDI Broadband 75 kHz Long-Ranger ADCP	5699	454 - 462 m	5149	u (cm/s)	-20.26	57.38	10.627	11.931
				v (cm/s)	-35.92	51.08	-2.078	12.469

Table C-6

Statistics from Mooring 3 Deployment 1 single point current meters for the u and v components of the currents measured.

Instrument	Serial Number	Depth	N	Parameter	Minimum	Maximum	Mean	Standard Deviation
S4	2129	0750 m	5148	u (cm/s)	-22.85	31.45	4.376	7.598
				v (cm/s)	-26.69	35.07	-0.405	8.177
Aanderaa RCM 7	12084	0998 m	5148	u (cm/s)	-25.95	27.07	1.612	6.624
				v (cm/s)	-19.68	35.77	0.798	7.152
Aanderaa RCM 8s	10643	1245 m	5148	u (cm/s)	-27.14	19.98	0.751	6.341
				v (cm/s)	-17.86	31.89	0.469	6.31
Aanderaa RCM 7	9480	1492 m	5148	u (cm/s)	-21.86	17.49	0.029	5.859
				v (cm/s)	-16.27	32.01	0.841	5.585
Aanderaa RCM 8s	9809	1996 m	5148	u (cm/s)	-27.96	20.91	0.913	6.701
				v (cm/s)	-20.28	32.16	-0.161	6.552
Aanderaa RCM 8	12808	2499 m	5148	u (cm/s)	-29.02	21.31	-0.498	7.767
				v (cm/s)	-19.59	33	0.422	6.676
Aanderaa RCM 8	12809	2699 m	5148	u (cm/s)	-28.3	19.91	-0.66	7.416
				v (cm/s)	-19.78	32.06	0.361	7

Table C-7

Statistics from Mooring 4 Deployment 1 single point current meters for the u and v components of the currents measured.

Instrument	Serial Number	Depth	N	Parameter	Minimum	Maximum	Mean	Standard Deviation
Aanderaa RCM 8s	10112	2530 m	5099	u (cm/s)	-13.8	9.7	-2.896	4.346
				v (cm/s)	-12.05	14.61	-0.17	4.123
Aanderaa RCM 8	12810	2630 m	5099	u (cm/s)	-14.25	10.58	-2.97	4.094
				v (cm/s)	-13.71	15.08	0.357	4.097

Table C-8

Statistics from Mooring 1 Deployment 2 ADCP for the u and v components of the currents measured.

Instrument	Serial Number	Bin Depth	N	Parameter	Minimum	Maximum	Mean	Standard Deviation
RDI Broadband 75 kHz Long-Ranger ADCP	4844	45 - 53 m	1692	u (cm/s)	-80.2	58.26	-10.158	16.831
				v (cm/s)	-95.91	66.99	4.59	15.709
RDI Broadband 75 kHz Long-Ranger ADCP	4844	53 - 61 m	3342	u (cm/s)	-86.45	38.5	-20.523	18.12
				v (cm/s)	-73.42	58.46	10.193	16.988
RDI Broadband 75 kHz Long-Ranger ADCP	4844	61 - 69 m	3707	u (cm/s)	-68.89	32.6	-21.542	17.228
				v (cm/s)	-40.02	60.49	10.159	16.53
RDI Broadband 75 kHz Long-Ranger ADCP	4844	69 - 77 m	3709	u (cm/s)	-65.67	30.2	-21.143	16.626
				v (cm/s)	-34.39	61.05	10.192	15.688
RDI Broadband 75 kHz Long-Ranger ADCP	4844	77 - 85 m	3709	u (cm/s)	-63.11	34.67	-20.774	16.119
				v (cm/s)	-29.73	60.29	10.278	15.055
RDI Broadband 75 kHz Long-Ranger ADCP	4844	85 - 93 m	3709	u (cm/s)	-60.96	33.21	-20.368	15.645
				v (cm/s)	-24.95	65.33	10.193	14.803
RDI Broadband 75 kHz Long-Ranger ADCP	4844	93 - 101 m	3709	u (cm/s)	-59.19	31.66	-20.212	15.174
				v (cm/s)	-22.97	71.35	9.996	14.476
RDI Broadband 75 kHz Long-Ranger ADCP	4844	101 - 109 m	3709	u (cm/s)	-57.1	33.48	-20.05	14.679
				v (cm/s)	-24.6	61.62	9.829	13.903
RDI Broadband 75 kHz Long-Ranger ADCP	4844	109 - 117 m	3709	u (cm/s)	-55.08	30.97	-20.005	14.24
				v (cm/s)	-23.23	48.72	9.577	13.255
RDI Broadband 75 kHz Long-Ranger ADCP	4844	117 - 125 m	3709	u (cm/s)	-53.1	27.92	-19.902	13.821
				v (cm/s)	-23.9	47.4	9.361	12.672
RDI Broadband 75 kHz Long-Ranger ADCP	4844	125 - 133 m	3709	u (cm/s)	-54.23	25.38	-19.596	13.555
				v (cm/s)	-23.73	50.66	9.14	12.395
RDI Broadband 75 kHz Long-Ranger ADCP	4844	133 - 141 m	3709	u (cm/s)	-56	23.99	-19.361	13.33
				v (cm/s)	-21.95	45.15	9.004	12.002
RDI Broadband 75 kHz Long-Ranger ADCP	4844	141 - 149 m	3709	u (cm/s)	-52.17	23.66	-19.054	12.972
				v (cm/s)	-22.85	45.83	8.838	11.749
RDI Broadband 75 kHz Long-Ranger ADCP	4844	149 - 157 m	3709	u (cm/s)	-55.61	20.2	-18.827	12.778
				v (cm/s)	-26.88	45.24	8.718	11.543
RDI Broadband 75 kHz Long-Ranger ADCP	4844	157 - 165 m	3709	u (cm/s)	-52.65	19.32	-18.633	12.443
				v (cm/s)	-28.1	46.33	8.602	11.312
RDI Broadband 75 kHz Long-Ranger ADCP	4844	165 - 173 m	3709	u (cm/s)	-52.82	19.22	-18.437	12.266
				v (cm/s)	-23.17	42.66	8.386	11.16
RDI Broadband 75 kHz Long-Ranger ADCP	4844	173 - 181 m	3709	u (cm/s)	-52.28	19.08	-18.173	12.14
				v (cm/s)	-23.48	41.67	8.296	11.022
RDI Broadband 75 kHz Long-Ranger ADCP	4844	181 - 189 m	3709	u (cm/s)	-50.28	16.66	-17.911	11.944
				v (cm/s)	-20.9	43.27	8.067	10.914
RDI Broadband 75 kHz Long-Ranger ADCP	4844	189 - 197 m	3709	u (cm/s)	-49.56	15.07	-17.667	11.79
				v (cm/s)	-20.41	40.14	8.032	10.787
RDI Broadband 75 kHz Long-Ranger ADCP	4844	197 - 205 m	3709	u (cm/s)	-48.28	17.75	-17.347	11.631
				v (cm/s)	-21.27	40.22	7.855	10.578
RDI Broadband 75 kHz Long-Ranger ADCP	4844	205 - 213 m	3709	u (cm/s)	-47.01	18.31	-17.078	11.497
				v (cm/s)	-22.53	39.81	7.726	10.43
RDI Broadband 75 kHz Long-Ranger ADCP	4844	213 - 221 m	3709	u (cm/s)	-47.8	16.88	-16.917	11.366
				v (cm/s)	-19.97	43.14	7.649	10.305
RDI Broadband 75 kHz Long-Ranger ADCP	4844	221 - 229 m	3709	u (cm/s)	-46.39	13.82	-16.613	11.234
				v (cm/s)	-21.56	40.71	7.449	10.15
RDI Broadband 75 kHz Long-Ranger ADCP	4844	229 - 237 m	3709	u (cm/s)	-46.78	14.63	-16.393	11.151
				v (cm/s)	-21.55	41.9	7.396	10.059
RDI Broadband 75 kHz Long-Ranger ADCP	4844	237 - 245 m	3709	u (cm/s)	-48.89	13.25	-16.283	11.079
				v (cm/s)	-22.56	40.5	7.248	10.048
RDI Broadband 75 kHz Long-Ranger ADCP	4844	245 - 253 m	3709	u (cm/s)	-47.18	14.31	-16.03	10.967
				v (cm/s)	-20.96	39.35	7.12	10.017

Table C-8. Statistics from Mooring 1 Deployment 2 ADCP for the u and v components of the currents measured (continued).

Instrument	Serial Number	Bin Depth	N	Parameter	Minimum	Maximum	Mean	Standard Deviation
RDI Broadband 75 kHz Long-Ranger ADCP	4844	253 - 261 m	3709	u (cm/s)	-43.7	14.62	-15.844	10.792
				v (cm/s)	-23.2	42.19	7.002	9.933
RDI Broadband 75 kHz Long-Ranger ADCP	4844	261 - 269 m	3709	u (cm/s)	-44.6	13.92	-15.468	10.453
				v (cm/s)	-20.51	38.5	6.991	9.629
RDI Broadband 75 kHz Long-Ranger ADCP	4844	269 - 277 m	3709	u (cm/s)	-43.87	14.21	-14.882	9.935
				v (cm/s)	-18.31	37.25	6.739	9.226
RDI Broadband 75 kHz Long-Ranger ADCP	4844	277 - 285 m	3709	u (cm/s)	-43.2	12.77	-14.914	9.89
				v (cm/s)	-21.9	35.14	6.636	9.078
RDI Broadband 75 kHz Long-Ranger ADCP	4844	285 - 293 m	3709	u (cm/s)	-43.5	12.79	-14.988	9.959
				v (cm/s)	-22.45	36.33	6.725	9.259
RDI Broadband 75 kHz Long-Ranger ADCP	4844	293 - 301 m	3709	u (cm/s)	-45.1	15	-14.836	10.041
				v (cm/s)	-22.18	37.4	6.604	9.166
RDI Broadband 75 kHz Long-Ranger ADCP	4844	301 - 309 m	3709	u (cm/s)	-45.08	13.64	-14.614	9.831
				v (cm/s)	-23.5	34.45	6.499	9.077
RDI Broadband 75 kHz Long-Ranger ADCP	4844	309 - 317 m	3709	u (cm/s)	-43.45	14.89	-14.382	9.622
				v (cm/s)	-23.72	32.74	6.393	8.925
RDI Broadband 75 kHz Long-Ranger ADCP	4844	317 - 325 m	3709	u (cm/s)	-42.97	14.17	-14.174	9.534
				v (cm/s)	-25.1	33.5	6.41	8.743
RDI Broadband 75 kHz Long-Ranger ADCP	4844	325 - 333 m	3709	u (cm/s)	-44.51	14.01	-14.052	9.353
				v (cm/s)	-23.74	32.27	6.399	8.597
RDI Broadband 75 kHz Long-Ranger ADCP	4844	333 - 341 m	3709	u (cm/s)	-41.59	12.88	-14.028	9.298
				v (cm/s)	-23.01	33.11	6.356	8.512
RDI Broadband 75 kHz Long-Ranger ADCP	4844	341 - 349 m	3709	u (cm/s)	-41.83	14.1	-13.914	9.154
				v (cm/s)	-22.89	32.67	6.313	8.456
RDI Broadband 75 kHz Long-Ranger ADCP	4844	349 - 357 m	3709	u (cm/s)	-41.19	15.88	-13.79	9.146
				v (cm/s)	-23.41	32.1	6.124	8.36
RDI Broadband 75 kHz Long-Ranger ADCP	4844	357 - 365 m	3709	u (cm/s)	-41.99	19.27	-13.635	9.107
				v (cm/s)	-23.42	33.24	5.97	8.327
RDI Broadband 75 kHz Long-Ranger ADCP	4844	365 - 373 m	3709	u (cm/s)	-41.69	17.58	-13.556	9.06
				v (cm/s)	-21.73	30.18	5.926	8.253
RDI Broadband 75 kHz Long-Ranger ADCP	4844	373 - 381 m	3709	u (cm/s)	-41.32	15.69	-13.357	8.985
				v (cm/s)	-20.74	33.85	5.879	8.244
RDI Broadband 75 kHz Long-Ranger ADCP	4844	381 - 389 m	3709	u (cm/s)	-41.69	14.39	-13.151	8.916
				v (cm/s)	-19.45	31.3	5.921	8.199
RDI Broadband 75 kHz Long-Ranger ADCP	4844	389 - 397 m	3709	u (cm/s)	-40.74	15.7	-12.914	8.841
				v (cm/s)	-19.62	33.69	5.79	8.208
RDI Broadband 75 kHz Long-Ranger ADCP	4844	397 - 405 m	3709	u (cm/s)	-42.13	18.64	-12.642	8.727
				v (cm/s)	-17.51	30.3	5.724	8.119
RDI Broadband 75 kHz Long-Ranger ADCP	4844	405 - 413 m	3709	u (cm/s)	-40.72	15.8	-12.455	8.65
				v (cm/s)	-19.18	34	5.62	8.136
RDI Broadband 75 kHz Long-Ranger ADCP	4844	413 - 421 m	3709	u (cm/s)	-38.83	17.89	-12.324	8.608
				v (cm/s)	-19.9	33.28	5.576	8.104
RDI Broadband 75 kHz Long-Ranger ADCP	4844	421 - 429 m	3709	u (cm/s)	-42.96	15.63	-12.206	8.573
				v (cm/s)	-19.12	30.05	5.565	8.099
RDI Broadband 75 kHz Long-Ranger ADCP	4844	429 - 437 m	3709	u (cm/s)	-41.39	14.54	-12.055	8.486
				v (cm/s)	-18.63	30.99	5.554	8.071
RDI Broadband 75 kHz Long-Ranger ADCP	4844	437 - 445 m	3709	u (cm/s)	-40.68	16.88	-11.85	8.474
				v (cm/s)	-19.37	32.78	5.488	8.107
RDI Broadband 75 kHz Long-Ranger ADCP	4844	445 - 453 m	3709	u (cm/s)	-40.65	16.8	-11.663	8.41
				v (cm/s)	-21.4	32.9	5.381	8.137
RDI Broadband 75 kHz Long-Ranger ADCP	4844	453 - 461 m	3709	u (cm/s)	-41.38	16.92	-11.471	8.304
				v (cm/s)	-21.2	31.47	5.306	8.107

Table C-8. Statistics from Mooring 1 Deployment 2 ADCP for the u and v components of the currents measured (continued).

Instrument	Serial Number	Bin Depth	N	Parameter	Minimum	Maximum	Mean	Standard Deviation
RDI Broadband 75 kHz Long-Ranger ADCP	4844	461 - 469 m	3709	u (cm/s)	-41.4	17.82	-11.318	8.242
				v (cm/s)	-18.96	31.83	5.157	8.067
RDI Broadband 75 kHz Long-Ranger ADCP	4844	469 - 477 m	3709	u (cm/s)	-37.33	17.34	-11.194	8.193
				v (cm/s)	-22.85	33.01	4.966	7.988
RDI Broadband 75 kHz Long-Ranger ADCP	4844	477 - 485 m	3709	u (cm/s)	-38.55	17.36	-10.853	8.06
				v (cm/s)	-18.58	32.49	4.883	7.875
RDI Broadband 75 kHz Long-Ranger ADCP	4844	485 - 493 m	3709	u (cm/s)	-36.97	20.26	-10.164	7.908
				v (cm/s)	-17.6	29.93	4.659	7.612

Table C-9

Statistics from Mooring 1 Deployment 2 single point current meters for the u and v components of the currents measured.

Instrument	Serial Number	Depth	N	Parameter	Minimum	Maximum	Mean	Standard Deviation
S4	78017	0749 m	3732	u (cm/s)	-40.02	42.19	-6.475	7.259
				v (cm/s)	-33.82	41.73	3.025	7.247
Aanderaa RCM 7	12805	0997 m	3732	u (cm/s)	-27.17	26.75	-3.792	6.002
				v (cm/s)	-24.73	29.7	2.762	5.804
Aanderaa RCM 7	7692	1244 m	1731	u (cm/s)	-15.05	11.45	-0.607	4.216
				v (cm/s)	-10.98	16.9	1.596	4.371
Aanderaa RCM 7	9722	1492 m	3732	u (cm/s)	-12.12	10.51	-0.427	2.902
				v (cm/s)	-11.03	12.82	0.879	2.57
Aanderaa RCM 8s	10053	1995 m	3732	u (cm/s)	-9.11	10.96	0.046	2.962
				v (cm/s)	-12.38	11.21	0.503	2.774
Aanderaa RCM 8	12085	2499 m	3733	u (cm/s)	-18.09	15.94	0.385	4.333
				v (cm/s)	-16.67	18.42	0.228	4.237

Table C-10

Statistics from Mooring 2 Deployment 2 ADCP for the u and v components of the currents measured.

Instrument	Serial Number	Bin Depth	N	Parameter	Minimum	Maximum	Mean	Standard Deviation
RDI Broadband 75 kHz Long-Ranger ADCP	5165	50 - 58 m	472	u (cm/s)	-47.39	18.05	-7.909	11.596
				v (cm/s)	-38.08	54.59	8.775	18.077
RDI Broadband 75 kHz Long-Ranger ADCP	5165	58 - 66 m	2867	u (cm/s)	-58.59	81.27	-5.148	20.853
				v (cm/s)	-58.43	59.11	5.982	24.036
RDI Broadband 75 kHz Long-Ranger ADCP	5165	66 - 74 m	3449	u (cm/s)	-88.28	77.46	-4.475	22.391
				v (cm/s)	-60.22	70.38	5.583	26.836
RDI Broadband 75 kHz Long-Ranger ADCP	5165	74 - 82 m	3621	u (cm/s)	-72.76	75.76	-4.441	21.899
				v (cm/s)	-60.15	73.08	5.866	27.446
RDI Broadband 75 kHz Long-Ranger ADCP	5165	82 - 90 m	3626	u (cm/s)	-69.67	67.49	-5.011	20.98
				v (cm/s)	-58.03	73.87	5.624	27.394
RDI Broadband 75 kHz Long-Ranger ADCP	5165	90 - 98 m	3626	u (cm/s)	-76.43	54.6	-5.367	20.038
				v (cm/s)	-57.95	69.04	5.333	26.984
RDI Broadband 75 kHz Long-Ranger ADCP	5165	98 - 106 m	3626	u (cm/s)	-77.88	50.32	-5.527	19.084
				v (cm/s)	-55.05	71.05	5.115	26.724
RDI Broadband 75 kHz Long-Ranger ADCP	5165	106 - 114 m	3626	u (cm/s)	-76.7	50.97	-5.739	18.217
				v (cm/s)	-51.95	75.44	4.957	26.47
RDI Broadband 75 kHz Long-Ranger ADCP	5165	114 - 122 m	3626	u (cm/s)	-75.35	49.47	-5.994	17.343
				v (cm/s)	-53.44	82.85	4.787	26.263
RDI Broadband 75 kHz Long-Ranger ADCP	5165	122 - 130 m	3626	u (cm/s)	-79.24	44.48	-6.189	16.451
				v (cm/s)	-57.15	82.71	4.832	26.175
RDI Broadband 75 kHz Long-Ranger ADCP	5165	130 - 138 m	3626	u (cm/s)	-72.87	41.58	-6.561	15.56
				v (cm/s)	-55.32	71.4	4.598	25.918
RDI Broadband 75 kHz Long-Ranger ADCP	5165	138 - 146 m	3626	u (cm/s)	-66.69	37.48	-6.787	14.916
				v (cm/s)	-56.93	70.56	4.261	25.659
RDI Broadband 75 kHz Long-Ranger ADCP	5165	146 - 154 m	3626	u (cm/s)	-65.54	33.31	-6.872	14.6
				v (cm/s)	-57.52	66.5	4.145	25.388
RDI Broadband 75 kHz Long-Ranger ADCP	5165	154 - 162 m	3626	u (cm/s)	-59.72	32.93	-7.01	14.32
				v (cm/s)	-56.76	65.98	4.026	25.176
RDI Broadband 75 kHz Long-Ranger ADCP	5165	162 - 170 m	3626	u (cm/s)	-58.61	34.36	-7.135	14.021
				v (cm/s)	-57.49	64.82	4.014	24.79
RDI Broadband 75 kHz Long-Ranger ADCP	5165	170 - 178 m	3626	u (cm/s)	-59.67	32.26	-7.228	13.61
				v (cm/s)	-54.38	63	3.922	24.438
RDI Broadband 75 kHz Long-Ranger ADCP	5165	178 - 186 m	3626	u (cm/s)	-56.01	33.52	-7.141	13.398
				v (cm/s)	-55.2	62.24	3.937	24.317
RDI Broadband 75 kHz Long-Ranger ADCP	5165	186 - 194 m	3626	u (cm/s)	-53.49	34.62	-7.067	13.169
				v (cm/s)	-55.02	58.05	3.981	24.186
RDI Broadband 75 kHz Long-Ranger ADCP	5165	194 - 202 m	3626	u (cm/s)	-48.17	33.44	-7.062	12.978
				v (cm/s)	-53.14	56.26	3.97	24.097
RDI Broadband 75 kHz Long-Ranger ADCP	5165	202 - 210 m	3626	u (cm/s)	-47.55	32.11	-7.051	12.809
				v (cm/s)	-51.5	56.34	3.824	23.799
RDI Broadband 75 kHz Long-Ranger ADCP	5165	210 - 218 m	3626	u (cm/s)	-48.66	28.71	-7.101	12.546
				v (cm/s)	-50.58	57.6	3.841	23.59
RDI Broadband 75 kHz Long-Ranger ADCP	5165	218 - 226 m	3626	u (cm/s)	-46.88	29.12	-7.096	12.287
				v (cm/s)	-53.39	57.63	3.736	23.295
RDI Broadband 75 kHz Long-Ranger ADCP	5165	226 - 234 m	3626	u (cm/s)	-46.8	27.91	-7.166	12.085
				v (cm/s)	-53.89	55.39	3.659	22.947
RDI Broadband 75 kHz Long-Ranger ADCP	5165	234 - 242 m	3626	u (cm/s)	-43.47	26.32	-7.139	11.953
				v (cm/s)	-53.89	57.8	3.613	22.789
RDI Broadband 75 kHz Long-Ranger ADCP	5165	242 - 250 m	3626	u (cm/s)	-44.9	30.46	-7.124	11.752
				v (cm/s)	-53.5	52.68	3.616	22.618
RDI Broadband 75 kHz Long-Ranger ADCP	5165	250 - 258 m	3626	u (cm/s)	-43.48	28.59	-7.004	11.538
				v (cm/s)	-51.9	51.95	3.546	22.257

Table C-10. Statistics from Mooring 2 Deployment 2 ADCP for the u and v components of the currents measured (continued).

Instrument	Serial Number	Bin Depth	N	Parameter	Minimum	Maximum	Mean	Standard Deviation
RDI Broadband 75 kHz Long-Ranger ADCP	5165	258 - 266 m	3626	u (cm/s)	-44.34	27.63	-6.982	11.292
				v (cm/s)	-51.68	52.15	3.368	21.843
RDI Broadband 75 kHz Long-Ranger ADCP	5165	266 - 274 m	3626	u (cm/s)	-42.9	26.79	-6.894	11.195
				v (cm/s)	-53.22	53.77	3.368	21.59
RDI Broadband 75 kHz Long-Ranger ADCP	5165	274 - 282 m	3626	u (cm/s)	-43.23	25.38	-6.916	11.018
				v (cm/s)	-51.51	52.58	3.328	21.259
RDI Broadband 75 kHz Long-Ranger ADCP	5165	282 - 290 m	3626	u (cm/s)	-42.5	25.42	-6.823	10.85
				v (cm/s)	-51.84	51.2	3.303	21.017
RDI Broadband 75 kHz Long-Ranger ADCP	5165	290 - 298 m	3626	u (cm/s)	-42.72	25.35	-6.724	10.779
				v (cm/s)	-46.9	54.34	3.287	20.703
RDI Broadband 75 kHz Long-Ranger ADCP	5165	298 - 306 m	3626	u (cm/s)	-43.03	24.08	-6.638	10.615
				v (cm/s)	-46.95	50.89	3.262	20.436
RDI Broadband 75 kHz Long-Ranger ADCP	5165	306 - 314 m	3626	u (cm/s)	-42.29	22.94	-6.559	10.451
				v (cm/s)	-46.61	52.72	3.153	20.216
RDI Broadband 75 kHz Long-Ranger ADCP	5165	314 - 322 m	3626	u (cm/s)	-45.14	23.58	-6.573	10.381
				v (cm/s)	-46.43	55.86	3.125	20.037
RDI Broadband 75 kHz Long-Ranger ADCP	5165	322 - 330 m	3626	u (cm/s)	-45.57	21.46	-6.574	10.365
				v (cm/s)	-44.25	50.67	3.037	19.779
RDI Broadband 75 kHz Long-Ranger ADCP	5165	330 - 338 m	3626	u (cm/s)	-43.79	23.84	-6.497	10.214
				v (cm/s)	-44.61	49.2	2.969	19.516
RDI Broadband 75 kHz Long-Ranger ADCP	5165	338 - 346 m	3626	u (cm/s)	-43.2	22.35	-6.434	10.154
				v (cm/s)	-42.52	47.67	2.859	19.182
RDI Broadband 75 kHz Long-Ranger ADCP	5165	346 - 354 m	3626	u (cm/s)	-43.93	25.94	-6.383	10.1
				v (cm/s)	-42.37	44.88	2.837	18.883
RDI Broadband 75 kHz Long-Ranger ADCP	5165	354 - 362 m	3626	u (cm/s)	-42.99	24.3	-6.274	10.068
				v (cm/s)	-47.19	47.68	2.793	18.543
RDI Broadband 75 kHz Long-Ranger ADCP	5165	362 - 370 m	3626	u (cm/s)	-42.47	23.02	-6.219	9.885
				v (cm/s)	-45.11	46.4	2.685	18.303
RDI Broadband 75 kHz Long-Ranger ADCP	5165	370 - 378 m	3626	u (cm/s)	-42.11	23.64	-6.105	9.791
				v (cm/s)	-44.95	43.3	2.539	17.983
RDI Broadband 75 kHz Long-Ranger ADCP	5165	378 - 386 m	3626	u (cm/s)	-43.11	24.57	-5.973	9.68
				v (cm/s)	-45.15	43.29	2.425	17.742
RDI Broadband 75 kHz Long-Ranger ADCP	5165	386 - 394 m	3626	u (cm/s)	-39.24	25.44	-5.827	9.613
				v (cm/s)	-45.52	40.94	2.398	17.385
RDI Broadband 75 kHz Long-Ranger ADCP	5165	394 - 402 m	3626	u (cm/s)	-40.47	25.48	-5.787	9.444
				v (cm/s)	-45.9	41.3	2.414	17.117
RDI Broadband 75 kHz Long-Ranger ADCP	5165	402 - 410 m	3626	u (cm/s)	-38.18	26.45	-5.641	9.207
				v (cm/s)	-43.94	41.59	2.372	16.784
RDI Broadband 75 kHz Long-Ranger ADCP	5165	410 - 418 m	3626	u (cm/s)	-36.09	25.8	-5.569	9.073
				v (cm/s)	-43.94	41.39	2.379	16.492
RDI Broadband 75 kHz Long-Ranger ADCP	5165	418 - 426 m	3626	u (cm/s)	-33.73	26.36	-5.47	8.987
				v (cm/s)	-43	43.78	2.412	16.284
RDI Broadband 75 kHz Long-Ranger ADCP	5165	426 - 434 m	3626	u (cm/s)	-36.45	27.16	-5.367	8.931
				v (cm/s)	-42.73	42.71	2.286	15.949
RDI Broadband 75 kHz Long-Ranger ADCP	5165	434 - 442 m	3626	u (cm/s)	-39.31	25.25	-5.241	8.94
				v (cm/s)	-40.73	41.68	2.222	15.739
RDI Broadband 75 kHz Long-Ranger ADCP	5165	442 - 450 m	3626	u (cm/s)	-38.53	26.2	-5.096	8.87
				v (cm/s)	-39.5	41.1	2.188	15.533
RDI Broadband 75 kHz Long-Ranger ADCP	5165	450 - 458 m	3626	u (cm/s)	-35.95	27.08	-5.001	8.859
				v (cm/s)	-37.85	39.75	2.074	15.241
RDI Broadband 75 kHz Long-Ranger ADCP	5165	458 - 466 m	3626	u (cm/s)	-38.25	26.84	-4.996	8.847
				v (cm/s)	-38.58	41.4	1.948	14.948

Table C-10. Statistics from Mooring 2 Deployment 2 ADCP for the u and v components of the currents measured (continued).

Instrument	Serial Number	Bin Depth	N	Parameter	Minimum	Maximum	Mean	Standard Deviation
RDI Broadband 75 kHz Long-Ranger ADCP	5165	466 - 474 m	3626	u (cm/s)	-39.52	22.09	-4.862	8.822
				v (cm/s)	-37.49	42.03	1.786	14.547
RDI Broadband 75 kHz Long-Ranger ADCP	5165	474 - 482 m	3626	u (cm/s)	-37.1	23.5	-4.693	8.733
				v (cm/s)	-36.6	42.99	1.651	14.138
RDI Broadband 75 kHz Long-Ranger ADCP	5165	482 - 490 m	3626	u (cm/s)	-35.43	23.43	-4.48	8.517
				v (cm/s)	-35.5	38.65	1.476	13.611
RDI Broadband 75 kHz Long-Ranger ADCP	5165	490 - 498 m	3626	u (cm/s)	-34.77	20.94	-4.158	8.057
				v (cm/s)	-34.41	40.25	1.275	12.836

Table C-11

Statistics from Mooring 2 Deployment 2 single point current meters for the u and v components of the currents measured.

Instrument	Serial Number	Depth	N	Parameter	Minimum	Maximum	Mean	Standard Deviation
S4	81617	0749 m	3626	u (cm/s)	-22.69	22.46	-2.137	5.749
				v (cm/s)	-24.71	23.93	0.239	7.433
Aanderaa RCM 7	7507	0997 m	3626	u (cm/s)	-17.56	18.19	-0.18	5.635
				v (cm/s)	-17.16	16.47	0.165	5.092
Aanderaa RCM 8s	7771	1244 m	3626	u (cm/s)	-18	20.29	0.575	5.628
				v (cm/s)	-12.68	13.5	0.045	3.884
Aanderaa RCM 8	12803	1492 m	3626	u (cm/s)	-20.44	27.19	1.254	6.659
				v (cm/s)	-12.89	16.7	0.226	4.2
Aanderaa RCM 8s	9807	1995 m	3626	u (cm/s)	-19.84	30.19	1.735	7.457
				v (cm/s)	-16.26	14.47	-0.529	4.172
Aanderaa RCM 8	12807	2499 m	1308	u (cm/s)	-23.13	18.84	2.164	7.852
				v (cm/s)	-16.2	11.94	-1.092	4.893

Table C-12

Statistics from Mooring 3 Deployment 2 ADCP for the u and v components of the currents measured.

Instrument	Serial Number	Bin Depth	N	Parameter	Minimum	Maximum	Mean	Standard Deviation
RDI Broadband 75 kHz Long-Ranger ADCP	5699	30 - 38 m	0	u (cm/s)	*****	*****	*****	*****
				v (cm/s)	*****	*****	*****	*****
RDI Broadband 75 kHz Long-Ranger ADCP	5699	38 - 46 m	553	u (cm/s)	-42.34	50.6	-1.641	18.334
				v (cm/s)	-15.54	46.56	16.196	11.756
RDI Broadband 75 kHz Long-Ranger ADCP	5699	46 - 54 m	1309	u (cm/s)	-44.01	74.5	6.679	22.472
				v (cm/s)	-38.09	61.1	10.61	17.875
RDI Broadband 75 kHz Long-Ranger ADCP	5699	54 - 62 m	3022	u (cm/s)	-46.46	100.36	26.049	28.589
				v (cm/s)	-83.64	83.8	5.182	25.276
RDI Broadband 75 kHz Long-Ranger ADCP	5699	62 - 70 m	3438	u (cm/s)	-46.32	99.89	28.92	29.353
				v (cm/s)	-79.98	88.51	3.06	26.419
RDI Broadband 75 kHz Long-Ranger ADCP	5699	70 - 78 m	3587	u (cm/s)	-46.17	107.91	29.979	30.111
				v (cm/s)	-79.6	87.71	2.632	26.529
RDI Broadband 75 kHz Long-Ranger ADCP	5699	78 - 86 m	3665	u (cm/s)	-48.86	104.36	30.252	30.513
				v (cm/s)	-78.16	90.76	2.609	26.377
RDI Broadband 75 kHz Long-Ranger ADCP	5699	86 - 94 m	3689	u (cm/s)	-47.23	109	29.398	30.098
				v (cm/s)	-80.17	98.92	2.511	26.336
RDI Broadband 75 kHz Long-Ranger ADCP	5699	94 - 102 m	3698	u (cm/s)	-51.82	103.86	28.538	29.561
				v (cm/s)	-74.97	105.08	2.574	26.326
RDI Broadband 75 kHz Long-Ranger ADCP	5699	102 - 110 m	3698	u (cm/s)	-59.1	105.41	27.566	28.934
				v (cm/s)	-71.52	100.75	2.724	26.124
RDI Broadband 75 kHz Long-Ranger ADCP	5699	110 - 118 m	3698	u (cm/s)	-62.63	105.01	26.575	28.304
				v (cm/s)	-68.67	96	2.864	25.813
RDI Broadband 75 kHz Long-Ranger ADCP	5699	118 - 126 m	3698	u (cm/s)	-60.91	107.68	25.662	27.563
				v (cm/s)	-74.43	96.11	2.853	25.368
RDI Broadband 75 kHz Long-Ranger ADCP	5699	126 - 134 m	3698	u (cm/s)	-56.07	107.74	24.723	26.691
				v (cm/s)	-73.04	92.36	2.86	24.976
RDI Broadband 75 kHz Long-Ranger ADCP	5699	134 - 142 m	3698	u (cm/s)	-48.16	103.88	23.911	25.99
				v (cm/s)	-75.31	90.9	2.956	24.52
RDI Broadband 75 kHz Long-Ranger ADCP	5699	142 - 150 m	3698	u (cm/s)	-47.51	101.38	23.226	25.207
				v (cm/s)	-72.39	86.14	3.173	24.079
RDI Broadband 75 kHz Long-Ranger ADCP	5699	150 - 158 m	3698	u (cm/s)	-42.3	98.42	22.575	24.461
				v (cm/s)	-69.69	81.52	3.288	23.774
RDI Broadband 75 kHz Long-Ranger ADCP	5699	158 - 166 m	3698	u (cm/s)	-38.54	98.89	22.11	23.848
				v (cm/s)	-67.08	79.29	3.31	23.382
RDI Broadband 75 kHz Long-Ranger ADCP	5699	166 - 174 m	3698	u (cm/s)	-39.7	94.35	21.531	23.284
				v (cm/s)	-64.77	75.57	3.334	23.012
RDI Broadband 75 kHz Long-Ranger ADCP	5699	174 - 182 m	3698	u (cm/s)	-38.71	93.75	20.988	22.738
				v (cm/s)	-64.63	73.9	3.28	22.558
RDI Broadband 75 kHz Long-Ranger ADCP	5699	182 - 190 m	3698	u (cm/s)	-40.72	90.7	20.365	22.157
				v (cm/s)	-64.18	74.5	3.243	22.249
RDI Broadband 75 kHz Long-Ranger ADCP	5699	190 - 198 m	3698	u (cm/s)	-37.47	90.35	19.891	21.783
				v (cm/s)	-62.6	73.17	3.239	21.987
RDI Broadband 75 kHz Long-Ranger ADCP	5699	198 - 206 m	3698	u (cm/s)	-39.85	86.29	19.43	21.328
				v (cm/s)	-61.18	74.04	3.311	21.665
RDI Broadband 75 kHz Long-Ranger ADCP	5699	206 - 214 m	3698	u (cm/s)	-36.33	83.08	18.988	20.972
				v (cm/s)	-59.99	73.6	3.269	21.46
RDI Broadband 75 kHz Long-Ranger ADCP	5699	214 - 222 m	3698	u (cm/s)	-33.99	79.74	18.576	20.653
				v (cm/s)	-58.06	75.23	3.197	21.113
RDI Broadband 75 kHz Long-Ranger ADCP	5699	222 - 230 m	3698	u (cm/s)	-33.94	77.28	18.111	20.264
				v (cm/s)	-57.64	71.7	3.082	20.893
RDI Broadband 75 kHz Long-Ranger ADCP	5699	230 - 238 m	3698	u (cm/s)	-34.93	75.89	17.784	19.942
				v (cm/s)	-56.95	71.05	3.056	20.607

Table C-12. Statistics from Mooring 3 Deployment 2 ADCP for the u and v components of the currents measured (continued).

Instrument	Serial Number	Bin Depth	N	Parameter	Minimum	Maximum	Mean	Standard Deviation
RDI Broadband 75 kHz Long-Ranger ADCP	5699	238 - 246 m	3698	u (cm/s)	-33.35	74.93	17.375	19.631
				v (cm/s)	-57.6	68.09	3.069	20.434
RDI Broadband 75 kHz Long-Ranger ADCP	5699	246 - 254 m	3698	u (cm/s)	-33.36	72.8	16.895	19.263
				v (cm/s)	-58.17	65.48	3.02	20.086
RDI Broadband 75 kHz Long-Ranger ADCP	5699	254 - 262 m	3698	u (cm/s)	-33.93	70.59	16.319	18.88
				v (cm/s)	-54.9	66.88	3.123	19.642
RDI Broadband 75 kHz Long-Ranger ADCP	5699	262 - 270 m	3698	u (cm/s)	-36.16	72.69	16.247	18.75
				v (cm/s)	-54.93	65.88	3.189	19.54
RDI Broadband 75 kHz Long-Ranger ADCP	5699	270 - 278 m	3698	u (cm/s)	-34.36	69.05	15.941	18.496
				v (cm/s)	-54.08	69.99	3.209	19.349
RDI Broadband 75 kHz Long-Ranger ADCP	5699	278 - 286 m	3698	u (cm/s)	-33.5	70.59	15.59	18.379
				v (cm/s)	-53.02	65.5	3.118	19.22
RDI Broadband 75 kHz Long-Ranger ADCP	5699	286 - 294 m	3698	u (cm/s)	-36.46	69.19	15.265	18.208
				v (cm/s)	-52.59	64.92	3.072	19.036
RDI Broadband 75 kHz Long-Ranger ADCP	5699	294 - 302 m	3698	u (cm/s)	-36.17	69.69	14.968	17.983
				v (cm/s)	-51.9	62.6	3.006	18.782
RDI Broadband 75 kHz Long-Ranger ADCP	5699	302 - 310 m	3698	u (cm/s)	-33.75	69.55	14.666	17.772
				v (cm/s)	-51.57	61.97	2.961	18.572
RDI Broadband 75 kHz Long-Ranger ADCP	5699	310 - 318 m	3698	u (cm/s)	-34.1	70.95	14.407	17.565
				v (cm/s)	-52.19	61.83	2.968	18.358
RDI Broadband 75 kHz Long-Ranger ADCP	5699	318 - 326 m	3698	u (cm/s)	-32.35	71.1	14.055	17.37
				v (cm/s)	-52.08	65.27	2.884	18.147
RDI Broadband 75 kHz Long-Ranger ADCP	5699	326 - 334 m	3698	u (cm/s)	-31.19	65.42	13.766	17.074
				v (cm/s)	-51.1	68.05	2.944	17.901
RDI Broadband 75 kHz Long-Ranger ADCP	5699	334 - 342 m	3698	u (cm/s)	-31.86	70.75	13.503	16.957
				v (cm/s)	-50.03	63.1	2.943	17.697
RDI Broadband 75 kHz Long-Ranger ADCP	5699	342 - 350 m	3698	u (cm/s)	-28.14	68.25	13.218	16.717
				v (cm/s)	-49.89	61.8	2.94	17.432
RDI Broadband 75 kHz Long-Ranger ADCP	5699	350 - 358 m	3698	u (cm/s)	-27.88	67.22	12.976	16.486
				v (cm/s)	-49.4	62.14	2.861	17.251
RDI Broadband 75 kHz Long-Ranger ADCP	5699	358 - 366 m	3698	u (cm/s)	-30.95	66.48	12.71	16.236
				v (cm/s)	-46.75	62.47	2.827	17.025
RDI Broadband 75 kHz Long-Ranger ADCP	5699	366 - 374 m	3698	u (cm/s)	-28.26	63.53	12.483	16.029
				v (cm/s)	-46.26	61.3	2.77	16.716
RDI Broadband 75 kHz Long-Ranger ADCP	5699	374 - 382 m	3698	u (cm/s)	-27.28	63.8	12.263	15.794
				v (cm/s)	-46.48	61.75	2.781	16.446
RDI Broadband 75 kHz Long-Ranger ADCP	5699	382 - 390 m	3698	u (cm/s)	-28.92	61.38	11.977	15.631
				v (cm/s)	-45.76	59.55	2.81	16.237
RDI Broadband 75 kHz Long-Ranger ADCP	5699	390 - 398 m	3698	u (cm/s)	-29.33	60.21	11.717	15.253
				v (cm/s)	-45.52	55.99	2.742	15.908
RDI Broadband 75 kHz Long-Ranger ADCP	5699	398 - 406 m	3698	u (cm/s)	-28.65	60.75	11.384	15.063
				v (cm/s)	-46.04	55.16	2.766	15.668
RDI Broadband 75 kHz Long-Ranger ADCP	5699	406 - 414 m	3698	u (cm/s)	-27.61	59.68	11.095	14.933
				v (cm/s)	-44.3	54.35	2.799	15.403
RDI Broadband 75 kHz Long-Ranger ADCP	5699	414 - 422 m	3698	u (cm/s)	-26.52	59.86	10.836	14.763
				v (cm/s)	-43.9	52.58	2.765	15.105
RDI Broadband 75 kHz Long-Ranger ADCP	5699	422 - 430 m	3698	u (cm/s)	-27.18	59.66	10.727	14.527
				v (cm/s)	-44.58	53.03	2.704	14.93
RDI Broadband 75 kHz Long-Ranger ADCP	5699	430 - 438 m	3698	u (cm/s)	-26.48	59.86	10.529	14.285
				v (cm/s)	-41.31	51.39	2.708	14.645
RDI Broadband 75 kHz Long-Ranger ADCP	5699	438 - 446 m	3698	u (cm/s)	-27.87	57.91	10.294	14.003
				v (cm/s)	-42.76	49.16	2.644	14.35

Table C-12. Statistics from Mooring 3 Deployment 2 ADCP for the u and v components of the currents measured.

Instrument	Serial Number	Bin Depth	N	Parameter	Minimum	Maximum	Mean	Standard Deviation
RDI Broadband 75 kHz Long-Ranger ADCP	5699	446 - 454 m	3698	u (cm/s)	-26.58	57.13	10.095	13.734
				v (cm/s)	-39.9	46.43	2.521	14.061
RDI Broadband 75 kHz Long-Ranger ADCP	5699	454 - 462 m	3698	u (cm/s)	-28.54	57.66	9.847	13.435
				v (cm/s)	-40.08	48.68	2.495	13.833
RDI Broadband 75 kHz Long-Ranger ADCP	5699	462 - 470 m	3698	u (cm/s)	-25.78	57.28	9.452	12.978
				v (cm/s)	-39.34	48.68	2.394	13.439

Table C-13

Statistics from Mooring 3 Deployment 2 single point current meters for the u and v components of the currents measured.

Instrument	Serial Number	Depth	N	Parameter	Minimum	Maximum	Mean	Standard Deviation
S4	8111	0750 m	3697	u (cm/s)	-24.79	35.02	3.411	9.003
				v (cm/s)	-34.32	35.4	0.689	9.546
Aanderaa RCM 7	12084	0997 m	3697	u (cm/s)	-18.24	20.63	-0.252	5.659
				v (cm/s)	-24.93	19.42	-0.107	6.629
Aanderaa RCM 8s	10643	1245 m	3697	u (cm/s)	-15.93	19.31	-1.461	5.182
				v (cm/s)	-23.07	20.75	-0.764	6.07
Aanderaa RCM 7	9480	1492 m	3697	u (cm/s)	-19.13	16.21	-1.7	4.955
				v (cm/s)	-18.49	22.07	-0.092	5.722
Aanderaa RCM 8s	9809	1996 m	3697	u (cm/s)	-21.85	14.29	-2.381	5.591
				v (cm/s)	-20.4	21.42	0.503	6.061
Aanderaa RCM 8	12808	2499 m	3697	u (cm/s)	-23.23	16.81	-2.225	6.367
				v (cm/s)	-20.31	21.9	-0.666	6.586
Aanderaa RCM 8	12809	2699 m	3697	u (cm/s)	-23.42	17.6	-2.206	6.253
				v (cm/s)	-21.38	22.53	-0.761	6.807

Table C-14

Statistics from Mooring 4 Deployment 2 single point current meters for the u and v components of the currents measured.

Instrument	Serial Number	Depth	N	Parameter	Minimum	Maximum	Mean	Standard Deviation
Aanderaa RCM 8s	10112	2530 m	3762	u (cm/s)	-17.14	13.51	-0.464	5.487
				v (cm/s)	-11.44	16.09	-0.724	3.806
Aanderaa RCM 8	12810	2630 m	3762	u (cm/s)	-17.77	12.93	-0.526	5.636
				v (cm/s)	-13.26	15.33	-0.818	3.973

APPENDIX D
Barotropic Tides

Tidal response analysis (Munk and Cartwright, 1966) determined the amplitude and phase for eight major tidal constituents (O1, K1, Q1, P1, M2, K2, N2, S2) from the six recovered bottom pressure records (PIES 1 through 6) within the array (Figures D-1, D-2, and Table D-1). Estimated phase and amplitude vary smoothly across the array as expected. Tidal amplitudes are generally small. The largest tidal amplitudes are near 14 cm for O1 and K1, near 5 cm for P1, and less than 5 cm for the remaining five constituents. Amplitudes have been converted to meters by dividing pressure by density times gravity, $\rho g = 1.02$.

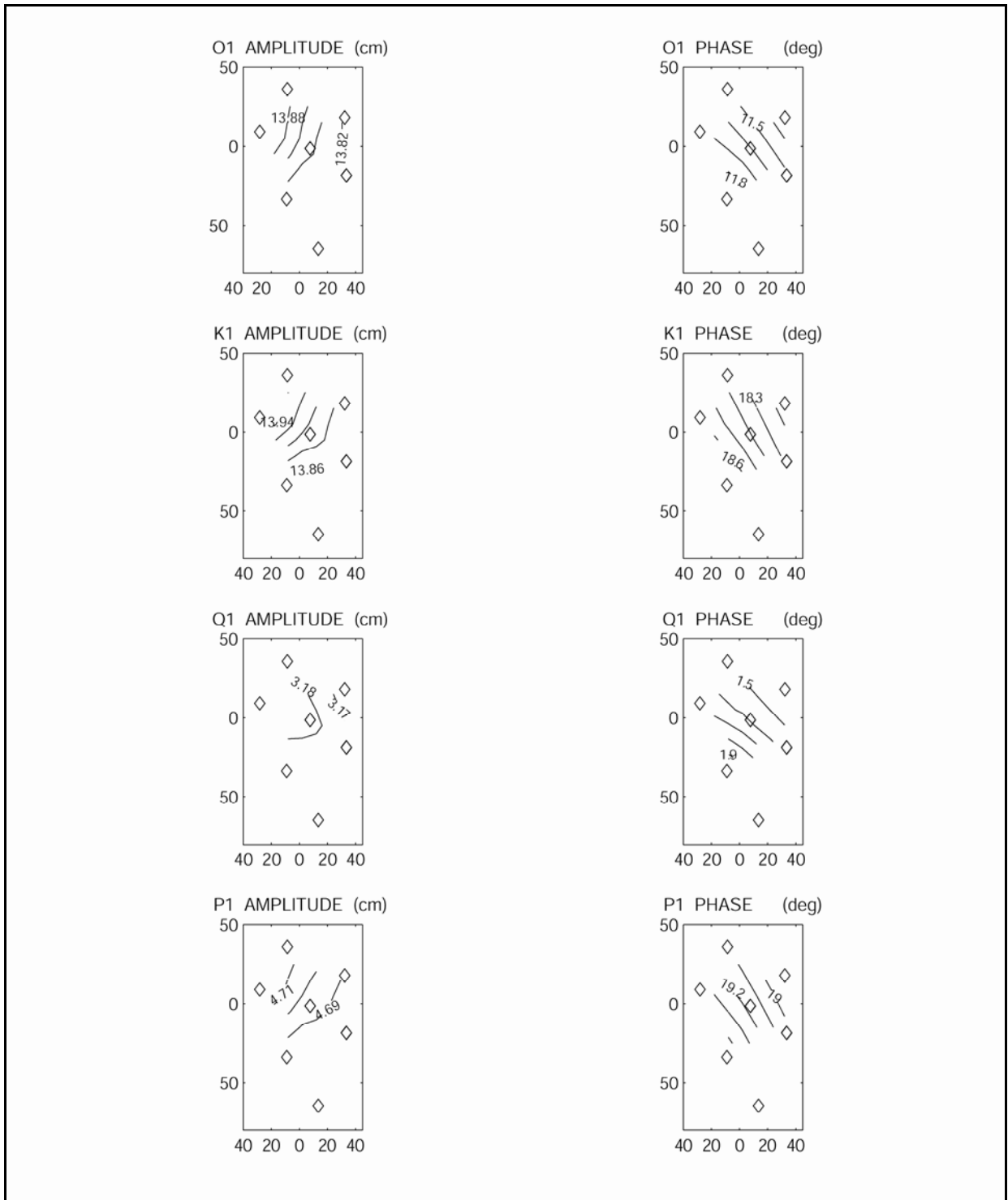


Figure D-1. Amplitude (left column) and phase (right column) of the O1, K1, Q1, and P1 constituents determined with the tidal response method (Munk and Cartwright, 1966) from the six bottom pressure records. PIES locations denoted by open diamonds. Note that PIES7 shown but did not contribute to the calculation because the telemetered data are daily averages.

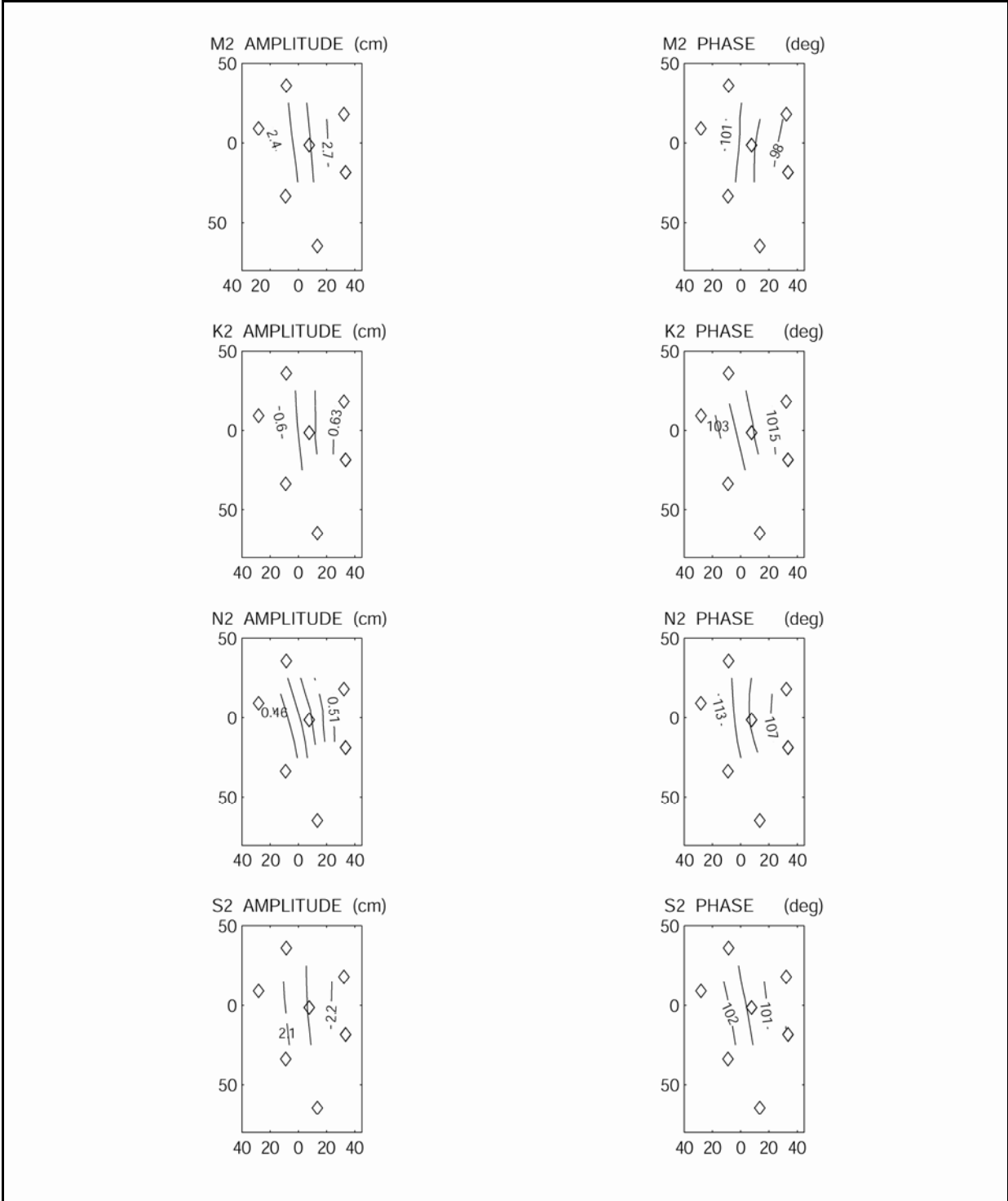


Figure D-2. Amplitude (left panels) and phase (right panels) of the M2, K2, N2, and S2 constituents determined with the tidal response method (Munk and Cartwright, 1966) from the six bottom pressure records. PIES locations denoted by open diamonds. Note that PIES7 shown but did not contribute to the calculation because the telemetered data are daily averages.

Table D-1

Amplitude in cm and phase in degrees for the eight major tidal constituents (O1, K1, Q1, P1, M2, K2, N2, S2) constituents determined with the tidal response method (Munk and Cartwright, 1966).

Site	O1		K1		Q1		P1	
	Amplitude (cm)	Phase (degrees)						
P1	13.96	12.17	13.97	18.37	3.23	354.94	4.62	19.75
P2	13.93	11.98	13.96	18.09	3.22	354.81	4.61	19.47
P3	13.84	11.79	13.86	17.9	3.2	354.74	4.58	19.26
P41	13.87	12.08	13.88	18.17	3.23	354.9	4.57	19.56
P42	13.87	12.08	13.88	18.17	3.23	354.9	4.57	19.56
P5	13.85	12.42	13.85	18.46	3.22	355.25	4.57	19.83
P61	13.85	11.98	13.85	18.02	3.22	354.99	4.57	19.4
P62	13.85	11.98	13.85	18.02	3.22	354.99	4.57	19.4
Site	M2		K2		N2		S2	
	Amplitude (cm)	Phase (degrees)						
P1	2.31	102.78	0.5	101.8	0.45	117.85	2.08	103.12
P2	2.49	100.57	0.51	100.54	0.49	113.11	2.15	101.97
P3	2.79	97.81	0.54	99.36	0.52	108.06	2.26	100.92
P41	2.58	98.94	0.52	100.38	0.49	110.68	2.2	101.75
P42	2.58	98.94	0.52	100.38	0.49	110.68	2.2	101.75
P5	2.4	100.25	0.51	101.44	0.46	114.84	2.13	102.71
P61	2.8	97.2	0.55	99.67	0.52	107.37	2.27	100.84
P62	2.8	97.2	0.55	99.67	0.52	107.37	2.27	100.84

APPENDIX E
Elliptical Fit Parameters

Elliptical fits to a kinematic feature model (Glenn et al., 1990) were found for Eddy Ulysses, Eddy Vortex, Eddy Walker, four small cyclonic eddies, and a brief period of closed circulation in the Loop Current. This appendix contains plots of the time series of fit parameters for each eddy or closed circulation as determined from the available Horizon Marine drifting buoy deployed in 2005. In some cases, more than one buoy orbited a feature. Independent solutions in those cases give an indication of the usefulness of the elliptical fits.

Figures E-1 – E-5 show the parameters of the fits in Eddy Ulysses. At the beginning of 2005, this was an old eddy in the far southwestern Gulf. The fits to the longitude of the center show that it was still translating steadily to the west. The fits to the latitude of the center do not agree as well, but the eddy appears to have moved slowly southward. The orbital periods were around 15 days. This period is in the range expected in old eddies. The eccentricity and orientation show that Eddy Ulysses was nearly circular, with the long axis trending near north-south.

The graphs for Eddy Vortex are broken into two sections. Figures E-6 – E-10 describe the eddy from the end of February through the middle of April. Figures E-11 – E-15 show its evolution from June through November. From April through June, the eddy re-attached to the Loop Current and there were no closed buoy orbits. During March, Eddy Vortex moved to the northwest. In the process, it got unusually close to the Mississippi Delta. At the end of April, the center of circulation moved back to the southeast as the eddy re-attached to the Loop Current. The orbital period when the eddy was definitely detached from the Loop Current in March was rather low, only about 7 days. During that period, it was fairly elongated with an eccentricity of about 0.6. The long axis of the ellipse rotated clockwise at about 4° per day. The sense and speed of the rotation are as predicted for an isolated eddy by Cushman-Roisin et al. (1985).

Figures E-11 – E-15 show the evolution of Eddy Vortex after it separated again in June. There are some gaps in the record because the eddy re-attached to the Loop Current several times, but the center of circulation moved steadily to the southwest. The various buoys gave very similar center positions. From June through August (Year days 160 – 240) the orbital period was long for a fresh eddy, but during this time the eddy was rather large. The orientation of the ellipse changed rapidly during June and the early part of July (Year days 160 – 200) but after that the regular clockwise rotation set in.

Eddy Walker first formed a closed circulation at the end of September, but did not completely separate from the Loop Current until 2006. There were only brief periods when buoys made closed orbits in it, as shown in Figures E-16 – E-20.

Several of the buoys became trapped in small anti-cyclonic (cold) eddies. Figures E-21 – E-25 show the fits to the first of these in February 2005. Cold Eddy 1 was in a meander on the eastern side of the Loop Current. Both buoys in this eddy showed that the center moved steadily southward. Buoy 1476 showed that the center longitude was steady, but buoy 1500 showed the center moving to the east. The reason is that buoy 1500 orbited at a larger radius, and went around a rather diffuse circulation to the east of the main center. This extension to the east is also seen in the eccentricity of the orbit of buoy 1500 and its longer rotational period.

Cold Eddy 2 was in a Loop Current meander far to the south near Cuba at about the same time as Cold Eddy 1 existed. Its parameters are shown in Figures E-26 – E-30. It moved to the southeast as the meander progressed into the Straits of Florida. This was a small feature, and its orbital period was low at 4 – 6 days.

Cold Eddy 3 was a persistent feature from the first of August through the middle of September. It was located on the northeast edge of Eddy Vortex as it was making its final separation. As Eddy Vortex moved to the west, Cold Eddy 3 moved with it. There is a gap in the solution from Yeardays 238 – 248, but the resumed circulation is apparently the same feature. The feature is small and its orbital period low until late in the record when the buoy moved out to a larger orbit.

Cold Eddy 4 was the final cold eddy that had closed buoy orbits. It was directly north of Eddy Walker as it began to separate from the Loop Current in December 2005. This feature moved north as the Loop Current extended and east as its meander propagated clockwise around the northern edge of what would become Eddy Walker. It was a small feature with an orbital period of only 4 days.

Finally, buoy 1669 made a closed orbit in the middle of the Loop Current during the last half of September 2005 after Eddy Vortex separated. At first the center of circulation moved to the northwest, but then it moved to the northeast as the Loop Current leaned to the east. The change of the orientation of the ellipse from north-northwest to north is consistent with this lean. The period of rotation lowers as the orbit becomes more circular.

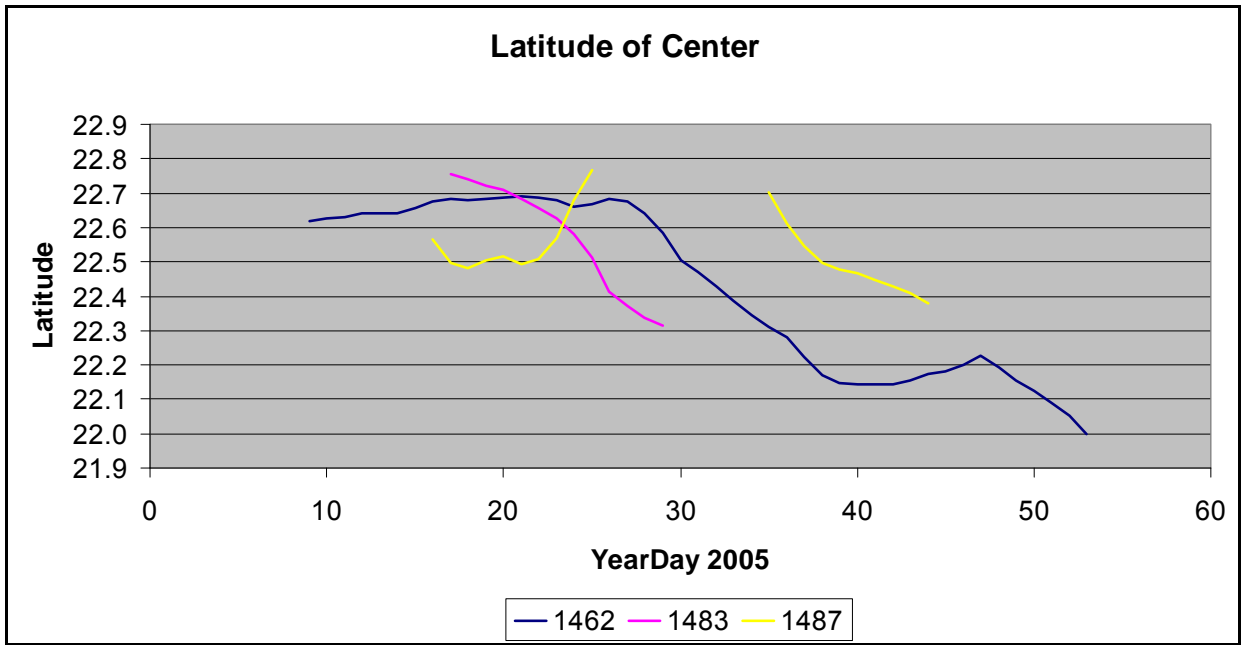


Figure E-1. Latitude of the center of Eddy Ulysses.

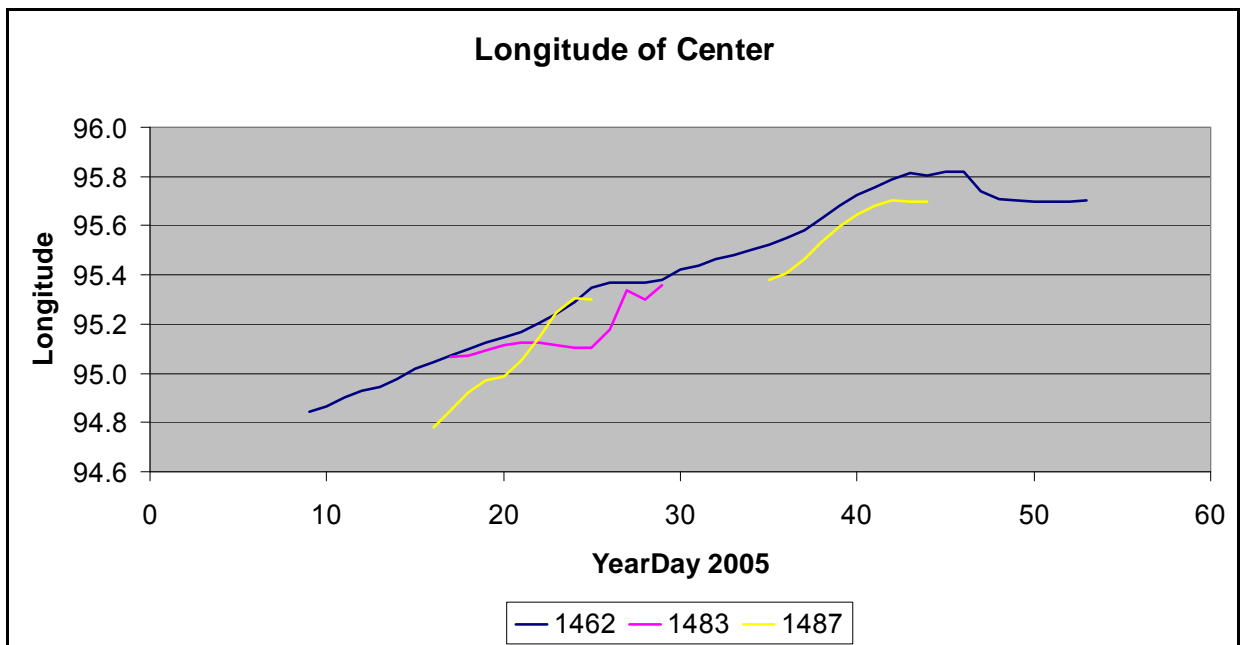


Figure E-2. Longitude of the center of Eddy Ulysses.

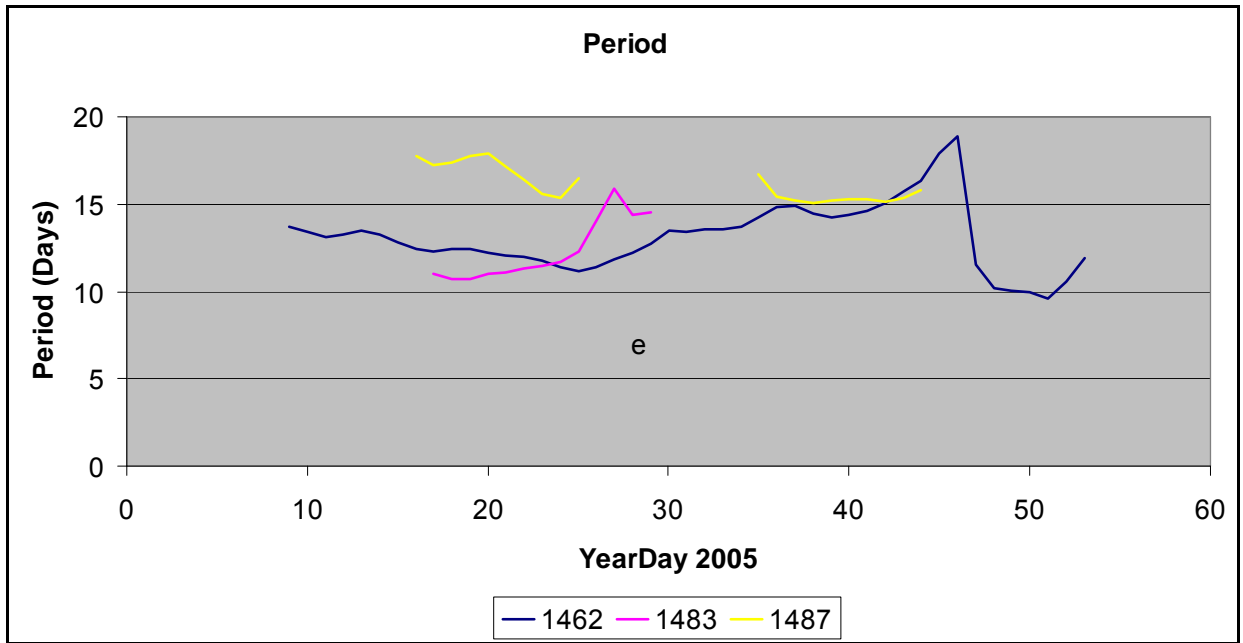


Figure E-3. Orbital period in Eddy Ulysses.

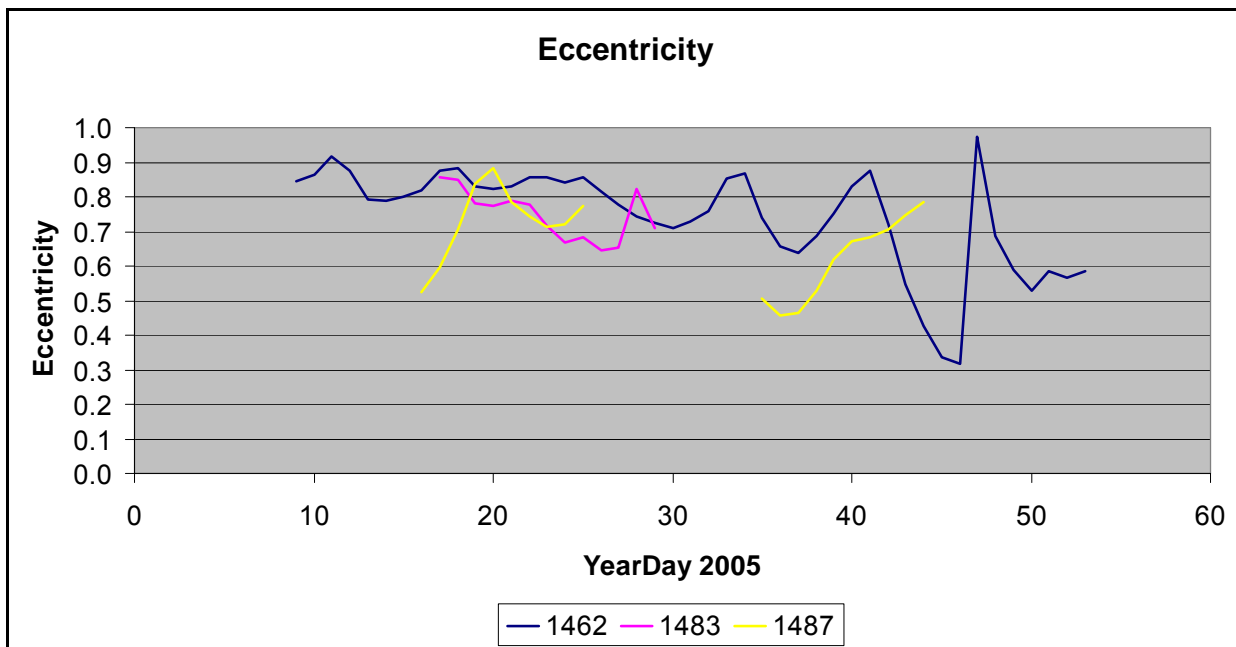


Figure E-4. Eccentricity of Eddy Ulysses.

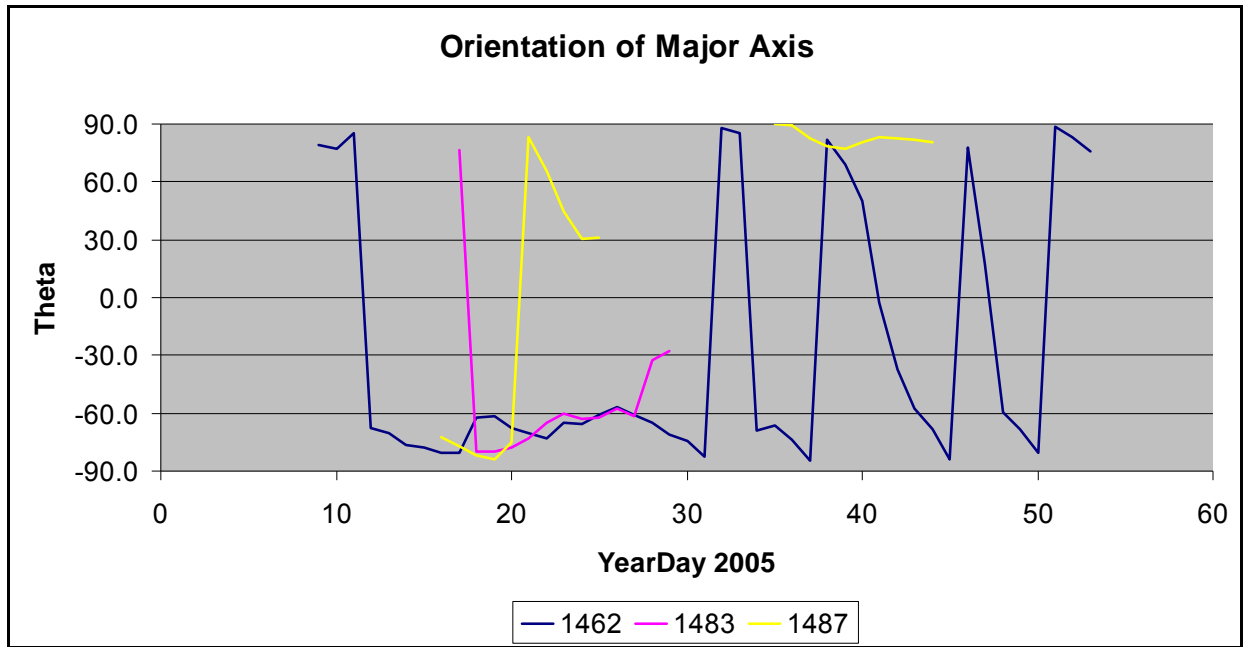


Figure E-5. Orientation of the major axis of Eddy Ulysses.

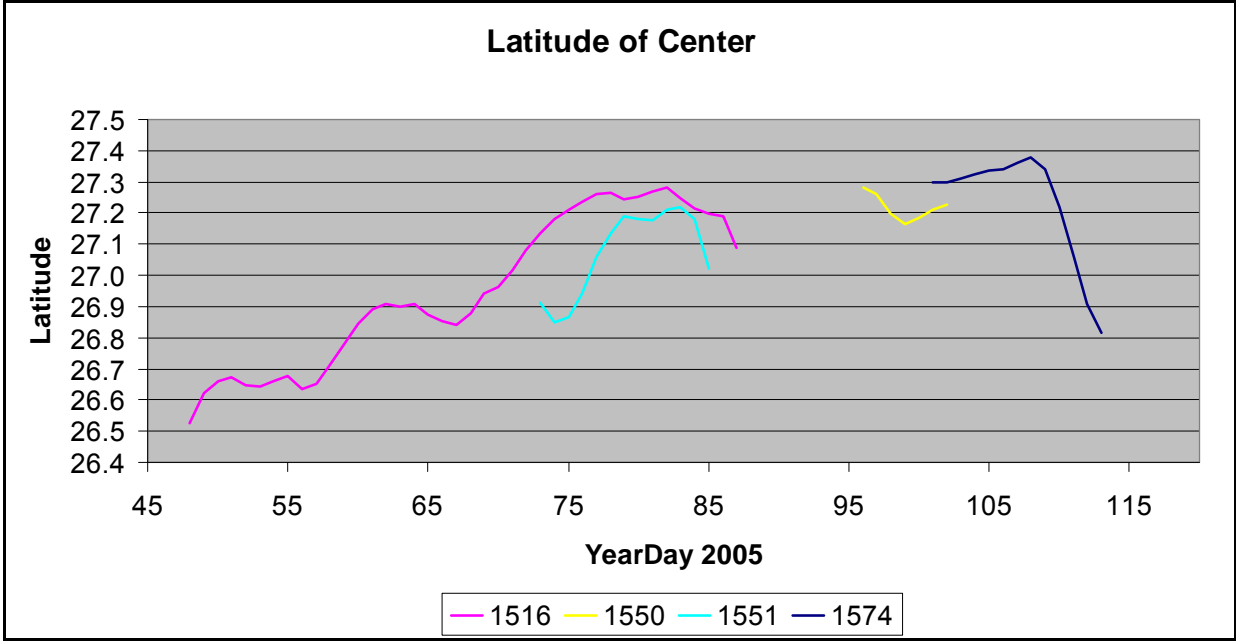


Figure E-6. Latitude of the center of Eddy Vortex early in 2005.

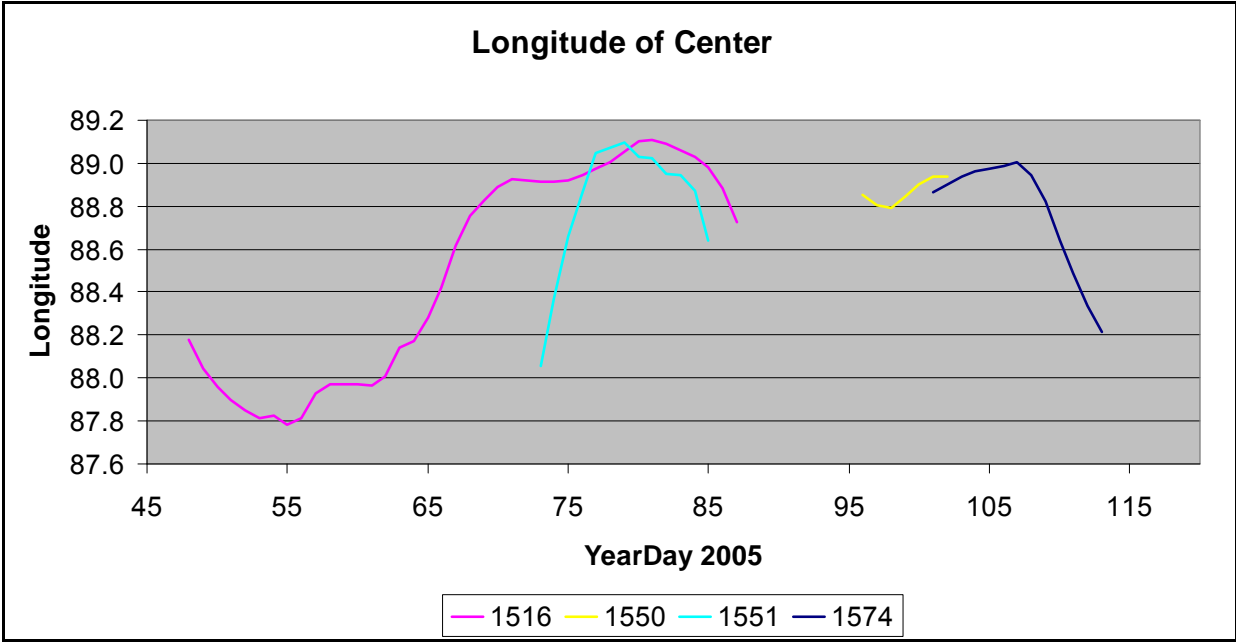


Figure E-7. Longitude of the center of Eddy Vortex early in 2005.

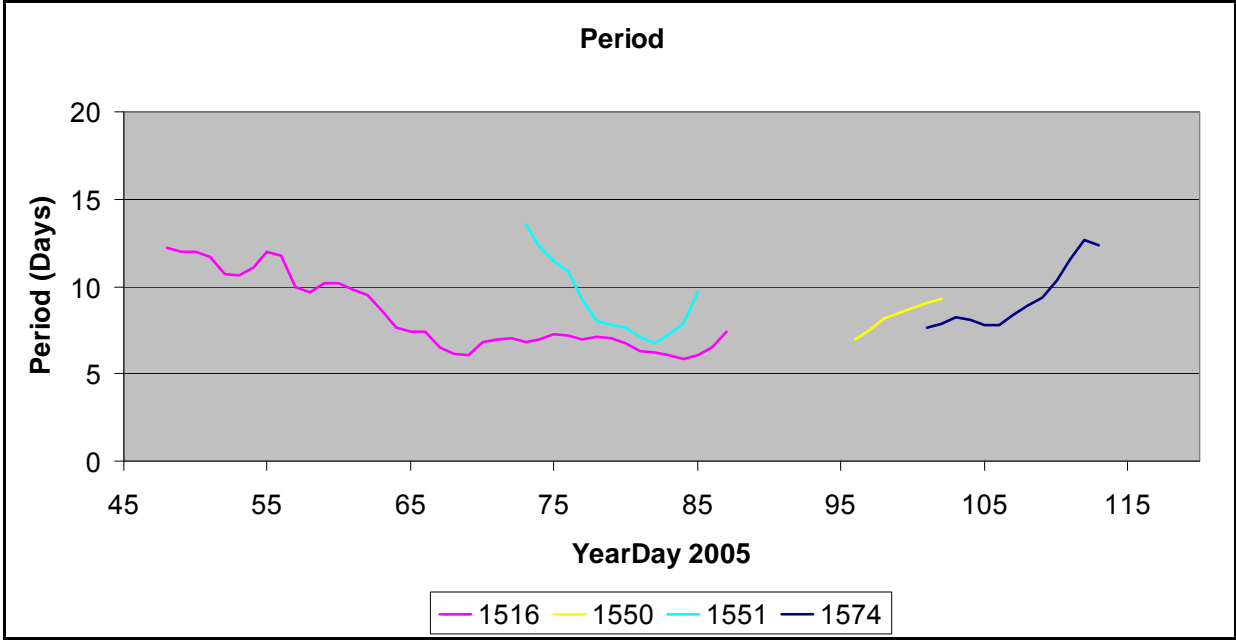


Figure E-8. Orbital period of Eddy Vortex early in 2005.

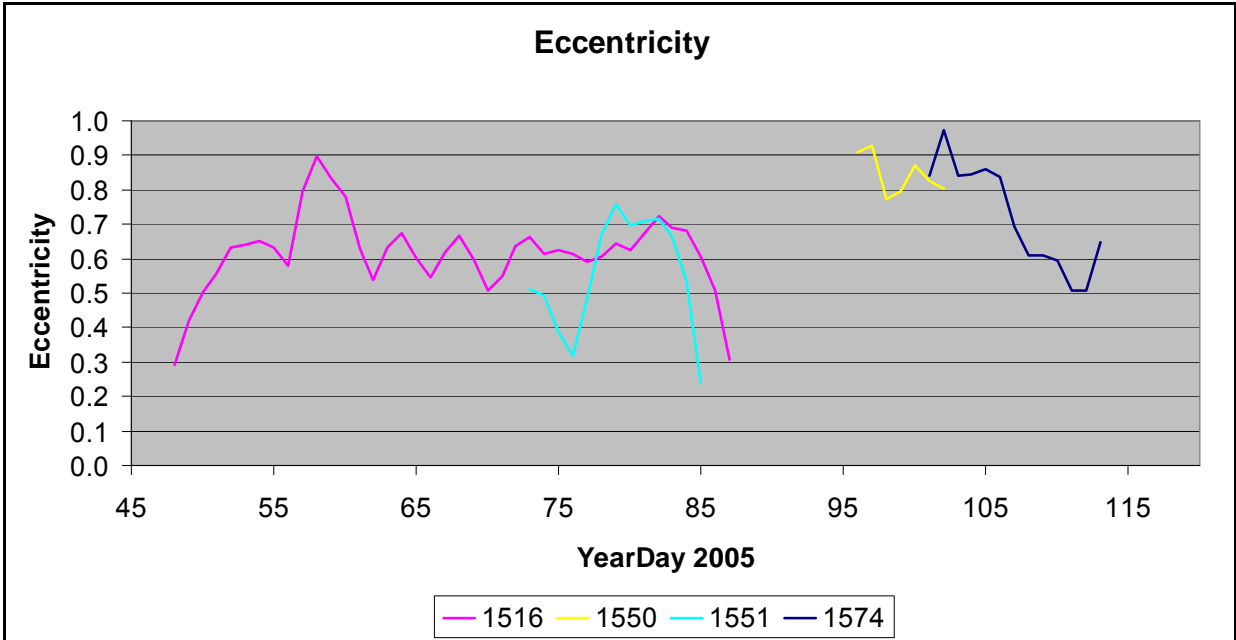


Figure E-9. Eccentricity of Eddy Vortex early in 2005.

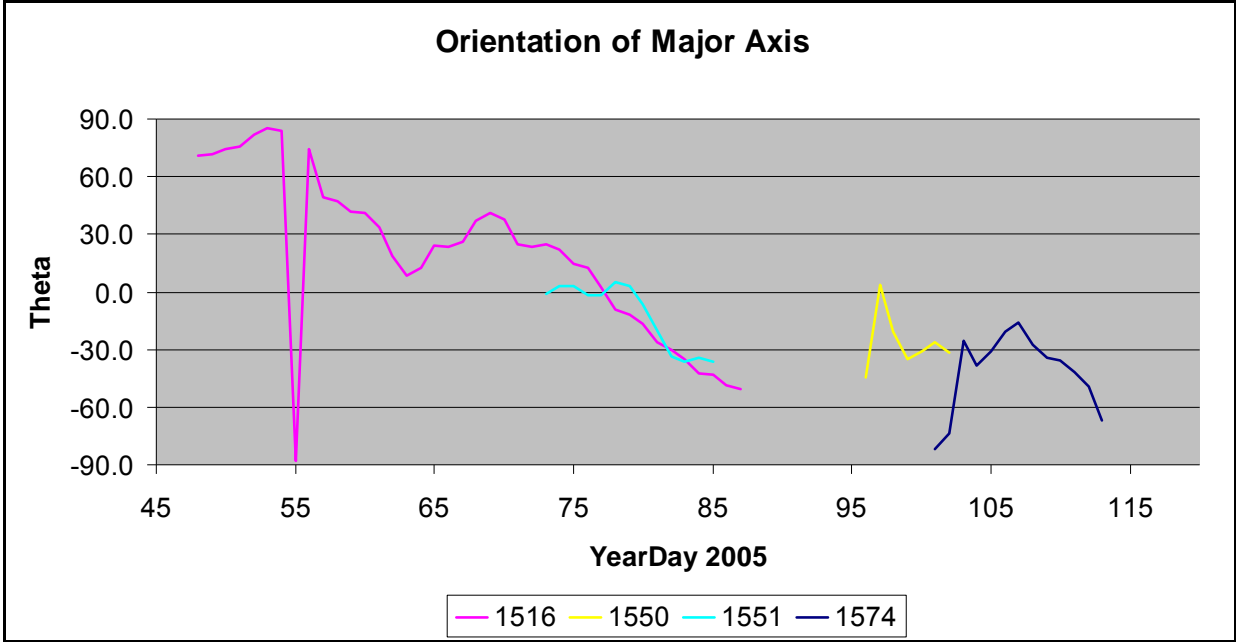


Figure E-10. Orientation of the major axis of Eddy Vortex early in 2005.

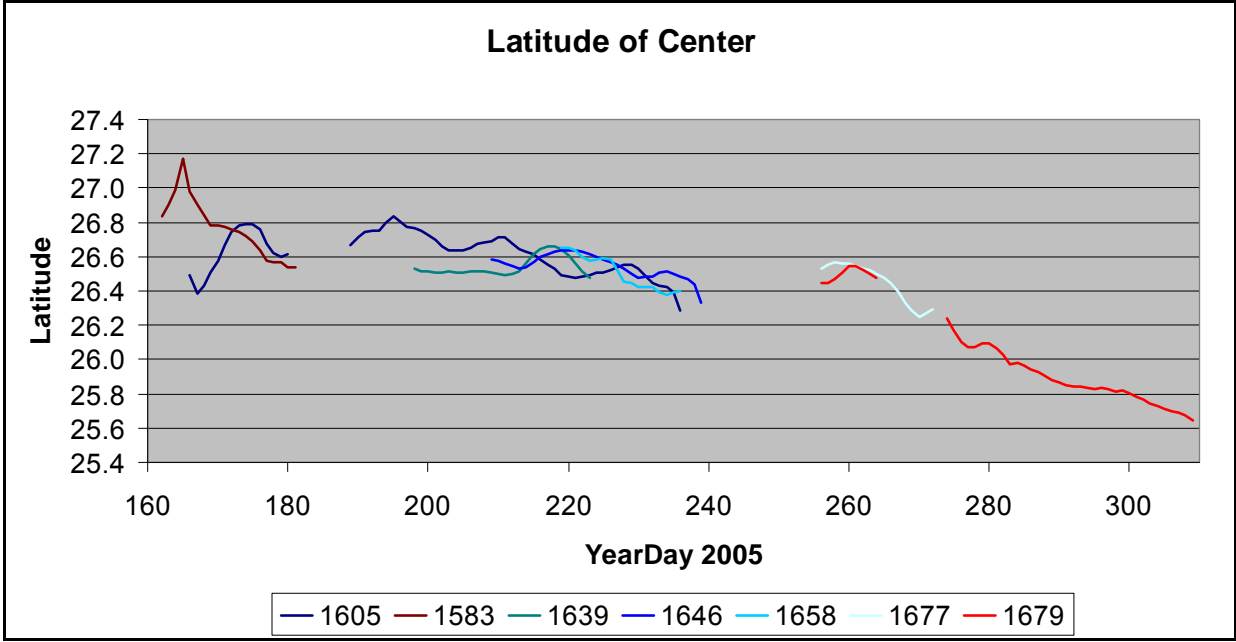


Figure E-11. Latitude of the center of Eddy Vortex late in 2005.

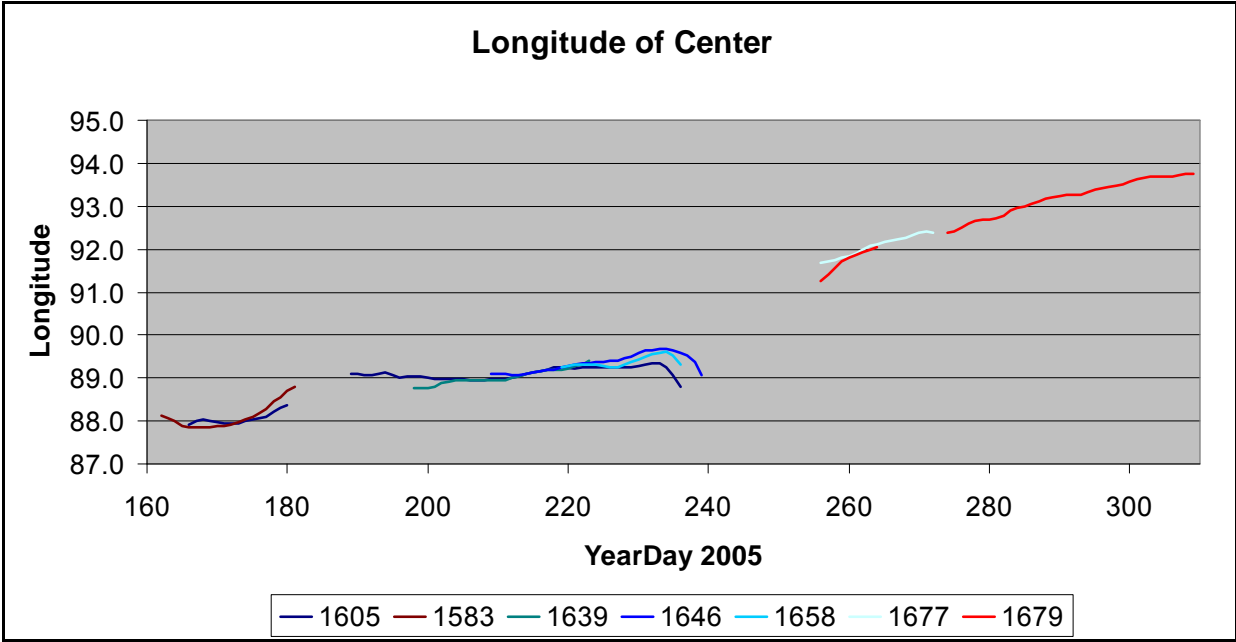


Figure E-12. Longitude of the center of Eddy Vortex late in 2005.

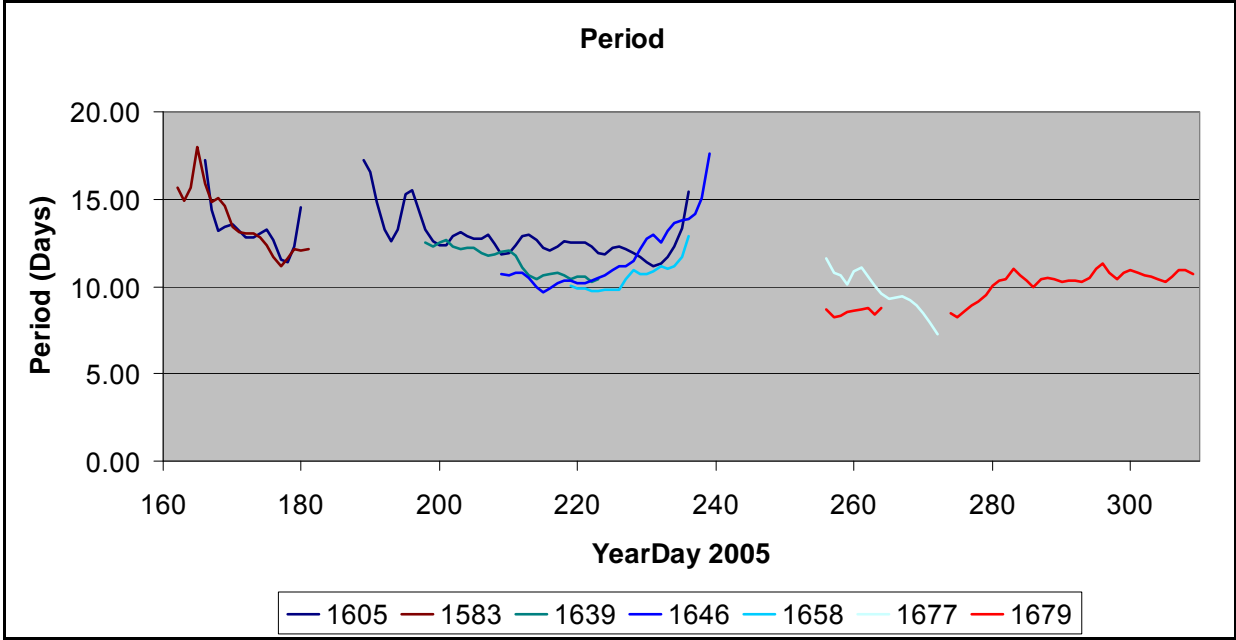


Figure E-13. Orbital period of Eddy Vortex late in 2005.

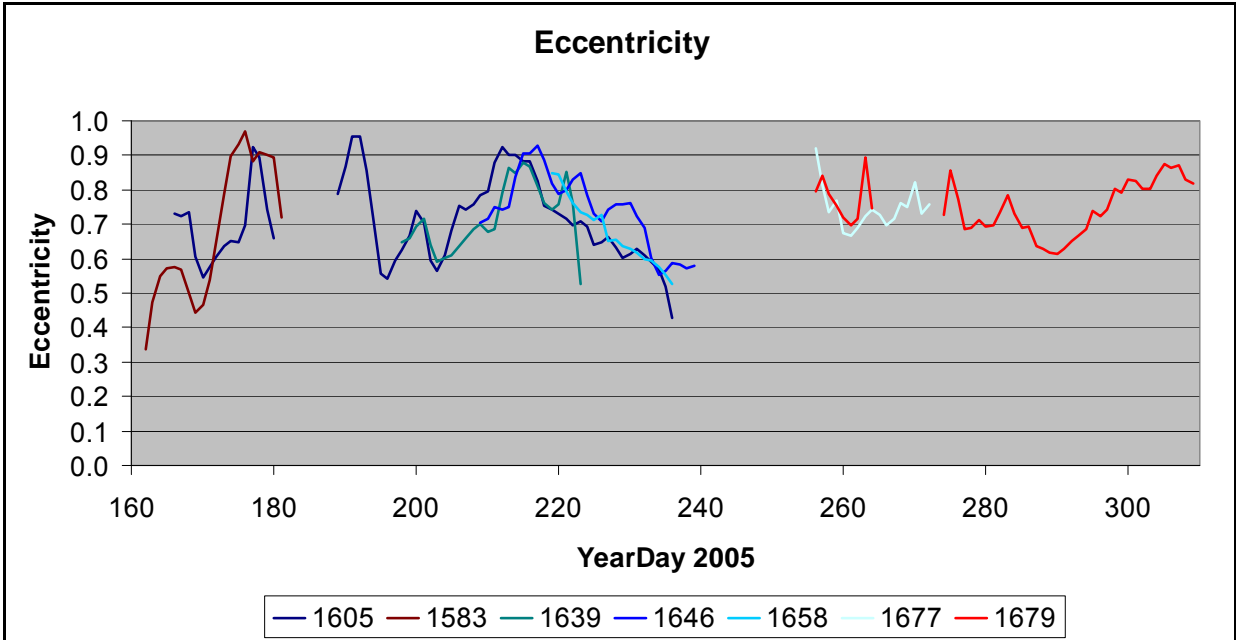


Figure E-14. Eccentricity of Eddy Vortex late in 2005.

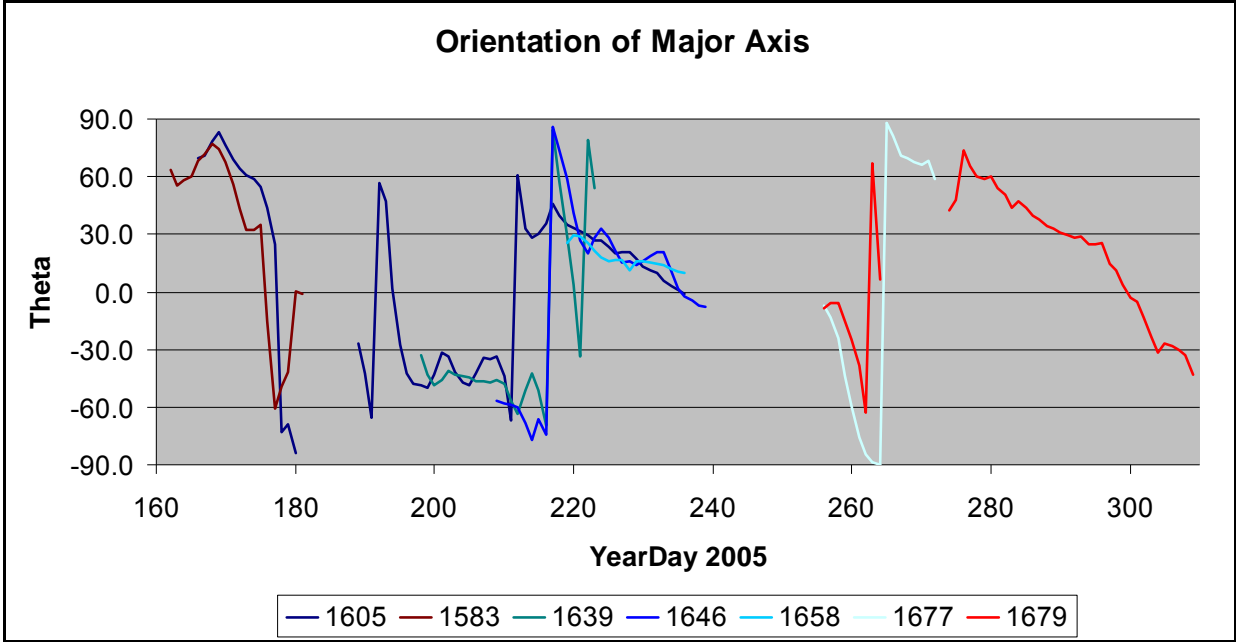


Figure E-15. Orientation of the major axis of Eddy Vortex late in 2005.

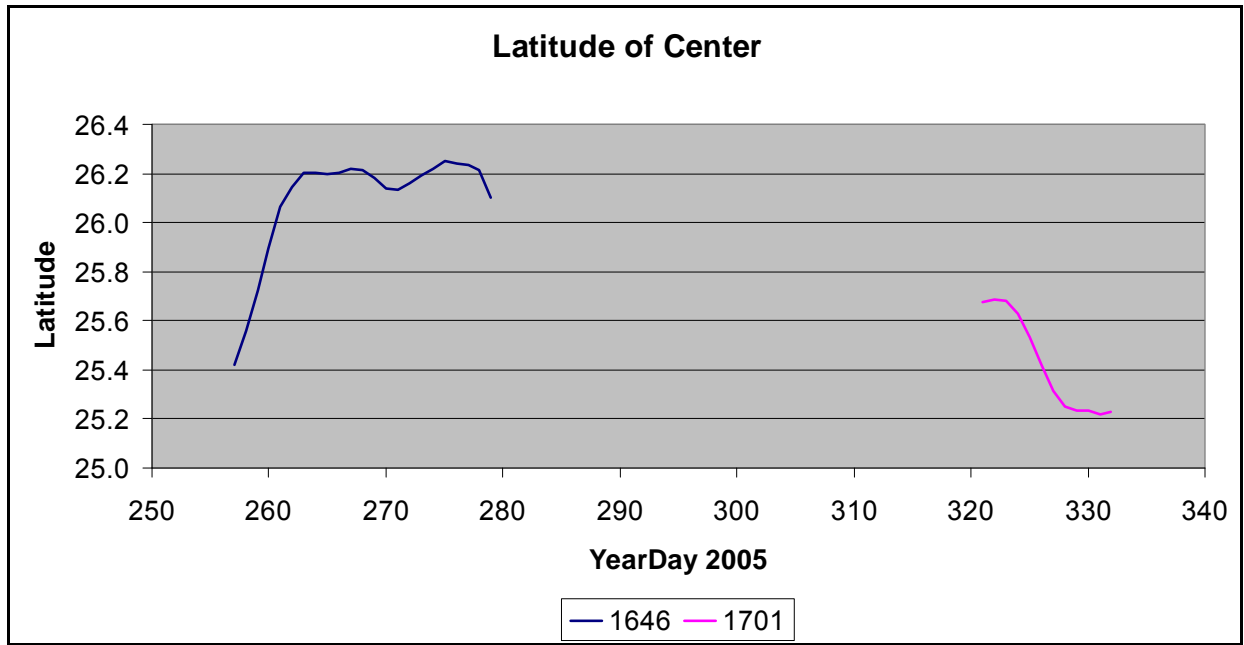


Figure E-16. Latitude of the center of Eddy Walker.

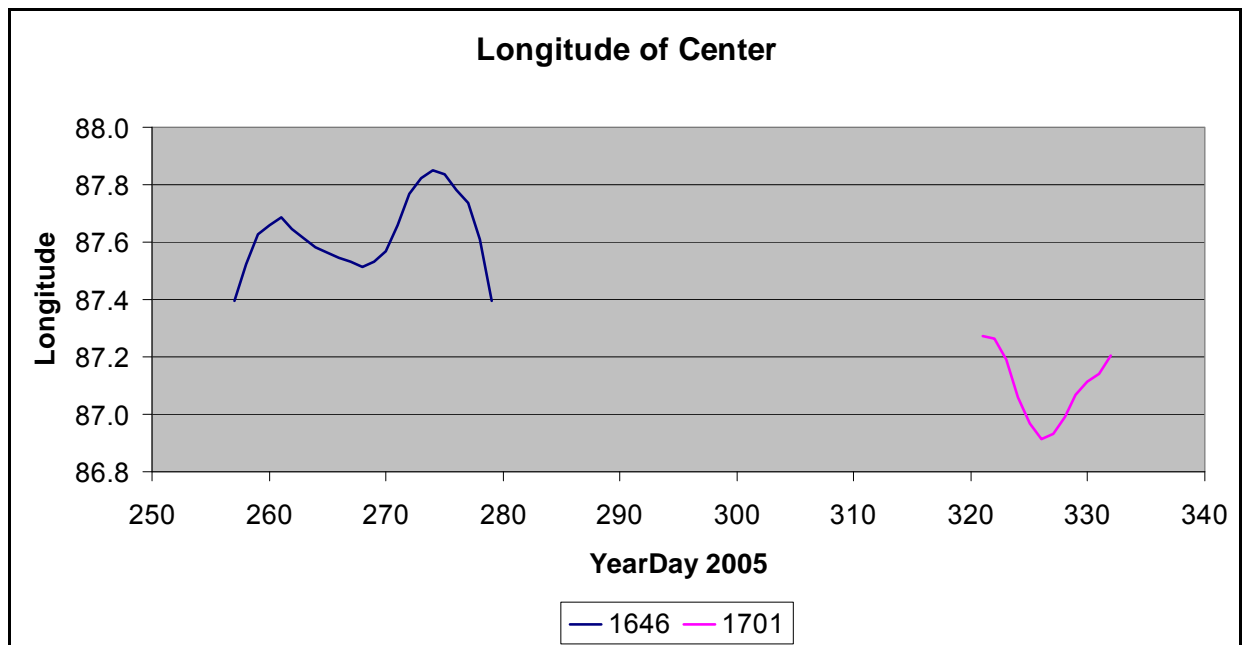


Figure E-17. Longitude of the center of Eddy Walker.

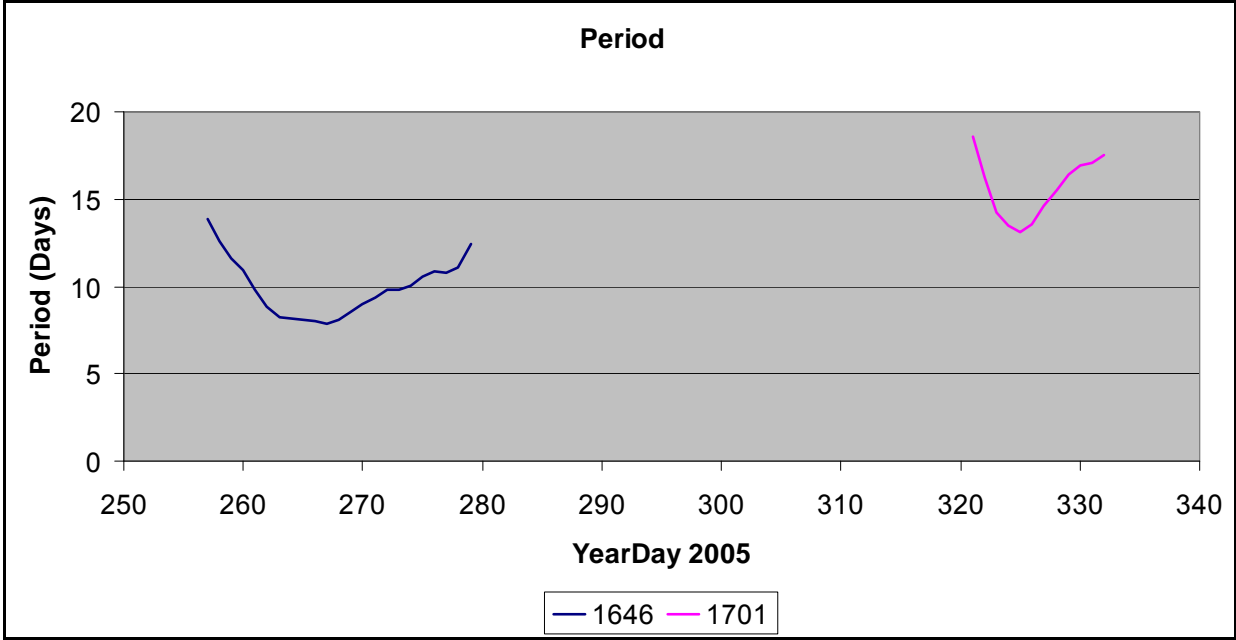


Figure E-18. Orbital period of Eddy Walker.

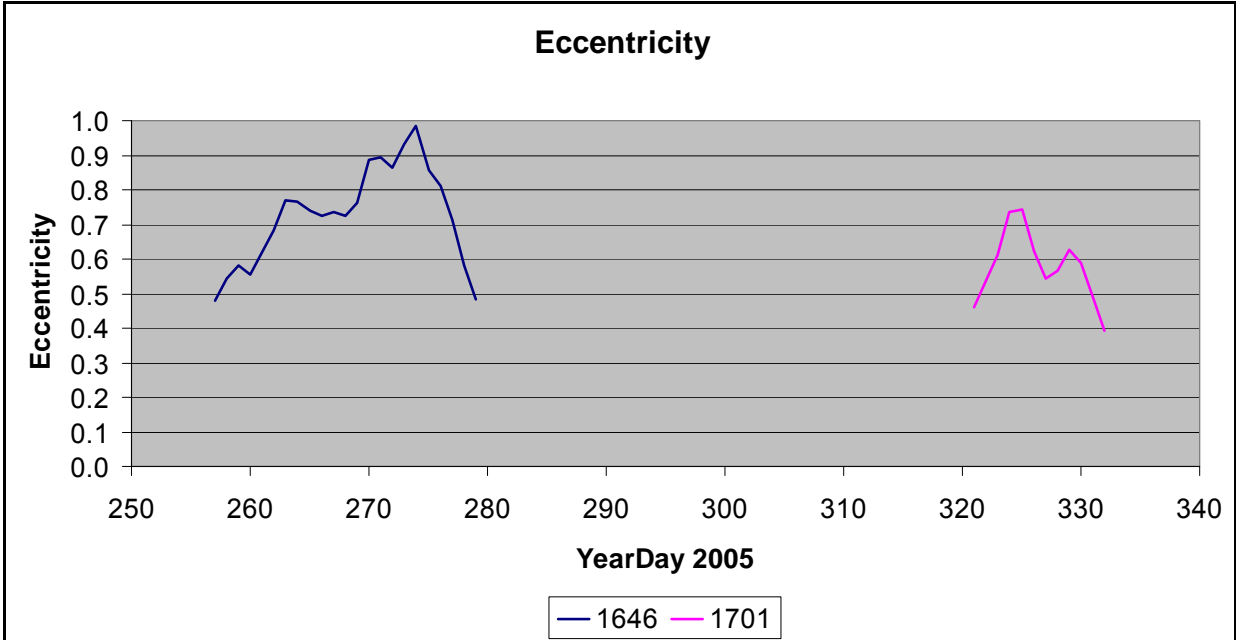


Figure E-19. Eccentricity of Eddy Walker.

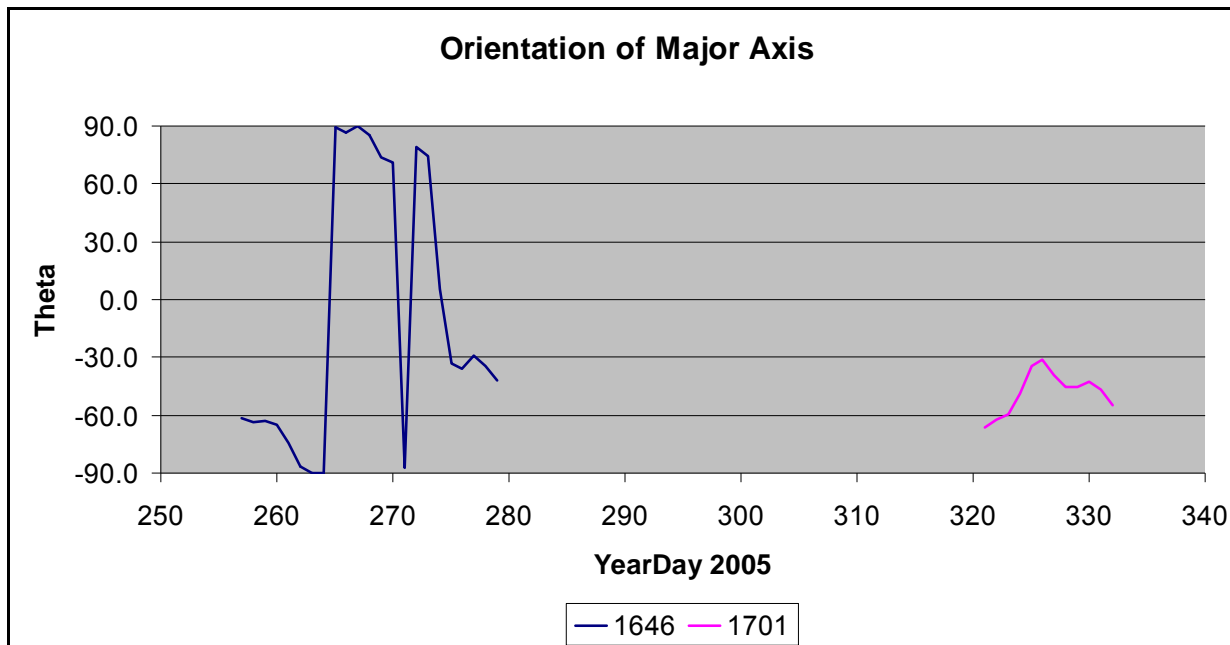


Figure E-20. Orientation of the major axis of Eddy Walker.

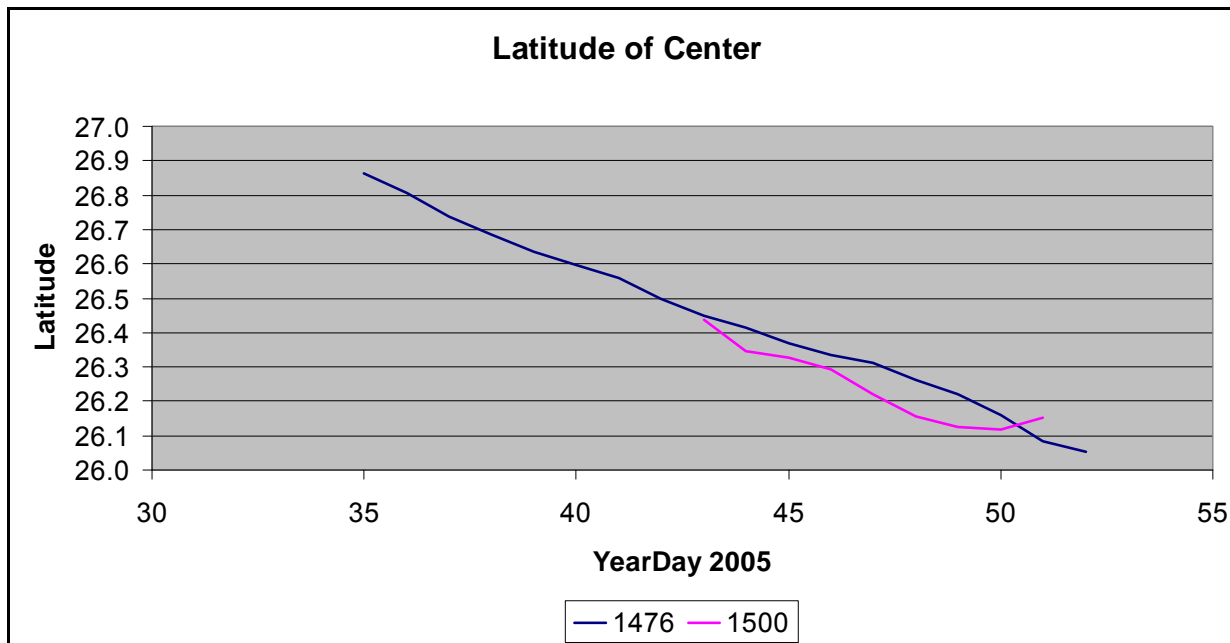


Figure E-21. Latitude of the center of Cold Eddy 1.

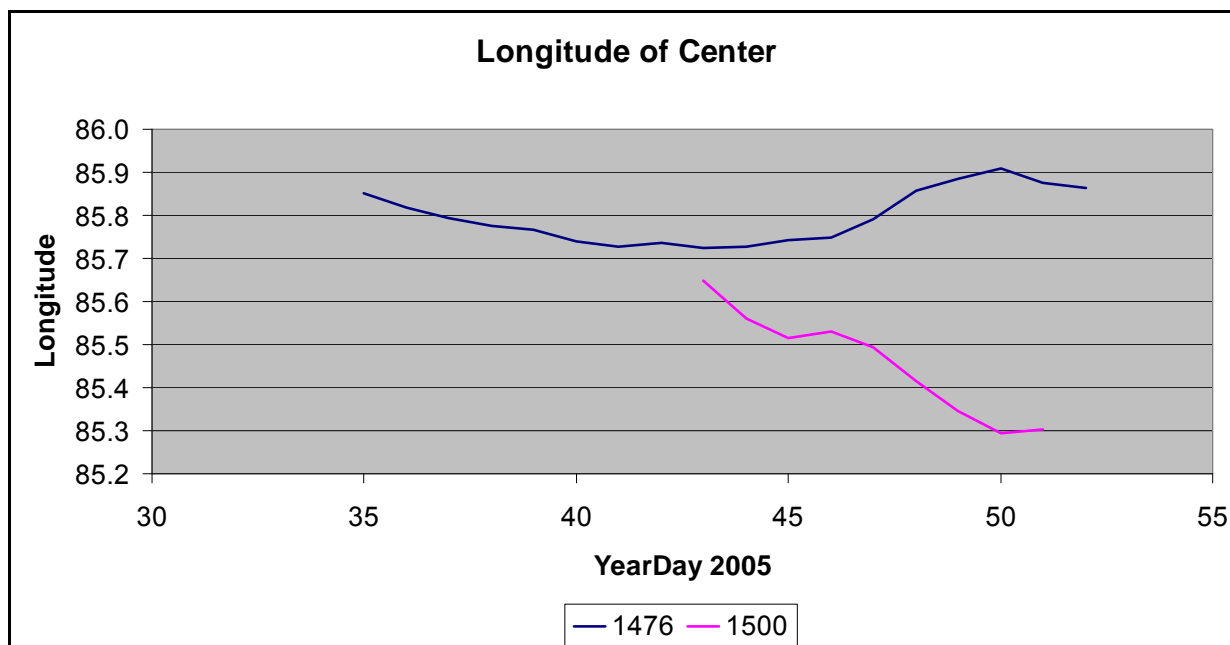


Figure E-22. Longitude of the center of Cold Eddy 1.

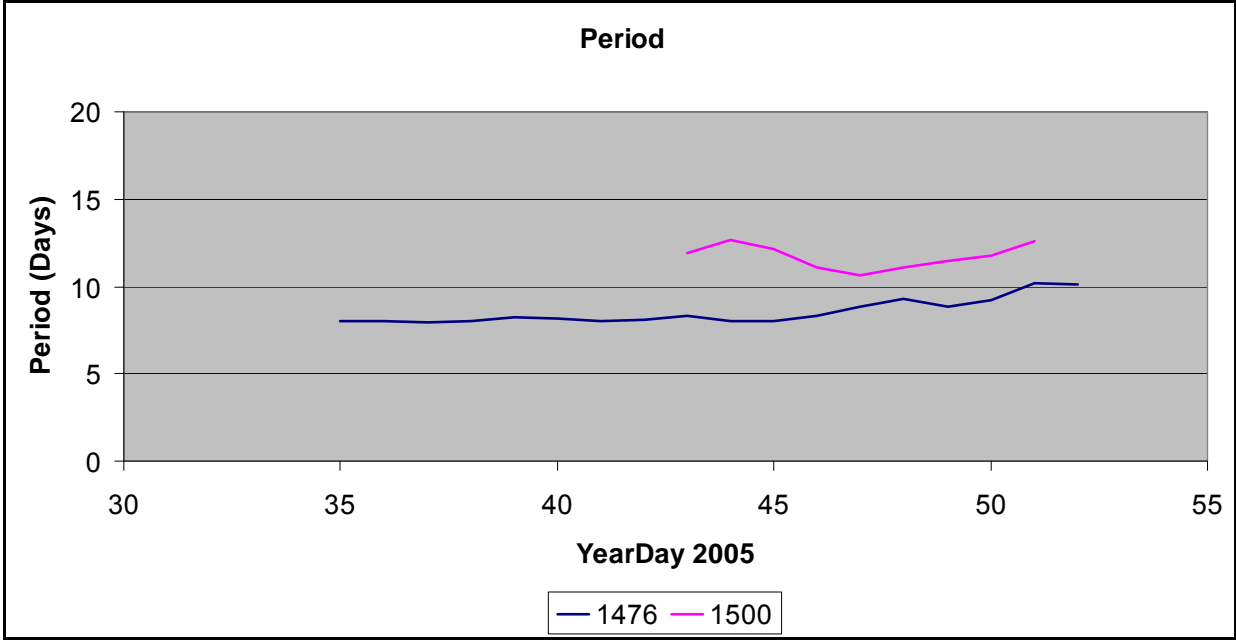


Figure E-23. Orbital period of Cold Eddy 1.

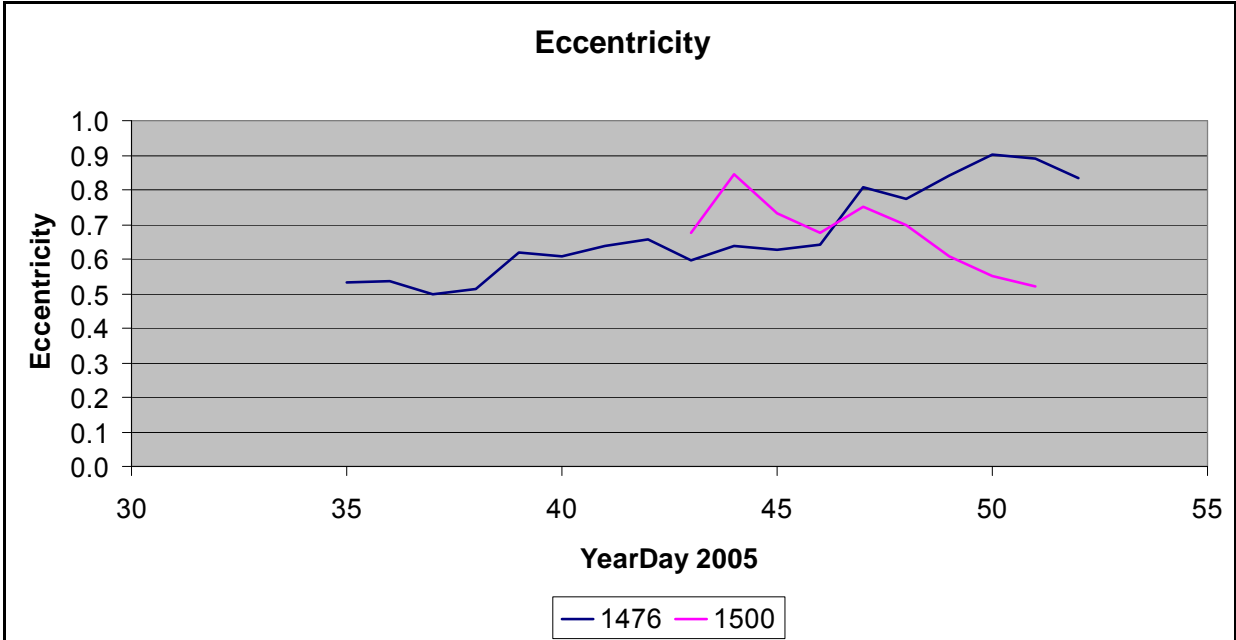


Figure E-24. Eccentricity of Cold Eddy 1.

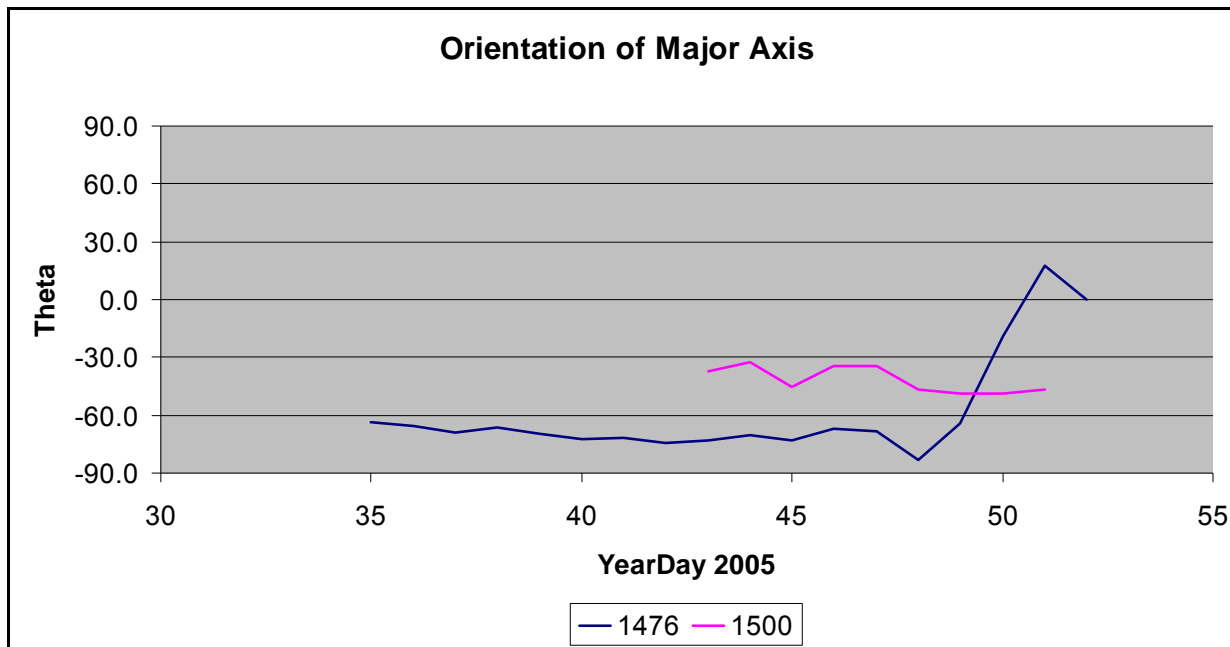


Figure E-25. Orientation of the major axis of Cold Eddy 1.

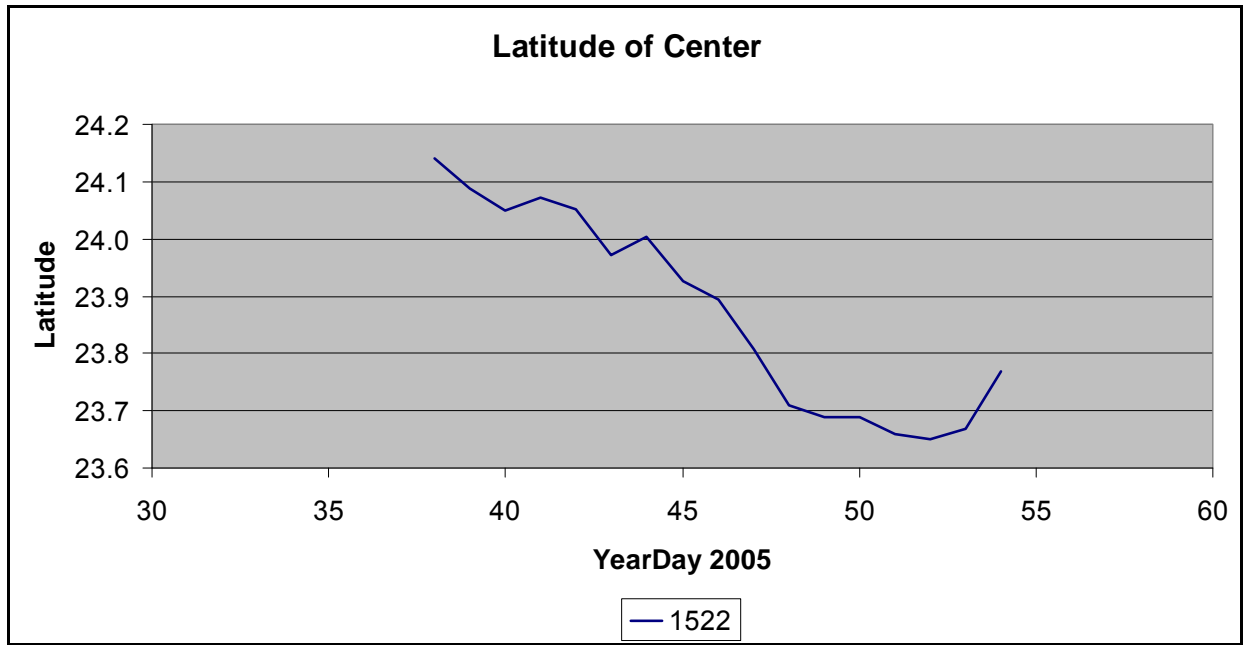


Figure E-26. Latitude of the center of Cold Eddy 2.

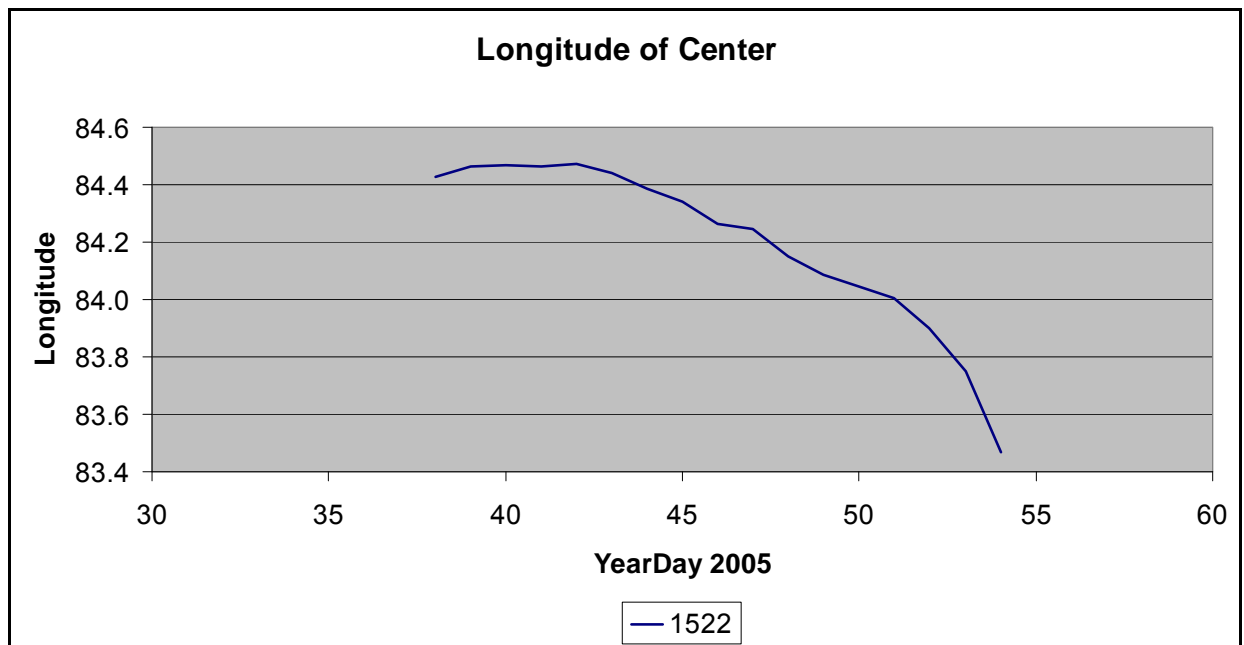


Figure E-27. Longitude of the center of Cold Eddy 2.

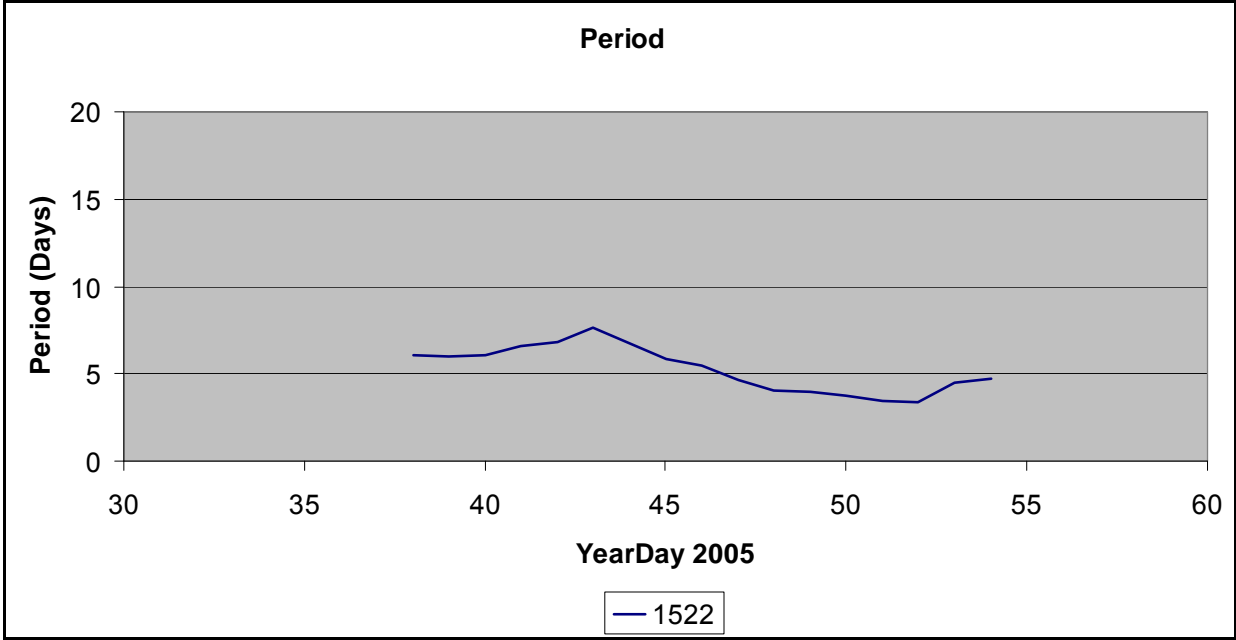


Figure E-28. Orbital period of Cold Eddy 2.

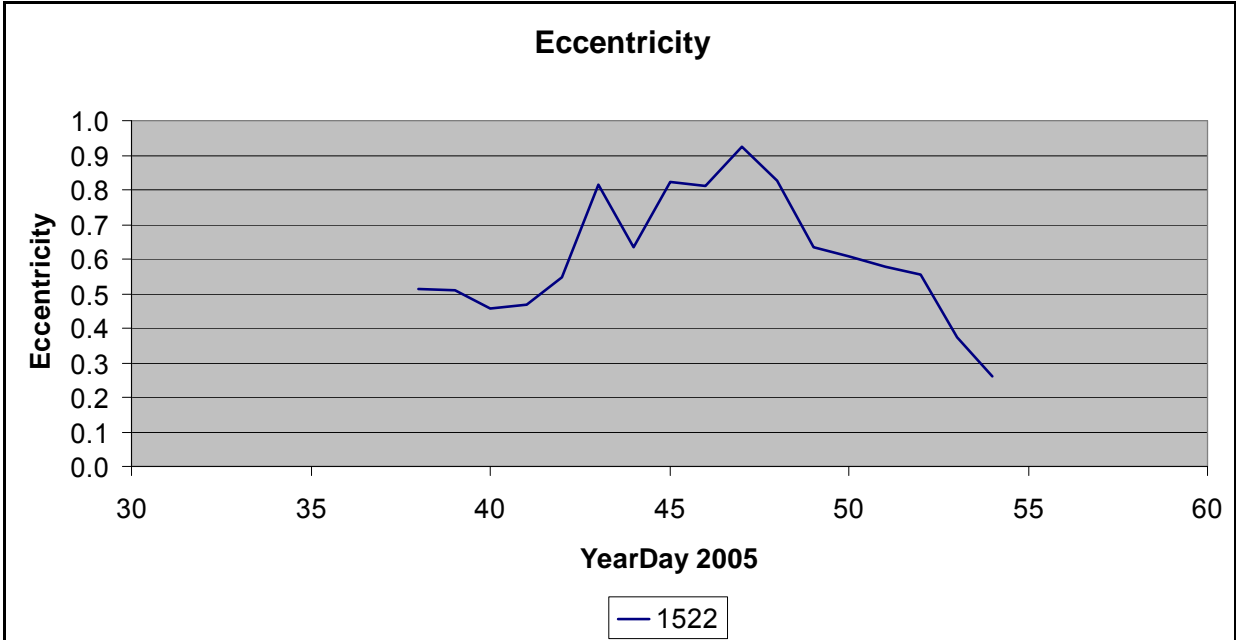


Figure E-29. Eccentricity of Cold Eddy 2.

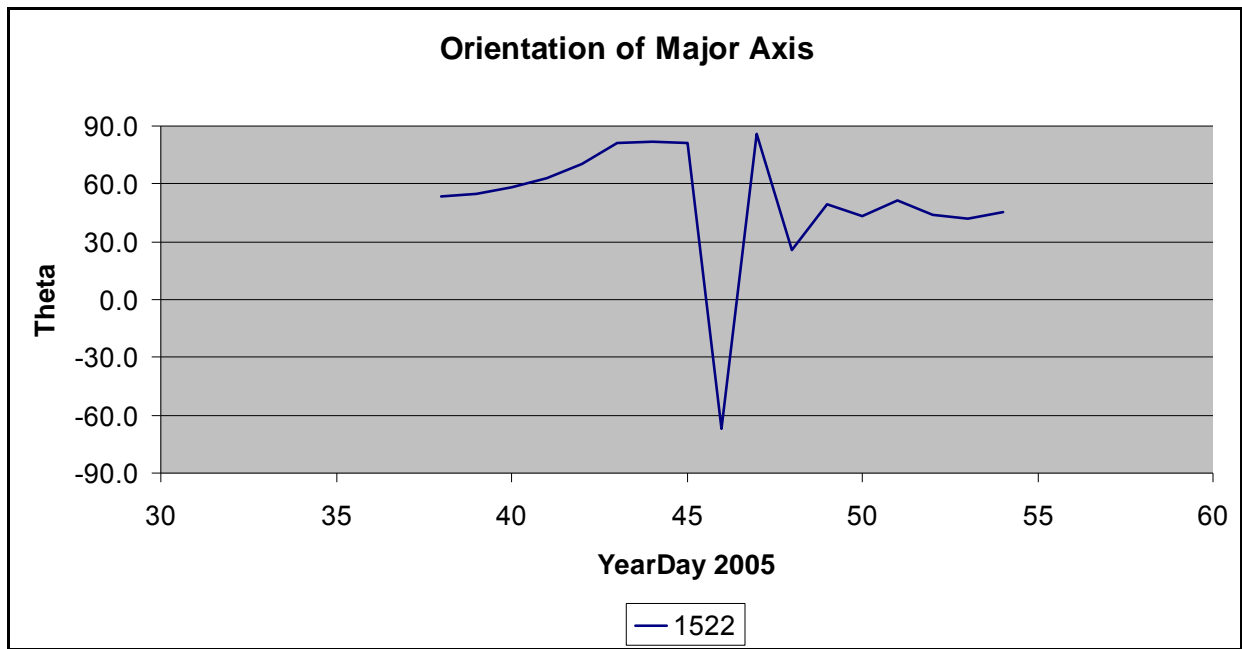


Figure E-30. Orientation of the major axis of Cold Eddy 2.

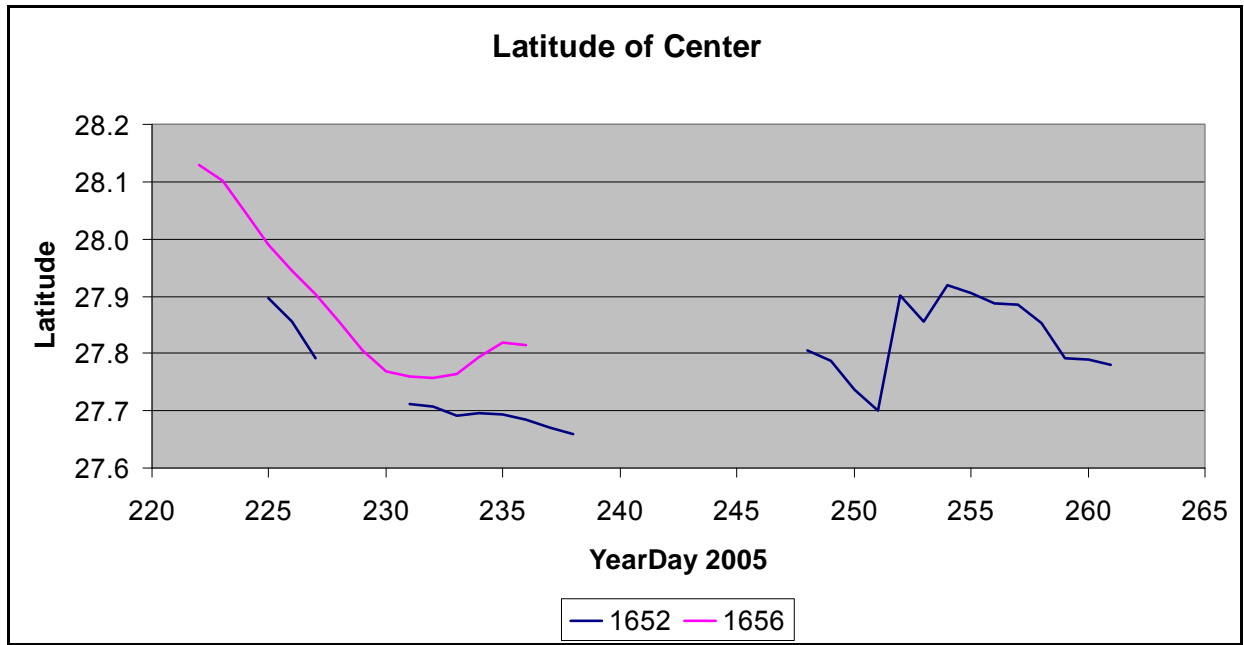


Figure E-31. Latitude of the center of Cold Eddy 3.

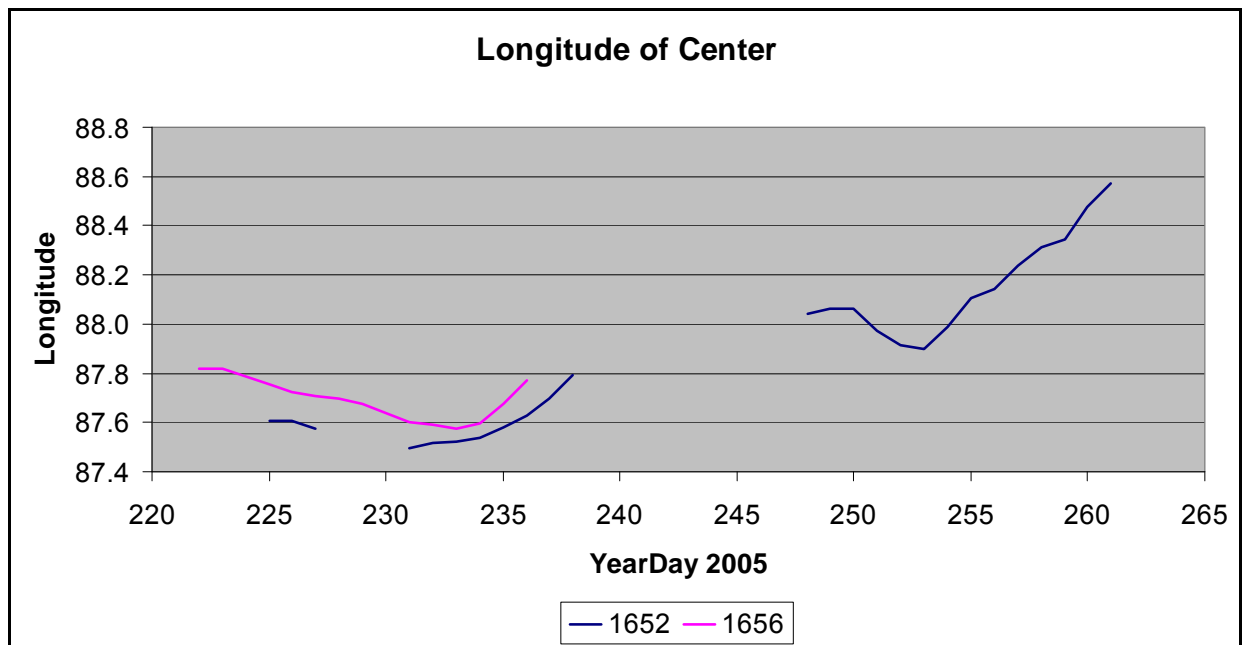


Figure E-32. Longitude of the center of Cold Eddy 3.

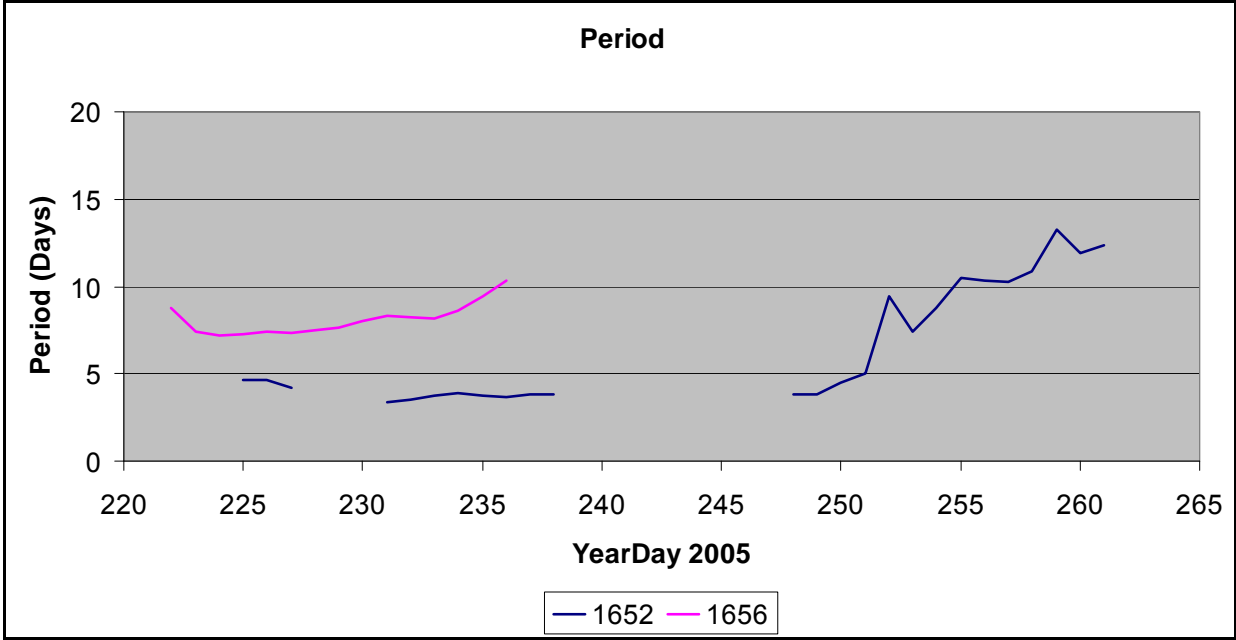


Figure E-33. Orbital period of Cold Eddy 3.

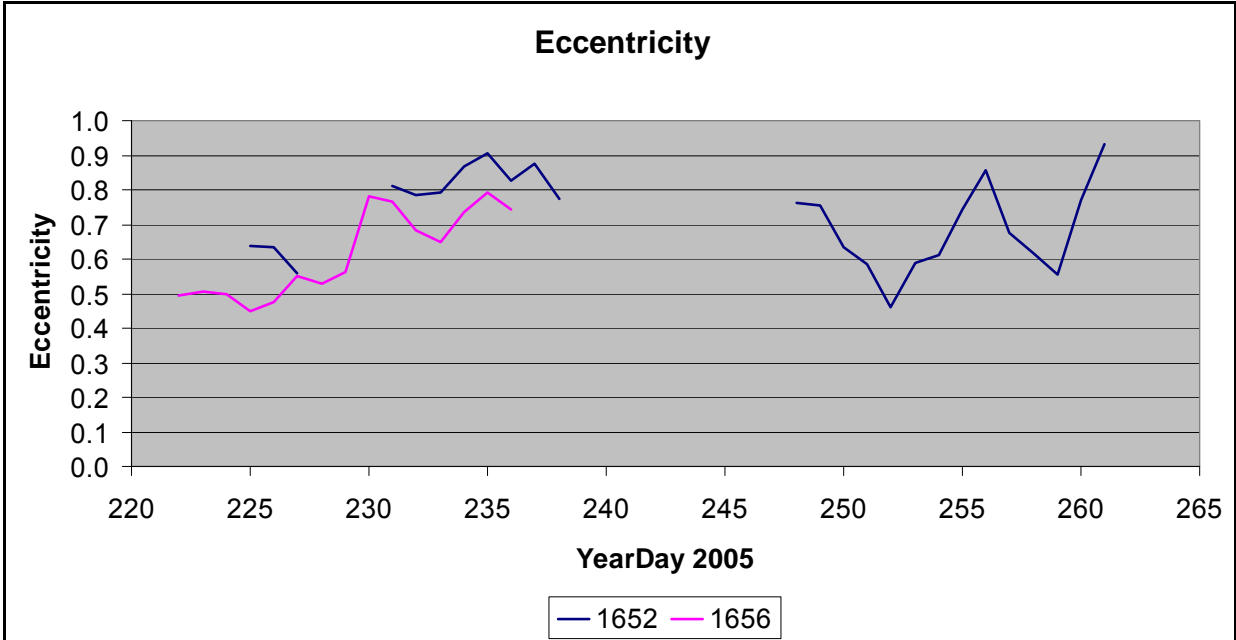


Figure E-34. Eccentricity of Cold Eddy 3.

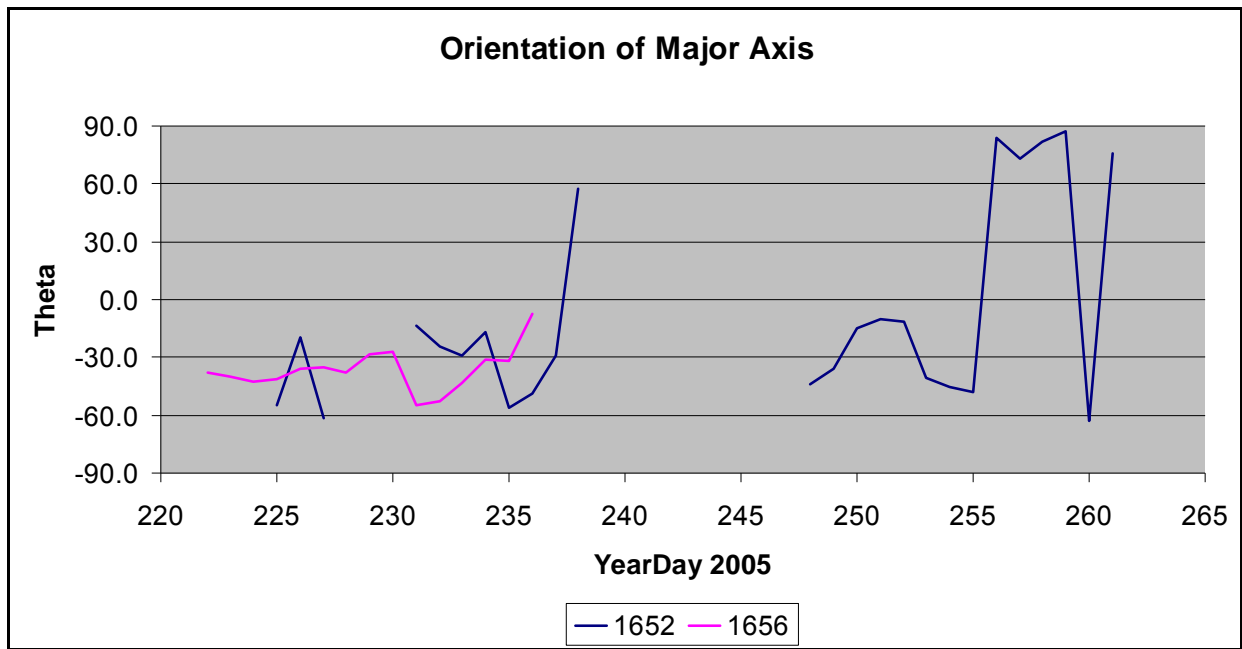


Figure E-35. Orientation of the major axis of Cold Eddy 3.

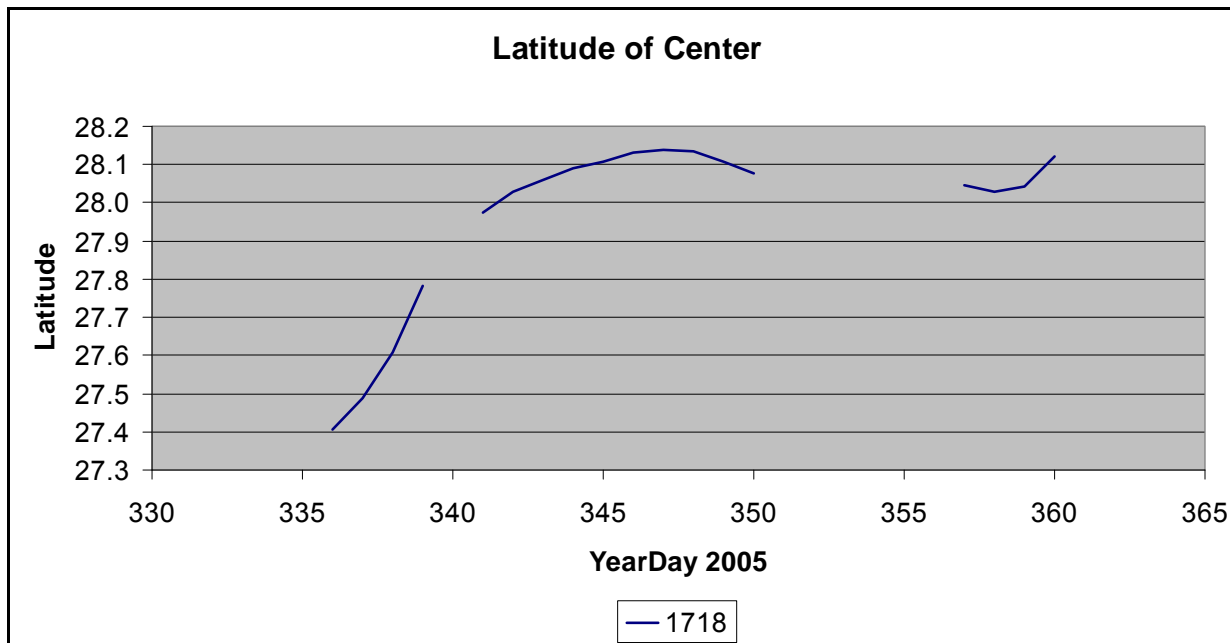


Figure E-36. Latitude of the center of Cold Eddy 4.

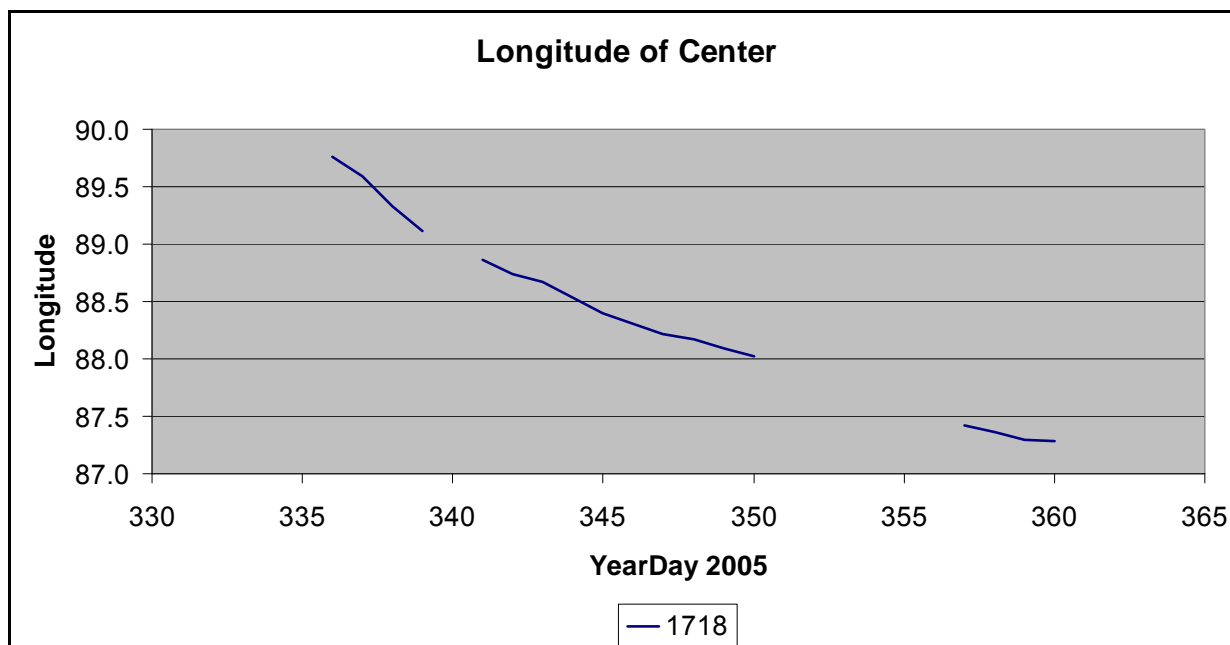


Figure E-37. Longitude of the center of Cold Eddy 4.

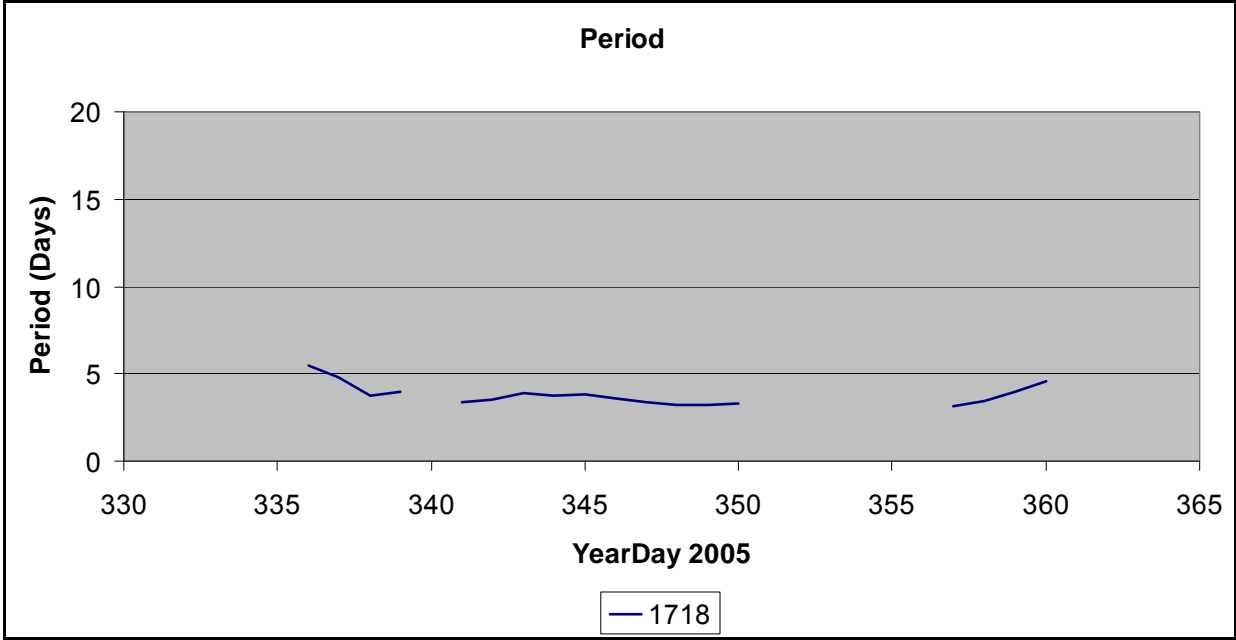


Figure E-38. Orbital period of Cold Eddy 4.

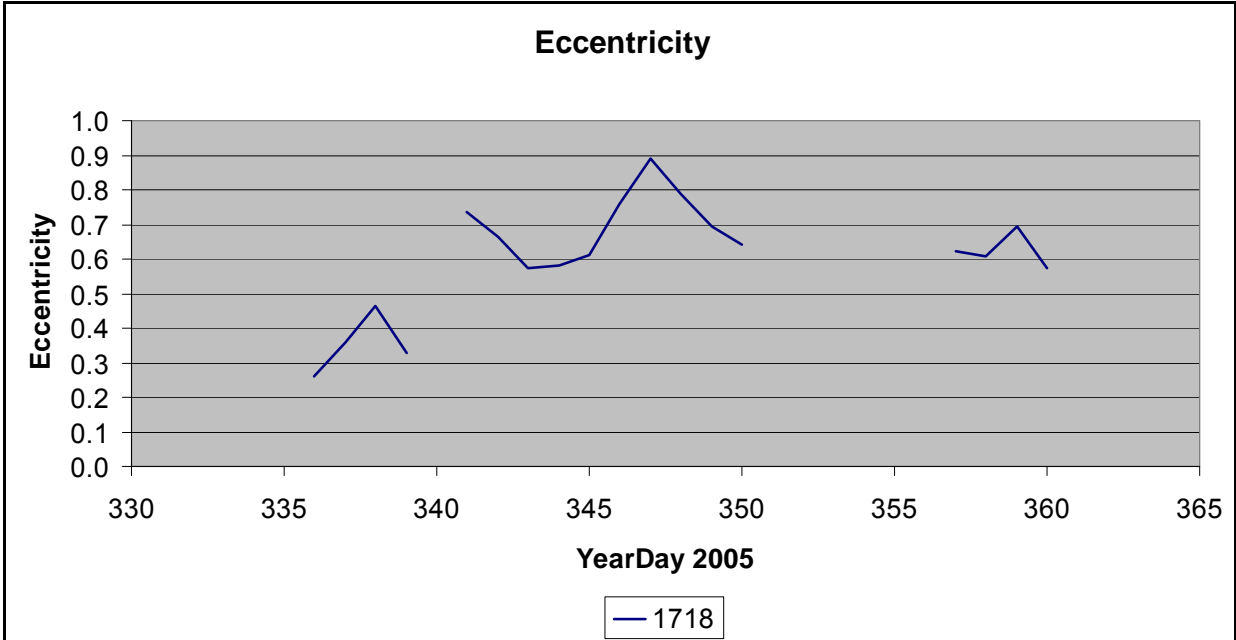


Figure E-39. Eccentricity of Cold Eddy 4.

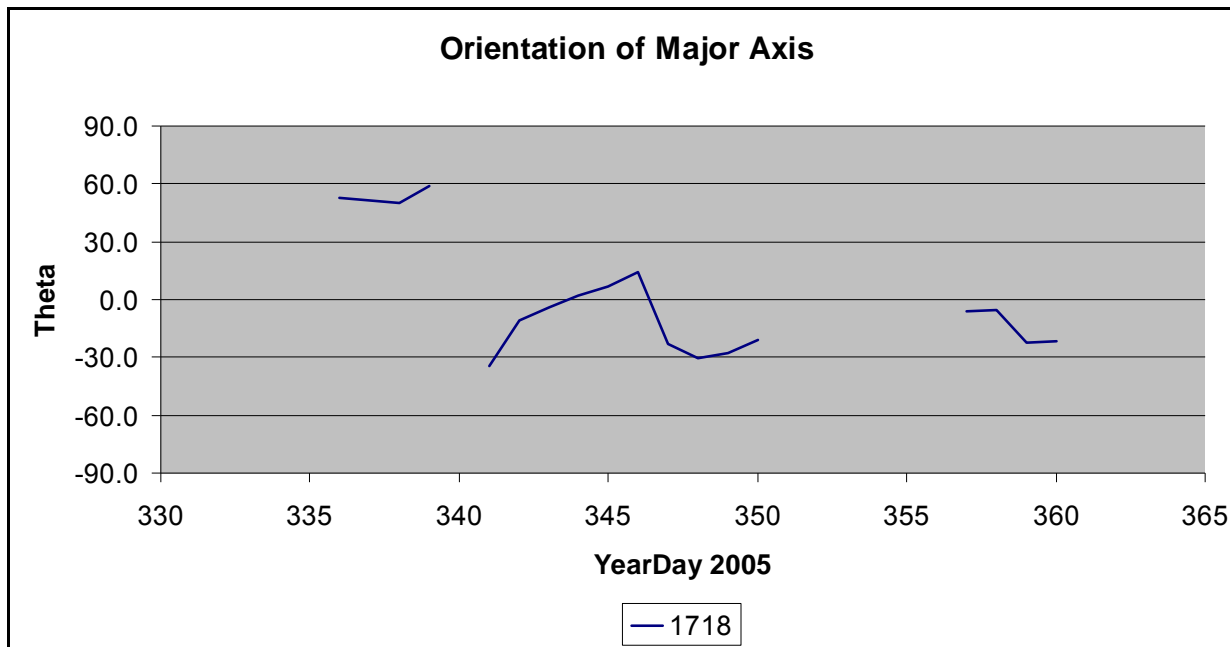


Figure E-40. Orientation of the major axis of Cold Eddy 4.

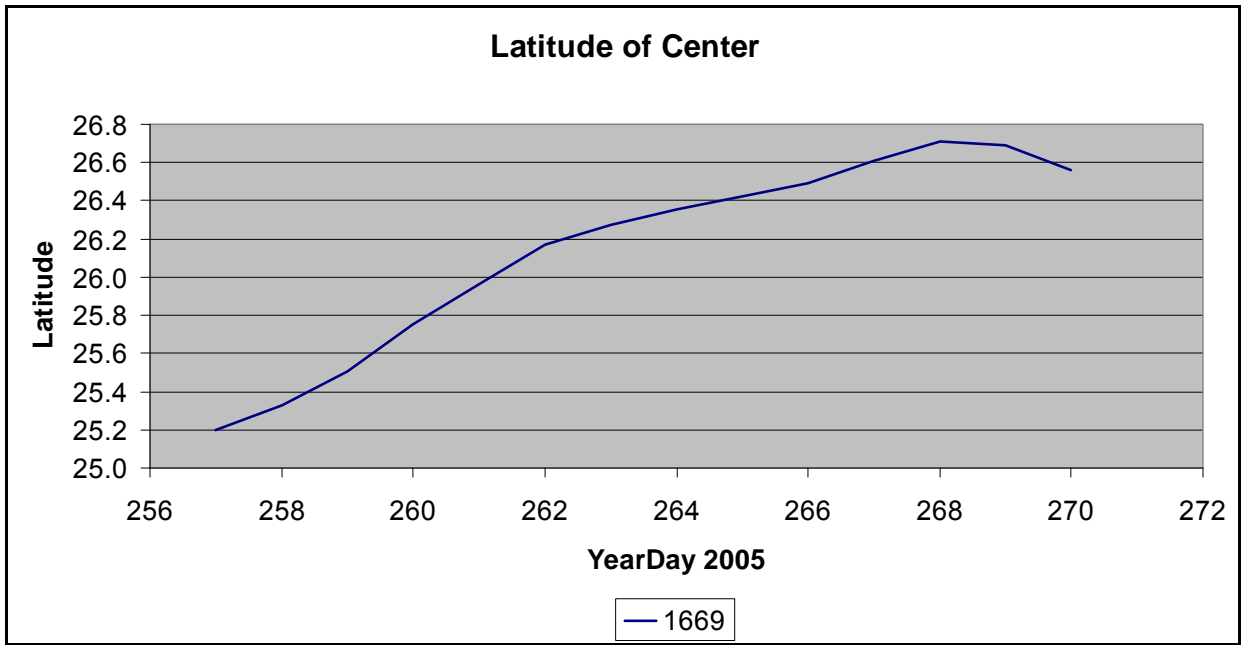


Figure E-41. Latitude of the center of the Loop Current.

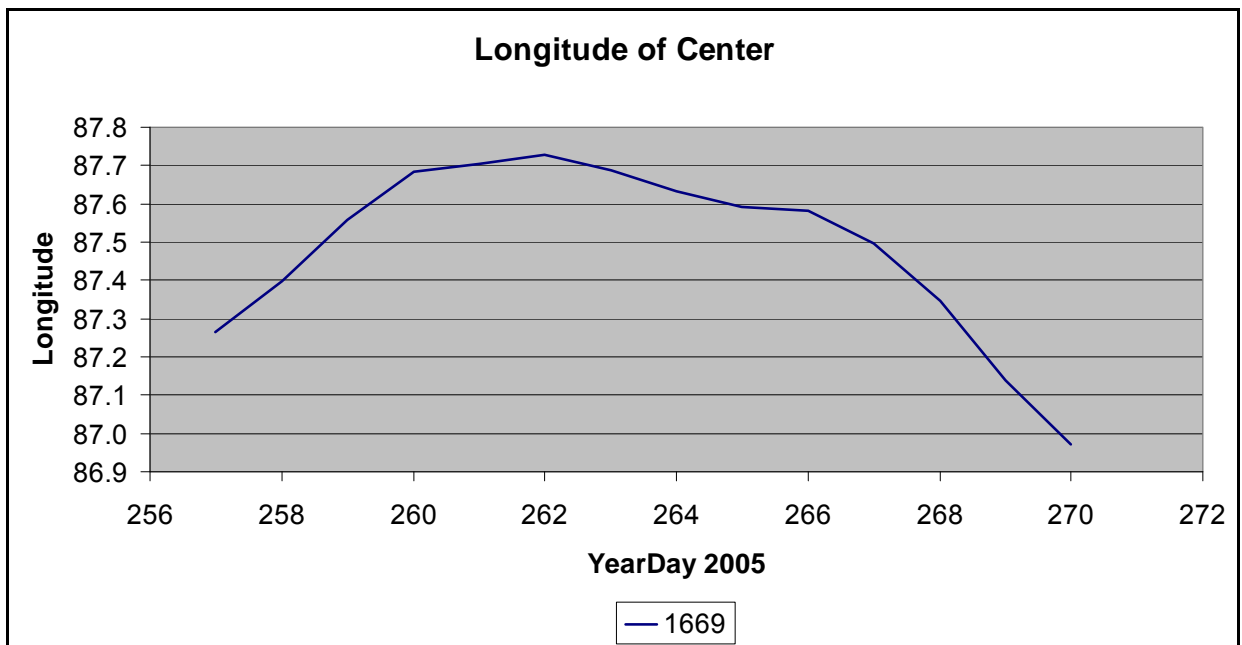


Figure E-42. Longitude of the center of the Loop Current.

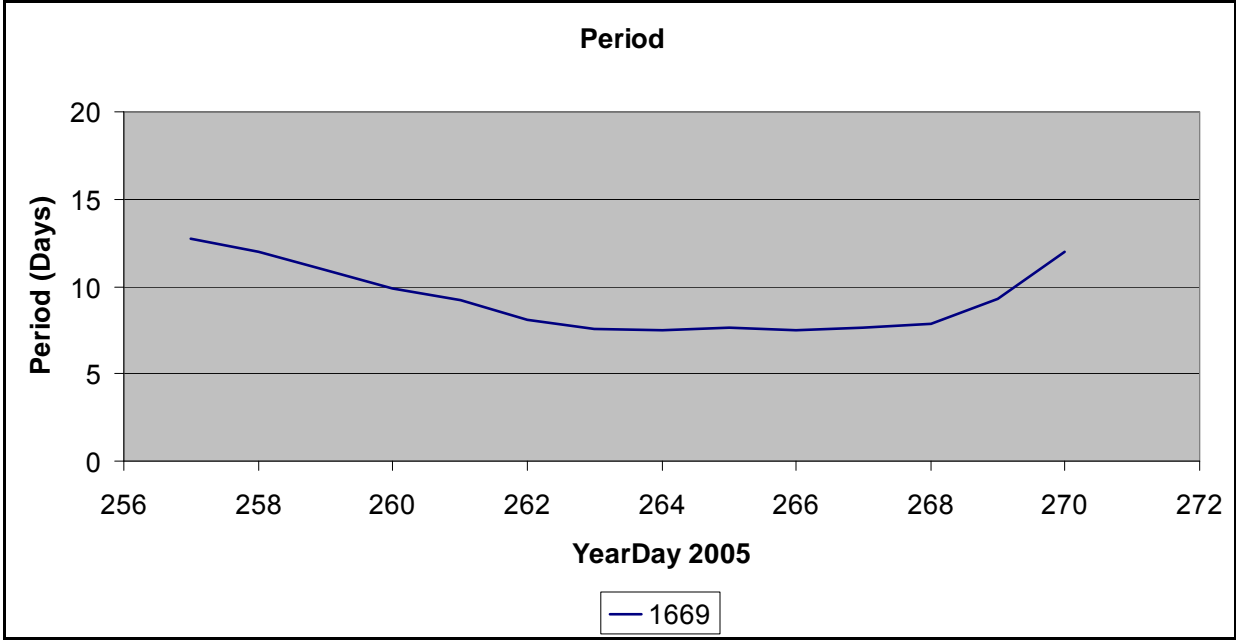


Figure E-43. Orbital period in the Loop Current.

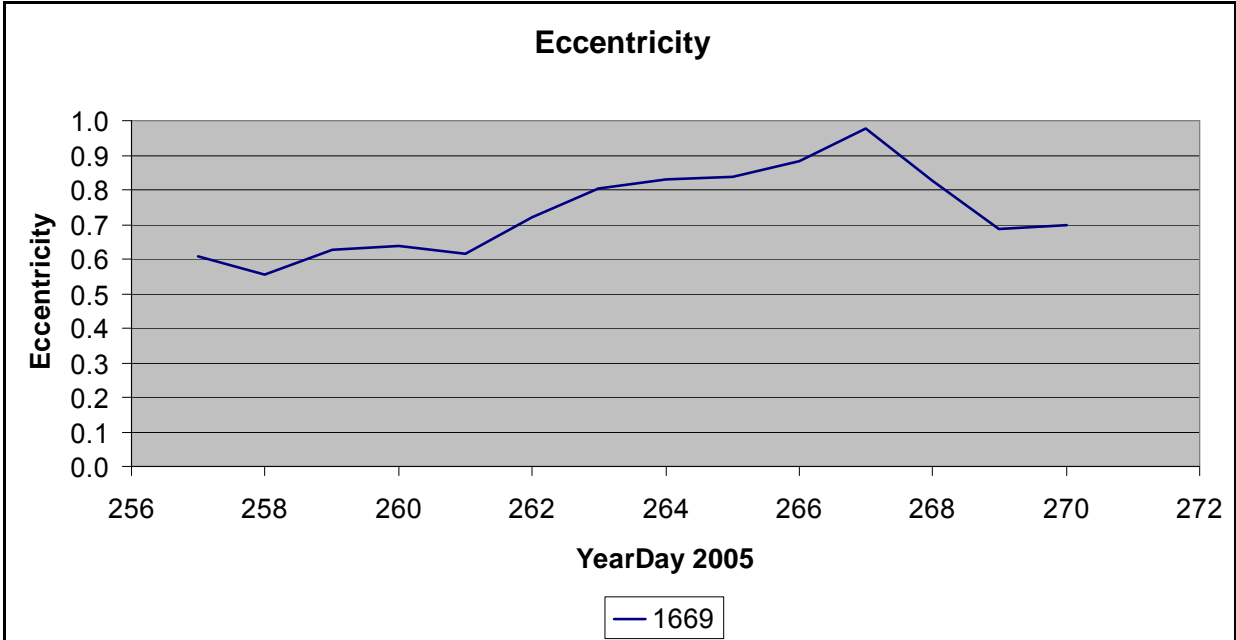


Figure E-44. Eccentricity of the Loop Current.

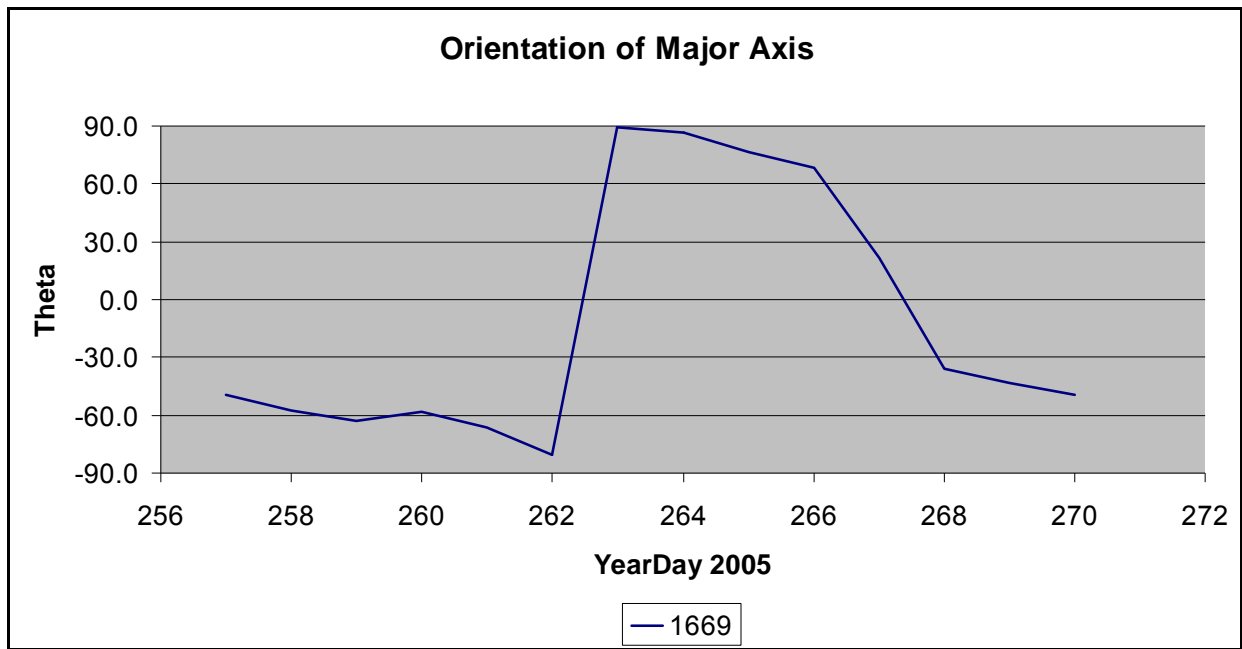


Figure E-45. Orientation of the major axis of the Loop Current.

APPENDIX F

Ocean Response to Hurricane Katrina in Presence of a Cyclone.

Report by Accurate Environmental Forecasting, Inc.

The following report was written by Accurate Environmental Forecasting, Inc. (AEF), and is enclosed as provided to Evans-Hamilton, Inc. This report was developed in support of the Climatology and Simulation of Eddies (CASE) Joint Industry Project (JIP). It was provided to the BOEMRE study team as part of an agreement in which AEF was provided measurement results from the present BOEMRE study, in return for AEF's analysis results and report to the JIP.

Ocean response to hurricane Katrina in presence of a cyclone
Ocean model validation study
Final report

Accurate Environmental Forecasting, Inc.

Narragansett, RI 02882

Tel: (401) 788-9031, Fax (401) 788-9034

www.accufore.com

August 25, 2007

Introduction

Presented in this report are the results of a validation study intended to assess the ability of the AEF version of the MIT GCM ocean model to simulate the ocean response to a hurricane in the presence of strong mesoscale features. The observational basis for the validation is provided by current measurements collected by a fixed instrument array during hurricane Katrina (2005). Preliminary data analysis indicates large spatial variability of the ocean response in the vicinity of the instrument array. A strong cyclonic mesoscale feature observed by the array just prior to the Katrina passage is presumed to be responsible for the observed variability.

Observations

The observational basis for this study is provided by the BOEMRE-funded ocean measurements program in the Eastern GOM. The measurements program covered the area located south of Mobile Bay in water depths ranging from 2000 to 2800 m (Figure F-1). Three tall (M1, M2, & M3) and one short (M4) moorings, along with seven PIES, were deployed from January 2006 to January 2007, with servicing of the moorings occurring in August 2006 just a few days prior to the arrival of hurricane Katrina. The tall moorings contained upward-looking 75 kHz ADCPs at 500 m depth, with single point current meters spaced at intervals from 750 m to near bottom. The tall moorings also contained combinations of temperature, or temperature-conductivity-pressure sensors at various depths. The short mooring contained two single point current meters near bottom.

The Eastern GOM array moorings have captured the ocean response to hurricane Katrina as it passed ~150 kilometers west of the array (Figure F-2). At the time of Katrina passage the mooring array was affected by a cold cyclonic eddy on the periphery of a Loop Current eddy. The approximate position of the cyclone is indicated by a surface drifter captured within its circulation (Figure F-2). Near-surface currents associated with the cyclone were on the order of 1.5 kts as indicated by the drifter speed and by ADCP measurements. As expected, the ocean response to Katrina primarily consisted of near-inertial oscillations. Preliminary analysis of near-inertial response was conducted by Forristall (2007) who applied a diurnal bandpass filter to the ADCP current time series. Results of this analysis at moorings 1 and 3 are shown in Figure F-3 and Figure F-4 respectively.

As expected, the oscillations have an upward phase propagation and downward energy propagation. The near-surface response at the Mooring 3 is about the same as at the Mooring 1, but at depth the oscillations are much stronger at Mooring 3 than at Mooring 1. Hurricane Katrina passed about the same distance from the two moorings, but they were in a different situation with respect to the cyclone shown in Figure F-2. Mooring 3 was in the middle of the cyclone and close to Loop Current Eddy Vortex. The enhanced inertial oscillations there are likely due to non-linear interaction between the cyclone and the hurricane. These measurements provide a good test case for validating the ability of three dimensional numerical models to adequately simulate non-linear ocean response to hurricanes in presence of background mesoscale ocean features.

Ocean Model

The ocean model is the Massachusetts Institute of Technology General Circulation Model (MIT GCM). The numerical formulation of the model is described in detail in Marshall et al. (1997); here we present a brief description. The model solves the incompressible Navier-Stokes equations using hydrostatic, quasi-hydrostatic, or non-hydrostatic approximations with rigid-lid or free-surface options. The equations are solved in a spherical geometry and with arbitrary complex coastlines, islands, and bathymetry using height as a vertical coordinate (z-coordinate system). For time integration the model uses a finite volume, predictor-corrector numerical procedure. The numerical scheme ensures that the evolving velocities are divergence free by solving the Poisson equation for the pressure with Neumann boundary conditions and then using this pressure to update the velocities. The pressure field is inverted using preconditioned conjugate-gradient methods. The equations are discretized using finite-volume methods with regular volumes based upon a uniform discretization of longitude, latitude, and depth. These volumes may take on irregular shapes and be “sculptured” to fit the boundary, improving the representation of both coastlines and topography. The model is also designed for parallel computation. Most of the parallelism is a so-called “fine-grained” data parallelism, available on the order of the total number of grid cells in the computational domain. In this approach the physical domain is partitioned by allocating equally sized vertical columns of the ocean to each processing unit. The model is well-tested; it has been employed to study numerous phenomena whose scales range from centimeters up to many thousands of kilometers (see Adcroft et al., 1997 and references therein).

For this study the model was configured for the Gulf of Mexico domain with uniform horizontal resolution of 4 km. The high horizontal resolution is necessary to adequately resolve a sharp baroclinic front associated with LC/LCEs. The uniformity of the numerical grid eliminates potential numerical artifacts associated with wave trapping in non-uniform grids. The model domain has open inflow/outflow boundaries in the Yucatan and Florida straights. The open boundary conditions allow a realistic simulation of the LC. The numerical grid has 50 vertical levels distributed uniformly with 10 m resolution in the upper 100 meters. The vertical resolution gradually transitions to a nearly uniform 15 meter resolution throughout most of the thermocline. Vertical resolution below the thermocline decreases gradually, reaching approximately 700 meters at the very bottom. Realistic bottom topography from ETOPO-2 1/30 degree resolution data base was prescribed throughout the entire domain except for regions shallower than 50 meters. Shallow regions are notorious for producing numerical instabilities under strong forcing conditions. Since this study is only concerned with deep ocean response, regions shallower than 50 meters were marked as land to simplify the model configuration and reduce the study cost.

Model Initialization

The model was initialized using the methodology described in Frolov et al. (2004). Similar methodology is used by the AEF-HMI eddy forecast system (Coholan et al., 2005) for operational forecasts of the GOM currents. In brief, the methodology utilizes a feature-oriented approach based on describing mesoscale ocean features with their Potential Vorticity (PV) field. This feature-oriented approach utilizes historical observations of the GOM features, i.e. the Loop Current (LC), Loop Current Eddies (LCEs), and cyclones, as well as our understanding of physical mechanisms controlling their evolution to reconstruct the initial 3-dimensional PV field on the basis of a few real-time observations. Using PV instead of density and/or velocity allows for clean separation between closely located features. The initial density and velocity are inferred from the constructed 3-d PV field by solving the system of intermediate equations. Since intermediate equations closely approximate the full set of primitive equations for the majority of slow-evolving solutions (Allen, 1997; McWilliams et al., 1986), the resulting initial density and velocity fields can be used to initialize a primitive equation model without any significant adjustments.

The fundamental assumption of this initialization methodology is that the PV structure of a mesoscale feature is conserved along the flow lines within that feature. In the case of the LC, its PV structure is expected to be conserved along the perimeter of the Loop. However, this assumption becomes invalid when the LC undergoes a process of merging with another anticyclonic feature, e.g. a warm-core eddy. During this process, the flow within the LC becomes disrupted and its PV structure undergoes a complex evolution while blending with the PV structure of the merging feature. In this situation a more accurate initialization approach is to use the primitive equations model itself to calculate the complex frontal structure resulting from the process of feature merging. With this approach, the primitive equations model is initialized prior to the merging event and is run forward to the target initialization date without any external forcing or data assimilation. The initial conditions prior to the merging event are adjusted iteratively to achieve a close agreement between the model and observations over the time period preceding the target initialization date.

Surface frontal analysis on August 20 shown in Figure F-5 indicates that the LC was undergoing the process of reconnecting with eddy Vortex (Figure F-6). The “connection” region is located just south of the Eastern Gulf Array and may have a significant impact on the ocean response to Katrina in its vicinity. Consequently, the alternative initialization approach (described above) had to be applied in order to realistically initialize frontal structure in the LC/Vortex connection region. The ocean model was initialized on August 18 when eddy Vortex was clearly separated from the LC enabling the application of the PV conservation assumption along the eddy front. After initialization on August 18 the model was allowed to evolve freely, i.e. without any external forcing or data assimilation. The simulated eddy-LC evolution was compared with observations, i.e. drifter trajectories and frontal positions; the initial conditions were adjusted iteratively to ensure a good agreement. The comparison between the model simulation and observations prior to the Katrina passage is shown in Figure F-7 through Figure F-10.

The cyclonic feature east of the eddy Vortex required special attention during the initialization since this feature is hypothesized to be primarily responsible for the spatial variability in the near-inertial response observed by the Eastern Gulf Array. Surface drifters captured within the feature indicate that it is not a frontal cyclone but rather an isolated cyclonic feature that is interacting with the LC. This conclusion is based on the fact that the location of the circulation center, as it is indicated by drifter trajectories, does not move any appreciable distance along the LC front over the time period since August 20 (compare Figure F-5 and Figure F-6). The cyclone was initialized using the Gaussian PV anomaly feature model previously developed by AEF for modeling isolated cyclones over the northern slope (Frolov et al., 2004). The position of the cyclone was derived from drifter trajectories and the Eastern Gulf Array current meter data. The latter was given a heavier weight in the analysis since the center of near-surface circulation derived from drifter trajectories can be significantly affected by the warm LC water being pulled into the cyclonic circulation. Parameters of the cyclonic feature model controlling its vertical structure were determined on the basis of the current observations from the Eastern Gulf Array. On the basis of these observations the core PV anomaly associated with the cyclone was placed at 200 meters, which is consistent with previous observations of isolated cyclones in the GOM (Hamilton et al., 2002).

Validation Results and Discussion

Simulated and observed currents at the mooring locations are shown in Figure F-11 through Figure F-13. Simulated currents are interpolated into the vertical coordinates moving with each mooring and truncated near the surface to make the comparison consistent. The comparison shows a very good agreement between the observed and simulated ocean response. The spatial variability in the near-inertial response observed and simulated in the vicinity of the cyclonic feature is consistent with the analytical work of Kunze (1985) and observational work of D'Asaro (1995). Near-inertial waves are being trapped and propagate downward in the zone of high horizontal shear within the cyclone. The southern mooring is located in the high shear zone within the cyclone, consequently, it experiences the strongest near-inertial response at depth. The northern mooring is located just outside of the cyclone, where the near-inertial response remains bound to the upper mixed layer with very little vertical propagation. The middle mooring is located within the cyclonic circulation but in the region of relatively low horizontal shear. The near-inertial response at this mooring penetrates below the mixed layer but at a slower rate relative to the southern mooring.

References

- Adcroft, A., C. Hill, and J. Marshall. 1997. Representation of topography by shaved cells in a height coordinate ocean model. *Mon. Weather Rev.* 125:2293-2315.
- Allen, J., J. Barth, and P. Newberger. 1990. On intermediate models for baroclinic continental shelf and slope flow fields. Part I: Formulation and comparison of exact solutions. *J. Phys. Oceanogr.* 25:2953-2958.
- Coholan, P.D., S.P. Anderson, and S.A. Frolov. 2005. Forecasting eddy Ulysses. *Proceedings of Dynamic Positioning Conference*. September 27-28, 2005.

- D'Asaro, E.A. 1995. Upper-ocean inertial currents forced by a strong storm. Part III: Interaction of inertial currents and mesoscale eddies. *J. Phys. Oceanogr.* 25:2953-2958.
- Forristall, G.Z. 2007. Industry Perspective on the Northeast Gulf of Mexico Current Measurements. Proc. Minerals Management Service, 24th Information Transfer Meeting. New Orleans. Jan 2007.
- Frolov, S.A., G.D. Rowe, L.M. Rothstein, and I. Ginis. 2004. Cross-shelf exchange processes and the deepwater circulation of the Gulf of Mexico: Dynamical effects of submarine canyons and the interactions of Loop Current Eddies with topography: Final Report. U.S. Dept. of the Interior, Minerals Management Service, Gulf of Mexico OCS Region, New Orleans, LA. 164 pp.
- Hamilton, P., T.J. Berger, and W. Johnson. 2002. On the structure and motions of cyclones in the northern Gulf of Mexico. *J. Geophys. Res.* 107(C12):3208-3219.
- Kunze, E. 1985. Near-inertial wave propagation in geostrophic shear. *J. Phys. Oceanogr.* 15:544-565.
- Marshall, J., A. Adcroft, C. Hill, L. Perelman, and C. Heisey. 1997. A finite-volume, incompressible Navier-Stokes model for studies of the ocean on parallel computers. *J. Geophys. Res.* 102(C3):5733-5752.
- McWilliams, J.C., P.R. Gent, and N.J. Norton. 1986. The evolution of balanced, low-mode vortices on the beta-plane. *J. Phys. Oceanogr.* 16:838-855.

MMS Study Area Cruise 2 Moorings and PIES

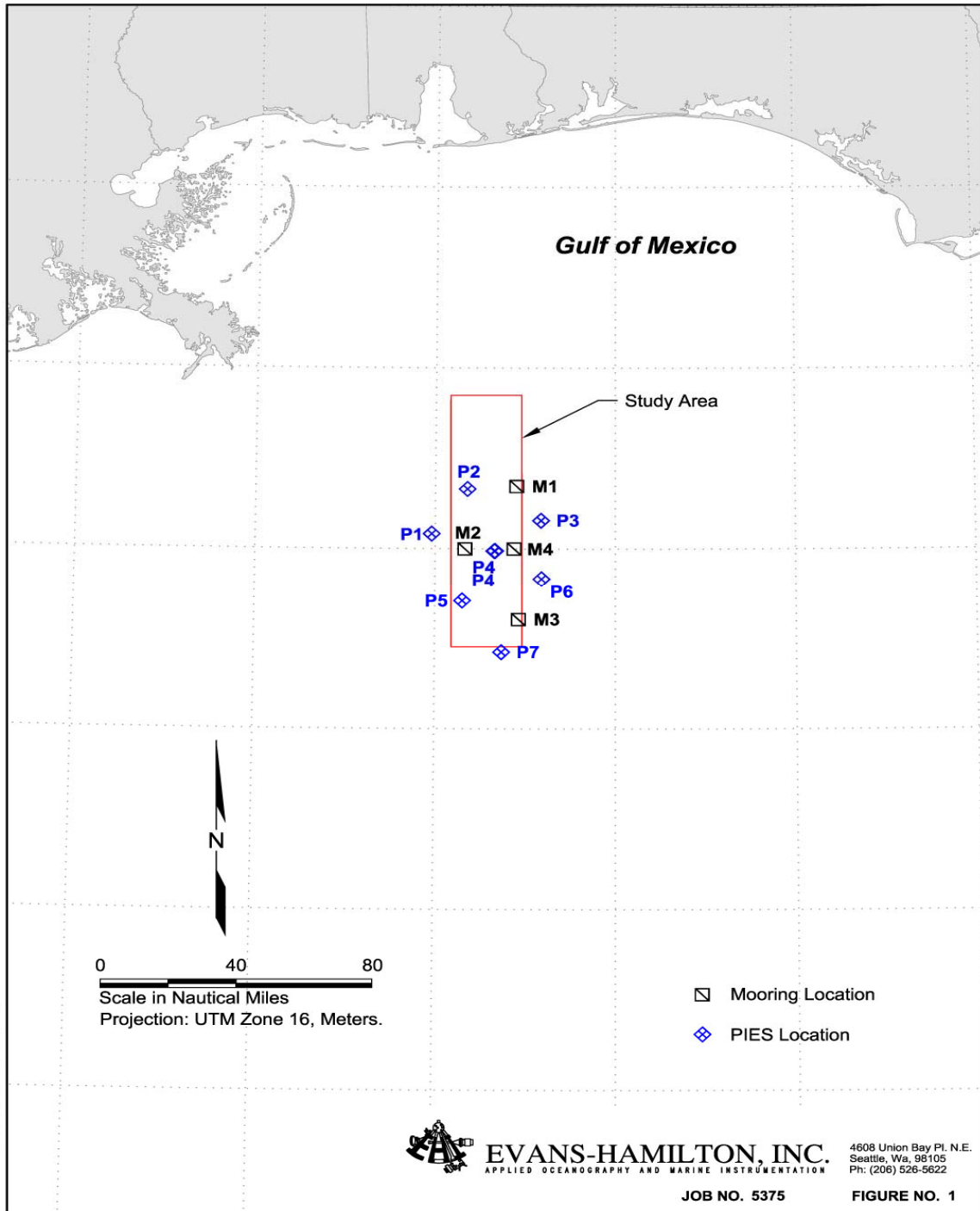


Figure F-1. Mooring map for the Eastern GOM observational program. (Image is taken from the ITM report by Evans Hamilton Inc., courtesy of Jeff Cox).

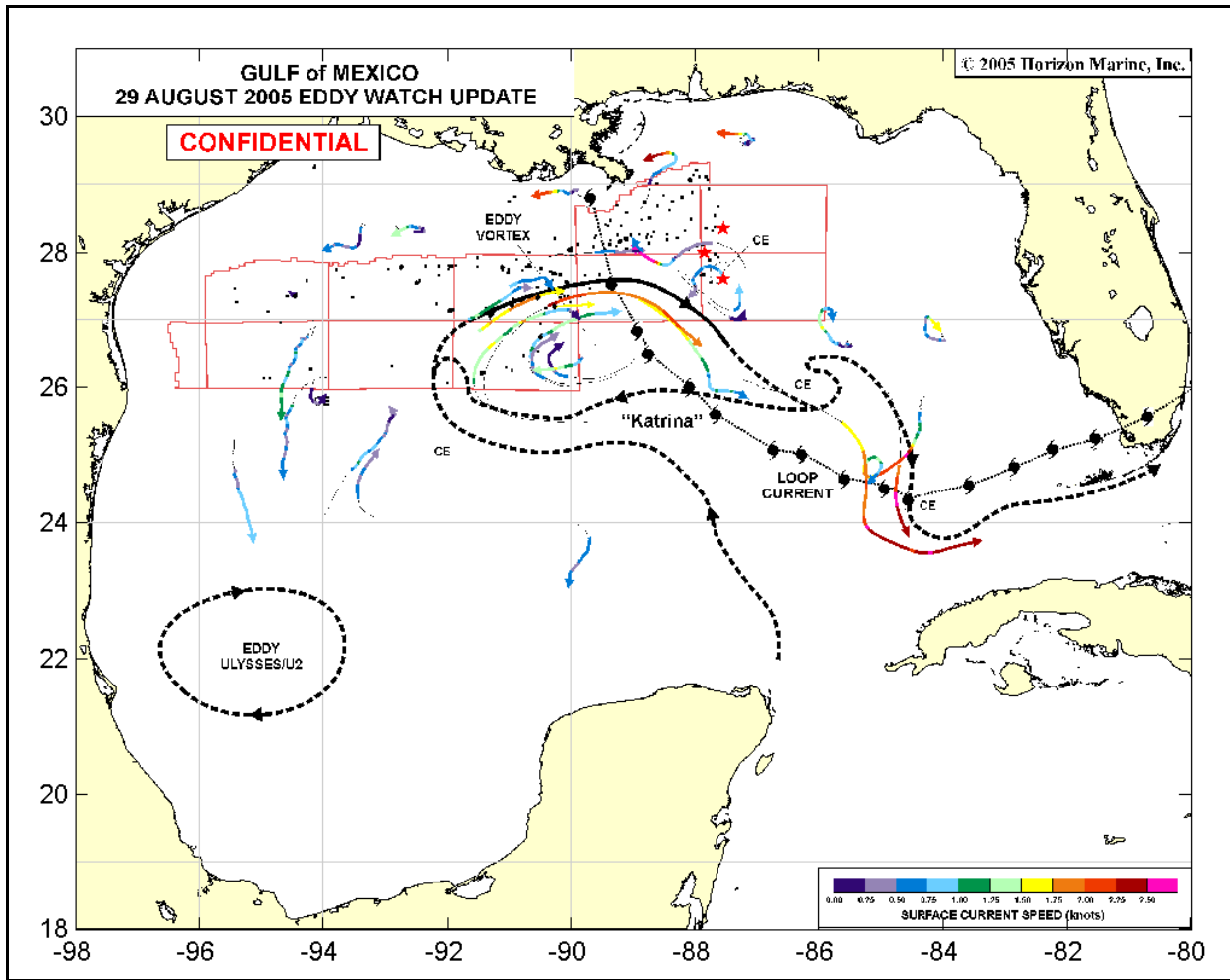


Figure F-2. Locations of tall moorings M1-M3 (shown with red stars) overlaid on the real-time analysis of surface fronts for August 29, 2005 (provided by Horizon Marine Inc.)

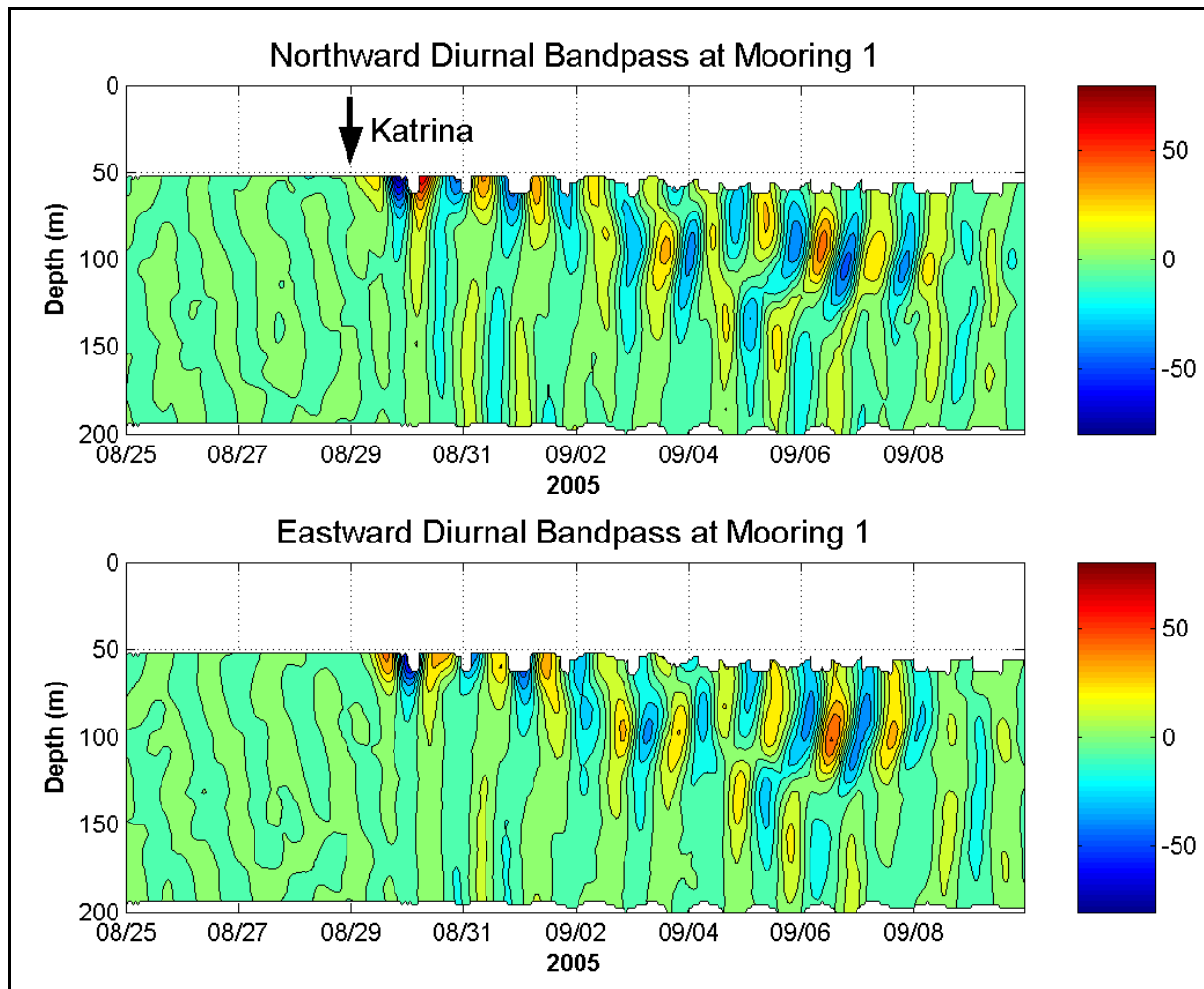


Figure F-3. Near-inertial response to hurricane Katrina at Mooring 1 (Forristall, 2007).

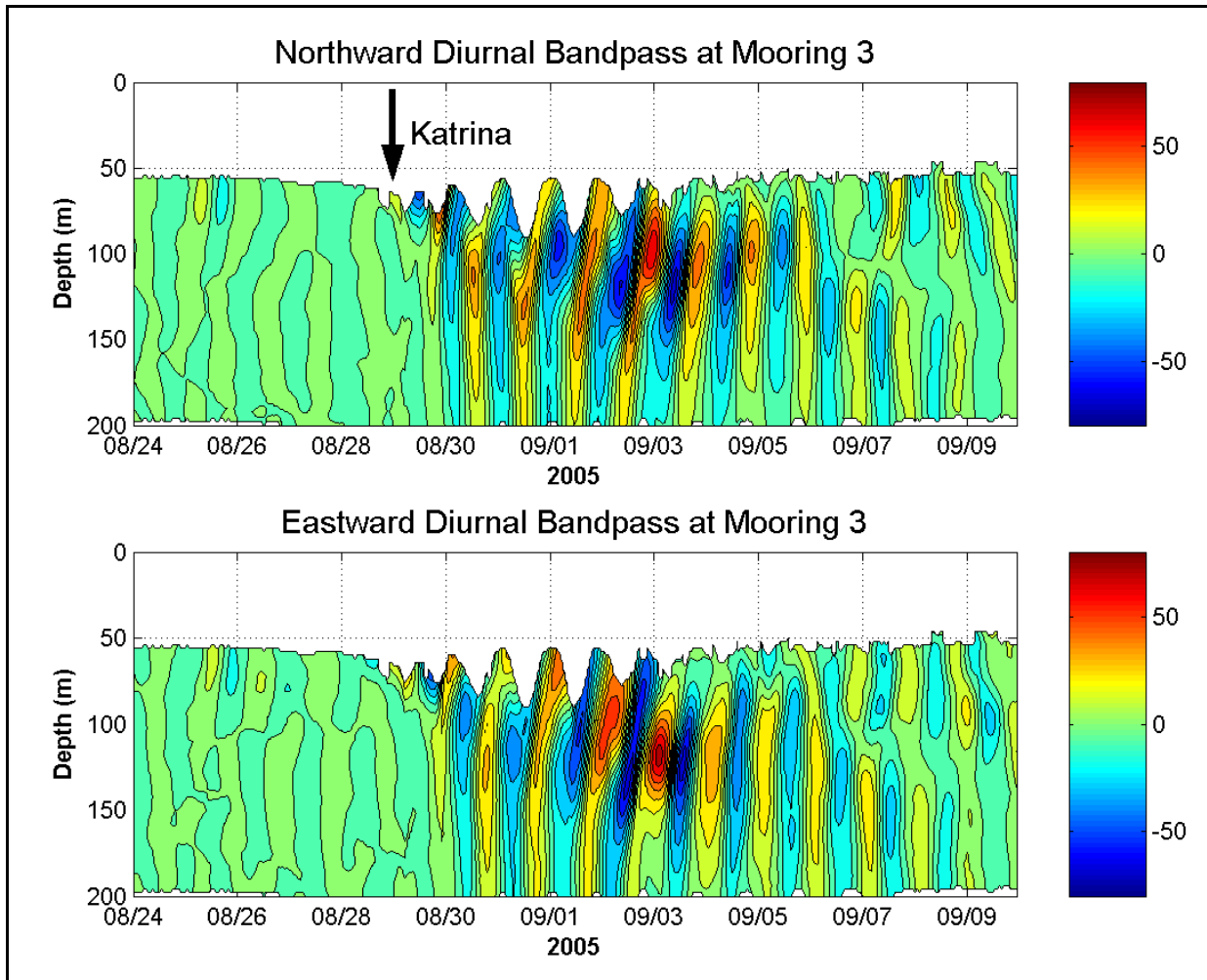


Figure F-4. Near-inertial response to hurricane Katrina at Mooring 3 (Forristall, 2007).

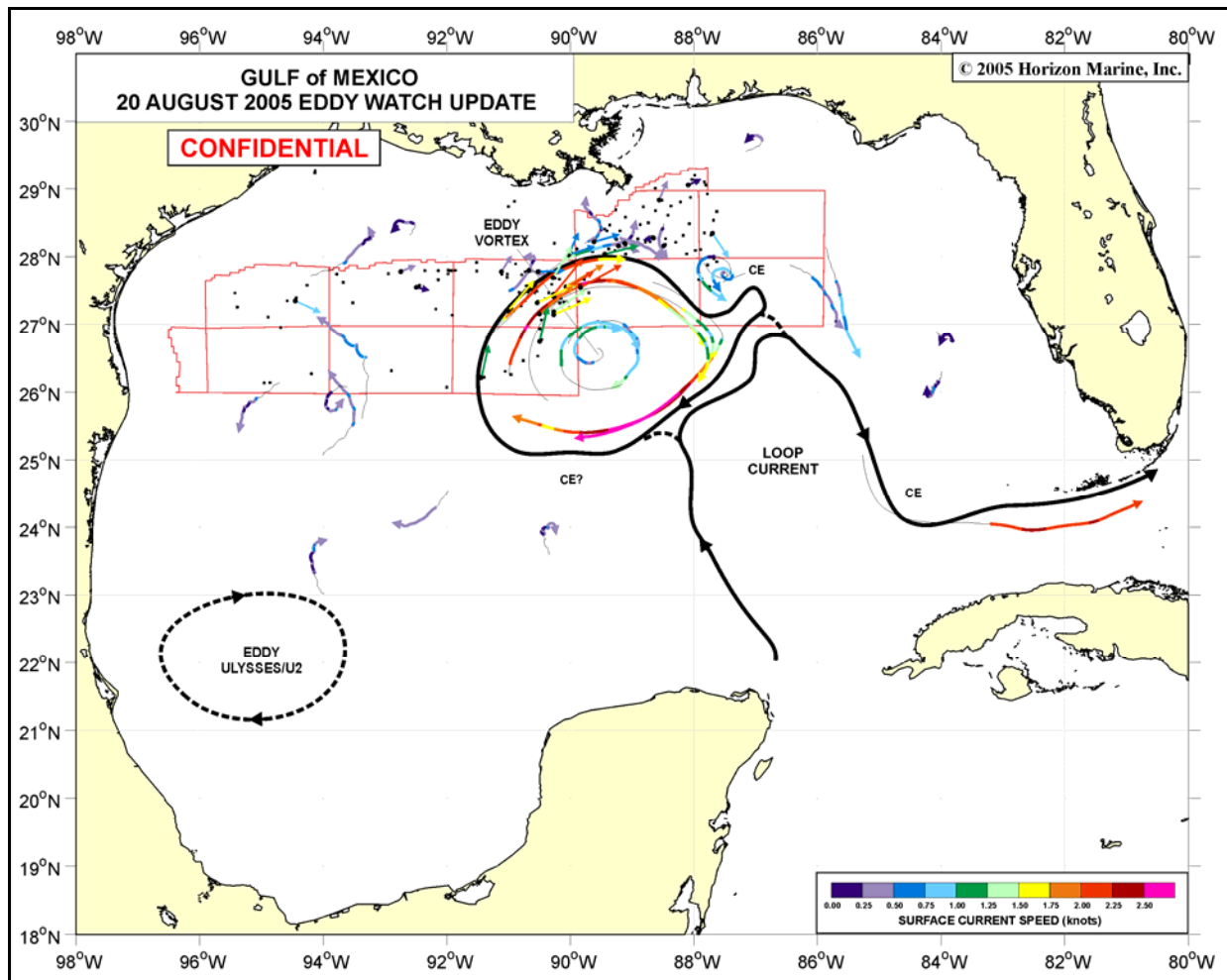


Figure F-5. Surface frontal analysis provided by Horizon Marine Inc. for August 20, 2005. Thick black lines indicate surface front positions. Colored lines indicate drifting buoy trajectories; color indicates the buoy speed, i.e. local current speed. All drifting buoys are drogued at 50 meters depth.

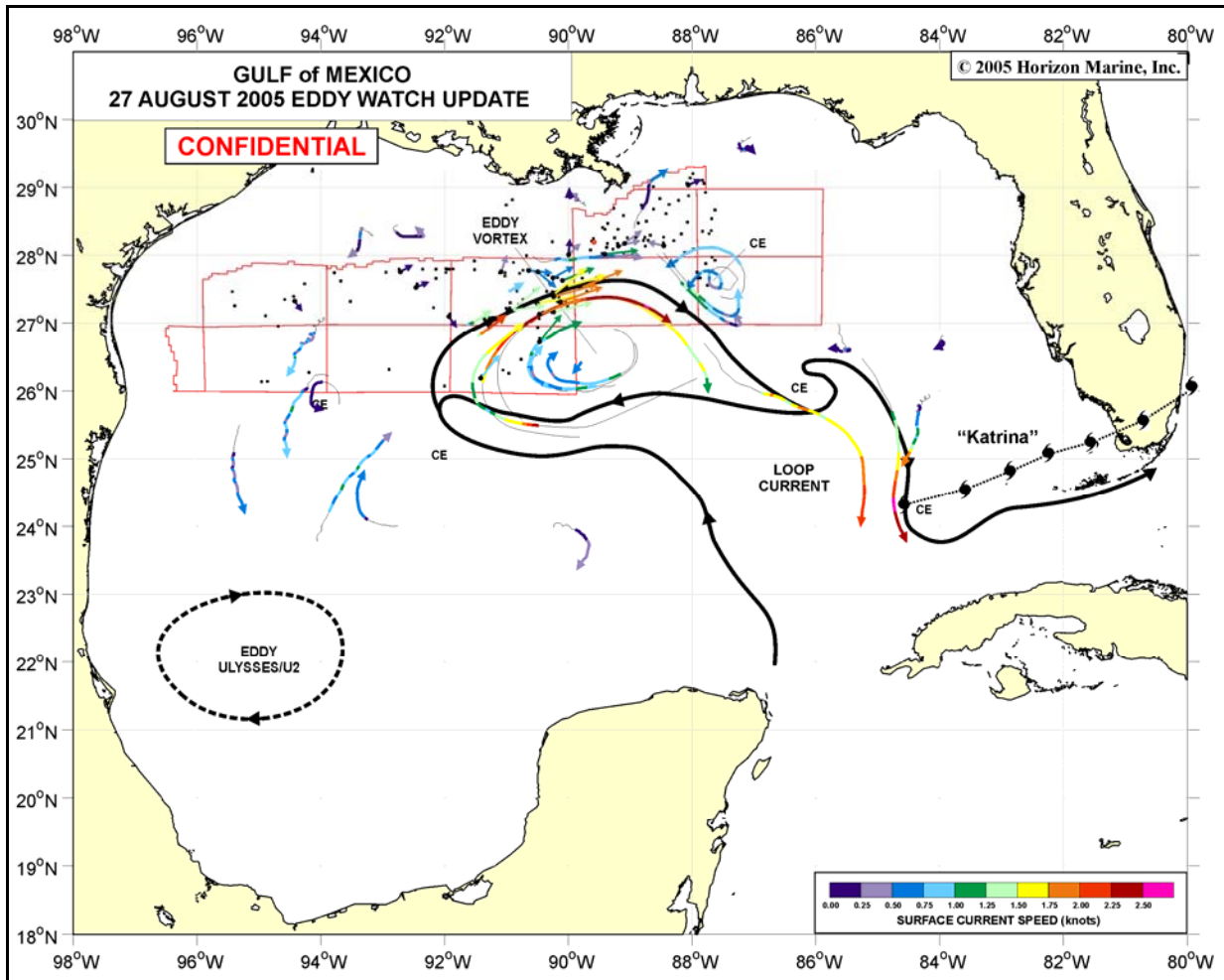


Figure F-6. Surface frontal analysis provided by Horizon Marine Inc. for August 27, 2005. Thick black lines indicate surface front positions. Colored lines indicate drifting buoy trajectories; color indicates the buoy speed, i.e. local current speed. All drifting buoys are drogued at 50 meters depth.

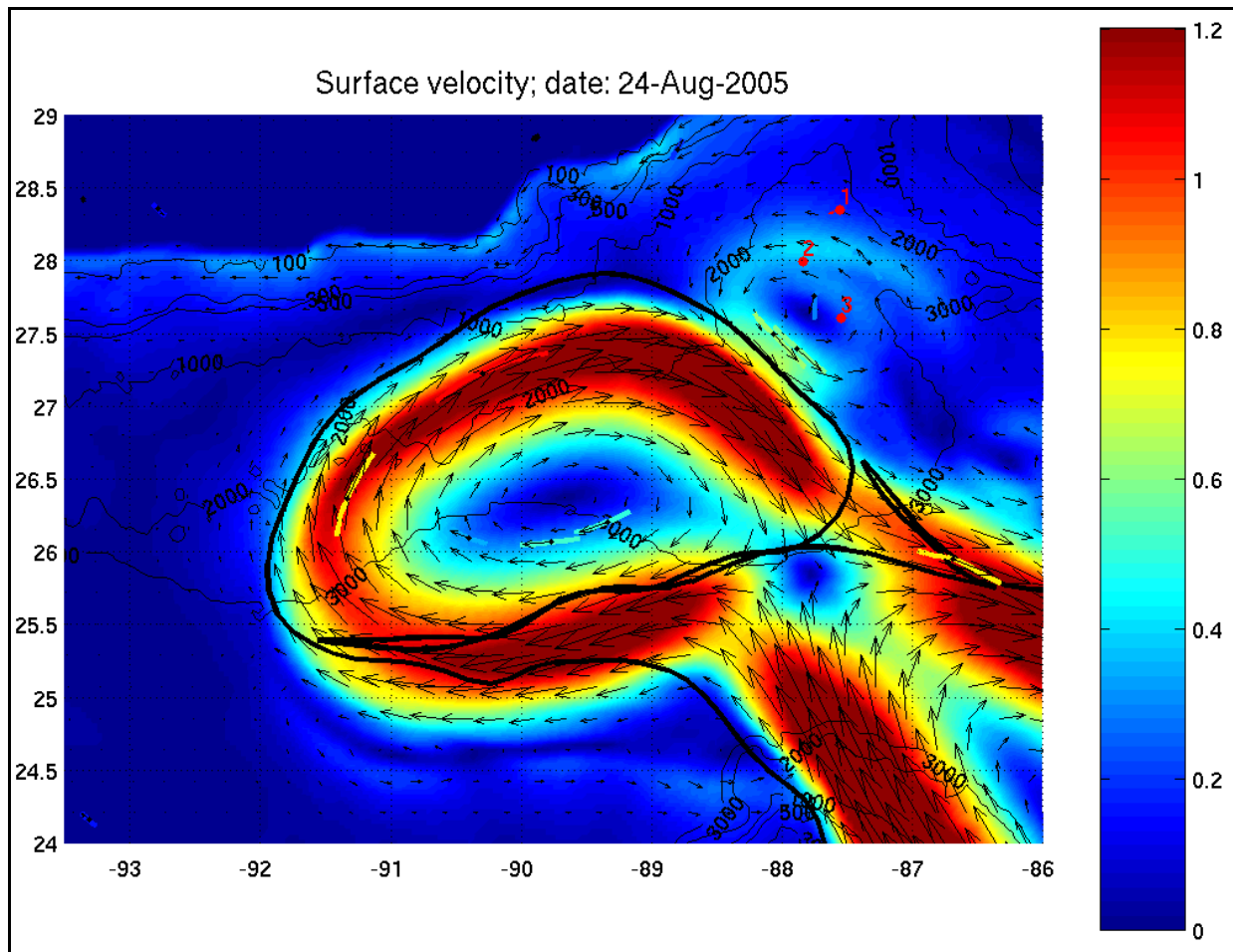


Figure F-7. Surface currents simulated during the “spinup” initialization on August 24, 2005. Thick black lines indicate surface front positions as they are digitized from the Horizon Marine charts. Drifter trajectories are shown with colored lines. The line color represents the average drifter speed over the shown portion of the trajectory (24 hours) with the color scale consistent with the rest of the figure. Mean drifter position and velocity are shown with black dots and arrows. The Eastern Gulf Array moorings are shown with red dots. The upper level current velocity measured at each mooring is shown with a red arrow. All arrow scales are consistent throughout the figure.

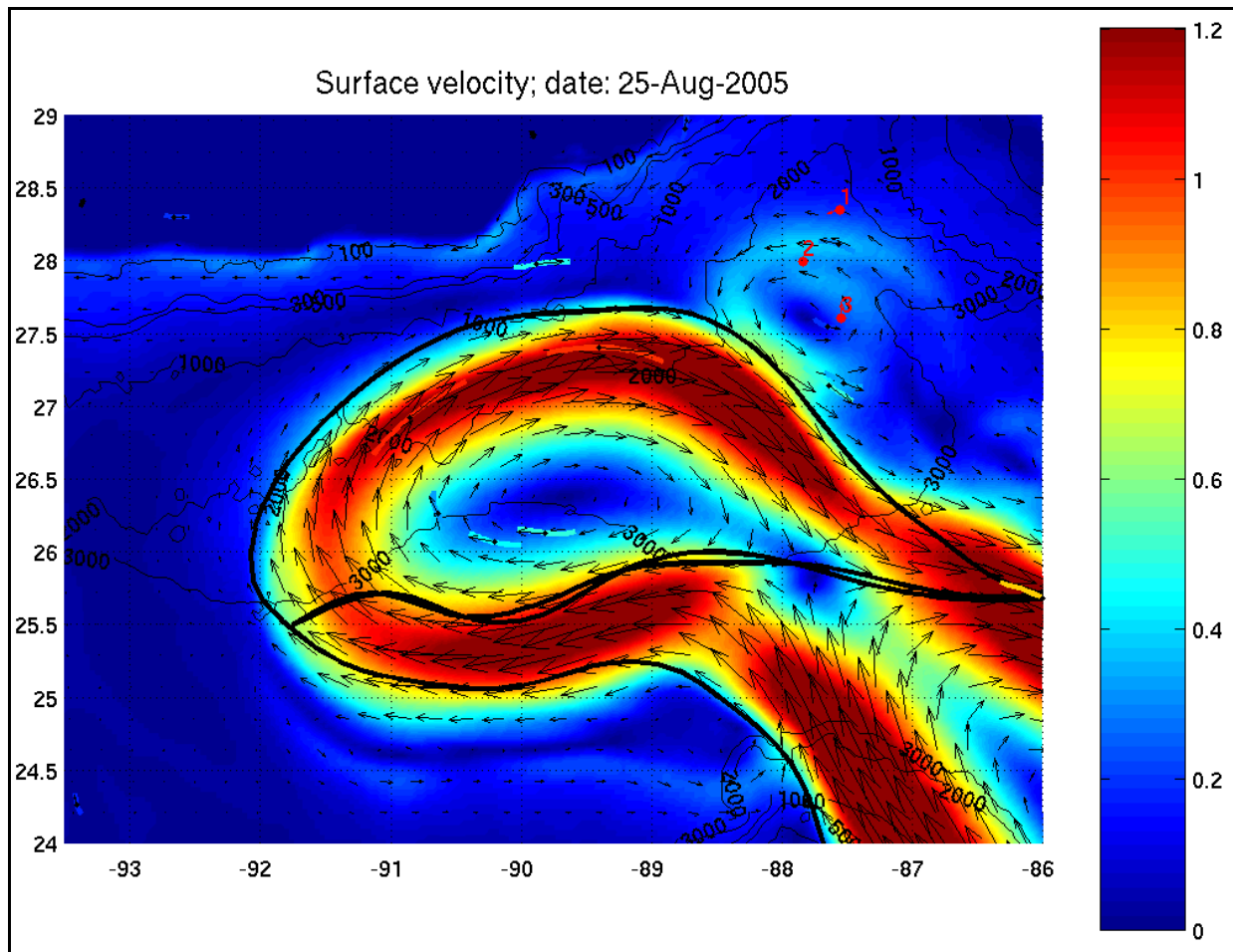


Figure F-8. Surface currents simulated during the “spinup” initialization on August 25, 2005. Thick black lines indicate surface front positions as they are digitized from the Horizon Marine charts. Drifter trajectories are shown with colored lines. The line color represents the average drifter speed over the shown portion of the trajectory (24 hours) with the color scale consistent with the rest of the figure. Mean drifter position and velocity are shown with black dots and arrows. The Eastern Gulf Array moorings are shown with red dots. The upper level current velocity measured at each mooring is shown with a red arrow. All arrow scales are consistent throughout the figure.

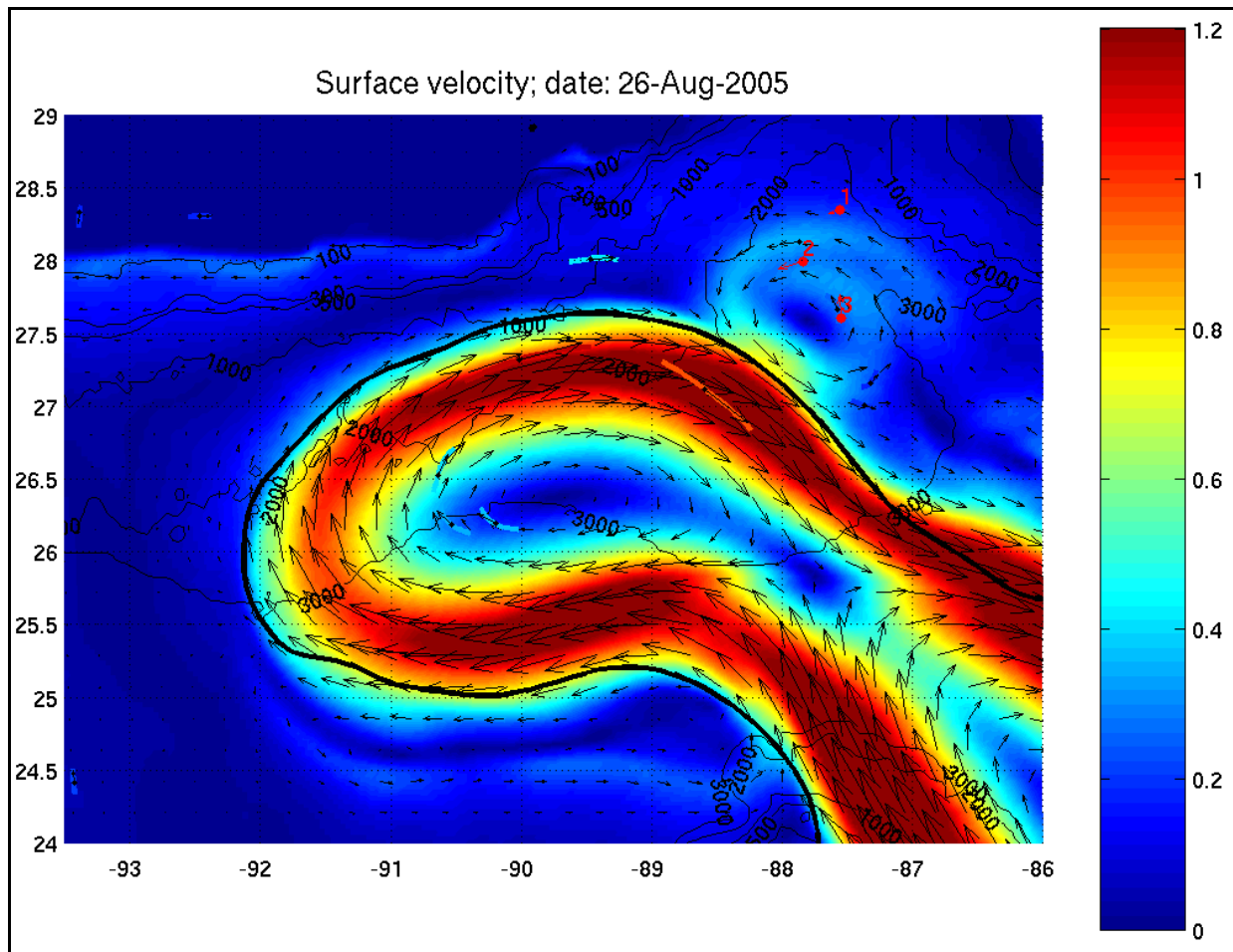


Figure F-9. Surface currents simulated during the “spinup” initialization on August 26, 2005. Thick black lines indicate surface front positions as they are digitized from the Horizon Marine charts. Drifter trajectories are shown with colored lines. The line color represents the average drifter speed over the shown portion of the trajectory (24 hours) with the color scale consistent with the rest of the figure. Mean drifter position and velocity are shown with black dots and arrows. The Eastern Gulf Array moorings are shown with red dots. The upper level current velocity measured at each mooring is shown with a red arrow. All arrow scales are consistent throughout the figure.

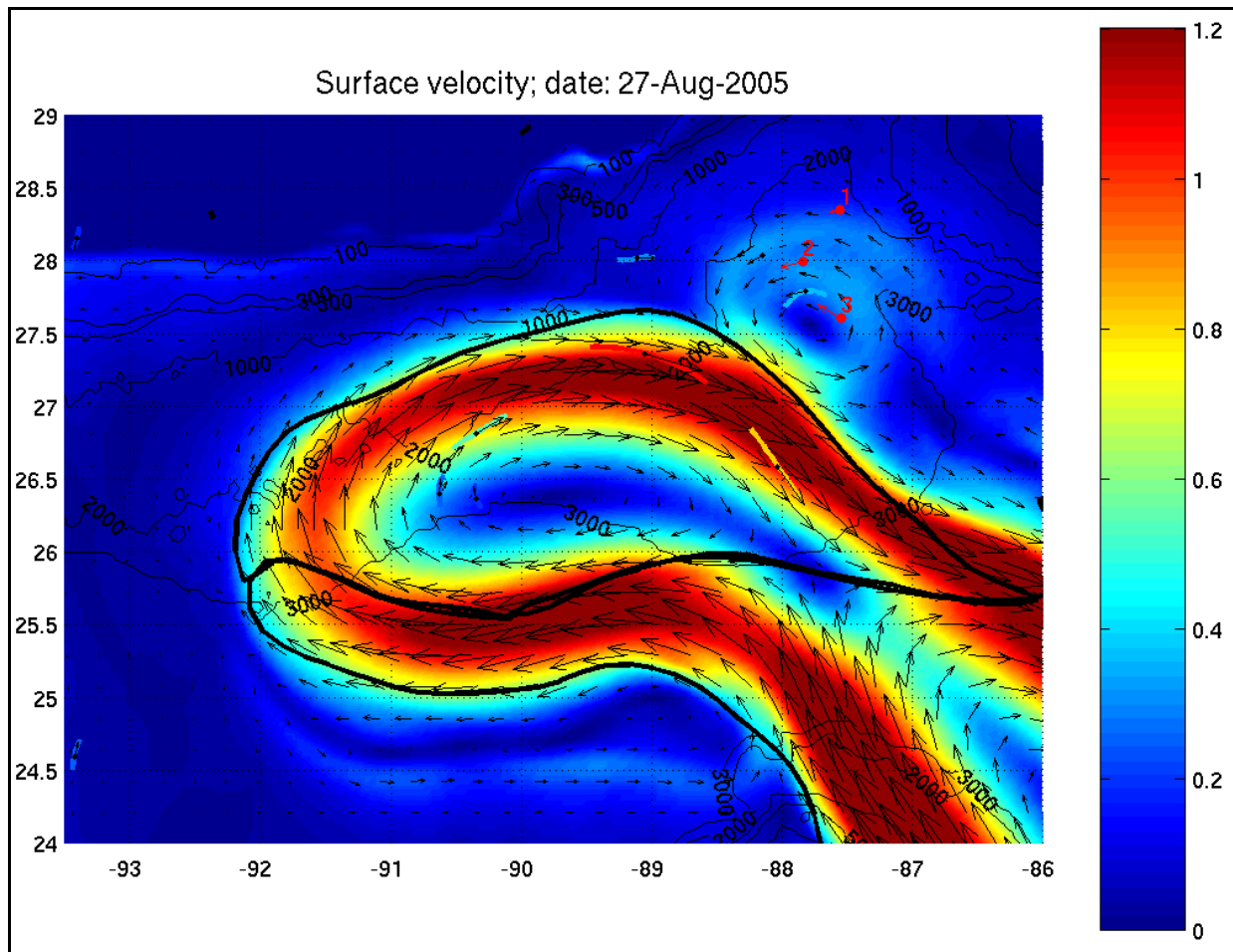


Figure F-10. Surface currents simulated during the “spinup” initialization on August 27, 2005. Thick black lines indicate surface front positions as they are digitized from the Horizon Marine charts. Drifter trajectories are shown with colored lines. The line color represents the average drifter speed over the shown portion of the trajectory (24 hours) with the color scale consistent with the rest of the figure. Mean drifter position and velocity are shown with black dots and arrows. The Eastern Gulf Array moorings are shown with red dots. The upper level current velocity measured at each mooring is shown with a red arrow. All arrow scales are consistent throughout the figure.

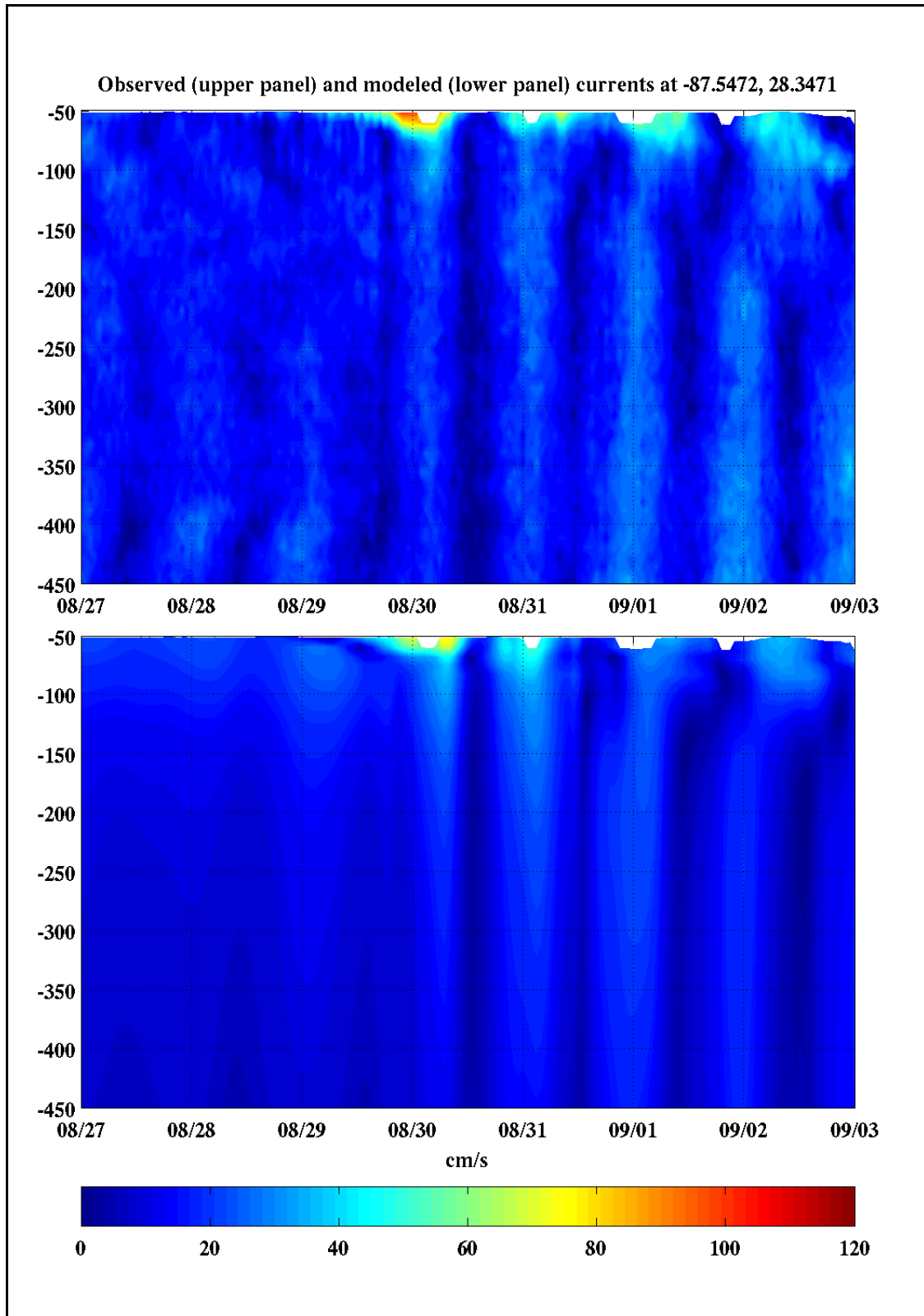


Figure F-11. Observed (upper panel) and simulated (lower panel) current speed at the northern mooring.

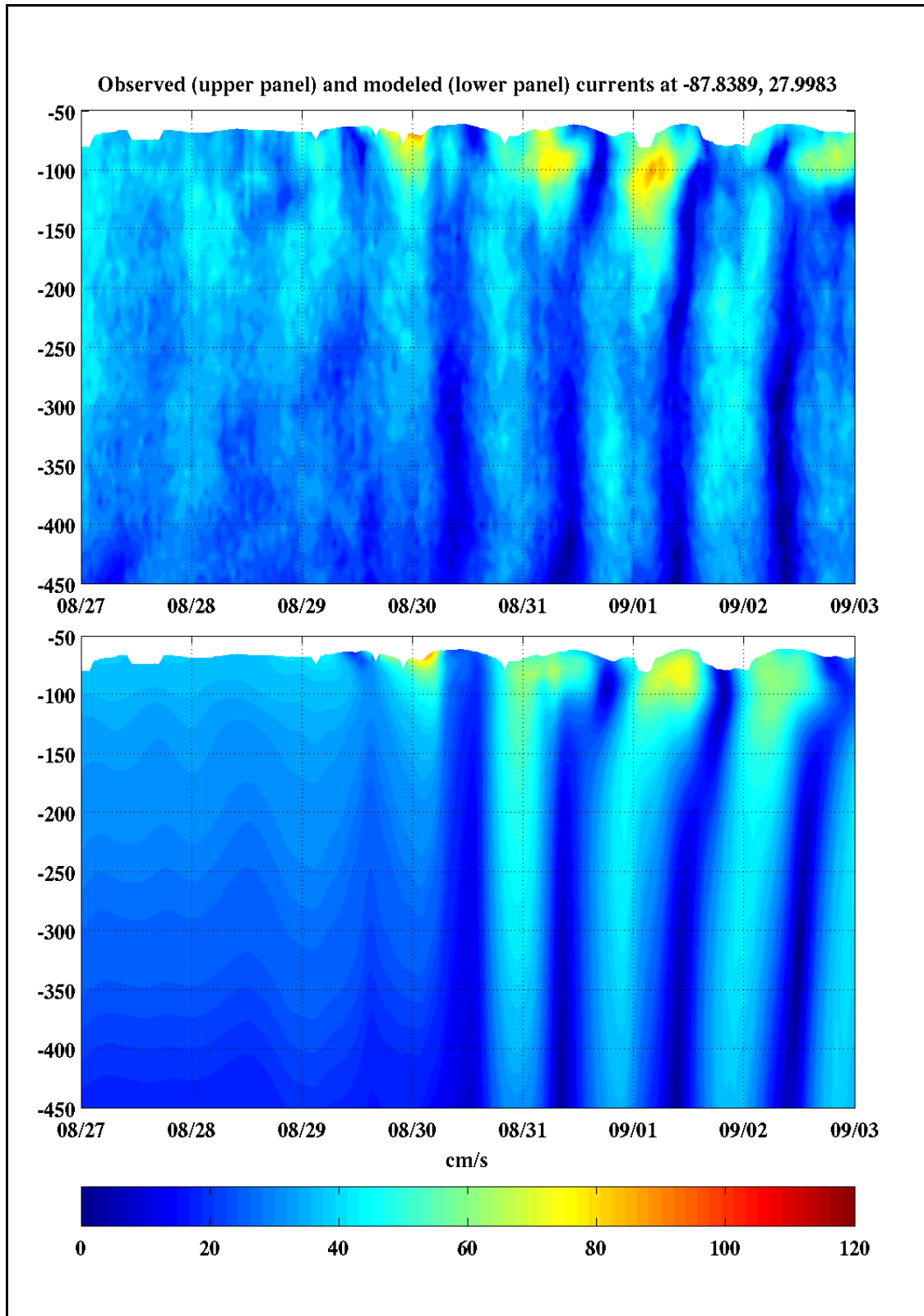


Figure F-12. Observed (upper panel) and simulated (lower panel) current speed at the middle mooring.

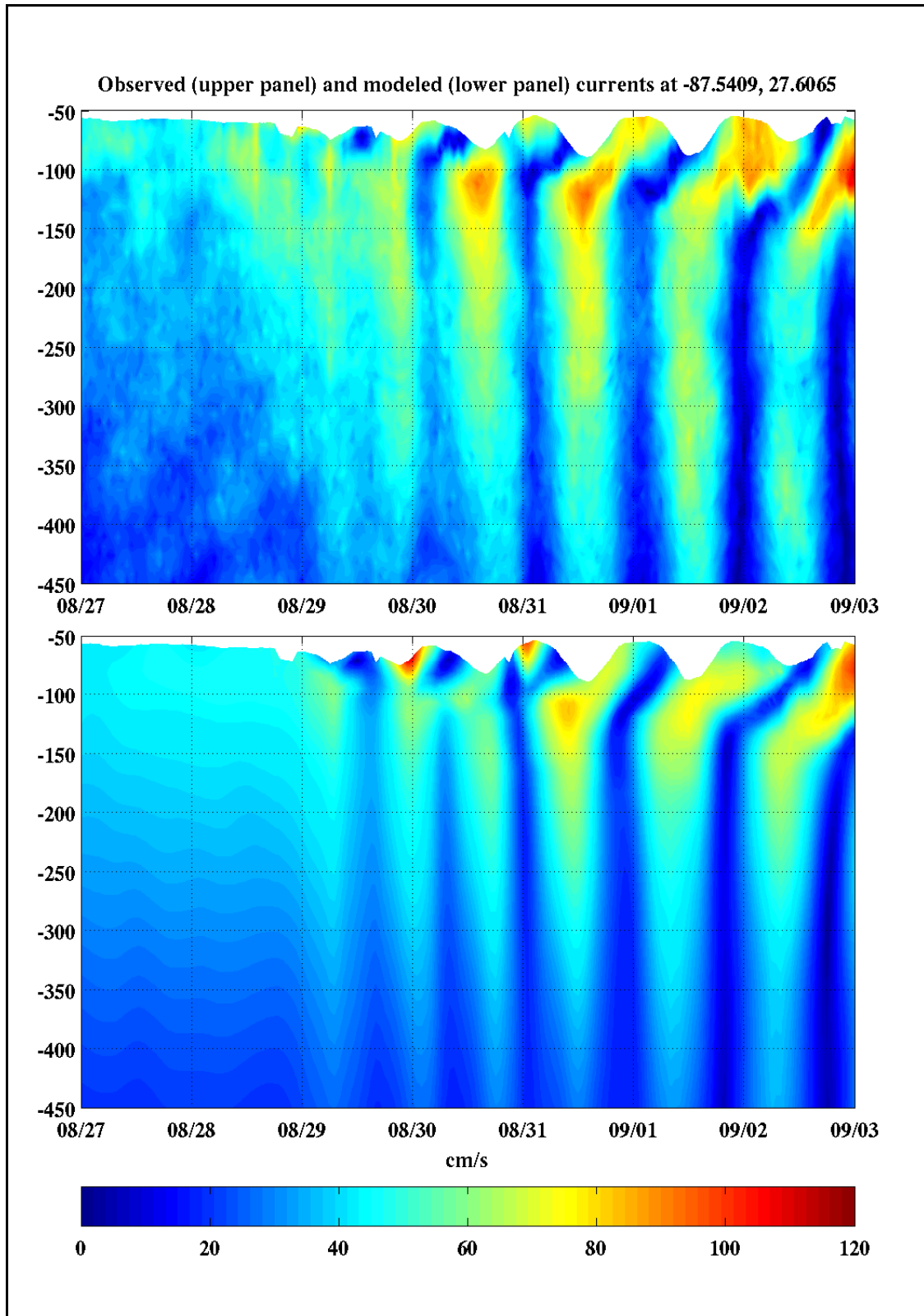


Figure F-13. Observed (upper panel) and simulated (lower panel) current speed at the southern mooring.